University of Stuttgart
Germany

Matthias
Rambausek

Magneto-electro-elasticity of soft bodies across scales

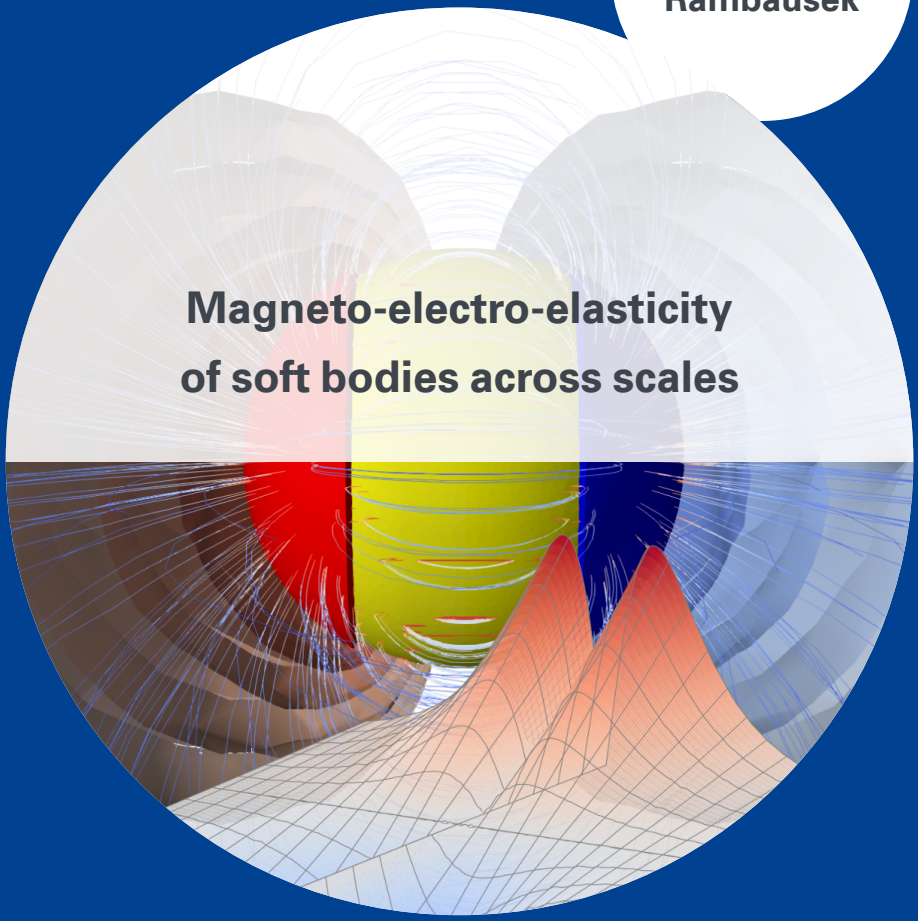

4

Publication series of the
Institute of Applied Mechanics (IAM)

Magneto-electro-elasticity of soft bodies across scales

Von der Fakultät Bau- und Umweltingenieurwissenschaften der Universität Stuttgart und dem Stuttgart Research Centre for Simulation Technology zur Erlangung der Würde eines Doktor-Ingenieurs (Dr.-Ing.) genehmigte Abhandlung

Vorgelegt von

Matthias Rambausek

aus Sankt Pölten

Hauptberichter:	Prof. Dr.-Ing. Marc-André Keip
Mitberichter:	Prof. Dr. Konstantinos Danas

Tag der mündlichen Prüfung: 14. Februar 2020

Institut für Mechanik (Bauwesen) der Universität Stuttgart

2020

Publication series of the Institute of Applied Mechanics (IAM), Volume 4
Institute of Applied Mechanics University of Stuttgart, Germany, 2020

© Matthias Rambausek
Institute of Applied Mechanics (Civil Engineering)
Chair of Materials Theory
University of Stuttgart
Pfaffenwaldring 7
70569 Stuttgart, Germany

ISBN 978 – 3 – 937399 – 52 – 2
(D 93 – Dissertation, Universität Stuttgart)

Danksagung/Acknowledgments
Die vorliegende Arbeit ist das Ergebnis meiner vierjährigen Tätigkeit am Institut für Mechanik im Bauwesen an der Universität Stuttgart unter Anleitung meines Doktorvaters Marc-André Keip, der mich Anfang 2015 unter seine Fittiche genommen hat und mich bis heute geduldig unterstützt und mit größtem Vertrauen fördert. Die Fertigstellung meiner Dissertation ist ein guter Zeitpunkt um zurück zu blicken und mir einige für meinen (nicht nur) beruflichen Werdegang wichtige Stationen, Ereignisse und Personen in Erinnerung zu rufen und "Danke!" zu sagen. Ich beginne im Jahr 2020 und wechsle kurz in die englische Sprache.

I want to thank my friends and colleagues at the LMS at the École Polytechnique, in particular Filippo Agnelli, Jérémie Chichignoud, Marco Moscatelli, Sofia Sakout, Nicole Tueni, Janis Waza and Othmane Zerhouni for all their support and company. Special thanks goes to my good friend, colleague and flatmate Nikolai Khailov. On the professional side, I want to thank Konstantinos Danas, who hosted me for a large portion of the time in which I actually wrote down this thesis, for the inspiring and fruitful discussions and his support over the last year. Moreover, I thank Dipayan Mukherjee for the excellent collaboration in parts of my current research and the whole LMS for welcoming me in the most friendly and supportive way. I could not have chosen a better place for my first Post-Doc period.

Nun zu meiner Zeit in Stuttgart: Großer Dank gebührt hier neben meinem Doktorvater auch meinen ehemaligen Kollegen Lukas Böger, Felix Göküzüm, Daniel Kienle, Steffen Mauthe, Khiem Nguyen, Elten Polukhov, Ashish Sridhar und insbesondere meinem Büro-Nachbarn Omkar Nadgir sowie der "Familia Meccanica" – Lukas Eurich, Aref Nateghi, Stefan Teichtmeister (bei dem ich mich nicht genug bedanken kann) und Daniel Vallicotti, die mir innerhalb sowie auch außerhalb der Arbeitszeiten stets eine gute Gesellschaft waren.

Dass ich überhaupt in Stuttgart landete, habe ich unter anderem Christian Celigoj, Katrin Ellermann und Stefan Hollerer zu verdanken. Christian Celigoj war auch jener Professor, der mich für die höhere Mechanik begeisterte und mir bis heute wichtiges Handwerkszeug vermittelte. Eine weitere überaus prägende Person am Institut für Festigkeitslehre war Michael Hammer, der mir die Grundlagen der Methode der finiten Elemente, insbesondere deren Implementierung, beibrachte und meine Diplomarbeit betreute. Daneben möchte ich auch Manfred Ulz erwähnen, durch den ich zum ersten Mal mit den Untiefen der Tensorrechnung in Kontakt kam.

Natürlich wäre ich nie so weit gekommen ohne meine Eltern Gudrun und Roland, die mich stets unterstützt und immer an mich geglaubt haben – auch wenn sie nicht immer verstanden habe, was ich eigentlich gerade so mache. Großer Dank gilt auch meiner Schwester Maria und meinen Großeltern Hilde und Herbert, die mir von meinen frühen Tagen an bis heute zur Seite stehen. Zu guter Letzt möchte ich mich bei Eva-Maria bedanken, die mich durch die Endphase meiner Promotion aus der Ferne begleitet hat.

Stuttgart und Palaiseau, im Februar 2020 Matthias Rambausek

Contents

Abstract

This thesis is concerned with continuum magneto-electro-elasticity in a quasi-static setting at large deformations. In other words, it is concerned with the description of the mechanical, electric and magnetic response of bodies under mechanical forces, electric field and magnetic field. The interesting part thereby is that magnetic fields cause deformation or changes in the electric polarization of a body, i.e. coupling phenomena. The overall topic, but also the sub-fields electro-elasticity and magneto-elasticity are actively researched in experiment, theory and simulation. In a more general context, applications range from micro-electronic devices such as computer memory, to sensors and actuators over display technology to artificial muscles.

The first project embraced by this thesis was the modeling of magnetorheological elastomers (MREs) – a type of composite that combines soft rubber with magnetic particles – across scales. In that course a number of experimentally observed effects, i.e. change of stiffness under magnetic field (Jolly et al., 1996) and deformation with response to magnetic field (Böse et al., 2012) in dependence of microscopic features of the composite (Danas et al., 2012) have been confirmed. Moreover, the conducted two-scale simulations shed light on what is called "shape effect": for instance, the influence of a specimen's shape on its the deformation response to magnetic fields. Somewhat counter-intuitively, bodies with given magnetization deform differently for different initial shapes even without mechanical forces being applied. This is not only an interesting phenomenon but a huge challenge for the experimental determination of *material properties* (Martin et al., 2006; Diguet et al., 2010; Bodelot et al., 2018) which are supposed to be local properties independent of specimen shape. One outcome of this thesis are suggestions on the design of experiments and insight on how to estimate the non-local effect of shape dependence from measurements.

Since MREs consist of an elastomer with dielectric properties and inclusions which can be regarded as either dielectric or conducting, it is a natural extension to also include electrostatics. The hope was to observe pronounced magneto-electric coupling, which as opposed to electro-magnetic coupling also exists in quasi-static settings. The most apparent application is the construction of magnetic field sensors (Martin et al., 2003). Interestingly, a phenomenon called magnetoreception – the ability of biological organisms to use (the earth's) magnetic field for orientation and navigation – is suspected to be rooted in a similar setting (Liu and Sharma, 2013). As reported in the thesis, the above mentioned shape effects play a big role in magneto-electric (ME) coupling. In fact, even materials without classical ME coupling coefficients can be employed for ME *devices*. This has been demonstrated for ellipsoidal bodies by analytical means as well as by finite element simulations. Another setting investigated are capacitor-like devices where

the dielectric medium that resides between the electrodes also features magnetic properties, e.g. a MRE between electrodes. Of course, also for such devices significant ME coupling can be observed. However, there are challenges in the numerical simulations: The geometry of the electrodes locally leads to extreme field concentrations which are difficult to capture by finite elements. Even worse, the unavoidable discretization errors yield electro-mechanical artifacts that potentially affect the accuracy and also the robustness of simulations. One such artifact are "spurious" deformations due to electric or magnetic fields in media which do not feature respective coupling properties. The present thesis does not provide a cure for these issues but at least some benchmark problems which hopefully prove useful for the deeper analysis and eventual resolution of this effect. One attempt to remove or at least reduce the spurious coupling was to go from commonly preferred scalar-potential formulations for electro- and magnetostatics to vector-potential and mixed formulations. Both of them can in fact be regarded as instances of linearly constrained minimization principles which distinguishes them from pure scalar potential formulations. As reported, these alternative formulations indeed seem to increase robustness but fail to provide a true solution. Another outcome of the investigations of alternative finite elements formulations for magneto-electro-elasticity was the observation that mixed formulations are potentially superior over vector potential-based formulations in terms of computation time and memory requirements while their solutions belong to closely related or even equivalent discrete function spaces. The reported observations are based on the use of direct linear solvers for the coupled system of equations. The extension of these studies to the case of iterative linear solvers requires efficient preconditioners of which the construction is not trivial and for now remains a future task.

The constrained minimization principles leading to mixed formulations for magneto-electro-elasticity also gave rise to another development. The linear constraints in that formulation are linear partial differential equations in space. Their finite element discretization leads to sparse matrices showing up in the off-diagonal blocks of the Karush-Kuhn-Tucker (KKT) matrix of the magneto-electric-elastic saddle point problem. But all they do is removing the divergence from a vector field. It was recognized that this operation, the projection of a general vector field to the space of divergence free vector fields is a mode-wise local operation in Fourier space and thus much cheaper than in finite elements. The result is the Fourier-based solver for magneto-mechanical problems at microscopic scales for the computation of effective material responses for the case of vanishing free currents. The latter restriction is, however, not an issue in the microscale modeling of MREs, which can be modeled an insulators. A particular appeal of the Fourier-type solver developed is the projection-based approach which has solid mathematical foundations, most importantly the Helmholtz decomposition theorem. Thanks to its structure the method can be directly extended to magneto-electro-elasticity in absence of free charges. A possible question for future investigations is how to also account for free current and charge densities.

Besides the studies above the thesis also revisits the theoretical foundations magneto-electro-mechanics. Accompanying the application-oriented work, the theoretical part is

quite extensive with the intention to provide a solid basis for future research beyond the quasi-static regime and beyond bulk materials in Euclidean space, e.g. films and shell structures or "partial differential equations on manifolds" in general. The theoretical approach presented heavily relies on a the framework on differential forms and "modern" differential geometry (Burke, 1996; Frankel, 2011; Bossavit, 2012). They are well known in certain communities, e.g. modern finite element theory (Arnold et al., 2006), but not so much in continuum mechanics where classical vector and tensor calculus are predominant. Notable exceptions are the works of Hirani (2003), Leok (2004) and Kanso et al. (2007). Hence, a considerable amount of work has gone into the introduction of this framework which is much richer in geometric objects than classical tensor and vector calculus. As a reward one gains a well-defined set of rules governing the operations on the objects encountered and clear geometrical interpretations that even give hints on the proper finite element discretization. Thus, a main task in the "new" framework is to find the appropriate mathematical object for the representation of a physical quantity. This automatically fixes the rules. By contrast, in tensor calculus things are not always that clear and it is thus much easier to unconsciously leave the path of physically reasonable mathematical operations. The thesis however does not stop at the translation of basic magnetic, electric and mechanical quantities to a new framework but goes further: invariants of tensorial quantities and forms in connection with the principles of material frame indifference and covariance are one of main topics waiting for further extension in future publications. Connected to that, the thesis contains a discussion of different parameterizations of energy functions, their time rates and relations between them.

Zusammenfassung

Die vorliegende Arbeit beschäftigt sich mit Magneto-Elektro-Elastizität im Rahmen der Kontinuumsmechanik unter großen Deformationen und quasi-statischer Prozesse. In anderen Worten: Es geht um die Beschreibung des mechanischen, magneto- und elektrostatischen Verhaltens von meso- und makroskopischen Körpern unter dem Einfluss von mechanischen Kräften, magnetischen Feldern und elektrischen Feldern. Ein besonders interessanter Aspekt ist dabei, die von magnetischen Feldern verursachte Deformation eines Körpers und der damit einhergehenden Änderung seiner elektrischen Eigenschaften, also magneto-elektrische Kopplung. Dieser Themenkomplex, der selbstverständlich auch die Subthemen Magneto-Elastizität und Elektro-Elastizität umfasst, ist Gegenstand aktueller Forschung auf experimenteller, theoretischer und simulationswissenschafltlicher Ebene. Zu möglichen Anwendungen der in diesem Bereich gewonnenen Erkenntnisse zählen unter anderem neuartige Speicherbausteine im Bereich der Mikroelektronik, Sensoren und Aktuatoren, haptischen Displays und künstliche Muskeln.

Das erste Projekt, dessen Resultate Eingang in diese Dissertationsschrift gefunden haben, war die Modellierung von magnetorheologischen Elastomeren (MREs). Bei MREs handelt es sich um den Verbund eines weichen Elastomers als Matrix und metallischen magnetischen Partikeln, weshalb bei der Modellierung von MREs, deren Mikrostruktur mit Hilfe von Mehrskalen-Methoden berücksichtigt werden muss. Im Zuge unserer Arbeit wurden verschiedene in Experimenten beobachtete Effekte – Veränderung der Steifigkeit unter Einfluss magnetischer Felder (Jolly et al., 1996), Deformation als Reaktion auf magnetische Felder (Böse et al., 2012) in Abhängigkeit der vorliegenden Mikrostruktur (Danas et al., 2012) – in Computersimulationen bestätigt. Darüber hinaus ermöglichten die Mehrskalen-Simulationen neue Einblicke in "Formeffekte" (engl. "shape effects"), das heißt, der Einfluss der Probengeometrie auf das magnetomechanische Verhalten. Überraschenderweise verformen sich nämlich Körper aus dem selben Material und mit der gleichen Magnetisierung unterschiedlich stark in Abhängigkeit von deren ursprünglicher Form. Das ist nicht nur ein interessanter Effekt an sich, sondern verkompliziert auch die experimentelle Bestimmung von *Materialeigenschaften* (Martin et al., 2006; Diguet et al., 2010; Bodelot et al., 2018), da bei den auftretenden großen Verfomungen die Berücksichtigung der Ausgangsform alleine nicht ausreichend ist, um Messungen von Formeffekten zu bereinigen.

MREs bestehen aus Elastomeren mit dielektrischen Eigenschaften sowie dielektrischen oder leitenden Einschlüssen. Daher war es nur natürlich, die Untersuchungen zur Magnetomechanik von MREs um das Gebiet der Elektrostatik zu erweitern. Dies geschah in der Hoffnung auf signifikante magnetoelektrische Kopplung im Bereich der

Quasistatik, also ohne elektrodynamische Effekte. Die naheliegendste Anwendung in diesem Bereich sind Sensoren für magnetische Felder (Martin et al., 2003). Interessanterweise kann vermutlich auch das Phänomen der Magnetorezeption – die Fähigkeit von Lebewesen sich an magnetischen Feldern zu orientieren – auf quasistatische Magnetoelektrische (ME) Kopplung zurückgeführt werden (Liu and Sharma, 2013). Wie im Zuge dieser Dissertationsschrift gezeigt wird, spielen die schon zuvor erwähnten Formeffekte auch bei der ME Kopplung bei weichen Materialien eine große Rolle. Die Formeffekte ermöglichen ME Kopplung sogar für Materialien, die von sich aus keine ME Kopplung zeigen. Das heißt, die Kopplung kann auch nur über die (veränderliche) Form eines Körpers zustande kommen. Einzige Voraussetzungen sind die Magnetisierbarkeit und Polarisierbarkeit des Körpers sowie eine relativ geringe Steifigkeit. Der umrissene Effekt wird in der vorliegenden Arbeit anhand von Ellipsoiden mittels analytischer Ansätze und numerischer Methoden demonstriert. Ein weiteres Szenario sind Plattenkondensatoren mit magnetisierbarem Dielektrikum, zum Beispiel ein MRE mit aufgeklebten Elektroden. Klarerweise kann auch in diesem Fall eine signifikante ME Kopplung beobachtet werden. Allerdings hält diese Anwendung einige Herausforderungen für numerischen Simulationen bereit: Die schlanke geometrische Form der Elektroden führt zu enormen Feldkonzentrationen, die in Finite-Elemente-Simulationen nur sehr schwierig abzubilden sind. Schlimmer noch: Die unvermeidbaren Diskretisierungsfehler führen zu elektromechanischen Artefakten, die sich negativ auf Genauigkeit und Stabilität der Simulationen auswirken. Ein solches Artefakt sind fälschlicherweise durch magnetische oder elektrische Felder verursachte Deformationen in Körpern, die keine entsprechenden Kopplungseigenschaften (auch nicht über Formeffekte) aufweisen. Die vorliegende Arbeit kann hier leider keine Abhilfe, aber zumindest Benchmarkbeipsiele bieten, die sich hoffentlich als nützlich für die weitergehende Analyse dieser numerischen Artefakte erweisen und letztlich zur Behebung dieser Probleme beitragen. Ein Versuch Abhilfe zu schaffen, mündete in der Untersuchung alternativer Diskretisierungsmethoden. Im Zuge dieser Untersuchungen wurde die Verwendung von dualen und gemischten Formulierungen anstelle der gängigen Variante basierend auf dem elektrischen Potential und dem magnetischen Skalarpotential vorgeschlagen. Beide Alternativen sind (linear restringierte) Minimierungsprinzipien und bringen tatsächlich eine Verbesserung. Bei näherer Betrachtung zeigt sich jedoch dass sie keine wirkliche Lösung des Problems bieten. Ein weiteres Ergebnis dieser Untersuchung war die Demonstration der Äquivalenz der gemischten und der dualen (Vektorpotential) Formulierung, wobei die gemischte Formulierung sich als wesentlich performanter herausstellte. Die zugrunde liegenden Laufzeiten wurden mit direkten Lösern für lineare Gleichungssysteme ermittelt. Entsprechende Tests mit iterativen Lösungsverfahren erfordern effiziente Vorkonditionierer, deren Konstruktion alles andere als trivial ist. Daher musste dieser Punkt leider offen bleiben.

Eine weitere Anwendung der restringierten Minimierungsprinzipien, welche als Basis für die gemischten Formulierungen fungieren, fand sich in Fourier-Diskretisierungen. Da die linearen Restriktionen nichts anderes erledigen als den Divergenz- beziehungsweise den Rotations-Anteil eines Vektorfeldes zu entfernen, reduziert sich de-

ren Realisierung im Fourier-Raum zu einfachen und vor allem lokalen Matrix-Vektor-Produkten. Aufgrund der Lokalität im Fourier-Raum ergibt sich eine großer Vorteil gegenüber Finite Elemente Implementierungen derselben Formulierung. Der resultierende Fourier-basierte Löser für magnetomechanische Probleme eignet sich zur Ermittlung von Materialeigenschaften von MRE durch Simulationen von deren Mikrostruktur. Ein besonderes Merkmal dieses Lösers ist der Projektionsansatz zur Erfüllung der divergenz- beziehungsweise rotationsfreiheit basierend auf der Helmholtz-Zerlegung von Vektorfeldern. Dieses Prinzip ermöglicht die einfache Erweiterung des entwickelten Lösers auf Magnetoelektromechanik aber auch auf viele andere Gebiete.

Neben den oben erwähnten anwendungsorientierten Untersuchungen widmet sich die vorliegende Arbeit auch den theoretischen Grundlagen der Magnetoelektromechanik. Die Absicht dahinter ist die Vorbereitung eines leistungsfähigen theoretischen Rahmens für künftige Forschungsvorhaben die über quasistatische Probleme in Euklidschen Räumen hinaus gehen; man denke and Schalen, Filme und partielle Differentialgleichungen auf Mannigfaltigkeiten im Allgemeinen. Der vorgestellte theoretische Ansatz basiert auf "modernen" differentialgeometrischen Werkzeugen wie den auf Élie Cartan zurückgehenden Differentialformen und dem *Exterior Calculus* (Burke, 1996; Frankel, 2011; Bossavit, 2012). Diese Werkzeuge sind wohlbekannt in einigen wissenschaftlichen *Communities* oder Gebieten wie zum Beispiel in der modernen Finite Elemente Theorie (Arnold et al., 2006), nicht jedoch in der Kontinuumsmechanik, wo bis heute klassische Tensoranalysis vorherrschend ist. Hierbei seien die Arbeiten von Hirani (2003), Leok (2004) und Kanso et al. (2007) als Ausnahmen hervorzuheben. Aufgrund deren geringer Verbreitung beschäftigt sich ein signifikanter Teil dieser Arbeit mit den Grundlagen des Exterior Calculus. Dieser bietet eine wesentliche größere Auswahl an mathematischen Objekten als klassischer Tensor-Calculus. Im Gegenzug erhält man einen wohldefinierten Satz an Operationen für die jeweiligen Objekte und klare geometrische Interpretationen, die in klassischer Tensorrechnung oft weit weniger eindeutig sind. Des Weiteren gibt die geometrische Interpretation auch direkt Auskunft über geeignete Finite Elemente Diskretisierungen. Daher ist der vielleicht wichtigste Punkt in der Verwendungen des "neuen" Frameworks das Finden des passenden mathematischen Objekts für die Representation einer physikalische Größe. Danach sind die erlaubten Operationen für diese Größe praktische fixiert. Im Gegensatz dazu ist es in der klassischen Tensorrechnung wesentlich leichter versehentlich physikalisch nicht sinnvolle Operationen durchzuführen, die zwar nicht automatisch falsch, aber jedenfalls mit äußerster Vorsicht zu interpretieren sind. Diese Dissertationsschrift geht aber über die reine "Übersetzung" vorhandener physikalischer Größen in Objekte des Exterior Calculus hinaus: Invarianten von tensoriellen Größen und Differentialformen in Verbindung mit den Prinzipien der "Unabhängigkeit vom materiellen Bezugssystem" und der "Kovarianz" bilden einen weiteren Themenkomplex, der zudem Stoff für weitergehende Arbeiten bietet. In Verbindung damit diskutiert diese Arbeit auch verschiedene Parameterisierungen von Energiefunktionen, deren Zeitableitungen und die Beziehungen zwischen den sich ergebenden Ausdrücken.

Chapter 1

Introduction

The research that is reported in this thesis started with studies of a soft elastic rubber-like material that in addition exhibits magnetization in response to an externally applied magnetic field. This is something peculiar since materials with pronounced magnetic properties are generally rather hard and stiff. Thus, to obtain a soft and at the same time magnetic material one has to resort to composites. In the present case a soft elastomer matrix is employed to hold magnetic particles which have characteristic dimensions in the range of microns. The production of such composites, so-called *magnetorheological elastomers*, is comparably easy and their deformation in response to magnetic fields is observable with the naked eye. This distinguishes them from "classical" magneto-mechanical (magneto-strictive) materials which undergo orders of magnitudes lower deformations (James and Kinderlehrer, 1993; Bednarek, 1999). Magnetorheological elastomers furthermore change their stiffness significantly when exposed to magnetic fields somewhat similar to magnetorheological fluids (Jolly et al., 1996). These properties lead to a wide range of proposed applications, from tunable shock-absorbers (Jolly et al., 1996; Böse and Röder, 2009) to actuators for valves (Böse et al., 2012). Moreover, their softness also brings along extremely rich buckling phenomena. They can be exploited to create deformation patterns controlled by magnetic fields for the design of haptic displays (Psarra et al., 2017, 2019). However, while it did not take long to achieve promising experimental results, the modeling of material properties to render them tractable for computation simulations of full *devices* turned out to be an extensive endeavor. The deformations of MRE's require a more rigorous geometric description than what is employed for magnetic materials undergoing small strains. The appropriate finite strain theory of elasticity has been extended to account for magnetic phenomena (Brown, 1966; Dorfmann and Ogden, 2003; Kankanala and Triantafyllidis, 2004; Bustamante et al., 2008) and is nowadays well-established. One of the remaining challenges is to capture the actual properties that should be fed into the theoretical framework (Danas et al., 2012). One possibility is to consider the individual constituents of which the properties and the behavior are quite well known and then just start computations at the microscopic scale. However, since the macroscopic specimens or devices are orders of magnitudes larger that the magnetic particles such an approach requires an extreme spatial resolution of simulations leading to prohibitive computational effort. Fortunately, there exist so-called "homogenization" techniques to extract the essential information ("effective response") from the microscopic features without

resolving the microstructure at every point of a body (Hill, 1952; Hashin and Shtrikman, 1962b,a; Willis, 1977; Ponte Castañeda and Galipeau, 2011; Moulinec and Suquet, 1994; Feyel and Chaboche, 2000; Miehe et al.). Precisely this issue, the treatment of magnetorheological elastomers *across* scales was the first task to be addressed in this project (Keip and Rambausek, 2016). During this simulation-focused work we wanted to compare our findings to experiments found in literature. In that course we learned that the experimental characterization of magnetorheological elastomers is more complicated than expected (Martin et al., 2006; Diguet et al., 2010). In fact, in experiments one always determines the properties of a specimen. When interested in material properties it is paramount to devise specimens and loading conditions that allow a precise and complete reconstruction of the state at some point inside the specimen from applied loads and measured response. For elastic materials there exist well-established procedures where the stress can be directly inferred from the applied forces and the strains are either measured directly or obtained from measured displacements. In magnetic materials, however, a similar reconstruction is currently not possible, at least not with the same degree of accuracy. The reason is that the shape of a specimen influences its response to applied magnetic field in a rather complicated nonlinear and nonuniform way. We addressed this challenge by regarding our two-scale simulations as in-silico experiments and trying to reconstruct (estimate) the complete magneto-mechanical state, i.e. stress, strain, magnetization and magnetic field (Keip and Rambausek, 2017). As a result we propose to conduct experiments on specimens of ellipsoidal shape, which is in line with findings of other groups in the field (Bodelot et al., 2018) and detailed in Chapter 7.

As a next step we thought about also considering electrostatics and entering the domain of magneto-electro-elasticity. The motivation for this was the hope to find competitive alternatives to existing magneto-electrically coupling materials (Spaldin and Fiebig, 2005; Fiebig, 2005; Lee et al., 2005), i.e. materials that change their polarization when exposed to magnetic field or vice-versa. Such effects can be used to construct novel types of magnetic field sensors (Fetisov et al., 2006) but also computer memory (Scott, 2007; Bibes and Barthélémy, 2008). Currently these application are realized by materials, "pure" or composites, that undergo only small deformations. However, as reported by Martin et al. (2003) magnetorheological elastomers could also be employed for sensing applications. In addition, the work of Liu and Sharma (2013) highlighted a possible mechanism for magneto-reception, the ability of biological organisms to detect (sense) magnetic fields (Mora et al., 2004; Holland et al., 2006; Wu and Dickman, 2011). Motivated by these findings we also investigated magneto-electric coupling in magnetorheological elastomers. We experimented with simulations of their magneto-electric coefficients and found some coupling, but not as much as we hoped for. However, remembering the fact that even magneto-mechanical coupling is heavily driven by non-local macroscopic effects we started to extend our models for purely macroscopic magneto-electro-mechanical coupling. With that the results were more satisfactory and we recognized that *material* coefficients make up only one, sometimes even negligible part of the coupling properties of a *body*. We also believe that the distinction between

properties of a material on the one hand and properties of bodies made of a material on the other hand are not always as clearly distinguished as it would be desirable. After our considerations on macroscopic magneto-electric coupling effects (Rambausek and Keip, 2018a) presented in Chapter 8 we returned to situations inspired by Liu and Sharma (2013), which can be summarized as "putting a magnetorheological elastomer between two electrodes" – a setting which we call "magneto-electric capacitor". Here we encountered challenges for our numerical tools that let us search for alternative formulations as documented in Chapter 9. While we did not resolve all issues we at least increased our capabilities for the simulation of magneto-electric capacitor setups. We studied their magneto-electric properties with quite simple material models that do not account for effects arising from the micro-morphology of magnetorheological elastomers as reported in Section 9.4. These results have then been compared with two-scale simulations in Chapter 10. The main observation in this comparison is that while magneto-electric coupling coefficients of the material do not seem to play an important role, the magneto- and electro-elastic material properties indeed do. This information is of great importance for the design and optimization of materials for magneto-electric devices. As a by-product of our experiments with (discrete) formulations for magneto-electro-mechanics we developed a computational homogenization scheme based on discrete Fourier transforms. As described in Chapter 11, by virtue of the transformation of spatial derivatives into vector products in Fourier space, the proposed formulation leads to an efficient numerical scheme along the lines of Zeman et al. (2017) and de Geus et al. (2017). Thanks to the structure of this recently published method (Rambausek et al., 2019) it can directly be extended to magneto-electro-elasticity.

The work outlined above is built on top of well-established theoretical foundations going back to Toupin (1956) and Brown (1966). The magneto-electro-mechanics was covered by, e.g., Pao and Hutter (1975) and Eringen and Maugin (1990). The monograph by Kovetz (2000) contributed additional momentum to the field and the by that time established theory was (partly) revisited by, *inter alia*, Dorfmann and Ogden (2003, 2005), Kankanala and Triantafyllidis (2004), McMeeking et al. (2007) and Ericksen (2006, 2007). Except for Kovetz (2000) who concentrated on electromagnetism, the given references after year 2000 focused on either the magneto- or the electro-mechanical but not the fully coupled setting. More recently it were Liu and Sharma (2013) and Liu (2013, 2014) who pushed into deformation-mediated ME coupling in soft media. Despite the potential applications, experimental and theoretical studies of the ME effects in MREs are still rare. Nevertheless, the above works offered sufficient background for our studies[1]. However, from time to time, when thinking about future projects, pushing limits and heading into new fields, theoretical details and subtleties gain importance. The up to now unmentioned first part of this thesis is devoted to a careful description of magneto-electro-elastic theory as it shall serve as a solid basis for future enterprises. It is not done in the fashion of the references cited above. Instead we tried to develop things starting

[1]This literature overview reports the path following which we entered the field and the community. It is thus by no means exhaustive. Moreover, we are not sure whether we can recommend to follow this path to newcomers.

from the very basis, that is the notions of energy, power and modern differential geometry. This route was motivated by Kanso et al. (2007) and Bossavit (2010, 2012). In these developments we heavily relied on the monographs by Marsden and Hughes (1994), Burke (1996) and Frankel (2011). The outcome, Part I, is a presentation of the theory which is more general, more detailed and more rigorous than necessary for what we present in Part II. Therefore, we decided to make the latter part largely self contained by delivering the necessary theory in the "common" way on-the-fly. Moreover, preceding Part I, Chapters 2 and 3 provide informal and brief introductions to continuum mechanics and electromagnetic theory, respectively.

Chapter 2

A primer in continuum mechanics

In the framework of continuum mechanics we consider bodies or portions of bodies at length scales much larger than atomic or molecular scales. At such a scale, bodies are modeled as "continuous" objects in space. This roughly means that we do not regard them as an aggregate of individual atoms or molecules, but as domains where material properties change very slowly in bulk, and "instantaneously" at boundaries and interfaces between two different bulk materials. Such a viewpoint yields accurate models and predictions down to surprisingly small scales and is the dominant perspective in both of engineering science and practice.

What follows in the present chapter can probably be found in every continuum mechanics text book. Our presentation follows the monograph by Tadmor et al. (2012) and also includes material from Marsden and Hughes (1994) and Bonet and Wood (2008). Both references provide further details on what is presented below and go far beyond the present scope.

A word on notation: We mainly use the notation employed by Bonet and Wood (2008) which is widely used in more or less the same form in large parts of the continuum mechanics community. Although we in some cases, most notably by not using boldface letters for positions, deviate from their notation, we believe that it is still comprehensible without rigorous introduction. The probably most apparent difference to mainstream notation is the use of the zero, "0", for any vanishing object, i.e. we do not distinguish between a scalar zero, a vector zero and a tensor zero. Moreover, we in general write anything that is position-like, e.g. coordinates and associated maps, in normal font in order to distinguish then from vectors in a differential-geometric sense.

2.1. Balance of mass

In the scope of this thesis we only deal with scenarios where mass is conserved. For a body $\mathcal{B}_t$ with mass density ρ at time t we write (Tadmor et al., 2012, Section 4.1)

$$\frac{\mathrm{d}}{\mathrm{d}t}\int_{\mathcal{B}_t} \rho \, dv = 0 \qquad \Leftrightarrow \qquad \int_{\mathcal{B}_t} \rho \, dv = \int_{\mathcal{B}} \rho_0 \, dV \tag{2.1}$$

with ρ_0 and $\mathcal{B}$ denoting the mass density and the configuration of the body, respectively, at time $t = 0$. The corresponding volume elements are denoted as dv and dV. For the

initial configuration at fixed time $t = 0$ it holds that

$$\frac{\mathrm{d}}{\mathrm{d}t}\int_{\mathcal{B}} \rho_0 \, dV = \int_{\mathcal{B}} \dot{\rho}_0 \, dV = 0 \qquad \Rightarrow \qquad \dot{\rho}_0 = 0. \tag{2.2}$$

Let J denote the change of volume[1] such that

$$\int_{\mathcal{B}_t} dv = \int_{\mathcal{B}} J \, dV. \tag{2.3}$$

Then we obtain the relation between the densities at time t and time $t = 0$ from (2.1) as

$$\int_{\mathcal{B}} \rho J \, dV = \int_{\mathcal{B}} \rho_0 \, dV \qquad \Rightarrow \qquad \rho = \frac{\rho_0}{J}. \tag{2.4}$$

An important general and useful result of the balance of mass is

$$\frac{\mathrm{d}}{\mathrm{d}t}\int_{\mathcal{B}_t} \rho\psi \, dv = \frac{\mathrm{d}}{\mathrm{d}t}\int_{\mathcal{B}} \rho_0\psi \, dV = \int_{\mathcal{B}} \rho_0\dot{\psi} \, dV = \int_{\mathcal{B}_t} \rho\dot{\psi} \, dv. \tag{2.5}$$

2.2. Balance of linear momentum

The continuum perspective leads to governing differential equations that differ from classical Newtonian particle mechanics. We begin with the global balance of linear momentum (Tadmor et al., 2012, Section 4.2)

$$\frac{\mathrm{d}}{\mathrm{d}t}\int_{\mathcal{B}_t} \rho \boldsymbol{v} \, dv = \int_{\mathcal{B}_t} \rho \boldsymbol{b} \, dv + \int_{\partial\mathcal{B}_t} \boldsymbol{t} \, da, \tag{2.6}$$

where $\boldsymbol{v}$ denotes the velocity of an infinitesimal portion dv of a body $\mathcal{B}_t$. On the right-hand-side of the above equation we have the body force per unit mass $\boldsymbol{b}$ and the surface traction $\boldsymbol{t}$ (force per unit surface area) exerted by agencies external to the body. Let us briefly discuss the concepts of force and traction. Force can be regarded as something that changes the state of motion of a body. They are of long range, e.g. gravity, or short range, e.g. contact forces, type. It is to our knowledge not possible to directly observe a force. What we basically observe are changes in the state of motion, the position or the deformation of some portion of matter. Forces are then indirectly determined via a mathematical relation, e.g., (2.6). A body force density is a long-range force per volume whereas traction is a short-range contact-type force per area. The latter forces can be imagined as the result of a limit process of body forces within a thin layer which is collapsed to form the boundary of body.

Besides the above mentioned (external) traction occurring at the boundary of a body, there also exists the concept of "internal" traction. Consider a pill-box shaped sub-body

[1] See Section 4.1.8 for details.

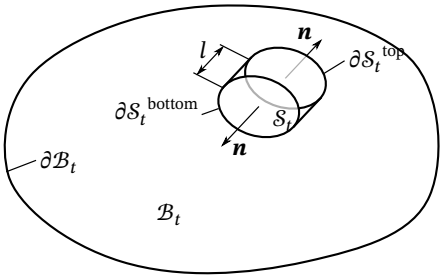

Figure 2.1: A pill-box shaped sub-body $\mathcal{S}$ of body $\mathcal{B}$ at time t. The sub-body is considered as a body in its own right and thus is susceptible to body force density and surface traction.

$\mathcal{S}$ that is cut out of the body $\mathcal{B}$ at rest as depicted in Figure 2.1. In general, $\mathcal{S}_t$ can be exposed to body forces and tractions. Let us take the limit of $l \to 0$ such that the three-dimensional pill-box degenerates to a two-dimensional object with surface but without volume. Then, from (2.6) only the two integrals over $\partial\mathcal{S}_t^{\text{top}}$ and $\partial\mathcal{S}_t^{\text{bottom}}$ remain, i.e.

$$\int_{\partial\mathcal{S}_t^{\text{top}}} \boldsymbol{t}\, da + \int_{\partial\mathcal{S}_t^{\text{bottom}}} \boldsymbol{t}\, da = 0. \tag{2.7}$$

Since this is supposed to hold for arbitrary sub-bodies we have

$$\boldsymbol{t}(x)\, da^{\text{top}} = -\boldsymbol{t}(x)\, da^{\text{bottom}}. \tag{2.8}$$

The area elements da^{top} and da^{bottom} can be characterized by the surface normal, i.e. da^{top} corresponds to the surface with extent da and unit normal $\boldsymbol{n}$ whereas da^{bottom} refers to the opposite surface with same extent da but normal $-\boldsymbol{n}$. Therefore, we rewrite (2.8) as

$$\boldsymbol{t}(x, \boldsymbol{n}) = -\boldsymbol{t}(x, -\boldsymbol{n}). \tag{2.9}$$

The peculiar dependence of the traction vector $\boldsymbol{t}$ on $\boldsymbol{n}$ shows that $\boldsymbol{t}$ is not only an odd function but also a linear function in $\boldsymbol{n}$. This is the essence of the famous Cauchy tetrahedron argument (see, e.g., Tadmor et al. (2012, Section 4.2.3)). An object that *linearly* relates two vectors is a (second-order) tensor. In the present case, this tensor is the *Cauchy stress tensor* $\boldsymbol{\sigma}$ which fulfills

$$\boldsymbol{t}(x, \boldsymbol{n}) = \boldsymbol{\sigma} \cdot \boldsymbol{n}. \tag{2.10}$$

Note that the pill-box above could also share one of its surfaces with $\mathcal{B}$ such that $\partial\mathcal{B}' \subset \partial\mathcal{B}$. Then, one $\boldsymbol{t}$ actually is the external traction $\boldsymbol{t}^{\text{e}}$. This observation yields to the classical boundary condition

$$\boldsymbol{t}(x, \boldsymbol{n}) = \boldsymbol{\sigma}(x) \cdot \boldsymbol{n} = \boldsymbol{t}^{\text{e}}. \tag{2.11}$$

By means of the Cauchy stress $\boldsymbol{\sigma}$, the boundary condition (2.11) and the divergence theorem we may reformulate (2.6)

$$\rho \dot{\boldsymbol{v}} = \operatorname{div} \boldsymbol{\sigma} + \rho \boldsymbol{b}. \tag{2.12}$$

We remark that the above discussion started from integral laws. As a consequence there is a certain non-uniqueness inherent to the resulting observations. Imagine a traction whose integral over the whole surface of a body vanishes. Such a traction does not result in a measurable net force on the body but rather in local deformation and possible changes in the distribution of reaction forces at supports. The same holds true for self-equilibrated body forces. Their determination is a true challenge and we will encounter such in Part II. We recommend the discussions of Eringen (1976) and also Brown (1966, Section 3.3) on localization of (momentum) balance laws.

2.3. Balance of moment of momentum

In continuum mechanics the balance of moment of momentum or balance of angular momentum is a principle in its own right (Tadmor et al., 2012, Section 4.3). Its integral form is given as

$$\frac{\mathrm{d}}{\mathrm{d}t} \int_{\mathcal{B}_t} \boldsymbol{r} \times \rho \boldsymbol{v} \, dv = \int_{\mathcal{B}_t} \boldsymbol{r} \times \rho \boldsymbol{b} \, dv + \int_{\partial \mathcal{B}_t} \boldsymbol{r} \times \boldsymbol{t} \, dv \tag{2.13}$$

If we assume that the continuum under consideration is only susceptible to force densities and tractions but not to body and surface "couple[2] densities", then the Cauchy stress tensor is symmetric

$$\boldsymbol{\sigma} = \boldsymbol{\sigma}^{\mathrm{T}}, \tag{2.14}$$

which is a localized form of the balance of angular momentum. For a derivation of this result we again refer to Tadmor et al. (2012). For theories that go beyond this assumption we refer to Eringen (1976).

2.4. Balance of energy

Balance of energy means that the change of energy in $\mathcal{B}$ equals the power exerted on $\mathcal{B}$. In case of only mechanical power we express this as (Tadmor et al., 2012, Section 5.6.1)

$$\frac{\mathrm{d}}{\mathrm{d}t} \int_{\mathcal{B}_t} \frac{1}{2} \rho \boldsymbol{v}^2 + \rho e \, dv = \int_{\mathcal{B}_t} \rho \boldsymbol{b} \cdot \boldsymbol{v} \, dv + \int_{\partial \mathcal{B}_t} \boldsymbol{t} \cdot \boldsymbol{v} \, da, \tag{2.15}$$

where the first integrand on the left-hand-side is the kinetic energy density and the second term is the internal energy density. Using (2.2), (2.10) and the divergence theorem

[2] This refers to "angular momentum sources" imprinted to infinitesimal volume or surface elements similar to force densities and tractions, i.e., "linear momentum sources".

we obtain

$$\int_{\mathcal{B}_t} \rho \boldsymbol{v} \cdot \dot{\boldsymbol{v}} + \rho \dot{e}\, dv = \int_{\mathcal{B}_t} \rho \boldsymbol{b} \cdot \boldsymbol{v}\, dv + \int_{\mathcal{B}_t} \operatorname{div}(\boldsymbol{\sigma} \cdot \boldsymbol{v})\, dv. \tag{2.16}$$

Then, we apply the product rule applied to the last integrand together with the localized balance of linear momentum to end up with (2.12)

$$\int_{\mathcal{B}_t} \rho \dot{e}\, dv = \int_{\mathcal{B}_t} \boldsymbol{\sigma} : \operatorname{grad} \boldsymbol{v}\, dv. \tag{2.17}$$

Furthermore, under (quasi-)static conditions, i.e. $\rho \dot{\boldsymbol{v}} = 0$, we obtain from (2.16)

$$\int_{\mathcal{B}_t} \rho \dot{e}\, dv - \int_{\mathcal{B}_t} \rho \boldsymbol{b} \cdot \boldsymbol{v}\, dv - \int_{\partial \mathcal{B}_t} \boldsymbol{t} \cdot \boldsymbol{v}\, da = 0. \tag{2.18}$$

This, however, does not change the result (2.17). We point out that $\dot{e}$ accounts for all kinds of changes of energy, not only the elastically stored contribution. Considering only mechanical power as "energy input" or output, we additively decompose the energy density rate[3] $\dot{e}$

$$\dot{e} = \dot{e}^{\mathrm{E}} + \dot{e}^{\mathrm{NE}}, \tag{2.19}$$

where $\dot{e}^{\mathrm{E}}$ denotes the "elastic" (reversible) rate of energy and $\dot{e}^{\mathrm{NE}}$ the remaining (irreversible) part. According to the second law of thermodynamics (cf. Tadmor et al. (2012, Sections 5.5, 5.6 and 6.2)), $\dot{e}^{\mathrm{NE}}$ will never be negative such that

$$\int_{\mathcal{B}_t} \rho \dot{e}^{\mathrm{E}}\, dv - \int_{\mathcal{B}_t} \rho \boldsymbol{b} \cdot \boldsymbol{v}\, dv - \int_{\partial \mathcal{B}_t} \boldsymbol{t} \cdot \boldsymbol{v}\, da \leq 0 \tag{2.20}$$

for *adiabatic* (no heat flux) processes and

$$\int_{\mathcal{B}_t} \rho \dot{\Psi}^{\mathrm{E}}\, dv - \int_{\mathcal{B}_t} \rho \boldsymbol{b} \cdot \boldsymbol{v}\, dv - \int_{\partial \mathcal{B}_t} \boldsymbol{t} \cdot \boldsymbol{v}\, da \leq 0 \tag{2.21}$$

for *isothermal* processes, whereby $\dot{\Psi}^{\mathrm{E}}$ is the elastically reversible rate of the (Helmholtz) *free* energy density $\Psi = e - \theta s$, where θ is the temperature and s the entropy. As can be seen from (2.20) and (2.21), there is no difference in the structure of equations for isentropic and isothermal processes. However, in (quasi-)statics the isothermal case often better reflects the experimental conditions, e.g. a tension test on a thermally non-insulated specimen with small strain rates. Thus, we will from now on work with the Helmholtz free energy density Ψ.

[3] This split does not reflect an additive decomposition of e but only the distinction of state variables associated with elastic and non-elastic changes of energy.

By grouping terms, equation (2.21) can be rewritten as

$$\dot{\Pi}^{\text{int}} - P^{\text{ext}} \leq 0 \tag{2.22a}$$

with

$$\dot{\Pi}^{\text{int}} = \int_{\mathcal{B}_t} \rho \dot{\Psi}^{\text{E}} \, dv, \qquad P^{\text{ext}} = \int_{\mathcal{B}_t} \rho \boldsymbol{b} \cdot \boldsymbol{v} \, dv + \int_{\partial \mathcal{B}_t} \boldsymbol{t} \cdot \boldsymbol{v} \, da, \tag{2.22b}$$

where equality only holds at static equilibrium, that is when the system does not change its state[4] any more. Since the present thesis is not concerned with the modeling of irreversible processes[5] but only with equilibrium states, we by a slight abuse of notation henceforth identify $\dot{\Psi}^{\text{E}}$ with $\dot{\Psi}$.

In case that there exists an external potential Π^{ext} such that the virtual work of external agencies also can be derived from that potential as $P^{\text{ext}} = -\dot{\Pi}^{\text{ext}}$ we may reformulate (2.22) to arrive at

$$\dot{\mathcal{L}} \leq 0 \qquad \text{with} \qquad \mathcal{L} = \Pi^{\text{int}} + \Pi^{\text{ext}}. \tag{2.23}$$

We did not make any assumptions on the velocity field $\boldsymbol{v}$ except for exclusion of dynamic effects such that equilibrium states, stable or not, can be solved for by requiring that equality in $(2.23)_1$ holds for any $\boldsymbol{v}$. In other words: At equilibrium, there exists no $\boldsymbol{v}$ for which $\dot{\mathcal{L}} < 0$. This is usually expressed as

$$\delta \mathcal{L} = 0, \tag{2.24}$$

where δ denotes a "variation". From (2.23) it furthermore follows that an equilibrium is only stable if the stationary point of $\mathcal{L}$ is a (local) infimum.

Remark 2.1. Replacing time rates with variations already in the equality case of (2.22) yields a form of the principle of virtual work, which does not require a potential of mechanical power and is thus more general than (2.24). However, this comes at the expense that equilibrium is not characterized by critical points of a scalar functional.

2.4.1. A constitutive relation for the Cauchy stress

Let us now discuss the localized balance of energy (2.17). We informally introduce the deformation gradient $\underline{\boldsymbol{F}}$

$$\underline{\boldsymbol{F}} = \frac{\partial \varphi(X,t)}{\partial X}, \tag{2.25}$$

[4] In this context by state we mean the final (deformed) size and shape of the body.

[5] Example for such processes are heat transfer, friction, viscous stresses and plasticity. We prefer to not delve further into the framework of continuum thermodynamics. For extensive treatments we refer to Truesdell and Noll (2004) and Tadmor et al. (2012).

where X denotes the initial position of a material point $X = x(t = 0)$ and φ is the deformation map relating initial and current positions[6] $x(t) = \varphi(X, t)$. From (2.17) and (2.22) we obtain at equilibrium (Tadmor et al., 2012, Section 5.6.1)

$$\int_{\mathcal{B}_t} \boldsymbol{\sigma} : \frac{\partial \boldsymbol{v}}{\partial x}\, dv = \int_{\mathcal{B}} \boldsymbol{\sigma} : \left(\frac{\partial \boldsymbol{v}}{\partial X} \cdot \underline{\boldsymbol{F}}^{-1}\right) J\, dV = \int_{\mathcal{B}} \left(J\boldsymbol{\sigma} \cdot \underline{\boldsymbol{F}}^{-\mathrm{T}}\right) : \dot{\underline{\boldsymbol{F}}}\, dV = \int_{\mathcal{B}} \rho_0 \dot{\Psi}\, dV, \quad (2.26)$$

in terms of integrals over the initial configuration $\mathcal{B}$. Since Ψ represents elastically stored energy and $\underline{\boldsymbol{F}}$ carries information on deformation we assume $\Psi = \Psi(\underline{\boldsymbol{F}})$. Combined with the final equation in (2.12) this suggests[7] that

$$\boldsymbol{\sigma} = \boldsymbol{\sigma}(\underline{\boldsymbol{F}}) = \rho \frac{\partial \Psi(\underline{\boldsymbol{F}})}{\partial \underline{\boldsymbol{F}}} \cdot \underline{\boldsymbol{F}}^{\mathrm{T}} =: \underline{\boldsymbol{\sigma}}, \quad (2.27)$$

which is an indirect constitutive relation for the Cauchy stress. In fact, the equation above involves the *first Piola-Kirchhoff stress* $\underline{\boldsymbol{P}}$ defined as (Bonet and Wood, 2008, Section 6.2)

$$\underline{\boldsymbol{P}} = \rho_0 \frac{\partial \Psi(\underline{\boldsymbol{F}})}{\partial \underline{\boldsymbol{F}}} \quad \Leftrightarrow \quad \underline{\boldsymbol{\sigma}} = \frac{1}{J} \underline{\boldsymbol{P}} \cdot \underline{\boldsymbol{F}}^{\mathrm{T}}. \quad (2.28)$$

Remark 2.2. In equation (2.27) we see two versions of the Cauchy stress, the non-mixed (here fully "contravariant") second order-tensor $\boldsymbol{\sigma}$ and mixed-type second order-tensor $\underline{\boldsymbol{\sigma}}$, respectively. In the present introductory scope these two objects are essentially equivalent and the reader should not bother too much with them for now. However, this issue is one of the many reasons that motivated us to delve into differential geometry in Chapter 4.

2.4.2. Invariances of the internal energy and constitutive relations

Let us come back to the assumption that both internal energy e and Cauchy stress $\boldsymbol{\sigma}$ depend on the deformation gradient $\underline{\boldsymbol{F}}$. It is certainly reasonable in the scope of elasticity to assume that both the internal energy density e and the Cauchy stress $\boldsymbol{\sigma}$ depend at least on the same deformation or strain measure, and, more importantly, that $\boldsymbol{\sigma}$ is a state variable. It turns out that $\underline{\boldsymbol{F}}$ is invariant by rigid body translation. As a consequence, a quasi-static translation of a body together with its support and loads from one place to another does not change its energetic state. However, $\underline{\boldsymbol{F}}$ is not invariant under rotations represented by a (constant) matrix $\boldsymbol{Q}$ with $\boldsymbol{Q}^{\mathrm{T}} = \boldsymbol{Q}^{-1}$ and $\det \boldsymbol{Q} = 1$. The rotated coordinates are denoted as $x' = \boldsymbol{Q} \cdot x$. Then,

$$\underline{\boldsymbol{F}}' = \frac{\partial \boldsymbol{Q} \cdot \varphi(X)}{\partial X} = \boldsymbol{Q} \cdot \underline{\boldsymbol{F}}. \quad (2.29)$$

[6] For an explanation of how a tensor like $\underline{\boldsymbol{F}}$ is obtained from to position-like quantities (not vectors) we refer to Section 4.1.

[7] Such a localization potential discards self-equilibrated stress fields which *in toto* do not add to the integral in (2.26). For an overview of advanced theories concerned with this case we refer to Eringen (1976).

There is of course experimental evidence that internal energy density e and thus also the free energy density Ψ as well as stresses are invariant with respect to quasi-static rigid-body rotations (negligible centrifugal force) in the same sense as they are invariant with respect to rigid-body translations (Tadmor et al., 2012, Section 6.3). Thus, they fulfill

$$\Psi(\underline{\boldsymbol{F}}) = \Psi(\boldsymbol{Q} \cdot \underline{\boldsymbol{F}}) \qquad \text{and} \qquad \boldsymbol{\sigma}(\underline{\boldsymbol{F}}) = \boldsymbol{\sigma}(\boldsymbol{Q} \cdot \underline{\boldsymbol{F}}). \tag{2.30}$$

It is easily seen that the so-called right Cauchy-Green deformation tensor

$$\mathbf{C} = \underline{\boldsymbol{F}}^{\mathrm{T}} \cdot \underline{\boldsymbol{F}} = (\boldsymbol{Q} \cdot \underline{\boldsymbol{F}})^{\mathrm{T}} \cdot (\boldsymbol{Q} \cdot \underline{\boldsymbol{F}}) \tag{2.31}$$

is such a rotation invariant quantity based on $\underline{\boldsymbol{F}}$. Moreover, $\mathbf{C}$ is symmetric by construction. Then, if $\Psi(\underline{\boldsymbol{F}}) = \widehat{\Psi}(\mathbf{C})$ (Tadmor et al., 2012, Section 6.3.5), we have

$$\frac{\partial \Psi}{\partial \underline{\boldsymbol{F}}} = \frac{\partial \widehat{\Psi}}{\partial \mathbf{C}} : \frac{\partial \mathbf{C}}{\partial \underline{\boldsymbol{F}}} = 2\underline{\boldsymbol{F}} \cdot \frac{\partial \widehat{\Psi}}{\partial \mathbf{C}} \qquad \text{and} \qquad \boldsymbol{\sigma} = 2\rho \underline{\boldsymbol{F}} \cdot \frac{\partial \widehat{\Psi}}{\partial \mathbf{C}} \cdot \underline{\boldsymbol{F}}^{\mathrm{T}}. \tag{2.32}$$

The above relation has interesting consequences. First of all, the equation for $\boldsymbol{\sigma}$ in (2.32) *ensures* that $\boldsymbol{\sigma}$ is symmetric and this implies that balance of angular momentum is fulfilled. Moreover, a rigid body rotation yields

$$\boldsymbol{\sigma}' = \boldsymbol{Q} \cdot \boldsymbol{\sigma} \cdot \boldsymbol{Q}^{\mathrm{T}}, \tag{2.33}$$

which is indeed the appropriate transformation law for $\boldsymbol{\sigma}$, that is the eigenvalues of $\boldsymbol{\sigma}$ are unaffected by this operation. If we allow for viscous stresses, e.g. $\boldsymbol{\sigma} = \boldsymbol{\sigma}^{\mathrm{e}}(\underline{\boldsymbol{F}}) + \boldsymbol{\sigma}^{\mathrm{v}}(\underline{\boldsymbol{F}}, \dot{\underline{\boldsymbol{F}}})$ the above argument is not sufficient to ensure balance of angular momentum. In that case one may follow Green and Rivlin (1964) and consider a rigid body rotation $\varphi_Q(x)$ with spatially uniform angular velocity represented by the skew-symmetric matrix $\dot{\underline{\boldsymbol{F}}}_Q = \dot{\boldsymbol{Q}}$. Then, from (2.17) we obtain under assumption that e is not affected by a motion $\boldsymbol{v} = \dot{\varphi}_Q(x)$

$$0 = \int_{\mathcal{B}_t} \boldsymbol{\sigma} \, dv : \dot{\boldsymbol{Q}}. \tag{2.34}$$

In arbitrary volumes the above equation is fulfilled for non-vanishing $\boldsymbol{\sigma}$ and any skew-symmetric $\dot{\boldsymbol{Q}}$ if and only if $\boldsymbol{\sigma}$ is symmetric.

To conclude the above considerations we highlight that the requirement of rotational invariance of e yields symmetry of the Cauchy stress which is a form of the balance of angular momentum as well as the appropriate transformation law under a change of coordinates. Moreover we point out that what is possible for rotational invariance is similarly valid for translational invariance. To see this, consider (2.16) under a rigid body translation that affects x and its time derivatives but does not affect $\underline{\boldsymbol{F}}$, i.e. $\dot{\underline{\boldsymbol{F}}} = 0$. Under assumption that e is unaffected, e.g. because $e = e(\underline{\boldsymbol{F}})$, we obtain (Green and

Rivlin, 1964)

$$\int_{\mathcal{B}_t} \rho \boldsymbol{v} \cdot \dot{\boldsymbol{v}} + 0 \, dv = \int_{\mathcal{B}_t} \rho \boldsymbol{b} \cdot \boldsymbol{v} + \operatorname{div}(\boldsymbol{\sigma}) \cdot \boldsymbol{v} + 0 \, dv. \tag{2.35}$$

For arbitrary but spatially uniform $\boldsymbol{v}$ and arbitrary volumes this results in

$$\rho \dot{\boldsymbol{v}} - \rho \boldsymbol{b} - \operatorname{div} \boldsymbol{\sigma} = 0 \tag{2.36}$$

which is nothing else than (2.12), the local balance of linear momentum. The results outlined above are more thoroughly discussed by Marsden and Hughes (1994, p. 145, Box 3.1).

Chapter 3

Fundamentals of electromagnetic theory

We now provide a short introduction to basic relations of electrodynamics. For this purpose we decided to mainly follow the probably rather unconventional approach of Kovetz (2000), which discusses electrodynamics not following historical developments but in terms of "modern" principles that have been discovered much later.

Having stated this plan we immediately deviate from it. This is because the "three principles" of electrodynamics (Kovetz, 2000, Chapters 3 to 5) are of abstract nature and do not provide a very smooth introduction for reader with a background in mechanics. Therefore, as a motivation we begin with the force on a classical (non-quantum) charged particle with mass m and charge q. First, consider the particle to be at rest where it "sees" an electric field $\boldsymbol{E}$. It experiences the force[1] $\boldsymbol{F}^q$ (Kovetz, 2000, Section 15)

$$\boldsymbol{F}^q = q\boldsymbol{E}. \tag{3.1}$$

It is important to note that in this context $\boldsymbol{E}$ does not include any contribution of the particle's electric field created by its charge q. When $\boldsymbol{E}$ is the field created by another particle with charge q_2 then (3.1) can be cast into the form of Coulomb's force law. However, it is also known that moving charges experience forces under magnetic field[2] $\boldsymbol{B}$. To be precise, we consider some inertial frame of reference in which we observe a magnetic field $\boldsymbol{B}$ and the charged particle moves relative to this frame with velocity $\boldsymbol{v}$. The force experienced by the particle is

$$\boldsymbol{F}^q = q\boldsymbol{v} \times \boldsymbol{B}. \tag{3.2}$$

Let us now consider how this situation looks like from the particle's perspective, this means from a frame in which the particle is at rest. We shall denote quantities in this frame with a "prime" ($'$). The charged particle would simply follow (3.1) with $\boldsymbol{E}'$. Since the force must be the same one concludes that in this case

$$\boldsymbol{E}' = \boldsymbol{v} \times \boldsymbol{B}. \tag{3.3}$$

Finally, when there is an electric field $\boldsymbol{E}$ and a magnetic field $\boldsymbol{B}$ in the un-primed inertial

[1] The symbol $\boldsymbol{F}^q$ not be confused with the deformation gradient $\underline{\boldsymbol{F}}$.

[2] Throughout this thesis, by "magnetic field" we refer to the $\boldsymbol{B}$-field, where as the $\boldsymbol{H}$ field will be referred to as "current potential" with "current" in the sense of electric current for reasons outline below.

frame then the force on the particle is the so-called Lorentz force

$$\boldsymbol{F}^q = q(\boldsymbol{E} + \boldsymbol{v} \times \boldsymbol{B}), \tag{3.4}$$

which reveals that

$$\boldsymbol{E}' = \boldsymbol{E} + \boldsymbol{v} \times \boldsymbol{B}. \tag{3.5}$$

This has the interesting consequence that it appears to be perfectly possible that in one frame there only exists an electric field whereas in another frame one only detects a magnetic field. This can only be the case if electric and magnetic field actually are two appearances of some "higher-level" structure or object (Kovetz, 2000, Chapter 4). The search for such structures was one of the most formidable tasks in physics that culminated in modern electromagnetism and, when extended to embrace mechanics, the theory of relativity.

3.1. The fundamental principles of electromagnetism

In this section, following Kovetz (2000), we present first the conservation of charge, then the dynamic relation between the electric and the magnetic field and finally the so-called aether-relations as the three principles of electromagnetic theory.

3.1.1. Conservation of charge

The first principle of electromagnetism is the conservation of charge (Kovetz, 2000, Chapter 3). In integral and differential form it is expressed as

$$\frac{\mathrm{d}}{\mathrm{d}t}\int_\Omega q\, dV + \int_{\partial\Omega} \boldsymbol{j}\cdot\boldsymbol{n}\, dA = 0 \qquad \text{and} \qquad \frac{\partial q}{\partial t} + \operatorname{div}\boldsymbol{j} = 0, \tag{3.6}$$

respectively, where the domain Ω is fixed in space, q is a charge density, $\boldsymbol{j}$ is a current (moving charge) density and $\boldsymbol{n}$ is the outward pointing unit normal of the closed surface $\partial\Omega$. It is indeed possible to obtain q and $\boldsymbol{j}$ from "potentials", i.e.

$$q = \operatorname{div}\boldsymbol{D} \qquad \text{and} \qquad \boldsymbol{j} = \operatorname{curl}\boldsymbol{H} - \frac{\partial \boldsymbol{D}}{\partial t}. \tag{3.7}$$

Then, (3.6) is fulfilled identically, whereby $\operatorname{curl}\boldsymbol{H}$ simply is a contribution to $\boldsymbol{j}$ that is undetermined by (3.6) since $\operatorname{div}\operatorname{curl}\boldsymbol{H} \equiv \boldsymbol{0}$. In Section 4.1 we provide some mathematical tools to put these considerations further. Although not very standard, we will call $\boldsymbol{D}$ the *charge potential* and $\boldsymbol{H}$ the *current potential*.

3.1.2. The electromagnetic field

The second principle is concerned with the electromagnetic field (Kovetz, 2000, Chapter 4) which is characterized by

$$\int_{\partial\Omega} \boldsymbol{B}\cdot\boldsymbol{n}\,dA = 0 \qquad \text{and} \qquad \frac{\mathrm{d}}{\mathrm{d}t}\int_{S} \boldsymbol{B}\cdot\boldsymbol{n}\,dA + \int_{\partial S} \boldsymbol{E}\cdot d\boldsymbol{L} = 0, \tag{3.8}$$

with $\partial\Omega$ denoting the *closed* surface of a fixed volume Ω and $\mathcal{S}$ a fixed *open* surface with boundary $\partial\mathcal{S}$ whereby the latter has an infinitesimal tangent element $d\boldsymbol{L}$. The differential versions are given as

$$\operatorname{div}\boldsymbol{B} = 0 \qquad \text{and} \qquad \frac{\partial \boldsymbol{B}}{\partial t} + \operatorname{curl}\boldsymbol{E} = 0. \tag{3.9}$$

Equations $(3.8)_2$ and $(3.9)_2$ are known as the Maxwell-Faraday law in integral and differential form.

Equations $(3.8)_1$ and $(3.9)_1$ tell us that the magnetic field $\boldsymbol{B}$ has no sources. The second equation in each of the two pairs somehow looks like a conservation law, but on a geometric object of less dimensionality than usually, i.e. an open surface instead of a closed volume. [3]

The actual second principle basically is the observation that $\boldsymbol{B}$ and $\boldsymbol{E}$ can be derived from the potentials $\boldsymbol{A}$ and ϕ, that is

$$\boldsymbol{B} = \operatorname{curl}\boldsymbol{A} \qquad \text{and} \qquad \boldsymbol{E} = -\operatorname{grad}\phi - \frac{\partial \boldsymbol{A}}{\partial t} \tag{3.10}$$

such that (3.9) are fulfilled automatically. The term $-\operatorname{grad}\phi$ (the minus is by convention) in $(3.10)_2$ is a contribution to $\boldsymbol{E}$ which is not determined by $(3.9)_2$. We point out that the scalar-valued electric potential ϕ can be interpreted as an energy per unit charge, which can be derived via the work done by moving a charge against an electric field. Moreover, because the vector-valued potential $\boldsymbol{A}$ completely determines $\boldsymbol{B}$ it is usually referred to as magnetic (vector) potential.

We will see in Section 4.2 that ϕ and $\boldsymbol{A}$ together form the *electromagnetic potential* and that both $\boldsymbol{E}$ and $\boldsymbol{B}$ are manifestations of this single underlying object.

3.1.3. The aether relations and Maxwell's equation in vacuum

The two disjoint pairs of equations (3.7) and (3.9) are the differential versions of what is known as Maxwell's equations. The third principle of electromagnetism is then that there exists at least one (Euclidean) inertial frame of reference (Kovetz, 2000, Chapter 5)

[3] By contrast to Kovetz (2000) we therefore prefer to not call them "conservation law". In this context we refer to the differential-geometric characterization of physical quantities in Section 4.1.8 and to discussion of Frankel (2011, Section 3.5d) on what certain types of geometric objects "measure".

for which the following relations hold:

$$\boldsymbol{D} = \epsilon_0 \boldsymbol{E} \qquad \text{and} \qquad \boldsymbol{H} = \boldsymbol{B}/\mu_0. \tag{3.11}$$

A reference frame in which above equations hold is called an "aether frame". In an aether frame, Maxwell's equations can be expressed as

$$\epsilon_0 \operatorname{div} \boldsymbol{E} = q \qquad \operatorname{curl} \boldsymbol{B}/\mu_0 - \epsilon_0 \frac{\partial \boldsymbol{E}}{\partial t} = \boldsymbol{j} \tag{3.12a}$$

$$\operatorname{div} \boldsymbol{B} = 0 \qquad \operatorname{curl} \boldsymbol{E} + \frac{\partial \boldsymbol{B}}{\partial t} = 0, \tag{3.12b}$$

The coefficients ϵ_0 and μ_0 are commonly referred to as the electric permittivity and magnetic permeability of vacuum. Their values can be determined from experiments and it can furthermore be shown that they are related to the speed of light c as

$$\sqrt{\epsilon_0 \mu_0} = \frac{1}{c}. \tag{3.13}$$

Despite looking like simple scalar numbers, each of ϵ_0 and μ_0 actually relates two physical quantities which transform differently.[4] Also note that we see from (3.11) that $\boldsymbol{D}$ and $\boldsymbol{H}$ are not merely potentials but physical fields in their own right.

Let us now turn to the question for the reference frames in which the relations (3.11) hold. Two inertial frames are usually related via a translation with relative velocity $\boldsymbol{v}$ that is uniform in space and time, i.e. a Galilean transform. The transformation rules for the electromagnetic quantities introduced so far are given as[5] (Kovetz, 2000)

$$q' = q, \qquad \boldsymbol{j}' = \boldsymbol{j} - \boldsymbol{v} q, \tag{3.14a}$$

$$\boldsymbol{D}' = \boldsymbol{D}, \quad \frac{\partial \boldsymbol{D}'}{\partial t} = \frac{\partial \boldsymbol{D}}{\partial t} + (\operatorname{grad} \boldsymbol{D}) \cdot \boldsymbol{v}, \quad \boldsymbol{H}' = \boldsymbol{H} - \boldsymbol{v} \times \boldsymbol{D}, \quad \boldsymbol{A}' = \boldsymbol{A}, \tag{3.14b}$$

$$\boldsymbol{B}' = \boldsymbol{B}, \quad \frac{\partial \boldsymbol{B}'}{\partial t} = \frac{\partial \boldsymbol{B}}{\partial t} + (\operatorname{grad} \boldsymbol{B}) \cdot \boldsymbol{v}, \quad \boldsymbol{E}' = \boldsymbol{E} + \boldsymbol{v} \times \boldsymbol{B}, \quad \phi' = \phi - \boldsymbol{v} \cdot \boldsymbol{A}. \tag{3.14c}$$

From these we see that (3.11) will in general not be fulfilled under such transformations and the form of (3.11) is thus not invariant in a case where the mechanical laws from Section 2 are. Instead, it is known that (3.11) are invariant under Lorentz transformations. The insight that inertial frames are actually connected via Lorentz transforms and thus can be identified with aether frames is an important feature of the theory of relativity (Kovetz, 2000, Section 12). Thus, we shall be warned of simply applying concepts from classical mechanics in the realm of electromagnetism, even at small velocities.

[4] The constants ϵ_0 and μ_0 fulfill a role similar to the elasticity tensor in continuum mechanics. We will revisit this point in Sections 4.1.7.10 and 4.1.8.8.

[5] This specific forms are derived via tensor transformation rules as by Kovetz (2000, Sections 6, 9 and 10). There exist other versions in literature which are based on small-velocity limits of the Lorentz transformations (Le Bellac and Lévy-Leblond, 1973).

3.2. Maxwell's equations in matter

With matter we actually mean a continuum in the sense of Section 2 such that we are not concerned with electrodynamic and quantum phenomena at atomistic length scales. Then we may roughly distinguish between charges that can move more or less freely within a continuum and charges whose motion is confined to a region which is very small in comparison. The latter kind of charges is denoted as "bound charge". A similar distinction shall be made for "free" and "bound" currents. We introduce the polarization $\boldsymbol{P}$ and the magnetization $\boldsymbol{M}$ as those parts of $\boldsymbol{D}$ and $\boldsymbol{H}$ that correspond to "bound" charges and currents. Furthermore, we let from now on refer $\boldsymbol{D}$ and $\boldsymbol{H}$ to the remaining portions of the charge and the current potential, respectively. Accordingly, q and $\boldsymbol{j}$ will also from now on refer to free charges and currents. The "aether relations" (3.11) then read as (Kovetz, 2000, Section 20)

$$\boldsymbol{D} = \epsilon_0 \boldsymbol{E} + \boldsymbol{P} \qquad \text{and} \qquad \boldsymbol{H} = \boldsymbol{B}/\mu_0 - \boldsymbol{M} \tag{3.15}$$

The laws for their changes under Galilean transformations are inherited from the corresponding original quantities. To remove the two additional vector-valued unknowns one considers material-dependent functions, e.g., $\boldsymbol{P} = \boldsymbol{P}(\boldsymbol{E})$ and $\boldsymbol{M} = \boldsymbol{M}(\boldsymbol{B})$, that are to be determined experimentally.

Under these changes Maxwell's equations are *formally* still the same (Kovetz, 2000, Section 21), i.e.

$$\operatorname{div} \boldsymbol{D} = q \qquad \operatorname{curl} \boldsymbol{H} - \frac{\partial \boldsymbol{D}}{\partial t} = \boldsymbol{j} \tag{3.16a}$$

$$\operatorname{div} \boldsymbol{B} = 0 \qquad \operatorname{curl} \boldsymbol{E} + \frac{\partial \boldsymbol{B}}{\partial t} = 0. \tag{3.16b}$$

However, we point out that now $\boldsymbol{D}$, $\boldsymbol{j}$, q and $\boldsymbol{H}$ refer to free charges, currents and their (partial) potentials. The corresponding jump conditions for a surface with unit normal $\boldsymbol{n}$, normal velocity v_n, free surface charge density q^{s} and free surface current density $\boldsymbol{j}^{\mathrm{s}}$ are given as

$$\boldsymbol{n} \cdot [\![\boldsymbol{D}]\!] = q^{\mathrm{s}} \qquad \boldsymbol{n} \times [\![\boldsymbol{H}]\!] + v_n [\![\boldsymbol{D}]\!] = \boldsymbol{j}^{\mathrm{s}} \tag{3.17a}$$

$$\boldsymbol{n} \cdot [\![\boldsymbol{B}]\!] = 0 \qquad \boldsymbol{n} \times [\![\boldsymbol{E}]\!] - v_n [\![\boldsymbol{B}]\!] = 0. \tag{3.17b}$$

For a derivation we once again refer to Kovetz (2000, Sections 7 and 8).

In vacuum, when there are neither free nor bound charges or currents, such that the equations (3.16) reduce to the "aether" versions (3.12) with $q = 0$ and $\boldsymbol{j} = \boldsymbol{0}$, i.e.

$$\epsilon_0 \operatorname{div} \boldsymbol{E} = 0 \qquad \operatorname{curl} \boldsymbol{B}/\mu_0 - \epsilon_0 \frac{\partial \boldsymbol{E}}{\partial t} = 0 \tag{3.18a}$$

$$\operatorname{div} \boldsymbol{B} = 0 \qquad \operatorname{curl} \boldsymbol{E} + \frac{\partial \boldsymbol{B}}{\partial t} = 0. \tag{3.18b}$$

So far we have introduced the governing equations of electromagnetism. In this thesis, however, we only consider quasi-static situations where the "dynamic" coupling of electric and magnetic does not occur. In the two sections to come we will first discuss the case of electrostatics and then move on to magnetostatics as preparation for magneto-electro-mechanics in a quasi-static setting.

3.3. Electrostatics

Electrostatics refers to the case where the time rates of the fields $\boldsymbol{E}$ and $\boldsymbol{D}$ are zero or at least negligible, whereby the latter case corresponds to "quasi"-statics. Moreover, we shall assume that if magnetic fields are present, their time rates are also negligible.

3.3.1. Electrostatic equations

The governing equations in this reduced scope are given as

$$\operatorname{div} \boldsymbol{D} = q \qquad \operatorname{curl} \boldsymbol{E} = 0 \qquad \boldsymbol{D} = \epsilon_0 \boldsymbol{E} + \boldsymbol{P}, \tag{3.19}$$

with jump conditions

$$\boldsymbol{n} \cdot [\![\boldsymbol{D}]\!] = q^{\mathrm{s}} \qquad \boldsymbol{n} \times [\![\boldsymbol{E}]\!] = 0. \tag{3.20}$$

This system is closed by some empiric relation for, e.g., $\boldsymbol{P} = \boldsymbol{P}(\boldsymbol{E})$. In electrostatics, $(3.10)_1$ reduces to

$$\boldsymbol{E} = -\operatorname{grad} \phi, \tag{3.21}$$

which we could have also seen from $(3.19)_2$.

3.3.2. Electrostatic work and energy

We begin this discussion with a free[6] charge density q which we move around in an electric field. Of course, we move q with very low velocity $\boldsymbol{v}$ such that electrodynamic effects can be neglected. The electrostatic *net* force on a domain Ω containing q is

$$\boldsymbol{F}^q = \int_\Omega q\boldsymbol{E}\, dV. \tag{3.22}$$

Note that this almost looks like the Lorentz force, but it is not exactly the same. Here we consider a charge density q instead of a single charged particle without saying what

[6] To be precise, "free" means that we may move this charge around independent of other charges, but we are also free to stick in to a piece of matter such that it can only move together with its new carrier. On the contrary, a bound charge can only be moved by a tiny distance such that it will go back to some equilibrium position when it is released. Both "free" and "bound" are of course idealizations. The essential question is how much energy is needed to arbitrarily move a certain charge and the transition is not always sharp.

q represents exactly.[7] It is important to note here that in absence of an external field, a body with a charge distribution may deform but never experience a net force just because of being charged or polarized in a uniform or non-uniform manner. Thus, the total force only depends on the external electric field in the sense that

$$\boldsymbol{F}^q = \int_\Omega q\boldsymbol{E}\, dV = \int_\Omega q\boldsymbol{E}^{\text{ext}}\, dV. \tag{3.23}$$

If one imagines polarization $\boldsymbol{P}$ as a pair of two charges of equal magnitude but opposite sign separated by only a small distance, one arrives at the following formula of the total force on a polarized domain of space (see, e.g., Pao and Hutter (1975))

$$\boldsymbol{F}^P = \int_\Omega \boldsymbol{P} \cdot \operatorname{grad} \boldsymbol{E}\, dV = \int_\Omega \boldsymbol{P} \cdot \operatorname{grad} \boldsymbol{E}^{\text{ext}}\, dV. \tag{3.24}$$

Such complications in the transition from particles towards densities and continua in the context of electrostatics and electromechanics are source of a lot of confusion in literature (cf. McMeeking and Landis (2004)). With these considerations in mind we introduce a "net force density" $\boldsymbol{f}^{\text{q}}$

$$\boldsymbol{f}^q = q\boldsymbol{E}^{\text{ext}}. \tag{3.25}$$

The associated infinitesimal work density for moving q against $\boldsymbol{f}^q$ is

$$dw^q = -q\boldsymbol{E}^{\text{ext}} \cdot d\boldsymbol{L}. \tag{3.26}$$

We obtain the work density w^{q} through integration where we make use of (3.21)

$$w^q(x = x_2 - x_1) = \int_{x_1}^{x_2} q \operatorname{grad} \phi^{\text{ext}} \cdot d\boldsymbol{L} = q\left(\phi^{\text{ext}}(x_2) - \phi^{\text{ext}}(x_1)\right) = q\Delta\phi^{\text{ext}}. \tag{3.27}$$

Therefore, $\Delta\phi^{\text{ext}} = w^q/q$ is a measure for work per charge. Conversely, we may call $\phi^{\text{ext}}(x)q$ the potential energy of q with respect to some initial position x_1 for which $\phi^{\text{ext}}(x_1) = 0$ similar to the potential energy of a mass under (external) gravity.

Next, consider a domain $\mathcal{B} \subset \mathbb{R}^3$ with boundary $\partial\mathcal{B}$. According to the above considerations, the power P^{ext} for "pumping" charge density into $\mathcal{B}$ and a surface charge

[7] For example, imagine that q represents charges which are attached to a rigid grid. If the grid were not rigid, it would deform until an equilibrium state is attained. But this would only complicate matters too much for now. Interestingly, in this sense the free charge density q is an aggregate of bound charges that move collectively.

density onto $\partial\mathcal{B}$ is[8] (McMeeking and Landis, 2004)

$$P^{\text{ext}} = \int_{\mathcal{B}} \phi\dot{q}\, dV + \int_{\partial\mathcal{B}} \phi\dot{q}^{\text{s}}\, dA. \tag{3.28}$$

Via the divergence theorem, the product rule, the jump conditions (3.20), $\dot{q} = 0$ in $\mathbb{R}^3 \setminus \mathcal{B}$ and $\phi, \boldsymbol{D} \to 0$ in great distance from $\mathcal{B}$ it is possible to transform (3.28) into the well-known form

$$P^{\text{ext}} = \int_{\mathcal{B}} \boldsymbol{E}\cdot\dot{\boldsymbol{D}}\, dV + \int_{\mathbb{R}^3\setminus\mathcal{B}} \boldsymbol{E}\cdot\dot{\boldsymbol{D}}\, dV = \int_{\mathbb{R}^3} \boldsymbol{E}\cdot\dot{\boldsymbol{D}}\, dV. \tag{3.29}$$

Let Π denote the stored energy in $\mathbb{R}^3$. Then, following the same line of thought as in Section 2.4, $\dot{\Pi} \leq P^{\text{ext}}$ where equality holds in equilibrium, we do not further investigate any dissipative processes but are only interested in an equilibrium state. Thus, we directly proceed with the assumption of an energy density $\Psi(\boldsymbol{D})$ in whole $\mathbb{R}^3$ – irrespective of the presence or absence of matter – such that (Suo et al., 2008)

$$\dot{\Pi}(\boldsymbol{D}) = \int_{\mathbb{R}^3} \dot{\Psi}(\boldsymbol{D})\, dV = \int_{\mathbb{R}^3} \boldsymbol{E}\cdot\dot{\boldsymbol{D}}\, dV \tag{3.30}$$

and

$$\boldsymbol{E} = \frac{\partial\Psi(\boldsymbol{D})}{\partial\boldsymbol{D}} \tag{3.31}$$

at equilibrium[9].

For the empty domain $\mathbb{R}^3\setminus\mathcal{B}$ we have in case of an aether frame the relation $\boldsymbol{E} = \boldsymbol{D}/\epsilon_0$ such that

$$\Psi(\boldsymbol{D}) = \Psi^{\text{vac}}(\boldsymbol{D}) = \frac{1}{2\epsilon_0}\boldsymbol{D}\cdot\boldsymbol{D} \quad \text{in } \mathbb{R}^3\setminus\mathcal{B}. \tag{3.32}$$

Next we bring together (3.28) and (3.30) under assumption that $-P^{\text{ext}}$ is the time rate of an external potential $\Pi^{\text{ext}}(q)$

$$\dot{\mathcal{L}}^{\text{e}} \leq 0 \qquad \text{with} \qquad \mathcal{L}^{\text{e}} = \int_{\mathbb{R}^3} \Psi(\boldsymbol{D})\, dV + \Pi^{\text{ext}}(q), \tag{3.33}$$

where equality holds at equilibrium.

Remark 3.1. The derivation of (3.30) started from charge densities. Despite that, it is naturally applicable to polarizable bodies.

[8] We recommend the contributions of McMeeking and Landis (2004) and Suo et al. (2008) for a discussion of these matters. While their considerations involve deformable media, their derivations can be easily broken down to the rigid setting.

[9] Note that rates cannot be of arbitrary magnitude in electro*statics* but they still can be of arbitrary direction, which is all we require in the present scope.

3.4. Magnetostatics

In magnetostatics we have basically the same conditions as in electrostatics, that is negligible time rates such that electric and magnetic phenomena are decoupled.

3.4.1. Magnetostatic equations

The magnetostatic equations are obtained as

$$\operatorname{div} \boldsymbol{B} = 0 \qquad \operatorname{curl} \boldsymbol{H} = \boldsymbol{j} \qquad \boldsymbol{H} = \boldsymbol{B}/\mu_0 - \boldsymbol{M}, \tag{3.34}$$

which are accompanied by the jump conditions

$$\boldsymbol{n} \cdot [\![\boldsymbol{B}]\!] = 0 \qquad \boldsymbol{n} \times [\![\boldsymbol{H}]\!] = \boldsymbol{j}^{\mathrm{s}}. \tag{3.35}$$

Like already before in the full electrodynamic case (3.10) the magnetic field $\boldsymbol{B}$ is obtained from the magnetic vector potential via

$$\boldsymbol{B} = \operatorname{curl} \boldsymbol{A}. \tag{3.36}$$

In addition, we have the identity

$$\operatorname{div} \boldsymbol{j} = \operatorname{div} \operatorname{curl} \boldsymbol{H} \equiv 0, \tag{3.37}$$

which is a direct consequence of $\dot{\boldsymbol{D}} = \boldsymbol{0}$. Moreover, in the case of vanishing currents, $\boldsymbol{H}$ can be expressed as the negative gradient of an (auxililary) scalar-valued magnetic potential ϕ^{m} in analogy to (3.21)

$$\boldsymbol{H} = -\operatorname{grad} \phi^{\mathrm{m}} \quad \Longleftrightarrow \quad \boldsymbol{j} = \boldsymbol{0}. \tag{3.38}$$

In this case the mathematical structure of magnetostatics is exactly the same as for electrostatics, except for the fact that $\operatorname{div} \boldsymbol{B} = 0$ holds always and everywhere. However, physically reasonable boundary conditions as well as relations between $\boldsymbol{M}$, $\boldsymbol{B}$ and $\boldsymbol{H}$ are quite different from their counterparts in electrostatics.

3.4.2. Magnetostatic force and energy

The fundamentals of magneto-mechanical interactions of deformable bodies are covered by the monograph of Brown (1966). Although we for now deal with magnetostatics of rigid bodies only, the present section is, with minor exceptions, based on the first sections of this standard reference.

In electrostatics the primitive object on which the field exerts a force is the charge or a charge density. In magnetostatics charge itself does not play a role. But from the Lorentz force (3.4) we see that moving charge represented by $q\boldsymbol{v}$ experiences a force in presence of $\boldsymbol{B}$. However, a moving or transported charge (density) is in this case equivalent to a

current (density). Hence, we consider the (net) force on a current density to be (Brown, 1966, Section 2.5)

$$\boldsymbol{F}^{\mathrm{m}} = \int_{\Omega} \boldsymbol{j}^{\mathrm{tot}} \times \boldsymbol{B}^{\mathrm{ext}}\, dV = \int_{\Omega} (\operatorname{curl} \boldsymbol{H} + \operatorname{curl} \boldsymbol{M}) \times \boldsymbol{B}^{\mathrm{ext}}\, dV = \int_{\Omega} \frac{1}{\mu_0} \operatorname{curl} \boldsymbol{B} \times \boldsymbol{B}^{\mathrm{ext}}\, dV, \tag{3.39}$$

where we note that by the "external" nature of $\boldsymbol{B}^{\mathrm{ext}}$, i.e. it is not produced by $\boldsymbol{j}^{\mathrm{tot}}$ such that $\operatorname{curl} \boldsymbol{B}^{\mathrm{ext}} = 0$ where $\boldsymbol{j}^{\mathrm{tot}} \neq 0$. Considering only free current densities the local force is

$$\boldsymbol{f}^{j} = \boldsymbol{j} \times \boldsymbol{B}. \tag{3.40}$$

From this formula we see that the force is normal to the the direction of the current. Thus a stationary current exposed to a stationary magnetic field does not do any work. Work is only done when driving charges against an electric field $\boldsymbol{E}$. Equation $(3.12b)_2$ tells us that an electric field aligned with the current is created by an instationary magnetic field $\boldsymbol{B}$. The corresponding power is

$$P^{\mathrm{ext}} = -\int_{\Omega} \boldsymbol{j} \cdot \boldsymbol{E}\, dV = \int_{\Omega} \boldsymbol{j} \times \dot{\boldsymbol{B}}\, dV, \tag{3.41}$$

which is the continuous version of the power of a current I in a coil (a closed circuit around $\mathcal{S}$) against[10] the induced electromotive force f^{em} (Brown, 1966, Section 2.6)

$$P^{\mathrm{ext}} = -I f^{\mathrm{em}} = -I(-\dot{\Phi}^{\mathrm{m}}) = I \int_{S} \frac{\partial \boldsymbol{B}}{\partial t} \cdot \boldsymbol{n}\, dA = I \int_{\partial S} \dot{\boldsymbol{A}} \cdot d\boldsymbol{L}. \tag{3.42}$$

The current potential $\boldsymbol{H}$ corresponding to I is computed as

$$\boldsymbol{H}(x) = -I \int_{\partial S} \frac{\boldsymbol{r}}{\|\boldsymbol{r}\|^3} \times d\boldsymbol{L} \tag{3.43}$$

with $\boldsymbol{r}$ denoting the distance vector from a point in $\partial\mathcal{S}$ to the position x. Conversely, the vector potential created by a magnetized domain Ω in great distance is (Brown, 1966, Section 2.3)

$$\boldsymbol{A}(x) = \mu_0 \int_{\Omega} \frac{\boldsymbol{M} \times \boldsymbol{r}}{\|\boldsymbol{r}\|^3}\, dV. \tag{3.44}$$

To distinguish fields from different "sources" we will below refer to $\boldsymbol{H}$ according to (3.43) as $\boldsymbol{H}^{\mathrm{c}}$ ("c" for coil) and to $\boldsymbol{A}$ according to (3.44) as $\boldsymbol{A}^{\mathrm{self}}$. Moreover, we from now

[10] The sign convention for the electromotive force might appear counter-intuitive for reader trained in mechanics. The notion itself refers to the fact that in order to move a charge against a field, one has to exert a force on that charge. However, this force usually comes as well from an electric field but must be distinguished from the electric field against which the work is done. The question is whether on uses the term electromotive force for the "driver" or for the "resistance". In this thesis we follow the terminology of (Brown, 1966, Section 2.6). Svendsen and Chanda (2005), for example, follow the converse convention.

on consider I as stationary and thus $\dot{\boldsymbol{A}} = \dot{\boldsymbol{A}}^{\text{self}}$. We employ (3.43) and (3.44) in (3.42), where one $\boldsymbol{r}$ is the negative of the other, and arrive at (Brown, 1966, Eq. (2.53))

$$\begin{aligned} P^{\text{ext}} &= \int_{\mathcal{B}} \mu_0 \boldsymbol{H}^{\text{c}} \cdot \dot{\boldsymbol{M}} \, dV = \int_{\mathcal{B}} \mu_0 \boldsymbol{H} \cdot \dot{\boldsymbol{M}} \, dV - \int_{\mathcal{B}} \mu_0 \boldsymbol{H}^{\text{self}} \cdot \dot{\boldsymbol{M}} \, dV \\ &= \int_{\mathcal{B}} \mu_0 \boldsymbol{H} \cdot \dot{\boldsymbol{M}} \, dV - \int_{\mathbb{R}^3} \frac{\mu_0}{2} \frac{\mathrm{d}(\boldsymbol{H}^{\text{self}})^2}{\mathrm{d}t} \, dV, \end{aligned} \tag{3.45}$$

or alternatively

$$\begin{aligned} \bar{P}^{\text{ext}} &= \int_{\mathcal{B}} \boldsymbol{B}^{\text{c}} \cdot \dot{\boldsymbol{M}} \, dV = \int_{\mathcal{B}} \boldsymbol{B} \cdot \dot{\boldsymbol{M}} \, dV - \int_{\mathcal{B}} \boldsymbol{B}^{\text{self}} \cdot \dot{\boldsymbol{M}} \, dV \\ &= \int_{\mathcal{B}} \boldsymbol{B} \cdot \dot{\boldsymbol{M}} \, dV + \int_{\mathbb{R}^3} \frac{1}{2\mu_0} \frac{\mathrm{d}(\boldsymbol{B}^{\text{self}})^2}{\mathrm{d}t} \, dV, \end{aligned} \tag{3.46}$$

Note that the last integral in both of (3.45) and (3.46) is over all space. They represent *non-local* contributions to the virtual work expended on the body $\mathcal{B}$. This means that the integrands $\mu_0 \boldsymbol{H}^{\text{self}} \cdot \dot{\boldsymbol{M}}$ and $\boldsymbol{B}^{\text{self}} \cdot \dot{\boldsymbol{M}}$ cannot be determined without any information about the shape of the domain $\mathcal{B}$ because the self-fields have to fulfill their differential equations and jump conditions not only inside $\mathcal{B}$ but everywhere in $\mathbb{R}^3$.

At equilibrium, following the reasoning in elasto- and electrostatics before, we equate the virtual magnetic work with the time rate of the stored magnetostatic energy $\Pi(\boldsymbol{M})$

$$\dot{\Pi}(\boldsymbol{M}) = P^{\text{ext}} = \int_{\mathcal{B}} \mu_0 \boldsymbol{H}^{\text{c}} \cdot \dot{\boldsymbol{M}} \, dV = \int_{\mathcal{B}} \mu_0 \boldsymbol{H} \cdot \dot{\boldsymbol{M}} - \mu_0 \boldsymbol{H}^{\text{self}} \cdot \dot{\boldsymbol{M}} \, dV = 0. \tag{3.47}$$

The last term is non-local as mentioned above such that we shall not include in some kind of internal energy density $\Psi(\boldsymbol{M})$. Neglecting any dissipative processes[11] we may define

$$\int_{\mathcal{B}} \Psi(\boldsymbol{M}) \, dV = \Pi(\boldsymbol{M}) + \int_{\mathcal{B}} \frac{\mu_0}{2} \boldsymbol{H}^{\text{self}} \cdot \boldsymbol{M} \, dV. \tag{3.48}$$

With that we finally arrive at a function $\mathcal{L}$

$$\mathcal{L} = \int_{\mathcal{B}} \Psi(\boldsymbol{M}) \, dV - \int_{\mathcal{B}} \frac{\mu_0}{2} \boldsymbol{H}^{\text{self}} \cdot \boldsymbol{M} \, dV - \int_{\mathcal{B}} \mu_0 \boldsymbol{H}^{\text{c}} \cdot \boldsymbol{M} \, dV \tag{3.49}$$

again fulfilling $\dot{\mathcal{L}} \leq 0$. Based on that the magnetostatic equilibrium condition is $\dot{\mathcal{L}} = 0$. The analogon of (3.49) derived using $\bar{P}^{\text{ext}}$ (3.46) is

$$\bar{\mathcal{L}} = \int_{\mathcal{B}} \bar{\Psi}(\boldsymbol{M}) \, dV + \int_{\mathcal{B}} \frac{1}{2\mu_0} \boldsymbol{B}^{\text{self}} \cdot \boldsymbol{M} \, dV - \int_{\mathcal{B}} \boldsymbol{B}^{\text{c}} \cdot \boldsymbol{M} \, dV. \tag{3.50}$$

[11] An important example is magnetic hysteresis, which we do not consider in this work.

The constitutive relations obtained from (3.49) and (3.50) are

$$\frac{\partial \Psi(\boldsymbol{M})}{\partial \boldsymbol{M}} = \mu_0 \boldsymbol{H} \qquad \text{and} \qquad \frac{\partial \bar{\Psi}(\boldsymbol{M})}{\partial \boldsymbol{M}} = \boldsymbol{B}, \tag{3.51}$$

respectively.

Deviating from Brown (1966), we now discuss the case when I consists of a current density $\boldsymbol{j}$. Then, (3.42) turns into

$$P^{\text{ext}} = \int_\Omega \boldsymbol{j} \times \dot{\boldsymbol{B}}\, dV = \int_\Omega \boldsymbol{j} \cdot \dot{\boldsymbol{A}}\, dV, \tag{3.52}$$

where Ω must fully enclose $\boldsymbol{j}$. When this is used as starting point instead of (3.45) or (3.46) it is natural to come up with an internal energy $\Pi(\boldsymbol{B})$. Since we do not see anything non-local terms in (3.52) we write the balance of energy at equilibrium as

$$\dot{\Pi}(\boldsymbol{B}) = \int_\Omega \frac{\partial \widehat{\Psi}(\boldsymbol{B})}{\partial \boldsymbol{B}} \cdot \dot{\boldsymbol{B}}\, dV = P^{\text{ext}} = \int_\Omega \boldsymbol{j} \cdot \dot{\boldsymbol{A}}\, dV, \tag{3.53}$$

where we note that for P^{ext} to assume the given form, Stokes' theorem has to be applicable, which reveals the auxiliary[12] nature of $\boldsymbol{A}$ and justifies the dependence of the internal energy Π on $\boldsymbol{B}$ instead of $\boldsymbol{A}$. Using the identity (see, e.g., Bustamante et al. (2008))

$$\operatorname{div}(\dot{\boldsymbol{A}} \times \boldsymbol{H}) = \boldsymbol{H} \cdot \dot{\boldsymbol{B}} - \operatorname{curl} \boldsymbol{H} \cdot \dot{\boldsymbol{A}} \tag{3.54}$$

one obtains with $\boldsymbol{B} = \operatorname{curl} \boldsymbol{A}$

$$\boldsymbol{H} = \frac{\partial \widehat{\Psi}(\boldsymbol{B})}{\partial \boldsymbol{B}} \qquad \text{such that} \qquad \operatorname{curl} \boldsymbol{H} = \boldsymbol{j}. \tag{3.55}$$

For $\boldsymbol{j}$ being the only external contribution the governing functional $\mathcal{L}$ follows as

$$\mathcal{L} = \int_{\mathbb{R}^3} \widehat{\Psi}(\boldsymbol{B}) - \boldsymbol{j} \cdot \boldsymbol{A}\, dV, \tag{3.56}$$

again with $\dot{\mathcal{L}} \leq 0$ and equality holding at equilibrium. This is in perfect agreement with (3.49) and (3.50). For a discussion of the relations between the many possible formulations of magnetostatics we refer to Bustamante et al. (2008)[13].

[12] In quantum-electrodynamics there exists the Aharonov-Bohm effect (Aharonov and Bohm, 1959) which allows a different conclusion (Feynman et al., 2011). But physicists are still concerned with the Aharonov-Bohm effect and the question of the physical (non-)significance of the electromagnetic potentials $(\phi, \boldsymbol{A})$, e.g. Pearle and Rizzi (2017).

[13] They actually cover magneto-mechanics. However, their results are also useful for pure magnetostatics.

— Part I —

General theory and mathematical concepts

General theory and mathematical concepts
This first part of the thesis comes in two main Chapters 4 and 5. The former is concerned with variational principles for magneto-electro-mechanics. In that chapter we devote the first section to differential geometry beyond "classical" tensor calculus which is mainly based on material from Marsden and Hughes (1994), Burke (1996) and Frankel (2011) and heavily inspired by Kanso et al. (2007) and Bossavit (2010, 2012). We then employ the "new" notions to re-classify the physical quantities of Chapters 2 and 3. After translating also the governing equations into the "new" language we present several variational principles for magneto-electro-elasticity in a quasi-static setting. The differential geometry framework chosen is not the most common one in the finite elasticity and magneto-electro-mechanics community. One could say that it just too complicated for what is usually done in this field. On the one hand this is true since we did not derive anything which does not yet exist in classical tensor calculus. Moreover, not everything can be expressed more elegantly in the "new" framework. On the other hand, many aspects which are difficult to master or to understand in tensor calculus are more natural or obvious in the "new" versions. Let us compare both approaches as follows: Tensor calculus has a small set of objects but a complex set of rules how to treat them. This leads to the situation that many of the "vectors" encountered do not transform as vectors under changes of coordinates but follow different transformation rules which are not imprinted in the objects themselves. The "new" differential-geometric approach has a rich set of different objects but in turn a much more consistent set of operations. In retrospective we appreciate the additional insight gained by translating one framework into the other. This was not always without pain though, since we had to derive several formulae and results of which the tensor-calculus version is readily available. Here we mention once again the works of Kanso et al. (2007) and Bossavit (2012) which served as excellent starting points.

After the main chapter on variational principles we in Chapter 5 provide a discussion of variational homogenization in nonlinear magneto-electro-elasticity within the framework developed in Chapter 4.

We note that it is not necessary to go through all that just as preparation for Part II, which is largely self-contained.

Chapter 4

Variational principles for magneto-electro-mechanics

In this chapter we first introduce several mathematical notions and tools before we proceed with our theoretical presentation of magneto-electro-elasticity.

4.1. An introduction to differential geometry

In Chapters 2 and 3 we worked with classical vector calculus in Euclidean space. Thereby, we did not assume that the reader has deep knowledge in this field and kept the mathematical presentation simple. However, we believe it is not only occasionally required but also beneficial for a deeper understanding to make the reader familiar with certain notions of differential geometry. Since this is a vast field by itself, we restrict the presentation to those aspects which are at the heart of variational principles from an engineering perspective. That is integration, differentiation of integrals and integral theorems like those of Gauß, Green and Stokes. Besides that we try to explain these concepts by means of quantities and equations presented in Chapters 2 and 3 above.

For the interested reader we recommend the monographs by Burke (1996) and Frankel (2011), which focus on the applications of differential geometry in physics as well as to Marsden and Hughes (1994) focusing on finite elasticity. Next to that, we complementarily mention the monographs of Epstein (2010) and Steinmann (2015). Moreover, we note that we did not start reading Tonti (2013) before completing the main work on the present chapter. However, this monograph with a scope somewhat similar to Frankel (2011) certainly deserves being mentioned for its outstanding focus on the big picture ("Tonti diagrams") and the numerous historical references.

A disclaimer regarding notation: We keep boldface letters for vectors, upright boldface letters for fully co- or contravariant second-order tensors and underlined symbols for objects of "mixed" type. However, below we will introduce many new (types of) objects and it is impossible to give all of them a dedicated font or font-style. Since we expect many readers to be unfamiliar with a large portion of the differential geometric quantities and objects, we introduce most of the notation step by step alongside the respective objects and occasionally comment on our choice. By that we hope to achieve good readability. It is the first time that we delve into this field and there are not many good examples from which to borrow notation. Furthermore, the necessity to cover not only mechanics but also electromagnetism leads to additional notation-clashes (even in classical notation). Thus, what follows will probably not be without any rough edges.

4.1.1. Differentiable manifolds

We begin with a brief definition of smooth n-manifolds

Definition 4.1. (Marsden and Hughes, 1994, p. 35, Definition 2.1)

> "A *smooth n-manifold* (or a manifold modeled on $\mathbb{R}^n$ is as set $\mathcal{M}$ such that: (1) For each $P \in \mathcal{M}$ there is a subset $\mathcal{U}$ of $\mathcal{M}$ containing P, and a one-to-one mapping, called *chart* or *coordinate system*, $\{x^\alpha\}$ from $\mathcal{U}$ onto an open set $\mathcal{V}$ in $\mathbb{R}^n$; x^α will denote the components of this mapping ($\alpha = 1, 2, \dots, n$). (2) If $\{x^\alpha\}$ and $\{\bar{x}^\alpha\}$ are two such mappings, the change of coordinate functions $\bar{x}^\alpha(x^1, x^2, \dots, x^n)$ are C^∞.
>
> If $\{\bar{\bar{x}}^\alpha\}$ maps a set $\mathcal{U} \subset \mathcal{M}$ one-to-one onto an open set in $\mathbb{R}^n$, and if the change of coordinate functions with the given coordinate functions are smooth (C^∞), then $\{\bar{\bar{x}}^\alpha\}$ will also be called a *chart* or *coordinate system*."

Please note that there exist other, more involved definitions of differentiable manifolds, e.g. as in Frankel (2011, Section 1.2). In the remainder of this thesis we simply use the term "n-manifold" (or simply "manifold") to refer to a *differentiable* or *smooth* n-manifold. A *body* is a special case of a manifold

Definition 4.2. (Marsden and Hughes, 1994, p. 25, Definition 1.1)

> "A *simple body* is an open set $\mathcal{B} \subset \mathbb{R}^n$. A *configuration* of $\mathcal{B}$ is a mapping $\varphi : \mathcal{B} \mapsto \mathbb{R}^n$. The set of all configurations of $\mathcal{B}$ is denoted $\mathscr{C}$, or by $\mathscr{C}(\mathcal{B})$ if there is danger of confusion. Points in $\mathcal{B}$ are labeled by capital letters, e.g. X. By convention, $(x^1, x^2, \dots, x^n) = x$ denote coordinates of $\mathbb{R}^n$."

During deformation, bodies attain different configurations. The configuration at initial time $t = 0$ is the *initial* configuration. We pick the coordinates of this configuration to label points in $\mathcal{B}$ such that $X = x = \varphi(X; t = 0)$, i.e. $\varphi(X; t = 0)$ is the identity map. Thus, we identify the initial configuration with the *Lagrangian* or *material* configuration. This, however, is not necessarily the case in general. Another term occasionally encountered is "referential configuration", which in the present context simply refers to the initial configuration. Moreover, we assume that the initial configuration is *undeformed*. Conversely, configurations at any time $t > 0$ are referred to as *deformed* configurations or "the *current* configuration" $\mathcal{B}_t = \varphi(\mathcal{B}, t)$. If there is no chance of confusion, we will emloy the symbol φ also for other mappings than the one between configurations of a body.

Remark 4.1. Neither x nor X represent vectors (see Section 4.1.2) on $\mathcal{B}_t$ or $\mathcal{B}$, respectively, but simply tuples of coordinate values. We shall not use the notion of "location vector" without explicitly mentioning it. Steinmann (2015, Part III) discusses the relation between Euclidean coordinates allowing for position vectors and general curvilinear coordinates in great detail.

Remark 4.2. In the above definitions neither bodies nor manifolds include their possibly existing boundaries. We explicitly refer to boundaries as $\partial\mathcal{B}$ or as $\partial\mathcal{M}$, respectively. A boundary is also a manifold and never has a boundary itself (Frankel, 2011).

Remark 4.3. In practical applications we encounter bodies with boundaries that contain edges or corners, that is they are smooth only almost[1] everywhere. However, boundaries will effectively appear mainly in integrals, such that we presently should not be too concerned about that.

4.1.2. Vectors and one-forms

In Chapters 2 and 3 we presumed some knowledge about "standard" vector calculus in $\mathbb{R}^n$. The only (second-order) tensors that occurred were the Cauchy stress tensor, the deformation gradient and right Cauchy-Green tensor. We did not elaborate on their nature beyond what had been absolutely necessary. In the present section we introduce various geometric objects to some of which people often refer to as "vectors" or "tensors". Indeed, this does not do great harm once we know a number of subtleties and only work with Cartesian coordinates and Euclidean space. However, we believe that it is instructive to at least inform about the zoo of different geometric objects we are actually dealing with.

Example 4.1. Velocity*: Consider the trajectory $c(t)$ of a particle in $\mathbb{R}^2$ as depicted in Figure 4.1. At time $t = t_1$ the particle's position is $c(t_1)$ and its velocity is $\dot{c}(t_1) = (\mathrm{d}c/\mathrm{d}t)(t_1)$. The velocity clearly is tangential to $c(t)$ and is most naturally illustrated by an arrow based at $c(t_1)$, which is the common representation of a* vector*. Then, at time $t = t_2$ the velocity $\dot{c}(t_2)$ is represented by a vector tangential to c at $c(t_2)$. It does not make sense to add the two vectors $\dot{c}(t_1)$ and $\dot{c}(t_2)$ since they correspond to velocities at different points in time and space.*

Next, consider another trajectory $c'(t')$. At time $t' = t'_1$ it shall be tangential to c, i.e. $c'(t'_1) = c(t_1)$ and $\dot{c}'(t'_1) = \lambda\dot{c}(t_1)$ with a scalar factor λ. In terminology of differential geometry, the two curves are tangential *if and only if $\lambda = 1$. For $\lambda \neq 1$ the curves are said to be in* contact*. Two tangential trajectories thus have the same velocity vector at their point of contact. Conversely, a single velocity vector may be understood as the (local) representation a all trajectories with velocity $\boldsymbol{v} = \dot{c}(t)$ at point $x = c(t)$ (Burke, 1996).*

Velocity is the prototypical example of what is referred to as a *tangent vector* or simply a *vector*. The space of (tangent) vectors based at a point $x \in \mathcal{M}$ is denoted as $\mathrm{T}\mathcal{M}_x$. The collection of all $\mathrm{T}\mathcal{M}_x$ over $\mathcal{M}$ is the *tangent bundle* $\mathrm{T}\mathcal{M}$. We emphasize here that displacement, i.e. a difference between two positions is not a *tangent* vector.

An important property of geometrical objects is how their representation changes under a change of coordinates. For the velocity vector of a parameterized curve $c(t)$ represented in coordinates $\{x^i\}$ as $c_{(x)}(t) = (x^1(t), x^2(t))$ and in $\{y^i\}$ as $c_{(y)}(t) = (y^1(t), y^2(t))$ we have the velocity *components*

$$\frac{\mathrm{d}y^i(t)}{\mathrm{d}t} = \sum_j \frac{\partial y^i}{\partial x^j}\frac{\mathrm{d}x^j(t)}{\mathrm{d}t}, \tag{4.1}$$

[1] We do not consider the case of fractals or similar objects.

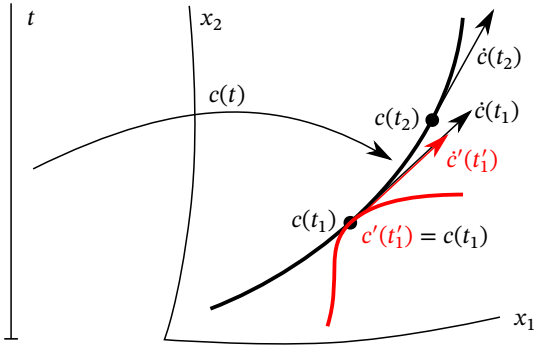

Figure 4.1: The curve $c(t)$ and two tangent vectors at $t = t_1$ and $t = t_2$. Of course, other curves that "touch" c at some point(s), e.g. c', could have the *same* tangents. Then, such curves are *tangent* to each other. If only the direction of respective tangents is the same, as is the case for $\dot{c}(t_1)$ and $\dot{c}'(t'_1)$, one speaks of *contact*. If we are only given a tangent vector we can think of it as the representation of all curves featuring exactly this tangent at this very point. Also the coordinate lines themselves are just curves.

or, using the Einstein summation convention which implies summation over double indices of different "vertical" position,

$$\frac{\mathrm{d}y^i(t)}{\mathrm{d}t} = \frac{\partial y^i}{\partial x^j}\frac{\mathrm{d}x^j(t)}{\mathrm{d}t}. \tag{4.2}$$

Some authors, e.g. Frankel (2011), define vectors by this transformation rule. However, we prefer to consider Example 4.1 as definition of a vector and by that follow Burke (1996).

Example 4.2. Electric potential and electric field*: Consider an electric potential ϕ in $\mathbb{R}^2$ with iso-lines (equipotential lines) as depicted in Figure 4.2. These iso-lines, although being lines, are not parameterized like trajectories in the example above. For them there is no natural definition of a velocity or tangent vector. However, for the iso-lines of the potential there still exists a natural local property, namely the "closeness" or density of iso-lines. Locally we may represent this by two parallel straight lines "tangent" to an iso-line as shown in Figure 4.2. Clearly, these two straight lines in red colour represent two iso-lines of infinitesimal potential difference at a certain point $x \in \mathbb{R}^2$. They are straight because they are only first-order representations in the same sense as tangent vectors, which also do not represent curvature. Similarly, they thus locally represent not only a single potential but all potentials of which the iso-lines at this very point coincide in the sense of being in contact.*

Now consider a unit test charge being moved from one iso-line to another with velocity $\boldsymbol{v} = \dot{c}(t)$. Let $\dot{\phi}$ denote the corresponding change in the potential seen by the charge during

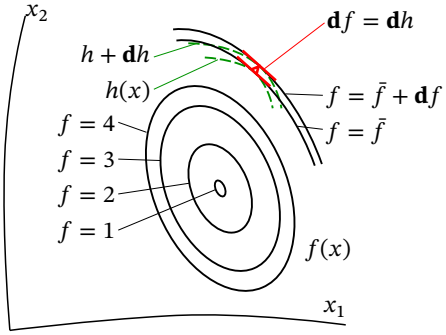

Figure 4.2: Equipotential (or "iso"-)lines (black) of the function $f(x)$. The one-form (red) here represents (infinitely) close iso-lines separated by a given potential difference characterized by $\mathbf{d}f$. Thus, one-forms measure the density of iso-lines. Moreover, in the infinitesimal limit, the curvature of the iso-lines does not play a role such that a one-form representing iso-lines of $f(x)$ at a point could at the same time represent iso-lines of $h(x)$ (green, dashed), i.e.$\mathbf{d}f = \mathbf{d}h$ and one point x. We also say that in such a case $f(x)$ and $h(x)$ are *locally* equivalent (at some point x and to first order).

an infinitesimal amount of time. In this limit, there is a linear relation $\dot{\phi} = -z_1 v^1 - z_2 v^2 = -\mathfrak{z}(\boldsymbol{v})$*, where* $\mathfrak{z}$ *is a linear map taking a (one) vector* $\boldsymbol{v}$ *and returning a scalar* $\dot{\phi}$*. In fact,* $\mathfrak{z}$ *plays the role of the electric field as in (3.26): this is the reason for the minus. Visually,* $\mathfrak{z}$ *can be understood as a measure of how many iso-lines with a certain infinitesimal potential difference are crossed by* $\boldsymbol{v}$ *and thus corresponds to the picture of iso-line density as visualized in Figure 4.3. From this discussion it is clear that* $\mathfrak{z}$ *is quite different from a (tangent) vector. Indeed, it is the dual concept in the same sense as force is dual to velocity.*

We shall refer to objects like $\mathfrak{z}$, that is linear functionals mapping vectors into scalars, as one-forms[2]. Later we will introduce higher-order forms such that we often write, e.g., ${}^1\mathfrak{z}$ to emphasize the degree. Also note that the components of ${}^1\mathfrak{z}$ are denoted as z_i.

In the example above, the one-form is obviously related to a scalar function, the electric potential ϕ. In components we would write for the derivative of ϕ with respect to the curve parameter t

$$\dot{\phi} = \frac{\partial \phi}{\partial x^i}\frac{\mathrm{d}x^i}{\mathrm{d}t} = v^i \frac{\partial \phi}{\partial x^i} = \left(\frac{\mathrm{d}x^i}{\mathrm{d}t}\frac{\partial}{\partial x^i}\right)\phi. \tag{4.3}$$

The term in braces features the components of the velocity and the partial differential operators corresponding to this spatial component. Indeed, this term is the full coordi-

[2]Some authors at this stage use the term co-vector and reserve one-form for fields. There does not seem to be a unique terminology.

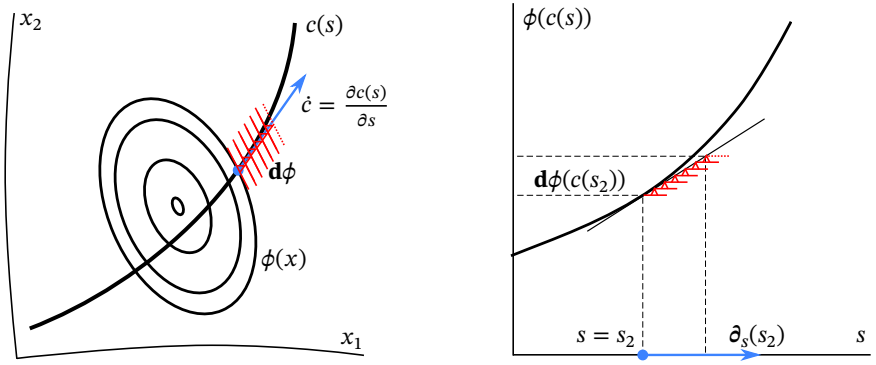

Figure 4.3: The "product" of a vector and a one-form can be thought of as the number of how many times one-forms can be crossed by the vector. On the left this is sketched by means of the graphs of ϕ and $c = c(s)$ in the x_1-x_2-plane. On the right, we show the same scene with ϕ plotted along the curve parameter s. In that case, the vector $\dot{c}$ appears in form of the basis vector ∂_s. The action of ∂_s on $\mathbf{d}\phi(c(s))$ in the sketch on the right boils down to the derivative $\mathrm{d}\phi/\mathrm{d}s$. Also note that while we used curvilinear coordinates for physical space on the left, we opted a Cartesian representation on the right. By this we reflect the different physical interpretations of the spaces spanned by the respective coordinates. However, on could formally introduce curvilinear coordinates in the ϕ-s plane as well.

nate expression of the velocity vector $\boldsymbol{v}$, i.e. components *and* basis,

$$\boldsymbol{v} = \frac{\mathrm{d}x^i}{\mathrm{d}t}\frac{\partial}{\partial x^i} = \frac{\mathrm{d}x^i}{\mathrm{d}t}\partial_{x^i} = v^i\partial_{x^i} \quad \Rightarrow \quad \boldsymbol{v}(f) = v^i\frac{\partial f}{\partial x^i} \tag{4.4}$$

where ∂_{x^i} is a shorthand for the *basis vector* connected to $\partial/\partial x^i$. It is important to note that the derivatives represented by ∂_{x^i} are never applied to the vector components but only to functions on which we apply the vector. From this discussion we also see that one may regard a vector $\boldsymbol{v}$ applied on a function f as the directional derivative operator (Marsden and Hughes, 1994; Burke, 1996). We point out that ∂_{x^i} when applied to functions does exactly the same as the differential operator. However, this is not necessarily the case when applied to other objects as we shall see in (4.14).

Converse to the viewpoint of a vector acting on a function as in (4.3), the partial derivatives $\partial\phi/\partial x^i$ can be interpreted as components to the basis $\mathbf{d}x^i$ forming an object on its own – the differential of ϕ denoted as $\mathbf{d}\phi$:

Definition 4.3. (Frankel, 2011, Section 2.1b)

> "Let $f : \mathcal{M} \mapsto \mathbb{R}$. The *differential* of f at x, written $\mathbf{d}f$ is the linear functional $\mathbf{d}f : \mathrm{T}\mathcal{M}_x \mapsto \mathbb{R}$ defined by
>
> $$\mathbf{d}f(\boldsymbol{v}) = \boldsymbol{v}(f)." \tag{4.5}$$

The coordinate representation is simply

$$\mathbf{d}f = \frac{\partial f}{\partial x^i}\mathbf{d}x^i. \tag{4.6}$$

If the components $z_i = \partial_{x^i} f$ are not the partial derivatives of a single function we face a (general) *one-form*

$$^1\mathfrak{z} = z_i \mathbf{d}x^i. \tag{4.7}$$

Remark 4.4. Given the components z_i of a one-form $^1\mathfrak{z}$ at some point x we can always find a differential $\mathbf{d}\phi$ with the same components at this one point. In case that $z_i(x) = \partial_{x^i}\phi(x)$ holds for all points x in the domain of $^1\mathfrak{z}$, the form $^1\mathfrak{z}$ is said to be *exact*. In fact, the term "exact" is the generalization of "can be written as the differential of a function" for forms of arbitrary degree (Frankel, 2011, Section 5.2).

The space of one-forms is the dual space $\mathrm{T}^*\mathcal{M}_x$ of the tangent space ($\mathrm{T}\mathcal{M}_x$). It is referred to as co-tangent space. Accordingly, $\mathrm{T}^*\mathcal{M}$ is the co-tangent bundle.

Let us now confirm that Definition 4.3 is consistent with (4.3) and (4.6). The last part of (4.3) obviously corresponds to $\boldsymbol{v}(\phi)$. Hence, we turn to $\mathbf{d}\phi(\boldsymbol{v})$:

$$\mathbf{d}\phi(\boldsymbol{v}) = \frac{\partial\phi}{\partial x^i}\mathbf{d}x^i\left(v^j\partial_{x^j}\right) = \frac{\partial\phi}{\partial x^i}v^j\underbrace{\mathbf{d}x^i\left(\partial_{x^j}\right)}_{\frac{\partial x^i}{\partial x^j}=\delta^i_j} = \frac{\partial\phi}{\partial x^i}v^i = v^i\partial_{x^i}(\phi) = \boldsymbol{v}(\phi), \tag{4.8}$$

where the "Kronecker-delta" δ^i_j is one if $i = j$ and zero otherwise. Since (4.8) is supposed to be independent of the coordinates used, the components of differentials and also one-forms transform as

$$\frac{\partial\phi}{\partial y^i} = \frac{\partial\phi}{\partial x^j}\frac{\partial x^j}{\partial y^i}, \tag{4.9}$$

which is converse to the transformation formula for vector components (4.2).

We note that not only the components of vectors and differentials transform under a change of coordinates but also the bases do, i.e.

$$\partial_{y^i} = \partial_{x^j}\frac{\partial x^j}{\partial y^i} \qquad \text{and} \qquad \mathbf{d}y^i = \frac{\partial y^i}{\partial x^j}\mathbf{d}x^j, \tag{4.10}$$

respectively. Thus, they transform in the inverse way such that actual object (the actual vector or one-form, respectively) is not affected by changes of coordinates. Indeed, using a prefix subscript "$_x$" or "$_y$" to indicate the coordinates to which a component refers, we

have

$$\boldsymbol{v} = {}_x v^i \, m\partial_{x^i} = {}_x v^i \, \frac{\partial y^j}{\partial x^i} \frac{\partial x^k}{\partial y^j} \, \partial_{x^k} = {}_y v^j \, \partial_{y^j} \tag{4.12}$$

$${}^1\mathfrak{z} = {}_x z_i \, \mathbf{d}x^i = {}_x z_i \, \frac{\partial x^i}{\partial y^j} \frac{\partial y^j}{\partial x^k} \, \mathbf{d}x^k = {}_y z_j \, \mathbf{d}y^j, \tag{4.13}$$

which confirms coordinate invariance of vectors $\boldsymbol{v}$ and one-forms ${}^1\mathfrak{z}$.

As the **d**-notation already suggests, a one-form is an object that can be integrated along a curve, that is it takes a tangent vector of a curve and returns a scalar. In other words, one-forms correspond to integrands of line integrals and vectors are the local representation of the domain of integration. A corresponding physical idea is the computation of the work done by moving a particle in a force field. For example, taking a charged particle from a place x_1 with electric potential ϕ_1 to a position x_2 with ϕ_2.

In the discussion above we outlined how vectors act on functions and differentials, and, conversely, how differentials act on vectors. The latter operation naturally extends to one-forms:

$$\boldsymbol{v}({}^1\mathfrak{z}) = {}^1\mathfrak{z}(\boldsymbol{v}) = z_i \, v^j \, \mathbf{d}x^i(\partial_{x^j}) = z_i v^i. \tag{4.14}$$

In (4.14) the essential ingredient is the orthogonality of the vector and the one-form bases, i.e. $\mathbf{d}x^i(\partial_{x^j}) = \partial_{x^i}(\mathbf{d}x^j) = \delta^i_j$. This relation is also used to read off the components of vectors and forms in a specific coordinate system, e.g.

$$v^i = \boldsymbol{v}(\mathbf{d}x^i) = v^j \partial_{x^j}(\mathbf{d}x^i) = v^j \delta^i_j \quad \text{and} \quad z_i = \mathfrak{z}\,(\partial_{x^i}) = z_j \, \mathbf{d}x^j\,(\partial_{x^i}) = z_j \delta^j_i. \tag{4.15}$$

At first sight, the action of a vector on a one-form seems a bit peculiar, since the basis vectors do not seem to act as differential operators anymore. However, the correct geometric interpretation is that a one-form represents an equivalence class of functions (Burke, 1996). The equivalence is in the sense that a vector applied to each of them will yield the same result. Thus, we may also think of a one-form representing a linear function such that the one-form's are constants. Then, the action of vector on the one-form components vanishes and only the natural pairing with the one-form basis remains. Consequently, when computing derivatives of vectors, forms or tensors instead of scalar functions we will need a different machinery.

4.1.3. Push-forward and pull-back

In (4.11) we have seen transformations under a change of coordinates. A related question is how to map vectors and one-forms from (speaking in mechanics language) one configuration to another. In the present case we are dealing with mappings of manifolds (Frankel, 2011, Section 1.3d).

Let $\varphi : \mathcal{M}^n \mapsto \mathcal{M}'^{n'}$ now denote a differentiable map[3] from one manifold of dimension n to another manifold of dimension n'. Let further X denote coordinates in some region of $\mathcal{M}$ and x those in $\mathcal{M}'$ such that $x = \varphi(X)$. In case of the configuration of bodies, we have $n = n'$.

A curve $C(s) \subset \mathcal{M}$ is mapped to $c(s) = \varphi(C(s)) \subset \mathcal{M}'$. By the chain rule the components of the vector $\boldsymbol{V}$ tangent to C transform as

$$v^i \partial_{x^i} = \partial_{x^i} \frac{\partial \varphi^i}{\partial X^J} V^J, \tag{4.16}$$

which is basically the same formula as for change of coordinates. Operations similar to (4.16), i.e. transitions of objects on a configuration to the configuration's image under a map, are generally referred to as push-forward and abstractly denoted as φ_*, e.g. $\varphi_*[\boldsymbol{v}]$ in the case of vectors. We introduce the mixed two-point tensor[4] $\underline{\boldsymbol{F}}$

$$\underline{\boldsymbol{F}} = \frac{\partial \varphi^i}{\partial X^J} \partial_{x^i} \otimes \mathbf{d}X^J \tag{4.17}$$

such that $\boldsymbol{v} = \varphi_*[\boldsymbol{V}] = \underline{\boldsymbol{F}}(\boldsymbol{V})$, i.e. $\underline{\boldsymbol{F}}$ takes a vector in $\mathrm{T}\mathcal{M}_X$ and returns a vector in $\mathrm{T}\mathcal{M}'_{\varphi(X)}$. From the bases in (4.17) we conclude that $\underline{\boldsymbol{F}}$ can be referred to as *vector-valued* one-form and also as linear transform. Moreover, $\underline{\boldsymbol{F}}$ has bases in two different manifolds and is thus a so-called *two-point* tensor. Since it maps tangents into tangents, we call $\underline{\boldsymbol{F}}$ the tangent map.

In continuum mechanics, when φ is a *deformation*, that is a map between configurations, $\underline{\boldsymbol{F}}$ is known as the deformation gradient. However, this name is misleading, since $\underline{\boldsymbol{F}}$ clearly is not a "gradient" (Marsden and Hughes, 1994).

Next we investigate relation (4.5) between functions, one-forms and vectors under a map φ. Using $f = f(x)$ and evaluating all symbols living in $\mathcal{M}'$ at $x = \varphi(X)$ we obtain

$$\begin{aligned} \mathbf{d}f(\boldsymbol{v} = \varphi_*[\boldsymbol{V}]) = \varphi_*[\boldsymbol{V}](f) &= \left(\frac{\partial \varphi^i}{\partial X^J} \partial_{x^i} \otimes \mathbf{d}X^J \left(V^K \partial_{X^K} \right) \right)(f) = \frac{\partial \varphi^i}{\partial X^J} V^J \frac{\partial f}{\partial x^i} \\ &= \varphi^*[\mathbf{d}f](\boldsymbol{V}), \end{aligned} \tag{4.18}$$

with

$$\varphi^*[\mathbf{d}f] = \frac{\partial f}{\partial x^i} \frac{\partial \varphi^i}{\partial X^J} \mathbf{d}X^J = \underline{\boldsymbol{F}}(f). \tag{4.19}$$

Obviously, the equation above is again the application of the chain rule to $f(x) = f(x = \varphi(X)) = f \circ \varphi$. Also note $\underline{\boldsymbol{F}}(f) = \underline{\boldsymbol{F}}(\mathbf{d}f)$, which corresponds to (4.14). In fact, the pull-back with $\underline{\boldsymbol{F}}$ not only works for differentials but also general one-forms, i.e.

$$\varphi^*[{}^1\boldsymbol{\vartheta}] = \underline{\boldsymbol{F}}({}^1\boldsymbol{\vartheta}). \tag{4.20}$$

[3] We hereby "upgrade" the symbol φ introduced for configurations bodies in $\mathbb{R}^n$ to use it on more general manifolds.

[4] By "mixed" we mean that $\underline{\boldsymbol{F}}$ has one-form and vector bases. By "two-point" we mean that some of the bases belong to the "first" configuration and the remaining bases belong to the "second" configuration.

We conclude that $\underline{\boldsymbol{F}}$ when applied to vectors "pushes" them forward to $x = \varphi(X)$ and conversely "pulls" back one-forms from $x = \varphi(X) \in \mathcal{M}'$ to $X \in \mathcal{M}$. In both cases we write $\underline{\boldsymbol{F}}(\bullet)$, i.e. $\underline{\boldsymbol{F}}({}^1\!\mathfrak{z})$ and $\underline{\boldsymbol{F}}(\boldsymbol{V})$, respectively. The appropriate operation is automatically performed since the basis of ${}^1\!\mathfrak{z}$ or $\boldsymbol{V}$ can only by paired with the vector or one-form basis, respectively, of $\underline{\boldsymbol{F}}$.

If φ is invertible and both φ and φ^{-1} are sufficiently smooth (differentiable) we may define the inverse tangent map as

$$\underline{\boldsymbol{f}} := f^I{}_i \, \partial_{X^I} \otimes \mathbf{d}x^i = \underline{\boldsymbol{F}}^{-1} \qquad \text{with} \qquad f^I{}_i = \frac{\partial(\varphi^{-1})^I}{\partial x^i} \tag{4.21}$$

such that

$$\underline{\boldsymbol{F}}^{-1} \cdot \underline{\boldsymbol{F}} = \delta^I_J \, \partial_{X^I} \otimes \mathbf{d}X^J \tag{4.22}$$

where "$\cdot$" denotes the contraction of the innermost bases of the product, $\mathbf{d}x^i$ and ∂_{x^j}, respectively. When we are in possession of $\underline{\boldsymbol{f}}$ we are able to push-forward one-forms and pull-back vectors. When in addition φ is an injective ("one-to-one") and surjective ("onto") we speak of a *diffeomorphism* (Frankel, 2011, Section 1.3d).

Remark 4.5. Although there is great similarity between pull-back/push-forward of objects and changes of objects through a change of coordinates, we shall distinguish them. With a "change of coordinates" we refer to switching between two coordinate charts at the same time for the same region of a single, unchanged manifold. By contrast, we reserve pull-back and push-forward for relations between objects on not necessarily identical manifolds and at possibly different points in time. The manifolds are not even required to have the same dimension. Thus, pull-back and push-forward go beyond changes of coordinates. This distinction is occasionally also reflected in notation. When focusing on changes of coordinates the involved coordinates are $\{y^i\}$ and $\{x^i\}$ with $y = y(x)$. If we allow for "different" manifolds we in most but not all cases employ coordinates x and X connected through a map φ such that $x = \varphi(X)$. In case of a diffeomorphism, both notions are equivalent (Carrol, 2019).

4.1.4. Metric tensors

A useful concept in the context of vectors is that of magnitude or, visually, the length of the arrow that we draw. A related question is: how to measure the length of a line? To address this, we require the notion of a metric tensor, which as the name suggests does the "measurement" under consideration. Our definition follows Marsden and Hughes (1994, p. 68)

Definition 4.4. The metric tensor $\mathbf{g}$ defines the inner product of two vectors $\boldsymbol{u}$ and $\boldsymbol{v} \in \mathrm{T}\mathcal{M}_x$. It represents the operation $\mathbf{g}(\boldsymbol{u}, \boldsymbol{v}) = g_{ij} u^i v^j$ with

$$\mathbf{g} = g_{ij} \, \mathbf{d}x^i \otimes \mathbf{d}x^j = \langle \partial_{x^i}, \partial_{x^j} \rangle_{\mathbf{g}} \, \mathbf{d}x^i \otimes \mathbf{d}x^j, \tag{4.23}$$

where $\langle , \rangle_{\mathbf{g}}$ denotes the corresponding inner product. We require that $\mathbf{g}(\boldsymbol{v}, \boldsymbol{u}) = \mathbf{g}(\boldsymbol{u}, \boldsymbol{v})$ and $\mathbf{g}(\boldsymbol{u}, \boldsymbol{v}) = 0 \iff (\boldsymbol{u} = \mathbf{0} \vee \boldsymbol{v} = \mathbf{0})$. Usually, one also requires that $\mathbf{g}(\boldsymbol{u}, \boldsymbol{u}) > 0$ for $\boldsymbol{u} \neq \mathbf{0}$. However, this is for example not the case in special and general relativity.

The inner product of a vector $\boldsymbol{u}$ with itself is the square of its "magnitude"

$$\|\boldsymbol{u}\| = \sqrt{\mathbf{g}(\boldsymbol{u}, \boldsymbol{u})}. \tag{4.24}$$

When $\mathbf{g}$ is only applied to a single vector $\boldsymbol{u}$ the resulting object $\mathfrak{u} = \mathbf{g}(\boldsymbol{u}, \bullet) = g_{ij} u^i \mathbf{d}x^j$ behaves like a one-form. We call it the "one-form *associated* with $\boldsymbol{u}$". Obviously, $\mathfrak{u}(\boldsymbol{v}) = \mathbf{g}(\boldsymbol{u}, \boldsymbol{v})$. In Euclidean space and Cartesian coordinates $g_{ij} = \delta_{ij}$ such that $\mathbf{g}(\boldsymbol{u}, \boldsymbol{v})$ reduces to the standard Euclidean norm. Then $u_i = u^i$ which is not a tensor equation, that means it breaks under a change of coordinates. This is easy to see from the different transformation rules for vectors and one-forms.

The inverse $\mathbf{g}^{-1}$ of the matrix expression for $\mathbf{g}$ can be somehow thought of as defining the magnitude of a one-form. This nicely fits into the picture of length indicating magnitude of vectors versus density of iso-lines indicating the magnitude of one-forms in $\mathbb{R}^2$. In full notation,

$$\mathbf{g}^{-1} = g^{ij} \partial_{x^i} \otimes \partial_{x^j}, \tag{4.25}$$

where $g^{ij} g_{jk} = \delta^i_k$. Similar to $\mathbf{g}(\boldsymbol{u}, \bullet)$ we may employ $\mathbf{g}^{-1}({}^1\mathfrak{z}, \bullet)$ to create a vector associated with ${}^1\mathfrak{z}$.

The components of $\mathbf{g}$ transform similar to those of one-forms

$$g'_{ij} = g_{kl} \frac{\partial x^k}{\partial y^i} \frac{\partial x^l}{\partial y^j}. \tag{4.26}$$

4.1.5. The covariant derivative of vector fields

Consider the following

Definition 4.5. (Marsden and Hughes, 1994, p. 72, Definition 4.16)

> "A *connection* on a manifold $\mathcal{M}$ is an operation $\boldsymbol{\nabla}$ that associates to each pair of vector fields $\boldsymbol{w}$, $\boldsymbol{u}$ on $\mathcal{M}$ a third vector field denoted $\boldsymbol{\nabla}_{\boldsymbol{w}} \boldsymbol{u}$ and called the *covariant derivative* of $\boldsymbol{u}$ along $\boldsymbol{w}$, such that:
>
> (i) $\boldsymbol{\nabla}_{\boldsymbol{w}} \boldsymbol{u}$ is linear in each of $\boldsymbol{w}$ and $\boldsymbol{u}$;
>
> (ii) $\boldsymbol{\nabla}_{f\boldsymbol{w}} \boldsymbol{u} = f \boldsymbol{\nabla}_{\boldsymbol{w}} \boldsymbol{u}$ for scalar functions f; and
>
> (iii) $\boldsymbol{\nabla}_{\boldsymbol{w}}(f\boldsymbol{u}) = f \boldsymbol{\nabla}_{\boldsymbol{w}} \boldsymbol{u} + [\boldsymbol{w}(f)]\boldsymbol{u}$."

Within this thesis we assume that all basis-vectors and -one-forms correspond to coordinate functions[5], that is we are considering coordinate frames only. The covariant

[5] We recommend Frankel (2011, Chapter 9) for some comments on the more general case and to Steinmann (2015, Part III) for the application of general connections in plasticity.

derivative can be understood as a derivative that applies not only to the components but also to the basis of a vector. We introduce the *Christoffel symbols* via the covariant derivative of basis vectors $\boldsymbol{e}_i$ (Marsden and Hughes, 1994, p. 72, Definition 4.17)

$$\Gamma^a_{bc}\boldsymbol{e}_a = \boldsymbol{\nabla}_{\boldsymbol{e}_b}\boldsymbol{e}_c. \tag{4.27}$$

If the $\boldsymbol{e}_i$ are vectors which are tangent to coordinate functions we have a coordinate frame for which the Christoffel symbols can be computed as (Marsden and Hughes, 1994, p. 31, Definition 1.9)

$$\Gamma^a_{bc} = \frac{\partial^2 y^i}{\partial x^c \partial x^b}\frac{\partial x^a}{\partial y^i} \tag{4.28}$$

where $\boldsymbol{e}_a = (\partial y^i/\partial x_b)\boldsymbol{i}_i$ and $\boldsymbol{i}_i$ are basis vectors of $\mathbb{R}^n$. Based on (4.27) we have the coordinate expression (Marsden and Hughes, 1994, p. 73, Proposition 4.18)

$$(\boldsymbol{\nabla}_{\boldsymbol{w}}\boldsymbol{u})^a = \frac{\partial u^a}{\partial x^b}w^b + \Gamma^a_{bc}w^b u^c = u^a{}_{|b}w^b \tag{4.29}$$

and

$$(\boldsymbol{\nabla}\boldsymbol{u})^a{}_b = \frac{\partial u^a}{\partial x^b} + \Gamma^a_{bc}u^c = u^a{}_{|b}. \tag{4.30}$$

Since the metric $\mathbf{g}$ is defined through basis vectors we have the important identity

$$\frac{\partial g_{ij}}{\partial x^k} = g_{bj}\Gamma^b_{ik} + g_{ib}\Gamma^b_{jk}. \tag{4.31}$$

This allows to define the Christoffel symbols[6] for a coordinate frame as (Frankel, 2011, p. 229)

$$\Gamma^a_{bc} = \frac{1}{2}g^{ra}\left(\frac{\partial g_{rb}}{\partial x^c} + \frac{\partial g_{cr}}{\partial x^b} - \frac{\partial g_{bc}}{\partial x^r}\right). \tag{4.32}$$

We remark that in case of coordinate frames the Christoffel symbols according to (4.28) and (4.32) are symmetric with respect to the bottom indices, i.e.

$$\Gamma^a_{bc} = \Gamma^a_{cb}. \tag{4.33}$$

In that case, one also speaks of a symmetric connection. Please note that Frankel (2011, Sections 8.5 and 9.1) employs the term "Christoffel" symbols for the "connection" symbols of coordinate frames whereas Marsden and Hughes (1994) use "Christoffel" symbols also for general, i.e. non-coordinate, frames.

The generalization of the covariant derivative to arbitrary tensors $\mathbf{t} = t^{i\ldots n}{}_{m\ldots w}\boldsymbol{\partial}_{x^i} \otimes$

[6] They are indeed no tensors (Marsden and Hughes, 1994).

$\cdots \otimes \partial_{x^n} \otimes \mathbf{d}x^o \otimes \cdots \otimes \mathbf{d}x^w$ is given as (Marsden and Hughes, 1994)

$$\begin{aligned} t^{ij\ldots n}{}_{mo\ldots w|a} = &\frac{\partial t^{ij\ldots n}{}_{op\ldots w}}{\partial x^a} \\ &+ t^{bj\ldots n}{}_{op\ldots w}\Gamma^i_{ba} + t^{ib\ldots n}{}_{op\ldots w}\Gamma^j_{ba} + \ldots \\ &- t^{ij\ldots m}{}_{bp\ldots w}\Gamma^b_{oa} - t^{ij\ldots n}{}_{ob\ldots w}\Gamma^b_{pa} - \ldots . \end{aligned} \tag{4.34}$$

In case that $\boldsymbol{w}(t) = \dot{\varphi}(X,t)$ is the (material) velocity of a motion φ at time t we may define the *material derivative of a vector field* as $\boldsymbol{\nabla}_{\dot{\varphi}(X,t)}\boldsymbol{u}$ (Marsden and Hughes, 1994, p. 73, Definition 4.19)

$$\boldsymbol{\nabla}_{\boldsymbol{w}(t)}\boldsymbol{u} =: \frac{\mathrm{d}\boldsymbol{u}}{\mathrm{d}t} = \dot{\boldsymbol{u}} = \frac{\partial \boldsymbol{u}}{\partial t} + \boldsymbol{\nabla}_{\boldsymbol{w}(t)}\boldsymbol{u}. \tag{4.35}$$

Components of the material time derivative will be denoted as $(\dot{\boldsymbol{u}})^i$. The generalization to tensors follows from (4.34).

Remark 4.6. We emphasize that $(\dot{\boldsymbol{u}})^i \neq \dot{u}^i$ unless the coordinate basis is constant in space and time. Thus, we do not introduce new symbols for the material time derivative but only distinguish whether a component or a complete object is "dotted".

Remark 4.7. A well-known and useful property of the covariant derivative is that

$$g_{ij|b} \equiv 0 \tag{4.36}$$

holds for the metric tensor of the corresponding coordinate system.

4.1.6. The concept of a *variation*

We already made heavy use of variations in Chapters 2 and 3. We assumed that the reader was at that point roughly familiar with the meaning of a variation. Now we give a not too formal description of this tool. Consider a function f defined on a manifold $\mathcal{M}$. Choosing coordinates $\{x^i\}$ we write $f = f(x^1, \ldots, x^n) = f(x)$. Then, the *variation* of f is denoted as δf and given in terms of the directional derivative (Marsden and Hughes, 1994, p. 183, Box 1.1) as

$$\delta f = \left.\frac{\mathrm{d}f(x + t\boldsymbol{u})}{\mathrm{d}t}\right|_{t=0} = \left.\frac{\partial f}{\partial x^i}\right|_x u^i = \mathbf{d}f|_x(\boldsymbol{u}) = \boldsymbol{u}(\mathbf{d}f) = \boldsymbol{u}(f) \tag{4.37}$$

where $\boldsymbol{u} \in \mathrm{T}\mathcal{M}$ is any (admissible) vector field on $\mathcal{M}$. Note that $x + t\boldsymbol{u}$ is only valid in the limit $t \to 0$, which brings everything to tangent space. Otherwise, we cannot add a point x and a vector $t\boldsymbol{u}$. In particular, this means that while φ is just a map, by no means a vector, its variation $\delta\varphi$ is indeed a vector (Marsden and Hughes, 1994, Section 4.2).

Consequently,

$$\delta\underline{\boldsymbol{F}} = \frac{\mathrm{d}}{\mathrm{d}t}\left(\frac{\partial\varphi + t\boldsymbol{u}}{\partial X^I}\right)\Big|_{t=0} \tag{4.38}$$

or, in components,

$$(\delta\underline{\boldsymbol{F}})^i{}_I = \frac{\partial u^i}{\partial X^I} + \Gamma^i_{jk}\frac{\partial\varphi^j}{\partial X^I}u^k = u^i{}_{|l}F^l{}_I = (\delta\varphi)^i{}_{|l}F^l{}_I, \tag{4.39}$$

where we in the last step identified $\boldsymbol{u}$ as $\delta\varphi$. Observe the similarity between $\delta\underline{\boldsymbol{F}}$ and the material time derivative $\dot{\underline{\boldsymbol{F}}}$ with $\delta\varphi$ playing the role of $\dot{\varphi}$ (see Section 4.1.5). If $f = f(x, h(x))$ then the chain rule applies as usual

$$\delta f = \frac{\partial f}{\partial x^i}\Big|_x \delta x^i + \frac{\partial f}{\partial h}\Big|_x \delta h = \frac{\partial f}{\partial x^i}\Big|_x \delta x^i + \frac{\partial f}{\partial h}\Big|_x \frac{\partial h}{\partial x^i}\Big|_x \delta x^i. \tag{4.40}$$

Remark 4.8. The manifold $\mathcal{M}$ on which we perform the variation is a quite abstract object in many cases. Consider an electrostatic energy density $\Psi(\boldsymbol{D}; X)$ defined in a fixed domain Ω. The manifold we consider for the variation is not Ω but, when is $\boldsymbol{D}$ is understood as a vector, the tangent bundle $\mathrm{T}\Omega$ with coordinates $\{X^1, X^2, X^3, D^1, D^2, D^3\}$. Since we considered Ω as fixed, admissible variations leave X unaffected and we have

$$\delta\Psi = \frac{\partial\Psi}{\partial D^i}\delta D^i = \delta\boldsymbol{D}(\mathbf{d}\Psi). \tag{4.41}$$

The notation suggests that $\delta\boldsymbol{D}$ and $\mathbf{d}\Psi$ are a vector and a one-form, respectively, *on the tangent bundle* $\mathrm{T}\Omega$. This is not to be confused with vectors and one-forms on Ω.

4.1.7. Differential forms: algebra and common operations

In this section we generalize the notion of one-forms (also known as co-vectors) to n-forms. We also present a set of mathematical operations on such forms which render a compact "language" of forms. This comes at the cost that we have to deal with a larger number of different objects. We start with the formal definition of n-forms (Marsden and Hughes, 1994, p. 104, Definition 7.1)

Definition 4.6. A differential n-form on a manifold $\mathcal{M}$ *linearly* maps an n-tuple of vectors $\{\boldsymbol{v}_1, \dots, \boldsymbol{v}_n\}$ at x from $T\mathcal{M}_x$ to $\mathbb{R}$ with the additional property that for a permutation p on indices $\{1, \dots, n\}$

$${}^n\beta(\boldsymbol{v}_{\mathrm{p}(1)}, \dots, \boldsymbol{v}_{\mathrm{p}(n)}) = \mathrm{sgn}(\mathrm{p})\,{}^n\beta(\boldsymbol{v}_1, \dots, \boldsymbol{v}_n) \tag{4.42}$$

with

$$\mathrm{sgn}(\mathrm{p}) = \begin{cases} +1 & \text{if p is even,} \\ -1 & \text{if p is odd.} \end{cases} \tag{4.43}$$

Thus, forms can be characterized as fully covariant skew-symmetric tensors. This

means that each "swap" of indices, changes the sign in the sense $z_{123} = -z_{321}$. The space of n-forms on a manifold $\mathcal{M}$ will be denoted as ${}^n\Lambda(\mathcal{M})$. Scalar-valued functions are understood as zero-forms. Moreover, n-forms on an n-manifold are scalar-valued, but they shall not be confused with scalars.

An extension of differential forms are n-form-*valued* forms:

Definition 4.7. An n-form-valued m-form ${}^m\underline{\underline{\mathfrak{z}}}$ is tensorial objects given as

$$z_{\underline{i^1\dots i^n}\ \underline{j^1\dots j^m}} = {}^m\underline{\underline{\mathfrak{z}}} \in {}^n\Lambda \otimes {}^m\Lambda, \tag{4.44}$$

which is skew-symmetric in its first n and last m "slots".

If not stated explicitly, forms $\mathfrak{z}$ and $\underline{\mathfrak{z}}$ consume all "inputs" from left to right. For vectors and strictly contravariant ("indices up") tensors the natural contraction is applied. When applied to vector-valued forms, the vector part is contracted with the leading one-form part but the form part of the argument is employed to form an exterior derivative. In the present work, we will only have use for one-form-valued forms and vector-valued one-forms, which we write as underlined vectors $\underline{\boldsymbol{v}}$. One example of such a "mixed"-type tensor is the tangent-map $\underline{\boldsymbol{F}}$. The actual operations of underlined objects are worked out in Section 4.1.8.10.

4.1.7.1. The exterior product

This is the "natural" product[7] of two differential forms. Wherever two forms are multiplied this product is employed.

Definition 4.8. (Marsden and Hughes, 1994)

> "Let ${}^n\mathfrak{y}$ be an n-form and ${}^m\mathfrak{z}$ and m-form. Define the $(n+m)$-form ${}^n\mathfrak{y}\wedge{}^m\mathfrak{z}$, called their *wedge* or *exterior* product, by (...)
>
> $$({}^n\mathfrak{y} \wedge {}^m\mathfrak{z})(\boldsymbol{v}_1, \dots, \boldsymbol{v}_n, \boldsymbol{v}_{n+1}, \dots, \boldsymbol{v}_{n+m}) = \underline{\sum} \operatorname{sgn}(\mathrm{p})\, {}^n\mathfrak{y}(\boldsymbol{v}_{\mathrm{p}(1)}, \dots, \boldsymbol{v}_{\mathrm{p}(n)})\, {}^m\mathfrak{z}(\boldsymbol{v}_{\mathrm{p}(n+1)}, \dots, \boldsymbol{v}_{\mathrm{p}(n+m)}) \tag{4.45}$$
>
> where $\underline{\sum}$ denotes the sum over permutations satisfying $\mathrm{p}(1) < \dots < \mathrm{p}(n)$ and $\mathrm{p}(n+1) < \dots < \mathrm{p}(n+m)$."

By convention, no $\wedge$ is written for the product of a zero-form with another form. In fact, one may also regard the component functions of any tensorial object as zero-forms.

The exterior product also occurs in the coordinate expression of an n-form ${}^n\mathfrak{z}$

$${}^n\mathfrak{z} = z_{\underline{i,\dots,n}} \mathbf{d}x^i \wedge \dots \wedge \mathbf{d}x^n, \tag{4.46}$$

[7] The usual tensor or dyadic product "$\otimes$" is not appropriate since it dues not maintain skew-symmetry, that is the result is not a higher-order form but general tensors.

where underlined indices indicate that only ordered sets $\underline{ij\dots n} = (i < j < \cdots < n)$ are considered. From this rule we see that exterior products where at least one n-form occurs more than once vanish identically. In particular, $\mathbf{d}x^i \wedge \mathbf{d}x^i = 0$ but also $\mathbf{d}x^i \wedge \mathbf{d}x^j \wedge \mathbf{d}x^i = 0$. Moreover, the "$\wedge$"-product is associative but not commutative, i.e.

$$({}^p\mathfrak{x} \wedge {}^q\mathfrak{y}) \wedge {}^r\mathfrak{z} = {}^p\mathfrak{x} \wedge ({}^q\mathfrak{y} \wedge {}^r\mathfrak{z}) = {}^p\mathfrak{x} \wedge {}^q\mathfrak{y} \wedge {}^r\mathfrak{z} \tag{4.47a}$$

$${}^p\mathfrak{x} \wedge {}^q\mathfrak{y} = (-1)^{pq}\, {}^q\mathfrak{y} \wedge {}^p\mathfrak{x}. \tag{4.47b}$$

Example 4.3. *The exterior product of two one-forms $\mathfrak{a}$ and $\mathfrak{b}$ is defined in terms of the usual tensor product "$\otimes$" as (Frankel, 2011)*

$${}^1\mathfrak{a} \wedge {}^1\mathfrak{b} = {}^1\mathfrak{a} \otimes {}^1\mathfrak{b} - {}^1\mathfrak{b} \otimes {}^1\mathfrak{a} \tag{4.48}$$

and results in a two-form, *a completely skew-symmetric covariant second-order tensor. This means, ${}^1\mathfrak{a} \wedge {}^1\mathfrak{b}$ takes* two *vectors and gives a scalar, i.e.*

$$\left({}^1\mathfrak{a} \wedge {}^1\mathfrak{b}\right)(\boldsymbol{u}, \boldsymbol{v}) = {}^1\mathfrak{a}(\boldsymbol{u}){}^1\mathfrak{b}(\boldsymbol{v}) - {}^1\mathfrak{b}(\boldsymbol{u}){}^1\mathfrak{a}(\boldsymbol{v}) \tag{4.49}$$

and in components

$$\begin{aligned}(a_i\mathbf{d}x^i) \wedge (b_j\mathbf{d}x^j) = a_ib_j(\mathbf{d}x^i \otimes \mathbf{d}x^j - \mathbf{d}x^j \otimes \mathbf{d}x^i) = \\ \sum_{i<j}(a_ib_j - a_jb_i)\mathbf{d}x^i \wedge \mathbf{d}x^j = \sum_{i<j}\gamma_{ij}\mathbf{d}x^i \wedge \mathbf{d}x^j = \gamma_{\underline{ij}}\mathbf{d}x^i \wedge \mathbf{d}x^j.\end{aligned} \tag{4.50}$$

Because of the properties

$$\mathbf{d}x^i \wedge \mathbf{d}x^j = -\mathbf{d}x^j \wedge \mathbf{d}x^i \tag{4.51a}$$

$$\mathbf{d}x^i \wedge \mathbf{d}x^i = 0 \tag{4.51b}$$

$$\gamma_{ij} = -\gamma_{ji} \tag{4.51c}$$

the restriction to ordered sets of indices $\underline{ij\dots n}$ is equivalent to restricting $ij\dots n$ to even permutations.

4.1.7.2. The interior product

While n-forms map from $T\mathcal{M}_x \overset{n}{\otimes} T\mathcal{M}_x$ to $\mathbb{R}$ there is also the common operation of a map taking a single vector $\boldsymbol{v}$ and returning an $(n-1)$-form (Marsden and Hughes, 1994, p .106,Definition 7.3).

Definition 4.9. The interior product of a vector $\boldsymbol{v} \in T\mathcal{M}_x$ with an n-form ${}^n\mathfrak{z}$ at x denoted as $\mathbb{i}_{\boldsymbol{v}}{}^n\mathfrak{z}$ is

$$(\mathbb{i}_{\boldsymbol{v}}{}^n\mathfrak{z})(\boldsymbol{v}_2, \dots, \boldsymbol{v}_n) = {}^n\mathfrak{z}(\boldsymbol{v}, \boldsymbol{v}_2, \dots, \boldsymbol{v}_n). \tag{4.52}$$

From the skew-symmetry of form it follows that

$$\mathbb{i}_{\boldsymbol{v}} \circ \mathbb{i}_{\boldsymbol{v}} = 0, \tag{4.53}$$

where use "$\circ$" as the symbols for the composition of two operators (or maps). Furthermore we have for the interior product of a vector with the exterior product of two forms

$$\mathbb{i}_{\boldsymbol{v}}({}^{n}\mathfrak{y} \wedge {}^{m}\mathfrak{z}) = (\mathbb{i}_{\boldsymbol{v}}{}^{n}\mathfrak{y}) \wedge {}^{m}\mathfrak{z} + (-1)^{n}\, {}^{n}\mathfrak{y} \wedge \mathbb{i}_{\boldsymbol{v}}{}^{m}\mathfrak{z}. \tag{4.54}$$

4.1.7.3. The exterior derivative

Consider a one-form field ${}^{1}\mathfrak{z}(x) = z_i(x)\mathbf{d}x^i$. We already know that the differential of a zero-form (scalar-function) yields a one-form $\mathbf{d}f = (\partial_{x^i} f)\,\mathbf{d}x^i$, which is a tensor-like object. Surprisingly, derivatives of the components of a one-form, i.e. $\partial_{x^j} z_i$ do not form the components of a tensor. However, $\partial_{x^j} z_i - \partial_{x^i} z_j$ do indeed form the components of a two-form (Frankel, 2011, p. 64, Theorem 2.42)

$$\mathbf{d}{}^{1}\mathfrak{z} = \sum_{\underline{ij}} (\partial_{x^j} z_i - \partial_{x^i} z_j)\,\mathbf{d}x^i \wedge \mathbf{d}x^j. \tag{4.55}$$

Note that we write the short-hand partial differentiation with a normal-faced ∂, e.g. ∂_{x^i}, to distinguish it from basis vectors with bold-faced $\boldsymbol{\partial}$, e.g. $\boldsymbol{\partial}_{x^i}$.

A definition of the exterior derivative (or differential) $\mathbf{d}$ in terms of a coordinate expression is given as (Frankel, 2011, Section 2.6a):

Definition 4.10. Consider an n-form ${}^{n}\mathfrak{z} = z_{\underline{i\ldots n}}\mathbf{d}x^i \wedge \cdots \wedge \mathbf{d}x^n$. Then

$$\mathbf{d}{}^{n}\mathfrak{z} = \mathbf{d}z_{\underline{i\ldots n}} \wedge \mathbf{d}x^i \wedge \cdots \wedge \mathbf{d}x^n, \tag{4.56}$$

where $\mathbf{d}z_{\underline{i\ldots n}}$ simply is the differential of the scalar component function $z_{\underline{i\ldots n}}$.

The exterior derivative features a number of important properties (see Marsden and Hughes (1994, p. 106, Theorem 7.4) and Frankel (2011, Theorem 2.53)):

Theorem 4.1. *On a manifold $\mathcal{M}$ there exists a unique linear operator $\mathbf{d}$ taking n-forms into $n+1$-forms, which satisfies*

(i) $\mathbf{d}(\mathbf{d}{}^{n}\mathfrak{z}) \equiv 0$.

(ii) $\mathbf{d}({}^{n}\mathfrak{y} + {}^{n}\mathfrak{z}) = \mathbf{d}{}^{n}\mathfrak{y} + \mathbf{d}{}^{n}\mathfrak{z}$.

(iii) $\mathbf{d}({}^{n}\mathfrak{y} \wedge {}^{m}\mathfrak{z}) = (\mathbf{d}{}^{n}\mathfrak{y}) \wedge {}^{m}\mathfrak{z} + (-1)^{n}\, {}^{n}\mathfrak{y} \wedge (\mathbf{d}{}^{m}\mathfrak{z})$.

(iv) $\mathbf{d}{}^{0}\mathfrak{z}$ *is the usual differential of a function.*

(v) $\mathbf{d}$ *commutes with restrictions ("$|$") to open subsets $\mathcal{U} \in \mathcal{M}$:* $\mathbf{d}({}^{n}\mathfrak{z}|_{\mathcal{U}}) = (\mathbf{d}{}^{n}\mathfrak{z})|_{\mathcal{U}}$.

Remark 4.9. We regard the exterior derivative as an operator that always belongs to the domain of its argument. Thus, we do not use a different symbol if we for example apply $\mathbf{d}$ in the current or in the initial configuration of a body.

4.1.7.4. A product rule for the exterior derivative of one-form-valued forms

In Sections 4.1.8.10 and 4.3 we will need some kind of product rule for the exterior derivative of two-forms obtained by paring a one-form-valued two-form with a vector, i.e. ${}^2\underline{\mathfrak{z}}(\boldsymbol{v})$. Besides simply computing the exterior derivative Kanso et al. (2007) define a derivative connecting the covariant (4.30) and the exterior derivative (4.56) in terms of a product rule:

Definition 4.11. Consider a one-form-valued 2-form ${}^2\underline{\mathfrak{z}} \in {}^1\Lambda(\mathcal{M}) \otimes {}^2\Lambda(\mathcal{M})$ and a vector field $\boldsymbol{v}(x) \in T_x\mathcal{M}$. Then, we define the derivative denoted as $\mathbb{d}$ by

$$(\mathbb{d}^2\underline{\mathfrak{z}})(\boldsymbol{v}) = \mathbf{d}[{}^2\underline{\mathfrak{z}}(\boldsymbol{v})] - {}^2\underline{\mathfrak{z}}(\boldsymbol{\nabla v}). \tag{4.57}$$

In components, by means of (4.30) and (4.56), this is written as

$$\begin{aligned}(\mathbb{d}^2\underline{\mathfrak{z}})(\boldsymbol{v}) &= \left(\frac{\partial z_{m\underline{kl}} v^m}{\partial x^j} - z_{i\underline{kl}}\left(\frac{\partial v^i}{\partial x^j} + \Gamma^i_{mj} v^m\right)\right)\mathbf{d}x^j \wedge \mathbf{d}x^k \wedge \mathbf{d}x^l \\ &= v^m\left(\frac{\partial z_{m\underline{kl}}}{\partial x^j} - z_{i\underline{kl}}\Gamma^i_{mj}\right)\mathbf{d}x^j \wedge \mathbf{d}x^k \wedge \mathbf{d}x^l \end{aligned} \tag{4.58}$$

and thus

$$\begin{aligned}\mathbb{d}^2\underline{\mathfrak{z}} &= \mathbb{d}\left(z_{m\underline{kl}}\mathbf{d}x^m \otimes \mathbf{d}x^k \wedge \mathbf{d}x^l\right) = \left(\frac{\partial z_{m\underline{kl}}}{\partial x^j} - z_{i\underline{kl}}\Gamma^i_{mj}\right)\mathbf{d}x^m \otimes \mathbf{d}x^j \wedge \mathbf{d}x^k \wedge \mathbf{d}x^l \\ &= \left(\frac{\partial z_{m\underline{kl}}}{\partial x^j} - z_{i\underline{kl}}\Gamma^i_{mj}\right)\epsilon^{j\underline{kl}}\,\mathbf{d}x^m \otimes \mathbf{d}x^1 \wedge \mathbf{d}x^2 \wedge \mathbf{d}x^3. \end{aligned} \tag{4.59}$$

Remark 4.10. Equation (4.59) interestingly contains the formula for the covariant derivative for the first index ("m") and otherwise is the standard exterior derivative on the form indices $\underline{kl}$.

Remark 4.11. Similar to $\mathbf{d}$ (see Remark 4.9) we use the same symbols for $\mathbb{d}$ and Γ on each manifold, as long as there is no chance of confusion.

4.1.7.5. Pull-back

The pull-back of a form from $\mathcal{M}$ to $\mathcal{M}'$ is simply defined by the application to vectors pushed forward (4.16) from $\mathcal{M}'$ to $\mathcal{M}$ (Frankel, 2011).

Definition 4.12. Under a map $\varphi : \mathcal{M}^n \to \mathcal{M}'^m$ the pull-back of a form ${}^n\mathfrak{z}'$ is given as

$${}^n\mathfrak{z}(\boldsymbol{v}_1, \ldots \boldsymbol{v}_n) = \varphi^*[{}^n\mathfrak{z}'](\boldsymbol{v}_1, \ldots \boldsymbol{v}_n) = {}^n\mathfrak{z}'(\varphi_*[\boldsymbol{v}_1], \ldots, \varphi_*[\boldsymbol{v}_n]), \tag{4.60}$$

where $\boldsymbol{v}_i$ are defined on $\mathcal{M}^n$.

The pull-back of a form commutes with the exterior derivative, i.e.

$$\mathbf{d}\varphi^*[{}^n\mathfrak{z}] = \varphi^*[\mathbf{d}^n\mathfrak{z}]. \tag{4.61}$$

4.1.7.6. Restriction of forms to sub-manifolds

A common operation is the restriction of an n-form ${}^n\mathfrak{z}$ that is defined on an m-manifold $\mathcal{M}^m$ to a sub-manifold $\mathcal{S}^k$ of dimension k. In fact, this is a special instance of a pull-back operation. Let us consider two examples: In the first we want to evaluate the two-form ${}^2\mathfrak{z}$ defined in $\mathcal{M}^3$ (coordinates $\{x^1, x^2, x^3\}$) on a surface in $\mathcal{S}$ (coordinates $\{u^1, u^2\}$). By combining (4.60) and (4.15) we obtain

$$ {}^2\mathfrak{z}\big|_{\mathcal{S}} = {}^2\mathfrak{z}(\varphi_* \partial_{u^1}, \varphi_* \partial_{u^2})\, \mathbf{d}u^1 \wedge \mathbf{d}u^2 \text{ with } x = \varphi(\boldsymbol{u}). \tag{4.62} $$

Clearly, the result has only a single component as is appropriate for a *two*-form on a *two*-manifold. In the second example, we consider a one-form instead of a two-form which yields

$$ {}^1\mathfrak{z}\big|_{\mathcal{S}} = {}^1\mathfrak{z}(\varphi_* \partial_{u^1})\, \mathbf{d}u^1 + {}^1\mathfrak{z}(\varphi_* \partial_{u^2})\, \mathbf{d}u^2. \tag{4.63} $$

Thus, by contrast to the two form, the one form contains two components instead of one. However, when we further restrict the one-form to a line it will also have only a single component.

Remark 4.12. Such operations for example occur in the evaluation of integrals (see Section 4.1.7.7) over boundaries and in the formulation of jump conditions. We note that the vector operations corresponding to (4.62) and (4.63) are $\boldsymbol{v} \cdot \boldsymbol{n}$ in the first and $\boldsymbol{v} - (\boldsymbol{v} \cdot \boldsymbol{n})\boldsymbol{n}$ in the second case (see also Section 4.1.8.12). We see that when dealing with forms, the degree of a form directly tells us the appropriate restriction whereas a vector by itself does not. In addition, when integrating restrictions of vectors we separately have to transform volume, area and line elements. Forms handle this intrinsically.

4.1.7.7. Integration of forms

Differential (n-)forms are the natural objects to be integrated over (n-)manifolds. Let us begin with the usual definition of the integral of a scalar function f over a region $\Omega^n \subset \mathbb{R}^n$

$$ \int_{\Omega^n} f(x)\, \mathbf{d}x^1 \dots \mathbf{d}x^n. \tag{4.64} $$

The occurrence of the basis one-forms $\mathbf{d}x^i$ is not by accident. However, we do not see any "$\wedge$" product such that the order of the $\mathbf{d}x^i$ has no influence on the result. The following definition specifies the integral of a form (Frankel, 2011):

Definition 4.13. The integral of a n-form over region Ω^n with orientation o is defined in terms of the usual integral of a function over Ω^n through

$$ \int_{(\Omega^n, o)} {}^n\mathfrak{z} = \int_{(\Omega^n, o)} \underline{z_{i,\dots,n}}(x)\, \mathbf{d}x^i \wedge \dots \wedge \mathbf{d}x^n := o(x) \int_{\Omega} \underline{z_{i,\dots,n}}(x)\, \mathbf{d}x^i \dots \mathbf{d}x^n \tag{4.65} $$

with $o(x) \pm 1$, whereby $o(x) = 1$ if and only if the basis $\{\partial_{x^1}, \dots, \partial_{x^n}\}$ has the same orientation as defined by o.

One can understand the orientation as an indicator of the parity of the permutation ("+1": even, "−1": odd) of the basis. That is, if we define $o(\{\partial_{x^1}, \partial_{x^2}, \partial_{x^3}\}) = 1$ then, e.g., $o(\{\partial_{x^3}, \partial_{x^1}, \partial_{x^2}\}) = +1$ and $o(\{\partial_{x^3}, \partial_{x^2}, \partial_{x^1}\}) = -1$.

An important property built into forms is that their integrals are independent of coordinates and invariant under pull-back operations. It is precisely the requirement of this invariance which is employed to derive the pull-back and push-forwards for physical quantities even when they are represented by classical vectors or tensors. Thus, although the magnetic field $\boldsymbol{B}$ and the current potential $\boldsymbol{H}$ are both represented by vectors in many instances, their transformation under pull-back and push-forward are different from the rules for real (tangent) vectors. In fact, one implicitly treats them as forms, i.e. as "vector-proxies" (Bossavit, 1998b).

To make this property transparent we consider an oriented region $(\Omega, o) \subset \mathbb{R}^n$ and a map χ mapping Ω^n to some manifold $\mathcal{M}^m$ of possibly greater dimension

$$\chi : \Omega^n \to \mathcal{M}^m. \tag{4.66}$$

Let ${}^n\mathfrak{z}$ be a form of degree n defined on $\mathcal{M}^m$. Then, the integral of ${}^n\mathfrak{z}$ over the image of Ω^n in $\mathcal{M}^m$ is defined as (Frankel, 2011)

$$\int_{\chi(\Omega^n, o)} {}^n\mathfrak{z} := \int_{(\Omega^n, o)} \chi^*[{}^n\mathfrak{z}], \tag{4.67}$$

where χ^* denotes the standard pull-back for an n-form (4.60). From (4.65) we see that we can only integrate n-forms over n-dimensional domains. Thus, if an n-form ${}^n\mathfrak{z}$ "lives" on an m-dimensional manifold we have to pull it back to an n-dimensional manifold for integration. Indeed, a two-form on a manifold $\mathcal{M}^3$ has three components and we do not have any means to integrate it directly. However, when pulled-back to a two-manifold $\mathcal{M}^2$ the result will be an integral of type (4.65).

4.1.7.8. Pseudo-forms

Despite their name, *pseudo*[8]-forms are an own class of objects. It just happens that we employ forms to express them (Burke, 1996).

Definition 4.14. A *pseudo*-(n-)form $\mathfrak{z}$ is a form which changes sign when orientation is reversed (Frankel, 2011)

$${}_o\mathfrak{z} = -_{(-o)}\mathfrak{z}. \tag{4.68}$$

By (naively) integrating ${}_o\mathfrak{z}$ via (4.65) we see that the sign of the integral of ${}_o\mathfrak{z}$ is independent of orientation. However, pseudo-forms are their own class of objects such

[8] Some sources, e.g. Burke (1996), use the attribute "twisted" instead.

that we shall not directly use formulae for forms, at least where orientation is involved. Importantly, pseudo-forms can be even integrated over non-orientable[9] manifolds. For pseudo-forms it is sufficient to have transverse orientation. The reader is referred to the monographs by Burke (1996) and Frankel (2011) for an accessible description of these subtleties.

4.1.7.9. The volume form

This is a (pseudo-)form of paramount importance. In fact, although called "volume form" this concept applies to n-manifolds in the sense that for example on a line it corresponds to arc-length and on a surface it corresponds to area. For general discussion, we denote the volume form on an n-manifold as ${}^n\mathfrak{v}$. However, for the special case of one-, two- and three-dimensional manifolds we will also use classical symbols like $dl = ds = {}^1\mathfrak{v}$, $da = {}^2\mathfrak{v}$ and $dv = {}^3\mathfrak{v}$. Note that we do not use an exterior differential "$\mathbf{d}$" because this is definitely not meant here. In $\mathbb{R}^3$ we have $dv = \mathbf{d}x\,\mathbf{d}y\,\mathbf{d}z$. In terms of forms we write, again for $\mathbb{R}^3$,

$$dv = o(x)\,\mathbf{d}x^1 \wedge \mathbf{d}x^2 \wedge \mathbf{d}x^3 = {}^3\mathfrak{v} \tag{4.69}$$

such that (also see 4.65)

$$\int o(x)\,\mathbf{d}x^1 \wedge \mathbf{d}x^2 \wedge \mathbf{d}x^3 = \int \mathbf{d}x^1\mathbf{d}x^2\mathbf{d}x^3 \text{ (indep. of } o(x)) \tag{4.70}$$

with $o(x)$ accounting for the orientation of the coordinate system $\{x^i\}$ and $\wedge$ denoting the *exterior product* of differential forms. The orientation is simply $+1$ if the orientation of coordinate system agrees with the orientation of space. Hence, if the space itself is right-handed then $o(x) = 1$ for $\{x^i\}$ being right-handed to $o(x) = -1$ if $\{x^i\}$ is left-handed.

It can be shown by direct computation that the (general $n-$)*volume-form* ${}^n\mathfrak{v}$ under a change of coordinates $y = y(x)$ (or a mapping φ) transforms as (Frankel, 2011, Section 2.8f)

$$\begin{aligned} {}^n\mathfrak{v} &= o(x)\,\mathbf{d}x^1 \wedge \cdots \wedge \mathbf{d}x^n = o(x)\det\left[\frac{\partial x}{\partial y}\right]\mathbf{d}y^1 \wedge \cdots \wedge \mathbf{d}y^n \\ &= o(y)\,|\det\left[\frac{\partial x}{\partial y}\right]|\,\mathbf{d}y^1 \wedge \cdots \wedge \mathbf{d}y^n, \end{aligned} \tag{4.71}$$

where x is a *locally orthonormal* basis. Another expression for $\det[\partial x/\partial y]$ is obtained in terms of the metric tensor $\mathbf{g}$ with determinant g

$$\det\left[\frac{\partial x}{\partial y}\right] = \sqrt{g} \tag{4.72}$$

[9] We do not give a precise definition but mention the Möbius strip as the prototypical example for a non-orientable manifold. By non-orientable we refer to the lack of "internal" orientation without resorting to any additional structure which embeds the manifold under consideration.

with

$$g_{ij} = \frac{\partial x^k}{\partial y^i}\frac{\partial x^l}{\partial y^j}\delta_{kl} \tag{4.73}$$

where δ_{kl} is the metric tensor in coordinates $\{x^i\}$, which we assumed to be (locally) orthonormal.

For mappings $x = \varphi(X)$ and $o(x) = o(X) = 1$ (4.71) reduces to the well-known change-of-volume formula (Marsden and Hughes, 1994, Section 1.5) which in fact holds for any dimension

$$\varphi^*[{}^n\mathfrak{v}] = \det \underline{\boldsymbol{F}} \frac{\sqrt{g}}{\sqrt{G}} {}^n\mathfrak{V} = J\, {}^n\mathfrak{V} \tag{4.74}$$

with uppercase symbols corresponding to the manifold with coordinates X. We emphasize that in the present case they are not at all the pull-backs, i.e.

$$\mathbf{G} \neq \varphi^*[\mathbf{g}] \qquad \text{and} \qquad {}^n\mathfrak{V} = \sqrt{G}\, \mathbf{d}X^1 \wedge \cdots \wedge \mathbf{d}X^n \neq \varphi^*[{}^n\mathfrak{v}]. \tag{4.75}$$

Note that (4.74) only works if $\underline{\boldsymbol{F}}$ has a square and full-rank matrix representation such that

$$\varphi^*[g] = \det\left(\varphi^*[\mathbf{g}]\right) = \left(\det \underline{\boldsymbol{F}}\right)^2 g. \tag{4.76}$$

Since ${}^n\mathfrak{v}$ is just a pseudo-form we also may readily apply the pull-back rules we know for forms but with keeping an eye on orientation. Then, even if $\underline{\boldsymbol{F}}$ is not square/full-rank it still holds that

$$\varphi^*[{}^n\mathfrak{v}] = \underbrace{\frac{\sqrt{\varphi^*[g]}}{\sqrt{G}}}_{J} {}^n\mathfrak{V} = \sqrt{\varphi^*[g]}\, \mathbf{d}X^1 \wedge \cdots \wedge \mathbf{d}X^n. \tag{4.77}$$

A use-case for the latter form is, for example, the pull-back of the area form of a surface in $\mathbb{R}^3$ to surface coordinates $\{u^1, u^2\}$.

4.1.7.10. Hodge operators

These are special operators that take a pseudo/true k-form and return an true/pseudo $(n-k)$-form (Bossavit, 2010; Frankel, 2011) such that

$$\star\, \mathfrak{z} \wedge \mathfrak{z} = \langle \mathfrak{z}, \mathfrak{z} \rangle\, dv \tag{4.78}$$

where $\langle \bullet, \bullet \rangle$ denotes an inner product appropriate for the type of arguments. This also allows for the interpretation that "$\star$" defines some metric involved in $\langle \bullet, \bullet \rangle$ (Arnold

et al., 2006). An example of a Hodge operation is

$$\begin{aligned}\star\,{}^1\mathfrak{h}\wedge{}^1\mathfrak{h} &= (\sqrt{g}\,g^{ij}\,h_j\,\epsilon_{i\underline{kl}}\,\mathbf{d}x^k\wedge\mathbf{d}x^l)\wedge(h_m\mathbf{d}x^m)\\ &= h^i\,\epsilon_{i\underline{kl}}\,h_m\sqrt{g}\,\mathbf{d}x^k\wedge\mathbf{d}x^l\wedge\mathbf{d}x^m = h^i\,h_i\,dv.\end{aligned}\tag{4.79}$$

The general formula for a k-form on an n-dimensional manifold is

$$(\star\,\mathfrak{z})_{l_1\dots l_{n-k}} = \sqrt{g}\,\epsilon_{\underline{k_1\dots k_k}l_1\dots l_{n-k}}\,g^{k_1j_1}\dots g^{k_kj_k}\,z_{j_1\dots j_k}.\tag{4.80}$$

Let us consider now the Hodge-dual of a two-form. It is obtained as

$$\star\,{}^2\mathfrak{z} = \sqrt{g}\,g^{ik}\,g^{jl}\,z_{ij}\,\epsilon_{\underline{kl}m}\,\mathbf{d}x^m\tag{4.81}$$

such that

$$\begin{aligned}\star\,{}^2\mathfrak{z}\wedge{}^2\mathfrak{z} &= \sqrt{g}\,g^{ik}\,g^{jl}\,z_{ij}\,\epsilon_{\underline{kl}m}\,z_{\underline{no}}\,\mathbf{d}x^m\wedge\mathbf{d}x^n\wedge\mathbf{d}x^o\\ &= g^{ik}\,g^{jl}\,z_{ij}\,z_{\underline{kl}}\,dv = \left(g^{ik}\,g^{jl}-g^{jk}\,g^{il}\right)z_{\underline{ij}}\,z_{\underline{kl}}\,dv.\end{aligned}\tag{4.82}$$

From (4.82) we see that the square of the norm of a two-form is computed as

$$\|^2\mathfrak{z}\|^2 = \langle\mathfrak{z},\mathfrak{z}\rangle = z_{\underline{ij}}\,z_{\underline{kl}}\,(\mathbb{cof}\,\mathbf{g}^{-1})^{ijkl},\tag{4.83}$$

with

$$(\mathbb{cof}\,\mathbf{g}^{-1})^{ijkl} := \left(g^{ik}\,g^{jl}-g^{il}\,g^{jk}\right)\tag{4.84}$$

denoting the "fourth-order" prototype[10] of the (second-order) co-factor (see also (4.120)).

4.1.7.11. The Helmholtz-Hodge decomposition

In a simply connected domain the Helmholtz decomposition of a vector field $\boldsymbol{v}(x)$ is given as

$$\boldsymbol{v} = \boldsymbol{w} + \operatorname{grad} f + \operatorname{curl}\boldsymbol{u}\tag{4.85}$$

where $\boldsymbol{w}$ is curl- and div-free, f is a scalar function and $\boldsymbol{u}$ is another vector field. The differential form version of above equation reads as

$${}^1\mathfrak{z} = {}^1\mathfrak{w} + \mathbf{d}f + \star\,\mathbf{d}\,{}^1\mathfrak{y} = {}^1\mathfrak{z}_0 + \mathbf{d}f + \star\,\mathbf{d}\star\,{}^2\mathfrak{y}\tag{4.86}$$

which is an instance of the generic *Hodge* decomposition (Frankel, 2011, Section14.2c)

$${}^n\mathfrak{z} = {}^n\mathfrak{w} + \mathbf{d}\,{}^{n-1}\mathfrak{x} + \mathbf{d}^*\,{}^{n+1}\mathfrak{y}\tag{4.87}$$

[10] We note that we did not fully specify the operator $\mathbb{cof}$ by not providing the tensor basis of its result. Depending on this definition one might need further a definition for the product on form with skew-symmetric contravariant (superscript indices by convention) tensors such that the expression (4.83) is maintained.

with

$$\mathbf{d}^* = \star\,\mathbf{d}\,\star \quad \text{and} \quad \mathbf{d}^n\mathfrak{w} = 0 = \mathbf{d}^{*n}\mathfrak{w}. \tag{4.88}$$

4.1.7.12. Stokes' theorem for differential forms

Stokes' theorem for forms and also pseudo forms is simply stated as (Frankel, 2011, Sections 3.3b and 3.4d)

$$\int_{\Omega^{n+1}} \mathbf{d}^n\mathfrak{z} = \int_{\partial\Omega^{n+1}} {}^n\mathfrak{z}, \tag{4.89}$$

where $\partial\Omega^{n+1}$ is a sub-manifold of dimension n. This holds for all dimensions and corresponds to the divergence theorem when $n = 2$.

4.1.7.13. The Lie derivative

Consider a family of maps φ_t with parameter t, which can be imagined as time, such that $\dot{\varphi}_t = \boldsymbol{v}$ is a time-independent velocity (vector) field. Then, φ_t is called a (time-independent) flow.

Definition 4.15. Given a flow φ_t with velocity field $\boldsymbol{v}$ and a second vector field $\boldsymbol{u}$. The difference between a vector $\boldsymbol{u}(\varphi_t(x))$ at $\varphi_t(x)$ and the push-forward $\varphi_{t*}[\boldsymbol{u}(x)]$ in the limit of $t \to 0$ defines the Lie derivative of the vector field $\boldsymbol{u}$ with respect to $\boldsymbol{v}$ (Frankel, 2011, Section 4.1)

$$\pounds_{\boldsymbol{v}}\,\boldsymbol{u} := \lim_{t\to 0} \frac{\boldsymbol{u}(\varphi_t(x)) - \varphi_{t*}[\boldsymbol{u}(x)]}{t}. \tag{4.90}$$

For forms the definition is slightly different since the pull-back is the more natural operation in this case.

Definition 4.16. Given a flow φ_t with velocity field $\boldsymbol{v}$ and an n-form $\mathfrak{z}$. The Lie derivative of $\mathfrak{z}$ with respect to $\boldsymbol{v}$ is (Frankel, 2011, Section 4.2)

$$\pounds_{\boldsymbol{v}}\,\mathfrak{z} := \lim_{t\to 0} \frac{\varphi_t^*[\mathfrak{z}(\varphi(x))] - \mathfrak{z}(x)}{t}. \tag{4.91}$$

Besides these two definitions, there exists a direct formula for the Lie derivative of a tensor $\mathbf{t} = t^{i\ldots n}{}_{o\ldots w}\partial_{x^i} \otimes \cdots \otimes \partial_{x^n} \otimes \mathbf{d}x^o \otimes \cdots \otimes \mathbf{d}x^w$ (Marsden and Hughes, 1994, p. 97)

$$\begin{aligned}(\pounds_{\dot{x}}\,\mathbf{t})^{ij\ldots n}{}_{op\ldots w} = &\frac{\partial t^{ij\ldots n}{}_{op\ldots w}}{\partial x^a}\dot{x}^a \\ &- t^{aj\ldots n}{}_{op\ldots w}\frac{\partial \dot{x}^i}{\partial x^a} - t^{ia\ldots n}{}_{op\ldots w}\frac{\partial \dot{x}^j}{\partial x^a} - \ldots \\ &+ t^{i\ldots n}{}_{ap\ldots w}\frac{\partial \dot{x}^a}{\partial x^o} + t^{i\ldots n}{}_{oa\ldots w}\frac{\partial \dot{x}^a}{\partial x^p} + \ldots,\end{aligned} \tag{4.92}$$

where we omitted the partial time derivative of $\boldsymbol{t}$ for consistency with (4.90) and (4.91). In case of curvilinear coordinates, the partial derivatives in above formula *can* be replaced by covariant derivatives (Section 4.1.5), as pointed out by Marsden and Hughes (1994, p. 97). Nevertheless, the Lie derivative itself does not rely on any notion of metric or covariant differentiation. Besides the formula above, for differential forms there also exists Cartan's formula (see Frankel (2011, p. 135) and Marsden and Hughes (1994, p. 108, Theorem 7.6))

$$\pounds_{\boldsymbol{v}}\, \boldsymbol{\mathfrak{z}} = \mathbf{d}(\mathbb{i}_{\boldsymbol{v}}\boldsymbol{\mathfrak{z}}) + \mathbb{i}_{\boldsymbol{v}}(\mathbf{d}\boldsymbol{\mathfrak{z}}). \tag{4.93}$$

The reason for excluding the partial time derivatives in (4.92) is that the general time-dependent case is handled following Frankel (2011, Section 4.3b): Define an extended velocity vector $\dot{\chi} = \boldsymbol{v} + \partial_t$. Then,

$$\pounds_{\dot{\chi}}\,(\bullet) = \pounds_{\boldsymbol{v}+\partial/\partial t}\,(\bullet) = \frac{\partial(\bullet)}{\partial t} + \pounds_{\boldsymbol{v}}\,(\bullet), \tag{4.94}$$

i.e. the Lie derivative with respect to $\dot{\chi}$ adds the partial time derivatives of $\boldsymbol{t}$ and $\boldsymbol{\mathfrak{z}}$ to (4.92) and (4.93), respectively.

Properties of the Lie derivative

As listed by Marsden and Hughes (1994, p. 109, Box 7.1), the Lie derivative has the (not necessarily independent) properties

$$\pounds_{\boldsymbol{v}}\,(\mathbf{t}_1 + \mathbf{t}_2) = \pounds_{\boldsymbol{v}}\,\mathbf{t}_1 + \pounds_{\boldsymbol{v}}\,\mathbf{t}_2 \tag{4.95a}$$

$$\pounds_{\boldsymbol{v}}\,(\mathbf{t}_1 \otimes \mathbf{t}_2) = \pounds_{\boldsymbol{v}}\,\mathbf{t}_1 \otimes \mathbf{t}_2 + \mathbf{t}_1 \otimes \pounds_{\boldsymbol{v}}\,\mathbf{t}_2 \tag{4.95b}$$

$$\pounds_{\boldsymbol{v}}\,(\boldsymbol{\mathfrak{y}} \wedge \boldsymbol{\mathfrak{z}}) = \pounds_{\boldsymbol{v}}\,\boldsymbol{\mathfrak{y}} \wedge \boldsymbol{\mathfrak{z}} + \boldsymbol{\mathfrak{y}} \wedge \pounds_{\boldsymbol{v}}\,\boldsymbol{\mathfrak{z}} \tag{4.95c}$$

$$\pounds_{\boldsymbol{v}+\dot{\boldsymbol{y}}}\,\mathbf{t} = \pounds_{\boldsymbol{v}}\,\mathbf{t} + \pounds_{\dot{\boldsymbol{y}}}\,\mathbf{t} \tag{4.95d}$$

$$\pounds_{\boldsymbol{v}}\,\mathbf{d}\boldsymbol{\mathfrak{z}} = \mathbf{d}(\pounds_{\boldsymbol{v}}\,\boldsymbol{\mathfrak{z}}) \tag{4.95e}$$

$$\varphi^*\,(\pounds_{\boldsymbol{v}}\,\mathbf{t}) = \pounds_{\varphi^*\boldsymbol{v}}\,(\varphi^*\mathbf{t}) \tag{4.95f}$$

$$\frac{\mathrm{d}(\varphi^*\mathbf{t})}{\mathrm{d}t} = \varphi^*\left(\pounds_{\boldsymbol{v}+\partial/\partial t}\,\mathbf{t}\right), \tag{4.95g}$$

where $\boldsymbol{v} = \dot{\varphi}$.

Some component results for Lie derivatives of forms

For later reference, we provide some component expressions for Lie derivatives of differential forms. For zero-forms, the Lie derivative reduces to the material time derivative

$$\pounds_{\dot{\chi}}\, f(t, x; a, b, \dots) = \dot{f} = \frac{\mathrm{d}f}{\mathrm{d}t} = \frac{\partial f}{\partial t} + \frac{\partial f}{\partial x^i}v^i + \frac{\partial f}{\partial a}\dot{a} + \frac{\partial f}{\partial b}\dot{b} + \dots \tag{4.96}$$

where $\dot{\chi} = \boldsymbol{v} + \partial/\partial t$ and the chain rule is applied as usual to all additional arguments $\{a, b \dots\}$. For one-forms the result is

$$\pounds_{\dot{\chi}}(z_i \mathbf{d}x^i) = \left(\pounds_{\dot{\chi}}\, z_i\right) \mathbf{d}x^i + z_i \left(\pounds_{\dot{\chi}}\, \mathbf{d}x^i\right) = \left(\frac{\mathrm{d}z_i}{\mathrm{d}t} + z_j \frac{\partial v^j}{\partial x^i}\right) \mathbf{d}x^i, \tag{4.97}$$

where the product rule (4.95c) has been applied with components z_i understood as zero-forms. For two-forms we obtain

$$\begin{aligned} \pounds_{\dot{\chi}}(z_{\underline{ij}} \mathbf{d}x^i \wedge \mathbf{d}x^j) &= \left(\pounds_{\dot{\chi}}\, z_{\underline{ij}}\right) \mathbf{d}x^i \wedge \mathbf{d}x^j + z_{\underline{ij}}\, \pounds_{\dot{\chi}} \left(\mathbf{d}x^i \wedge \mathbf{d}x^j\right) \\ &= \left(\frac{\mathrm{d}z_{\underline{ij}}}{\mathrm{d}t} + z_{\underline{ij}} \frac{\partial v^k}{\partial x^k} - z_{\underline{mn}} \epsilon^{\underline{lmn}} \frac{\partial v^k}{\partial x^l} \epsilon_{k\underline{ij}}\right) \mathbf{d}x^i \wedge \mathbf{d}x^j, \end{aligned} \tag{4.98}$$

which is also known as "flux derivative" (Kovetz, 2000, p. 89). We note that (4.98) can either be obtained through use of (4.93) or (4.95g). In the latter case one needs the pull-back of a two-form given in (4.117).

Finally, the Lie derivative of a three-form on a three-manifold is

$$\begin{aligned} \pounds_{\dot{\chi}}(f \mathbf{d}x^1 \wedge \mathbf{d}x^2 \wedge \mathbf{d}x^3) &= \left(\pounds_{\dot{\chi}}\, f\right) \mathbf{d}x^1 \wedge \mathbf{d}x^2 \wedge \mathbf{d}x^3 + f\, \pounds_{\dot{\chi}} \left(\mathbf{d}x^1 \wedge \mathbf{d}x^2 \wedge \mathbf{d}x^3\right) \\ &= \left(\dot{f} + f \frac{\partial v^i}{\partial x^i}\right) \mathbf{d}x^1 \wedge \mathbf{d}x^2 \wedge \mathbf{d}x^3 \end{aligned} \tag{4.99a}$$

or, alternatively,

$$\begin{aligned} \pounds_{\dot{\chi}}(f \mathbf{d}x^1 \wedge \mathbf{d}x^2 \wedge \mathbf{d}x^3) &= \frac{\partial f}{\partial t} \mathbf{d}x^1 \wedge \mathbf{d}x^2 \wedge \mathbf{d}x^3 + \mathbf{d}\left(f v^i \epsilon_{i\underline{jk}} \mathbf{d}x^j \wedge \mathbf{d}x^k\right) \\ &= \left(\frac{\partial f}{\partial t} + \frac{\partial f v^i}{\partial x^i}\right) \mathbf{d}x^1 \wedge \mathbf{d}x^2 \wedge \mathbf{d}x^3. \end{aligned} \tag{4.99b}$$

Remark 4.13. From above equations as well as (4.95g) we see that the material time derivative, except for zero-forms, in general does not commute with pull-back and push-forward

$$\varphi^* \left[\frac{\mathrm{d}\mathfrak{z}}{\mathrm{d}t}\right] \neq \frac{\mathrm{d}}{\mathrm{d}t} \varphi^*[\mathfrak{z}]. \tag{4.100}$$

4.1.7.14. Differentiation of integrals

An important mathematical operation in mechanics is the differentiation of integrals with respect to time or, equivalently, their variation. Consider the time derivative of the integral of the n-form $\mathfrak{z}$ over the time-varying n-domain Ω_t. Let φ be a map taking the fixed domain Ω to Ω_t. Then

$$\frac{\mathrm{d}}{\mathrm{d}t} \int_{\Omega_t} \mathfrak{z} = \frac{\mathrm{d}}{\mathrm{d}t} \int_{\Omega} \varphi^* \mathfrak{z} = \int_{\Omega} \frac{\mathrm{d}(\varphi^* \mathfrak{z})}{\mathrm{d}t} = \int_{\Omega_t} \varphi_* \left[\frac{\mathrm{d}(\varphi^* \mathfrak{z})}{\mathrm{d}t}\right], \tag{4.101}$$

where we assume that pull-back (φ^*) and push-forward (φ_*) are well-defined. It turns out that the final integrand is an operation equivalent to the Lie derivative (Bonet and Wood, 2008; Frankel, 2011)

$$\varphi_* \left[\frac{\mathrm{d}(\varphi^* \mathfrak{z})}{\mathrm{d}t} \right] = \pounds_{(v + \partial/\partial t)} \mathfrak{z} \qquad \text{with} \qquad \boldsymbol{v} = \dot{\varphi}, \tag{4.102}$$

by (4.95g). However, the definition of the Lie derivative of a form (4.91) does not explicitly involve a map from a fixed to the actual domain nor do the formulae (4.92) and (4.93). This reflects the fact that the result of (4.101) is independent of the actual choice of fixed domain Ω and map φ.

4.1.8. Differential geometric interpretation of physical quantities

In Section 4.1.2 we introduced the notions of vectors and one-forms and in Section 4.1.7 we extended one-forms to general n-forms along-side their algebra. Below we provide a geometric (re-)characterization of the physical quantities encountered so far.

Notation
As above, Fraktur letters ($\mathfrak{a}, \mathfrak{b}, \mathfrak{c}, \mathfrak{d} \ldots$) will be used to denote n-forms whereas the associated vectors will be denoted by the serif (roman) version. All lowercase quantities will be considered to "live" in the current configuration. Conversely, uppercase symbols indicate the corresponding objects in the initial configuration.

4.1.8.1. Velocity

We already employed velocity as the prototype of a (tangent) vector. Considering an infinitesimal time interval $\mathrm{d}t$ the corresponding infinitesimal element of a t-parameterized curve $c(t)$ is $\dot{c}(t)\,\mathrm{d}t$. Obviously, such a line element, being a scalar multiple of $\dot{c}$, is also an example of a (tangent) vector, i.e. living in tangent space of c at $c(t)$.

4.1.8.2. Electric potential and electric field

As already outlined above, the electric potential ϕ is a scalar function. In Example 4.2 we mentioned that the electric field is a quantity that is most naturally represented by a one-form (Burke, 1996; Frankel, 2011; Bossavit, 2012). This can also be seen from the "natural" operations one performs with the electric field: integration along a line to obtain the electric potential (difference) and computing the curl, which via Stokes' theorem also relates to a line integral. In terms of the electric field ${}^1\mathfrak{e}$ and the electric potential ϕ we have

$$-\int_{c'} {}^1\mathfrak{e}' = \phi'(c'(t_2)) - \phi'(c'(t_1)) = -\int_{c} {}^1\mathfrak{e} = \phi(c(t_2)) - \phi(c(t_1)), \tag{4.103}$$

with $c' = \varphi(c)$, ${}^1\mathbf{e} = \varphi^*[{}^1\mathbf{e}']$ and $\phi(x) = \phi'(\varphi(x))$. In index notation using (4.18) this reads as

$$-\int_{c'} \mathbf{e}'_i \, \mathbf{d}y^i = -\int_c \mathbf{e}'_i \frac{\partial y^i}{\partial x^j} \mathbf{d}x^j = -\int_c \mathbf{e}_j \mathbf{d}x^j. \tag{4.104}$$

In "naive vector notation" tacitly assuming Euclidean space and Cartesian coordinates we would (correctly) write with $E'^i = \mathbf{e}'_i$

$$-\int_{c'} \boldsymbol{E}' \cdot d\boldsymbol{L}' = -\int_c \boldsymbol{E}' \cdot (\underline{\boldsymbol{F}} \cdot d\boldsymbol{L}) = -\int_c (\boldsymbol{E}' \cdot \underline{\boldsymbol{F}}) \cdot d\boldsymbol{L}, \tag{4.105}$$

such that $\boldsymbol{E} = \boldsymbol{E}' \cdot \underline{\boldsymbol{F}}$. This, however, is based on the transformation for $\mathbf{d}\boldsymbol{L}' = \underline{\boldsymbol{F}} \cdot d\boldsymbol{L}$ and the requirement that the integrals over c' and c give the same results. We conclude that, although we do not have different notions for the "vectors" $\boldsymbol{E}$ and $d\boldsymbol{L}$, we have to employ different transformation rules for them. Hence, in the naive vector notation, we could not tell how to correctly transform a "vector" without putting it into an integral that corresponds to its role in physical equations. This is a strong point for the rigorous differential geometric approach.

In electrostatics, the electric field one-form ${}^1\mathbf{e}$ is fully characterized by the differential of ϕ, i.e. ${}^1\mathbf{e} = \mathbf{d}\phi$. This relation between functions and differentials as a subset of all one-forms suggests the term *zero*-form for scalar functions.

4.1.8.3. Charge and mass density

Charge density q and mass density ρ are integrated over volume to give the total charge Q and the total mass M, respectively, that is contained in that volume. What applies to q also applies to ρ and vice-versa such that we base our discussion on ρ only. We have with $\rho_0 = \rho(t = 0)$

$$M = \int_{\mathcal{B}} \rho_0 \, dV. \tag{4.106}$$

Both, the mass density ρ_0 and the volume three-form dV (see Section 4.1.7.9) are scalar in the sense that both of them can be described by a single number. However, their nature is nevertheless different as we see from a deformation $\varphi(\mathcal{B})$ which shall leave M invariant (see also (2.1))

$$M = \int_{\mathcal{B}} \rho_0 \, dV = \int_{\varphi(\mathcal{B})} \rho \, dv = \int_{\varphi(\mathcal{B})} {}^3\mathbf{m}. \tag{4.107}$$

From formula (4.74) we see that

$$M = \int_{\varphi(\mathcal{B})} \rho(x) \, dv(x) = \int_{\mathcal{B}} J(X)\rho(\varphi(X)) \, dV(X) = \int_{\mathcal{B}} \rho_0(X) \, dV(X) \tag{4.108}$$

and thus,

$$\rho_0 = \rho J. \tag{4.109}$$

Above equation is the general transformation for volume densities under orientation-preserving mappings and changes of coordinates.

Remark 4.14. The volume form is a so-called *pseudo-form*. This means that even if the coordinate system changes orientation, the volume, but also mass or total charge do not change sign (see Section 4.1.7.7). In solid mechanics deformation maps are required to have $\det \underline{\boldsymbol{F}} > 0$. A violation of this corresponds to self-penetration of body.

4.1.8.4. The free-charge potential

By use of the divergence theorem we obtain an integral version of equation $(3.19)_1$

$$\int_{\partial\Omega} \boldsymbol{D} \cdot \boldsymbol{N}\, dA = \int_{\Omega} q\, dV, \tag{4.110}$$

which indicates that $\boldsymbol{D}$ represents an object that is to be integrated over closed surfaces (for what in classical notation one explicitly needs to form the normal-projection at the surface). Respecting our convention of using lowercase symbols for Eulerian quantities, we rewrite the above equation as

$$\int_{\partial\Omega} \boldsymbol{d} \cdot \boldsymbol{n}\, da = \int_{\Omega} q\, dv, \tag{4.111}$$

where $\boldsymbol{d}\cdot\boldsymbol{n}$ can be considered as the scalar[11] multiplied with the two-form da restricted[12] to $\partial\Omega$. Consequently, the form corresponding to $\boldsymbol{d}$ is a two-form, which (when restricted to a surface) takes two vectors tangent to the surface (spanning a surface element) and returns the flux through the corresponding surface element. We shall denote this two-form as ${}^2\mathfrak{d}$, in terms of which we have

$$\int_{\partial\Omega} {}^2\mathfrak{d} = \int_{\Omega} q\, dv, \tag{4.112}$$

where the restriction of ${}^2\mathfrak{d}$ to $\partial\Omega$ is natural and thus not explicitly stated. The relation between $\boldsymbol{d}$ and ${}^2\mathfrak{d}$ is established through the volume three-form dv (Frankel, 2011, Section 2.9b)

$${}^2\mathfrak{d}(\boldsymbol{u}, \boldsymbol{v}) = dv(\boldsymbol{d}, \boldsymbol{u}, \boldsymbol{v}) = \mathbb{i}_{\boldsymbol{d}}\, dv \tag{4.113}$$

[11] In classical treatments, e.g. (Bonet and Wood, 2008), $\boldsymbol{n}\, da$ is regarded as a kind of "vectorial" surface element written like $\boldsymbol{da}$. From a purely algebraic point of view, we may understand this as a vector-valued two-form, of which the vector part is contracted with $\boldsymbol{d}$ (using a metric tensor).

[12] Recall Sections 4.1.7.7 and 4.1.7.9.

where $\mathbin{⨽}_{\boldsymbol{d}}$ denotes the interior product (4.52). In coordinates this is expressed as

$$d_{\underline{jk}}\mathbf{d}x^j \wedge \mathbf{d}x^k = \sqrt{g}\,\epsilon_{i\underline{jk}}d^i\mathbf{d}x^j \wedge \mathbf{d}x^k, \tag{4.114}$$

where $g = \det \mathbf{g}$ is the determinant of the metric tensor corresponding to coordinates x^i. From that one can also see that both a vector and a two-form (and also one-forms) on a three-manifold have three independent components, which leads to the confusion of two-forms with one-forms and vectors[13]. Equation (4.113) also defines the pull-back of $\boldsymbol{d}$ since it must hold that (Marsden and Hughes, 1994, p. 116, Definition 7.18)

$$\varphi^*[{}^2\mathfrak{d}] = i_{\varphi^*[\boldsymbol{d}]}\,\varphi^*[\,dv] = i_{J\varphi^*[\boldsymbol{d}]}\,dV, \tag{4.115}$$

where $\varphi^*[\boldsymbol{d}]$ is the pull-back operation of a vector, which is not the complete "pull-back" of $\boldsymbol{d}$ for the integral (4.111) to be invariant under φ. In fact, the full *Piola*-type transform is

$$\boldsymbol{D} = J\underline{\boldsymbol{F}}^{-1} \cdot \boldsymbol{d}. \tag{4.116}$$

Another possibility to obtain this formula is to investigate the transformation of $\boldsymbol{n}\,da$ which via Nanson's formula finally yields (4.116) as described by Bonet and Wood (2008). The latter approach also works via volumes and can thus be regarded as the vector-calculus version of the approach outlined above.

Remark 4.15. We conclude that the transform of an *associated* vector has to be derived either from its special definition or from the transformation rule for the underlying form (in the present scope this applies to one- and two-forms). Thus, we shall not treat associated vectors as "true" vectors. Besides "associated vector" there also exists the term "vector proxy" (Bossavit, 1998b).

Based on (4.114) and (4.116) we may come up with a coordinate formula for the pull-back of ${}^2\mathfrak{d}$, i.e.

$$(\varphi^*[\mathfrak{d}])_{JK} = D_{JK} = \sqrt{G}\epsilon_{IJK}\left(J\frac{\partial X^I}{\partial x^i}\epsilon^{i\underline{jk}}\frac{1}{\sqrt{g}}d_{\underline{jk}}\right) = \epsilon_{IJK}\det\underline{\boldsymbol{F}}\,\frac{\partial X^I}{\partial x^i}\epsilon^{i\underline{jk}}d_{\underline{jk}}, \tag{4.117}$$

where the last result contains the *adjugate* (adj) or *co-factor* (cof)

$$\operatorname{adj}\underline{\boldsymbol{F}} = \det(\underline{\boldsymbol{F}})\,\underline{\boldsymbol{F}}^{-1} = \operatorname{cof}\underline{\boldsymbol{F}}^{\mathrm{T}} \quad \Leftrightarrow \quad (\operatorname{adj}\underline{\boldsymbol{F}})^I{}_i = \det\underline{\boldsymbol{F}}\,\frac{\partial X^I}{\partial x^i} = (\operatorname{cof}\underline{\boldsymbol{F}})_i^I. \tag{4.118}$$

Another way to obtain the pull-back of ${}^2\mathfrak{d}$ is the generic formula (4.60). Applied to ${}^2\mathfrak{d}$

[13] Please note that the two underlined subscript indices of $d_{\underline{jk}}$ indicate that this symbol denotes components of a two-form while the superscript index of d^i indicates that the latter refers to components of a vector. The full symbol, that is with indices, should be understood as an entity. For example, just a d without indices has nothing to do with $d_{\underline{jk}}$ or d^i nor are the latter two intrinsically connected in any way just be cause they share the d in their name, which is inherited from their respective parent objects. It is just the relations explicitly established, such as Equation (4.113) that specify their relation.

we have

$$
\begin{aligned}
(\varphi^*[{}^2\mathfrak{d}])_{IJ} = \varphi^*[{}^2\mathfrak{d}]\,(\partial_{X^I}, \partial_{X^J}) &= {}^2\mathfrak{d}\left(\frac{\partial \varphi^i}{\partial X^I}\partial_{x^i}, \frac{\partial \varphi^j}{\partial X^J}\partial_{x^j}\right) \\
&= d_{\underline{kl}}\left[\mathbf{d}x^k\left(\frac{\partial \varphi^i}{\partial X^I}\partial_{x^i}\right)\mathbf{d}x^l\left(\frac{\partial \varphi^j}{\partial X^J}\partial_{x^j}\right) - \mathbf{d}x^l\left(\frac{\partial \varphi^i}{\partial X^I}\partial_{x^i}\right)\mathbf{d}x^k\left(\frac{\partial \varphi^j}{\partial X^J}\partial_{x^j}\right)\right] \\
&= d_{\underline{kl}}\left(F^k{}_I F^l{}_J - F^l{}_I F^k{}_J\right), \qquad (4.119)
\end{aligned}
$$

where the last term in braces shall be denoted as $\mathbb{cof}\,\underline{\boldsymbol{F}}$ due to the fact that it contains the building blocks of $\operatorname{cof}\underline{\boldsymbol{F}}$, that is

$$
(\operatorname{cof}\underline{\boldsymbol{F}})_i^I = \epsilon_{\underline{ijk}}\epsilon^{\underline{IJK}}(\mathbb{cof}\,\underline{\boldsymbol{F}})^{jk}_{JK} \quad \text{with} \quad (\mathbb{cof}\,\underline{\boldsymbol{F}})^{jk}_{JK} = \left(F^j{}_J F^k{}_K - F^k{}_J F^j{}_K\right). \qquad (4.120)
$$

Remark 4.16. This structure corresponds to the "×"-product in the contributions of de Boer (1982), Bonet et al. (2015) and Gil and Ortigosa (2016) among others.

Remark 4.17. While (4.117) features the inverse tangent map $\underline{\boldsymbol{F}}^{-1} = \underline{\boldsymbol{f}}$ we see from (4.119) and (4.120) that $\underline{\boldsymbol{f}}$ is actually not required. Otherwise it would not be possible to pull-back a two-from from a three- to a two-dimensional manifold for integration since the corresponding tangent map is not invertible. In fact, the pull-back of a form *never* requires the inverse of the tangent map as can be seen from (4.60).

We already saw in (4.83) another instance where co-factors play a role in operations involving two-forms, namely in computing their norm. Let us compare (4.83) applied to $\mathfrak{d}$ with the norm of the associated vector $\boldsymbol{d}$

$$
\begin{aligned}
\|\boldsymbol{d}\|^2 = d^i\, g_{ij}\, d^j &= d_{\underline{kl}}\frac{1}{\sqrt{g}}\epsilon^{\underline{ikl}}\, d_{\underline{mn}}\frac{1}{\sqrt{g}}\epsilon^{\underline{jmn}}\, g_{ij} \\
&= d_{\underline{kl}}\,\epsilon^{\underline{ikl}}\, d_{\underline{mn}}\,\epsilon^{\underline{jmn}}\,\frac{g_{ij}}{\det \mathbf{g}} = d_{\underline{kl}}\, d_{\underline{mn}}\left(\mathbb{cof}\,\mathbf{g}^{-1}\right)^{klmn} = \|{}^2\mathfrak{d}\|^2 \qquad (4.121)
\end{aligned}
$$

where $\mathbb{cof}\,\mathbf{g}^{-1}$ is in components

$$
\left(\mathbb{cof}\,\mathbf{g}^{-1}\right)^{ijkl} = g^{ik}\, g^{jl} - g^{il}\, g^{jk}. \qquad (4.122)
$$

Thus, the definition of the associated vector of a two-form is consistent with the corresponding Hodge-dual.

Remark 4.18. The two-form ${}^2\mathfrak{d}$ is actually a pseudo-form since it is related to the charge density q, which is a pseudo-(three-)form. Similarly, since the polarization $\boldsymbol{P}$ (or $\boldsymbol{p}$ in the current configuration) accounts for bound charges, it is also a pseudo-two-form.

4.1.8.5. The magnetic field

The governing equation for the magnetic field $\boldsymbol{b}$ in magneto-statics is $\operatorname{div} \boldsymbol{b} = 0$ (3.34). In terms of an integral of the two-form ${}^2\mathfrak{b}$ we write

$$\int_{\partial\Omega} {}^2\mathfrak{b} = 0. \tag{4.123}$$

What seems geometrically similar to $\boldsymbol{d}$ before still features a subtle difference: $\boldsymbol{d}$ is integrated over closed surfaces to measure the charge density in the interior. The magnetic field, however, measures a flux through an *open* surface. This can be observed in the integral version of $(3.12)_4$

$$\int_S \frac{\partial \boldsymbol{b}}{\partial t} \cdot \boldsymbol{n}\, da = -\int_{\partial S} \boldsymbol{e} \cdot d\boldsymbol{l} \qquad \text{or} \qquad \int_S \frac{\partial^2 \mathfrak{b}}{\partial t} = -\int_{\partial S} {}^1\mathfrak{e}, \tag{4.124}$$

where the integral of $\partial_t \boldsymbol{b}$ or $\partial_t {}^2\mathfrak{b}$ is over S which is in general not a boundary (if it were, then $\partial S \equiv 0$). Furthermore, since $\operatorname{div} \boldsymbol{b} = 0$ holds everywhere, the integral of $\boldsymbol{b}$ over a closed surface always vanishes. As detailed by Frankel (2011, Section 2.9b), a vector-type quantity corresponding to a two-form is a *pseudo-vector*, i.e. a vector obtained as the cross product of two vectors or as the curl of a vector potential. This is indeed the case for $\boldsymbol{b}$. Nevertheless, we may use the same formula as for the relation between $\boldsymbol{d}$ and the pseudo-form ${}^2\mathfrak{d}$, that is

$${}^2\mathfrak{b} = \mathbb{i}_{\boldsymbol{b}}\, dv. \tag{4.125}$$

Consequently, the pull back of $\boldsymbol{b}$ is performed via (4.119).

Remark 4.19. The difference between pseudo- and "true" vectors or forms becomes apparent under changes of orientation. "Pseudo" refers to "*a change of sign with a change of orientation*" (see Section 4.1.7.8 and Frankel (2011, Section 2.8e)). Otherwise they transform in the same way.

4.1.8.6. Magnetic vector potential

The magnetic vector potential $\boldsymbol{a}$ has a corresponding one-form ${}^1\mathfrak{a}$ and follows the same rules as $\boldsymbol{e}$ or ${}^1\mathfrak{e}$, respectively.

4.1.8.7. Current density and the current potential

The current potential $\boldsymbol{H}$ as well as the magnetization $\boldsymbol{M}$ measure currents traversing a surface. Hence, they are naturally integrated over closed curves, i.e. boundaries of surfaces. Thus, they correspond to pseudo-one-forms ${}^1\mathfrak{h}$ and ${}^1\mathfrak{m}$, respectively. Based on

${}^1\mathfrak{h}$, ${}^2\mathfrak{d}$ and $(3.7)_2$ the (electric) current ${}^2\mathfrak{j}$ is the pseudo two-form obtained as

$$ {}^2\mathfrak{j} = \mathbf{d}\,{}^1\mathfrak{h} - \frac{\partial^2 \mathfrak{d}}{\partial t}. \tag{4.126} $$

4.1.8.8. Permittivity and permeability

The two constants ϵ_0 and μ_0, while often regarded as simple scalars, can be understood as Hodge-star operators "$\star$" (Bossavit, 2010; Frankel, 2011). In fact, one may regard them as representations of (incremental) constitutive laws connecting two work-conjugate quantities, of which one is a pseudo/true k-form and the other a true/pseudo $(n-k)$-form where n is the dimension of space. Thus, also the elasticity tensor can be understood as a Hodge operator (Bossavit, 2010; Kanso et al., 2007).

Let us comment on (4.79). The components h^i can either be understood as components of the vector associated with the one-form $\mathfrak{h}$ or as the vector associated with the Hodge-dual $\star\,\mathfrak{h}$. In the latter case, think of inserting a multiplication with μ_0 to obtain a Hodge operation

$$ \star_{\mu_0}\mathfrak{h} = \mu_0(\star\,\mathfrak{h}) \tag{4.127} $$

which can be read as $\mathfrak{b} = \star_{\mu_0}\mathfrak{h}$ in vacuum. Clearly, $\star_{\mu_0}\mathfrak{h}\wedge\mathfrak{h}$ is the magnetostatic energy density in empty space expressed in terms of $\mathfrak{h}$. We note that $\boldsymbol{b}$ (associated with ${}^2\mathfrak{b}$) transforms transforms differently than $\boldsymbol{h}$ (associated with ${}^1\mathfrak{h}$). In vector-notation we would write $\boldsymbol{b} = \mu_0\boldsymbol{h}$. Here the different transforms for $\boldsymbol{b}$ and $\boldsymbol{h}$ also indicate that there is an additional (hidden) operator. Otherwise $\mu_0\boldsymbol{h}$ could not transform differently than $\boldsymbol{h}$. However, understanding both objects, $\boldsymbol{b}$ and $\boldsymbol{h}$ as vectors and μ_0 as a scalar constant obstructs us from seeing the operator. Instead, it seems that this simple constitutive relation is not preserved under pull-back operations as stated by Dorfmann and Ogden (2005, Eq. 20).

4.1.8.9. Force and momentum

We prefer the viewpoint that force simply is a linear functional taking velocity (or virtual displacement) and returning mechanical power (or virtual work). Accordingly, we regard force as a one-form. However, this notion is not a complete characterization of force *densities* $\rho\boldsymbol{b}$ as in (2.6). Indeed, let us consider $\rho\boldsymbol{b}\,dv$, or better $(\rho\boldsymbol{b}\cdot\boldsymbol{v})\,dv$ as in the balance of energy (2.15). Clearly, $\rho\boldsymbol{b}\cdot\boldsymbol{v}$ is the scalar component of a three-form as indicated by dv. We ask for the geometric character of $\rho\boldsymbol{b}\;dv$. Without further ado (Definition 4.7), we refer to an object which takes a vector and returns a pseudo three-form in $\mathbb{R}^3$ as *one-form-valued* pseudo three-form as an extension to standard scalar-valued three-forms. The latter is obtained once the former is paired with a vector; velocity in this case. We highlight that a one-form-valued three-form in $\mathbb{R}^3$ is not a four-form in $\mathbb{R}^3$ because any $(n+1)$-form on an n-dimensional manifold vanishes identically (this follows from (4.46)). The essential difference is that we do not require a one-form-valued

three-form in $\mathbb{R}^3$ to be totally skew-symmetric. In mathematical notation with $\rho\boldsymbol{b}$ corresponding to the one-form $\mathfrak{f}$

$$\rho\boldsymbol{b}\cdot\boldsymbol{v}\,dv = \mathbb{i}_{\boldsymbol{v}}(\mathfrak{f}\otimes dv) = \mathbb{i}_{\boldsymbol{v}}\mathfrak{f}\;dv. \tag{4.128}$$

Occasionally, we will compactly denote a one-form-valued three-form as, e.g.

$$\mathfrak{f}\otimes dv = {}^3\underline{\mathfrak{f}}. \tag{4.129}$$

Remark 4.20. A huge benefit of exterior calculus and differential forms compared with classical vector calculus is that this framework works for any spatial dimension, not only up to three such that they may be naturally employed for four-dimensional space time. However, we did not explore this application. Nevertheless, we note that in such a situation the current discussion has to be revisited; i.e. new objects which combine two already known objects emerge. As an example we mention the energy-momentum vector in special relativity (Frankel, 2011) and the electromagnetic four-potential discussed in Section 4.2.5.

At this point, we also need to digress on the magnetic force term $\boldsymbol{j}\times\boldsymbol{b}$ as in (3.40). Above we reasoned that electric current as well as magnetic field are two-forms in $\mathbb{R}^3$ (without loss of generality). Thus, their exterior product vanishes identically. This means, the translation of (3.40) which would come to one's mind at first, i.e. $\mathfrak{j}\wedge\mathfrak{b}$, fails. However, the problem can be solved by investigating the Lorentz-type force density (3.4) which we rewrite as a one-form-valued three-form

$$\boldsymbol{f}^{\mathrm{m}} = q\,(\boldsymbol{e}+\boldsymbol{v}\times\boldsymbol{b})\;dv \quad\Leftrightarrow\quad \left({}^1\mathfrak{e}-\mathbb{i}_{\boldsymbol{v}}{}^2\mathfrak{b}\right)\otimes{}^3\mathfrak{q} = \left(q\,{}^1\mathfrak{e}-q\,\mathbb{i}_{\boldsymbol{v}}{}^2\mathfrak{b}\right)\otimes dv = {}^1\mathfrak{f}^{\mathrm{m}}\otimes dv. \tag{4.130}$$

The interesting part is

$$\left(q\,\mathbb{i}_{\boldsymbol{v}}{}^2\mathfrak{b}\right)\otimes dv = \left(\mathbb{i}_{q\boldsymbol{v}}{}^2\mathfrak{b}\right)\otimes dv \tag{4.131}$$

because we have

$$\mathbb{i}_{\boldsymbol{v}}{}^3\mathfrak{q} = q\,\dot{x}^i\,dv(\partial_{x^i}) = q\,\dot{x}^i\varepsilon_{\underline{ijk}}\sqrt{q}\,\mathbf{d}x^j\wedge\mathbf{d}x^k = {}^2\mathfrak{j}. \tag{4.132}$$

Hence, $q\dot{x}^i$ are the components of a vector $\boldsymbol{j}$ associated with the two-form $\mathfrak{j}$ (see also (4.113)). The same vector components also appear in the interior product in (4.131). This suggests to understand $\boldsymbol{j}\times\boldsymbol{b}\,dv$ as

$$\boldsymbol{f}^{\mathrm{m}} = \boldsymbol{j}\times\boldsymbol{b}\,dv \qquad\Leftrightarrow\qquad {}^1\mathfrak{f}^{\mathrm{m}}\otimes dv = \left(\mathbb{i}_{\boldsymbol{j}}{}^2\mathfrak{b}\right)\otimes dv = {}^3\underline{\mathfrak{f}}^{\mathrm{m}}. \tag{4.133}$$

In fact, when working with a current, we are free to write it in terms of charge and velocity whereby only their product counts but not their individual values.

4.1.8.10. Stress

Stresses as represented by the Cauchy stress tensor $\boldsymbol{\sigma}$ are objects of which we take the divergence and which we integrate over surfaces (2.10). This obviously indicates a two-form character. However, similar to force and force densities also stress has a natural pairing with velocity (2.35) as well as with the velocity gradient (2.16). To shed some light on the details, we consider equations (2.10) and (2.26). The last integral in (2.26) features the Piola-type transformation already encountered for $\boldsymbol{D}$ and $\boldsymbol{B}$ applied to the second "slot" (from the right) of $\boldsymbol{\sigma}$. Moreover, $\underline{\boldsymbol{F}}$ is already the tangent map. This is also in agreement with the normal vector occurring in (2.10) and leading to integrands $\boldsymbol{\sigma}\cdot\boldsymbol{n}\,da$. If we insert (2.10) into the integral balance of energy (2.15) we obtain $(\boldsymbol{\sigma}\cdot\boldsymbol{n})\cdot\boldsymbol{v}\,da$. Hence, when integrating over a surface, the first slot of $\boldsymbol{\sigma}$ takes a velocity vector and is therefore understood to represent a one-form similar to force. We conclude that stress can be represented by a one-form-valued two-form ${}^2\underline{\underline{\mathfrak{s}}}$ as detailed by Kanso et al. (2007)

$$\int_{\partial\mathcal{B}_t}(\boldsymbol{\sigma}\cdot\boldsymbol{n})\cdot\boldsymbol{v}\,da \;\Rightarrow\; \int_{\partial\mathcal{B}_t}\mathbb{i}_{\boldsymbol{v}}s_{i\underline{jk}}\mathbf{d}x^i\otimes\mathbf{d}x^j\wedge\mathbf{d}x^k=\int_{\partial\mathcal{B}_t}(\dot{x}^i s_{i\underline{jk}})\,\mathbf{d}x^j\wedge\mathbf{d}x^k. \tag{4.134}$$

The last integral features a two-form such that we may naturally apply the generalized Stokes' theorem (4.89) and rewrite the last integral in (4.134) as

$$\begin{aligned}\int_{\partial\mathcal{B}_t}(\dot{x}^i s_{i\underline{jk}})\,\mathbf{d}x^j\wedge\mathbf{d}x^k &= \int_{\mathcal{B}_t}\mathbf{d}\left((\dot{x}^i s_{i\underline{jk}})\,\mathbf{d}x^j\wedge\mathbf{d}x^k\right)=\int_{\mathcal{B}_t}\frac{\partial\dot{x}^i s_{i\underline{kl}}}{\partial x^j}\mathbf{d}x^j\wedge\mathbf{d}x^k\wedge\mathbf{d}x^l\\ &=\int_{\mathcal{B}_t}\left(s_{i\underline{kl}}\frac{\partial\dot{x}^i}{\partial x^j}+\dot{x}^i\frac{\partial s_{i\underline{kl}}}{\partial x^j}\right)\mathbf{d}x^j\wedge\mathbf{d}x^k\wedge\mathbf{d}x^l \qquad (4.135)\end{aligned}$$

or by (4.57)

$$=\int_{\mathcal{B}_t}\left[\mathbb{i}_{\boldsymbol{v}}\,\mathbb{d}\underline{\underline{\mathfrak{s}}}+\underline{\underline{\mathfrak{s}}}(\boldsymbol{\nabla}\boldsymbol{v})\right]. \tag{4.136}$$

From (4.136) we see that $\mathbb{d}\underline{\underline{\mathfrak{s}}}$ plays the role of the (covariant) divergence (Marsden and Hughes, 1994, p. 82, Box 4.1) of the associated stress tensor with components $s_i{}^j$ (see (4.137b) below), but for the differential form version. Remarkably, (4.135) is the simplest statement when it comes to coordinate expressions.

To not too much surprise both of the final integrands (4.135) and (4.136) have the same component-wise structure as $\boldsymbol{\sigma}:\operatorname{grad}\boldsymbol{v}+\operatorname{div}(\boldsymbol{\sigma})\cdot\boldsymbol{v}$ in $\mathbb{R}^3$ and both approaches are equivalent in their further results. However, the fact that the covariant derivative of metric tensors vanishes identically (4.36) renders (4.136) and related formulations favorable as we shall see in Section 4.1.8.13

It now remains to characterize the expression $\rho\partial\Psi(\underline{\boldsymbol{F}})/\partial\underline{\boldsymbol{F}}$ arising in (2.26) and (2.27). The double-contraction with $\dot{\underline{\boldsymbol{F}}}$ suggests that $\partial\Psi(\underline{\boldsymbol{F}})/\partial\underline{\boldsymbol{F}}$ has the structure of a one-form $\otimes$-multiplied with a vector. However, suppose we do not want to use the "tensor-style" double contraction but rather the exterior product of the stress form's two-form part and

the tangent-map's one-form part. Then we may apply a vector-to-two-form conversion (4.113) as we also did in the case of the vectors $\boldsymbol{d}$ and $\boldsymbol{b}$ which here correspond to the vector part of the classical stress tensor. In detail, this works as

$$\rho \frac{\partial \Psi(\underline{\boldsymbol{F}})}{\partial \underline{\boldsymbol{F}}}\, dv = \rho_0 \left(\frac{\partial \Psi(\underline{\boldsymbol{F}})}{\partial F^i_{\ I}}\, \mathbf{d}x^i \partial_{X^I} \right) dV = P_i^{\ I}\, \epsilon_{I\underline{KL}} \sqrt{G}\, \mathbf{d}x^i \otimes \mathbf{d}X^K \wedge \mathbf{d}X^L \tag{4.137a}$$

or

$$= \frac{1}{J} P_i^{\ I}\, \mathbf{d}x^i \frac{\partial \varphi^j}{\partial X^I} \partial_{x^j}\, dv = s_i^{\ j}\, \epsilon_{j\underline{kl}} \sqrt{g}\, \mathbf{d}x^i \otimes \mathbf{d}x^k \wedge \mathbf{d}x^l. \tag{4.137b}$$

Recalling (4.113) we see that

$$s_i^{\ j}\, \epsilon_{j\underline{kl}} \sqrt{g} = s_{i\underline{kl}} \qquad \text{and} \qquad P_i^{\ J}\, \epsilon_{J\underline{KL}} \sqrt{G} = P_{i\underline{KL}}. \tag{4.138}$$

The one-form-valued two-forms ${}^2\underline{\mathfrak{s}}$ and ${}^2\underline{\mathfrak{P}}$ act on $\boldsymbol{\nabla v}$ and $\underline{\dot{\boldsymbol{F}}}$, respectively, such that

$${}^2\underline{\mathfrak{s}}\,(\boldsymbol{\nabla v}) = s_{i\underline{kl}}\, \mathbf{d}x^i \otimes (\mathbf{d}x^k \wedge \mathbf{d}x^l) \left((\boldsymbol{\nabla v})^i_{\ j}\, \mathbf{d}x^j \partial_{x^i} \right) = s_{i\underline{kl}} (\boldsymbol{\nabla v})^i_{\ j}\, \mathbf{d}x^j \wedge \mathbf{d}x^k \wedge \mathbf{d}x^l \tag{4.139}$$

and

$${}^2\underline{\mathfrak{P}}\,(\underline{\dot{\boldsymbol{F}}}) = P_{i\underline{KL}}\, \mathbf{d}x^i \otimes (\mathbf{d}X^K \wedge \mathbf{d}X^L) \left((\dot{\boldsymbol{F}})^i_{\ J}\, \mathbf{d}X^J \partial_{x^i} \right) = P_{i\underline{KL}} (\dot{\boldsymbol{F}})^i_{\ J}\, \mathbf{d}X^J \wedge \mathbf{d}X^K \wedge \mathbf{d}X^L. \tag{4.140}$$

For further aspects on the treatment of forces, tractions and stresses in terms of forms we refer to Kanso et al. (2007). We mention that we derived the above results by our own calculations and compared them against the latter reference. We also note that we deliberately did not follow the corresponding material in (Frankel, 2011, Chapter $\mathcal{O}$), where the discussion is based on the treatment of force as vector and not as one-form. This is not only contrasting the starting point of Kanso et al. (2007) but also inconsistent with the treatment of, e.g., the Lorentz force in the same monograph (Frankel, 2011, Section 3.5b,p. 120).

4.1.8.11. Traction and surface charge density

Surface charge density ${}^2\mathfrak{q}^{\mathrm{s}}$ is a two-form as is the charge potential ${}^2\mathfrak{d}$. However, while ${}^2\mathfrak{d}$ is usually defined on a three-manifold $\mathcal{M}^3$ and thus has an associated vector, ${}^2\mathfrak{q}^{\mathrm{s}}$ is only defined on a surface. Hence, ${}^2\mathfrak{q}^{\mathrm{s}}$ is naturally scalar-valued, which is also the case for ${}^2\mathfrak{d}$ when restricted onto a surface.

Tractions are the mechanical counterpart of surface charge densities. We represent them as one-form-valued two-forms defined on a surface only. Notably, tractions make only sense if the surface is embedded in a higher-dimensional manifold of which the vectors are paired with the tractions one-form part.

The relation between stresses and traction in this framework is quite natural. Since tractions are two-forms on a two-(sub-)manifold they have corresponding two-forms in three-manifolds which are stresses. They are connected by the restriction of the stresses

to the domain of the tractions, i.e. a surface. This can be best demonstrated by means of (4.135). Consider the case where the bases $\mathbf{d}x^1$ and $\mathbf{d}x^2$ do not only serve as (two of three) basis forms of $\mathbb{R}^3$ but at the same time correspond to the two coordinate functions on the surface $\mathcal{S}_t$, where $\underline{jk} = \{1, 2\}$. Then, the restriction of the stress form $\underline{\mathfrak{s}}$ gives

$$\underline{\mathfrak{s}}\big|_{\mathcal{S}_t} = s_{i12}\mathbf{d}x^i. \tag{4.141}$$

That is, we extract the "traction"-part of the stress form $\underline{\mathfrak{s}}$ which is represented by only three components.

We remark that surface charges actually correspond to the difference of the restrictions of the charge potential from both sides of the surface, i.e. the jump of ${}^2\mathfrak{d}$. Similarly, tractions correspond to jumps in stress across a surface. However, in mechanics the stress outside a body is usually zero such the notion of a jump is mostly superfluous. However, in magneto-electro-mechanics stress exists also in free space (air) such that the notion of tractions as jumps in stress fields across boundaries of bodies is a necessity.

4.1.8.12. Surface currents

On two-dimensional manifolds exist two kinds of one forms: The first possibility are usual one-forms such as the one employed for the electric field. The second type is a two-form restricted to a two-domain $\mathcal{M}_1^2$ which is then collapsed to a line being part of a traversing two-manifold $\mathcal{M}_2^2$. For this to be possible, both two-domains have to be embedded in a higher-dimensional space where the original two-form is defined. The form restricted to $\mathcal{M}_1^2 \cap \mathcal{M}_2^2$ seems like a one-form on $\mathcal{M}_2^2$, but has the flux-type character of a two-form in a three-domain. We may think of it as an $(n-1)$-form which just happens to be a one-form for $n = 2$. Mathematically, one might construct such an object by means of the Dirac-δ for the one-form's out-of-plane dimension (the collapsed dimension). Figure 4.4 depicts a surface $\mathcal{S}_t$ with coordinates $\{u^1, u^2\}$. In subplot (a) we see a standard one-form (red) paired with a vector tangent to u^2. In (b) we have a two-form (red) with a component corresponding to a traversing coordinate t. The tangents to u^2 and t span an area element $\partial_{u^2} \wedge \partial_t$ with which we may associate a normal vector (dashed). When t corresponds to some (infinitesimal) thickness of the surface the two-form may shrink in t (increasing its local value) and look like a one-form on $\mathcal{S}_t$. However, it will not lose its connection to the orientation of the degenerate area-element.

The most important example for this is the notion of a surface current analogous to surface charge. We suggest a special notion for one-forms originating from two-forms on a collapsed domain which is as follows: Assume a surface (a two-manifold) with coordinates $\{u^1, u^2\}$. Let u^3 denote the coordinate function defined by means of a curve traversing the surface. Assume now a current two-form, e.g., $\mathfrak{j} = j_{23}\mathbf{d}u^2 \wedge \mathbf{d}u^3$, on a manifold spanned by the coordinate curves u^2 and u^3. This manifold shall now be collapsed such that the u^3 extent vanishes but at the same time $\mathfrak{j}$ is scaled such that the integral value remains the same. The resulting surface current "collapsed two-form" $\mathfrak{j}^{\mathrm{s}}$

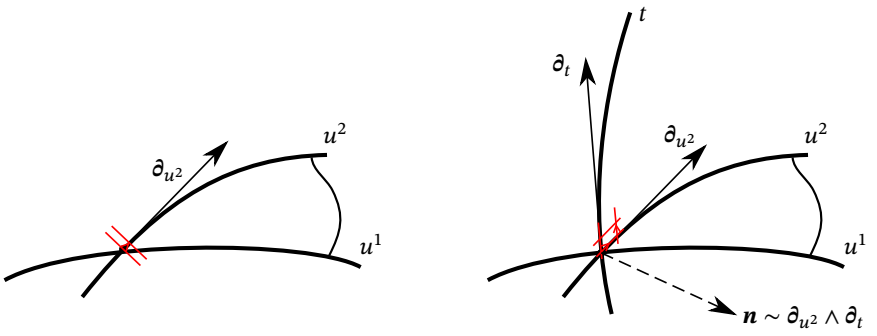

(a) a one-form in the u^1-u^2 plane

(b) a two-form with a t component

Figure 4.4: A one-form in the u^1-u^2 plane (a) versus a two-form with an "out-of-plane" component in the t coordinate (b). If we let the t direction collapse, e.g. as an infinitesimal thickness, the two-form looks like a one-form but we shall not forget that there remains a natural notion of orientation and traversal which is not encoded by the one-form. Note that the wedge product of two vectors can be defined in analogy to that for one-forms, that is $\boldsymbol{a} \wedge \boldsymbol{b} = \boldsymbol{a} \otimes \boldsymbol{b} - \boldsymbol{b} \otimes \boldsymbol{a}$ (see (4.48)).

will be expanded as

$$\mathbf{j}^{\mathrm{s}} = j^{\mathrm{s}}_{23} \mathbf{d}u^2 \wedge \text{⌀}u^3 + j^{\mathrm{s}}_{31} \text{⌀}u^3 \wedge \mathbf{d}u^1 = (j^{\mathrm{s}}_{13} \mathbf{d}u^1 + j^{\mathrm{s}}_{23} \mathbf{d}u^2) \wedge \text{⌀}u^3. \tag{4.142}$$

The collapsed basis $\text{⌀}u^3$ helps to keep track of signs with the standard rules of exterior calculus summarized in Section 4.1.7. As a consequence it allows for a natural treatment of the jump condition for the current potential $\mathfrak{h}$ and corresponds to operations like $\boldsymbol{n} \times \boldsymbol{j}$.

Remark 4.21. We are not aware of a situation where a notation as in (4.142) is useful for tractions or surface charges. However, the approach should be applicable also in other situations.

4.1.8.13. Considerations on invariants prototypical for energy densities

In this section we by "invariant" mean a scalar quantity computed from non-scalar objects which is invariant under a change of coordinates. The most familiar invariant is probably the norm of a vector

$$\|\boldsymbol{v}\| = \sqrt{\langle \boldsymbol{v}, \boldsymbol{v} \rangle} = v^i g_{ij} v^j, \tag{4.143}$$

which represents the *length* of a vector, hence also the name *metric* tensor for $\mathbf{g}$.

The principle of material frame indifference

Material frame indifference of the mechanical or more general physical equations is a principle of central importance (Truesdell and Noll, 2004; Noll, 2006). It demands the

independence of observations made in different observer frames connected by a length- and orientation-preserving transform $y = \chi(x)$ *within* the Eulerian frame (Marsden and Hughes, 1994, Section 3.2, Axiom 2.9). By length-preserving we mean

$$\|\boldsymbol{v}\|^2 = \langle \boldsymbol{v}, \boldsymbol{v} \rangle_{\mathbf{g}} = \langle \chi_*[\boldsymbol{v}], \chi_*[\boldsymbol{v}] \rangle_{\mathbf{g}} \tag{4.144}$$

One can show that the tangent map of χ has to fulfill

$$v^i \frac{\partial \chi^a}{\partial x^i} g_{ab} \frac{\partial \chi^b}{\partial x^j} v^j = v^i g_{ij} v^j \qquad \Leftrightarrow \qquad g_{ab} \frac{\partial \chi^b}{\partial x^j} g^{jk} = \frac{\partial \chi^{-1}{}^k}{\partial y^a}. \tag{4.145}$$

With $F^a{}_i = \partial_{x^i} \chi^a$ this boils down to $\underline{\boldsymbol{F}}^{\tau} = \underline{\boldsymbol{F}}^{-1}$ (adjoint = inverse)[14], which characterizes *isometries* (in $\mathbb{R}^3$: the special orthogonal group $SO(3)$, i.e. rotation matrices).

Material frame indifference is the generalization of the common notion of an "invariant" as something "not affected by rotations" to "invariant under length preserving transforms". The invariants as the vector norm above clearly meet this requirement given that the involved objects really follow the usual tensor transformation rules. Material frame indifference shall, however, also hold for observations by moving observers as well as for equations, e.g. the balance of energy. If we allow for relative motion of observers, velocity transforms in case of $y = \chi(x,t) = \chi(\varphi(X,t),t) = \hat{\chi}(X,t)$ as

$$\dot{y} = \dot{\chi} = \frac{\mathrm{d}}{\mathrm{d}t} (\chi(x,t)) = \underline{\boldsymbol{F}}(\dot{x}) + \frac{\partial \chi}{\partial t} \tag{4.146}$$

and thus

$$\|\dot{y}\|_{\mathbf{g}} \neq \|\dot{x}\|_{\mathbf{g}} \tag{4.147}$$

even if χ is an isometry (4.145). Hence, velocity and kinetic energy are not material frame indifferent. The balance of energy, however, is material frame indifferent by virtue of the balance of linear momentum and the balance of moment of momentum[15]. Tensors that keep their tensorial transformation rule in case of moving observers are sometimes called *objective*. Only such objects can safely be used to form material-frame-indifferent "invariants". We highlight that Lie rates (Section 4.1.7.13), are always objective (Marsden and Hughes, 1994, Section 1.6, Box 6.1). Since we shall stay in the quasi-static and non-dissipative context, we need not elaborate further on invariance and objectivity of time derivatives. Nevertheless, the interested reader is referred to the extensive discussions of material frame indifference by Marsden and Hughes (1994, Section2.3; Section 3.2, Axiom 2.9) and Tadmor et al. (2012, Section 6.3).

[14] Here we slightly deviate from the notation employed by Marsden and Hughes (1994) who use a superscript T to denote the adjoint, whereas we instead use τ and reserve T for the usual transposition from linear algebra. See also Appendix C. In many cases, most notably Cartesian coordinates with Euclidean metric, this distinction is dropped for simplicity.

[15] Or, conversely: postulating material frame indifference of the balance of energy yields the balance of linear momentum and balance of moment of momentum. See Section 2.4.2 and Marsden and Hughes (1994, Chapter 2, Boxes 3.1–3.3).

Invariance under general changes of coordinates
As an extension of material frame indifference we are also interested in invariance under general changes of coordinates or diffeomorphisms, i.e. *covariance* (Marsden and Hughes, 1994, Sections 2.4 and 3.3). Norms such as $\|\boldsymbol{v}\|$ (provided that $\boldsymbol{v}$ is objective) are zero-forms such that their point-value is invariant under pull-back operations with respect to a change of coordinates φ. In particular, for vectors we have

$$\|\boldsymbol{v}\| = \|\boldsymbol{v}\|_{\mathbf{g}} = \sqrt{v^i g_{ij} v^j} = \sqrt{V^I C_{IJ} V^J} = \|\varphi^*[\boldsymbol{v}]\|_{\varphi^*[\mathbf{g}]} \tag{4.148}$$

with

$$(\mathbf{C})_{IJ} = C_{IJ} = \varphi^*[\mathbf{g}]_{IJ} = F^i{}_I F^j{}_J g_{ij}. \tag{4.149}$$

Below we shall focus on invariance in precisely this sense where we will, however, restrict ourselves to what is needed in a quasi-static context.

Invariants of differential forms
By analogy to (4.143) one can guess that the corresponding operation for one-forms is

$$\|{}^1\boldsymbol{\imath}\| = \sqrt{\langle {}^1\boldsymbol{\imath}, {}^1\boldsymbol{\imath}\rangle} = \sqrt{z_i g^{ij} z_j}. \tag{4.150}$$

When $\boldsymbol{v} = \mathbf{g}^{-1}(\boldsymbol{\imath})$ is the vector associated with the one-form $\boldsymbol{\imath}$ it is easy to verify that (4.105) and (4.150) are consistent in the sense that the norms of associated objects evaluate to the same number. Moreover, for forms of all degrees we have by (4.78)

$$\|\boldsymbol{\imath}\|^2 = \langle \boldsymbol{\imath}, \boldsymbol{\imath}\rangle = \frac{\star\, \boldsymbol{\imath} \wedge \boldsymbol{\imath}}{dv}. \tag{4.151}$$

In particular, for two-forms this boils down to the formula (4.83). As demonstrated by (4.121), the norm of a two-form according to (4.151) is consistent with the norm of the associated vector (4.113). For one-forms it holds that

$$\|{}^1\boldsymbol{\imath}\| = \|{}^1\boldsymbol{\imath}\|_{\mathbf{g}^{-1}} = \|\varphi^*[{}^1\boldsymbol{\imath}]\|_{\varphi^*[\mathbf{g}^{-1}]} = \sqrt{Z_I C^{IJ} Z_J} \tag{4.152}$$

with

$$(\mathbf{C}^{-1})^{IJ} = C^{IJ} = (\varphi^*[\mathbf{g}^{-1}])^{IJ} = f^I{}_i f^J{}_j g^{ij} = (\varphi^*[\mathbf{g}]^{-1})^{IJ} \quad \text{and} \quad \underline{\boldsymbol{f}} = \underline{\boldsymbol{F}}^{-1}. \tag{4.153}$$

From (4.153) we see that the pull-back commutes with inversion, i.e.

$$\varphi^*[\mathbf{g}^{-1}] = \varphi^*[\mathbf{g}]^{-1}. \tag{4.154}$$

For two-forms it can be shown that (see (4.121))

$$\|{}^2\boldsymbol{\imath}\| = \|{}^2\boldsymbol{\imath}\|_{\mathbb{cof}\,\mathbf{g}^{-1}} = \|\varphi^*[{}^2\boldsymbol{\imath}]\|_{\varphi^*[\mathbb{cof}\,\mathbf{g}^{-1}]} \tag{4.155}$$

with

$$\varphi^*[\mathbb{cof}\,\mathbf{g}^{-1}] = \mathbb{cof}\,(\varphi^*[\mathbf{g}]^{-1}). \tag{4.156}$$

This result is either obtained through the norm of the associated vector expressed in pull-backs or via the general n-form formula

$$\|\mathfrak{z}\|^2 = \langle \mathfrak{z}, \mathfrak{z} \rangle = \frac{\varphi^*[\star\, \mathfrak{z}] \wedge \varphi^*[\mathfrak{z}]}{\varphi^*[\, dv]}. \tag{4.157}$$

The norms given above can be applied to the vectors and forms such as the electric field $\mathfrak{e}$, the free-charge potential $\mathfrak{d}$, the free-current potential $\mathfrak{h}$ and the magnetic field $\mathfrak{b}$ as well as to their associated vectors. Furthermore, norms with respect to, e.g., the push-forward of $\mathbf{G}$ or $\mathbf{G}^{-1}$ are also possible in principle and can be treated in a similar manner.

Strain measures

Different considerations are in order for invariants of strain measures. The fundamental quantity encoding deformation is the tangent map (4.17) of the motion $x = \varphi(X)$

$$\underline{\boldsymbol{F}}(X) = \frac{\partial \varphi^i(X)}{\partial X^I} \partial_{x^i} \otimes \mathbf{d}X^I. \tag{4.158}$$

Based on $\underline{\boldsymbol{F}}$ there exists a range of strain or deformation measures reflecting the idea of comparing lengths in the initial configuration (with coordinates X) with lengths in the current configuration (with coordinates x). One such strain tensor is the *Green* or *Lagrangian* strain tensor $\mathbf{E}$ (not to be confused with the electric field vector) which compares the length of the push-forward with the length of the original vector $\boldsymbol{V}(X)$

$$\frac{1}{2}\left(\langle \varphi_*[\boldsymbol{V}], \varphi_*[\boldsymbol{V}] \rangle_{\mathbf{g}} - \langle \boldsymbol{V}, \boldsymbol{V} \rangle_{\mathbf{G}}\right) = \frac{1}{2}\left(\langle \boldsymbol{V}, \boldsymbol{V} \rangle_{\varphi^*[\mathbf{g}]} - \langle \boldsymbol{V}, \boldsymbol{V} \rangle_{\mathbf{G}}\right) = E_{IJ} V^I V^J \tag{4.159}$$

with

$$E_{IJ} = \frac{1}{2}\left(F^i{}_I F^j{}_J g_{ij} - G_{IJ}\right) = \frac{1}{2}\left(C_{IJ} - G_{IJ}\right). \tag{4.160}$$

Another strain measure is the *Eulerian*, *spatial* or Almansi strain tensor $\mathbf{e}$

$$\frac{1}{2}\left(\langle \boldsymbol{v}, \boldsymbol{v} \rangle)_{\mathbf{g}} - \langle \varphi^*[\boldsymbol{v}], \varphi^*[\boldsymbol{v}] \rangle_{\mathbf{G}}\right) = \frac{1}{2}\left(\langle \boldsymbol{v}, \boldsymbol{v} \rangle_{\mathbf{g}} - \langle \boldsymbol{v}, \boldsymbol{v} \rangle_{\varphi_*[\mathbf{G}]}\right) = e_{ij} v^i v^j \tag{4.161}$$

with

$$e_{ij} = \frac{1}{2}\left(g_{ij} - f^I{}_i f^J{}_j G_{IJ}\right) = \frac{1}{2}\left(g_{ij} - (\varphi_*[G])_{IJ}\right), \tag{4.162}$$

The term $f^I{}_i f^J{}_j G_{IJ} = (\varphi_*[\mathbf{G}])_{ij}$ is also denoted as $(\mathbf{c})_{ij} = c_{ij} = (\varphi_*[\mathbf{G}])_{ij}$.

Of course, neither $\mathbf{E}$ nor $\mathbf{e}$ are yet invariants. To obtain such we may compute their *eigenvalues* which have this property. Moreover, any scalar computed from $\mathbf{E}$ or $\mathbf{e}$ via proper contractions trough metric tensors, e.g.,

$$G^{IJ} E_{IJ} = G^{AI} E_{IJ}\, \delta^J{}_A = \mathrm{Tr}\left(E^I{}_J\, \partial_{X^I} \otimes \mathbf{d}X^J\right) = \mathrm{Tr}_{\mathbf{G}^{-1}} \mathbf{E} \tag{4.163}$$

or

$$g^{ij}\, e_{ij} = g^{ai}\, e_{ij}\, \delta^j{}_a = \mathrm{tr}\left(e^i{}_j\, \partial_{x^i} \otimes \mathbf{d}x^j\right) = \mathrm{tr}_{\mathbf{g}^{-1}}\, \mathbf{e} \tag{4.164}$$

is an invariant in the above sense. When we are interested in invariants computed via eigenvalues we have to solve equations (Frankel, 2011, Section 2.4d)

$$E^I{}_J\, V^J = \Lambda\, V^I \qquad \text{or} \qquad e^i{}_j\, v^j = \lambda\, v^i, \tag{4.165}$$

which work with the "mixed" versions $\underline{\boldsymbol{E}}$ and $\underline{\boldsymbol{e}}$, respectively. What Frankel (2011) essentially points out is that when using standard linear algebra procedures to compute scalar invariants of second-order tensors we have to work with the "mixed" versions. Otherwise, for example (4.165) would not be proper tensor equations, i.e. their results would not be independent of the chosen coordinates. If we are about to work with E_{IJ} or e_{ij} one would need to employ procedures where the traces or eigenvalues are computed with respect to the corresponding metric[16], which is equivalent to working with mixed quantities. Thus, we shall give the components

$$(\underline{\boldsymbol{E}})^I{}_J = \frac{1}{2}\left(C^I{}_J - \delta^I_J\right) \qquad \text{and} \qquad (\underline{\boldsymbol{e}})^i{}_j = \frac{1}{2}\left(\delta^i_j - c^i{}_j\right) \tag{4.166}$$

with

$$(\underline{\boldsymbol{C}})^I{}_J = G^{IA}\, F^i{}_A\, F^j{}_J\, g_{ij} \qquad \text{and} \qquad (\underline{\boldsymbol{c}})^i{}_j = g^{ia}\, f^I{}_a\, f^J{}_j\, G_{IJ}. \tag{4.167}$$

We remark that Marsden and Hughes (1994, Section 1.3) directly refer to the mixed $\underline{\boldsymbol{C}}$ as *right Cauchy-Green* tensor and not to $\mathbf{C}$ with components C_{IJ}[17]. Based on these considerations, an elastic energy density may be parameterized by any of $\{\underline{\boldsymbol{F}}, \mathbf{g}, \mathbf{G}\}$, $\underline{\boldsymbol{C}}$, $\underline{\boldsymbol{c}}$, $\underline{\boldsymbol{E}}$ or $\underline{\boldsymbol{e}}$.

Anisotropy

Due to the lack of material (Lagrangian) information, *purely* spatial invariants as in (4.143) to (4.151) are incapable to account for *anisotropy*, that is the presence of "preferred" directions of the material. Conversely, anisotropy can only be represented in a spatial invariant if the quantity acting as the metric for that invariant encodes information about the Lagrangian configuration. The probably most apparent way of doing so is to use the push-forward of some Lagrangian metric-like tensor $\mathbf{K}$ to compute an invariant, for example

$$\|\boldsymbol{v}\|^2_{\varphi_*[\mathbf{K}]} = \langle \boldsymbol{v}, \boldsymbol{v}\rangle_{\varphi_*[\mathbf{K}]} = v^i f^I{}_i\, f^J{}_j\, K_{IJ}\, v^j = \langle \boldsymbol{V}, \boldsymbol{V}\rangle_{\mathbf{K}}. \tag{4.168}$$

Of course, we may set $\mathbf{K} = \mathbf{G}$ which still represents material isotropy as long as $\mathbf{G}$ is "spherical". Then, the matrix representation of $\mathbf{K}$ is (a multiple of) the unit-matrix and, thus, all its eigenvalues coincide. As soon as not all eigenvalues of $\mathbf{K}$ are equal, we have

[16] In linear algebra parlance such fall into the class of "generalized eigenvalue problems".

[17] Please note that Marsden and Hughes (1994) employ a different notation: for example, their $\mathbf{C}$ is our $\underline{\boldsymbol{C}}$. Moreover, there does not seem to be a name for $\underline{\boldsymbol{c}}$ but for $\underline{\boldsymbol{b}} = \underline{\boldsymbol{c}}^{-1}$, i.e. the *Finger* or *left Cauchy-Green* tensor.

anisotropy. The idea sketched above naturally extends to invariants of forms. Next, considering strain or deformation tensors, we see from (4.167) that we obtain anisotropic invariants as soon as **G** is a non-spherical tensor or replaced by such. In literature, the most common approach is to use a set of *structural tensors* $\{\mathbf{M}_i\}$ each of which encodes a single preferred direction. They can either be directly employed instead of **K** or in combination with **G** to yield anisotropic invariants. We note that the anisotropic invariants are still invariant with respect tochanges of Lagrangian coordinates, which are applied to all Lagrangian tensors. However, in general they are not invariant with respect to rotations applied to the structural tensors only, except for those in the symmetry group of the material (see e.g. Schröder and Neff (2003)). In equations this is expressed as

$$I(\mathbf{C},\mathbf{G},\mathbf{M}) = I(\Phi_*[\mathbf{C}],\Phi_*[\mathbf{G}],\Phi_*[\mathbf{M}]) \neq I(\mathbf{C},\mathbf{G},\Phi_*[\mathbf{M}]), \tag{4.169}$$

where Φ_* represents the transform associated with a rotation in the initial configuration that is not part of the material's (the structural tensor's) symmetry group. In the equality in (4.169), Φ_* is related to a change of coordinates whereas at the very right-hand-side Φ_* represents a change of internal material orientation.

We close this brief digression on anisotropy by pointing the reader to the work of Spencer (1971) for invariant theory. We recommend the contributions of Schröder and Neff (2003) and Schröder et al. (2005) for an extensive discussion of anisotropy in the context finite elasticity.

4.1.8.14. A closing remark

All transformations of a vector into an associated form and vice-versa are trivial operations in Cartesian coordinates in $\mathbb{R}^n$, i.e. the transform does not change the values of the components. Thus, in implementations of standard finite element procedures one usually does not have to take care of them but just work in components. Things are different however for shells or when it comes to the actual evaluation of integrals in finite element procedures, which eventually heavily rely on pull-backs. In these applications, the exterior calculus of differential forms reveals its strengths (see, e.g., Arnold et al. (2006)).

4.2. Reformulation of some important equations in terms of differential form language

After finding the differential form representatives of various physical quantities we are in the position to express essential equations from Chapters 2 and 3 in terms of the "new" language. Subsequently, we turn to variational principles for magneto-electro-elasticity. To reduce notational clutter we omit the degree-indicating numbers for forms. As in 4.1.7.13 we use $\dot{\chi} = \dot{x} + \partial/\partial_t$. We point out that the "new" versions of equations given below can be directly obtained by expressing time derivatives in terms of Lie

derivatives, e.g. for the charge three-form the transition is done by

$$\frac{\partial q}{\partial t} \Rightarrow \pounds_{\dot{\chi}}\, \mathfrak{q} - \mathbf{d}(\mathbb{i}_{\boldsymbol{v}}\mathfrak{q}). \tag{4.170}$$

As a side effect, the reformulated electromagnetic equations feature the Galilean invariants summarized in (3.14).

4.2.1. Conservation of mass

By means of (4.106), (4.107) and the Lie derivative of a three-form (4.99) we rewrite (2.1) as

$$\begin{aligned}\pounds_{\dot{\chi}}\, \mathfrak{m} &= \pounds_{\dot{\chi}} \left(\sqrt{g}\rho\, \mathbf{d}x^1 \wedge \mathbf{d}x^2 \wedge \mathbf{d}x^3\right) = \frac{\partial \rho}{\partial t}\, dv + \mathbf{d}\left(\sqrt{g}\rho \dot{x}^i \epsilon_{\underline{ijk}}\, \mathbf{d}x^j \wedge \mathbf{d}x^k\right) \\ &= \left(\sqrt{g}\dot{\rho} + \rho \frac{\partial \sqrt{g}\dot{x}^i}{\partial x^i}\right) \mathbf{d}x^1 \wedge \mathbf{d}x^2 \wedge \mathbf{d}x^3 = \dot{\rho}\, dv + \rho\, \mathrm{div}\, \boldsymbol{v}\, dv = 0\end{aligned} \tag{4.171}$$

with

$$\begin{aligned}\mathrm{div}\, \boldsymbol{v} &:= \frac{1}{\sqrt{g}} \frac{\partial \sqrt{g}\dot{x}^i}{\partial x^i} = \frac{1}{\sqrt{g}} \left(\frac{1}{2\sqrt{g}} \frac{\partial g}{\partial x^i} \dot{x}^i + \sqrt{g} \frac{\partial \dot{x}^i}{\partial x^i}\right) \\ &= \frac{g^{kl}}{2} \underbrace{\left(g_{ol}\Gamma^o_{ki} + g_{ko}\Gamma^o_{li}\right) \dot{x}^i}_{\dot{g}_{kl}} + \frac{\partial \dot{x}^i}{\partial x^i} = \Gamma^o_{li}\, \dot{x}^i\, \delta^l_o + \frac{\partial \dot{x}^i}{\partial x^i} = \dot{x}^i_{|j}\, \delta^j_i = \underline{\boldsymbol{\delta}} : \boldsymbol{\nabla} \boldsymbol{v}\end{aligned} \tag{4.172}$$

being the divergence in general coordinates (Marsden and Hughes, 1994, p. 78, Definition 4.27). Alternatively, we could write

$$\begin{aligned}\pounds_{\dot{\chi}}\, \mathfrak{m} &= \pounds_{\dot{\chi}} \left(\sqrt{g}\rho\, \mathbf{d}x^1 \wedge \mathbf{d}x^2 \wedge \mathbf{d}x^3\right) \\ &= \frac{\partial \sqrt{g}\rho}{\partial t} \mathbf{d}x^1 \wedge \mathbf{d}x^2 \wedge \mathbf{d}x^3 + \mathbf{d}\left(\sqrt{g}\rho \dot{x}^i \epsilon_{\underline{ijk}}\, \mathbf{d}x^j \wedge \mathbf{d}x^k\right) \\ &= \left(\frac{\mathrm{d}\sqrt{g}\rho}{\mathrm{d}t} + \sqrt{g}\rho \frac{\partial \dot{x}^i}{\partial x^i}\right) \mathbf{d}x^1 \wedge \mathbf{d}x^2 \wedge \mathbf{d}x^3 \\ &= \left(\frac{1}{\sqrt{g}} \frac{\mathrm{d}\sqrt{g}\rho}{\mathrm{d}t} + \rho \frac{\partial \dot{x}^i}{\partial x^i}\right) dv = 0.\end{aligned} \tag{4.173}$$

4.2.2. Balance of momentum

The integral balance of momentum suffers from the fact that in general there does not exist any notion of an integral of a vector- (or a one-form-)valued three-form. However, we saw in Section 2.4 that we do not need it as an independent statement. Locally, it could be reformulated rigorously by means of the "covariant derivative" (Marsden and Hughes, 1994; Frankel, 2011). We will encounter the weak form of the balance of linear

momentum in terms of the "new" machinery in Section 4.3.2.

4.2.3. Mechanical power

With our considerations in Section 4.1.8.9 and Section 4.1.8.10 mechanical power can directly be rewritten as

$$P^{\text{mech}} = \int_{\mathcal{B}_t} \mathfrak{m}\mathfrak{f}^{\flat}(\boldsymbol{v}) + \int_{\partial\mathcal{B}_t} \underline{\mathfrak{t}}(\boldsymbol{v}). \tag{4.174}$$

4.2.4. Conservation of charge

The local form of conservation of charge (3.6) becomes

$$\pounds_{\dot{\chi}}\, \mathfrak{q} + \mathbf{d}(\mathfrak{j} - \mathbb{i}_{\boldsymbol{v}}\mathfrak{q}) = \pounds_{\dot{\chi}}\, \mathfrak{q} + \mathbf{d}\check{\mathfrak{j}} = 0, \tag{4.175}$$

where $\mathfrak{j} - \mathbb{i}_{\boldsymbol{v}}\mathfrak{q} = \check{\mathfrak{j}}$ is the Galilei-invariant current two-form. Moreover, (3.7) now read as[18]

$$\mathfrak{q} = \mathbf{d}\mathfrak{d} \qquad \text{and} \qquad \check{\mathfrak{j}} = \mathbf{d}\check{\mathfrak{h}} - \pounds_{\dot{\chi}}\, \mathfrak{d} \qquad \text{with} \qquad \check{\mathfrak{h}} = \mathfrak{h} + \mathbb{i}_{\boldsymbol{v}}\mathfrak{d}, \tag{4.176}$$

where $\check{\mathfrak{h}}$ is the Galilean-invariant current-potential two-form (see also Section 3.1.3). The integral form for possibly *moving* domains of (4.175) is

$$\int_{\Omega_t} \pounds_{\dot{\chi}}\, \mathfrak{q} + \int_{\partial\Omega_t} \check{\mathfrak{j}} = 0. \tag{4.177}$$

From the above equations the jump conditions for $\mathfrak{d}$ and $\check{\mathfrak{h}}$ across a surface $\mathcal{S}$ can be derived by means of (4.62) and (4.63)

$$[\![\pounds_{\dot{\chi}}\, \mathfrak{d}\,(\partial_{u^1}, \partial_{u^2})]\!]\, \mathbf{d}u^1 \wedge \mathbf{d}u^2 = \mathfrak{q}^{\mathrm{s}}\, \mathbf{d}u^1 \wedge \mathbf{d}u^2 \tag{4.178a}$$

and

$$[\![\check{\mathfrak{h}}\,(\partial_{u^i})]\!]\, \mathbf{d}u^i = -\check{j}^{\mathrm{s}}_{i3}\, \mathbf{d}u^i \wedge \text{⌀}u^3 = -\check{\mathfrak{j}}^{\mathrm{s}} \tag{4.178b}$$

where $\check{\mathfrak{j}}^{\mathrm{s}}$ is a current one-form defined on the surface, $\{u^1, u^2\}$ are the (Gaußian) coordinates of the surface and $\text{⌀}u^3$ indicates the traversing direction. See Section 4.1.8.12 for the peculiar notation employed for $\check{\mathfrak{j}}^{\mathrm{s}}$.

A digression: spacetime
Recalling that we somehow used (3.6) as justification for (3.7) we now switch to four-dimensional space with coordinates $\{t, x^1, x^2, x^3\}$. All the operations for differential forms introduced above are still valid in this case, by contrast to operations like cross products of vectors. By inspection one may come up with the pseudo two-form (see

[18] See (3.14) for the Galilei-invariants in classical tensor notation and (A.2) for their translation in form language. In particular, note the two occurrences of the cross product.

(Frankel, 2011, Section 3.5) and (Kovetz, 2000, Chapter 3, Section 6))

$$\mathfrak{c} = \mathfrak{h} \wedge \mathbf{d}t + d_{\underline{ij}}\, \mathbf{d}x^i \wedge \mathbf{d}x^j. \tag{4.179}$$

Computing the exterior derivative yields

$$\begin{aligned}\mathbf{d}\mathfrak{c} &= \sum_{\underline{ij}} \frac{\partial h_j}{\partial x^i}\, \mathbf{d}x^i \wedge \mathbf{d}x^j \wedge \mathbf{d}t + \frac{\partial d_{\underline{ij}}}{\partial t}\, \mathbf{d}t \wedge \mathbf{d}x^i \wedge \mathbf{d}x^j + \frac{\partial d_{\underline{ij}}}{\partial x^k}\, \mathbf{d}x^k \wedge \mathbf{d}x^i \wedge \mathbf{d}x^j \\ &= \sum_{\underline{ij}} \left[\left(\frac{\partial h_j}{\partial x^i} - \frac{\partial d_{\underline{ij}}}{\partial t}\right) \mathbf{d}x^i \wedge \mathbf{d}x^j\right] \wedge \mathbf{d}t + \frac{\partial d_{\underline{ij}}}{\partial x^k}\, \mathbf{d}x^k \wedge \mathbf{d}x^i \wedge \mathbf{d}x^j = \mathfrak{j} \wedge \mathbf{d}t + \mathfrak{q}. \end{aligned} \tag{4.180}$$

Then, using Theorem 4.1, we have the conservation of charge stated as

$$\mathbf{d}\,\mathbf{d}\mathfrak{c} = \left(\frac{\partial j_{\underline{jk}}}{\partial x^i} e^{\underline{ijk}} + \frac{\partial \mathfrak{q}}{\partial t}\right) \mathbf{d}x^1 \wedge \mathbf{d}x^2 \wedge \mathbf{d}x^3 \wedge \mathbf{d}t = 0. \tag{4.181}$$

4.2.5. The Maxwell-Faraday equation and the electromagnetic field

In Section 3.1.2 we pointed out that $\boldsymbol{E}$ and $\boldsymbol{B}$ actually belong to a single object, the *electromagnetic potential*. Before we come to that, we restate (3.8) using the Lie derivative as

$$\mathbf{d}\mathfrak{b} = 0 \qquad \text{and} \qquad \pounds_{\dot{\chi}}\, \mathfrak{b} + \mathbf{d}\underbrace{(\mathfrak{e} - \mathbb{i}_{\mathfrak{v}}\mathfrak{b})}_{\check{\mathfrak{e}}} = \pounds_{\dot{\chi}}\, \mathfrak{b} + \mathbf{d}\check{\mathfrak{e}} = 0, \tag{4.182}$$

with the Galilean-invariant electric field $\check{\mathfrak{e}}$. The exactly same expressions holds for the electromotive force $\mathfrak{f}^{\text{em}}$ following the sign convention of Brown (1966, Section 2.6). Next, turning to (3.10) we have

$$\check{\mathfrak{e}} = -\mathbf{d}\check{\phi} - \pounds_{\dot{\chi}}\, \mathfrak{a} \qquad \text{and} \qquad \mathfrak{b} = \mathbf{d}\mathfrak{a}, \tag{4.183}$$

with $\check{\phi} = \phi - \mathbb{i}_{\mathfrak{v}}\mathfrak{a}$ being the Galilean-invariant electric potential. The integral form of $(4.182)_2$ reads as

$$\int_{\partial \mathcal{S}_t} \pounds_{\dot{\chi}}\, \mathfrak{a} = -\int_{\partial \mathcal{S}_t} \check{\mathfrak{e}}. \tag{4.184}$$

We assume that the potentials $\check{\phi}$ and $\mathfrak{a}$ are continuous. In that case the jump conditions for $\check{\mathfrak{e}}$ and $\mathfrak{b}$ are given by

$$[\![\check{\mathfrak{e}}(\partial_{u^i})]\!]\, \mathbf{d}u^i = 0\,(\mathbf{d}u^1 + \mathbf{d}u^2) \quad \text{and} \quad [\![\mathfrak{b}(\partial_{u^1}, \partial_{u^2})]\!]\, \mathbf{d}u^1 \wedge \mathbf{d}u^2 = 0\, \mathbf{d}u^1 \wedge \mathbf{d}u^2. \tag{4.185}$$

A digression: spacetime again
Now consider again four-dimensional space with coordinates $\{t, x^1, x^2, x^3\}$. We introduce the *electromagnetic potential* $\mathfrak{u} = -\phi\,\mathbf{d}t + a_i\,\mathbf{d}x^i$ (cf. (Frankel, 2011, Section 3.5) and (Kovetz, 2000, Chapter 4)). Then, the exterior derivative (4.56) yields

$$\mathbf{d}\mathfrak{u} = -\frac{\partial\phi}{\partial x^i}\,\mathbf{d}x^i \wedge \mathbf{d}t + \frac{\partial a_i}{\partial t}\,\mathbf{d}t \wedge \mathbf{d}x^i + \sum_{\underline{ij}} \frac{\partial a_i}{\partial x^j}\,\mathbf{d}x^j \wedge \mathbf{d}x^i. \tag{4.186}$$

Separating the purely spatial and the mixed space-time components gives

$$\mathfrak{e} \wedge \mathbf{d}t = -\left(\frac{\partial\phi}{\partial x^i} + \frac{\partial a_i}{\partial t}\right)\mathbf{d}x^i \wedge \mathbf{d}t \qquad \text{and} \qquad \mathfrak{b} = \sum_{\underline{ij}} \frac{\partial a_i}{\partial x^j}\mathbf{d}x^j \wedge \mathbf{d}x^i, \tag{4.187}$$

where $\mathfrak{e}$ and $\mathfrak{b}$ are the electric field one-form and the magnetic field two-form, respectively. The space-time two-form $\mathfrak{g} = \mathbf{d}\mathfrak{u}$ is the electro-magnetic field. In terms of this new quantity Equation (3.9) is simply

$$\mathbf{d}\mathfrak{g} = \mathbf{d}\,\mathbf{d}\mathfrak{u} = 0. \tag{4.188}$$

4.2.6. Electromagnetic power

The power expended for moving charges (as density or current) against an electromotive force has been the starting point for both the electric (3.28) and the magnetic (3.52) power. We therefore investigate first the volume power density $-\mathfrak{f}^{\text{em}} \wedge \mathfrak{j}$ and the surface power density $-\mathfrak{f}^{\text{em}} \wedge \mathfrak{j}^{\text{s}}$ expended by moving charges for *volumes and surfaces at rest*

$$\begin{aligned}
P^{\text{j}} &= -\int_{\Omega_t} \mathfrak{f}^{\text{em}} \wedge \mathfrak{j} - \int_{\mathcal{S}_t} \mathfrak{f}^{\text{em}} \wedge \mathfrak{j}^{\text{s}} = \int_{\Omega_t} \left(\frac{\partial \mathfrak{a}}{\partial t} + \mathbf{d}\phi\right) \wedge \mathfrak{j} + \int_{\mathcal{S}_t} \left(\frac{\partial \mathfrak{a}}{\partial t} + \mathbf{d}\phi\right) \wedge \mathfrak{j}^{\text{s}} \\
&= \int_{\Omega_t} \frac{\partial \mathfrak{a}}{\partial t} \wedge \mathfrak{j} + \int_{\Omega_t} \mathbf{d}\phi \wedge \mathfrak{j} + \int_{\mathcal{S}_t} \frac{\partial \mathfrak{a}}{\partial t} \wedge \mathfrak{j}^{\text{s}} + \int_{\mathcal{S}_t} \mathbf{d}\phi \wedge \mathfrak{j}^{\text{s}} \\
&= \int_{\Omega_t} \frac{\partial \mathfrak{a}}{\partial t} \wedge \mathfrak{j} + \int_{\Omega_t} \mathbf{d}(\phi\mathfrak{j}) - \int_{\Omega_t} \phi\,\mathbf{d}\mathfrak{j} + \int_{\mathcal{S}_t} \frac{\partial \mathfrak{a}}{\partial t} \wedge \mathfrak{j}^{\text{s}} + \int_{\mathcal{S}_t} \mathbf{d}(\phi\mathfrak{j}^{\text{s}}) - \int_{\mathcal{S}_t} \phi\,\mathbf{d}\mathfrak{j}^{\text{s}} \\
&= \int_{\Omega_t} \mathfrak{j} \wedge \frac{\partial \mathfrak{a}}{\partial t} + \int_{\partial\Omega_t} \phi\mathfrak{j} - \int_{\mathcal{S}_t} \phi\,[\![\mathfrak{j}]\!] + \int_{\Omega_t} \phi\frac{\partial \mathfrak{q}}{\partial t} \\
&\quad + \int_{\mathcal{S}_t} \frac{\partial \mathfrak{a}}{\partial t} \wedge \mathfrak{j}^{\text{s}} + \int_{\partial\mathcal{S}_t} \phi\mathfrak{j}^{\text{s}} + \int_{l_t} \phi\,[\![\mathfrak{j}^{\text{s}}]\!] - \int_{\mathcal{S}_t} \phi\,\mathbf{d}\mathfrak{j}^{\text{s}},
\end{aligned} \tag{4.189}$$

where $\mathcal{S}_t$ includes all surfaces of discontinuity for $\mathfrak{j}$ and l does so for $\mathfrak{j}^{\text{s}}$. We assume that the boundary and jump terms for $\mathfrak{j}^{\text{s}}$ vanish and furthermore replace $-[\![\mathfrak{j}]\!] - \mathbf{d}\mathfrak{j}^{\text{s}}$ with

$\partial \mathfrak{q}^{\mathrm{s}}/\partial t$ to arrive at

$$P^{\mathrm{i}} = \int_{\Omega_t} \mathfrak{j} \wedge \frac{\partial \mathfrak{a}}{\partial t} + \int_{\Omega_t} \phi \frac{\partial \mathfrak{q}}{\partial t} + \int_{\partial\Omega_t} \phi \mathfrak{j} + \int_{\mathcal{S}_t} \phi \frac{\partial \mathfrak{q}^{\mathrm{s}}}{\partial t} + \int_{\mathcal{S}_t} \mathfrak{j}^{\mathrm{s}} \wedge \frac{\partial \mathfrak{a}}{\partial t}. \tag{4.190}$$

The equation above clearly contains the sum of electric and magnetic power as given in (3.28) and (3.52), respectively, but also an additional term for the conserved part of a current traversing a surface and general currents traversing the outer boundary $\partial\Omega_t$. For moving domains we have

$$P^{\check{\mathrm{i}}} = \int_{\Omega_t} \check{\mathfrak{j}} \wedge \pounds_{\dot{\chi}} \mathfrak{a} + \int_{\Omega_t} \check{\phi} \pounds_{\dot{\chi}} \mathfrak{q} + \int_{\partial\Omega_t} \check{\phi} \check{\mathfrak{j}} + \int_{\mathcal{S}_t} \check{\phi} \pounds_{\dot{\chi}} \mathfrak{q}^{\mathrm{s}} + \int_{\mathcal{S}_t} \check{\mathfrak{j}}^{\mathrm{s}} \wedge \pounds_{\dot{\chi}} \mathfrak{a}. \tag{4.191}$$

Note that we explicitly wrote $\mathfrak{f}^{\mathrm{em}}$ instead of $\mathfrak{e}$ to distinguish this approach from a different (but equivalent) viewpoint commonly advocated by physicists, e.g. Kovetz (2000, Section 54) and Feynman et al. (2011) and also employed for example by Kankanala and Triantafyllidis (2004). Considering (3.6), (4.178b) and $(4.185)_1$ in their forms for a system at rest we have the identity

$$\begin{aligned}
&- \int_{\Omega_t} \mathfrak{e} \wedge \mathfrak{j} - \int_{\mathcal{S}_t} \mathfrak{e} \wedge \mathfrak{j}^{\mathrm{s}} \\
&= - \int_{\Omega_t} \mathfrak{e} \wedge \left(\mathbf{d}\mathfrak{h} - \frac{\partial \mathfrak{d}}{\partial t} \right) + \int_{\mathcal{S}_t} \mathfrak{e} \wedge [\![\mathfrak{h}]\!] \\
&= \int_{\Omega_t} \mathbf{d}(\mathfrak{e} \wedge \mathfrak{h}) - \int_{\Omega_t} \mathbf{d}\mathfrak{e} \wedge \mathfrak{h} + \int_{\Omega_t} \mathfrak{e} \wedge \frac{\partial \mathfrak{d}}{\partial t} + \int_{\mathcal{S}_t} \mathfrak{e} \wedge [\![\mathfrak{h}]\!] \\
&= \int_{\partial\Omega_t} \mathfrak{e} \wedge \mathfrak{h} - \int_{\mathcal{S}_t} \mathfrak{e} \wedge [\![\mathfrak{h}]\!] + \int_{\Omega_t} \mathfrak{h} \wedge \frac{\partial \mathfrak{b}}{\partial t} + \int_{\Omega_t} \mathfrak{e} \wedge \frac{\partial \mathfrak{d}}{\partial t} + \int_{\mathcal{S}_t} \mathfrak{e} \wedge [\![\mathfrak{h}]\!] \\
&= \int_{\partial\Omega_t} \mathfrak{e} \wedge \mathfrak{h} + \int_{\Omega_t} \mathfrak{h} \wedge \frac{\partial \mathfrak{b}}{\partial t} + \int_{\Omega_t} \mathfrak{e} \wedge \frac{\partial \mathfrak{d}}{\partial t},
\end{aligned} \tag{4.192}$$

which is a form of *Poynting's theorem* (Frankel, 2011; Bossavit, 2016) and the vector corresponding to the two-form $\mathfrak{e} \wedge \mathfrak{h}$ is known as the *Poynting vector*. The equation above can be rearranged such that the boundary integral stands alone

$$- \int_{\partial\Omega_t} \mathfrak{e} \wedge \mathfrak{h} = \int_{\Omega_t} \mathfrak{e} \wedge \mathfrak{j} + \int_{\mathcal{S}_t} \mathfrak{e} \wedge \mathfrak{j}^{\mathrm{s}} + \int_{\Omega_t} \mathfrak{h} \wedge \frac{\partial \mathfrak{b}}{\partial t} + \int_{\Omega_t} \mathfrak{e} \wedge \frac{\partial \mathfrak{d}}{\partial t} = P^{\mathrm{EM}}, \tag{4.193}$$

where the left-hand-side is considered as electromagnetic energy entering the system instead of P^{i} (cf. Kovetz (2000, Section 54), Kankanala and Triantafyllidis (2004) and Feynman et al. (2011, Part II, Chapter 27)). We emphasize that for in form of electromagnetic power, $\mathfrak{e}$ in the is the field *driving* the current such that both are aligned.

As pointed out by Bossavit (2016) there have been (maybe not yet settled) debates on

the physical significance of the Poynting vector and the terms $\mathfrak{e} \wedge \partial\mathfrak{d}/\partial t$ and $\mathfrak{h} \wedge \partial\mathfrak{b}/\partial t$. Without going into detail we follow the argumentation of Bossavit (2016) and interpret $\mathfrak{e} \wedge \mathfrak{h}$ as a flux of electromagnetic energy and $\mathfrak{e} \wedge \partial\mathfrak{d}/\partial t$ and $\mathfrak{h} \wedge \partial\mathfrak{b}/\partial t$ as rates of electric and magnetic energy, respectively. We note in particular that despite the Poynting "vector", i.e. actually the Poynting two-form, only appears in terms of its exterior derivative (corresponding to divergence in this case) and the corresponding boundary integral in (4.192) it is unique under reasonable assumptions as established by Birkeland (1894) and summarized by Bossavit (2016). We mention, however, that for example Kovetz (2000, Section 54) is less confident in this regard. We close this discussion with the remark that this issue is similar to the localization procedure that leads to the usual constitutive relations for stresses, e.g. (4.137a) and (4.137b).

For completeness, we also provide moving-domain versions of (4.193). First, we replace $\mathfrak{e}$ by $\check{\mathfrak{e}}$ and $\mathfrak{j}$ by $\check{\mathfrak{j}}$ as these are involved in, e.g. (4.182) and (4.175). Using in addition (4.183) we obtain

$$\begin{aligned} P^{\mathrm{EM}} &= -\int_{\partial\Omega_t} \check{\mathfrak{e}} \wedge \check{\mathfrak{h}} = -\int_{\Omega_t} \mathbf{d}(\check{\mathfrak{e}} \wedge \check{\mathfrak{h}}) \\ &= \int_{\Omega_t} \check{\mathfrak{e}} \wedge \check{\mathfrak{j}} + \int_{\mathcal{S}_t} \check{\mathfrak{e}} \wedge \check{\mathfrak{j}}^{\mathrm{s}} + \int_{\Omega_t} \left(\check{\mathfrak{h}} \wedge \pounds_{\dot{\chi}} \mathfrak{b} + \check{\mathfrak{e}} \wedge \pounds_{\dot{\chi}} \mathfrak{d} \right) \end{aligned} \tag{4.194}$$

Further expanding the terms containing $\check{\mathfrak{j}}$ or $\check{\mathfrak{j}}^{\mathrm{s}}$ as in (4.190) yields

$$\begin{aligned} P^{\mathrm{EM}} &= -\int_{\Omega_t} \mathbf{d}(\check{\mathfrak{e}} \wedge \check{\mathfrak{h}}) \\ &= \int_{\Omega_t} \left(\check{\mathfrak{h}} \wedge \pounds_{\dot{\chi}} \mathfrak{b} + \check{\mathfrak{e}} \wedge \pounds_{\dot{\chi}} \mathfrak{d} \right) + \int_{\Omega_t} \left(-\mathbf{d}\check{\phi} \wedge \check{\mathfrak{j}} - \pounds_{\dot{\chi}} \mathfrak{a} \wedge \check{\mathfrak{j}} \right) \\ &\quad + \int_{\mathcal{S}_t} \left(-\mathbf{d}\check{\phi} \wedge \check{\mathfrak{j}}^{\mathrm{s}} - \pounds_{\dot{\chi}} \mathfrak{a} \wedge \check{\mathfrak{j}}^{\mathrm{s}} \right) \end{aligned} \tag{4.195a}$$

$$\begin{aligned} &= \int_{\Omega_t} \left(\check{\mathfrak{h}} \wedge \pounds_{\dot{\chi}} \mathfrak{b} + \check{\mathfrak{e}} \wedge \pounds_{\dot{\chi}} \mathfrak{d} \right) - \int_{\Omega_t} \left(\check{\phi}\, \pounds_{\dot{\chi}} \mathfrak{q} + \check{\mathfrak{j}} \wedge \pounds_{\dot{\chi}} \mathfrak{a} \right) \\ &\quad - \int_{\partial\Omega_t} \check{\phi}\check{\mathfrak{j}} - \int_{\mathcal{S}_t} \left(\check{\phi}\, \pounds_{\dot{\chi}} \mathfrak{q}^{\mathrm{s}} + \pounds_{\dot{\chi}} \mathfrak{a} \wedge \check{\mathfrak{j}}^{\mathrm{s}} \right). \end{aligned} \tag{4.195b}$$

4.3. Variational principles for coupled magneto-electro-elasticity in a quasi-static setting

In Sections 2.4, 3.3.2 and 3.4.2 we discussed the balance of energy in three different settings. In Section 4.2.6 we digressed into electromagnetic power which embraces the electro- and magnetostatic case. The aim of the present section is to combine these developments to a variational principle governing quasi-static coupled magneto-electro-

elasticity. In that course we make use of the mathematical tools introduced in Sections 4.1 and 4.2. The setting of bodies $\mathcal{B}^i$ in the otherwise empty domain Ω under consideration is depicted in Figure 4.5.

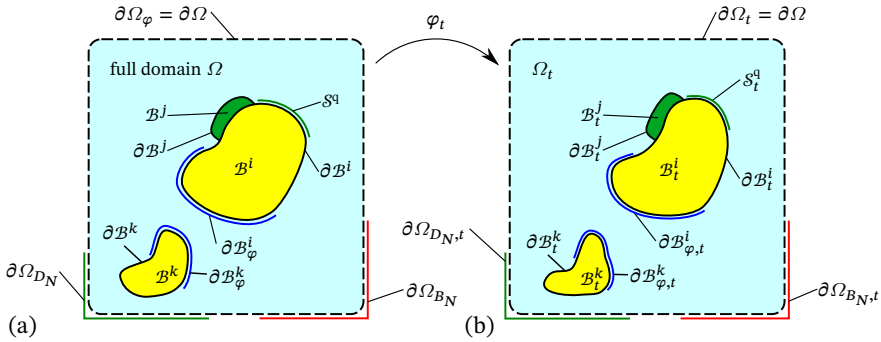

Figure 4.5: Bodies in free space: (a) initial and (b) current configuration. The bodies $\mathcal{B}^i$, $\mathcal{B}^j$ and $\mathcal{B}^k$ are embedded into Ω. On subsets of boundaries denoted with subscripts, e.g. $\partial\mathcal{B}^i_\varphi$, Ω_φ, $\Omega_\mathfrak{D}$ or $\Omega_\mathfrak{N}$, we put constraints on the corresponding quantity in terms of essential (Dirichlet) boundary conditions. For simplicity we assume that $\partial\Omega_\varphi = \partial\Omega = \partial\Omega_t$ (Keip and Rambausek, 2016, 2017). The surface $\mathcal{S}^q$ denotes a surface where the free charge surface density $\mathfrak{q}^s$ does not vanish. The collection of all bodies is $\mathcal{B} = \bigcup_i \mathcal{B}^i \subset \Omega$. The "empty" part of Ω is denoted as $\mathcal{B}' = \Omega \setminus \mathcal{B}$.

The mechanical power has already been given in (4.174) in appropriate form. For the electromagnetic energy flow we employ (4.191) which is already in a convenient format. Notably, the Lie rates in that equation are either magneto- or electro-mechanical quantities. In a quasi-static setting they are better represented by variations in the same sense as virtual displacements replace velocity in mechanical power. The quantities $\check{\mathfrak{h}}$, $\check{\mathfrak{e}}$, $\check{\phi}$, $\check{\mathfrak{j}}$ and $\check{\mathfrak{j}}^s$, however, feature magnetic and electric contributions. Since we are only interested in (quasi-)static processes we neglect all coupling in the mentioned quantities by dropping the velocity-related part. What remains are the original non-Galilei-invariant fields $\mathfrak{h}$, $\mathfrak{e}$, ϕ, $\mathfrak{j}$ and $\mathfrak{j}^s$. Concerning the integrand $\phi\mathfrak{j}$ on $\partial\Omega_t$ we note that we consider the boundary $\partial\Omega_t$ as fixed and disjoint from any body or somehow conducting matter (see Figure 4.5). Thus, we drop the whole term $\phi\mathfrak{j}$. To summarize these considerations we give the electro- and magneto-static power derived from $P^{\check{\mathfrak{j}}}$ (4.195b) together with the mechanical power (4.174) as

$$P^{\mathrm{MEM}} = \underbrace{\int_{\mathcal{B}_t} \mathfrak{m}\, \mathfrak{f}^{\flat}(\boldsymbol{v}) + \int_{\partial\mathcal{B}_t} \underline{\mathfrak{t}}(\boldsymbol{v})}_{P^{\mathrm{mech}}} + \underbrace{\int_{\mathcal{B}_t} \phi\, \pounds_{\dot{\chi}}\, \mathfrak{q} + \int_{\partial\mathcal{B}_t} \phi\, \pounds_{\dot{\chi}}\, \mathfrak{q}^s}_{P^{\mathrm{elec}}} + \underbrace{\int_{\Omega_t} \mathfrak{j} \wedge \pounds_{\dot{\chi}}\, \mathfrak{a} + \int_{\mathcal{S}_t} \mathfrak{j}^s \wedge \pounds_{\dot{\chi}}\, \mathfrak{a}}_{P^{\mathrm{magn}}} \tag{4.196}$$

with $\mathcal{B}_t \cap \mathcal{S}_t = \emptyset$. In what follows we do not consider any surface currents ($\mathfrak{j}^s = 0$).

With above results we arrive at the quasi-static balance of energy

$$\dot{U} = \underbrace{\int_{\mathcal{B}_t} \mathfrak{m}\, \mathfrak{f}^{\mathrm{b}}(\boldsymbol{\upsilon}) + \int_{\partial\mathcal{B}_t} \underline{\mathfrak{t}}(\boldsymbol{\upsilon})}_{P^{\mathrm{mech}}} + \underbrace{\int_{\mathcal{B}_t} \phi\, \pounds_{\dot{\chi}}\, \mathfrak{q} + \int_{\partial\mathcal{B}_t} \phi\, \pounds_{\dot{\chi}}\, \mathfrak{q}^{\mathrm{s}}}_{P^{\mathrm{elec}}} + \underbrace{\int_{\Omega_t} \mathfrak{j} \wedge \pounds_{\dot{\chi}}\, \mathfrak{a}}_{P^{\mathrm{magn}}}, \tag{4.197}$$

with U denoting internal energy and Ω_t the full domain under consideration and thus containing $\mathcal{B}_t$. Next we only consider stored elastic, electric and magnetic energy contributions which we summarize as Π^{int} such that $\Pi^{\mathrm{int}} \leq U$ and $\dot{\Pi}^{\mathrm{int}} \leq \dot{U}$

$$\dot{\Pi}^{\mathrm{int}} - \underbrace{(P^{\mathrm{mech}} + P^{\mathrm{elec}} + P^{\mathrm{magn}})}_{P^{\mathrm{ext}}} \leq 0, \tag{4.198}$$

where equality characterizes equilibrium. When the powers collected by P^{ext} are the (negative) time rate of a potential Π^{ext}, i.e. $P^{\mathrm{ext}} = -\dot{\Pi}^{\mathrm{ext}}$, we may introduce

$$\mathcal{L} = \Pi^{\mathrm{int}} + \Pi^{\mathrm{ext}} \qquad \text{and} \qquad \dot{\mathcal{L}} \leq 0. \tag{4.199}$$

This is of course too early to stop. Indeed, we will use the power expressions in (4.197) together with the generic statement (4.199) as starting point for the derivation of concrete variational principles.

Next we turn from mechanical, magnetic and electric power to internal energy. In Section 4.1.8.13 we elaborated a bit on possible internal structure, i.e. dependence on invariants of the full arguments. We saw that all these invariants can be built from $\underline{\boldsymbol{F}}$, the Eulerian metric $\mathbf{g}$, the (spherical) Lagrangian metric $\mathbf{G}$, structural tensors $\mathbf{M}_i$ as well as Eulerian or Lagrangian electric and magnetic quantities. The power in (4.197) suggests that internal energy is, besides some deformation measure and metric tensors, a function of $\mathfrak{d}$ and $\mathfrak{b}$ since these are the fields related to $\mathfrak{q}$ and $\mathfrak{a}$. This is also in line with the parameterizations of energy densities (3.30) and (3.53). Moreover, in presence of matter it is reasonable to assume that some part of the energy density is bound to mass. Thus, a possible parameterization in terms of Eulerian quantities is

$$\psi = \rho\psi^{\mathrm{mat}}(\mathbf{g}, \mathfrak{d}, \mathfrak{b}, \varphi_*[\mathbf{G}], \varphi_*[\mathbf{M}_i]) + \psi^{\mathrm{vac}}(\mathbf{g}, \mathfrak{d}, \mathfrak{b}). \tag{4.200}$$

A possible parameterization of a Lagrangian energy density is

$$\Psi_0 = \rho_0\Psi^{\mathrm{mat}}(\mathbf{C}, \mathfrak{D}, \mathfrak{B}; \mathbf{G}, \mathbf{M}_i) + \Psi_0^{\mathrm{vac}}(\mathbf{C}, \mathfrak{D}, \mathfrak{B}; \mathbf{G}), \tag{4.201}$$

with $\{\mathbf{C}, \mathfrak{D}, \mathfrak{B}\} = \varphi^*[\{\mathbf{g}, \mathfrak{d}, \mathfrak{b}\}]$. The main difference between Eulerian and Lagrangian parameterization becomes apparent when computing the total time derivatives of ψ and Ψ, both per mass or current volume but with different arguments. Regarding the time rates of Eulerian quantities we may choose between the covariant and the component time rates as long as we use both time derivatives consistently when it comes to derivatives of the Eulerian metric tensor $\mathbf{g}$. By contrast, the time rates of Lagrangian quantities directly translate into Lie rates of their Eulerian counterparts. Since Lie rates contain

time rates, all forms of time derivatives of energy densities can be translated into each other. Which approach to use is just a matter of taste and convenience. Moreover, one can also mix both approaches which is exactly what we will do below.

4.3.1. Rates of energy densities

In this subsection we provide several expressions for the rates of Eulerian and Lagrangian energy densities. We first consider an energy density with Lagrangian parameterization $\Psi(\mathbf{C}, \mathfrak{D}, \mathfrak{B}; \mathbf{G}, \mathbf{M}_i)$ where we shall not distinguish between mass- and volume-bound densities as this has no influence on what is to be shown. The tensors $\mathbf{G}$ and $\mathbf{M}_i$ represent the (spherical) Lagrangian metric and possibly present structural tensors for anistropy. In case of Lagrangian quantities we need not distinguish between covariant and component time rates. Moreover, since everything works the same way for both $\mathfrak{D}$ and $\mathfrak{B}$ we only consider $\mathfrak{D}$ in the demonstration below. With that we have

$$\begin{aligned}\frac{\mathrm{d}\Psi(\mathbf{C}, \mathfrak{D}; \mathbf{G}, \mathbf{M}_i)}{\mathrm{d}t} &= \frac{\partial \Psi}{\partial C_{IJ}} \dot{C}_{IJ} + \frac{\partial \Psi}{\partial \underline{D_{IJ}}} \dot{D}_{\underline{IJ}} \\ &= \varphi_* \left[\frac{\partial \Psi}{\partial \mathbf{C}}\right]^{ij} \pounds_{\dot{\chi}} [\mathbf{g}]_{ij} + \varphi_* \left[\frac{\partial \Psi}{\partial \mathfrak{D}}\right]^{\underline{ij}} \pounds_{\dot{\chi}} [\mathfrak{d}]_{\underline{ij}} \\ &= \left[\frac{\partial \widehat{\Psi}}{\partial \mathbf{g}}\right]^{ij} \pounds_{\dot{\chi}} [\mathbf{g}]_{ij} + \left[\frac{\partial \widehat{\Psi}}{\partial \mathfrak{d}}\right]^{\underline{ij}} \pounds_{\dot{\chi}} [\mathfrak{d}]_{\underline{ij}} = \frac{\mathrm{d}\widehat{\Psi}(\mathbf{g}, \mathfrak{d}, \varphi_*[\mathbf{G}], \varphi_*[\mathbf{M}_i])}{\mathrm{d}t},\end{aligned} \tag{4.202}$$

where we used the general relation for functions of invariants of tensors, i.e. objective functions, $\widehat{\Psi}(\mathbf{t}) = \Psi(\varphi^*[\mathbf{t}]) = \Psi(\mathbf{T})$[19]

$$\frac{\partial \widehat{\Psi}(\mathbf{t})}{\partial \mathbf{t}} = \frac{\partial \Psi(\varphi^*[\mathbf{t}])}{\partial \varphi^*[\mathbf{t}]} \frac{\partial \varphi^*[\mathbf{t}]}{\partial \mathbf{t}} = \varphi_* \left[\frac{\partial \Psi(\mathbf{T} = \varphi^*[\mathbf{t}])}{\partial \varphi^*[\mathbf{t}]}\right], \tag{4.203}$$

as shown for the case of $\partial_{\mathbf{C}} \Psi$ by Marsden and Hughes (1994, p. 196). We emphasize that the derivatives above do not involve explicit derivatives of Ψ and $\widehat{\Psi}$ with respect to $\underline{\boldsymbol{F}}$. Rates of $\underline{\boldsymbol{F}}$ of course appear when for example $\pounds_{\dot{\chi}}[\mathbf{g}]$ is expanded out. When we let Ψ or $\widehat{\Psi}$, respectively, explicitly depend on $\underline{\boldsymbol{F}}$ we would obtain a different structure compared with above, while the total rate itself is equivalent. We mention these subtle complications at this point because of the many different objects which are identified as some kind of stress in literature (Brown, 1966; Kovetz, 2000; Kankanala and Triantafyllidis, 2004; Bustamante et al., 2009b). However, since we did not yet put energy rates in context with mechanical, electric and magnetic power we defer the identification of a stress measure to a later stage.

For comparison, we now turn to the rate of the Eulerian energy density $\psi(\mathbf{g}, \mathfrak{d}, \mathbf{c}, \mathbf{m}_i)$

[19] We note that this relation holds if both of Ψ and $\widehat{\Psi}$ are defined per unit mass or on the same configuration, i.e. only the parameters are connected via pull-back/push-forward.

with $\mathbf{m}_i = \varphi_*[\mathbf{M}_i]$. Recall that we write the time rate of coordinate functions as $\dot{g}^{ij}$ whereas the components of a covariant time derivative are denoted as $(\dot{\mathbf{g}})^{ij}$. This means, we do not distinguish between "different" time derivatives of tensorial objects but rather whether we take time rates of components only or of the full objects including their possible non-constant bases. Let us elaborate a bit on that in the context of rates of invariants. Consider any (scalar) invariant $I(\underline{\boldsymbol{c}})$ of $\underline{\boldsymbol{c}}$, for example $c^i{}_i = g^{ia}\, c_{aj}\, \delta^j_i$. It holds that

$$\begin{aligned}\dot{I}(\underline{\boldsymbol{c}}) &= \frac{\mathrm{d}I(\underline{\boldsymbol{c}}(\mathbf{c},\mathbf{g}^{-1}))}{\mathrm{d}t} = \frac{\partial I(\underline{\boldsymbol{c}})}{\partial c^i{}_j}\left(\frac{\partial c^i{}_j}{\partial c_{kl}}\frac{\mathrm{d}c_{kl}}{\mathrm{d}t} + \frac{\partial c^i{}_j}{\partial g^{kl}}\frac{\mathrm{d}g^{kl}}{\mathrm{d}t}\right)\\ &= \frac{\partial I(\underline{\boldsymbol{c}})}{\partial c^i{}_j}\left(g^{ik}\dot{c}_{kj} + \dot{g}^{ik}c_{kj}\right) = \frac{\partial I(\underline{\boldsymbol{c}})}{\partial c^i{}_j}\left(g^{ik}\dot{f}^I{}_k f^J{}_j G_{IJ} + g^{ik}f^I{}_k\dot{f}^J{}_j G_{IJ} + \dot{g}^{ik}c_{kj}\right)\end{aligned} \tag{4.204a}$$

or

$$= \frac{\partial I(\underline{\boldsymbol{c}})}{\partial c^i{}_j}\dot{c}^i{}_j. \tag{4.204b}$$

No covariant derivatives appear since all basis vectors and basis one-forms compensate each other when forming the invariant. When we insist on employing covariant derivatives, we obtain for example

$$\begin{aligned}\dot{I}(\underline{\boldsymbol{c}}) &= \frac{\mathrm{d}I(\underline{\boldsymbol{c}}(\mathbf{c},\mathbf{g}^{-1}))}{\mathrm{d}t} = \frac{\partial I(\underline{\boldsymbol{c}})}{\partial c^i{}_j}\left(\frac{\partial c^i{}_j}{\partial c_{kl}}\left(\frac{\mathrm{d}\mathbf{c}}{\mathrm{d}t}\right)_{kl} + \frac{\partial c^i{}_j}{\partial g^{kl}}\left(\frac{\mathrm{d}\mathbf{g}^{-1}}{\mathrm{d}t}\right)^{kl}\right)\\ &= \frac{\partial I(\underline{\boldsymbol{c}})}{\partial c^i{}_j}g^{ik}\left(\frac{\mathrm{d}\mathbf{c}}{\mathrm{d}t}\right)_{kj},\end{aligned} \tag{4.205}$$

because the covariant derivative of $\mathbf{g}^{-1}$ vanishes (4.36). Since $c_{ij} = f^I{}_i f^J{}_j G_{IJ}$ we have

$$\left(\frac{\mathrm{d}\mathbf{c}}{\mathrm{d}t}\right)_{ij} = \left(\underline{\dot{\boldsymbol{f}}}\right)^I{}_i f^J{}_j G_{IJ} + F^I_i\left(\underline{\dot{\boldsymbol{f}}}\right)^J{}_j G_{IJ}. \tag{4.206}$$

However, also the derivatives of basis vectors and basis one-forms compensate each other in $I(\underline{\boldsymbol{c}})$. This can easily be shown by direct calculations using (4.34). Hence, from (4.205) and (4.204b) we conclude that

$$\dot{c}^i{}_j = g^{ik}\,\dot{c}_{kj} + \dot{g}^{ik}\,c_{kj} = g^{ik}\left(\frac{\mathrm{d}\mathbf{c}}{\mathrm{d}t}\right)_{kj}, \tag{4.207}$$

which can be checked with (4.31), (4.34) and (4.206). The same procedure works for tensors $\hat{\underline{\boldsymbol{c}}} = \varphi_*\mathbf{K}(\mathbf{G},\mathbf{M})$ which feature structural tensors to account for anisotropy (see also Section 4.1.8.13). Quite similar considerations also apply to invariants of $\mathfrak{d}$ which are formed via contractions using $\mathbf{g}^{-1}$.

The essential difference in the further use of component or covariant derivatives, respectively, is the appearance of rates of the metric tensor. Accordingly, using component derivatives we have

$$\frac{\mathrm{d}\psi(\mathbf{g},\mathfrak{d},\mathbf{c},\mathbf{m})}{\mathrm{d}t} = \frac{\partial\psi}{\partial g_{ij}}\dot{g}_{ij} + \frac{\partial\psi}{\partial \underline{d_{ij}}}\underline{\dot{d}_{ij}} + \frac{\partial\psi}{\partial c_{ij}}\dot{c}_{ij} + \frac{\partial\psi}{\partial m_{ij}}\dot{m}_{ij}, \tag{4.208}$$

with $\mathbf{m} = \varphi_*[\mathbf{M}]$. Conversely, using covariant derivatives throughout yields[20]

$$\frac{\mathrm{d}\psi(\mathbf{g},\mathfrak{d},\mathbf{c},\mathbf{m})}{\mathrm{d}t} = \frac{\partial\psi}{\partial \underline{d_{ij}}}(\dot{\mathfrak{d}})_{\underline{ij}} + \frac{\partial\psi}{\partial c_{ij}}(\dot{\mathbf{c}})_{ij} + \frac{\partial\psi}{\partial \mathbf{m}_{ij}}(\dot{\mathbf{m}})_{ij}. \tag{4.209}$$

A final important observation is that

$$\frac{\mathrm{d}\mathbf{C}}{\mathrm{d}t} = \frac{\mathrm{d}\varphi^*[\mathbf{g}]}{\mathrm{d}t} = (\underline{\dot{\boldsymbol{F}}})^i{}_I\, F^j{}_J\, g_{ij} + F^i{}_I\, (\underline{\dot{\boldsymbol{F}}})^j{}_J\, g_{ij} = \dot{F}^i{}_I F^j{}_J\, g_{ij} + F^i{}_I F^j{}_J\, \dot{g}_{ij} + F^i{}_I \dot{F}^j{}_J\, g_{ij}, \tag{4.210}$$

which lets us arrive at a commonly used parameterization in terms of $\underline{\boldsymbol{F}}$

$$\frac{\mathrm{d}\Psi(\mathbf{C},\mathfrak{D})}{\mathrm{d}t} = \frac{\mathrm{d}\tilde{\Psi}(\underline{\boldsymbol{F}},\mathfrak{D},\mathbf{g})}{\mathrm{d}t} = \left(\frac{\partial\tilde{\Psi}}{\partial\underline{\boldsymbol{F}}}\right)^I_i (\underline{\dot{\boldsymbol{F}}})^i{}_I + \frac{\partial\tilde{\Psi}}{\partial \underline{D_{IJ}}}\underline{\dot{D}_{IJ}}. \tag{4.211}$$

Remark 4.22. Different parameterizations can still refer to the same energy density. Thus, as at least partially worked out in the discussion above, the main effect of parameterization are the individual rates that make up $\dot{\Psi}$ or $\dot{\psi}$, respectively. Indeed, as a simple example consider $\Psi^{\mathrm{D}}(\mathbf{C},\mathfrak{D}) = \langle\mathfrak{D},\mathfrak{D}\rangle_{\mathrm{cof}\,\mathbf{C}^{-1}} = \langle\mathfrak{d},\mathfrak{d}\rangle_{\mathrm{cof}\,\mathbf{g}^{-1}} = \widehat{\Psi}^{\mathrm{d}}(\mathbf{g},\mathfrak{d})$. For the rate we have a range of equivalent expressions

$$\frac{\mathrm{d}}{\mathrm{d}t}\Psi^{\mathrm{D}} = \frac{\partial\Psi}{\partial C_{IJ}}\dot{C}_{IJ} + \frac{\partial\Psi}{\partial \underline{D_{IJ}}}\underline{\dot{D}_{IJ}} = \frac{\partial\widehat{\Psi}}{\partial g_{ij}}(\pounds_{\dot{\chi}}\,\mathbf{g})_{ij} + \frac{\partial\widehat{\Psi}}{\partial \underline{d_{ij}}}(\pounds_{\dot{\chi}}\,\mathfrak{d})_{\underline{ij}} \tag{4.212a}$$

$$= \frac{\partial\widehat{\Psi}}{\partial g_{ij}}\underbrace{(\dot{\mathbf{g}})_{ij}}_{\equiv 0} + \frac{\partial\widehat{\Psi}}{\partial \underline{d_{ij}}}(\dot{\mathfrak{d}})_{\underline{ij}} = \frac{\partial\widehat{\Psi}}{\partial g_{ij}}\dot{g}_{ij} + \frac{\partial\widehat{\Psi}}{\partial \underline{d_{ij}}}\underline{\dot{d}_{ij}} = \frac{\mathrm{d}}{\mathrm{d}t}\widehat{\Psi}^{\mathrm{d}}. \tag{4.212b}$$

4.3.2. Stationary conditions

In what follows we opt for an energy density per current volume but with a Lagrangian-type parameterization, i.e.

$$\Psi = \widehat{\Psi}(\rho,\mathbf{g},\mathfrak{d},\mathfrak{b},\varphi_*[\mathbf{G}],\varphi_*[\mathbf{M}_i]) = \Psi(\rho,\varphi^*[\mathbf{g}],\varphi^*[\mathfrak{d}],\varphi^*[\mathfrak{b}];\mathbf{G},\mathbf{M}_i). \tag{4.213}$$

[20] We admit that this may look quite puzzling at first. The reason why this works lies in the way energy-densities depend on the metric $\mathbf{g}$ through invariants (of objective quantities). The equivalence of (4.208) and (4.209) for such invariants can verified using the formula for the covariant derivative (4.34).

To avoid clutter we misuse notation and write $\Psi(\rho, \mathbf{g}, \mathfrak{d}, \mathfrak{b}, \varphi_*[\mathbf{G}], \varphi_*[\mathbf{M}_i])$ without the hat "$\widehat{\ }$"

$$\begin{aligned} \Pi^{\text{int}} &= \int_{\Omega_t} \Psi(\rho, \mathbf{g}, \mathfrak{d}, \mathfrak{b})\, dv \\ &= \int_{\Omega_t} \left(\rho \Psi^{\text{mat}}(\mathbf{g}, \mathfrak{d}, \mathfrak{b}) + \Psi^{\text{vac}}(\mathbf{g}, \mathfrak{d}, \mathfrak{b})\right) dv \end{aligned} \tag{4.214}$$

with

$$\dot{\Pi}^{\text{int}} = \int_{\Omega_t} \left(\rho \dot{\Psi}^{\text{mat}} + \dot{\Psi}^{\text{vac}} + \Psi^{\text{vac}} \operatorname{div} \boldsymbol{v}\right) dv = \int_{\Omega_t} \left(\dot{\Psi} + \Psi \operatorname{div} \boldsymbol{v}\right) dv. \tag{4.215}$$

We do so because we anticipate that the rates $\dot{\Psi}^{\text{mat}}$ and $\dot{\Psi}^{\text{vac}}$ are computed following (4.202) which will lead to simplifications through canceling Lie-rates.

As a drawback, we have to think about the meaning of deformation in empty space $\Omega \setminus \mathcal{B}$. We keep in mind, however, that the vacuum energy density[21] actually is independent of local deformation. Thus, we may formally extend the deformation map φ from bodies $\mathcal{B}$ to whole Ω with great "freedom". In the derivation below we shall not bother with this issue. Instead, we simply assume some continuous non-degenerate deformation map. In numerical simulations this point is more critical and will be discussed in greater detail in Part II.

We begin with inserting (4.215) in (4.198) from which we obtain by using (4.202)

$$\begin{aligned} &\int_{\Omega_t} \left(\frac{\partial \Psi}{\partial g_{ij}} \pounds_{\dot{\chi}}[\mathbf{g}]_{ij} + \frac{\partial \Psi}{\partial \underline{d_{ij}}} \pounds_{\dot{\chi}}[\mathfrak{d}]_{\underline{ij}} + \frac{\partial \Psi}{\partial \underline{b_{ij}}} \pounds_{\dot{\chi}}[\mathfrak{b}]_{\underline{ij}} + \Psi \operatorname{div} \boldsymbol{v} \right) dv \\ &\quad - \int_{\mathcal{B}_t} \mathfrak{m}\, \mathfrak{f}^{\flat}(\boldsymbol{v}) - \int_{\partial \mathcal{B}_t} \underline{\mathfrak{t}}(\boldsymbol{v}) - \int_{\mathcal{B}_t} \phi\, \pounds_{\dot{\chi}}\, \mathfrak{q} - \int_{\partial \mathcal{B}_t} \phi\, \pounds_{\dot{\chi}}\, \mathfrak{q}^{\mathrm{s}} - \int_{\Omega_t} \mathfrak{j} \wedge \pounds_{\dot{\chi}}\, \mathfrak{a} \leq 0, \end{aligned} \tag{4.216}$$

where equality holds at equilibrium which is the case considered from now on. Next, we formally replace the traction two-form[22] by the negative jump of the (stress) two-form $\underline{\mathfrak{s}}$ and the surface charges by the jump in $\mathfrak{d}$ and invoke $(4.176)_1$ as well as $(3.10)_2$. Then we rearrange the equation above by forming groups according to the argument of the

[21] Concrete expressions will be given in Part II.

[22] This step is not necessary. In many derivations the traction remains until the end. However, the current procedure is equivalent, at least in the present scope.

time rates to obtain

$$\begin{aligned}
&\int_{\Omega_t}\left(\Psi\delta_i^j+2\frac{\partial\Psi}{\partial g_{kj}}g_{ik}\right)v^i{}_{|j}\,dv-\int_{\mathcal{B}_t}\mathfrak{m}\,\mathfrak{f}^{\flat}(\boldsymbol{v})+\int_{\partial\mathcal{B}_t}[\![\underline{\mathfrak{s}}(\boldsymbol{v})]\!]\\
&+\int_{\Omega_t}\frac{\partial\Psi}{\partial d_{\underline{ij}}}(\pounds_{\dot\chi}\,\mathfrak{d})_{\underline{ij}}\,dv-\int_{\mathcal{B}_t}\phi\,\pounds_{\dot\chi}(\mathbf{d}\mathfrak{d})-\int_{\partial\mathcal{B}_t}\phi\,[\![\pounds_{\dot\chi}\,\mathfrak{d}]\!]\\
&+\int_{\Omega_t}\frac{\partial\Psi}{\partial b_{\underline{ij}}}(\pounds_{\dot\chi}\,\mathbf{d}\mathfrak{a})_{\underline{ij}}\,dv-\int_{\Omega_t}\mathfrak{j}\wedge\pounds_{\dot\chi}\,\mathfrak{a}=0,
\end{aligned}\tag{4.217}$$

where we used the relations

$$\pounds_{\dot\chi}[\mathbf{g}]_{ij}=g_{ik}v^k{}_{|j}+g_{kj}v^k{}_{|i}\quad\text{and}\quad\frac{\partial\Psi}{\partial g_{ij}}=\frac{\partial\Psi}{\partial g_{ji}}.\tag{4.218}$$

We proceed by invoking manipulations as in (4.138) and (4.114) to express all integrands fully in terms of forms. Furthermore, we get rid of the jump in stress across boundaries $\partial\mathcal{B}_t$ along the lines of (4.134) and in addition employ the product rule for the exterior derivative as well as Stokes' theorem in each of the last two lines. Since there are no prescribed tractions at the free-space boundary $\partial\Omega_t$ we arrive at

$$\begin{aligned}
&\int_{\Omega_t}\underbrace{\sqrt{g}\epsilon_{m\underline{kl}}\left(\Psi\delta_i^m+2\frac{\partial\Psi}{\partial g_{nm}}g_{in}\right)}_{r^{\mathfrak{g}}_{\underline{kl}}}v^i{}_{|j}\,\epsilon^{jkl}\,\mathbf{d}x^1\wedge\mathbf{d}x^2\wedge\mathbf{d}x^3-\int_{\mathcal{B}_t}\mathfrak{m}\,\mathfrak{f}^{\flat}(\boldsymbol{v})+\int_{\partial\mathcal{B}_t}[\![\underline{\mathfrak{s}}(\boldsymbol{v})]\!]\\
&\quad+\int_{\Omega_t}\underbrace{\sqrt{g}\,\epsilon_{m\underline{kl}}\frac{\partial\Psi}{\partial d_{\underline{kl}}}}_{r^{\mathfrak{d}}_m}\pounds_{\dot\chi}[\mathfrak{d}]_{\underline{ij}}\,\epsilon^{mij}\,\mathbf{d}x^1\wedge\mathbf{d}x^2\wedge\mathbf{d}x^3+\int_{\Omega_t}\mathbf{d}\phi\wedge\pounds_{\dot\chi}\,\mathfrak{d}-\int_{\partial\Omega_t}\phi\,[\![\pounds_{\dot\chi}\,\mathfrak{d}]\!]\\
&\quad+\int_{\Omega_t}\underbrace{\sqrt{g}\,\epsilon_{m\underline{kl}}\frac{\partial\Psi}{\partial b_{\underline{kl}}}}_{r^{\mathfrak{b}}_m}\pounds_{\dot\chi}[\mathbf{d}\mathfrak{a}]_{\underline{ij}}\,\epsilon^{mij}\,\mathbf{d}x^1\wedge\mathbf{d}x^2\wedge\mathbf{d}x^3-\int_{\Omega_t}\mathfrak{j}\wedge\pounds_{\dot\chi}\,\mathfrak{a}\\
&=\int_{\Omega_t}(\underline{\mathfrak{r}}^{\mathfrak{g}}-\underline{\mathfrak{s}})\,(\boldsymbol{\nabla}\boldsymbol{v})-\int_{\Omega_t}\mathbb{i}_{\boldsymbol{v}}\left(\mathfrak{f}^{\flat}\otimes\mathfrak{m}+\mathbb{d}\underline{\mathfrak{s}}\right)-\int_{\partial\Omega_t}\underline{\mathfrak{s}}(\boldsymbol{v})\\
&\quad+\int_{\Omega_t}(\mathfrak{r}^{\mathfrak{b}}+\mathbf{d}\phi)\wedge\pounds_{\dot\chi}\,\mathfrak{d}+\int_{\partial\Omega_t}\phi\,\pounds_{\dot\chi}\,\mathfrak{d}\\
&\quad+\int_{\Omega_t}(\mathbf{d}\mathfrak{r}^{\mathfrak{b}}-\mathfrak{j})\wedge\pounds_{\dot\chi}\,\mathfrak{a}+\int_{\partial\mathcal{B}_t}[\![\mathfrak{r}^{\mathfrak{b}}]\!]\wedge\pounds_{\dot\chi}\,\mathfrak{a}-\int_{\partial\Omega_t}\mathfrak{r}^{\mathfrak{b}}\wedge\pounds_{\dot\chi}\,\mathfrak{a}=0,
\end{aligned}\tag{4.219}$$

where we extended $\mathfrak{f}^{\flat}$ to all of Ω_t by $\mathfrak{f}^{\flat} = 0$ in $\Omega_t \setminus \mathcal{B}_t$. Obviously, (4.219) is fulfilled if

$$\mathbb{d}\underline{\mathfrak{s}} = -\mathfrak{f}^{\flat} \otimes \mathfrak{m} \tag{4.220a}$$

$$\underline{\mathfrak{r}}^{\mathfrak{g}} = \sqrt{g}\,\epsilon_{m\underline{kl}}\left(\Psi\delta_i^m + 2\frac{\partial\Psi}{\partial g_{nm}}g_{in}\right)\mathbf{d}x^i \otimes \mathbf{d}x^k \wedge \mathbf{d}x^l = \underline{\mathfrak{s}} \tag{4.220b}$$

$$\mathfrak{r}^{\mathfrak{d}} = \sqrt{g}\,\epsilon_{m\underline{kl}}\frac{\partial\Psi}{\partial d_{\underline{kl}}}\mathbf{d}x^m = -\mathbf{d}\phi = \mathfrak{e} \tag{4.220c}$$

$$\mathbf{d}\mathfrak{r}^{\mathfrak{b}} = \mathbf{d}\left(\sqrt{g}\,\epsilon_{m\underline{kl}}\frac{\partial\Psi}{\partial b_{\underline{kl}}}\mathbf{d}x^m\right) = \mathfrak{j} = \mathbf{d}\mathfrak{h} \;\Rightarrow\; \mathfrak{h} = \sqrt{g}\,\epsilon_{m\underline{kl}}\frac{\partial\Psi}{\partial b_{\underline{kl}}}\mathbf{d}x^m \tag{4.220d}$$

in Ω_t and

$$[\![\mathfrak{r}^{\mathfrak{b}}]\!]|_{\partial\mathcal{B}_t} = 0 \tag{4.220e}$$

$$\mathfrak{r}^{\mathfrak{b}}|_{\partial\Omega_t} = 0 \tag{4.220f}$$

$$\mathfrak{s}(\boldsymbol{v})|_{\partial\Omega_t} = 0. \tag{4.220g}$$

Equation (4.220a) is the localized balance of linear momentum. The stationary conditions (4.220b), (4.220c) and (4.220d) are constitutive relations in terms of differential forms. In addition we have the magnetic jump condition (4.220e). The remaining integrals over the outer boundary (4.220f) and (4.220g) vanish identically for an infinite domain, e.g. $\mathbb{R}^3$, and represent (by default homogeneous) natural boundary conditions otherwise. Alternatively, one might also regard $\partial\Omega_t$ as fixed in space which means (4.220g) vanishes by $\boldsymbol{v} = 0$.

Besides (4.220) we of course have to fulfill the relations assumed in the derivation

$$[\![\underline{\mathfrak{s}}]\!]|_{\partial\mathcal{B}_t} = -\boldsymbol{t}, \qquad [\![\mathfrak{d}]\!]|_{\partial\mathcal{B}_t} = \mathfrak{q}^{\mathfrak{s}} \qquad \text{and} \qquad \mathbf{d}\mathfrak{d} = q \tag{4.220h}$$

which completes the set of stationary conditions.

Remark 4.23. The balance of angular momentum (see Section 2.3) is automatically fulfilled. This can be seen from the symmetry of the Cauchy-type total stress

$$s^{mn} = \left(\Psi g^{mn} + 2\frac{\partial\Psi}{\partial g_{nm}}\right) \tag{4.221}$$

consistent with $\underline{\mathfrak{s}}$. Of course, this also holds in case of anisotropy of electric and magnetic properties. Thus, symmetry of the total stress in this sense does not exclude phenomena like electric or magnetic body *couples*, i.e. angular momentum sources.

Remark 4.24. If we would not have based our energy rate on (4.202) but on a direct computation without Lie rates the latter were still present in (4.217) through the external power terms. To obtain stationary conditions we then would have to split off the time

rates from the Lie rates, i.e. $\pounds_{\dot\chi}\,\mathfrak{y} = \dot{\mathfrak{y}} + (\pounds_{\dot\chi}\,\mathfrak{y} - \dot{\mathfrak{y}})$, where

$$\pounds_{\dot\chi}\,\mathfrak{y} - \dot{\mathfrak{y}} = \varphi_* \left[\frac{\partial \varphi^*[\mathfrak{y}]}{\partial \underline{\boldsymbol{F}}}\right]^j_i (\boldsymbol{\nabla} \boldsymbol{v})^i_j. \tag{4.222}$$

By doing so, one recognizes stress contributions (in the sense of being products with $\boldsymbol{\nabla} \boldsymbol{v}$) which even are possibly non-symmetric. They, however, simply "replace" stress terms "lost" in the alternative rate version for the energy rate such that the "total" stress $\underline{\mathfrak{s}}$ remains the same. The such obtained expression of the total stress features magnetic and electric contributions of which the *form* is independent of the actual material model. They are often referred to as "Maxwell" stress (Kankanala and Triantafyllidis, 2004; Bustamante et al., 2009b), which is however non-unique in presence of matter. See also Remark 4.26.

Remark 4.25. In a purely mechanical context, (4.220b) reduces to the Doyle-Ericksen formula (Doyle and Ericksen, 1956; Marsden and Hughes, 1994)

$$\sqrt{g}\epsilon_{m\underline{kl}}\left(2\rho\frac{\partial \Psi^{\text{mat}}}{\partial g_{nm}} g_{in}\right) = s_{i\underline{kl}} \tag{4.223}$$

where $\underline{\mathfrak{s}}$ is the one-form-valued two-form corresponding to the Cauchy stress tensor $\boldsymbol{\sigma}$.

Remark 4.26. In *empty* space we may find Ψ from (4.220c) and (4.220d) and the aether relations (3.11)

$$\begin{aligned}\Psi^{\text{vac}}(\mathbf{g}, \mathfrak{d}, \mathfrak{b})\, dv &= \left(\frac{1}{2\epsilon_0}\langle \mathfrak{d}, \mathfrak{d}\rangle + \frac{1}{2\mu_0}\langle \mathfrak{b}, \mathfrak{b}\rangle\right) dv \\ &= \frac{1}{2}\left(\frac{\star\, \mathfrak{d} \wedge \mathfrak{d}}{\epsilon_0} + \frac{\star\, \mathfrak{b} \wedge \mathfrak{b}}{\mu_0}\right).\end{aligned} \tag{4.224}$$

Employing the above energy density in (4.220b) yields (recall (4.83))

$$\underline{\mathfrak{s}} = \left(\frac{\star\, \mathfrak{d} \otimes \mathfrak{d}}{\epsilon_0} - \frac{\langle \mathfrak{d}, \mathfrak{d}\rangle}{2\epsilon_0}\right) \mathbf{d}x^i \otimes dv(\partial_{x^i}) + \left(\frac{\star\, \mathfrak{b} \otimes \mathfrak{b}}{\mu_0} - \frac{\langle \mathfrak{b}, \mathfrak{b}\rangle}{2\mu_0}\right) \mathbf{d}x^i \otimes dv(\partial_{x^i}), \tag{4.225}$$

which in classical vector notation reads as

$$\mathbf{s} = \frac{1}{\epsilon_0}\boldsymbol{d} \otimes \boldsymbol{d} - \frac{1}{2\epsilon_0}(\boldsymbol{d} \cdot \boldsymbol{d})\mathbf{1} + \frac{1}{\mu_0}\boldsymbol{b} \otimes \boldsymbol{b} - \frac{1}{2\mu_0}(\boldsymbol{b} \cdot \boldsymbol{b})\mathbf{1}, \tag{4.226}$$

an expression known as the *Maxwell* stress. It is important to note that the notion of the Maxwell stress is only unique, if not to say valid, where the aether relations hold. Only then it can be employed to compute the net force on a body. We refer to Brown (1966) for a discussion of the Maxwell stress in the magneto-static case as well as to Schlömerkemper (2002, 2005) and Schlömerkemper and Schmidt (2009) for a thorough discussion of magnetic forces at small scales and their transition to continuum-level notions. We also remark that the correct expression for the Maxwell stress is obtained

from (4.220b) when the two-form $\mathfrak{d}$ is kept fixed, not its vector counterpart $\boldsymbol{d}$ despite that the norms of both evaluate to the same value. The reason is the occurrence of $\det \mathbf{g}$ in relation (4.114).

4.3.3. The variational energy principle

We now consider the case of $P^{\text{ext}} = -\dot{\Pi}^{\text{ext}}$ such that we are in the position to state a variational principle that corresponds to (4.199). We remark that the stationary conditions (4.220) were derived from (4.198) via (4.216) with the assumption of an energy density $\Psi = \Psi(\rho, \mathbf{C}, \mathfrak{D}, \mathfrak{B})$ in the sense of (4.202). Below we exploit the fact that the Lie rates appearing in (4.216) are the push-forwards of the times rate of the corresponding Lagrangian (or pulled backs) quantities (4.95f). By that we arrive at the Lagrangian version of (4.216)

$$\begin{aligned}\frac{\mathrm{d}}{\mathrm{d}t}(\Pi^{\text{int}} + \Pi^{\text{ext}}) = \int_\Omega \frac{\partial \Psi_0}{\partial C_{ij}}\dot{C}_{ij} + \frac{\partial \Psi_0}{\partial \underline{D}_{ij}}\dot{\underline{D}}_{ij} + \frac{\partial \Psi_0}{\partial \underline{B}_{ij}}\dot{\underline{B}}_{ij}\, dV \\ - \int_{\mathcal{B}} \left(\varphi^*[\mathfrak{m}]\, \mathbb{i}_{\boldsymbol{v}} \mathfrak{f}^{\flat} + \phi \frac{\mathrm{d}\varphi^*[\mathfrak{q}]}{\mathrm{d}t} + \varphi^*[\mathfrak{j}] \wedge \dot{\mathfrak{A}} \right) \\ - \int_{\partial\mathcal{B}} \left(\varphi^*[\mathbb{i}_{\boldsymbol{v}} \underline{\mathfrak{t}}] + \phi \frac{\mathrm{d}\varphi^*[\mathfrak{q}^{\mathrm{s}}]}{\mathrm{d}t} \right) = 0 \end{aligned} \tag{4.227}$$

where

$$\Psi_0(\mathbf{C}, \mathfrak{D}, \mathfrak{B}) = \rho_0 \Psi^{\text{mat}}(\mathbf{C}, \mathfrak{D}, \mathfrak{B}) + \frac{1}{J}\Psi^{\text{vac}}(\mathbf{C}, \mathfrak{D}, \mathfrak{B}) \quad \text{and} \quad J = \sqrt{\frac{\det \mathbf{C}}{\det \mathbf{G}}}. \tag{4.228}$$

A few comments are in order. The pull-backs go along with a change of domain of integration. Conversely, we only pull back those parts of the objects involved, which are affected by that. This means, we only pull back those forms or parts of forms as required for integration over the Lagrangian (initial) domains. Noteworthy, considering $\mathbb{i}_{\boldsymbol{v}} \mathfrak{f}^{\flat}$ which evaluates to a scalar does not require an "individual" pull-back of $\mathbb{i}_{\boldsymbol{v}}$ and $\mathfrak{f}^{\flat}$. A "collective" (and trivial) pull-back of the scalar result is sufficient. Along this line of thinking we also only pull back the two-form part of the traction $\underline{\mathfrak{t}}$ such that

$$\mathbb{i}_{\boldsymbol{v}} \underline{\mathfrak{T}} = \varphi^*[\mathbb{i}_{\boldsymbol{v}} \mathfrak{t}]. \tag{4.229}$$

In addition, we employed $\mathfrak{b} = \mathbf{d}\mathfrak{a}$, which will be replaced by its referential version $\mathfrak{B} = \mathbf{d}\mathfrak{A}$, as well as $\mathfrak{q} = \mathbf{d}\mathfrak{d}$ and the corresponding jump condition $\mathfrak{q}^{\mathrm{s}} = [\![\mathfrak{d}]\!]$. The latter two equations are of particular interest since they removed all traces of charge density which were part of the electric power. Therefore, we have to respect the Lagrangian versions of $\mathfrak{q} = \mathbf{d}\mathfrak{d}$ and $\mathfrak{q}^{\mathrm{s}} = [\![\mathfrak{d}]\!]$ in a variational principle.

Following these considerations the actual minimization principle is formulated as

$$\{\hat{\varphi}, \hat{\mathfrak{D}}, \hat{\mathfrak{A}}\} = \arg\left\{ \inf_{\varphi,\mathfrak{D},\mathfrak{A}} \int_\Omega \Psi_0(\mathbf{C}, \mathfrak{D}, \mathfrak{B} = \mathbf{d}\mathfrak{A})\, dV + \Pi^{\text{ext}}(\varphi, \mathfrak{D}, \mathfrak{A}) \right\} \tag{4.230a}$$

with Π^{ext} such that

$$\dot{\Pi}^{\text{ext}} = -\left(P^{\text{mech}} + P^{\text{elec}} + P^{\text{magn}}\right) \tag{4.230b}$$

and under the (Lagrangian) constraints

$$\mathfrak{Q} = \mathbf{d}\mathfrak{D} \quad \text{and} \quad \mathfrak{Q}^{\text{s}} = [\![\mathfrak{D}]\!]\,. \tag{4.230c}$$

A principle that directly incorporates the constraints (4.230c) is obtained via the method of Lagrange multipliers. In the present case this is achieved by setting

$$\Pi^{\text{ext}}_{\mathfrak{D}}(\phi, \mathfrak{D}) = -\int_\Omega \phi\,(\mathbf{d}\mathfrak{D} - \mathfrak{Q}) - \int_{\partial\mathcal{B}} \phi\,([\![\mathfrak{D}]\!] - \mathfrak{Q}^{\text{s}}) \tag{4.231}$$

with ϕ in the role of the Lagrange multiplier and $\mathfrak{Q}$ as well as $\mathfrak{Q}^{\text{s}}$ are assumed to be given. Then, the corresponding variation is

$$\delta\Pi^{\text{ext}}_{\mathfrak{D}}(\phi, \mathfrak{D}) = -\int_\Omega \delta\phi\,(\mathbf{d}\mathfrak{D} - \mathfrak{Q}) - \int_{\partial\mathcal{B}} \delta\phi\,([\![\mathfrak{D}]\!] - \mathfrak{Q}^{\text{s}}) - \int_\Omega \phi\,\mathbf{d}\delta\mathfrak{D} - \int_{\partial\mathcal{B}} \phi\,[\![\delta\mathfrak{D}]\!]\,. \tag{4.232}$$

In the case when $\mathfrak{q}$ and $\mathfrak{q}^{\text{s}}$ are given instead of $\mathfrak{Q}$ and $\mathfrak{Q}^{\text{s}}$, respectively, the potential $\Pi^{\text{ext}}_{\mathfrak{D}}$ also depends on $\underline{\boldsymbol{F}}$ such that (4.232) has to be modified accordingly. Below, we shall however assume that $\mathfrak{Q}$ and $\mathfrak{Q}^{\text{s}}$ are given. With $\Pi^{\text{ext}}_{\mathfrak{D}}$ we reformulate (4.230) to arrive at

$$\{\hat{\varphi}, \hat{\mathfrak{D}}, \hat{\mathfrak{A}}, \hat{\phi}\} = \arg\left\{ \inf_{\varphi,\mathfrak{D},\mathfrak{A}} \sup_{\phi} \int_\Omega \Psi_0(\mathbf{C}, \mathfrak{D}, \mathfrak{B})\, dV + \Pi^{\text{ext}}_{\varphi}(\varphi) + \Pi^{\text{ext}}_{\mathfrak{D}}(\phi, \mathfrak{D}) + \Pi^{\text{ext}}_{\mathfrak{A}}(\mathfrak{A}) \right\}. \tag{4.233}$$

This constrained minimization principle serves us as starting point for a set of variational principles for coupled magneto-electro-elasticity. For brevity we excluded detailed specifications of the function spaces and essential (Dirichlet) boundary conditions for φ, $\mathfrak{D}$, $\mathfrak{A}$ and ϕ. We shall discuss these aspects in detail below.

The stationary conditions corresponding to (4.233) can be shown to be the referential

versions[23] of (4.220). That is, at a state $\{\hat{\varphi}, \hat{\mathfrak{D}}, \hat{\mathfrak{A}}, \hat{\phi}\}$ we have

$$\underline{\mathfrak{P}} = 2\sqrt{G}\,\epsilon_{M\underline{KL}}\,\frac{\partial \Psi_0}{\partial C_{NM}}\,F^i{}_N\,\mathbf{d}x^i \otimes (\mathbf{d}X^K \wedge \mathbf{d}X^L) \tag{4.234a}$$

$$\mathfrak{E} = -\,\mathbf{d}\phi(X) = \sqrt{G}\,\epsilon_{M\underline{KL}}\,\frac{\partial \Psi_0}{\partial D_{\underline{KL}}}\,\mathbf{d}X^M \tag{4.234b}$$

$$\mathbf{d}\mathfrak{H} = \mathfrak{J} = \mathbf{d}\left(\sqrt{G}\,\epsilon_{M\underline{KL}}\,\frac{\partial \Psi_0}{\partial B_{\underline{KL}}}\,\mathbf{d}X^M\right) \tag{4.234c}$$

$$\mathbb{d}\underline{\mathfrak{P}} = -\mathfrak{f}^{\mathrm{b}} \otimes \mathfrak{M} \tag{4.234d}$$

$$\left[\!\left[\underline{\mathfrak{P}}\right]\!\right]\Big|_{\partial\mathcal{B}} = -\varphi^*[\mathfrak{t}] = -\mathfrak{T} \tag{4.234e}$$

$$\mathbf{d}\mathfrak{D} = \mathfrak{Q} \tag{4.234f}$$

$$[\![\mathfrak{D}]\!]\big|_{\partial\mathcal{B}} = \mathfrak{Q}^{\mathrm{s}}, \tag{4.234g}$$

where $\mathfrak{P}$ is the total Piola-Kirchoff stress, $\mathfrak{E}$ there Lagrangian electric field, $\mathfrak{H}$ the Lagrangian current potential, $\mathfrak{M}$ the Lagrangian mass three-form and $\mathfrak{T}$ the Lagrangian traction.

4.3.3.1. Function Spaces and discretization

We will not elaborate too much on the involved mathematics of functional analysis but instead opt for a practical and pragmatic outline of this topic. For rigorous mathematical treatments which focus on discretization aspects we refer to the classical monograph by Boffi et al. (2013) and to Arnold et al. (2006) whose *Finite Element Exterior Calculus* (FEEC) heavily relies on the geometrical concepts presented in Section 4.1. In both of the two references one also finds detailed specifications of finite elements for the discretization of the function spaces introduced below. Finite element software frameworks such as `deal.II` (Bangerth et al., 2007; Alzetta et al., 2018) and `FEniCS` (Rognes et al., 2009; Logg et al., 2012) provide corresponding implementations. In this context we refer to an overview over a wide range of generic finite elements provided at femtable.org (Arnold and Logg, 2014). Besides that, we recommend Bossavit (1998a, 2010) for mathematically solid "engineering" perspectives on subsets of the present scope.

Somewhat beyond the present scope is the framework of Discrete Exterior Calculus (Hirani, 2003; Leok, 2004), short "DEC", which aims to establish the discrete counterparts of all the objects and operators outlined in Section 4.1. This undertaking starts from a different perspective and goes in a different direction than FEEC in the sense that DEC is not built around finite elements in first place. Nevertheless, there are close relations, in particular for lowest order schemes as mentioned by Arnold et al. (2006). For the interested reader we point out applications of DEC in computational electromagnetism (Stern et al., 2015), computergraphics (Desbrun et al., 2003; Crane et al.,

[23] Again, only the form-parts are pulled-back as it was the case for the derivation of (4.230).

2013) and computational fluid mechanics (Hirani et al., 2015; Mohamed et al., 2016).

The deformation map φ

We begin our analysis with the deformation map φ. From Section 4.1 we know that φ basically is a tuple-valued[24] function or zero-form. In (4.230a) the deformation map occurs in two instances: in the external energy $\Pi^{\text{ext}}_{\varphi}(\varphi)$ and in the energy density $\Psi_0(\mathbf{C} = \varphi^*[\mathbf{g}], \dots)$ with $\varphi^*[\mathbf{g}]_{IJ} = (\partial\varphi^i/\partial X^I)(\partial\varphi^j/\partial X^J)\, g_{ij}$. An appropriate space for this case is given as

$$\mathscr{W}_{\varphi}(\Omega) = \left\{ \varphi^i \in {}^0\Lambda \mid \{\varphi, \mathbf{d}(\varphi^i(X))\} \in \mathscr{L}^2(\Omega), \pi_{\varphi}(\varphi - \varphi^{\text{D}}) = 0 \text{ on } \partial\Omega \cup \left(\bigcup_i \partial\mathcal{B}^i_{\varphi} \right) \right\} \tag{4.235}$$

where $\mathbf{d}$ now represents the exterior derivative with respect to Lagrangian coordinates, $\mathscr{L}^2$ denotes the space of Lebesgue square-integrable functions functions[25] and π_{φ} is an abstract projection that specifies the direction(s) in which φ is subject to a constraint at $\partial\mathcal{B}^i_{\varphi}$. The natural discretization of this space are (component-wise) finite elements of Lagrange type, i.e. continuous piecewise polynomials with nodal degrees of freedom. In FEEC notation (Arnold et al., 2006, Section 5), this element type is denoted as $\mathcal{P}_r{}^0\Lambda(\mathcal{T})$ where $\mathcal{P}_r$ stands for polynomials of degree up to r, ${}^0\Lambda(\mathcal{T})$ for the space of zero-forms (see Definition 4.6) and $\mathcal{T}$ for a triangulation of Ω_t.

The Lagrangian vector potential $\mathfrak{A}$

Next we turn to the one-form $\mathfrak{A}$ which occurs by value in $\Pi^{\text{ext}}_{\mathfrak{A}}$ and as $\mathfrak{B} = \mathbf{d}\mathfrak{A}$ in Ψ_0. While also having dim components, the natural space is different from $\mathscr{W}_{\varphi}$ due to the different geometrical character. However, since $\mathbf{d}$ automatically respects this difference, the specification of the function space is almost the same as before (note the ${}^1\Lambda$ instead of ${}^0\Lambda$)

$$\mathscr{W}_{\mathfrak{A}}(\Omega) = \left\{ \mathfrak{A} \in {}^1\Lambda \mid \{\mathfrak{A}, \mathbf{d}\mathfrak{A}\} \in \mathscr{L}^2(\Omega), \pi_{\mathfrak{A}}(\mathfrak{A} - \mathfrak{A}^{\text{D}}) = 0 \vee \mathbf{d}\mathfrak{A} - \mathfrak{B} = 0 \text{ on } \partial\Omega_{\mathfrak{A}} \right\}. \tag{4.236}$$

While $\pi_{\mathfrak{A}}(\mathfrak{A} - \mathfrak{A}^{\text{D}}) = 0$ is just a slightly generalized Dirichlet-type boundary condition, the type of the second deserves closer attention. Indeed, the restriction $\mathbf{d}\mathfrak{A}|_{\partial\Omega_{\mathfrak{A}}}$ reads in surface coordinates $\{u_1, u_2\}$ as

$$\mathbf{d}\mathfrak{A}|_{\partial\Omega_{\mathfrak{A}}} = -\frac{\partial^u A_1}{\partial u^2} + \frac{\partial^u A_2}{\partial u^1}. \tag{4.237}$$

Thus, it only depends on components of the restricted vector potential $\mathfrak{A}|_{\partial\Omega_{\mathfrak{A}}}$ and on surface coordinates. Hence, it is also a suitable boundary condition for FE discretiza-

[24] We reserve "vector-valued" function to functions whose value is a true (tangent-type) vector and not only a tuple of values.

[25] When dealing with forms of degree greater than zero or with vectors we use their "square" norms as given in Section 4.1.8.13

tions in the sense that it only depends on discrete degrees of freedom and derivatives "belonging" to the boundary. Staying with finite elements for $\mathscr{W}_{\mathfrak{A}}$, there are two big classes found in literature. A common choice, in particular in the magneto- and electro-mechanics community, are exactly the same component-wise Lagrange elements as for $\mathscr{W}_{\varphi}$. This is motivated by the fact that in a simplified vector-calculus context both φ (and displacements $\boldsymbol{u} = \varphi - X$) as well as $\mathfrak{A}$ are regarded as vectors which in turn are identified with vector-valued functions. Indeed, in two-dimensional problems where only the out-of-plane component of $\mathfrak{A}$ is non-zero, Lagrange elements for this single component are a proper choice. Another reason is the ease of implementation and the simplicity of Lagrange elements. However, in three dimensions, while in principle appropriate, Lagrange elements are not the most natural choice because one-forms are different from tuple-valued zero-forms and the requirement that all first partial derivatives of $\mathfrak{A}$ are to be in $\mathscr{L}^2$ is over-restrictive. In fact, such observations have been made long ago and led to the development of what we now call "Nédélec (edge) elements" due to Nédélec (1980, 1986) or simply "edge elements" because their degrees of freedom "live" on edges. Within the class of Nédélec elements one distinguishes elements of first and second kind, of which the former feature a reduced and the latter a complete polynomial space over a single element[26]. In FEEC notation, $\mathcal{P}_r^{-\,(n-2)}\Lambda(\mathcal{T})$ and $\mathcal{P}_r^{\,(n-2)}\Lambda(\mathcal{T})$ stand for Nédélec edge elements of first and second kind, respectively, with n being the dimension of space – either two or three. From this we also see that in two-dimensional space, where $n-2=0$, the framework automatically suggests to discretize $\mathfrak{A}$ as a *scalar-valued* zero-form, at least as long as there are no out-of-plane magnetic fields.

The free-charge potential $\mathfrak{D}$

The two-form $\mathfrak{D}$ occurs in its actual form in Ψ_0, but also as $\mathbf{d}\mathfrak{D}$ and $[\![\mathfrak{D}]\!]$ in $\Pi^{\text{ext}}_{\mathfrak{D}}$. Thus,

$$\mathscr{W}_{\mathfrak{D}}(\Omega) = \left\{\mathfrak{D} \in {}^2\Lambda \mid \{\mathfrak{D}, \mathbf{d}\mathfrak{D}\} \in \mathscr{L}^2(\Omega \setminus \partial\mathcal{B}), [\![\mathfrak{D}]\!] \in \mathscr{L}^2(\partial\mathcal{B}), \mathfrak{D} = \mathfrak{D}^{\text{D}} \text{ on } \partial\Omega_{\mathfrak{D}}\right\} \tag{4.238}$$

where the only notable conceptual difference to (4.235) and (4.236) is that we do not need a projection for the boundary condition since the restriction of a two-form to a surface is scalar-valued already. In classical notation this means that we only define the normal component of the associated vector $\boldsymbol{D}$, i.e. $\boldsymbol{N} \cdot \boldsymbol{D} = D_N$.

Zero-forms are evaluated at points, one-forms are integrated over lines and two-forms over surfaces. Correspondingly, the natural finite elements for two-forms are Nédélec face elements or short "face elements" (Nédélec, 1980, 1986). Again, there are elements of first and second kind featuring reduced and complete polynomial space, respectively. In FEEC they are denoted as $\mathcal{P}_r^{-\,(n-1)}\Lambda(\mathcal{T})$ and $\mathcal{P}_r^{\,(n-1)}\Lambda(\mathcal{T})$.

Remark 4.27. There is an interesting ambiguity between discretizations of one-forms and two-forms in two dimensions. The key to resolve this is the consideration of a two-dimensional problem as the limit of a three-dimensional one, when appropriate. Regarding a surface embedded in three-dimensional space the exterior derivative of an

[26] This is at least the case for simplicial meshes consisting of lines, triangles and tetrahedra.

in-plane one-form is completely out-of-plane. If we do not allow for any out-of-plane quantities created by derivatives, all in-plane one-forms have to vanish such that, e.g. only the out-of-plane component of the one-form-valued potential $\mathfrak{A}$ remains. In that case, the only non-scalar-valued branch of "one-forms" are flux-type objects. They are however to be regarded as two-forms that have been collapsed to a plane. Otherwise, the exterior derivative would correspond to the curl instead of divergence. Accordingly, only the in-plane components of "real" one-forms vanish identically and only their out-plane-component, e.g., of the magnetic potential $\mathfrak{A}$, survives. Conversely, what appears as a one-form in two dimensions, often is a "collapsed" two-form. Hence, one should always distinguish collapsed $(n-p)$-forms which originally were $n-p+1$-forms from "real" $(n-p)$ forms. See also Section 4.1.8.12.

Remark 4.28. *Inter-element continuity*: Above we implicitly assumed inter-element continuity of the discretized fields. However, (4.233) features surface charges that imply jumps in $\mathfrak{D}$. In a discrete context we assume that surface charges are bound to element boundaries such that their presence locally destroys inter-element continuity. In computer implementations, inter-element continuity is usually implicitly enforced during the assembly of global matrices and vectors (in linear algebra sense). Thus, to locally give up on inter-element continuity the assembly procedures and the maps connecting element-local and global degrees of freedom have to be modified. Another possibility is to generally enforce continuity weakly by Lagrange multipliers. Such approaches are known as *hybrid* finite element methods (Brezzi, 1974; Trykozko et al., 2001; Boffi et al., 2013).

The electric potential ϕ

The electric potential ϕ is a zero-form. However, by contrast with φ, there do not occur any derivatives of ϕ in (4.233) such that we do not have to pose any constraints on $\mathbf{d}\phi$. Hence,

$$\mathscr{W}_\phi(\Omega) = \left\{ \phi \in {}^0\Lambda \mid \phi \in \mathscr{L}^2(\Omega), \phi = \phi^{\mathrm{D}} \text{ in } \Omega_\phi \cup \left(\bigcup_i \mathcal{B}^i_\phi \right) \right\} \tag{4.239}$$

which can be discretized by *piecewise continuous* polynomials. The corresponding FEEC elements are $\mathcal{P}_r^{-\,n}\Lambda(\mathcal{T})$ and $\mathcal{P}_r^{\,n}\Lambda(\mathcal{T})$. We note that element-wise constants are denoted as $\mathcal{P}_1^{-\,n}\Lambda(\mathcal{T})$ whereas $\mathcal{P}_2^{-\,n}\Lambda(\mathcal{T}) = \mathcal{P}_1^{\,n}\Lambda(\mathcal{T})$ are element-wise linear polynomials without inter-element continuity. From the notation we see that these elements are actually intended for n-forms in an n-space. However, such forms are related to zero-forms by simple scaling (a trivial Hodge operation). Thus, there is no need to define separate finite elements. We note that variational principles that feature derivatives of ϕ accordingly require the usual Lagrange elements $\mathcal{P}_r^0\Lambda(\mathcal{T})$ as we shall see later. Thus, (4.239) shall not be regarded as a universal specification of a function space for ϕ but only as the appropriate one for the variational principle under consideration. This also applies to the other function spaces given above.

4.3.4. A variational principle in terms of the electromagnetic potential

Using the variational energy-principle (4.233) as a starting point we now obtain a principle with primary variables $\{\varphi, \phi, \mathfrak{A}\}$. This is achieved by solving for $\mathfrak{D}$, i.e. finding the infimum with respect to $\mathfrak{D}$, beforehand. Formally, this means

$$\{\hat{\varphi}, \hat{\phi}, \hat{\mathfrak{A}}\} = \arg\left\{\inf_{\varphi,\mathfrak{A}} \sup_{\phi} \left\{\inf_{\mathfrak{D}} \int_\Omega \Psi_0(\mathbf{C}, \mathfrak{D}, \mathfrak{B})\, dV + \Pi^{\text{ext}}_\varphi(\varphi) + \Pi^{\text{ext}}_{\mathfrak{D}}(\phi, \mathfrak{D}) + \Pi^{\text{ext}}_{\mathfrak{A}}(\mathfrak{A})\right\}\right\}. \tag{4.240}$$

Let us further investigate the above statement. Consider the terms of interest

$$\begin{aligned}
&\int_\Omega \Psi_0(\mathbf{C}, \mathfrak{D}, \mathfrak{B})\, dV + \Pi^{\text{ext}}_{\mathfrak{D}}(\phi, \mathfrak{D}) = \\
&\quad \left(\int_\Omega \Psi_0(\mathbf{C}, \mathfrak{D}, \mathfrak{B})\, dV - \int_\Omega \phi\, \mathbf{d}\mathfrak{D} - \int_{\partial\mathcal{B}} \phi\, [\![\mathfrak{D}]\!]\right) + \int_\Omega \phi\mathfrak{Q} + \int_{\partial\mathcal{B}} \phi\mathfrak{Q}^{\text{s}} = \\
&\quad \left(\int_\Omega \Psi_0(\mathbf{C}, \mathfrak{D}, \mathfrak{B})\, dV + \int_\Omega \mathbf{d}\phi \wedge \mathfrak{D} - \int_{\partial\Omega} \phi\mathfrak{D}\right) + \int_\Omega \phi\mathfrak{Q} + \int_{\partial\mathcal{B}} \phi\mathfrak{Q}^{\text{s}},
\end{aligned} \tag{4.241}$$

which implies the requirement of $\mathbf{d}\phi \in \mathscr{L}^2$. Note that only the expressions in braces depend on $\mathfrak{D}$. Using the above intermediate calculation and, additionally, *weakly* enforcing possible boundary conditions on $\mathfrak{D}$ via a boundary term $\phi(\mathfrak{D}-\mathfrak{D}^{\text{D}})$, the infimum with respect to $\mathfrak{D}$ in (4.240) becomes

$$\begin{aligned}
&\inf_{\mathfrak{D}} \int_\Omega \Psi_0(\mathbf{C}, \mathfrak{D}, \mathfrak{B})\, dV + \int_{\partial\Omega} \phi(\mathfrak{D} - \mathfrak{D}^{\text{D}}) + \Pi^{\text{ext}}_{\mathfrak{D}}(\phi, \mathfrak{D}) + \Pi^{\text{ext}}_\varphi(\varphi) + \Pi^{\text{ext}}_{\mathfrak{A}}(\mathfrak{A}) = \\
&\quad \inf_{\mathfrak{D}} \int_\Omega \Psi_0(\mathbf{C}, \mathfrak{D}, \mathfrak{B})\, dV + \int_\Omega \mathbf{d}\phi \wedge \mathfrak{D} \\
&\quad - \int_{\partial\Omega} \phi\mathfrak{D}^{\text{D}} + \int_\Omega \phi\mathfrak{Q} + \int_{\partial\mathcal{B}} \phi\mathfrak{Q}^{\text{s}} + \Pi^{\text{ext}}_\varphi(\varphi) + \Pi^{\text{ext}}_{\mathfrak{A}}(\mathfrak{A}).
\end{aligned} \tag{4.242}$$

This motivates the definition

$$\widehat{\Psi}_0(\mathbf{C}, \mathfrak{E}, \mathfrak{B})\, dV := \inf_{\mathfrak{D}} \{\Psi_0(\mathbf{C}, \mathfrak{D}, \mathfrak{B})\, dV - \mathfrak{E} \wedge \mathfrak{D}\} \quad \text{with} \quad \mathfrak{E} = -\mathbf{d}\phi, \tag{4.243}$$

which is nothing else than a *Legendre-Fenchel* transform. Next, using $\widehat{\Psi}_0(\mathbf{C}, \mathfrak{E}, \mathfrak{B})$ we can rewrite (4.240) as

$$\{\hat{\varphi}, \hat{\phi}, \hat{\mathfrak{A}}\} = \arg\left\{\inf_{\varphi,\mathfrak{A}} \sup_{\phi} \int_\Omega \widehat{\Psi}_0(\mathbf{C}, \mathfrak{E}, \mathfrak{B})\, dV + \Pi^{\text{ext}}_\varphi(\varphi) + \Pi^{\text{ext}}_\phi(\phi) + \Pi^{\text{ext}}_{\mathfrak{A}}(\mathfrak{A})\right\} \tag{4.244}$$

with

$$\Pi^{\text{ext}}_{\phi}(\phi) = -\int_{\partial\Omega} \phi\mathfrak{D}^{\text{D}} + \int_{\Omega} \phi\mathfrak{Q} + \int_{\partial\mathcal{B}} \phi\mathfrak{Q}^{\text{s}}. \tag{4.245}$$

This leads to electrostatic stationary conditions dual to those in (4.234)

$$\sqrt{G}\frac{\partial\widehat{\Psi}_0}{\partial E_I}\epsilon_{IJ\underline{K}} = -D_{JK}, \qquad \mathbf{d}\mathfrak{D} = \mathfrak{Q} \qquad \text{and} \qquad [\![\mathfrak{D}]\!]|_{\partial\mathcal{B}} = \mathfrak{Q}^{\text{s}}. \tag{4.246}$$

The function spaces for the primary quantities φ and $\mathfrak{A}$ are the same as for (4.233). For ϕ, however, we now need

$$\mathcal{W}_{\phi}(\Omega) = \left\{\phi \in {}^0\Lambda \mid \{\phi, \mathbf{d}(\phi)\} \in \mathscr{L}^2(\Omega), \phi = \phi^{\text{D}} \text{ on } \partial\Omega_{\phi} \cup \left(\bigcup_i \partial\mathcal{B}^i_{\phi}\right)\right\} \tag{4.247}$$

which is discretized in terms of $\mathcal{P}^0_r\Lambda(\mathcal{T})$ and agrees with the requirement on ϕ for (4.241).

Remark 4.29. The above variational principle is the quasi-static version of what can be found in the monograph by Kovetz (2000, Chapter 15) and the article of Thomas and Triantafyllidis (2009). Both of them use the Poynting two-form as energy flux as a starting point (see (4.193) – (4.195b)).

4.3.5. A variational principle in terms of the electric and magnetic scalar potentials

Another principle can be obtained for the case of vanishing free currents. Then, $\mathbf{d}\mathfrak{H} \equiv 0$ and thus one can write $\mathfrak{H} = -\mathbf{d}\phi^{\text{m}}(X)$. The scalar magnetic potential ϕ^{m} is an auxiliary quantity mostly useful in current-free boundary value problems in magnetostatics. Nevertheless, it is widely used and so is the associated variational principle (Bossavit, 1998a; Bustamante et al., 2008).

Instead of rigorously deriving the variational principle below we merely state the magnetostatic part by analogy to the electrostatic part. Accordingly, $\mathfrak{H}$ plays the role of $\mathfrak{E}$ and $\mathfrak{B}$ that of $\mathfrak{D}$. The essential difference is the general absence of "magnetic charge". However, we still consider the loading potential $\Pi^{\text{ext}}_{\phi^{\text{m}}}(\phi^{\text{m}})$ which allows to specify $\mathfrak{B}$ at least at (parts of) the outer boundary $\partial\Omega$. The variational principle finally is

$$\{\hat{\varphi}, \hat{\phi}, \hat{\phi^{\text{m}}}\} = \arg\left\{\inf_{\varphi}\sup_{\phi,\phi^{\text{m}}} \int_{\Omega} \widehat{\widehat{\Psi}}_0(\mathbf{C}, \mathfrak{E}, \mathfrak{H})\, dV + \Pi^{\text{ext}}_{\varphi}(\varphi) + \Pi^{\text{ext}}_{\phi}(\phi) + \Pi^{\text{ext}}_{\phi^{\text{m}}}(\phi^{\text{m}})\right\} \tag{4.248}$$

with

$$\widehat{\widehat{\Psi}}_0(\mathbf{C}, \mathfrak{E}, \mathfrak{H}) = \inf_{\mathfrak{B}} \widehat{\Psi}_0(\mathbf{C}, \mathfrak{E}, \mathfrak{B})\, dV - \mathfrak{H} \wedge \mathfrak{B} \tag{4.249}$$

and

$$\Pi^{\text{ext}}_{\phi^{\text{m}}}(\phi^{\text{m}}) = -\int_{\partial\Omega} \phi^{\text{m}} \mathfrak{B}^{\text{D}} \quad \text{and} \quad \mathfrak{H} = -\,\mathbf{d}\phi^{\text{m}}. \tag{4.250}$$

We note that $\mathfrak{B}^{\text{D}}$ is related to $\mathfrak{A}^{\text{D}}$ (see (4.236)) via the exterior derivative but is applied as a natural boundary condition. The function space for ϕ^{m} is the same as for ϕ given by (4.247).

4.3.6. A variational principle in terms of $\mathfrak{D}$, $\mathfrak{B}$ and scalar potentials

Again by analogy to electrostatics we come up with a variational principle treating magnetostatics by means of the magnetic field $\mathfrak{B}$ and the scalar magnetic potential ϕ^{m}

$$\{\hat{\varphi}, \hat{\mathfrak{D}}, \hat{\mathfrak{B}}, \hat{\phi}, \hat{\phi^{\text{m}}}\} = \\ \arg\left\{ \inf_{\varphi,\mathfrak{D},\mathfrak{B}} \sup_{\phi,\phi^{\text{m}}} \int_{\Omega} \Psi_0(\mathbf{C},\mathfrak{D},\mathfrak{B})\, dV + \Pi^{\text{ext}}_{\varphi}(\varphi) + \Pi^{\text{ext}}_{\mathfrak{D}}(\phi,\mathfrak{D}) + \Pi^{\text{ext}}_{\mathfrak{B}}(\phi^{\text{m}},\mathfrak{B}) \right\} \tag{4.251}$$

with

$$\Pi^{\text{ext}}_{\mathfrak{B}}(\phi^{\text{m}},\mathfrak{B}) = -\int_{\partial\Omega} \phi^{\text{m}}(\mathfrak{B}^{\text{D}} - \mathfrak{B}) - \int_{\Omega} \phi^{\text{m}}\, \mathbf{d}\mathfrak{B}. \tag{4.252}$$

Obviously, the above principle is only valid for vanishing free currents.

The main difference between (4.248) and (4.251) is that only the latter is energy-based. In fact, it is a minimization problem constrained by linear PDEs, whereas the former has a more general saddle-point structure.

4.3.7. A variational principle in terms of electric and magnetic vector potentials

In case of vanishing free charge such that $\mathbf{d}\mathfrak{D} \equiv 0$ we may employ an electric vector potential $\mathfrak{A}^{\text{e}}$ with $\mathbf{d}\mathfrak{A}^{\text{e}} = \mathfrak{D}$ in analogy to $\mathbf{d}\mathfrak{A} = \mathfrak{B}$. The corresponding energy principle is obtained directly from (4.233)

$$\{\hat{\varphi}, \hat{\mathfrak{A}^{\text{e}}}, \hat{\mathfrak{A}}\} = \arg\left\{ \inf_{\varphi,\mathfrak{A}^{\text{e}},\mathfrak{A}} \int_{\Omega} \Psi_0(\mathbf{C},\mathfrak{D},\mathfrak{B})\, dV + \Pi^{\text{ext}}_{\varphi}(\varphi) + \Pi^{\text{ext}}_{\mathfrak{A}}(\mathfrak{A}) \right\}. \tag{4.253}$$

Note that in electrostatics $\mathbf{d}\mathfrak{E} = 0$ such that we *cannot* apply electric loads by a $\Pi^{\text{ext}}_{\mathfrak{A}^{\text{e}}}(\mathfrak{A}^{\text{e}})$ similar to $\Pi^{\text{ext}}_{\mathfrak{A}}(\mathfrak{A})$. Instead, the restriction of $\mathfrak{D}$ can be prescribed on $\partial\Omega_{\mathfrak{A}^{\text{e}}}$ as contained in the definition of the function space following (4.236)

$$\mathscr{W}_{\mathfrak{A}^{\text{e}}}(\Omega) = \\ \left\{ \mathfrak{A}^{\text{e}} \in {}^1\Lambda \,|\, \{\mathfrak{A}^{\text{e}}, \mathbf{d}\mathfrak{A}^{\text{e}}\} \in \mathscr{L}^2(\Omega),\, \pi_{\mathfrak{A}^{\text{e}}}(\mathfrak{A}^{\text{e}} - \mathfrak{A}^{\text{e,D}}) = 0 \vee \mathbf{d}\mathfrak{A}^{\text{e}} - \mathfrak{D} = 0 \text{ on } \partial\Omega_{\mathfrak{A}^{\text{e}}} \right\}. \tag{4.254}$$

Chapter 5

Variational homogenization and multiscale methods

This Chapter deals with techniques for the treatment of small-scale heterogeneities in material properties. We present computational homogenization in terms of the differential geometric quantities and notation discussed in Chapter 4 in a variational setting. In Part II of this thesis, we will apply the variational homogenization principles outlined below, but only after a transition to classical notation. Parts of the material discussed below can also be found in Keip and Rambausek (2017), Rambausek et al. (2019) and hopefully in some future publications.

5.1. Introduction to homogenization

Many technically relevant materials are inhomogeneous, meaning that at some length scale they exhibit different phases. A phase can be considered as being itself a material such that the different atoms in a continuum do not constitute a phase yet. In the present context we shall call a material homogeneous if each material sample, no matter of which size, ranging from microns to meters, has approximately the same properties. If this is not the case, we say the material is inhomogeneous. We also say that an inhomogeneous material has a microstructure, that is a special structure only observable at small scales.

There a many reasons for materials to be or to become inhomogeneous. In the case of metal alloys, the temperature dependence of both the crystal structure and the mutual solubility of the constituents are main drivers of the development of microstructures. However, for example deformation, thermal treatment or chemical reactions may also trigger the emergence or evolution of microstructures. Another "source" of inhomogeneity is the production of *composite materials* which are composed of two or more materials which never make up a single phase in the whole production process. Two important examples of such (classes of) composite materials are fibre-reinforced plastics and steel-reinforced concrete.

In the present work, composites made of a soft elastomer matrix and stiff magnetic filler particles, so-called magnetorheological elastomers (MREs), will be discussed in Part II. The overall macroscopically observable ("effective") mechanical and magnetic properties of such composites greatly differ from those of its constituents. Nevertheless, there is a strong dependence of the effective properties on the distribution and properties of the individual phases. This is the main motivation for the production of composites

in general.

Because of the remarkable effects of small-scale structures on macroscopic properties of many engineering materials, a whole scientific discipline, called *homogenization*, has emerged. It is concerned with the prediction of effective properties based on microstructural features. The fundamental idea behind is that fast-varying but, more or less, repeating microscopic features lead to physical responses of which only certain types of averages play a role in macroscopic considerations, at least to a certain extent. Thus, homogenization heavily relies on the mathematics of averaging and (in more general cases) filtering.

Early ideas about homogenization theory date back to the works of Voigt (1887), Reuss (1929), Hill (1952) and Eshelby and Peierls (1957). The work of Lippmann and Schwinger (1950), though in a different domain of physics, also had great impact on what we nowadays call homogenization. Later, the seminal works of Hashin and Shtrikman (1962b,a,c, 1963) established variational approaches and therefrom derived bounds for the mechanical but also magnetic behaviour of multiphase materials. Their results have been extended to anisotropic materials by Willis (1977), Milton and Kohn (1988) and Ponte-Castañeda (1991), among others. Parallel to these developments, Hill (1963, 1964, 1965a,b) made several central contributions to the field. In subsequent developments, homogenization has been and still is applied to various classes of more complicated materials and nonlinear material behaviour. Moreover, homogenization theory has been connected to "higher-order" materials and non-local theories by Gambin and Kröner (1989), Drugan and Willis (1996) and Forest (1998) to name a few. We also mention the monograph of Nemat-Nasser and Hori (2010) for an in-depth introduction to homogenization techniques in continuum mechanics. Homogenization of coupled magneto-mechanics within the present scope has recently been studied by Ponte Castañeda and Galipeau (2011), Galipeau and Ponte Castañeda (2012, 2013a,b).

Computational homogenization

The treatment of increasingly difficult scenarios has also lead to the demand for computational techniques that allow to obtain results where analytical approaches fail. This domain was pioneered by Moulinec and Suquet (1994) with their numerical scheme based on the Lippmann-Schwinger equation and the Fast Fourier Transform (FFT). This methodology was improved over the years by Eyre and Milton (1999) who came up with a faster version (the *accelerated scheme*) of what was proposed by Moulinec and Suquet (1994). An important development was also the possibility to treat infinite phase-contrast contributed by Michel et al. (2001). The use of conjugate gradient methods instead of a fixed-point scheme for the Lippmann-Schwinger equation was proposed by Brisard and Dormieux (2010) and Zeman et al. (2010). Gélébart and Mondon-Cancel (2013) and Kabel et al. (2014) documented the significant advantages of these methods such as high convergence rates. Another recent addition was the consideration of FFT-based schemes for the weak instead of the strong form of the equations under consideration by (Brisard and Dormieux, 2012). This is intimately connected to understanding the Green's operator in the Lippmann-Schwinger equation as special instance

of a more general projection viewpoint (Vondřejc et al., 2014). Based on these two contributions it was possible to view at the Fourier-based schemes from a finite element perspective (Zeman et al., 2017; de Geus et al., 2017). Despite their high degree of maturity, Fourier-based homogenization schemes still have some issues (Moulinec et al., 2018), in particular near interfaces of high contrast (Willot et al., 2014). We mention the works of Schneider et al. (2017) and Leuschner and Fritzen (2017) who address the latter issue by combining finite element and FFT schemes.

Spectral methods, and Fourier methods in particular, were applied to a wide range of problems in solid mechanics and materials science by, e.g., Lebensohn (2001), Brenner (2010), Berbenni et al. (2014), Kochmann et al. (2016), Lebensohn and Needleman (2016), Vidyasagar et al. (2017), Göküzüm and Keip (2018) and Göküzüm et al. (2019).

Another line of computational homogenization centered in continuum mechanics and tailored for finite element implementations was initiated by Miehe et al. (1999), Miehe et al., Feyel and Chaboche (2000), Terada and Kikuchi (2001) as well as Kouznetsova et al. (2001). By constrast to the community around FFT-based homogenization, here there was great interest in embedding the homogenization results directly and on-the-fly in macroscopic finite element (FE) simulations. This use case is termed "FE^2-method".

The initial works were followed by contributions in the field of solid mechanics, e.g. the contributions of Miehe and Koch (2002) in plasticity, Miehe et al. (2002) in stability analysis and of Terada et al. (2003) in finite elasticity. Research on schemes that consider higher derivatives of macroscopic deformation were conducted by Kouznetsova et al. (2002, 2004) and more recently by Forest and Trinh (2011).

Finite-element based homogenization techniques were successfully applied to coupled problems in magneto-electro-mechanics and subsets thereof by Schröder (2009), Schröder and Keip (2012), Javili et al. (2013), Keip et al. (2014), Galipeau et al. (2014), Miehe et al. (2015), Miehe et al. (2016), Lefèvre and Lopez-Pamies (2017b,a), Lefèvre et al. (2017) and Danas (2017). For a more detailed overview on (computational) FE- and FFT-based homogenization we refer also to our recent contributions Keip and Rambausek (2017) and Rambausek et al. (2019), respectively.

We conclude this brief literature overview by mentioning the framework of asymptotic homogenization (Engquist and Souganidis, 2008) and the heterogeneous multiscale method (Abdulle et al., 2012) which provide additional mathematical structure and generalizations. However, we will not make use of them in what follows.

Outline of the chapter

The present thesis contributes to the field of multiscale magneto-electro-mechanics by computational homogenization. We present FFT- as well as finite-element-based techniques in Part II. As preparation for that task we outline the fundamental concepts of (computational) homogenization in Section 5.2 below. Then we formulate variational homogenization principles for microscopic boundary value problems in Section 5.3, which will be based on the more general principles introduced in Section 4.3. After that, we describe an abstract software framework for the implementation of the FE^2-method and its generalization in Section 5.4.

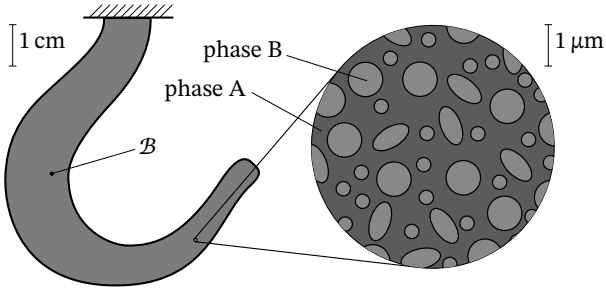

Figure 5.1: A macroscopically homogeneous body with microstructure. Many important engineering materials have their distinctive properties from their heterogeneous structure at small scale. Just consider concrete, the various kinds of steel or fibre-reinforced composites. They can consist of different phases of quite similar constituents but also of quite different basic ingredients.

5.2. Fundamental concepts of computational homogenization

Below we shall *assume* that the microscopic features and responses vary at length scales much smaller than macroscopically relevant scales. From a mathematical modeling point of view this means that the averages of the quantities $\underline{\boldsymbol{F}}$, $\mathfrak{D}$, $\mathfrak{B}$, $\underline{\dot{\mathfrak{P}}}$, $\mathfrak{E}$ and $\mathfrak{H}$ are practically constant for "averaging-windows" on some sub-macroscopic scale. Hence, we may decompose the actual fields into macroscopically effective and remaining purely microscopic contributions. We thus speak of *scale separation*.

5.2.1. Geometric setting and kinematics

In what follows we consider a body $\mathcal{B}$ with microstructure as illustrated in Figure 5.1. We let Lagrangian coordinates X denote the true scale-agnostic coordinates whereas $\overline{X}$ represent "macroscopic" coordinates where the smallest relevant increment is orders of magnitude larger than the characteristic length of the microstructure and the size of appropriate averaging windows.

We expect that such a body will under load deform in such a way that one observes deformation modes of macroscopic scale and also modes of microscopic scale as depicted in Figure 5.2. We thus decompose the deformation φ into a macroscopic and a microscopic part denoted as $\overline{\varphi}$ and $\widetilde{\varphi}$, respectively

$$\varphi(X) = \overline{\varphi}(X) + \widetilde{\varphi}(X). \tag{5.1}$$

Such an *additive* decomposition is sound because we assume that we actually deal with *Euclidean* space at the microscopic scale. From the macroscopic point of view this is consistent with a manifold being locally equivalent to Euclidean space.

If it is, as in Figure 5.2, the case that there are not any modes of intermediate scale we have scale separation. Then we may define $\widetilde{\varphi}$ to collect all of φ that is not macroscopic.

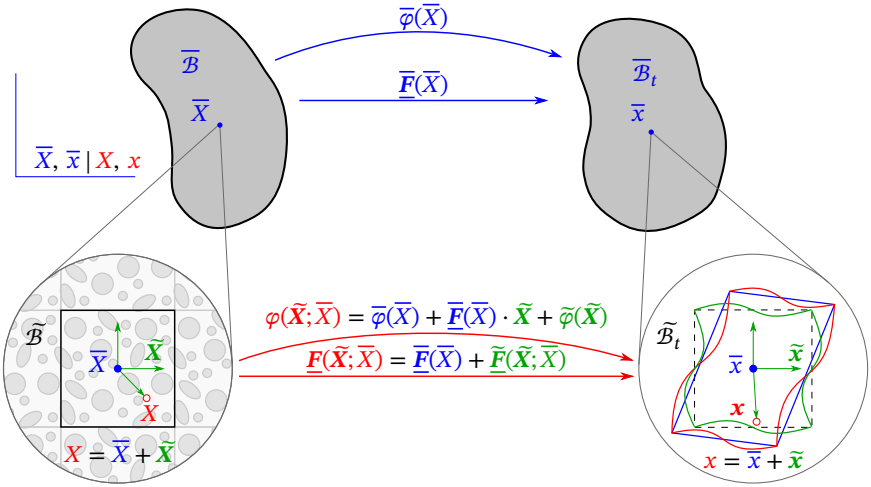

Figure 5.2: Kinematic ansatz of first-order homogenization. The total deformation φ (red) consists is up to first order governed by macroscopic expansion coefficients (blue). Higher-order "fluctuation" terms (green) are attributed to the microscopic scale.

The remaining question is in the choice of $\overline{\varphi}$. Since we are interested in macroscopic deformation the corresponding map $\overline{\varphi}(X)$ cannot be a constant. To proceed, let us consider as suggested by Figure 5.2 the microscopically *representative* domain $\widetilde{\mathcal{B}}[\overline{X}]$ around some fixed point $\overline{X}$. The domain $\widetilde{\mathcal{B}}[\overline{X}]$ is often referred to as *representative volume element* ($\mathcal{RVE}$) where representative is understood in terms of effective material properties of a sample $\widetilde{\mathcal{B}}[\overline{X}]$. It thus has to be large enough to capture the essential micromorphology but still much smaller than macroscopic lengths. Within $\widetilde{\mathcal{B}}[\overline{X}]$ we observe a *linear* $\overline{\varphi}(X)$ with superimposed small-scale fluctuations $\widetilde{\varphi}(X)$. The Euclidean setting also furthermore allows us to specify (5.1) within $\widetilde{\mathcal{B}}[\overline{X}]$ using $\widetilde{X} = X - \overline{X} = \widetilde{\boldsymbol{X}}$ to obtain an expansion[1]

$$\varphi(X)|_{\widetilde{\mathcal{B}}[\overline{X}]} = \varphi(\widetilde{\boldsymbol{X}}; \overline{X}) = \underbrace{\overline{\varphi}(\overline{X}) + \overline{\boldsymbol{F}}(\overline{X}) \cdot \widetilde{\boldsymbol{X}}}_{\overline{\varphi}(X)} + \widetilde{\varphi}(\widetilde{\boldsymbol{X}}) \tag{5.2}$$

where we have zeroth- and first-order terms $\overline{\varphi}(\overline{X})$ and $\overline{\boldsymbol{F}}(\overline{X}) \cdot \widetilde{\boldsymbol{X}}$, respectively, and higher-order terms $\widetilde{\varphi}(\widetilde{\boldsymbol{X}})$. In the equation above we care about the arguments of the quantities involved and therefore resort to the dot product "$\cdot$" to express the action of $\overline{\boldsymbol{F}}$ (evaluated at $\overline{X}$) on $\widetilde{\boldsymbol{X}}$. Note that we write $\widetilde{\boldsymbol{X}}$ in boldface to emphasize that we regard it not only as a position but also as a *position vector*. Also, we did not yet specify how $\overline{\varphi}(\overline{X})$ and $\overline{\boldsymbol{F}}(\overline{X})$ are obtained from φ. As indicated, we adopt an imprecise notation and do not

[1] Such a Taylor expansion requires that $\widetilde{X}$ can be regarded as a vector, which is not possible on a general manifold.

use distinguished symbols for $\varphi(X)$ and $\varphi(\widetilde{\boldsymbol{X}};\overline{X})$, although they are not exactly the same thing. However, in the present multiscale context we will from now on by φ always mean $\varphi(\widetilde{\boldsymbol{X}};\overline{X})$ unless explicitly stated otherwise.

The tangent map based on $\varphi(\widetilde{\boldsymbol{X}};\overline{X})$ is obtained as

$$\underline{\boldsymbol{F}}(\widetilde{\boldsymbol{X}};\overline{X}) = \frac{\partial\varphi^i}{\partial\widetilde{X}^I}\partial_{x^i}\otimes\mathbf{d}X^I = \left(\overline{F}^i{}_I + \frac{\partial\widetilde{\varphi}^i}{\partial\widetilde{X}^I}\right)\partial_{x^i}\otimes\mathbf{d}X^I. \tag{5.3}$$

Remark 5.1. We emphasize that the concept of scale separation as reflected in (5.2) is a central modeling *assumption*. The case when scales are not perfectly separated, i.e. when higher order expansion terms of $\overline{\varphi}$ appear on the "small" scale, other tools than (first-order) homogenization, which do not rely on strict scale separation, need to be employed (Hou and Wu, 1997; Hughes et al., 1998; Kouznetsova et al., 2004; Forest and Trinh, 2011).

5.2.2. The averaging filter

From now on, in addition to Euclidean space, we shall also restrict ourselves to orthonormal coordinates in $\widetilde{\mathcal{B}}[\overline{X}]$ and $\widetilde{\mathcal{B}}_t[\overline{X}]$. In the present scope of *first order* homogenization "averages" play a central role. In fact, we attain the viewpoint that small-scale (in the sense of "wavelength", not magnitude) fluctuations can be filtered[2] out by averaging. Whatever passes the "filter" is identified with some macroscopic or (macroscopically) *effective* quantity.

The average of $\varphi(X)$ over $\widetilde{\mathcal{B}}[\overline{X}]$ (short $\widetilde{\mathcal{B}}$) is

$$\langle\varphi\rangle_{\widetilde{\mathcal{B}}} = \frac{1}{|\widetilde{\mathcal{B}}|}\int_{\widetilde{\mathcal{B}}}\varphi(X)\,dV = \overline{\varphi}(\overline{X}) + \underline{\overline{\boldsymbol{F}}}(\overline{X})\cdot\langle\widetilde{\boldsymbol{X}}\rangle_{\widetilde{\mathcal{B}}} + \langle\widetilde{\varphi}(\widetilde{\boldsymbol{X}})\rangle_{\widetilde{\mathcal{B}}}. \tag{5.4}$$

We identify the macroscopic position of $\widetilde{\mathcal{B}}[\overline{X}]$ via the average[3] of $\varphi|_{\widetilde{\mathcal{B}}[\overline{X}]}$

$$\langle\varphi\rangle_{\widetilde{\mathcal{B}}} := \overline{\varphi}(\overline{X}) \qquad \text{such that} \qquad \underline{\overline{\boldsymbol{F}}}\cdot\langle\widetilde{\boldsymbol{X}}\rangle_{\widetilde{\mathcal{B}}} + \langle\widetilde{\varphi}(\widetilde{\boldsymbol{X}})\rangle_{\widetilde{\mathcal{B}}} = 0. \tag{5.5}$$

Then, it is convenient to set $\overline{X} = \langle X\rangle_{\widetilde{\mathcal{B}}}$ which leads to $\langle\widetilde{\boldsymbol{X}}\rangle_{\widetilde{\mathcal{B}}} = 0$ and, further, $\langle\widetilde{\varphi}(\widetilde{\boldsymbol{X}})\rangle_{\widetilde{\mathcal{B}}} = 0$. However, such considerations only play a role in the presence of body forces varying at microscopic length, which is beyond the present scope.

Before we continue, let us comment on notation. The averaging operator $\langle\bullet\rangle$, i.e. angle brackets with one argument, is not to be confused with the inner product $\langle\bullet,\bullet\rangle$ taking two arguments. Moreover, since we assumed Euclidean space and Cartesian coordinates in $\widetilde{\mathcal{B}}$, component-wise integrals of tensors make sense.

[2] It may immediately come to one's mind that the filtering perspective naturally opens the door to generalizations of what is shown below. See, e.g., the work of Yvonnet and Bonnet (2014).

[3] We refer to Larsson et al. (2010) for an approach where this condition is not met.

Next we come to the average of the tangent map. If φ is smooth we can write

$$\langle \underline{\boldsymbol{F}} \rangle_{\widetilde{\mathcal{B}}} = \frac{1}{|\widetilde{\mathcal{B}}|} \int_{\widetilde{\mathcal{B}}} \underline{\boldsymbol{F}}(X)\, dV = \underline{\overline{\boldsymbol{F}}} + \left\langle \frac{\partial \widetilde{\varphi}^i}{\partial \widetilde{X}^I}\, \partial_{x^i} \otimes \mathbf{d}X^I \right\rangle_{\widetilde{\mathcal{B}}} = \left(\overline{F}^i{}_I + \left\langle \frac{\partial \widetilde{\varphi}^i}{\partial \widetilde{X}^I} \right\rangle_{\widetilde{\mathcal{B}}} \right) \partial_{x^i} \otimes \mathbf{d}X^I. \tag{5.6}$$

In case of φ being non-smooth we may consider a sequence of *smooth* maps φ_n for which $\lim_{n\to 0} \varphi_{(n)} = \varphi$ and define

$$\langle F^i{}_I \rangle_{\widetilde{\mathcal{B}}} = \lim_{(n)\to 0} \left\langle \frac{\partial \varphi^i_{(n)}}{\partial \widetilde{X}^I} \right\rangle_{\widetilde{\mathcal{B}}} = \overline{F}^i{}_I + \lim_{n\to 0} \left\langle \frac{\partial \widetilde{\varphi}^i_{(n)}}{\partial \widetilde{X}^I} \right\rangle_{\widetilde{\mathcal{B}}}. \tag{5.7}$$

For smooth $\widetilde{\varphi}$ (or $\widetilde{\varphi}_{(n)}$) and exploiting Euclidean space and Cartesian coordinates in $\widetilde{\mathcal{B}}[\overline{X}]$ one can show that

$$\left\langle \frac{\partial \widetilde{\varphi}^i}{\partial \widetilde{X}^I} \right\rangle_{\widetilde{\mathcal{B}}} = \frac{1}{|\widetilde{\mathcal{B}}|} \int_{\widetilde{\mathcal{B}}} \mathbf{d}\left(\epsilon_{IJ\underline{K}}\, \widetilde{\varphi}^i\, \mathbf{d}X^J \wedge \mathbf{d}X^K \right) = \frac{1}{|\widetilde{\mathcal{B}}|} \int_{\partial\widetilde{\mathcal{B}}} \epsilon_{IJ\underline{K}}\, \widetilde{\varphi}^i\, \mathbf{d}X^J \wedge \mathbf{d}X^K. \tag{5.8}$$

In classical notation this is nothing else than (Miehe et al., 1999)

$$\left\langle \frac{\partial \widetilde{\varphi}^i}{\partial \widetilde{X}^I} \right\rangle_{\widetilde{\mathcal{B}}} = \frac{1}{|\widetilde{\mathcal{B}}|} \int_{\partial\widetilde{\mathcal{B}}} \widetilde{\varphi}^i \otimes N_I\, dA. \tag{5.9}$$

From the two equations above we see that C^1-continuity (almost everywhere; C^0 elsewhere) of $\widetilde{\varphi}$ is actually enough for (5.6) to hold. We only need to resort to (5.7) or directly to (5.8) if $\widetilde{\varphi}$ has jumps. In fact, the boundary integrals immediately inform us about the continuity and smoothness requirements on the integrand: if the integrand of the boundary integral is continuous everywhere in $\widetilde{\mathcal{B}}[\overline{X}]$ then the boundary integral average coincides with the volume integral average.

When we identify the average of $\underline{\boldsymbol{F}}$ as the macroscopic tangent map $\underline{\overline{\boldsymbol{F}}}$ we obtain one more constraint on $\widetilde{\varphi}$

$$\underline{\overline{\boldsymbol{F}}} := \langle \underline{\boldsymbol{F}} \rangle_{\widetilde{\mathcal{B}}} \qquad \Rightarrow \qquad \left\langle \frac{\partial \widetilde{\varphi}^i}{\partial \widetilde{X}^I} \right\rangle_{\widetilde{\mathcal{B}}} = 0. \tag{5.10}$$

By assumption, the position vectors $\widetilde{\boldsymbol{X}}$ are restricted to very small magnitudes compared with possible coordinate values of $\overline{X}$. The same holds for the relation between $\widetilde{\varphi}$ and $\overline{\varphi}$. This motivates us to introduce a coarse grained version of $\mathcal{B}$ denoted as $\overline{\mathcal{B}}$ which is parameterized by $\overline{X}$. It in this sense serves us as the domain of quantities depending on $\overline{X}$ instead of X such as $\overline{\varphi}(\overline{X})$ and $\underline{\overline{\boldsymbol{F}}}(\overline{X})$. Of course, on $\overline{\mathcal{B}}$ the tensor $\underline{\overline{\boldsymbol{F}}}$ represents the tangent map of $\overline{\varphi}$ with components

$$\overline{F}^i{}_I = \frac{\partial \overline{\varphi}^i}{\partial \overline{X}^I}. \tag{5.11}$$

The considerations on averaging over $\widetilde{\mathcal{B}}[\overline{X}]$ above can be readily adapted for other quantities: Any effective primary field is simply averaged like φ in (5.5). For quantities derived from primary fields procedures similar to that from (5.6) to (5.8) can be applied. The essential ingredients are a limit as in (5.7) and a possibly artificially constructed exterior derivative to employ Stokes' theorem as in (5.8). We refer to Miehe et al. (2016) for definitions of the macroscopic mechanical, electric and magnetic quantities in vector-calculus notation. In what follows we will restrict ourselves to the case where standard volume averages are sufficient for the determination of effective quantities.

5.3. Variational homogenization principles for magneto-electro-elasticity

Within this thesis, homogenization will be used solely for the determination of effective *material properties* from boundary values problems at the microscopic scale. Accordingly, as mentioned above, we will not consider the case of fast varying body forces or other "loads". Since we encode magneto- and electrostatic forces via constitutive laws for the *total* stress, the most obvious remaining force to think about is gravitation. Indeed, since gravitation is bound to mass density it can vary significantly on microscopic scales. However, we argue that the local effect, i.e. the effect of the local gravitational force density on the equilibrium state of a boundary value problem (BVP) on the microscale is negligible. The cumulative effect of gravitation from other parts of the body are of much greater importance. Just imagine a fibre-reinforced composite pole structure under self-weight: The bottom part has to support the full weight of the structure above, which is orders of magnitude more than the gravitational force exerted of the few fibres located in a small region on the structure in their vicinity. The picture can change for extremely soft carrier ("matrix") materials or certain dynamic scenarios such as the emerging field of acoustic meta-materials. We refer to Sridhar et al. (2016) for a recent contribution on homogenization in this area and to Hussein et al. (2014) for a general overview on the larger class of "phononic" materials.

Concerning free charge and current densities we for now assume that both of them vanish in materials for which we employ homogenization. This means that we treat the individual phases as insulators without free charge compartments. For MREs in quasi-static condition these are reasonable modeling assumptions.

5.3.1. The variational principle on the micropscopic scale

We first outline the homogenization procedure by means of the variational principle (4.233) in Section 4.3.3 and then present analogous results for the other principles discussed in Sections 4.3.4, 4.3.5 and 4.3.6. For convenience, we recall the scale-agnostic

(or full-scale) principle (4.233)

$$\{\hat{\varphi},\hat{\mathfrak{D}},\hat{\mathfrak{A}},\hat{\phi}\} = \arg\left\{\inf_{\varphi,\mathfrak{D},\mathfrak{A}}\sup_{\phi}\int_{\Omega}\Psi_0(\mathbf{C},\mathfrak{D},\mathfrak{B})\,dV + \Pi_{\varphi}^{\text{ext}}(\varphi) + \Pi_{\mathfrak{D}}^{\text{ext}}(\phi,\mathfrak{D}) + \Pi_{\mathfrak{A}}^{\text{ext}}(\mathfrak{A})\right\}.$$

When considering only a microscopic portion $\widetilde{\mathcal{B}} \subset \mathcal{B} \subset \Omega$ the above is written as

$$\{\hat{\varphi},\hat{\mathfrak{D}},\hat{\mathfrak{A}},\hat{\phi}\}\big|_{\widetilde{\mathcal{B}}} = \arg\left\{\inf_{\varphi,\mathfrak{D},\mathfrak{A}}\sup_{\phi}\int_{\widetilde{\mathcal{B}}}\Psi_0(\mathbf{C},\mathfrak{D},\mathfrak{B})\,dV - \int_{\widetilde{\mathcal{B}}}\phi\,\mathbf{d}\mathfrak{D}\right\} \tag{5.12}$$

which is equivalent to

$$\{\hat{\varphi},\hat{\mathfrak{D}},\hat{\mathfrak{A}},\hat{\phi}\}\big|_{\widetilde{\mathcal{B}}} = \arg\left\{\inf_{\varphi,\mathfrak{D},\mathfrak{A}}\sup_{\phi}\langle\Psi_0(\mathbf{C},\mathfrak{D},\mathfrak{B}) - \phi\,\mathbf{d}\mathfrak{D}\rangle_{\widetilde{\mathcal{B}}}\right\}. \tag{5.13}$$

The according restrictions of the primary fields are given as

$$\varphi|_{\widetilde{\mathcal{B}}} = \varphi(\widetilde{\boldsymbol{X}};\overline{X}) = \overline{\varphi} + \underbrace{\overline{\underline{\boldsymbol{F}}}(\overline{\boldsymbol{X}})}_{=\overline{\underline{\boldsymbol{F}}}(\overline{\boldsymbol{X}})\cdot\widetilde{\boldsymbol{X}}} + \widetilde{\varphi} \tag{5.14a}$$

$$\mathfrak{D}|_{\widetilde{\mathcal{B}}} = \mathfrak{D}(\widetilde{\boldsymbol{X}};\overline{X}) = \overline{\mathfrak{D}}(\overline{X}) + \widetilde{\mathfrak{D}}(\widetilde{\boldsymbol{X}}) \tag{5.14b}$$

$$\mathfrak{A}|_{\widetilde{\mathcal{B}}} = \mathfrak{A}(\widetilde{\boldsymbol{X}};\overline{X}) = \overline{\mathfrak{A}} + \frac{1}{2}\mathbb{i}_{\widetilde{\boldsymbol{X}}}\overline{\mathfrak{B}} + \widetilde{\mathfrak{A}} \tag{5.14c}$$

$$\phi|_{\widetilde{\mathcal{B}}} = \phi(\widetilde{\boldsymbol{X}};\overline{X}) = \overline{\phi} + \widetilde{\phi} \tag{5.14d}$$

of which (5.14c) is only valid for the three-dimensional case. In two dimensions, the factor 1/2 has to be dropped. Since $\mathfrak{D}$ directly enters Ψ_0 and we did not consider free charge densities (as maybe given by charged inclusions) there is no need to account for a linear macroscopic term. Similarly, we do not require a linear expansion of $\overline{\phi}$.

We regard the macroscopic quantities denoted with an overline as inputs or parameters for (5.12), e.g. $\hat{\varphi}|_{\widetilde{\mathcal{B}}[\overline{X}]} = \hat{\varphi}|_{\widetilde{\mathcal{B}}[\overline{X}]}(\overline{\varphi},\overline{\underline{\boldsymbol{F}}},\overline{\mathfrak{D}},\overline{\mathfrak{A}},\overline{\phi})$. The parameterization enters through the definition of the spaces for $\{\varphi,\mathfrak{D},\mathfrak{A},\phi\}|_{\widetilde{\mathcal{B}}}$ in (5.12)

$$\mathscr{W}_{\varphi}\left(\overline{\varphi},\overline{\underline{\boldsymbol{F}}};\widetilde{\mathcal{B}}\right) = \left\{\varphi^i \in {}^0\Lambda \,|\, \{\varphi,\mathbf{d}(\varphi^i)\} \in \mathscr{L}^2\left(\widetilde{\mathcal{B}}\right), \langle\varphi\rangle_{\widetilde{\mathcal{B}}} = \overline{\varphi}, \langle\mathbf{d}\varphi^i\rangle_{\widetilde{\mathcal{B}}} = \overline{F}^i{}_I\,\mathbf{d}\widetilde{X}^I\right\} \tag{5.15a}$$

$$\mathscr{W}_{\mathfrak{D}}\left(\overline{\mathfrak{D}};\widetilde{\mathcal{B}}\right) = \left\{\mathfrak{D} \in {}^2\Lambda \,|\, \{\mathfrak{D},\mathbf{d}\mathfrak{D}\} \in \mathscr{L}^2\left(\widetilde{\mathcal{B}}\right), \langle\mathfrak{D}\rangle_{\widetilde{\mathcal{B}}} = \overline{\mathfrak{D}}\right\} \tag{5.15b}$$

$$\mathscr{W}_{\mathfrak{A}}\left(\overline{\mathfrak{A}},\overline{\mathfrak{B}};\widetilde{\mathcal{B}}\right) = \left\{\mathfrak{A} \in {}^1\Lambda \,|\, \{\mathfrak{A},\mathbf{d}\mathfrak{A}\} \in \mathscr{L}^2\left(\widetilde{\mathcal{B}}\right), \langle\mathfrak{A}\rangle_{\widetilde{\mathcal{B}}} = \overline{\mathfrak{A}}, \langle\mathbf{d}\mathfrak{A}\rangle_{\widetilde{\mathcal{B}}} = \overline{\mathfrak{B}}\right\} \tag{5.15c}$$

$$\mathscr{W}_{\phi}\left(\overline{\phi};\widetilde{\mathcal{B}}\right) = \left\{\phi \in {}^0\Lambda \,|\, \phi \in \mathscr{L}^2\left(\widetilde{\mathcal{B}}\right), \langle\phi\rangle_{\widetilde{\mathcal{B}}} = \overline{\phi}\right\}. \tag{5.15d}$$

5.3.2. Stationary conditions and effective energy density

We now investigate the stationary conditions of (5.13), which essentially says that at a stationary point the quantity $\langle \Psi_0 - \phi(\mathbf{d}\mathfrak{D})\rangle_{\widetilde{\mathcal{B}}}$ is to first-order independent of microscopic fluctuations. Below we use "δ" to denote "full" variations in terms of macro- and microscopic fields and $\tilde{\delta}$ as well as $\overline{\delta}$ to refer to variations of the respective contribution such that $\delta = \tilde{\delta} + \overline{\delta}$. We begin with the full variations

$$
\begin{aligned}
\delta\langle \Psi_0 - \phi\,\mathbf{d}\mathfrak{D}\rangle_{\widetilde{\mathcal{B}}} = \\
&\Big\langle \underline{\mathfrak{P}}(\delta\underline{\boldsymbol{F}}) + \mathfrak{E}\wedge\delta\mathfrak{D} + \mathfrak{H}\wedge\mathbf{d}(\delta\mathfrak{A}) - \delta\phi\,\mathbf{d}\mathfrak{D} - \phi\,\mathbf{d}(\delta\mathfrak{D})\Big\rangle_{\widetilde{\mathcal{B}}} = \\
&\Big\langle \underline{\mathfrak{P}}(\tilde{\delta}\underline{\boldsymbol{F}}) + \mathfrak{E}\wedge\tilde{\delta}\mathfrak{D} + \mathfrak{H}\wedge\tilde{\delta}\mathfrak{B} - \tilde{\delta}\phi\,\mathbf{d}\mathfrak{D} - \phi\,\mathbf{d}(\tilde{\delta}\mathfrak{D})\Big\rangle_{\widetilde{\mathcal{B}}} \\
&\quad + \Big\langle \underline{\mathfrak{P}}\Big\rangle_{\widetilde{\mathcal{B}}}(\overline{\delta}\underline{\boldsymbol{F}}) + \langle\mathfrak{E}\rangle_{\widetilde{\mathcal{B}}}\wedge\overline{\delta}\mathfrak{D} + \langle\mathfrak{H}\rangle_{\widetilde{\mathcal{B}}}\wedge\overline{\delta}\mathfrak{B} - \overline{\delta}\phi\,\langle\mathbf{d}\mathfrak{D}\rangle_{\widetilde{\mathcal{B}}} - \langle\phi\rangle_{\widetilde{\mathcal{B}}}\mathbf{d}(\overline{\delta}\mathfrak{D}) = \\
&\Big\langle \underline{\mathfrak{P}}(\delta\widetilde{\boldsymbol{F}}) + \mathfrak{E}\wedge\delta\widetilde{\mathfrak{D}} + \mathfrak{H}\wedge\delta\widetilde{\mathfrak{B}} - \delta\widetilde{\phi}\,\mathbf{d}\mathfrak{D} - \phi\,\mathbf{d}(\delta\widetilde{\mathfrak{D}})\Big\rangle_{\widetilde{\mathcal{B}}} \\
&\quad + \Big\langle \underline{\mathfrak{P}}\Big\rangle_{\widetilde{\mathcal{B}}}(\delta\overline{\boldsymbol{F}}) + \langle\mathfrak{E}\rangle_{\widetilde{\mathcal{B}}}\wedge\delta\overline{\mathfrak{D}} + \langle\mathfrak{H}\rangle_{\widetilde{\mathcal{B}}}\wedge\delta\overline{\mathfrak{B}} - \delta\overline{\phi}\,\langle\mathbf{d}\mathfrak{D}\rangle_{\widetilde{\mathcal{B}}} - \overline{\phi}\,\underbrace{\mathbf{d}(\delta\overline{\mathfrak{D}})}_{\equiv 0}.
\end{aligned}
\tag{5.16}
$$

Now, at a *stationary* point of (5.13) we have

$$
\tilde{\delta}\langle \Psi_0 - \phi\,\mathbf{d}\mathfrak{D}\rangle_{\widetilde{\mathcal{B}}} = \Big\langle \underline{\mathfrak{P}}(\delta\widetilde{\boldsymbol{F}}) + \mathfrak{E}\wedge\delta\widetilde{\mathfrak{D}} + \mathfrak{H}\wedge\delta\widetilde{\mathfrak{B}} - \delta\widetilde{\phi}\,\mathbf{d}\mathfrak{D} - \phi\,\mathbf{d}(\delta\widetilde{\mathfrak{D}})\Big\rangle_{\widetilde{\mathcal{B}}} = 0 \tag{5.17}
$$

such that (5.16) reduces to the generalized Hill-Mandel condition

$$
\delta\langle \Psi_0 - \phi\,\mathbf{d}\mathfrak{D}\rangle_{\widetilde{\mathcal{B}}} = \Big\langle \underline{\mathfrak{P}}\Big\rangle_{\widetilde{\mathcal{B}}}(\delta\overline{\boldsymbol{F}}) + \langle\mathfrak{E}\rangle_{\widetilde{\mathcal{B}}}\wedge\delta\overline{\mathfrak{D}} + \langle\mathfrak{H}\rangle_{\widetilde{\mathcal{B}}}\wedge\delta\overline{\mathfrak{B}} - \delta\overline{\phi}\,\langle\mathbf{d}\mathfrak{D}\rangle_{\widetilde{\mathcal{B}}}. \tag{5.18}
$$

Because of (5.14b) and $\delta\widetilde{\phi}\,\mathbf{d}\mathfrak{D} = 0$ as required from (5.17), the term $\langle\mathbf{d}\mathfrak{D}\rangle_{\widetilde{\mathcal{B}}}$ vanishes. Thus, there is no use for a $\overline{\phi}$ with the character of a macroscopic Lagrange multiplier at the microscale such we can drop them to obtain a reduced Hill-Mandel condition

$$
\delta\langle \Psi_0\rangle_{\widetilde{\mathcal{B}}} = \Big\langle \underline{\mathfrak{P}}\Big\rangle_{\widetilde{\mathcal{B}}}(\delta\overline{\boldsymbol{F}}) + \langle\mathfrak{E}\rangle_{\widetilde{\mathcal{B}}}\wedge\delta\overline{\mathfrak{D}} + \langle\mathfrak{H}\rangle_{\widetilde{\mathcal{B}}}\wedge\delta\overline{\mathfrak{B}}. \tag{5.19}
$$

In accordance with the identification of averages with macroscopic or effective quantities we shall define

$$
\overline{\underline{\mathfrak{P}}} := \Big\langle \underline{\mathfrak{P}}(\hat{\underline{\boldsymbol{F}}}, \hat{\mathfrak{D}}, \hat{\mathfrak{B}})\Big\rangle_{\widetilde{\mathcal{B}}} \qquad \overline{\mathfrak{E}} := \Big\langle \mathfrak{E}(\hat{\underline{\boldsymbol{F}}}, \hat{\mathfrak{D}}, \hat{\mathfrak{B}})\Big\rangle_{\widetilde{\mathcal{B}}} \qquad \overline{\mathfrak{H}} := \Big\langle \mathfrak{H}(\hat{\underline{\boldsymbol{F}}}, \hat{\mathfrak{D}}, \hat{\mathfrak{B}})\Big\rangle_{\widetilde{\mathcal{B}}} \tag{5.20}
$$

at and only at a solution $\{\hat{\varphi}, \hat{\mathfrak{D}}, \hat{\mathfrak{A}}, \hat{\phi}\}\big|_{\widetilde{\mathcal{B}}}$ of (5.13). In the same spirit, we define the effective energy density to be

$$
\overline{\Psi}_0(\overline{\underline{\boldsymbol{F}}}, \overline{\mathfrak{D}}, \overline{\mathfrak{B}}) := \Big\langle \Psi_0(\hat{\underline{\boldsymbol{F}}}, \hat{\mathfrak{D}}, \hat{\mathfrak{B}})\Big\rangle_{\widetilde{\mathcal{B}}} \tag{5.21}
$$

exclusively at a solution state of the microscopic BVP. Then we can also write

$$\overline{P}_{i\underline{JK}} = \frac{\partial\overline{\Psi}_0}{\partial\overline{F}^i_{\ I}}\epsilon_{IJK} \qquad \overline{E}_I = \frac{\partial\overline{\Psi}_0}{\partial\overline{D}_{\underline{JK}}}\epsilon_{IJK} \qquad \overline{H}_I = \frac{\partial\overline{\Psi}_0}{\partial\overline{B}_{\underline{JK}}}\epsilon_{IJK} \tag{5.22}$$

resembling the constitutive relations contained in (4.234) but with all metrics replaced with the Euclidean ones, which we have omitted.

Remark 5.2. The potentials $\overline{\varphi}$ and $\overline{\mathfrak{A}}$ do not appear at all in (5.18); only $\underline{\overline{\boldsymbol{F}}}$ and $\overline{\mathfrak{B}}$ do so such that both of $\overline{\varphi}$ and $\overline{\mathfrak{A}}$ can also be set to zero. Of course, the actual values of $\overline{\phi}$, $\overline{\varphi}$ and $\overline{\mathfrak{A}}$ play a role on the macroscopic scale but they do not affect the solution of (5.13).

Remark 5.3. We regard the generalized Hill-Mandel statement (5.19) as the implicit definition of the effective quantities work-conjugate to the macroscopic inputs. From this point of view there is no need to define the effective duals beforehand and there is also no need to ask whether their volume integrals coincide with some boundary integrals. For example, we see from the boundary-integral definition of $\underline{\overline{\mathfrak{P}}}$ or $\underline{\overline{\boldsymbol{P}}}$, respectively, that the required continuity is that (in classical notation) $\underline{\boldsymbol{P}}\cdot\boldsymbol{N}$ is continuous; see for example (Keip et al., 2014; Miehe et al., 2016). This is of course always the case in the absence of tractions within $\widetilde{\mathcal{B}}[\overline{X}]$, which was one of the essential assumptions in the derivation. If we wanted to allow for internal tractions or also body forces, we would have to revisit the whole derivation.

5.3.3. Boundary conditions for the microscopic BVP

The definition of spaces (5.15) for the restrictions of the primary fields to $\widetilde{\mathcal{B}}$ already contain constraints on averages. However, these do not make up the full set of boundary conditions. To gain insight, we manipulate (5.17)

$$\begin{aligned}
&\left\langle \underline{\mathfrak{P}}(\delta\underline{\widetilde{\boldsymbol{F}}}) + \mathfrak{E}\wedge\delta\widetilde{\mathfrak{D}} + \mathfrak{H}\wedge\delta\widetilde{\mathfrak{B}} - \delta\widetilde{\phi}\,\mathbf{d}\mathfrak{D} - \phi\,\mathbf{d}(\delta\widetilde{\mathfrak{D}})\right\rangle_{\widetilde{\mathcal{B}}} = \\
&\left\langle -\mathbb{i}_{\delta\widetilde{\varphi}}\,\mathbb{d}\underline{\mathfrak{P}} + (\mathfrak{E}+\mathbf{d}\phi)\wedge\delta\widetilde{\mathfrak{D}} + \mathbf{d}\mathfrak{H}\wedge\delta\widetilde{\mathfrak{A}} - \delta\widetilde{\phi}\,\mathbf{d}\mathfrak{D}\right\rangle_{\widetilde{\mathcal{B}}} \\
&\quad + \frac{1}{|\widetilde{\mathcal{B}}|}\int_{\partial\widetilde{\mathcal{B}}}\left(\mathbb{i}_{\delta\widetilde{\varphi}}\underline{\mathfrak{P}} - \phi\delta\widetilde{\mathfrak{D}} - \mathfrak{H}\wedge\delta\widetilde{\mathfrak{A}}\right) = 0
\end{aligned} \tag{5.23}$$

wherein we recognize the weak forms of the governing equations in $\widetilde{\mathcal{B}}$ as well as boundary terms. Since we actually solve (5.23) by some method, the integrals over $\widetilde{\mathcal{B}}$ and $\partial\widetilde{\mathcal{B}}$ are going to vanish. The question is thus whether we have enough boundary conditions to end up with a non-singular system and what the solution will look like. Let us first discuss the case of constraints on the averages of the primary fields (and their fluctuations) only. These are already formulated in (5.14). In this case, vanishing boundary

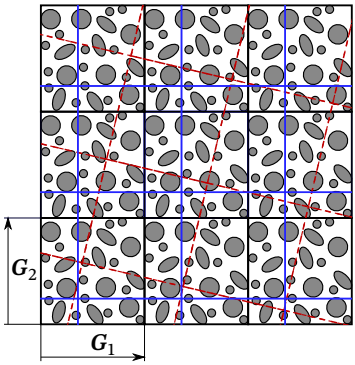

Figure 5.3: A grid of smallest possible ("unit"-)cells for a material with periodic microstructure. The grid vectors could also represent the blue grid which is just a translated version of the original (black) one. The red grid, however, is not equivalent to the other two and also does not conform to the periodicity of the microstructure.

integrals require (Keip et al., 2014)

$$\underline{\mathfrak{P}}\big|_{\partial\widetilde{\mathcal{B}}} = \overline{\underline{\mathfrak{P}}}\big|_{\partial\widetilde{\mathcal{B}}} \qquad \phi|_{\partial\widetilde{\mathcal{B}}} = \overline{\phi}\big|_{\partial\widetilde{\mathcal{B}}} = 0 \qquad \mathfrak{H}|_{\partial\widetilde{\mathcal{B}}} = \overline{\mathfrak{H}}\big|_{\partial\widetilde{\mathcal{B}}} \tag{5.24}$$

or in classical notation

$$\underline{\boldsymbol{P}} \cdot \boldsymbol{N}\big|_{\partial\widetilde{\mathcal{B}}} = \overline{\underline{\boldsymbol{P}}} \cdot \boldsymbol{N}\big|_{\partial\widetilde{\mathcal{B}}} \qquad \phi|_{\partial\widetilde{\mathcal{B}}} = \overline{\phi}\big|_{\partial\widetilde{\mathcal{B}}} = 0 \qquad \boldsymbol{H}\times\boldsymbol{N}|_{\partial\widetilde{\mathcal{B}}} = \overline{\boldsymbol{H}}\times\boldsymbol{N}\big|_{\partial\widetilde{\mathcal{B}}}\,. \tag{5.25}$$

These are just constant natural (Neumann) boundary conditions[4] which reduce to the respective homogeneous natural boundary conditions for the fluctuations.

By contrast, when we require the restrictions of fluctuations and hence also of their variations to vanish on the boundary, i.e. homogeneous essential (Dirichlet) boundary conditions, the boundary integral vanishes identically irrespective of $\underline{\mathfrak{P}}$, ϕ and $\mathfrak{H}$.

A third option is to require periodic fluctuations. With vectors $\boldsymbol{G}_i$ $(i = \{1, \dots, dim\})$ describing the desired periodicity as depicted in Figure 5.3 we write

$$\widetilde{\varphi}(\widetilde{\boldsymbol{X}}) = \widetilde{\varphi}(\widetilde{\boldsymbol{X}} + \boldsymbol{G}_i) \qquad \widetilde{\mathfrak{D}}(\widetilde{\boldsymbol{X}}) = \widetilde{\mathfrak{D}}(\widetilde{\boldsymbol{X}} + \boldsymbol{G}_i) \qquad \widetilde{\mathfrak{A}}(\widetilde{\boldsymbol{X}}) = \widetilde{\mathfrak{A}}(\widetilde{\boldsymbol{X}} + \boldsymbol{G}_i). \tag{5.26}$$

This goes beyond the notion of *boundary* conditions because periodicity is not restricted to boundaries. Supposed the microstructure really has the given periodicity, it rather implies that it does not matter where the boundary actually is. By that, it automatically reflects a fundamental idea in first order homogenization: it does not really matter whether we look at region centered at $\overline{X}$ or a region of same dimensions but translated by some $\widetilde{\boldsymbol{X}}$. This feature clearly distinguishes the requirements (5.26) from homogeneous natural and essential boundary conditions. Thinking in terms of finite elements,

[4] Recall that the restrictions to the boundary encode the appropriate pull-backs (see Section 4.1.7.6).

(5.26) is implemented via boundary conditions

$$\widetilde{\varphi}|_{\partial\widetilde{\mathcal{B}}} = \widetilde{\varphi}|_{\partial\widetilde{\mathcal{B}}+\boldsymbol{G}_i} \qquad \widetilde{\mathfrak{D}}|_{\partial\widetilde{\mathcal{B}}} = \widetilde{\mathfrak{D}}|_{\partial\widetilde{\mathcal{B}}+\boldsymbol{G}_i} \qquad \widetilde{\mathfrak{A}}|_{\partial\widetilde{\mathcal{B}}} = \widetilde{\mathfrak{A}}|_{\partial\widetilde{\mathcal{B}}+\boldsymbol{G}_i} \tag{5.27}$$

but this is not the case for all methods. For example, Fourier-based schemes feature basis functions that are periodic by construction. For the dual quantities in the boundary integral in (5.23) we obtain at a solution

$$\underline{\mathfrak{P}}\big|_{\partial\widetilde{\mathcal{B}}} = \underline{\mathfrak{P}}\big|_{\partial\widetilde{\mathcal{B}}+\boldsymbol{G}_i} \qquad \phi|_{\partial\widetilde{\mathcal{B}}} = \phi|_{\partial\widetilde{\mathcal{B}}+\boldsymbol{G}_i} \qquad \mathfrak{H}|_{\partial\widetilde{\mathcal{B}}} = \mathfrak{H}|_{\partial\widetilde{\mathcal{B}}+\boldsymbol{G}_i}. \tag{5.28}$$

We point out that by $\partial\widetilde{\mathcal{B}} + \boldsymbol{G}_i$ we mean the "shift" of $\partial\widetilde{\mathcal{B}}$ by $\boldsymbol{G}_i$. If we rather regard $\boldsymbol{G}_i$ to link two *opposite* portions of the boundary $\partial_i\widetilde{\mathcal{B}}^+$ and $\partial_i\widetilde{\mathcal{B}}^-$, respectively and their orientations are determined by the outward pointing normals, the above becomes

$$\underline{\mathfrak{P}}\big|_{\partial_i\widetilde{\mathcal{B}}^+} = -\underline{\mathfrak{P}}\big|_{\partial_i\widetilde{\mathcal{B}}^-} \qquad \phi|_{\partial_i\widetilde{\mathcal{B}}^+} = \phi|_{\partial_i\widetilde{\mathcal{B}}^-} \qquad \mathfrak{H}|_{\partial_i\widetilde{\mathcal{B}}^+} = -\mathfrak{H}|_{\partial_i\widetilde{\mathcal{B}}^-} \tag{5.29}$$

which reads in classical notation as

$$\underline{\boldsymbol{P}}\cdot\boldsymbol{N}\big|_{\partial_i\widetilde{\mathcal{B}}^+} = -\underline{\boldsymbol{P}}\cdot\boldsymbol{N}\big|_{\partial_i\widetilde{\mathcal{B}}^-} \qquad \phi|_{\partial_i\widetilde{\mathcal{B}}^+} = \phi|_{\partial_i\widetilde{\mathcal{B}}^-} \qquad \boldsymbol{H}\times\boldsymbol{N}\big|_{\partial_i\widetilde{\mathcal{B}}^+} = -\boldsymbol{H}\times\boldsymbol{N}\big|_{\partial_i\widetilde{\mathcal{B}}^-}. \tag{5.30}$$

However, we note that this anti-periodicity of *restrictions* to the boundary is connected to the orientation of the boundary. The dual quantities themselves, indeed, feature periodic fluctuations. Moreover, (5.28) or (5.29), respectively, are the *outcome* of the microscopic boundary value problem with periodicity of primary fields (5.26).

Concerning uniqueness we state the following: The averaging constraints on φ (5.15a) and ϕ (5.15d) are sufficient to uniquely determine their fluctuations, i.e. remove "rigid-body modes". Depending on the discretization technique, these constraints can be implemented more conveniently via classical essential boundary conditions. Also the free charge potential $\mathfrak{D}$ is fully determined by (5.15b) and the conditions discussed above. The magnetic potential $\mathfrak{A}$, however, may still need[5] gauge fixing in three-dimensional problems (Semenov et al., 2006; Miehe et al., 2016). A common choice is the Coulomb gauge $\operatorname{Div}\boldsymbol{A} = 0$ or, in terms of exterior calculus[6], $\star\,\mathbf{d}(\star\,\mathfrak{A}) = 0$, respectively. Since the problems under considerations are nonlinear, uniqueness in the sense of fully determined potentials does not translate to uniqueness of solutions.

Remark 5.4. Note the special role of ϕ in the above discussion: It represents a Lagrange multiplier for $\mathbf{d}\mathfrak{D}$ in the variational problem under consideration. Thus, ϕ is not a true primary field and is indeed treated as a dual field when it comes to boundary conditions.

Remark 5.5. We mentioned that periodic conditions are related to invariance with respect to translations of the averaging window $\widetilde{\mathcal{B}}[\overline{X}]$. We note that this only holds if the microstructure is indeed periodic. Invariances with respect to rotations of $\widetilde{\mathcal{B}}[\overline{X}]$ (characterized by $\boldsymbol{G}_i$) are related to material symmetries as mentioned in Section 4.1.8.13.

[5] Depending on the linear solver (Bossavit, 1998a; Biro et al., 1996).
[6] See Frankel (2011, Sections 14.1 and 14.2).

Remark 5.6. The size of $\widetilde{\mathcal{B}}[\overline{X}]$ has a certain influence of the computed homogenized response. In case of homogeneous essential or natural boundary conditions the convergence of the response with respect to $|\widetilde{\mathcal{B}}[\overline{X}]|$ is usually slower than with periodic conditions. In fact, for a truly periodic microstructure periodic conditions may lead to a converged response for the smallest possible $\widetilde{\mathcal{B}}[\overline{X}]$, which we call "unit-cell". However, it is possible that the true response has a periodicity of larger wavelength such that the unit-cell does not provide the converged response. Such changes of wavelength of the microscopic solution are associated with material instabilities as studied by, e.g. Miehe et al. (2002) and Polukhov et al. (2018).

5.3.4. An alternative formulation in terms of tangent map, free-charge potential and magnetic field

As discussed above, the electric potential ϕ in (5.12) plays the role of a Lagrange multiplier enforcing $\mathbf{d}\mathfrak{D} = 0$ whereby its actual effective value is not of interest as long as there is no effective free charge. In this case we may equivalently consider the constraints $\mathbf{d}\mathfrak{D} = 0$ as being part of the specification of the function space for $\mathfrak{D}$. Similarly, in the present scope the actual effective value of φ is not of interest and we may instead directly employ $\underline{\boldsymbol{F}}$ as a primary field under the constraint that it is derived from a tuple-valued function φ_F. Thus we require $\mathbf{d}(F^i_{\ I}\,\mathbf{d}X^I) = 0$. Finally, along the same lines of reasoning we employ $\mathfrak{B}$ as a primary field together with $\mathbf{d}\mathfrak{B} = 0$[7]. This brings us to the variational minimization principle

$$\{\hat{\underline{\boldsymbol{F}}}, \hat{\mathfrak{D}}, \hat{\mathfrak{B}}\}\big|_{\widetilde{\mathcal{B}}} = \arg\left\{\inf_{\underline{\boldsymbol{F}},\mathfrak{D},\mathfrak{A}} \int_{\widetilde{\mathcal{B}}} \Psi_0(\mathbf{C}, \mathfrak{D}, \mathfrak{B})\, dV\right\} \tag{5.31}$$

or, equivalently,

$$\{\hat{\underline{\boldsymbol{F}}}, \hat{\mathfrak{D}}, \hat{\mathfrak{B}}\}\big|_{\widetilde{\mathcal{B}}} = \arg\left\{\inf_{\underline{\boldsymbol{F}},\mathfrak{D},\mathfrak{B}} \langle \Psi_0(\mathbf{C}, \mathfrak{D}, \mathfrak{B})\rangle_{\widetilde{\mathcal{B}}}\right\} \tag{5.32}$$

of which the specification is completed by the set of function spaces

$$\mathscr{W}_{\underline{\boldsymbol{F}}}\left(\overline{\underline{\boldsymbol{F}}}; \widetilde{\mathcal{B}}\right) = \left\{F^i_{\ I}\,\mathbf{d}X^I \in {}^1\Lambda \mid \underline{\boldsymbol{F}} \in \mathscr{L}^2\left(\widetilde{\mathcal{B}}\right), \mathbf{d}(F^i_{\ I}\,\mathbf{d}X^I) = 0, \langle \underline{\boldsymbol{F}}\rangle_{\widetilde{\mathcal{B}}} = \overline{\underline{\boldsymbol{F}}}\right\} \tag{5.33a}$$

$$\mathscr{W}_{\mathfrak{D}}\left(\overline{\mathfrak{D}}; \widetilde{\mathcal{B}}\right) = \left\{\mathfrak{D} \in {}^2\Lambda \mid \mathfrak{D} \in \mathscr{L}^2\left(\widetilde{\mathcal{B}}\right), \mathbf{d}\mathfrak{D} = 0, \langle \mathfrak{D}\rangle_{\widetilde{\mathcal{B}}} = \overline{\mathfrak{D}}\right\} \tag{5.33b}$$

$$\mathscr{W}_{\mathfrak{B}}\left(\overline{\mathfrak{B}}; \widetilde{\mathcal{B}}\right) = \left\{\mathfrak{B} \in {}^2\Lambda \mid \mathfrak{B} \in \mathscr{L}^2\left(\widetilde{\mathcal{B}}\right), \mathbf{d}\mathfrak{B} = 0, \langle \mathfrak{B}\rangle_{\widetilde{\mathcal{B}}} = \overline{\mathfrak{B}}\right\}. \tag{5.33c}$$

The actual implementation of such constraints leads either to linearly-constrained minimization methods or to projection-based Fourier-homogenization solvers (Vondřejc et al., 2014; de Geus et al., 2017; Rambausek et al., 2019). For the latter case we also refer to Chapter 11.

[7] This is more natural than in the case of $\mathfrak{D}$ where $\mathbf{d}\mathfrak{D} = 0$ actually is a restriction on modeling.

5.3.5. Other variational homogenization principles

For completeness, we below summarize the homogenization principles based on the scale-agnostic variational principles given in Sections 4.3.4 to 4.3.6. The spaces given below do contain "modeling" boundary conditions, i.e. periodic or essential boundary conditions. We leave to the user of the principles to choose between natural, essential or periodic boundary conditions as discussed in Section 5.3.3.

In terms of the electromagnetic potential
The homogenization principle corresponding to (4.244) can be obtained along the lines of the original one and is given as

$$\{\hat{\varphi}, \hat{\phi}, \hat{\mathfrak{A}}\}\big|_{\widetilde{\mathcal{B}}} = \arg\left\{ \inf_{\varphi,\mathfrak{A}} \sup_{\phi} \int_{\widetilde{\mathcal{B}}} \widehat{\Psi}_0(\mathbf{C}, \mathfrak{E}, \mathfrak{B})\, dV \right\} \tag{5.34}$$

and spaces for $\{\varphi, \mathfrak{A}, \phi\}|_{\widetilde{\mathcal{B}}}$

$$\mathscr{W}_\varphi\left(\overline{\varphi}, \overline{\underline{F}}; \widetilde{\mathcal{B}}\right) = \left\{\varphi^i \in {}^0\Lambda \,|\, \{\varphi, \mathbf{d}(\varphi^i)\} \in \mathscr{L}^2\left(\widetilde{\mathcal{B}}\right), \langle\varphi\rangle_{\widetilde{\mathcal{B}}} = \overline{\varphi}, \langle \mathbf{d}\varphi^i\rangle_{\widetilde{\mathcal{B}}} = \overline{F}^i_I \mathbf{d}X^I\right\} \tag{5.35a}$$

$$\mathscr{W}_{\mathfrak{A}}\left(\overline{\mathfrak{A}}, \overline{\mathfrak{B}}; \widetilde{\mathcal{B}}\right) = \left\{\mathfrak{A} \in {}^1\Lambda \,|\, \{\mathfrak{A}, \mathbf{d}\mathfrak{A}\} \in \mathscr{L}^2\left(\widetilde{\mathcal{B}}\right), \langle\mathfrak{A}\rangle_{\widetilde{\mathcal{B}}} = \overline{\mathfrak{A}}, \langle \mathbf{d}\mathfrak{A}\rangle_{\widetilde{\mathcal{B}}} = \overline{\mathfrak{B}}\right\} \tag{5.35b}$$

$$\mathscr{W}_\phi\left(\overline{\phi}, \overline{\mathfrak{E}}; \widetilde{\mathcal{B}}\right) = \left\{\phi \in {}^0\Lambda \,|\, \{\phi, \mathbf{d}\phi\} \in \mathscr{L}^2\left(\widetilde{\mathcal{B}}\right), \langle\phi\rangle_{\widetilde{\mathcal{B}}} = \overline{\phi}, \langle \mathbf{d}\phi\rangle_{\widetilde{\mathcal{B}}} = -\overline{\mathfrak{E}}\right\}. \tag{5.35c}$$

Concerning further constraints such as periodicity similar considerations as in Section 5.3.3 apply.

In terms of the electric and magnetic scalar potentials
In this case we have

$$\{\hat{\varphi}, \hat{\phi}, \hat{\phi^{\mathrm{m}}}\}\big|_{\widetilde{\mathcal{B}}} = \arg\left\{ \inf_{\varphi} \sup_{\phi,\phi^{\mathrm{m}}} \int_{\widetilde{\mathcal{B}}} \widehat{\widehat{\Psi}}_0(\mathbf{C}, \mathfrak{E}, \mathfrak{H})\, dV \right\} \tag{5.36}$$

with the same protoype spaces for each component φ^i as well as ϕ and ϕ^{m}

$$\mathscr{W}_f\left(\overline{f}, \mathbf{d}\overline{f}; \widetilde{\mathcal{B}}\right) = \left\{f \in {}^0\Lambda \,|\, \{f, \mathbf{d}(f)\} \in \mathscr{L}^2\left(\widetilde{\mathcal{B}}\right), \langle f\rangle_{\widetilde{\mathcal{B}}} = \overline{f}, \langle \mathbf{d}f\rangle_{\widetilde{\mathcal{B}}} = (\mathbf{d}\overline{f})_I \mathbf{d}X^I\right\} \tag{5.37a}$$

such that

$$\varphi^i\big|_{\widetilde{\mathcal{B}}} \in \mathscr{W}_f(\overline{\varphi}^i, \overline{F}^i_I\, \mathbf{d}X^i) \qquad \phi|_{\widetilde{\mathcal{B}}} \in \mathscr{W}_f(\overline{\phi}, -\overline{\mathfrak{E}}) \qquad \phi^{\mathrm{m}}|_{\widetilde{\mathcal{B}}} \in \mathscr{W}_f(\overline{\phi^{\mathrm{m}}}, -\overline{\mathfrak{H}}). \tag{5.37b}$$

In terms of $\mathfrak{D}$, $\mathfrak{B}$ and scalar potentials
The homogenization principle is obtained by treating the magnetic and the electric parts in the same way as in (5.12), i.e.

$$\{\hat{\varphi}, \hat{\mathfrak{D}}, \hat{\mathfrak{B}}, \hat{\phi}, \hat{\phi^{\mathrm{m}}}\}\big|_{\widetilde{\mathcal{B}}} = \arg\left\{ \inf_{\varphi,\mathfrak{D},\mathfrak{B}} \sup_{\phi,\phi^{\mathrm{m}}} \int_{\widetilde{\mathcal{B}}} \Psi_0(\mathbf{C}, \mathfrak{D}, \mathfrak{B})\, dV \right\} \tag{5.38}$$

where the spaces for $\{\varphi, \mathfrak{D}, \mathfrak{B}, \phi, \phi^{\mathrm{m}}\}|_{\widetilde{\mathcal{B}}}$ are given as

$$\mathscr{W}_{\varphi}\left(\overline{\varphi}, \underline{\overline{\boldsymbol{F}}}; \widetilde{\mathcal{B}}\right) = \left\{\varphi^i \in {}^0\Lambda \mid \{\varphi, \mathbf{d}(\varphi^i)\} \in \mathscr{L}^2\left(\widetilde{\mathcal{B}}\right), \langle\varphi\rangle_{\widetilde{\mathcal{B}}} = \overline{\varphi}, \left\langle \mathbf{d}\varphi^i \right\rangle_{\widetilde{\mathcal{B}}} = \overline{F}^i{}_I \, \mathbf{d}\widetilde{X}^I\right\} \tag{5.39a}$$

$$\mathscr{W}_{\mathfrak{W}}\left(\overline{\mathfrak{W}}; \widetilde{\mathcal{B}}\right) = \left\{\mathfrak{W} \in {}^2\Lambda \mid \{\mathfrak{W}, \mathbf{d}\mathfrak{W}\} \in \mathscr{L}^2\left(\widetilde{\mathcal{B}}\right), \langle\mathfrak{W}\rangle_{\widetilde{\mathcal{B}}} = \overline{\mathfrak{W}}\right\} \tag{5.39b}$$

$$\mathscr{W}_{\chi}\left(\overline{\chi}; \widetilde{\mathcal{B}}\right) = \left\{\phi \in {}^0\Lambda \mid \phi \in \mathscr{L}^2\left(\widetilde{\mathcal{B}}\right), \langle\chi\rangle_{\widetilde{\mathcal{B}}} = \overline{\chi}\right\} \tag{5.39c}$$

and $\mathfrak{D} \in \mathscr{W}_{\mathfrak{W}}\left(\overline{\mathfrak{D}}; \widetilde{\mathcal{B}}\right)$, $\phi \in \mathscr{W}_{\chi}\left(\overline{\phi}; \widetilde{\mathcal{B}}\right)$, $\mathfrak{B} \in \mathscr{W}_{\mathfrak{W}}\left(\overline{\mathfrak{B}}; \widetilde{\mathcal{B}}\right)$ and $\phi^{\mathrm{m}} \in \mathscr{W}_{\chi}\left(\overline{\phi^{\mathrm{m}}}; \widetilde{\mathcal{B}}\right)$.

In terms of electric and magnetic vector potentials $\mathfrak{A}^{\mathrm{e}}$ and $\mathfrak{A}$
Finally, the principle resulting from (4.253) is given as

$$\{\hat{\varphi}, \hat{\mathfrak{A}}^{\mathrm{e}}, \hat{\mathfrak{A}}\} = \arg\left\{\inf_{\varphi, \mathfrak{A}^{\mathrm{e}}, \mathfrak{A}} \int_{\Omega} \Psi_0(\mathbf{C}, \mathfrak{D}, \mathfrak{B})\, dV\right\} \tag{5.40}$$

with spaces for $\{\varphi, \mathfrak{A}\mathrm{e}, \mathfrak{A}\}|_{\widetilde{\mathcal{B}}}$

$$\mathscr{W}_{\varphi}\left(\overline{\varphi}, \underline{\overline{\boldsymbol{F}}}; \widetilde{\mathcal{B}}\right) = \left\{\varphi^i \in {}^0\Lambda \mid \{\varphi, \mathbf{d}(\varphi^i)\} \in \mathscr{L}^2\left(\widetilde{\mathcal{B}}\right), \langle\varphi\rangle_{\widetilde{\mathcal{B}}} = \overline{\varphi}, \left\langle \mathbf{d}\varphi^i \right\rangle_{\widetilde{\mathcal{B}}} = \overline{F}^i{}_I \, \mathbf{d}\widetilde{X}^I\right\} \tag{5.41a}$$

$$\mathscr{W}_{\mathfrak{W}}\left(\overline{\mathfrak{W}}, \overline{\mathbf{d}\mathfrak{W}}; \widetilde{\mathcal{B}}\right) = \left\{\mathfrak{W} \in {}^1\Lambda \mid \{\mathfrak{W}, \mathbf{d}\mathfrak{W}\} \in \mathscr{L}^2\left(\widetilde{\mathcal{B}}\right), \langle\mathfrak{W}\rangle_{\widetilde{\mathcal{B}}} = \overline{\mathfrak{W}}, \langle\mathbf{d}\mathfrak{W}\rangle_{\widetilde{\mathcal{B}}} = \overline{\mathbf{d}\mathfrak{W}}\right\} \tag{5.41b}$$

where $\mathfrak{A}^{\mathrm{e}} \in \mathscr{W}_{\mathfrak{W}}\left(\overline{\mathfrak{A}}^{\mathrm{e}}, \overline{\mathfrak{D}}; \widetilde{\mathcal{B}}\right)$ and $\mathfrak{A} \in \mathscr{W}_{\mathfrak{W}}\left(\overline{\mathfrak{A}}, \overline{\mathfrak{B}}; \widetilde{\mathcal{B}}\right)$.

5.4. A computation strategy for two-scale problems

Having described the solution of the microscopic BVP we naturally come to the question of what to do on the macroscopic scale. This requires knowledge of the material response in terms of effective constitutive "duals" such as $\underline{\overline{\mathfrak{P}}}$. Moreover, in most cases (depending on the problem and the solver on the macroscopic scale) one also requires the sensitivities of the effective duals with respect to the macroscopic inputs to the micro-BVP.

5.4.1. Linearization of the microscopic stationary conditions

Suppose one has to solve a macroscopic boundary value problem where the material response is obtained through homogenization. In Section 5.3.2 we presented expressions for the effective constitutive quantities $(\{\underline{\overline{\mathfrak{P}}}, \overline{\mathfrak{E}}, \overline{\mathfrak{H}}\})$ dual to the macroscopic inputs $(\{\underline{\overline{\boldsymbol{F}}}, \overline{\mathfrak{D}}, \overline{\mathfrak{B}}\})$ in (5.20) and (5.22) as well as for the effective energy density $\overline{\Psi}_0(\underline{\overline{\boldsymbol{F}}}, \overline{\mathfrak{D}}, \overline{\mathfrak{B}})$ (5.21). Of similar interest are the effective moduli, i.e. the sensitivities of the duals with respect to the macroscopic inputs, e.g., for nonlinear solvers or simply as mate-

rial data. Consider for example the sensitivities of $\overline{P}_{i\underline{JK}} = \left\langle P_{i\underline{JK}}(\hat{\underline{F}}, \hat{\mathfrak{D}}, \hat{\mathfrak{B}}) \right\rangle_{\tilde{\mathcal{B}}}$ which can be expressed as

$$\frac{\Delta \overline{P}_{i\underline{JK}}}{\Delta \overline{F}^{j}{}_{L}} = \frac{\partial \overline{P}_{i\underline{JK}}}{\partial \hat{F}^{k}{}_{M}} \frac{\Delta \hat{F}^{k}{}_{M}}{\Delta \overline{F}^{j}{}_{L}} + \frac{\partial \overline{P}_{i\underline{JK}}}{\partial \hat{D}_{\underline{MN}}} \frac{\Delta \hat{D}_{\underline{MN}}}{\Delta \overline{F}^{j}{}_{L}} + \frac{\partial \overline{P}_{i\underline{JK}}}{\partial \hat{B}_{\underline{MN}}} \frac{\Delta \hat{B}_{\underline{MN}}}{\Delta \overline{F}^{j}{}_{L}}. \tag{5.42}$$

We explicitly write Δ instead of ∂ where more than simple partial derivatives are involved. Then, we have

$$\frac{\partial \hat{F}^{k}{}_{M}}{\partial \overline{F}^{j}{}_{L}} = \frac{\partial \overline{F}^{k}{}_{M}}{\partial \overline{F}^{j}{}_{L}} = \delta^{k}{}_{j}\delta^{M}{}_{L} \qquad \frac{\partial \hat{D}_{\underline{MN}}}{\partial \overline{F}^{j}{}_{L}} = 0 \qquad \frac{\partial \hat{B}_{\underline{MN}}}{\partial \overline{F}^{j}{}_{L}} = 0. \tag{5.43}$$

However, the fluctuation parts $\{\hat{\underline{F}}, \hat{\mathfrak{D}}, \hat{\mathfrak{B}}\}$ of the solutions $\{\hat{\underline{F}}, \hat{\mathfrak{D}}, \hat{\mathfrak{B}}\}$ also depend on $\overline{F}^{j}{}_{L}$ via the homogenization principle. Let us for a more compact notation introduce the generalized state $\mathrm{Y} = \{\varphi, \mathfrak{D}, \mathfrak{A}, \phi\}$ and the corresponding fluctuations $\widetilde{\mathrm{Y}}$. The non-trivial macroscopic parameters are collected by $\overline{\mathrm{M}} = \{\overline{\underline{F}}, \overline{\mathfrak{D}}, \overline{\mathfrak{B}}\}$. Then, when meaning fluctuations $\hat{\widetilde{\mathrm{Y}}}$ of a solution state $\hat{\mathrm{Y}}$ for given $\overline{\mathrm{M}}$ we shall write explicitly $\hat{\widetilde{\mathrm{Y}}} = \hat{\widetilde{\mathrm{Y}}}(\overline{\mathrm{M}})$. We recall that $\hat{\mathrm{Y}}$ is the solution of (5.17) or of an equivalent equation for other homogenization principles. Thus, we can employ the linearization of such a stationary condition to establish an implicit relation between increments in $\Delta\widetilde{\mathrm{Y}}$ and $\Delta\overline{\mathrm{M}}$. In fact, in the linearized setting we shall consider both of $\hat{\widetilde{\mathrm{Y}}}$ and $\overline{\mathrm{M}}$ as given and fixed. Also note that $\Delta\widetilde{\mathrm{Y}}$ is considered independent of $\Delta\overline{\mathrm{M}}$. With that we obtain the equation (which is not an identity)

$$\begin{aligned}\Delta\tilde{\delta}\left\langle \Psi_0 - \phi\,\mathbf{d}\mathfrak{D}\right\rangle_{\tilde{\mathcal{B}}} &= \widetilde{\Delta}\tilde{\delta}\left\langle \Psi_0 - \phi\,\mathbf{d}\mathfrak{D}\right\rangle_{\tilde{\mathcal{B}}} + \overline{\Delta}\tilde{\delta}\left\langle \Psi_0 - \phi\,\mathbf{d}\mathfrak{D}\right\rangle_{\tilde{\mathcal{B}}} \\ &= \underbrace{\frac{\Delta\tilde{\delta}\left\langle \Psi_0 - \phi\,\mathbf{d}\mathfrak{D}\right\rangle_{\tilde{\mathcal{B}}}}{\Delta\widetilde{\mathrm{Y}}_\alpha}\Delta\widetilde{\mathrm{Y}}_\alpha}_{\widetilde{\Delta}} + \underbrace{\frac{\Delta\tilde{\delta}\left\langle \Psi_0 - \phi\,\mathbf{d}\mathfrak{D}\right\rangle_{\tilde{\mathcal{B}}}}{\Delta\overline{\mathrm{M}}_\beta}\Delta\overline{\mathrm{M}}_\beta}_{\overline{\Delta}} = 0\end{aligned} \tag{5.44}$$

where $\widetilde{\Delta}$ and $\overline{\Delta}$ are analogous to $\tilde{\delta}$ and $\overline{\delta}$, respectively. In the equation above the $\Delta\overline{\mathrm{M}}_\beta$ are regarded as arbitrary and can be chosen individually. Then, if we want to fulfill the equation we have to solve for $\Delta\widetilde{\mathrm{Y}}$ (collectively). This solution, which linearly depends on $\Delta\overline{\mathrm{M}}$, is denoted as $\Delta\hat{\widetilde{\mathrm{Y}}} = \Delta\hat{\widetilde{\mathrm{Y}}}(\Delta\overline{\mathrm{M}}) = \mathrm{K}\cdot\Delta\overline{\mathrm{M}}$. Of course, the linear operator K has to be found by some analytical or numerical method. For now we remain in the symbolic (and continuous) setting. Using $\overline{\mathrm{M}}_\gamma = \overline{F}^{j}{}_{L}$ we can finally compute the desired sensitivity (5.42) as

$$\frac{\Delta\overline{P}_{i\underline{JK}}}{\Delta\overline{\mathrm{M}}_\gamma} = \frac{\Delta\left\langle P_{i\underline{JK}}\right\rangle_{\tilde{\mathcal{B}}}}{\Delta\overline{\mathrm{M}}_\gamma} + \frac{\Delta\left\langle P_{i\underline{JK}}\right\rangle_{\tilde{\mathcal{B}}}}{\Delta\widetilde{\mathrm{Y}}_\alpha}\mathrm{K}^{\gamma}_{\alpha}. \tag{5.45}$$

Remark 5.7. We once again stress that the effective dual quantities are not mere averages. They are by definition only functions of the macroscopic parameters which im-

plies constraints on the fluctuations as discussed in Section 5.3.2. They thus do not have any sensitivities with respect to fluctuations. By contrast, the corresponding averages are defined for any state – not only at stationary points. This difference is essential in (5.45).

Let us now be even a bit more abstract to get a better perspective on what is going on. Suppose we are about to find the macroscopic parameters $\overline{\mathrm{M}}$ that correspond to a desired dual state $\overline{\mathrm{P}} = \partial\overline{\Psi}_0(\overline{\mathrm{M}})/\partial\overline{\mathrm{M}}$. Implicitly, we also have to solve for $\hat{\widetilde{\mathrm{Y}}}(\overline{\mathrm{M}})$. The problem can thus be written as

$$\begin{pmatrix} \widetilde{\delta}\,\langle \Psi_0 - \phi\,\mathbf{d}\mathfrak{D}\rangle_{\widetilde{\mathcal{B}}} \\ \overline{\delta}\langle \Psi_0 - \phi\,\mathbf{d}\mathfrak{D}\rangle_{\widetilde{\mathcal{B}}} \end{pmatrix} = \begin{pmatrix} \widetilde{\delta}\,\langle \Psi_0 - \phi\,\mathbf{d}\mathfrak{D}\rangle_{\widetilde{\mathcal{B}}} \\ \overline{\delta}\langle \Psi_0\rangle_{\widetilde{\mathcal{B}}} \end{pmatrix} = \begin{pmatrix} 0 \\ \delta\overline{\mathrm{M}}\cdot\overline{\mathrm{P}} \end{pmatrix}. \tag{5.46}$$

Since this system is nonlinear in general, we need to employ some iterative scheme like Newton's method for its solution. For that we need the linearization of (5.46). At a guess $\{\widetilde{\mathrm{Y}}^{[n]}, \overline{\mathrm{M}}^{[n]}\}$ we have

$$\begin{pmatrix} \widetilde{\delta}\,\langle \Psi_0 - \phi\,\mathbf{d}\mathfrak{D}\rangle_{\widetilde{\mathcal{B}}}\big|^{(n)} \\ \overline{\delta}\,\langle \Psi_0 - \phi\,\mathbf{d}\mathfrak{D}\rangle_{\widetilde{\mathcal{B}}}\big|^{(n)} \end{pmatrix} + \begin{pmatrix} \widetilde{\Delta\delta}\,\langle \Psi_0 - \phi\,\mathbf{d}\mathfrak{D}\rangle_{\widetilde{\mathcal{B}}}\big|^{(n)} & \overline{\Delta\delta}\,\langle \Psi_0 - \phi\,\mathbf{d}\mathfrak{D}\rangle_{\widetilde{\mathcal{B}}}\big|^{(n)} \\ \widetilde{\Delta\delta}\,\langle \Psi_0 - \phi\,\mathbf{d}\mathfrak{D}\rangle_{\widetilde{\mathcal{B}}}\big|^{(n)} & \overline{\Delta\delta}\,\langle \Psi_0 - \phi\,\mathbf{d}\mathfrak{D}\rangle_{\widetilde{\mathcal{B}}}\big|^{(n)} \end{pmatrix} = \begin{pmatrix} 0 \\ \delta\overline{\mathrm{M}}\cdot\overline{\mathrm{P}} \end{pmatrix} \tag{5.47}$$

which we rewrite as

$$\begin{pmatrix} \delta\widetilde{\mathrm{Y}} & \delta\overline{\mathrm{M}} \end{pmatrix}\cdot\begin{pmatrix} \widetilde{\mathrm{R}} \\ \overline{\mathrm{P}} \end{pmatrix}\Big|^{(n)} + \begin{pmatrix} \delta\widetilde{\mathrm{Y}} & \delta\overline{\mathrm{M}} \end{pmatrix}\cdot\begin{pmatrix} \mathrm{A}_{\widetilde{\mathrm{Y}}\widetilde{\mathrm{Y}}} & \mathrm{A}_{\widetilde{\mathrm{Y}}\overline{\mathrm{M}}} \\ \mathrm{A}_{\overline{\mathrm{M}}\widetilde{\mathrm{Y}}} & \mathrm{A}_{\overline{\mathrm{M}}\overline{\mathrm{M}}} \end{pmatrix}\Big|^{(n)}\cdot\begin{pmatrix} \Delta\widetilde{\mathrm{Y}} \\ \Delta\overline{\mathrm{M}} \end{pmatrix}\Big|^{(n)} = \begin{pmatrix} \delta\widetilde{\mathrm{Y}} & \delta\overline{\mathrm{M}} \end{pmatrix}\cdot\begin{pmatrix} 0 \\ \overline{\mathrm{P}} \end{pmatrix} \tag{5.48}$$

and which has to be fulfilled for all admissible $\{\delta\widetilde{\mathrm{Y}}, \delta\overline{\mathrm{M}}\}$. We eliminate $\Delta\widetilde{\mathrm{Y}}^{[n]}$ to obtain a linear system for $\Delta\overline{\mathrm{M}}^{[n]}$

$$\Big[\mathrm{A}_{\overline{\mathrm{M}}\overline{\mathrm{M}}} - \underbrace{\mathrm{A}_{\overline{\mathrm{M}}\widetilde{\mathrm{Y}}}\cdot\left(\mathrm{A}_{\widetilde{\mathrm{Y}}\widetilde{\mathrm{Y}}}\right)^{-1}\cdot\mathrm{A}_{\widetilde{\mathrm{Y}}\overline{\mathrm{M}}}}_{-\mathrm{K}}\Big]\Big|^{(n)}\cdot\Delta\overline{\mathrm{M}}^{[n]} = \overline{\mathrm{P}} - \overline{\mathrm{P}}^{[n]} + \left(\mathrm{A}_{\widetilde{\mathrm{Y}}\widetilde{\mathrm{Y}}}\right)^{-1}\Big|^{(n)}\cdot\widetilde{\mathrm{R}}^{[n]}. \tag{5.49}$$

Obviously, when we solve for stationary points $\hat{\mathrm{Y}}$ before linearization, then $\widetilde{\mathrm{R}}^{[n]}$ vanishes from above. In that case, the operator in square braces represents the linearizations of the effective dual quantities, i.e. the effective (material) *moduli*, and thus also $\Delta\overline{P}_{iJ\underline{K}}/\Delta\overline{\mathrm{M}}_{\gamma}$. In a discrete setting, it is called the Schur complement of the (full) system matrix as in (5.48). We refer to Schröder et al. (2016) for a similar but less abstract description in the scope of magneto-electro-elasticity.

Remark 5.8. Another approach for the determination of effective moduli is adjoint sensitivity analysis where the effective duals are the quantities of interest and the effective inputs $\overline{\mathrm{M}}$ play the role of control variables as pointed out by Larsson and Runesson (2007).

5.4.2. An abstract two-scale solution framework

The probably most prominent instance of two-scale simulation schemes is the so-called FE^2 method (Miehe et al., 1999; Feyel and Chaboche, 2000; Terada and Kikuchi, 2001). This approach has been successfully applied not only to mechanical problems such as finite elasticity, crystal plasticity and fibre-reinforced composites, but also in coupled magneto-electro-mechanics and subsets thereof (Keip et al., 2014; Schröder et al., 2016; Keip et al., 2015; Keip and Rambausek, 2016, 2017). However, the global procedure is not tied to a particular discretization scheme. It is for example perfectly possible to employ an FE discretization for the macroscopic scale and Fourier-based solvers for the microscopic problem under periodic conditions as documented by Rambausek et al. (2019) and also described in Chapter 11. In literature, the FE^2 method is often presented as an algorithm on its own. This may be an appropriate presentation of the respective implementations but over time we abandoned this point of view. Instead, we strive to design homogenization solvers that offer an interface that is identical to conventional material routines. The macroscopic solver shall not know whether the subroutine it calls to compute stresses, the elasticity matrix or some other material response data is a "one-liner" or a full-featured FE software. This in the end also allows for *encapsulation* of the homogenization tool such that it can be used by totally different solvers or packages for the macroscopic BVP. Then the question of the overall algorithm does not arise at all. As a consequence, we will not present an FE^2 (or alike) scheme but instead highlight the independence of macroscopic and microscopic solvers in Figure 5.4. The main task to achieve a true two-scale simulation is then, besides the implementation of a homogenization solver itself, of course the implementation of the interface required by the macroscale solver for the material class[8] under consideration. As indicated on the "material data provider"-side, one could also include reduced-order modeling (ROM) as done by, e.g., Fritzen and Leuschner (2013, 2015); Fritzen and Kunc (2018), solution databases or other data-mining/machine-learning approaches (Temizer and Wriggers, 2007; Le et al., 2015; Klusemann and Ortiz, 2015; Bhattacharjee and Matouš, 2016; Bessa et al., 2017) to accelerate or even largely avoid the costly solution of the homogenization problems.

[8] For example, depending on the solver or software, a plastic material of which the response depends on history could be called differently than elastic materials.

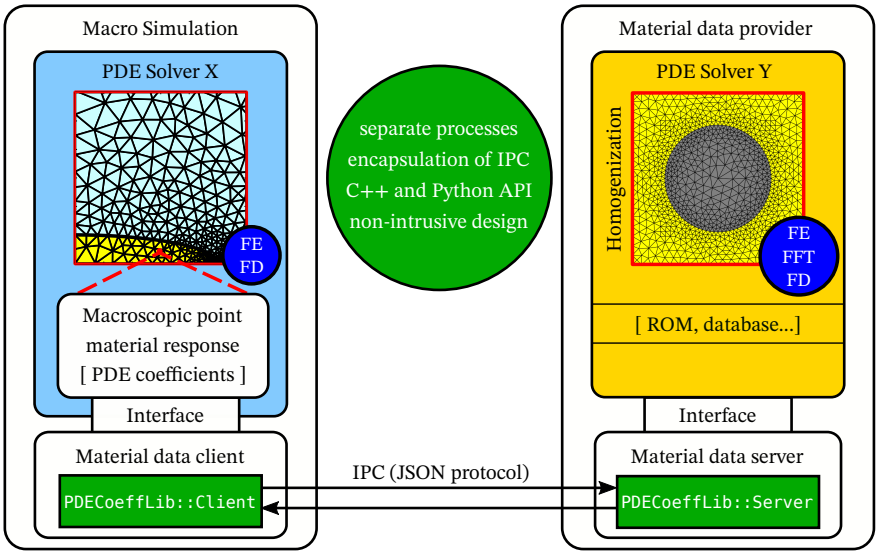

Figure 5.4: Conceptual sketch of a (not-only) two-scale simulation framework. Consider a macroscopic BVP for which "PDE Solver X" is the computation tool of choice. It demands a certain function signature, i.e. an *interface*, to be fulfilled by any material model. Instead of a standard material routine one implements a compact client fulfilling this interface. This client processes the input from the solver and send a request to a server which returns the material response. These messages can be in some generic format like JSON but also an MPI-based implementation could do the job. The client then processes the response of the server an passes it on to "PDE Solver X" in the required format. Through this design the solver on the microscale is completely hidden from the macroscopic one. In our implementation we moved the server part to a separate process to avoid issues arising from global variables as present in almost any solver. As a further consequence, one has sufficient freedom to not only implement two-scale schemes but many variants of sophisticated simulation- and/or data-based material-models. There are certain challenges regarding the management of, e.g., internal state. However, these issues can be solved with limited effort. In a student project (Harsch, 2017b,a), a simplified implementation of this scheme has been successfully adapted to crystal plasticity. The material model was employed in numerical simulations with `FEniCS` (Alnæs et al., 2015), `DUNE` (Blatt et al., 2016) and `FEAP` (Taylor, 2014) for a couple of representative scenarios taken from literature. By that it proved to be a useful ingredient for the comparison of different solvers in challenging real-world problems.

Chapter 6

Conclusion and Outlook

This first part of the thesis revisited the established theory of quasi-static magneto-electro-elasticity starting from notions of energy and power. In that course the commonly used framework of vector and tensor-calculus was given up in favor of an up-to-date differential geometric framework featuring a wider range of objects, most notably differential forms. In fact, it has been and still is one of our main objectives to provide a sound and smooth transition between these two approaches beginning from the governing physical equations down to the appropriate formulations of energy densities and their time rates. The latter aspects are usually not included in texts written by physicists. By taking them into account we hope that the present work appeals in particular to readers coming from (nonlinear) continuum mechanics for which the latter aspects are of great importance. In addition, we carried over the differential-geometric approach to variational homogenization by employing scale separation to justify the the Euclidean setting of the boundary value problems at the microscale.

What remains open are the extension to magneto-electro-elasto-dynamics, the consideration of coupled electromagnetic phenomena and irreversible processes. Another possible extension is to account for higher-order constitutive theories which are certainly of interest given that characteristic sizes of representative volume elements for magnetorheological elastomers can reach almost up to millimeters. Besides that, the above mentioned interpretation of scale separation was sufficient for the present scope, but it might need to be revisited for more general settings. At least we currently do not see how locally Euclidean space from the macroscopic perspective would exclude non-Euclidean structure on smaller scales as long as they are compatible in some average sense.

— Part II —

Computational Characterization of Soft Magneto-Electric Composites Across Scales

Computational Characterization of Soft Magneto-Electric Composites
In this second part the focus is shifted from theory to applications. It begins with Chapter 7 focusing on magneto-mechanical coupling. The matter of study are magnetorheological elastomers, which exhibit rich coupling phenomena through their composite nature. Most of our investigations rely on finite element simulations and computational homogenization. However, we also employ (semi-)analytical models for the interpretation of the observed effects. Chapter 8 puts the analytical tools further to characterize a scale-independent magneto-electric coupling effect. After that, Chapter 9 discusses a constrained-minimization formulation of magneto-electro-elasticity in the absence of free currents, which has some interesting features for finite element discretizations. In that course, we investigate prototypical magneto-electric devices for their coupling properties and also highlight some open problems in currently available numerical schemes. Chapter 10 extends these studies to a two-scale setting where we analyze the sources of macroscopic magneto-electric coupling. Finally, Chapter 11 is a digression to Fourier-based homogenization solvers which turn out to be an efficient numerical method for the constrained-minimization formulation of magneto-electro-elasticity.

Besides the focus on numerics and applications the content below comes with a certain degree of magneto-electro-mechanical theory. This is, on the one hand, done for readers mainly interested in the numerical part such that they do not have to go through all of Part I, which is admittedly not too short. On the other hand, it helps readers of the first part to recall the essential equations for the setting under consideration[1]. We point out that the compact presentations of theory below are close to existing literature in the respective fields and in many cases not following the approach to magneto-electro-elasticity of Part I. As a consequence we will extensively refer to theory publications which have not been considered in the developments presented in the first part. For better readability we also opted for a notation closer to current conventions and a simplified geometric setting, i.e. Euclidean space and Cartesian coordinates: Points (coordinates) will simply be denoted by plain letters, e.g. $X = (X_1, X_2, X_3)$. Vector-like quantities, i.e. everything that is not a point and can be represented by a tuple of dim numbers will be boldfaced, e.g. $\boldsymbol{v} = (v_1, v_2, v_3)$. In settings where position vectors are required, these will also be set in boldface. Second-order tensors that are usually represented by $dim \times dim$ matrices are either denoted by upright boldface letters ($\mathbf{C}$), or in case of two-point tensors, by boldface underlined symbols ($\underline{\boldsymbol{F}}$). Fourth-order tensors are recognized by their blackboard-boldface font. Domains will be denoted by uppercase calligraphic letters with two exceptions: when referring to "all space under consideration" we generally use Ω and for the space of real numbers we employ $\mathbb{R}$. Function spaces are in "script" font, a variant of the calligraphic one. Besides that, expansion coefficients for discretizations are indicated by upright sans-serif symbols. For other kinds of objects we do not offer regular notational distinctions.

[1] Appendix A provides translations between differential geometric notions and the corresponding ones in vector- and tensor-calculus in Euclidean space with Cartesian coordinates.

Chapter 7

Two-scale studies on the magneto-mechanical response of magnetorheological elastomers

In the present chapter we study the magneto-mechanical response of (MREs), a prototypical magneto-mechanical material. MREs are composites that consist of a soft, non-magnetic, elastomer matrix and stiff magnetic inclusions. They show pronounced deformations (macroscopic strains in the order of 10 %) when exposed to moderate magnetic fields. Furthermore, they exhibit a change in their mechanical stiffness in response to magnetic loads. Consequently, MREs are candidate materials for a range of innovative applications, i.e. tunable valves and shock absorbers (Jolly et al., 1996; Böse and Röder, 2009; Böse et al., 2012) as well as haptic displays (Psarra et al., 2017). Their interesting properties and, thus, also their performance in a certain application strongly depend on their micro-morphology. Hence, there arises the question which microstructure serves best for the application under consideration. It has been shown that the micromorpholgy can be tuned by the presence of a magnetic field during the solidification of an MRE ("curing") (Kallio, 2005; Boczkowska and Awietjan, 2012). In the absence of magnetic field the magnetic particles distribute randomly resulting in a macroscopically isotropic response. With applied field, by contrast, the particles form chain-like structures which lead to transversely isotropic or orthotropic properties. The observed deformation under magnetic field depends on the particular structure of the chains as documented by Danas et al. (2012): straight chains generally lead to contraction whereas wavy chains may also drive extension in the direction of the applied field. In the case of (almost) spherical particles the magneto-mechanical response is governed by long-range particle-particle interactions. Slender ellipsoidal or needle-like particles, however, also experience magnetic torque, i.e. they try to align their major axis with the applied magnetic field. This leads to particle rotations as a second contribution to the deformation response under magnetic load (Galipeau and Ponte Castañeda, 2013a). The situation is even more complex if the magnetic inclusions form clusters which itself may have a distinguished shape such that another length scale enters the game. Thus, from a modeling perspective it is important to account for the microstructural effects on the macrostructural response. For simulations of macroscopic boundary value problems this can be accomplished by fitting a sufficiently complex macroscopic material model to experimentally observed data, at least in theory. For MREs, however, such an approach turned out to be surprisingly difficult in practice. Another possibility is to characterize an MRE on the microscopic scale, where one resolves matrix and

inclusion. This enables the modeler to employ simple and better-known material models for both phases. For numerical simulations this usually results in prohibitive numerical effort. Fortunately it is sufficient to extract *macroscopically effective* properties of the microstructure and transfer only this information to the targeted macroscopic scale. Then, from a macroscopic perspective the obtained material properties are seemingly those of a homogeneous material. This explains why the associated mathematical process is commonly known as "homogenization", which heavily relies on averaging techniques. In the context of MREs, there exist analytical (Ponte Castañeda and Galipeau, 2011; Galipeau and Ponte Castañeda, 2012), semi-analytical (Lefèvre et al., 2017) as well as fully numerical (computational) homogenization schemes (Javili et al., 2013; Spieler et al., 2013; Ethiraj et al., 2015; Keip and Rambausek, 2016). Analytical homogenization is a powerful tool that not only allows for modeling the effective response but also gives theoretical bounds on effective properties. Computational homogenization, in contrast, is more expensive from a numerical point of view and does not deliver theoretical bounds. However, they are more accurate and can take into account more complex phenomena on the microscopic scale. Furthermore, the associated numerical simulations on the micro-scale lead to additional insights on governing mechanisms. In this context the interested reader is referred to the works of Kalina et al. (2016), Kalina et al. (2017), Danas (2017) and Lefèvre et al. (2017).

Besides the well-documented microstructural effects, the macroscopic shape of a soft body plays an equally important role not only for the purely magnetic but also for the magneto-mechanical behavior. This might not be surprising in first place. However, this has important implications on the design of experiments for the determination of macroscopic material behavior. The works of Martin et al. (2006) and Diguet et al. (2010) demonstrate that shape effects render the inference of material parameters from experiments a non-trivial task. Pössinger (2015) studied the shortcomings of cylindrical MRE specimens and proposed to employ cigar-shaped MREs instead. Bodelot et al. (2018) present recent progress in this direction. In other words, the use of homogenization techniques to obtain effective material properties is not enough when we want to *connect* simulations and theoretical findings for micro-scale phenomena to macroscopic experiments and real-world scenarios in general.

In the present chapter, which is mainly based on Keip and Rambausek (2016, 2017) and parts of Rambausek and Keip (2018a), we address micro- and macroscopic magneto-mechanical interactions of MREs by means of numerical simulations. For this purpose we employ computational homogenization. Thereby we do not stop at the determination of effective magneto-mechanical material properties from simulations on the micro-scale but embed these results into a macroscopic finite element framework in an FE^2 sense (Smit et al., 1998; Miehe et al., 1999; Feyel and Chaboche, 2000; Terada and Kikuchi, 2001). This enables us to separately characterize macroscopic shape effects and constitutive responses governed by an MRE's micro-morphology. For better readability the content of this chapter is given in a self-contained manner.

7.1. Theoretical background

In the present section we summarize the fundamentals of variational magneto-elasticity in a two-scale context. We first give the governing equations in quasi-static setting. Then, we proceed with a variational formulation and finally employ the concepts of scale separation and homogenization to obtain the macroscopic and microscopic boundary value problems. For theoretical details we refer to Chapters 4 and 5. We close this section with an overview of the corresponding finite element discretization.

Notation: In what follows we model the physical space by means of the Euclidean space $\mathbb{R}^3$ and work with Cartesian coordinates. Hence, we do not strictly distinguish between vectors, co-vectors and so forth.

7.1.1. Governing equations of continuum magneto-elasticity

In the present context of MREs we consider Maxwell's equations in matter reduced to magneto-statics and vanishing currents. This is justified since the mechanical response is much slower than the magnetic one and because possibly conductive magnetic particles are embedded in an electrically insulating matrix.

Let x denote the coordinates of a point fixed in space, i.e. Eulerian coordinates with grad, curl and div denoting the corresponding differential operators. Then, we have for the (free) current potential[1] $\boldsymbol{h}$ and the magnetic field $\boldsymbol{b}$

$$\operatorname{curl} \boldsymbol{h} = \boldsymbol{0} \qquad \text{and} \qquad \operatorname{div} \boldsymbol{b} = 0, \tag{7.1}$$

with jump conditions

$$\boldsymbol{n} \times [\![\boldsymbol{h}]\!] = \boldsymbol{0} \qquad \text{and} \qquad \boldsymbol{n} \cdot [\![\boldsymbol{b}]\!] = 0 \tag{7.2}$$

across a surface s with normal $\boldsymbol{n}$ where $[\![\bullet]\!] = \{\bullet\}^+ - \{\bullet\}^-$ and $\boldsymbol{n}$ pointing towards "+". From above equation we see that we may express $\boldsymbol{h}$ and $\boldsymbol{b}$ via the gradient of a scalar magnetic potential ϕ^{m} and the curl of a (magnetic) vector potential $\boldsymbol{a}$, respectively

$$\boldsymbol{h} = -\operatorname{grad} \phi^{\mathrm{m}} \qquad \text{and} \qquad \boldsymbol{b} = \operatorname{curl} \boldsymbol{a}. \tag{7.3}$$

In vacuum, $\boldsymbol{h}$ is related to $\boldsymbol{b}$ in terms of the vacuum permeability μ_0

$$\boldsymbol{h} = \frac{\boldsymbol{b}}{\mu_0}, \tag{7.4}$$

[1] Here we deviate from the usual names for $\boldsymbol{h}$ and $\boldsymbol{b}$, the "magnetic field" and "magnetic induction", respectively. This is simply for consistency with the presentation of electromagnetic theory in Chapter 3, which in this regard follows the monograph by Kovetz (2000). There one can find the physical motivation for the terminology employed in the present work.

whereas in matter we have the relation

$$\boldsymbol{h} = \frac{\boldsymbol{b}}{\mu_0} - \boldsymbol{m}, \tag{7.5}$$

with $\boldsymbol{m}$ denoting the magnetization per unit volume.

Let X denote the labels of material points of a body $\mathcal{B}$, i.e. Lagrangian coordinates. We follow the convention to identify the Lagrangian coordinates X of a body with the Eulerian coordinates x of the respective material points at initial time $t = 0$. Accordingly, the differential operators {grad, curl, div} and their counterparts {Grad, Curl, Div} are defined in terms of derivatives with respect to x and X, respectively. We introduce the deformation map $\varphi(X, t)$ that at time t assigns to each Lagrangian coordinate X the Eulerian coordinate $x = \varphi(X, t)$. The image of the body $\mathcal{B}$ under φ at time t is denoted as $\mathcal{B}_t \subset \mathbb{R}^3$, also named Eulerian or current configuration. Conversely, $\mathcal{B} = \mathcal{B}_{t=0} \subset \mathbb{R}^3$ is referred to as Lagrangian or initial configuration. The derivative of φ with respect to x is the "deformation gradient" $\underline{\boldsymbol{F}}$

$$\underline{\boldsymbol{F}} = \frac{\partial \varphi}{\partial X} = \operatorname{Grad} \varphi. \tag{7.6}$$

The magneto-mechanical quantity dual to $\underline{\boldsymbol{F}}$ is the total[2] first Piola-Kirchoff stress $\underline{\boldsymbol{P}}$. In a quasi-static setting in absence of body forces the tensors $\underline{\boldsymbol{F}}$ and $\underline{\boldsymbol{P}}$ are required to fulfill the compatibility condition and the balance of momentum, respectively,

$$\operatorname{Curl} \underline{\boldsymbol{F}} = \boldsymbol{0} \quad \text{and} \quad \operatorname{Div} \underline{\boldsymbol{P}} = \boldsymbol{0} \quad \text{in } \mathcal{B} \tag{7.7}$$

defined on the initial configuration of body. Note that the differential operators in above equation act in a row-wise manner[3].

As jump conditions across a surface $\mathcal{S}$ with normal $\boldsymbol{N}$ we have

$$[\![\underline{\boldsymbol{F}}]\!] \times \boldsymbol{N} = \boldsymbol{0} \quad \text{and} \quad [\![\underline{\boldsymbol{P}}]\!] \cdot \boldsymbol{N} = -\boldsymbol{t}_0^{\text{mech}} \quad \text{across } \mathcal{S}, \tag{7.8}$$

where $\boldsymbol{t}_0^{\text{mech}}$ is the vector of mechanical tractions on $\mathcal{S}$, that is Eulerian surface force per Lagrangian area.

Obviously, (7.1) involves Eulerian differential operators curl and div, whereas (7.1) contains derivatives with respect to Lagrangian coordinates. However, we may pull back $\boldsymbol{h}$ and $\boldsymbol{b}$ to the initial configuration via

$$\boldsymbol{H} = \underline{\boldsymbol{F}}^{\mathrm{T}} \cdot \boldsymbol{h} = -\operatorname{Grad} \phi^{\mathrm{m}} \quad \text{and} \quad \boldsymbol{B} = J\, \underline{\boldsymbol{F}}^{-1} \cdot \boldsymbol{b} = \operatorname{Curl} \boldsymbol{A} \quad \text{with} \quad J = \det \underline{\boldsymbol{F}}, \tag{7.9}$$

to obtain their Lagrangian counterparts $\boldsymbol{H}$ and $\boldsymbol{B}$, respectively. This is clearly feasible

[2] The concept of total stress accounts for the fact that it is in general not clear how to separate stress into mechanical and magneto-mechanical contributions. As a consequence, total stress reduces to the classical mechanical stress in the absence of (macroscopic) electro-magnetic fields on the one hand and to the Maxwell stress in empty space on the other hand (McMeeking and Landis, 2004; Kankanala and Triantafyllidis, 2004).

[3] By "row" we refer to rows of the matrix representation of these second-order tensors. This means, that the differential operators act only on the rightmost index or "slot" of a tensor.

in a domain in space that is occupied by a body for which we already introduced a Lagrangian configuration. In free space, where (7.1) also hold, the definition of an initial configuration does not make sense from a physical point of view. However, this should not prevent us from formally "extending" the Lagrangian coordinates of the body into the surrounding space (Kankanala and Triantafyllidis, 2004), denoted as $\mathcal{B}'$. We then define the motion of the free-space in terms of the deformation of an auxiliary elastic material glued to the surface of the deformable body. From this we also get the Eulerian configuration $\mathcal{B}'_t$ as the image of $\mathcal{B}'$ under φ, which is now defined in $\mathcal{B} \cup \mathcal{B}' = \Omega \subseteq \mathbb{R}^3$. Clearly, the auxiliary material must not exert any *mechanical* tractions on the body. How this enters the numerical simulations will be described in Section 7.1.3. If we for now simply accept this idea we end up with

$$\operatorname{Curl} \boldsymbol{H} = \boldsymbol{0} \quad \text{and} \quad \operatorname{Div} \boldsymbol{B} = 0 \quad \text{in } \Omega, \tag{7.10a}$$

$$[\![\boldsymbol{H}]\!] \times \boldsymbol{N} = \boldsymbol{0} \quad \text{and} \quad [\![\boldsymbol{B}]\!] \cdot \boldsymbol{N} = 0 \quad \text{across } \mathcal{S}. \tag{7.10b}$$

Alternatively, we could express the mechanical equations in the Eulerian configuration resulting in

$$\operatorname{curl}(\underline{\boldsymbol{F}} \cdot \underline{\boldsymbol{F}}^{-1}) = \boldsymbol{0} \quad \text{and} \quad \operatorname{div} \boldsymbol{\sigma} = 0 \quad \text{in } \Omega_t, \tag{7.11a}$$

$$[\![\underline{\boldsymbol{F}} \cdot \underline{\boldsymbol{F}}^{-1}]\!] \times \boldsymbol{N} = \boldsymbol{0} \quad \text{and} \quad [\![\boldsymbol{\sigma}]\!] \cdot \boldsymbol{N} = -\boldsymbol{t}^{\text{mech}} \quad \text{across } s. \tag{7.11b}$$

Therein, $\Omega_t = \mathcal{B}'_t \cup \mathcal{B}_t$ and $\boldsymbol{\sigma} = \frac{1}{J} \underline{\boldsymbol{P}} \cdot \underline{\boldsymbol{F}}^{\mathrm{T}}$ is the total Cauchy stress. The Eulerian versions of the equations for $\underline{\boldsymbol{F}}$ are trivial in the present scope. This directly follows from considering $\underline{\boldsymbol{F}}$ being the tangent map corresponding to φ and being the basic distortion measure at the same time. However, when we do not consider (7.6) as the definition of $\underline{\boldsymbol{F}}$ but simply as another equation, the picture is different. For an in-depth discussion of *compatibility* in continuum mechanics the interested reader is referred to Steinmann (2015). Also note that we did not mention the balance of moment of momentum, which in the present scope is fulfilled by the symmetry of $\boldsymbol{\sigma}$.

Depending on problem at hand, the Eulerian or Lagrangian form of the governing equations is preferred. In solid mechanics the Lagrangian perspective is advantageous in many cases and will also be adopted in what follows.

7.1.2. Variational formulation of finite-deformation magneto-elasticity

Within the present chapter we opt for the deformation map φ and the scalar magnetic potential ϕ^{m}

$$\varphi : \begin{cases} \Omega \times \mathcal{T} & \to \mathbb{R}^3 \\ (X,t) & \mapsto \varphi(X,t) \end{cases} \quad \text{and} \quad \phi^{\mathrm{m}} : \begin{cases} \Omega \times \mathcal{T} & \to \mathbb{R} \\ (X,t) & \mapsto \phi^{\mathrm{m}}(X,t) \end{cases} \tag{7.12}$$

as primary variables on the Lagrangian configuration of the full space Ω and for time $t \in \mathcal{T}$. Thus, by (7.6) and $(7.3)_1$ the equations (7.10) and (7.7) for $\underline{\boldsymbol{F}}$ and $\boldsymbol{H}$, respectively, are fulfilled trivially. The same holds for the associated jump conditions. Based on that, the equations for the respective dual fields $\underline{\boldsymbol{P}}$ and $\boldsymbol{B}$ are the Euler-Lagrange equations of the variational saddle-point principle[4]

$$\{\hat{\varphi}, \hat{\phi^{\mathrm{m}}}\} = \arg\left\{ \inf_{\substack{\varphi \\ \in \\ \mathscr{W}_\varphi}} \sup_{\substack{\phi^{\mathrm{m}} \\ \in \\ \mathscr{W}_{\phi^{\mathrm{m}}}}} \Pi(\varphi, \phi^{\mathrm{m}}) \right\} \tag{7.13}$$

with the spaces $\mathscr{W}_\varphi$ and $\mathscr{W}_{\phi^{\mathrm{m}}}$ given as[5]

$$\mathscr{W}_\varphi = \{\varphi \mid \varphi_{\mathrm{i}} \in \mathscr{H}(\mathrm{Grad}, \Omega),\ \pi_\varphi(\varphi) = \pi_\varphi(\varphi_{\mathrm{D}}) \text{ on } \partial\Omega_\varphi \cup \partial\mathcal{B}_\varphi\} \quad \text{and} \tag{7.14a}$$

$$\mathscr{W}_{\phi^{\mathrm{m}}} = \{\phi^{\mathrm{m}} \mid \phi^{\mathrm{m}} \in \mathscr{H}(\mathrm{Grad}, \Omega),\ \phi^{\mathrm{m}} = \phi^{\mathrm{m}}_{\mathrm{D}} \text{ on } \partial\Omega_{\phi^{\mathrm{m}}}\}. \tag{7.14b}$$

The potential Π in equation (7.15) is based on a free-energy density $\Psi(\underline{\boldsymbol{F}}, \boldsymbol{H})$ and loading potentials $\mathcal{P}^t$ and $\mathcal{P}^b$

$$\Pi = \int_\Omega \Psi(\underline{\boldsymbol{F}}, \boldsymbol{H})\, dV - \int_{\partial\mathcal{B}} \mathcal{P}^t\, dA - \int_{\partial\Omega} \mathcal{P}^b\, dA, \tag{7.15}$$

where the loading potentials give the mechanical tractions as well as the magnetic field projected on the normal to the boundary according to

$$\boldsymbol{t}_0^{\mathrm{mech}} = \frac{\partial \mathcal{P}^t}{\partial \varphi} \quad \text{and} \quad \boldsymbol{B}_N = \frac{\partial \mathcal{P}^b}{\partial \phi^{\mathrm{m}}}. \tag{7.16}$$

Figure 7.1 depicts the domains under consideration.

[4] The magneto-mechanical version of (4.248) in Part I)

[5] Notation: π_φ denotes an abstract operation that specifies the direction(s) in which φ is constrained. Furthermore, with $\mathscr{H}(\mathrm{Grad})$ we refer to the space where the function and its first gradient are square integrable, i.e. in L_2. This space is commonly denoted as $\mathcal{H}^1$. However, for consistency with the terminology for spaces, of which the definition relies on other differential operators, we prefer to be explicit about the differential operator in charge.

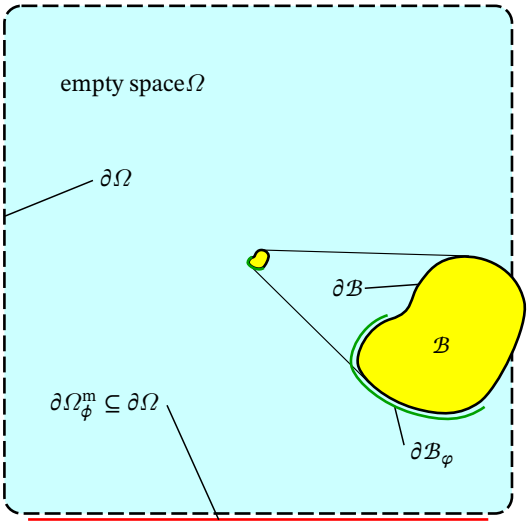

Figure 7.1: A magnetic body $\mathcal{B}$ embedded in a free space domain Ω, i.e. $\mathcal{B} \subset \Omega$. The body is considered to be positioned by some boundary condition $\varphi = \varphi_{\mathrm{D}}$ at $\mathcal{B}_\varphi$. Moreover, we require a certain behavior of φ and ϕ^{m} towards the boundary of the (theoretically infinite) domain Ω. In the case of φ it is natural to assume the identity map on all $\partial\Omega$. For ϕ^{m} we may prescribe specific values on $\partial\Omega_\phi^{\mathrm{m}}$. In Section 7.1.3 we discuss magnetic boundary conditions in greater detail.

A stationary point of Π is characterized by a vanishing first variation

$$\begin{aligned}
\delta\Pi &= \int_\Omega \frac{\partial\Psi}{\partial\underline{\boldsymbol{F}}} : \frac{\partial\delta\varphi}{\partial X} - \frac{\partial\Psi}{\partial\boldsymbol{H}} \cdot \frac{\partial\delta\phi^{\mathrm{m}}}{\partial X}\, dV - \int_{\partial\mathcal{B}} \frac{\partial\mathcal{P}^t}{\partial\varphi} \cdot \delta\varphi\, dA - \int_{\partial\Omega} \frac{\partial\mathcal{P}^b}{\partial\phi^{\mathrm{m}}} \cdot \delta\phi^{\mathrm{m}}\, dA \\
&= -\int_\Omega \mathrm{Div}\left[\frac{\partial\Psi}{\partial\underline{\boldsymbol{F}}}\right] \cdot \delta\varphi + \mathrm{Div}\left[-\frac{\partial\Psi}{\partial\boldsymbol{H}}\right] \delta\phi^{\mathrm{m}}\, dV \\
&\quad + \int_{\partial\mathcal{B}} \left(-\left[\!\left[\frac{\partial\Psi}{\partial\underline{\boldsymbol{F}}}\right]\!\right] \cdot \boldsymbol{N} - \frac{\partial\mathcal{P}^t}{\partial\varphi}\right) \cdot \delta\varphi\, dA \\
&\quad + \int_{\partial\Omega\setminus\partial\Omega_{\phi^{\mathrm{m}}}} \left(-\frac{\partial\Psi}{\partial\boldsymbol{H}} \cdot \boldsymbol{N} - \frac{\partial\mathcal{P}^b}{\partial\phi^{\mathrm{m}}}\right) \delta\phi^{\mathrm{m}}\, dA = 0 \quad \forall\, \delta\varphi \in \mathscr{W}_\varphi \text{ and } \delta\phi^{\mathrm{m}} \in \mathscr{W}_{\phi^{\mathrm{m}}}.
\end{aligned} \tag{7.17}$$

From above equation we recover the balance of linear momentum and the magnetic

Gauss law

$$\operatorname{Div} \underline{\boldsymbol{P}} = \boldsymbol{0} \qquad \text{with} \qquad \underline{\boldsymbol{P}} = \frac{\partial \Psi}{\partial \underline{\boldsymbol{F}}} \qquad \text{in } \Omega \qquad \text{and} \tag{7.18a}$$

$$\operatorname{Div} \boldsymbol{B} = 0 \qquad \text{with} \qquad \boldsymbol{B} = -\frac{\partial \Psi}{\partial \boldsymbol{H}} \qquad \text{in } \Omega, \tag{7.18b}$$

respectively. Furthermore we obtain the natural boundary conditions

$$-\left[\!\!\left[\frac{\partial \Psi}{\partial \underline{\boldsymbol{F}}} \right]\!\!\right] \cdot \boldsymbol{N} = \boldsymbol{t}_0^{\text{mech}} \quad \text{on } \partial\mathcal{B} \setminus \partial\mathcal{B}_\varphi \quad \text{and} \quad -\frac{\partial \Psi}{\partial \boldsymbol{H}} \cdot \boldsymbol{N} = B_N \quad \text{on } \partial\Omega \setminus \partial\Omega_{\phi^{\text{m}}}. \tag{7.19}$$

7.1.3. Experimentally motivated boundary conditions

In the current chapter we are concerned with the computational characterization of MREs. For comparison with experimental works we strive to mimic real world situations and measurements. In the case of mechanically soft magnetic bodies this task is complicated by the fact that such bodies magneto-mechanically interact with the surrounding free space. By that we refer to the magneto-mechanical tractions acting on the whole surface of a magnetized body. A soft body may undergo significant deformations just because of these tractions. Moreover, the tractions are not known in advance since they themselves depend on the current shape of body. The remedy is to solve boundary value problems in a spatial domain which is much larger than the actual body of interest as already indicated in Section 7.1.1. The additional empty domain $\mathcal{B}'$ can be filled with a very soft elastic material with the magnetic properties of vacuum. Then the magneto-mechanical stresses due to the magnetostatic energy contribution naturally act on the embedded body. This obviously comes with an error due to the elastic contribution in $\mathcal{B}'$. However, if the artificial elastic material in $\mathcal{B}'$ is sufficiently soft, i.e. much softer than that in $\mathcal{B}$), this error is usually negligible. Unfortunately, due to discretization errors (see Section 9.3.1) there is a lower limit on the stiffness in $\mathcal{B}'$. An alternative approach is to block all deformation *outside* $\mathcal{B}$ in a first solution step, solve the coupled problem and afterwards solve an auxiliary "material redistribution" or "mesh motion" problem in $\mathcal{B}'$. Such a method has been described in greater detail by Pelteret et al. (2016). Based on their work we came up with our own version presented in Appendix B.

Another challenge is the magnetic boundary condition. In experiments there usually is a magnetic body and separate magnetic loading devices. In most cases the magnetic loading devices are electromagnets of finite extent. Consequently, when we solve boundary value problems in an approximation of full space we not only need to compute the magnetic field of the body (the self-field) but also need precise knowledge of the applied fields. In some scenarios this requires possibly complicated models of the loading devices. We shall not follow this direction. Instead we restrict ourselves to the case where a magnetic body is placed in a region of homogeneous *applied* magnetic field $\boldsymbol{b}^\infty$ or $\boldsymbol{h}^\infty = \boldsymbol{b}^\infty/\mu_0$, respectively. This region of homogeneity is assumed to be large enough

for the body's self-field to be negligible at the outer domain boundaries as depicted in Figure 7.2 (Vu and Steinmann, 2010; Bustamante, 2009; Keip and Rambausek, 2016).

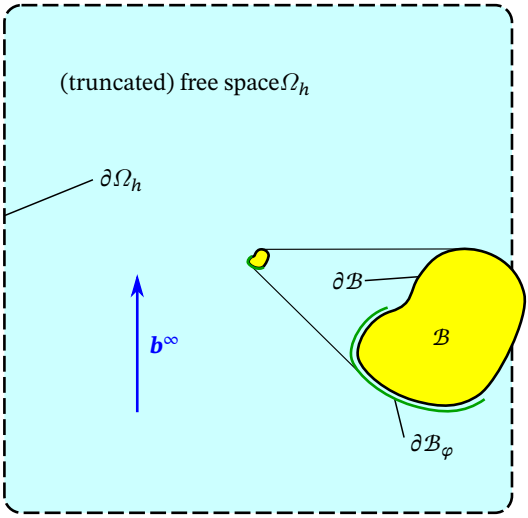

Figure 7.2: A magnetic body $\mathcal{B}$ embedded in a (truncated) free space domain Ω_h exposed to *uniform* applied magnetic field $\boldsymbol{b}^\infty$. Such a setting corresponds to a the specimen located between to comparably large magnetic poles of which the distance is much larger than the size of the specimen. The body is considered to be positioned by some boundary condition $\varphi = \varphi_\mathrm{D}$ on $\mathcal{B}_\varphi$. The domain $\mathcal{B}' = \Omega_h \setminus \mathcal{B}$ is empty, i.e. has the properties of air or vacuum.

An appropriate set of boundary conditions for this situation are

$$\varphi(X) = X \quad \text{and} \quad \phi^\mathrm{m}(x) = -\int_{\bar{x}=0}^{\bar{x}=x} \boldsymbol{h}^\infty \cdot d\boldsymbol{l} \quad \text{on } \partial\Omega_h, \tag{7.20}$$

where, because of the former, the latter is equivalent to

$$\phi^\mathrm{m}(X) = -\int_{\bar{X}=0}^{\bar{X}=X} \boldsymbol{h}^\infty \cdot d\boldsymbol{L}. \tag{7.21}$$

Recall that all we need from ϕ^m is the differential such that even shifted origins do not destroy equivalence here. In the present scope of Euclidean space and Cartesian coordinates the integrals reduce to dot-products

$$\phi^\mathrm{m}(x) = -\boldsymbol{h}^\infty \cdot x = \phi^\mathrm{m}(X) = -\boldsymbol{h}^\infty \cdot X \quad \text{on } \partial\Omega_h. \tag{7.22}$$

Moreover, (7.20) reflects the approximation that the scalar magnetic potential $\phi^\mathrm{m}_\mathrm{s}$ asso-

ciated with the body's (self-) current-potential $\boldsymbol{h}_\mathrm{s}$ decays to zero (or some other constant independent of x) for x approaching $\partial\Omega_h$. This motivates to decompose ϕ^m either into

$$\phi^\mathrm{m}(x) = -\boldsymbol{h}^\infty \cdot x + \phi^\mathrm{m}_\mathrm{s}(x) \quad \text{or} \quad \phi^\mathrm{m}(X) = -\boldsymbol{h}^\infty \cdot X + \phi^\mathrm{m}_\mathrm{p}(X), \tag{7.23}$$

where in the first version we have the self-potential $\phi^\mathrm{m}_\mathrm{s}(x)$ which is different from the abstract perturbation potential $\phi^\mathrm{m}_\mathrm{p}(x)$ in the second case. While both coincide on the boundary $\partial\Omega_h$ they differ elsewhere. Whether to opt for ϕ^m, $\phi^\mathrm{m}_\mathrm{s}$ or $\phi^\mathrm{m}_\mathrm{p}$ as actual degree of freedom in FE discretizations is a question of implementation. The results obtained are of course equivalent and can be recasted in either form. Note, however, that only ϕ^m and $\phi^\mathrm{m}_\mathrm{s}$ have physical meaning. Figure 7.3 illustrates the difference between $\phi^\mathrm{m}_\mathrm{s}$ and $\phi^\mathrm{m}_\mathrm{p}$ by means of a *non-magnetic* body exposed to a homogeneous $\boldsymbol{h}^\infty$ and undergoing deformation.

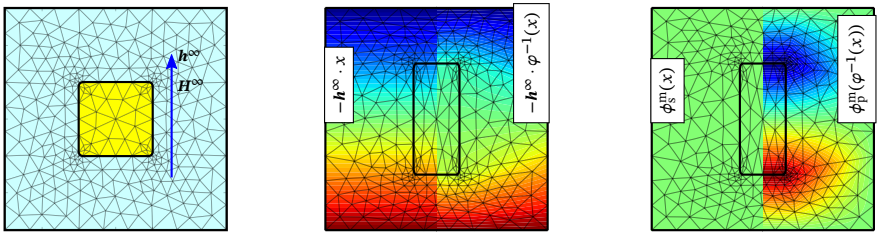

(a) (b) (c)

Figure 7.3: Review of two decompositions of the scalar magnetic potential by means of a *non-magnetic* body in free space under uniform field. The initial configuration is depicted in (a). In (b) we show a deformed configuration and contour plots of $-\boldsymbol{h}^\infty \cdot x$ versus $-\boldsymbol{h}^\infty \cdot X = -\boldsymbol{h}^\infty \cdot \varphi^{-1}(x)$. Clearly, only the formed corresponds to the uniform applied field which in the resent case is the full field since the the body is non-magnetic by definition. In (c) we plot $\phi^\mathrm{m}_\mathrm{s}(x) = \phi^\mathrm{m} - \boldsymbol{h}^\infty \cdot x$ and $\phi^\mathrm{m}_\mathrm{p}(x) = -\phi^\mathrm{m} - \boldsymbol{h}^\infty \cdot X$. This highlights the fact that $\phi^\mathrm{m}_\mathrm{p}$ cannot be the self-field of the body, which would vanish here. Indeed, only $\phi^\mathrm{m}_\mathrm{s}(x)$ has this property.

As an alternative to $(7.20)_2$ we could of course also employ the natural boundary condition

$$\boldsymbol{b}(x) \cdot \boldsymbol{n}(x) = \mu_0 \boldsymbol{h}^\infty \cdot \boldsymbol{n}(x) \quad \text{on } \partial\Omega_h, \tag{7.24}$$

which under $(7.20)_1$ is equivalent to $\boldsymbol{B}(X) \cdot \boldsymbol{N}(X) = \mu_0 \boldsymbol{h}^\infty \cdot \boldsymbol{N}(X)$.

7.1.4. Finite-deformation magneto-elasticity across scales

Based on the outline of the governing (and scale-agnostic) variational principle in Section 7.1.2 we now provide details on the scale-bridging for MREs. For this purpose we consider the coordinates X as "true" or full-scale coordinates valid for macroscopic and

microscopic length scales. Consider a representative[6] microscopic material sample $\widetilde{\mathcal{B}}$ of which the spatial extent is orders of magnitudes smaller than that of the whole MRE body $\mathcal{B}$, i.e. $\widetilde{\mathcal{B}} \subset \mathcal{B}$ and $|\widetilde{\mathcal{B}}| \lll |\mathcal{B}|$. In the spirit of scale separation we associate such a representative volume element ($\mathcal{RVE}$) to each macroscopic material point $\overline{X}$. Within $\widetilde{\mathcal{B}}$ at $\overline{X}$ (short $\widetilde{\mathcal{B}}$) we decompose[7] X into

$$X|_{\widetilde{\mathcal{B}}} = \overline{X} + \widetilde{\boldsymbol{X}}, \tag{7.25}$$

where $\widetilde{\boldsymbol{X}}$ denotes microscopic (fine-scale) coordinates within $\widetilde{\mathcal{B}}$. Furthermore, we assume within $\widetilde{\mathcal{B}}$ following expansions of φ and ϕ^{m} (see Section 5.2)

$$\varphi(X)|_{\widetilde{\mathcal{B}}} = \varphi(\overline{X} + \widetilde{\boldsymbol{X}}) = \langle \varphi \rangle_{\widetilde{\mathcal{B}}} + \left\langle \frac{\partial \varphi}{\partial X} \right\rangle_{\widetilde{\mathcal{B}}} \cdot \widetilde{\boldsymbol{X}} + \widetilde{\varphi}(\widetilde{\boldsymbol{X}}) \quad \text{and} \tag{7.26a}$$

$$\phi^{\mathrm{m}}(X)|_{\widetilde{\mathcal{B}}} = \phi^{\mathrm{m}}(\overline{X} + \widetilde{\boldsymbol{X}}) = \langle \phi^{\mathrm{m}} \rangle_{\widetilde{\mathcal{B}}} + \left\langle \frac{\partial \phi^{\mathrm{m}}}{\partial X} \right\rangle_{\widetilde{\mathcal{B}}} \cdot \widetilde{\boldsymbol{X}} + \widetilde{\phi}^{\mathrm{m}}(\widetilde{\boldsymbol{X}}), \tag{7.26b}$$

where $\langle (\bullet) \rangle_{\widetilde{\mathcal{B}}}$ is an appropriate[8] averaging operator. Accordingly, we have for the derived fields $\underline{\boldsymbol{F}}$ and $\boldsymbol{H}$

$$\underline{\boldsymbol{F}}(\overline{X} + \widetilde{\boldsymbol{X}}) = \left\langle \frac{\partial \varphi}{\partial X} \right\rangle_{\widetilde{\mathcal{B}}} + \frac{\partial \widetilde{\varphi}}{\partial \widetilde{\boldsymbol{X}}} \quad \text{and} \tag{7.27a}$$

$$\boldsymbol{H}(\overline{X} + \widetilde{\boldsymbol{X}}) = -\left\langle \frac{\partial \phi^{\mathrm{m}}}{\partial X} \right\rangle_{\widetilde{\mathcal{B}}} - \frac{\partial \widetilde{\phi}^{\mathrm{m}}}{\partial \widetilde{\boldsymbol{X}}}, \tag{7.27b}$$

where we identify the effective deformation gradient $\overline{\underline{\boldsymbol{F}}}$ and the effective current potential $\overline{\boldsymbol{H}}$ as

$$\overline{\underline{\boldsymbol{F}}} = \left\langle \frac{\partial \varphi}{\partial X} \right\rangle_{\widetilde{\mathcal{B}}} \quad \text{and} \quad \overline{\boldsymbol{H}} = -\left\langle \frac{\partial \phi^{\mathrm{m}}}{\partial X} \right\rangle_{\widetilde{\mathcal{B}}}. \tag{7.28}$$

Next we define the effective energy density $\overline{\Psi}(\overline{\underline{\boldsymbol{F}}}, \overline{\boldsymbol{H}})$ in terms of the microscopic variational principle (Miehe et al., 2016)

$$\overline{\Psi}(\overline{\underline{\boldsymbol{F}}}, \overline{\boldsymbol{H}}) = \inf_{\substack{\widetilde{\varphi} \\ \in \\ \mathscr{W}_{\widetilde{\varphi}}}} \sup_{\substack{\widetilde{\phi}^{\mathrm{m}} \\ \in \\ \mathscr{W}_{\widetilde{\phi}^{\mathrm{m}}}}} \left\langle \Psi\left(\underline{\boldsymbol{F}}, \boldsymbol{H}\right) \right\rangle_{\widetilde{\mathcal{B}}}. \tag{7.29}$$

[6] "Representative" regarding the effective (macroscopic) properties. Consider a macroscopic body consisting of a periodic pattern of such a microscopic sample. Then the properties of the body should be invariant with respect to changes of the sample's size (within a certain range).

[7] For comments on the geometric setting, in particular the distinction of macroscopic points and microscopic position vectors we please see Section 5.2.

[8] In the present scope this is simply the volume average $\frac{1}{|\widetilde{\mathcal{B}}|} \int_{\widetilde{\mathcal{B}}} (\bullet)\, dV$. For a more general discussion of the notion of averages over an $\mathcal{RVE}$ we refer to Section 5.2.2.

The spaces $\mathscr{W}_{\widetilde{\varphi}}$ and $\mathscr{W}_{\widetilde{\phi}^{\mathrm{m}}}$ are given as

$$\mathscr{W}_{\widetilde{\varphi}} = \left\{\widetilde{\varphi} \mid \widetilde{\varphi}_{\mathrm{i}} \in \mathscr{H}(\mathrm{Grad}, \widetilde{\mathcal{B}}),\ \widetilde{\varphi}(\widetilde{\boldsymbol{X}}^{+}) = \widetilde{\varphi}(\widetilde{\boldsymbol{X}}^{-}),\ \widetilde{\varphi}(\widetilde{\boldsymbol{X}}^{c}) = \boldsymbol{0}\right\} \quad \text{and} \tag{7.30a}$$

$$\mathscr{W}_{\widetilde{\phi}^{\mathrm{m}}} = \left\{\widetilde{\phi}^{\mathrm{m}} \mid \widetilde{\phi}^{\mathrm{m}} \in \mathscr{H}(\mathrm{Grad}, \widetilde{\mathcal{B}}),\ \widetilde{\phi}^{\mathrm{m}}(\widetilde{\boldsymbol{X}}^{+}) = \widetilde{\phi}^{\mathrm{m}}(\widetilde{\boldsymbol{X}}^{-}),\ \widetilde{\phi}^{\mathrm{m}}(\widetilde{\boldsymbol{X}}^{c}) = 0\right\}, \tag{7.30b}$$

where pairs $\{\widetilde{\boldsymbol{X}}^{+}, \widetilde{\boldsymbol{X}}^{-}\}$ denote opposite boundary points of $\widetilde{\mathcal{B}}$ and $\widetilde{\boldsymbol{X}}^{c}$ denotes the set of corners of $\widetilde{\mathcal{B}}$. Hence, (7.30) enforce periodic boundary conditions and remove "rigid body modes" from the solutions. We point out that there is an important distinction between $\overline{\Psi}$ and $\langle \Psi \rangle_{\widetilde{\mathcal{B}}}$, namely

$$\delta_{\{\widetilde{\varphi}, \widetilde{\phi}^{\mathrm{m}}\}} \overline{\Psi} \equiv 0 \qquad \text{by definition, whereas} \tag{7.31a}$$

$$\delta_{\{\widetilde{\varphi}, \widetilde{\phi}^{\mathrm{m}}\}} \langle \Psi \rangle_{\widetilde{\mathcal{B}}} = 0 \qquad \text{is the equation to be solved.} \tag{7.31b}$$

At this point, for notational convenience, we introduce the variation symbols

$$\delta = \tilde{\delta} + \overline{\delta}, \quad \tilde{\delta} = \delta_{\{\widetilde{\varphi}, \widetilde{\phi}^{\mathrm{m}}\}} \quad \text{and} \quad \overline{\delta} = \delta_{\{\overline{\underline{\boldsymbol{F}}}, \overline{\boldsymbol{H}}\}}. \tag{7.32}$$

Analogously, we define

$$\Delta = \widetilde{\Delta} + \overline{\Delta}, \quad \widetilde{\Delta} = \Delta_{\{\widetilde{\varphi}, \widetilde{\phi}^{\mathrm{m}}\}} \quad \text{and} \quad \overline{\Delta} = \Delta_{\{\overline{\underline{\boldsymbol{F}}}, \overline{\boldsymbol{H}}\}}. \tag{7.33}$$

From (7.31) we know that $\tilde{\delta}\overline{\Psi} = 0$ and thus $\delta\overline{\Psi} = \overline{\delta}\overline{\Psi}$, that is

$$\left\langle \underline{\boldsymbol{P}}(\hat{\underline{\boldsymbol{F}}}, \hat{\boldsymbol{H}}) : \delta\underline{\boldsymbol{F}} - \boldsymbol{B}(\hat{\underline{\boldsymbol{F}}}, \hat{\boldsymbol{H}}) \cdot \delta\boldsymbol{H} \right\rangle_{\widetilde{\mathcal{B}}} = \overline{\underline{\boldsymbol{P}}} : \delta\overline{\underline{\boldsymbol{F}}} - \overline{\boldsymbol{B}} \cdot \delta\overline{\boldsymbol{H}}. \tag{7.34}$$

Above equation is nothing else than a generalized Hill-Mandel statement, where the effective dual quantities $\overline{\underline{\boldsymbol{P}}}$ and $\overline{\boldsymbol{B}}$ are computed as

$$\overline{\underline{\boldsymbol{P}}} = \frac{\partial \overline{\Psi}}{\partial \overline{\underline{\boldsymbol{F}}}} = \left\langle \underline{\boldsymbol{P}}(\hat{\underline{\boldsymbol{F}}}, \hat{\boldsymbol{H}}) \right\rangle_{\widetilde{\mathcal{B}}} \quad \text{and} \quad \overline{\boldsymbol{B}} = -\frac{\partial \overline{\Psi}}{\partial \overline{\boldsymbol{H}}} = \left\langle \boldsymbol{B}(\hat{\underline{\boldsymbol{F}}}, \hat{\boldsymbol{H}}) \right\rangle_{\widetilde{\mathcal{B}}}, \tag{7.35}$$

where $\{\hat{\underline{\boldsymbol{F}}}, \hat{\boldsymbol{H}}\} = \{\overline{\underline{\boldsymbol{F}}} + \mathrm{Grad}\,\hat{\widetilde{\varphi}}, \overline{\boldsymbol{H}} - \mathrm{Grad}\,\hat{\widetilde{\phi}}^{\mathrm{m}}\}$ with $\{\hat{\widetilde{\varphi}}, \hat{\widetilde{\phi}}^{\mathrm{m}}\}$ being solutions of (7.29). We emphasize that the volume averages in (7.35) are in general not the definitions of $\overline{\underline{\boldsymbol{P}}}$ and $\overline{\boldsymbol{B}}$. At equilibrium, we merely identify the terms that go with $\delta\overline{\underline{\boldsymbol{F}}}$ and $\delta\overline{\boldsymbol{H}}$ as effective duals. In the present case, these terms turn out to be precisely the volume averages in (7.35), but this does not hold in general. Please refer to Sections 5.2.2 and 5.3.3 for an in-depth discussion of and effective quantities and Hill-Mandel consistency.

For numerical simulations we also need the linearizations of $\overline{\underline{\boldsymbol{P}}}$ and $\overline{\boldsymbol{B}}$ with respect to

$\overline{\underline{\boldsymbol{F}}}$ and $\overline{\boldsymbol{H}}$ in the form

$$\begin{aligned}\overline{\Delta\delta\Psi} &= \overline{\Delta}\left(\overline{\underline{\boldsymbol{P}}} : \delta\overline{\underline{\boldsymbol{F}}} - \overline{\boldsymbol{B}} \cdot \delta\overline{\boldsymbol{H}}\right) \\ &= \left\langle \delta\overline{\underline{\boldsymbol{F}}} : \left(\mathbb{A} : \overline{\Delta}\hat{\underline{\boldsymbol{F}}}\right) - \delta\overline{\underline{\boldsymbol{F}}} : \left(\mathbf{q}^{\mathrm{T}} \cdot \overline{\Delta}\hat{\boldsymbol{H}}\right) - \delta\overline{\boldsymbol{H}} \cdot \left(\mathbf{q} : \overline{\Delta}\hat{\underline{\boldsymbol{F}}}\right) - \delta\overline{\boldsymbol{H}} \cdot \left(\boldsymbol{\mu} \cdot \overline{\Delta}\hat{\boldsymbol{H}}\right)\right\rangle_{\widetilde{\mathcal{B}}} \end{aligned} \tag{7.36}$$

with the moduli

$$\mathbb{A} = \partial_{\underline{\boldsymbol{F}}}\underline{\boldsymbol{P}}, \quad \mathbf{q} = \partial_{\underline{\boldsymbol{F}}}\boldsymbol{B} = -\left[\partial_{\boldsymbol{H}}\underline{\boldsymbol{P}}\right]^{\mathrm{T}} \quad \text{and} \quad \boldsymbol{\mu} = \partial_{\boldsymbol{H}}\boldsymbol{B} \tag{7.37}$$

and the linearizations $\overline{\Delta}\{\hat{\underline{\boldsymbol{F}}}, \hat{\boldsymbol{H}}\}$

$$\overline{\Delta}\hat{\underline{\boldsymbol{F}}} = \frac{\partial\overline{\underline{\boldsymbol{F}}}}{\partial\overline{\underline{\boldsymbol{F}}}} : \Delta\overline{\underline{\boldsymbol{F}}} + \frac{\partial\hat{\underline{\boldsymbol{F}}}}{\partial\overline{\underline{\boldsymbol{F}}}} : \Delta\overline{\underline{\boldsymbol{F}}} + \frac{\partial\hat{\underline{\boldsymbol{F}}}}{\partial\overline{\boldsymbol{H}}} \cdot \Delta\overline{\boldsymbol{H}} \quad \text{and} \tag{7.38a}$$

$$\overline{\Delta}\hat{\boldsymbol{H}} = \frac{\partial\overline{\boldsymbol{H}}}{\partial\overline{\boldsymbol{H}}} \cdot \Delta\overline{\boldsymbol{H}} + \frac{\partial\hat{\boldsymbol{H}}}{\partial\overline{\boldsymbol{H}}} \cdot \Delta\overline{\boldsymbol{H}} + \frac{\partial\hat{\boldsymbol{H}}}{\partial\overline{\underline{\boldsymbol{F}}}} : \Delta\overline{\underline{\boldsymbol{F}}}. \tag{7.38b}$$

Using $\partial_{\overline{\underline{\boldsymbol{F}}}}\overline{\underline{\boldsymbol{F}}} = \mathbb{I}$ and $\partial_{\overline{\boldsymbol{H}}}\overline{\boldsymbol{H}} = \mathbf{1}$ we see that (7.36) can be written as

$$\begin{aligned}&\overline{\Delta\delta\Psi} = \\ &\delta\overline{\underline{\boldsymbol{F}}} : \langle\mathbb{A}\rangle_{\widetilde{\mathcal{B}}} : \Delta\overline{\underline{\boldsymbol{F}}} - \delta\overline{\underline{\boldsymbol{F}}} : \langle\mathbf{q}\rangle_{\widetilde{\mathcal{B}}}^{\mathrm{T}} \cdot \Delta\overline{\boldsymbol{H}} - \delta\overline{\boldsymbol{H}} \cdot \langle\mathbf{q}\rangle_{\widetilde{\mathcal{B}}} : \Delta\overline{\underline{\boldsymbol{F}}} - \delta\overline{\boldsymbol{H}} \cdot \langle\boldsymbol{\mu}\rangle_{\widetilde{\mathcal{B}}} \cdot \Delta\overline{\boldsymbol{H}} \\ &+ \delta\overline{\underline{\boldsymbol{F}}} : \left\langle \mathbb{A} : \frac{\partial\hat{\underline{\boldsymbol{F}}}}{\partial\overline{\underline{\boldsymbol{F}}}} - \mathbf{q}^{\mathrm{T}} \cdot \frac{\partial\hat{\boldsymbol{H}}}{\partial\overline{\underline{\boldsymbol{F}}}} \right\rangle_{\widetilde{\mathcal{B}}} : \Delta\overline{\underline{\boldsymbol{F}}} + \delta\overline{\underline{\boldsymbol{F}}} : \left\langle \mathbb{A} : \frac{\partial\hat{\underline{\boldsymbol{F}}}}{\partial\overline{\boldsymbol{H}}} - \mathbf{q}^{\mathrm{T}} \cdot \frac{\partial\hat{\boldsymbol{H}}}{\partial\overline{\boldsymbol{H}}} \right\rangle_{\widetilde{\mathcal{B}}} \cdot \Delta\overline{\boldsymbol{H}} \\ &- \delta\overline{\boldsymbol{H}} \cdot \left\langle \mathbf{q} : \frac{\partial\hat{\underline{\boldsymbol{F}}}}{\partial\overline{\underline{\boldsymbol{F}}}} + \boldsymbol{\mu} \cdot \frac{\partial\hat{\boldsymbol{H}}}{\partial\overline{\underline{\boldsymbol{F}}}} \right\rangle_{\widetilde{\mathcal{B}}} : \Delta\overline{\underline{\boldsymbol{F}}} - \delta\overline{\boldsymbol{H}} \cdot \left\langle \mathbf{q} : \frac{\partial\hat{\underline{\boldsymbol{F}}}}{\partial\overline{\boldsymbol{H}}} + \boldsymbol{\mu} \cdot \frac{\partial\hat{\boldsymbol{H}}}{\partial\overline{\boldsymbol{H}}} \right\rangle_{\widetilde{\mathcal{B}}} \cdot \Delta\overline{\boldsymbol{H}}. \end{aligned} \tag{7.39}$$

It is important to note that the derivatives $\partial\{\hat{\underline{\boldsymbol{F}}}, \hat{\boldsymbol{H}}\}/\partial\{\overline{\underline{\boldsymbol{F}}}, \overline{\boldsymbol{H}}\}$ are nontrivial since they involve the sensitivities of solutions $\{\hat{\varphi}, \hat{\phi}^{\mathrm{m}}\}$ to (7.29) with respect to the "inputs" $\{\overline{\underline{\boldsymbol{F}}}, \overline{\boldsymbol{H}}\}$. These sensitivities can be computed as follows: Linearization of the micro-equilibrium condition $\delta\langle\Psi\rangle_{\widetilde{\mathcal{B}}} = 0$ at a micro-equilibrium point where $\langle\Psi\rangle_{\widetilde{\mathcal{B}}} = \overline{\Psi}$ yields

$$\begin{aligned}\Delta\delta\overline{\Psi} = \Bigg\langle &\frac{\partial\delta\widetilde{\varphi}}{\partial\widetilde{\boldsymbol{X}}} : \mathbb{A} : \left(\frac{\partial\Delta\hat{\varphi}}{\partial\widetilde{\boldsymbol{X}}} + \Delta\overline{\underline{\boldsymbol{F}}}\right) - \frac{\partial\delta\widetilde{\varphi}}{\partial\widetilde{\boldsymbol{X}}} : \mathbf{q}^{\mathrm{T}} \cdot \left(-\frac{\partial\Delta\hat{\phi}^{\mathrm{m}}}{\partial\widetilde{\boldsymbol{X}}} + \Delta\overline{\boldsymbol{H}}\right) \\ &+ \frac{\partial\delta\widetilde{\phi}^{\mathrm{m}}}{\partial\widetilde{\boldsymbol{X}}} \cdot \mathbf{q} : \left(\frac{\partial\Delta\hat{\varphi}}{\partial\widetilde{\boldsymbol{X}}} + \Delta\overline{\underline{\boldsymbol{F}}}\right) + \frac{\partial\delta\widetilde{\phi}^{\mathrm{m}}}{\partial\widetilde{\boldsymbol{X}}} \cdot \boldsymbol{\mu} \cdot \left(-\frac{\partial\Delta\hat{\phi}^{\mathrm{m}}}{\partial\widetilde{\boldsymbol{X}}} + \Delta\overline{\boldsymbol{H}}\right)\Bigg\rangle_{\widetilde{\mathcal{B}}} \\ = 0. \end{aligned} \tag{7.40}$$

We rearrange this equation into the form $\widetilde{\Delta}\delta\overline{\Psi} = -\overline{\Delta}\delta\overline{\Psi}$

$$\left\langle \left(\frac{\partial \delta\widetilde{\varphi}}{\partial \widetilde{\boldsymbol{X}}} : \mathbb{A} + \frac{\partial \delta\widetilde{\phi}^{\mathrm{m}}}{\partial \widetilde{\boldsymbol{X}}} \cdot \mathbf{q} \right) : \frac{\partial \Delta\hat{\widetilde{\varphi}}}{\partial \widetilde{\boldsymbol{X}}} \right\rangle_{\widetilde{\mathcal{B}}} + \left\langle \left(\frac{\partial \delta\widetilde{\varphi}}{\partial \widetilde{\boldsymbol{X}}} : \mathbf{q}^{\mathrm{T}} - \frac{\partial \delta\widetilde{\phi}^{\mathrm{m}}}{\partial \widetilde{\boldsymbol{X}}} \cdot \boldsymbol{\mu} \right) \cdot \frac{\partial \Delta\hat{\widetilde{\phi}}^{\mathrm{m}}}{\partial \widetilde{\boldsymbol{X}}} \right\rangle_{\widetilde{\mathcal{B}}} =$$
$$- \left\langle \frac{\partial \delta\widetilde{\varphi}}{\partial \widetilde{\boldsymbol{X}}} : \mathbb{A} + \frac{\partial \delta\widetilde{\phi}^{\mathrm{m}}}{\partial \widetilde{\boldsymbol{X}}} \cdot \mathbf{q} \right\rangle_{\widetilde{\mathcal{B}}} : \Delta\underline{\overline{\boldsymbol{F}}} - \left\langle - \frac{\partial \delta\widetilde{\varphi}}{\partial \widetilde{\boldsymbol{X}}} : \mathbf{q}^{\mathrm{T}} + \frac{\partial \delta\widetilde{\phi}^{\mathrm{m}}}{\partial \widetilde{\boldsymbol{X}}} \cdot \boldsymbol{\mu} \right\rangle_{\widetilde{\mathcal{B}}} \cdot \Delta\overline{\boldsymbol{H}}, \tag{7.41}$$

which represents a linear system for the micro-equilibrium perturbations $\{\Delta\hat{\widetilde{\varphi}}, \Delta\hat{\widetilde{\phi}}^{\mathrm{m}}\}$ in terms of macro-perturbations $\{\Delta\underline{\overline{\boldsymbol{F}}}, \Delta\overline{\boldsymbol{H}}\}$.

7.1.5. Finite element discretization for the macroscopic setting

The spatial domain to be discretized is Ω, which of course includes $\mathcal{B}$. Since we will not employ techniques such as "infinite elements" or boundary element methods (Chen and Konrad, 1997; Vu and Steinmann, 2010, 2012) that would allows us to consider all of $\mathbb{R}^3$ as computational domain, we just consider a finite domain Ω_h together with appropriate boundary conditions on $\partial\Omega_h$. For the discrete vacuum domain $\mathcal{B}'_h$ we do not have to consider separate scales. From an implementation perspective $\mathcal{B}'_h$ is part of the macroscopic boundary value problem. Thus the primary fields to be discretized in Ω_h are simply the fields (7.12) belonging to spaces specified in (7.14). Within the discretized MRE body $\mathcal{B}_h$ we consider[9] $\langle\varphi\rangle_{\widetilde{\mathcal{B}}} = \overline{\varphi}(\overline{X})$ and $\langle\phi^{\mathrm{m}}\rangle_{\widetilde{\mathcal{B}}} = \overline{\phi}^{\mathrm{m}}(\overline{X})$ as primary macroscopic fields, also belonging to the spaces $\mathscr{W}_{\varphi}$ and $\mathscr{W}_{\phi^{\mathrm{m}}}$. These spaces will be discretized in terms of triangular Lagrange elements of polynomial degree two.

For notational convenience we denote macroscopic quantities $\overline{(\bullet)}$ in $\mathcal{B}$ with un-annotated ones $(\bullet)$ in $\overline{\mathcal{B}}$, e.g. $\overline{\varphi}(\overline{X})$ in $\mathcal{B} \Leftrightarrow \varphi(X)$ in $\overline{\mathcal{B}}$.[10] Furthermore, we introduce the following abstract FEM matrix notation for discrete primary fields $\varphi_h(X)$ and $\phi_h^{\mathrm{m}}(X)$:

$$\varphi_h(X) = \underline{\mathbf{N}}(X) \cdot \underline{\mathbf{d}} \quad \Leftrightarrow \quad \varphi_h^{\mathrm{e}}(X) = \underline{\mathbf{N}}^{\mathrm{e}}(X) \cdot \underline{\mathbf{d}}, \tag{7.42a}$$
$$\operatorname{Grad}\varphi_h(X) = \underline{\mathbf{B}}(X) \cdot \underline{\mathbf{d}} \quad \Leftrightarrow \quad \operatorname{Grad}\varphi_h^{\mathrm{e}}(X) = \underline{\mathbf{B}}^{\mathrm{e}}(X) \cdot \underline{\mathbf{d}}, \tag{7.42b}$$
$$\phi_h^{\mathrm{m}}(X) = \underline{\mathrm{N}}(X) \cdot \underline{\mathbf{d}} \quad \Leftrightarrow \quad \phi_h^{\mathrm{m,e}}(X) = \underline{\mathrm{N}}^{\mathrm{e}}(X) \cdot \underline{\mathbf{d}}, \tag{7.42c}$$
$$\operatorname{Grad}\phi_h^{\mathrm{m}}(X) = \underline{\mathrm{B}}(X) \cdot \underline{\mathbf{d}} \quad \Leftrightarrow \quad \operatorname{Grad}\phi_h^{\mathrm{m,e}}(X) = \underline{\mathrm{B}}^{\mathrm{e}}(X) \cdot \underline{\mathbf{d}}. \tag{7.42d}$$

In above equation $\underline{\mathbf{d}}$ is the global array of discrete degrees of freedom, $\underline{\mathbf{N}}$ and $\underline{\mathrm{N}}$ denote appropriate matrices of shape functions at X; $\underline{\mathbf{B}}$ and $\underline{\mathrm{B}}$ are the corresponding derivatives. A superscript "e" indicates a restriction to a specific element. The spaces for the discretized primary fields φ_h and ϕ_h^{m} are denoted as $\mathscr{W}_{\varphi,h}$ and $\mathscr{W}_{\phi^{\mathrm{m}},h}$ which are restrictions of $\mathscr{W}_{\varphi}$ and $\mathscr{W}_{\phi^{\mathrm{m}}}$ (see (7.14)) to piecewise quadratic polynomials on the meshed domain Ω_h. It follows that the discrete degrees of freedom $\underline{\mathbf{d}}$ have to be adjusted such

[9] Here the overlines remind us that domain $\mathcal{B}$ is treated in a special way, i.e. by homogenization.

[10] This twist reflects the fact, that from an implementation point of view, the routines serving the homogenized material properties should have the same interface as standard material routines. The homogenization procedure should be hidden from the macroscopic FEM solver.

that the essential boundary conditions specified by $\mathscr{W}_{\varphi}$ and $\mathscr{W}_{\phi^{\mathrm{m}}}$ are fulfilled. Moreover, we have

$$\underline{\boldsymbol{F}}_h = \operatorname{Grad} \varphi_h, \qquad \delta\underline{\boldsymbol{F}}_h = \operatorname{Grad} \delta\varphi_h, \tag{7.43a}$$

$$\boldsymbol{H}_h = -\operatorname{Grad} \phi_h^{\mathrm{m}}, \qquad \delta\boldsymbol{H}_h = -\operatorname{Grad} \delta\phi_h^{\mathrm{m}}. \tag{7.43b}$$

Based on that we write the discrete macroscopic BVP in equilibrium form

$$\delta\Pi_h = \delta\underline{\mathbf{d}} \cdot \left(\underline{\mathbf{R}}^{\mathrm{int}} + \underline{\mathbf{R}}^{\mathrm{ext}}\right) = \delta\underline{\mathbf{d}} \cdot \underline{\mathbf{R}} = 0, \tag{7.44}$$

with

$$\underline{\mathbf{R}}^{\mathrm{int}} = \sum_{e\in\mathcal{I}(\overline{\mathcal{B}}_h)} \int_{\overline{\mathcal{B}}_h^{\mathrm{e}}} \underline{\boldsymbol{P}} : \underline{\mathbf{B}}^{\mathrm{e}} + \boldsymbol{B} \cdot \underline{\mathbb{B}}^{\mathrm{e}}\, dV + \sum_{e\in\mathcal{I}(\mathcal{B}'_h)} \int_{\mathcal{B}_h^{\infty,e}} \underline{\boldsymbol{P}} : \underline{\mathbf{B}}^{\mathrm{e}} + \boldsymbol{B} \cdot \underline{\mathbb{B}}^{\mathrm{e}}\, dV \quad \text{and} \tag{7.45a}$$

$$\underline{\mathbf{R}}^{\mathrm{ext}} = \sum_{e\in\mathcal{I}(\overline{\mathcal{B}}_h)} \int_{\partial\overline{\mathcal{B}}_h^{\mathrm{e}}\cap\partial\overline{\mathcal{B}}_h} -\frac{\partial\mathcal{P}^t}{\partial\varphi} \cdot \underline{\mathbf{N}}^{\mathrm{e}}\, dA + \sum_{e\in\mathcal{I}(\mathcal{B}'_h)} \int_{\partial\mathcal{B}_h^{\infty,e}\cap\partial\Omega_h} -\frac{\partial\mathcal{P}^b}{\partial\phi^{\mathrm{m}}} \underline{\mathbb{N}}^{\mathrm{e}}\, dA. \tag{7.45b}$$

Obviously, the integrands of both integrals in $\underline{\mathbf{R}}^{\mathrm{int}}$ only differ in the material laws used to compute $\underline{\boldsymbol{P}}$ and $\boldsymbol{B}$. Since $\underline{\boldsymbol{P}} = \underline{\boldsymbol{P}}(\underline{\boldsymbol{F}}, \boldsymbol{H})$ and $\boldsymbol{B} = \boldsymbol{B}(\underline{\boldsymbol{F}}, \boldsymbol{H})$ are in general nonlinear relations, (7.44) is a nonlinear equation in $\underline{\mathbf{d}}$. Its taylor expansion up to first order at state $\underline{\mathbf{d}}^{[n]}$ is obtained as

$$0 = \delta\Pi_h(\underline{\mathbf{d}}^{[n]}) + \Delta\delta\Pi_h(\underline{\mathbf{d}}^{[n]}) = \delta\underline{\mathbf{d}} \cdot \underline{\mathbf{R}}(\underline{\mathbf{d}}^{[n]}) + \delta\underline{\mathbf{d}} \cdot \left(\underline{\mathbf{K}}(\underline{\mathbf{d}}^{[n]}) \cdot \Delta\underline{\mathbf{d}}\right), \tag{7.46}$$

with $\underline{\mathbf{K}}$ being the linearization of $\underline{\mathbf{R}}^{\mathrm{int}}$ (tacitly assuming that $\underline{\mathbf{R}}^{\mathrm{ext}}$ does not depend on $\underline{\mathbf{d}}$)

$$\underline{\mathbf{K}} = \sum_{e\in\mathcal{I}(\overline{\mathcal{B}}_h)} \int_{\overline{\mathcal{B}}_h^{\mathrm{e}}} \underline{\mathbf{B}}^{\mathrm{e}} : \left(\mathbb{A} : \underline{\mathbf{B}}^{\mathrm{e}} + \mathbf{q}^{\mathrm{T}} \cdot \underline{\mathbb{B}}^{\mathrm{e}}\right) + \underline{\mathbb{B}}^{\mathrm{e}} \cdot \left(\mathbf{q} : \underline{\mathbf{B}}^{\mathrm{e}} - \boldsymbol{\mu} \cdot \underline{\mathbb{B}}^{\mathrm{e}}\right) dV + \sum_{e\in\mathcal{I}(\mathcal{B}'_h)} \int_{\mathcal{B}_h^{\infty,e}} \underline{\mathbf{B}}^{\mathrm{e}} : \left(\mathbb{A} : \underline{\mathbf{B}}^{\mathrm{e}} + \mathbf{q}^{\mathrm{T}} \cdot \underline{\mathbb{B}}^{\mathrm{e}}\right) + \underline{\mathbb{B}}^{\mathrm{e}} \cdot \left(\mathbf{q} : \underline{\mathbf{B}}^{\mathrm{e}} - \boldsymbol{\mu} \cdot \underline{\mathbb{B}}^{\mathrm{e}}\right) dV. \tag{7.47}$$

For arbitrary $\delta\underline{\mathbf{d}}$ (7.46) we have the linearized system of equations at state $\underline{\mathbf{d}}^{[n]}$

$$\underline{\mathbf{K}}(\underline{\mathbf{d}}^{[n]}) \cdot \Delta\underline{\mathbf{d}} = -\underline{\mathbf{R}}(\underline{\mathbf{d}}^{[n]}), \tag{7.48}$$

of which we denote the solution as $\Delta\underline{\mathbf{d}}^{[n]}$. A new state is obtained as $\underline{\mathbf{d}}^{[n+1]} = \underline{\mathbf{d}}^{[n]} + \Delta\underline{\mathbf{d}}^{[n]}$. Repeated solution of (7.48) and state updates render the well-known Newton-Raphson procedure, by which we may obtain an equilibrium state $\hat{\underline{\mathbf{d}}}$.

7.1.6. Finite element discretization for the microscopic setting

On the microscale we employ the same type of finite element shape functions as for the macroscopic BVP. However, now the "fluctuations" $\widetilde{\varphi} \in \mathscr{W}_{\widetilde{\varphi},h}$ and $\widetilde{\phi}^{\mathrm{m}} \in \mathscr{W}_{\widetilde{\phi}^{\mathrm{m}},h}$ subject to periodic boundary conditions[11] are employed as discrete primary fields. In the present context the macroscopic coordinate $\overline{X}$ does not play a role for the microscopic BVP which thus can be completely specified in coordinates $\widetilde{\boldsymbol{X}} = X - \overline{X}$. We have

$$\widetilde{\varphi}_h(\widetilde{\boldsymbol{X}}) = \underline{\mathbf{N}}(\widetilde{\boldsymbol{X}}) \cdot \underline{\tilde{\mathbf{d}}} \quad \Leftrightarrow \quad \widetilde{\varphi}^{\mathrm{e}}_h(\widetilde{\boldsymbol{X}}) = \underline{\mathbf{N}}^{\mathrm{e}}(\widetilde{\boldsymbol{X}}) \cdot \underline{\tilde{\mathbf{d}}}, \tag{7.49a}$$

$$\operatorname{Grad} \widetilde{\varphi}_h(\widetilde{\boldsymbol{X}}) = \underline{\mathbf{B}}(\widetilde{\boldsymbol{X}}) \cdot \underline{\tilde{\mathbf{d}}} \quad \Leftrightarrow \quad \operatorname{Grad} \widetilde{\varphi}^{\mathrm{e}}_h(\widetilde{\boldsymbol{X}}) = \underline{\mathbf{B}}^{\mathrm{e}}(\widetilde{\boldsymbol{X}}) \cdot \underline{\tilde{\mathbf{d}}}, \tag{7.49b}$$

$$\widetilde{\phi}^{\mathrm{m}}_h(\widetilde{\boldsymbol{X}}) = \underline{\mathrm{N}}(\widetilde{\boldsymbol{X}}) \cdot \underline{\tilde{\mathbf{d}}} \quad \Leftrightarrow \quad \widetilde{\phi}^{\mathrm{m,e}}_h(\widetilde{\boldsymbol{X}}) = \underline{\mathrm{N}}^{\mathrm{e}}(\widetilde{\boldsymbol{X}}) \cdot \underline{\tilde{\mathbf{d}}}, \tag{7.49c}$$

$$\operatorname{Grad} \widetilde{\phi}^{\mathrm{m}}_h(\widetilde{\boldsymbol{X}}) = \underline{\mathrm{B}}(\widetilde{\boldsymbol{X}}) \cdot \underline{\tilde{\mathbf{d}}} \quad \Leftrightarrow \quad \operatorname{Grad} \widetilde{\phi}^{\mathrm{m,e}}_h(\widetilde{\boldsymbol{X}}) = \underline{\mathrm{B}}^{\mathrm{e}}(\widetilde{\boldsymbol{X}}) \cdot \underline{\tilde{\mathbf{d}}} \tag{7.49d}$$

and consequently, with $\underline{\overline{\boldsymbol{F}}}$ and $\overline{\boldsymbol{H}}$ regarded as mere inputs to the BVP,

$$\underline{\boldsymbol{F}}_h(\widetilde{\boldsymbol{X}}) = \underline{\overline{\boldsymbol{F}}} + \underline{\widetilde{\boldsymbol{F}}}_h = \underline{\overline{\boldsymbol{F}}} + \operatorname{Grad} \widetilde{\varphi}_h, \qquad \delta\underline{\widetilde{\boldsymbol{F}}}_h(\widetilde{\boldsymbol{X}}) = \operatorname{Grad} \delta\widetilde{\varphi}_h, \tag{7.50a}$$

$$\boldsymbol{H}_h(\widetilde{\boldsymbol{X}}) = \overline{\boldsymbol{H}} + \widetilde{\boldsymbol{H}}_h = \overline{\boldsymbol{H}} - \operatorname{Grad} \widetilde{\phi}^{\mathrm{m}}_h, \qquad \delta\widetilde{\boldsymbol{H}}_h(\widetilde{\boldsymbol{X}}) = -\operatorname{Grad} \delta\widetilde{\phi}^{\mathrm{m}}_h. \tag{7.50b}$$

Based on the equations right above, the discrete version of the micro-equilibrium equation (7.31b) is

$$\tilde{\delta} \langle \Psi \rangle_{\widetilde{\mathcal{B}}} = \delta\underline{\tilde{\mathbf{d}}} \cdot \underline{\tilde{\mathbf{r}}} = 0, \tag{7.51}$$

with

$$\underline{\tilde{\mathbf{r}}} = \frac{1}{|\widetilde{\mathcal{B}}|} \sum_e \int_{\widetilde{\mathcal{B}}^{\mathrm{e}}[\overline{X}]} \underline{\boldsymbol{P}}(\underline{\boldsymbol{F}}_h, \boldsymbol{H}_h) : \underline{\mathbf{B}}^{\mathrm{e}} + \boldsymbol{B}(\underline{\boldsymbol{F}}_h, \boldsymbol{H}_h) \cdot \underline{\mathrm{B}}^{\mathrm{e}} \, dV. \tag{7.52}$$

Following a similar route as in Section 7.1.5 for the linearization of (7.51), we arrive at

$$0 = \tilde{\delta} \left\langle \Psi(\underline{\tilde{\mathbf{d}}}^{[n]}) \right\rangle_{\widetilde{\mathcal{B}}} + \widetilde{\Delta}\tilde{\delta} \left\langle \Psi(\underline{\tilde{\mathbf{d}}}^{[n]}) \right\rangle_{\widetilde{\mathcal{B}}} = \delta\underline{\tilde{\mathbf{d}}} \cdot \underline{\tilde{\mathbf{r}}}(\underline{\tilde{\mathbf{d}}}^{[n]}) + \delta\underline{\tilde{\mathbf{d}}} \cdot \left(\underline{\tilde{\mathbf{k}}}(\underline{\tilde{\mathbf{d}}}^{[n]}) \cdot \Delta\underline{\tilde{\mathbf{d}}} \right), \tag{7.53}$$

with

$$\underline{\tilde{\mathbf{k}}} = \frac{1}{|\widetilde{\mathcal{B}}|} \sum_e \int_{\widetilde{\mathcal{B}}^{\mathrm{e}}[\overline{X}]} \underline{\mathbf{B}}^{\mathrm{e}} : \left(\mathbb{A} : \underline{\mathbf{B}}^{\mathrm{e}} + \mathbf{q}^{\mathrm{T}} \cdot \underline{\mathrm{B}}^{\mathrm{e}} \right) + \underline{\mathrm{B}}^{\mathrm{e}} \cdot \left(\mathbf{q} : \underline{\mathbf{B}}^{\mathrm{e}} - \boldsymbol{\mu} \cdot \underline{\mathrm{B}}^{\mathrm{e}} \right) dV. \tag{7.54}$$

The resulting linearized system at the heart of a Newton scheme is then

$$\underline{\tilde{\mathbf{k}}}(\underline{\tilde{\mathbf{d}}}^{[n]}) \cdot \Delta\underline{\tilde{\mathbf{d}}} = -\underline{\tilde{\mathbf{r}}}(\underline{\tilde{\mathbf{d}}}^{[n]}). \tag{7.55}$$

Next we come back to the micro-macro sensitivity relation (7.41). In the discrete set-

[11] For an in-depth study of boundary conditions at the microscale we refer to Zabihyan et al. (2018)

ting, this equations becomes

$$\delta\underline{\tilde{\mathbf{d}}} \cdot \left(\underline{\mathbf{k}}(\underline{\hat{\tilde{\mathbf{d}}}}) \cdot \Delta\underline{\tilde{\mathbf{d}}}\right) = -\delta\underline{\tilde{\mathbf{d}}} \cdot \left(\underline{\mathbf{L}}(\underline{\hat{\tilde{\mathbf{d}}}}) \cdot \Delta\underline{\overline{\mathbf{g}}}\right), \tag{7.56}$$

where $\underline{\hat{\tilde{\mathbf{d}}}}$ denotes a solution of (7.51) and $(\Delta)\underline{\overline{\mathbf{g}}}$ represents the one-dimensional array collecting the values of $(\Delta)\{\overline{\boldsymbol{F}}, \overline{\boldsymbol{H}}\}$. The matrix $\underline{\mathbf{L}}(\underline{\hat{\tilde{\mathbf{d}}}})$ is given as

$$\underline{\mathbf{L}} = \frac{1}{|\widetilde{\mathcal{B}}|} \sum_e \int_{\widetilde{\mathcal{B}}^e[\overline{X}]} \underline{\mathbf{B}}^e : \left(\mathbb{A}(\underline{\hat{\tilde{\mathbf{d}}}}) : \underline{\mathbf{D}} + \mathbf{q}^{\mathrm{T}}(\underline{\hat{\tilde{\mathbf{d}}}}) \cdot \underline{\mathsf{D}}\right) + \underline{\mathsf{B}}^e \cdot \left(\mathbf{q}(\underline{\hat{\tilde{\mathbf{d}}}}) : \underline{\mathbf{D}} - \boldsymbol{\mu}(\underline{\hat{\tilde{\mathbf{d}}}}) \cdot \underline{\mathsf{D}}\right) dV. \tag{7.57}$$

wherein $\underline{\mathbf{d}}$ and $\underline{\mathsf{D}}$ are defined such that

$$\overline{\boldsymbol{F}} = \underline{\mathbf{d}} \cdot \underline{\overline{\mathbf{g}}} \quad \text{and} \quad \overline{\boldsymbol{H}} = -\underline{\mathsf{D}} \cdot \underline{\overline{\mathbf{g}}}. \tag{7.58}$$

From (7.56) we eventually obtain the *discrete* micro-macro sensitivities[12]

$$\frac{\Delta\underline{\tilde{\mathbf{d}}}}{\Delta\underline{\overline{\mathbf{g}}}} = \left(\left\langle \underline{\mathbf{k}}(\underline{\hat{\tilde{\mathbf{d}}}}) \right\rangle_{\widetilde{\mathcal{B}}}\right)^{-1} \cdot \left(\underline{\mathbf{L}} \cdot \underline{\hat{\tilde{\mathbf{d}}}}\right). \tag{7.59}$$

The matrix $\underline{\mathbf{L}}$ can be regarded as a tuple of column vectors $\underline{\mathsf{L}}_{\mathrm{i}}$ such that the left-hand-side of (7.59) is the tuple of solution vectors $\frac{\Delta\underline{\tilde{\mathbf{d}}}}{\Delta\underline{\overline{\mathbf{g}}}_{\mathrm{i}}}$ to the linear systems $\langle \underline{\mathbf{k}} \rangle_{\widetilde{\mathcal{B}}} \cdot \frac{\Delta\underline{\tilde{\mathbf{d}}}}{\Delta\underline{\overline{\mathbf{g}}}_{\mathrm{i}}} = \underline{\mathsf{L}}_{\mathrm{i}}$. This is the perspective on which we based our implementation. Finally we arrive at the discrete version of (7.36) based on the effective energy density $\overline{\Psi}$

$$\overline{\delta\Delta\Psi} = \delta\underline{\overline{\mathbf{g}}} \cdot \underbrace{\left[\left\langle \frac{\partial^2\Psi}{\partial\underline{\overline{\mathbf{g}}}\,\partial\underline{\overline{\mathbf{g}}}} \right\rangle_{\widetilde{\mathcal{B}}} + \underline{\mathbf{L}}^{\mathrm{T}} \cdot \left(\langle \underline{\mathbf{k}} \rangle_{\widetilde{\mathcal{B}}}\right)^{-1} \cdot \underline{\mathbf{L}}\right]}_{\underline{\overline{\mathbf{k}}}} \cdot \Delta\underline{\overline{\mathbf{g}}}. \tag{7.60}$$

Remember that from a macroscopic point of view, the equation above is at a point $\overline{X}$. Thus, the matrix $\underline{\overline{\mathbf{k}}}$ is the linearized material response at a macroscopic point and thus should not be confused with the "stiffness" matrix of a finite element. Similarly, in (7.60) $\delta\underline{\overline{\mathbf{g}}}$ and $\Delta\underline{\overline{\mathbf{g}}}$ only represent the tuples of variations and increments, respectively, of $\{\overline{\boldsymbol{F}}, \overline{\boldsymbol{H}}\}$ at $\overline{X}$.

[12] The sensitivities for the continuous setting are discussed in Sections 5.4.1 and 7.1.4.

7.2. The magneto-mechanical response of a square magnetorheological elastomer specimen

In what follows we study the response of a square-shaped MRE specimen under magnetic and magneto-mechanical loading in two spatial dimensions. Besides investigations of different loading conditions we also vary the volume fraction of magnetic inclusions as well as the alignment of the orthotropic microstructure in the initial configuration. The results presented in this section have been published in (Keip and Rambausek, 2016).

7.2.1. Material models

The free-energy density present in (7.15) describes the local properties of the material under consideration. On the macroscopic scale we need a description for the material behavior of the MRE, which is provided by the homogenization procedure described in Section 7.1.4. In addition, we have to employ a material model with magnetic properties of vacuum. The mechanical properties of this free-space "material" are chosen such that the free space does not exert significant mechanical tractions on the body in response to deformation. On the microscale we model the elastomer matrix as a perfectly elastic, non-magnetic and almost incompressible material. The inclusions are modeled by a linear magnetic material and are furthermore mechanically very stiff compared to the matrix. We employ a free-energy density of the form (Javili et al., 2013)

$$\begin{aligned}\widehat{\Psi}(\underline{\boldsymbol{F}}, \boldsymbol{H}) = \frac{1}{2}\mu(\boldsymbol{C} - 3) + \frac{\lambda}{4}\left(J^2 - 1\right) - \left(\frac{\lambda}{2} + \mu\right)\ln J \\ - \frac{1}{2}\mu_0\left(1 + \frac{\chi^{\mathrm{m}}}{J}\right) J\left[\boldsymbol{C}^{-1} : (\boldsymbol{H} \otimes \boldsymbol{H})\right],\end{aligned} \tag{7.61}$$

with $\boldsymbol{C} = \underline{\boldsymbol{F}}^{\mathrm{T}} \cdot \underline{\boldsymbol{F}}$ and $J = \det \underline{\boldsymbol{F}}$. The parameters μ and λ are the classical Lamé parameters and χ^{m} denotes the magnetic susceptibility. The basically same energy-density is a common model for electro-elastic materials (see, e.g., Keip et al. (2014)) where the magnetic quantities are of course replaced by their electric counterparts.

The vacuum permeability is $\mu_0 = 4\pi \times 10^{-1}\,\mu\mathrm{N/A}^2$. The material-specific parameters are summarized in Table 7.1. The parameters for the matrix correspond to $E = 0.2\,\mathrm{MPa}$ and $\nu = 0.499$, those for the inclusion give $E = 200\,\mathrm{MPa}$ and $\nu = 0.3$.

Table 7.1: Material parameters on both scales

Material	λ / MPa	μ / MPa	χ^{m} / 1
Matrix	33.289	0.067	0.000
Inclusion	115.385	76.923	100.000
Free space	0.000	0.001	0.000

7.2.2. Spatial discretization of the magnetorheological elastomer specimen and the free-space domain

The spatial discretizations on both scales are depicted in Figure 7.4.

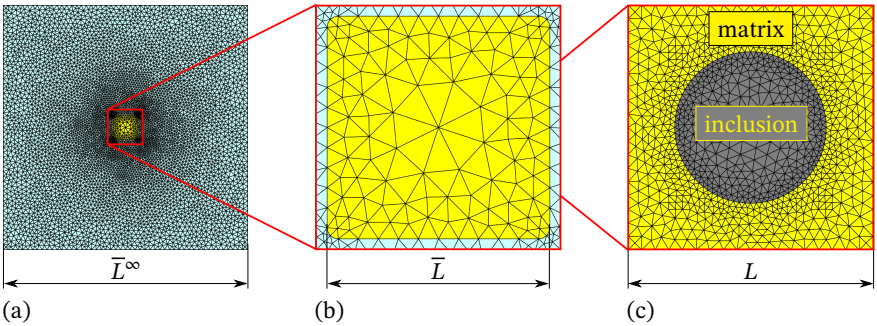

Figure 7.4: The full macroscopic domain is shown in (a). In (b) we present a zoomed view of the MRE specimen. Subplot (c) we depicts the a sample microstructure discretization with an inclusion volume fraction of 30 % (Keip and Rambausek, 2016).

The finite elements shown are of isoparametric Lagrange type with polynomial degree two. We employ three Gauß points per element for quadrature. Numerical tests confirmed that this number leads to sufficient accuracy. The macroscopic mesh consists of roughly 12 000 elements, of which *231* are for the MRE body. The size of the free-space box $L^{\infty} = 200\,\mathrm{mm}$, which is ten times bigger than the dimension $L = 20\,\mathrm{mm}$ of the MRE body. The corners of the MRE are rounded with $R = 1\,\mathrm{mm}$. On the microscale we have about 2000 elements, depending on the volume fraction of the inclusion. The length of the unit cell depicted in Figure 7.4 is in the order of[13] $\tilde{L} \approx 10\,\mu\mathrm{m}$. In the present chapter we use the unit cell of the microstructural material pattern as $\mathcal{RVE}$. This greatly reduces the numerical effort at a certain cost: we exclude phenomena, e.g. deformation patterns, with wavelength greater than a single unit cell. The (numerical) determination of the minimal $\mathcal{RVE}$ that captures all relevant wavelengths is one major topic of multiscale stability analysis. We refer to Kankanala and Triantafyllidis (2008), Rudykh and Bertoldi (2013), Miehe et al. (2016) and in particular the recent contribution of Polukhov et al. (2018) for further information.

7.2.3. Deformation in response to a homogeneous external magnetic field

Below we characterize the deformation response of the MRE body under consideration (see Sections 7.2.1 and 7.2.2 above). Figure 7.5a schematically depicts the specific

[13] Precise dimensions do not matter here because of the assumption of strict scale separation.

loading and boundary conditions for the body. On the macroscopic scale we vary the magnitude of the magnetic loading in terms of $h^\infty = \|\boldsymbol{h}^\infty\| \in [0, 0.6]\,\mathrm{MA\,m^{-1}}$. Besides that we consider microstructures with volume fractions $\widetilde{\mathcal{B}}^{\mathrm{inc}}/\widetilde{\mathcal{B}} = \mathfrak{v} \in \{10\,\%, 20\,\%, 30\,\%\}$ and orientations $\angle(\eta, X_2) = \gamma \in [0, \pi/4]$ as indicated in Figure 7.5b.

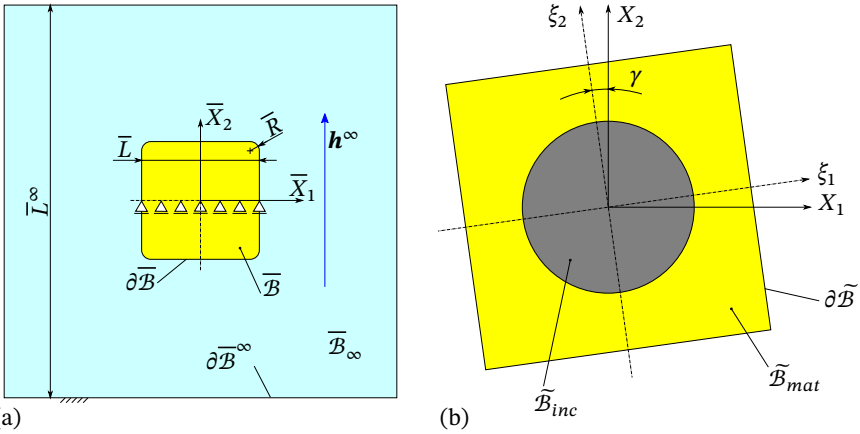

Figure 7.5: Macro(a)- and microscopic (b) setting for investigations of an MREs deformation response. The MRE specimen is prevented from rigid body rotations. These would be expected for microstructure orientations that are not symmetric with respect to $\{X\}$, which is itself of course aligned with $\{\overline{X}\}$ (Keip and Rambausek, 2016).

We measure the deformation in vertical direction in terms of the $\langle F_{22}\rangle_{\overline{\mathcal{B}}}$, i.e. the "22" component of the deformation gradient averaged over the MRE specimen. For a volume fraction of $\mathfrak{v} = 20\,\%$ we obtain the deformation responses depicted in Figure 7.6a.

We observe a nonlinear increase of the deformation magnitude with magnetic load. Depending on the microstructure orientation γ the deformation mode is either elongation (most pronounced for $\gamma = \pi/4$) or contraction (strongest for $\gamma = 0$) in direction of $\boldsymbol{h}^\infty$. Interestingly, for $\gamma = \pi/8$ there is almost no overall deformation in vertical direction for $h^\infty < 0.3\,\mathrm{MA\,m^{-1}}$. In this case, however, the shear deformation $\langle F_{12}\rangle_{\overline{\mathcal{B}}}$ is most pronounced, as visible in Figure 7.6b. To obtain an impression of the microstructural deformation Figure 7.7 plots the final deformed configuration of $\mathcal{RVE}$s with $\gamma \in \{0, \pi/8, \pi/4\}$. The influence of the volume fraction $\mathfrak{v}$ can be seen from Figure 7.8. As somewhat expected, a higher volume fraction leads to stronger deformation. This tendency, however, can not be extrapolated to very high volume fractions, because of the significant increase of the effective mechanical stiffness.

We close this study of the deformation response with a remark on the MRE-averages $\langle F_{12}\rangle_{\overline{\mathcal{B}}}$ and $\langle F_{22}\rangle_{\overline{\mathcal{B}}}$. For the MRE specimen under consideration we cannot expect uni-

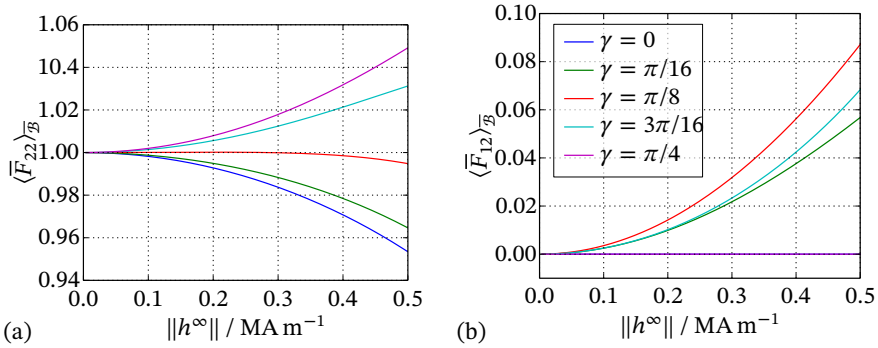

Figure 7.6: Deformation of an MRE specimen in terms of the averaged macroscopic deformation gradient in response to applied magnetic field. The volume fraction of magnetic inclusions is 20 %. For "symmetric" microstructure orientations $\gamma = \{0, \pi/4\}$ the deformation is dominated by contraction and elongation in field direction, respectively. For $\gamma = \pi/8$ one observes pronounced shear deformation of the specimen (Keip and Rambausek, 2016).

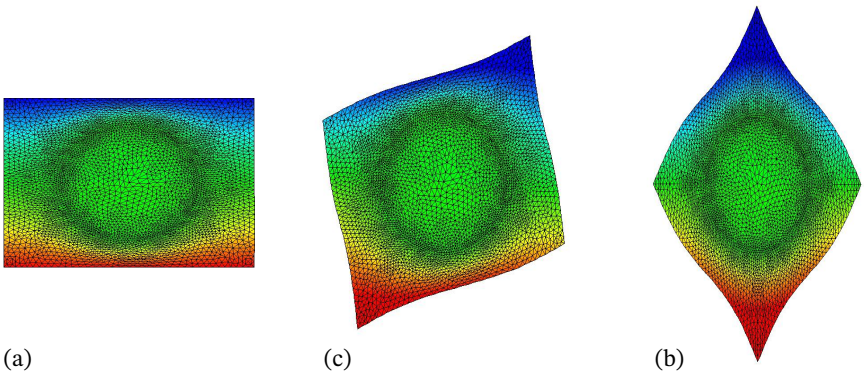

Figure 7.7: Deformed MRE microstructures with orientations (a) $\gamma = 0$, (b) $\gamma = \pi/8$ and (c) $\gamma = \pi/4$ (Keip and Rambausek, 2016).

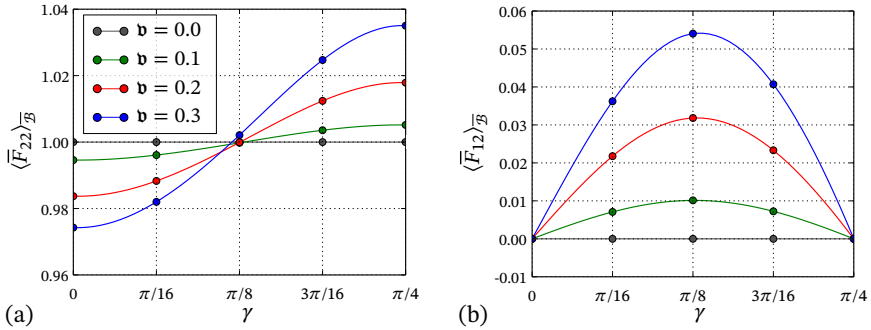

Figure 7.8: Deformation of an MRE specimen in terms of the averaged macroscopic deformation gradient in response to applied magnetic field. We compare different volume fraction $\mathfrak{v} \in \{0, 10, 20, 30\}\,\%$ at a magnetic load of $h^{\infty} = 0.5\,\mathrm{MA\,m^{-1}}$. As expected, for $\mathfrak{v} = 0$ (absence of magnetic inclusions) the deformation response vanishes (Keip and Rambausek, 2016).

form (effective) magnetization in response to the homogeneous external field[14] . Moreover, even if that would be the case the MRE would still exhibit a non-uniform deformation due to non-uniform magneto-mechanical tractions around the corners. Consequently it is notoriously problematic to characterize the MRE specimens' deformation by a single number. Figure 7.9 illustrates the inhomogeneity of the material state within the MRE domain $\mathcal{B}$.

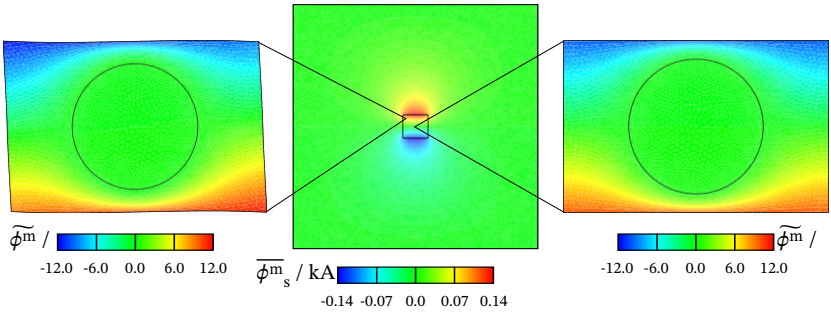

Figure 7.9: Magnetic self-potential of a deformed square MRE body and microstructures at selected points. Clearly, the magnetic self-field is non-uniform and so is the deformation as can be directly seen from the deformed microstructures (Keip and Rambausek, 2016).

We will come back to these issues in Section 7.3.

[14] It is known that this is only the case for elliptical and ellipsoidal bodies (Osborn, 1945).

7.2.4. Magnetic modulation of shear stiffness

Now we turn to another experimentally observable effect of practical relevance: the change of an MRE's stiffness under magnetic field, often referred to as "magnetorheological" effect and thus name-giving for MREs (Jolly et al., 1996). Resembling the experimental setting[15] of Danas et al. (2012) we "glue" rigid plates onto the top and the bottom edges of the MRE as depicted in Figure 7.10a.

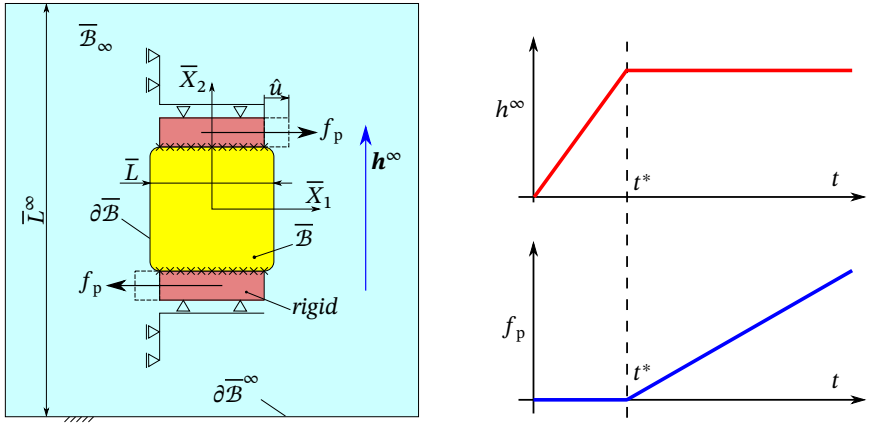

Figure 7.10: Deformation of an MRE in response to mechanical shear load under magnetic field. The overall setting is depicted in (a) whereas (b) shows the application of magnetic h^∞ and mechanical load f_p over time t (Keip and Rambausek, 2016).

In the simulations we first ramp up h^∞ to the desired magnitude (see Figure 7.10b. Then we keep the magnetic load fixed and ramp up the force f_p under which the plates can move in horizontal direction. The resulting displacement is denoted as $\hat{u}$ and the derivative $\mathrm{d}f_\mathrm{p}\,/\,\mathrm{d}\hat{u}$ is a measure for the shear stiffness.

The first study is concerned with an MRE microstructure with $\gamma = 0$ and volume fractions $\mathfrak{v} \in \{10\,,20\,,30\,\}\,\%$. In Figure 7.11a we show the displacement $\hat{u}$ plotted over applied force f_p for $\mathfrak{v} = 30\,\%$ and various magnetic loads h^∞. Figure 7.11b reports the initial stiffness, i.e. $\mathrm{d}f_\mathrm{p}\,/\,\mathrm{d}\hat{u}\big|_{\hat{u}=0}$. Obviously the initial stiffness increases under magnetic load.

Next we study the change of stiffness with increasing $\hat{u}$. A detailed plot for $\mathfrak{v} = 30\,\%$ is shown in Figure 7.12a. There we see that the graphs seem to converge such that one might imagine that they will intersect at some point. This also means that for the microstructure under consideration the stiffness increases with displacement $\hat{u}$ for low h^∞

[15] Despite the simulation give us access to a wide range of possible scenarios we believe that it is most valuable to contribute to the understanding of experiments, at least at the current state of research.

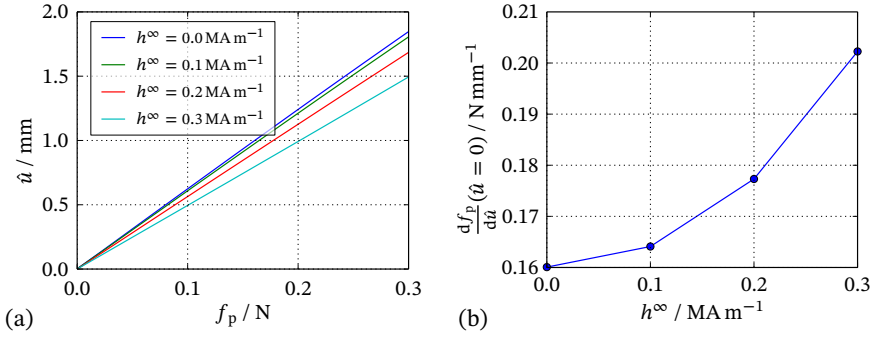

Figure 7.11: Shear stiffness of an MRE ($\mathfrak{v} = 30\,\%, \gamma = 0$) under magnetic load in terms of displacement over force (a) and initial force-displacement ratio (b). The stiffness clearly increases with the applied field.

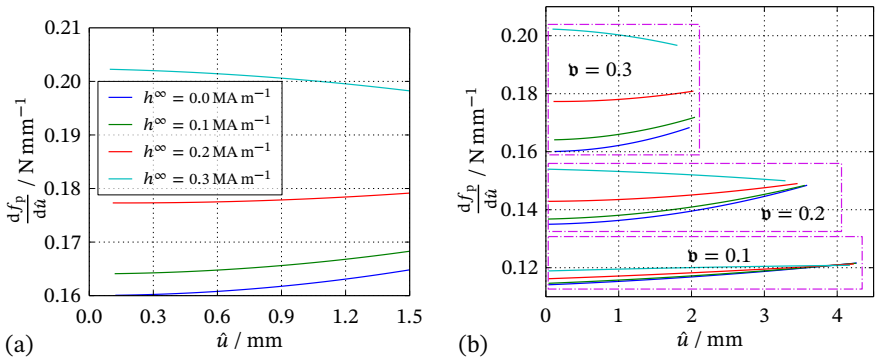

Figure 7.12: Change of stiffness of a MREs ($\gamma = 0$) under magnetic field at deformed states. Subplot (a) show a graph for an inclusion volume fraction of $\mathfrak{v} = 30\,\%$. In (b) we present the corresponding plots for $\mathfrak{v} \in \{10, 20, 30\}\,\%$.

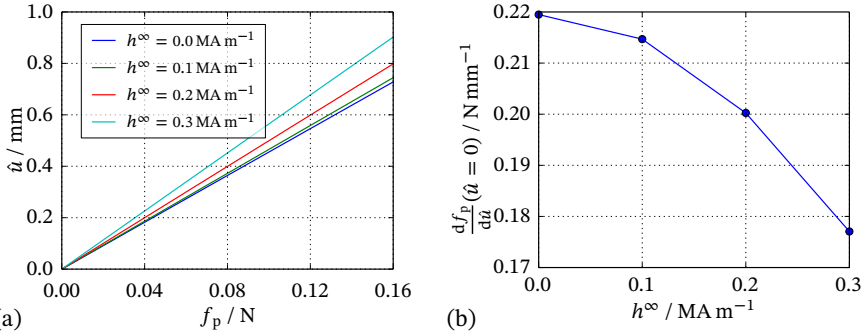

Figure 7.13: Shear stiffness of an MRE ($\mathfrak{v} = 30\,\%$, $\gamma = \pi/4$) under magnetic load in terms of displacement over force (a) and initial force-displacement ratio (b). By contrast to the MRE with $\gamma = 0$ the shear stiff decreases in the present case (Keip and Rambausek, 2016).

but exhibits the opposite tendency under high magnetic load. Figure 7.12b depicts the results for all volume fractions under consideration. There we indeed find intersecting graphs for $\mathfrak{v} = 10\,\%$.

Besides microstructures with $\gamma = 0$ we also studied the case of $\gamma = \pi/4$ with $\mathfrak{v} = 30\,\%$. In this case we expect different results since we already saw in Section 7.2.3 that $\gamma = 0$ leads to contraction in direction of $\boldsymbol{h}^\infty$ whereas $\gamma = \pi/4$ leads to elongation. The actual results for $\hat{u}$ versus f_p and stiffness versus magnetic load are shown in Figure 7.13a and Figure 7.13b, respectively. As can be seen in both plots the initial stiffness now decreases with increasing h^∞. The explanation for this effect lies in the different deformation states after magnetic loading. Note however, that the initial stiffness for the material with $\gamma = \pi/4$ and $\mathfrak{v} = 30\,\%$ for $h^\infty = 0$ is larger than the value for $\gamma = 0$ and $\mathfrak{v} = 30\,\%$ at $h^\infty = 0.3\,\mathrm{MA\,m^{-1}}$.

7.3. A characterization of macro- and micro-structural effects in the magneto-mechanics of soft bodies

It is known from experiments (Martin et al., 2006; Diguet et al., 2010) that the magneto-mechanical response of an MRE body exposed to homogeneous magnetic fields does not only depend on material properties but also on the shape of the MRE. This dependence is quite complex and can be imagined as a deformation dependent boundary condition. This renders the direct identification of material parameters from experiments a difficult, if not impossible, task. A partial remedy is the design of new specimen shapes, e.g. cigar shapes as proposed by Pössinger (2015) and Bodelot et al. (2018), which reduce the inhomogeneity of the state inside the specimen. Then, one might be able to reconstruct the actual boundary conditions at a specimen's surface. Whether or how it is possible to fully describe the state, i.e. all of $\underline{\boldsymbol{F}}$, $\boldsymbol{H}$, $\underline{\boldsymbol{P}}$ and $\boldsymbol{B}$, at a certain point inside the MRE with sufficient accuracy is still an open question[16]. We believe that computational methods are the right tool to solve this problem, since simulations not only give access to experimentally observable quantities but to the state at virtually every point in the computational domain.

In the current section we present results form two-scale simulations that are intended to foster the understanding of the complications mentioned above. We begin with a demonstration of the difficulties in the characterization of the deformation of rectangular MRE specimens in response to magnetic fields (Subsection 7.3.2). After that, in Subsection 7.3.3 we switch over to elliptically shaped specimens which we expect to be better suited for the experimental determination of material parameters. In Subsection 7.3.4 we propose an analytical estimate for the internal stress state. Based on this estimate we quantify the accuracy of approaches for the reconstruction of the internal stress state from measurements. Next to that, similar studies are carried out for deformation measures and magnetic quantities such that eventually the complete internal state can be approximated. The findings outline below can also be found in (Keip and Rambausek, 2017).

7.3.1. Material models

In the present section we extend the generic material model from Section 7.2.1 to capture magnetic saturation. The new energy-density is given as

$$\begin{aligned}\widehat{\Psi}(\underline{\boldsymbol{F}},\boldsymbol{H}) = \frac{1}{2}\mu(\boldsymbol{C}-3)+\frac{\lambda}{4}\left(J^2-1\right)-\left(\frac{\lambda}{2}+\mu\right)\ln J \\ -\frac{J}{2}\mu_0\left[\boldsymbol{C}^{-1}:(\boldsymbol{H}\otimes\boldsymbol{H})\right]-\mu_0\frac{{m_\mathrm{s}}^2}{\chi_0^\mathrm{m}}\ln\left[\cosh\left(\frac{\chi_0^\mathrm{m}}{m_\mathrm{s}}\sqrt{\boldsymbol{C}^{-1}:(\boldsymbol{H}\otimes\boldsymbol{H})}\right)\right],\end{aligned} \tag{7.62}$$

[16] In prominent purely mechanical (e.g. tension) tests this is trivial because we know how to craft specimens that exhibit homogeneous states in a certain region. These regions then allow us to "extrapolate" the state from the inside to the surface where have easy access via measurements.

where the m_s is the magnetization at saturation, χ_0^m is the magnetic susceptibility at $\boldsymbol{h} = 0$ and $\mu_0 = 4\pi \times 10^{-1}\,\mu\text{N/A}^2$. In Figure 7.14 we show a plot of $\|\boldsymbol{B}\|$ versus $\|\boldsymbol{H}\|$ for

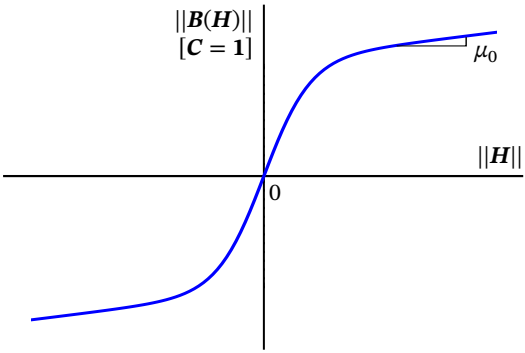

Figure 7.14: Isotropic magnetic material response $\boldsymbol{B}(\boldsymbol{H})$ with saturation.

$\boldsymbol{C} = \mathbf{1}$. The parameters employed for the matrix, the inclusions and the free space are summarized in Table 7.2. The values chosen are in the range of what can be found in literature (Diguet et al., 2010; Spieler et al., 2013). The Lamé parameters for the matrix

Table 7.2: Material parameters on both scales

Material	λ / MPa	μ / MPa	χ_0^m / 1	m_s / MA m^{-1}
Matrix	33.289	0.067	0.0	0.0
Inclusion	33 289.000	66.711	10.0	1.0
Free space	0.000	0.001	0.0	0.0

correspond to $E = 0.2\,\text{MPa}$ and $\nu = 0.499$. The inclusions have the same ν but $E = 200\,\text{MPa} = 1 \times 10^3\, E_{\text{matrix}}$.

7.3.2. Characterization of the shape-dependent magneto-mechanical response of rectangular specimens of various aspect ratios

The basic setup of the boundary value problem under consideration is depicted in Figure 7.15a. This is essentially the same situation as in Section 7.2 such that we do not go again into detail regarding boundary conditions. The actual specimen shapes under consideration are shown in Figure 7.15b.

A sample discretization for the macroscopic BVP as well as the FE mesh for the $\mathcal{RVE}$ are shown in Figure 7.16. Within the current subsection we restrict ourselves to a microstructure with volume fraction $\mathfrak{v} = 30\,\%$ and orientation $\gamma = 0$ (as depicted).

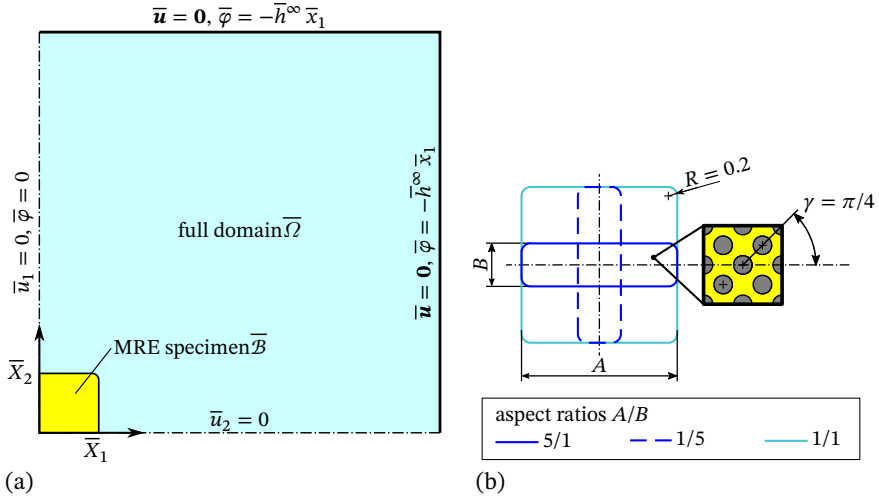

Figure 7.15: Boundary value problem (a) and rectangular MRE specimen geometries (b). The prescribed scalar magnetic potential corresponds to a uniform magnetic field $\mu_0 \boldsymbol{h}^{\infty}$ in x_1-direction. The displacements $\boldsymbol{u} = \varphi - X$ are fixed on the outer boundary of $\overline{\Omega}$. Dash-dotted lines indicate symmetry boundaries (Keip and Rambausek, 2017).

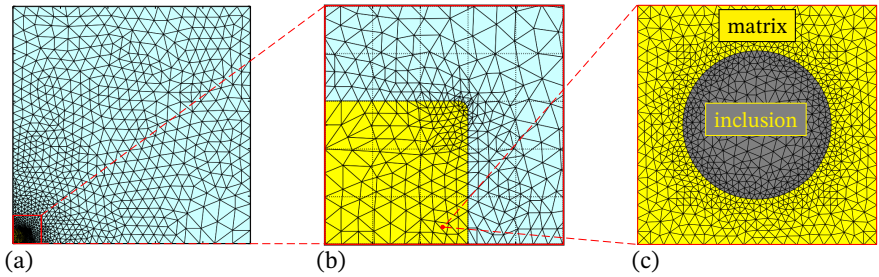

Figure 7.16: Representative meshes for investigation of shape effects with rectangular specimens. The full domain (of which we only consider a quarter) is a square box with a width and height of 100 cm (a), the depicted specimen (b) is square shaped with dimensions $a = b = 3$ cm. The microstructure (c) has an inclusion volume fraction of 30 % (Keip and Rambausek, 2017).

In case of rectangular specimens we have several options for the determination of "the" deformation. In Figure 7.17 we depict several points at the boundary of such a specimen based on which we define different measures for the deformation in x_1-

direction, symbolically denoted as $\varepsilon[\bullet]$,

$$\varepsilon\left[u_1^{\mathrm{A}}\right] = \left(u_1^{\mathrm{A}} - u_1^{\mathrm{A'}}\right)/a, \qquad \varepsilon\left[u_1^{\mathrm{B}}\right] = \left(u_1^{\mathrm{B}} - u_1^{\mathrm{B'}}\right)/a, \tag{7.63a}$$

$$\varepsilon\left[u_2^{\mathrm{C}}\right] = \frac{1}{1 + \left(u_2^{\mathrm{C}} - u_2^{\mathrm{C'}}\right)/b} - 1, \qquad \varepsilon\left[u_2^{\mathrm{D}}\right] = \frac{1}{1 + \left(u_2^{\mathrm{D}} - u_2^{\mathrm{D'}}\right)/b} - 1, \tag{7.63b}$$

$$\varepsilon\left[F_{11}^{\mathrm{D}}\right] = F_{11}^{\mathrm{D}} - 1, \qquad \varepsilon\left[F_{22}^{\mathrm{A}}\right] = 1/F_{22}^{\mathrm{A}} - 1. \tag{7.63c}$$

Note that both matrix and inclusion are almost incompressible such that $F_{11}^{\mathrm{A}} \approx 1/F_{22}^{\mathrm{A}}$ for plane strain.

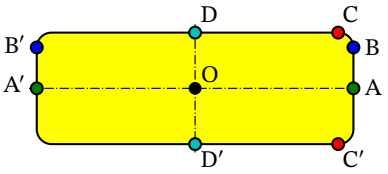

Figure 7.17: Different measurement locations for strain characterization of rectangular MRE specimens.

The deformation response in terms of the measures (7.63) of the two-scale simulations is presented in Figure 7.18.

When we compare these graphs with the measurements reported by Diguet et al. (2010) we see that only $\varepsilon\left[u_1^{\mathrm{B}}\right]$ and $\varepsilon\left[F_{11}^{\mathrm{D}}\right]$ are in qualitative agreement with the experiment. That is, they monotonically decrease with increasing aspect ratio A/B. Interestingly, the four remaining graphs fit to the prediction of the analytical model of Diguet et al. (2010). The explanation for this counter-intuitive observation lies in the inhomogeneous deformation of the specimens, in particular for that with $A/B = 1/5$. Figure 7.19 provides a detailed view highlighting this effect. From above observations we conclude that rectangular (hexahedral or cylindrical in 3D) specimens are sub-optimal for material characterizations in case of MREs.

7.3.3. Characterization of the shape-dependent magneto-mechanical response of elliptical specimens of various aspect ratios

As an alternative to rectangular specimens we below investigate elliptical MREs. The overall BVP and material parameters remain unchanged. Under such conditions we expect (almost) homogeneous magnetic fields in $\mathcal{B}$. The aspect ratios considered are in the range of $\{1/10 \ldots 10\}$. A subset of the actual specimens is depicted in Figure 7.20.

As second parameter we have the microstructure orientation $\gamma \in \{0, \pi/4\}$ (see also Section 7.2 above). Both parameters, aspect ratio A/B and orientation γ, together enable us to identify macroscopic and microscopic influences on an MRE's magneto-mechanical response. For sample discretizations on both scales see Figure 7.21.

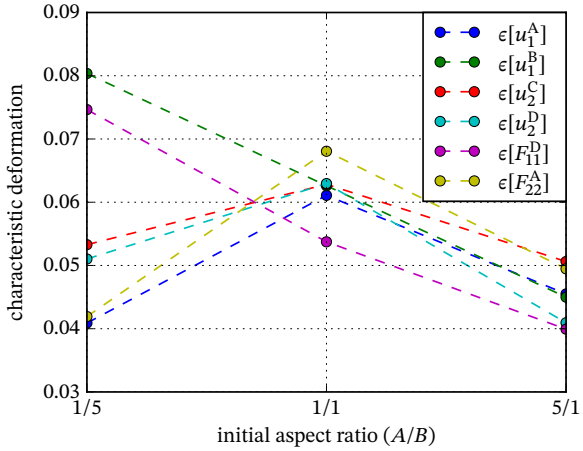

Figure 7.18: Deformation of rectangular MRE specimens with rotated microstructure ($\gamma = \pi/4$) at $m_1 = 0.25\,\mathrm{MA\,m^{-1}}$. The different deformation measure are given in (7.63). Obviously, the different measures do not agree everywhere (Keip and Rambausek, 2017).

Before we analyze the influence of aspect ratio and micro-structure we have a look at deformation in the interior and in the proximity of the magnetically saturated MRE bodies. Figure 7.22 shows plots of $\det \underline{\boldsymbol{F}}$ (a), F_{11} (b), F_{12} (c) and F_{21} (d) for an elliptical specimen with aspect ratio $A/B = 5/1$.

It can be observed that these quantities are not perfectly homogeneous in $\mathcal{B}$. Nevertheless, the situation is much better than for rectangular specimens. The self-potential ϕ_s^m for specimens with $A/B = 5/1$ is depicted in Figure 7.23, whereas a similar plot can be found in Figure 7.24 for $A/B = 1/5$.

In both cases we observe straight, equidistant and parallel iso-lines around the center of $\mathcal{B}_t$. Near the corners of the MRE with $A/B = 5/1$, however, the iso-lines are curved. This is in contrast with $A/B = 1/5$ where such an observation cannot be made. The effect of these inhomogeneities will be discussed in Subsection 7.3.4.

Next we turn to the macroscopic deformation response in terms of F_{11} at the center of the specimen. Figure 7.25 visualizes results obtained for $\gamma = 0$ in terms of F_{11} at the specimen center versus h_1 (a), m_1 (b) and the applied h_1^∞ (c). Figure 7.26 shows the same for $\gamma = \pi/4$.

In both figures the deformation truly saturates for higher magnetic loads. As in Section 7.2 we observe elongation in direction of $\boldsymbol{h}$ for $\gamma = \pi/4$ and contraction for $\gamma = 0$. Moreover, we see that the deformation response also strongly depends on the aspect ratio. This holds for the sensitivity of F_{11} with respect to magnetic quantities but also for the final deformation at saturation.

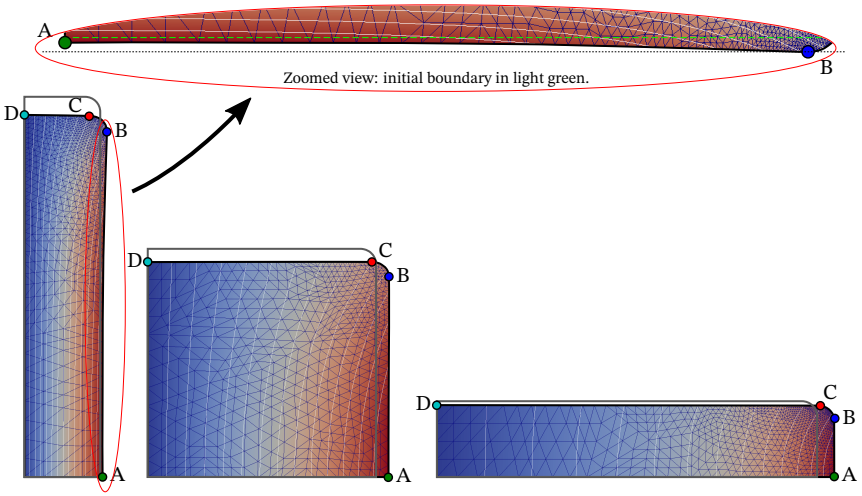

Figure 7.19: Deformed rectangular MRE specimens with rotated microstructure ($\gamma = \pi/4$) at $m_1 = 0.25\,\mathrm{MA\,m^{-1}}$. The contour plots depict the scalar magnetic self-potential ϕ_s^m, which clearly is non-uniform within the specimens. The outlines of the initial configurations are indicated in gray (Keip and Rambausek, 2017).

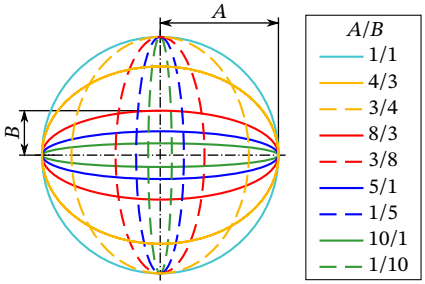

Figure 7.20: A subset of the elliptical MRE specimen geometries for the investigation of shape effects.

For a deeper analysis of this shape-effect we investigate the deformation at saturation in dependence of the aspect ratio A/B. For that purpose we compare deformation

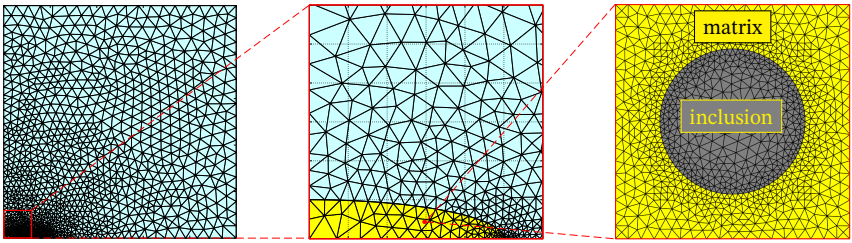

Figure 7.21: Representative meshes for investigation of shape effects with elliptical specimens. The full domain (of which we only consider a quarter) is a square box with a width and height of 100 cm (a), the depicted specimen (b) is ellipse-shaped with dimensions $a = 5$ cm and $b = 1$ cm. The microstructure (c) has an inclusion volume fraction of 30 % (Keip and Rambausek, 2017).

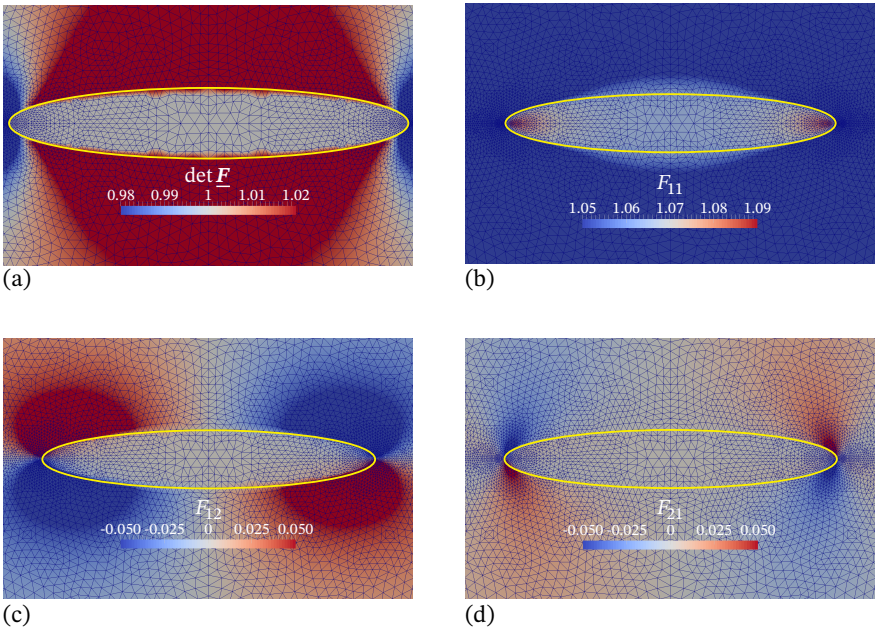

Figure 7.22: Deformed elliptical MRE specimen with aspect ratio 5/1 and rotated microstructure ($\gamma = \pi/4$) at magnetic saturation. The boundaries of the specimens are indicated in yellow (Keip and Rambausek, 2017).

measures

$$\varepsilon[u_1] = u_1/a, \qquad \varepsilon[u_2] = 1/(1+u_2/b) - 1, \tag{7.64a}$$

$$\varepsilon[F^{\mathrm{s}}_{11}] = F^{\mathrm{s}}_{11} - 1, \qquad \varepsilon[F^{\mathrm{s}}_{22}] = 1/F^{\mathrm{s}}_{22} - 1, \tag{7.64b}$$

$$\varepsilon[\mathcal{O}] = F_{11} - 1. \tag{7.64c}$$

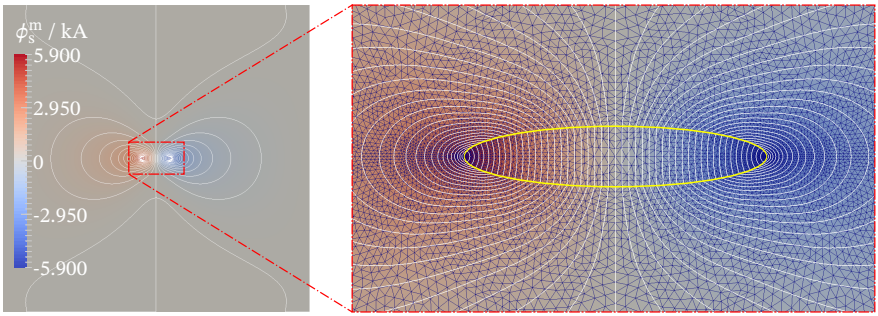

Figure 7.23: Scalar magnetic self-potential ϕ_s^m at the macroscopic scale for an elliptical MRE specimen with aspect ratio $A/B = 5/1$ and microstructure orientation $\gamma = 0$ in the *deformed configuration* (Keip and Rambausek, 2017). Overall perspective (a) and zoomed view (b).

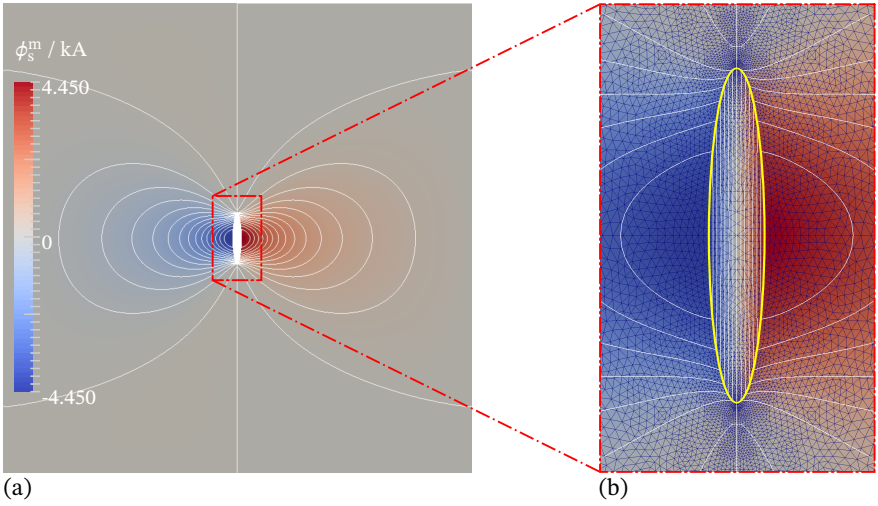

Figure 7.24: Scalar magnetic self-potential ϕ_s^m at the macroscopic scale for an elliptical MRE specimen with aspect ratio $A/B = 1/5$ and microstructure orientation $\gamma = 0$ in the *deformed configuration* (Keip and Rambausek, 2017). Overall perspective (a) and zoomed view (b).

similar to what we previously did in Subsection 7.3.2. The corresponding measurement locations are indicated in Figure 7.27.

When we look at the resulting plots shown in Figure 7.28 we immediately see that the graphs for $\varepsilon[\mathcal{O}]$, $\varepsilon[u_1]$ and $\varepsilon[u_2]$ are in qualitative agreement.

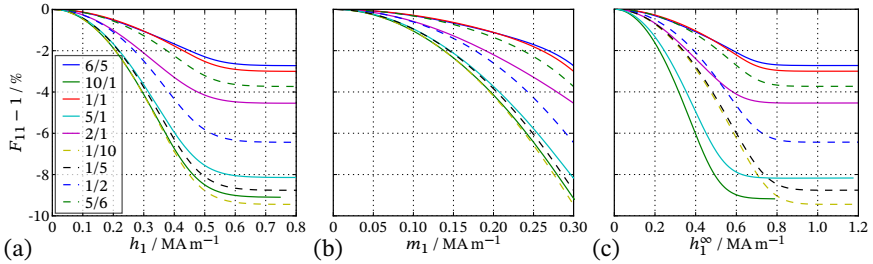

Figure 7.25: Deformation responses for elliptical MRE specimens with different aspect ratios and microstructure orientation $\gamma = 0$. Subplot (a) depicts the deformation measure $F_{11} - 1$ over the *local* field h_1. In (b) $F_{11} - 1$ is plotted over the magnetization m_1 and in (c) over the *applied* field h_1^∞. Similar to square specimens with $\gamma = 0$, one observes contraction in field direction (Keip and Rambausek, 2017).

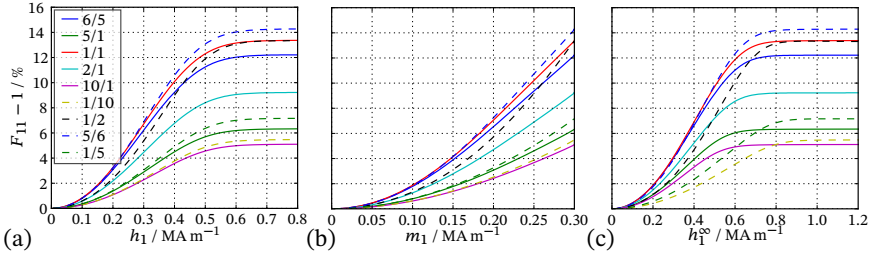

Figure 7.26: Deformation responses for elliptical MRE specimens with different aspect ratios and microstructure orientation $\gamma = \pi/4$. Subplot (a) depicts the deformation measure $F_{11} - 1$ over the *local* field h_1. In (b) $F_{11} - 1$ is plotted over the magnetization m_1 and in (c) over the *applied* field h_1^∞. By contrast to the case of $\gamma = 0$, one now observes elongation in field direction (Keip and Rambausek, 2017).

Comparing these measures for $\gamma = 0$ (a) and $\gamma = \pi/4$ (b) we observe that their characteristic features are mostly independent from γ. For both orientations the maximum deformation is obtained for shapes with A/B near 1. By contrast, the deformations in terms of $\varepsilon[F_{11}^{\mathrm{s}}]$ and $\varepsilon[F_{22}^{\mathrm{s}}]$ show a different behavior.

The explanation of the effect captured by $\varepsilon[\mathcal{O}]$, $\varepsilon[u_1]$ and $\varepsilon[u_2]$ is one of the things discussed in Subsection 7.3.4 below.

7.3.4. Investigation of an approach for the reconstruction of the internal state

From Figures 7.22, 7.23 and 7.24 we know that for MREs of elliptical shape of certain aspect ratios we can expect a good degree of homogeneity in $\underline{\boldsymbol{F}}$ and $\boldsymbol{H}$. Hence, we can

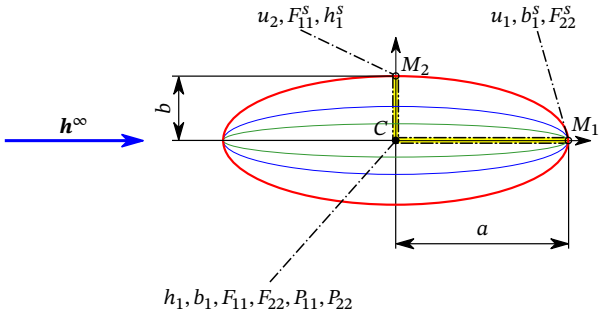

Figure 7.27: Measurement locations for the characterization of the deformation response of elliptical MRE specimens. The indicated kinematic quantities are employed in the strain measures (7.64).

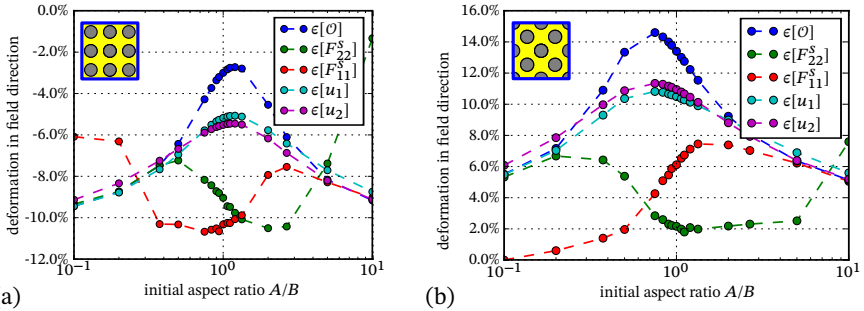

Figure 7.28: Deformation of elliptical MRE specimens at magnetic saturation. The results corresponding to microstructure with $\gamma = 0$ are shown in (a), those for $\gamma = \pi/4$ in (b). In both cases one observes a "peak" near $A/B = 1$ which reflects a tendency for elongation in field direction. However, in (a) the overall contracting deformation caused by the microstructure with $\gamma = 0$ is stronger. In (b), by contrast, this "shape effect" supports the elongation driven by the MREs rotated microstructure (Keip and Rambausek, 2017).

directly relate measurements of these quantities from the specimens surface to its center. For the complete determination of the state at some point inside the specimen we also need access to their duals $\underline{\boldsymbol{P}}$ and $\boldsymbol{B}$. The jump condition (7.2) informs us that we have to measure $\boldsymbol{b}$ at a point or region at the surface where the normal $\boldsymbol{n}$ is aligned with the outside magnetic field $\boldsymbol{b}$. Conversely, $\boldsymbol{h}$ is to be measured where $\boldsymbol{h}$ is tangent to the surface.

With the above considerations in mind we define relative deviations between detectable (evaluated at some point at the surface) and "true" (evaluated at the specimen's center) values. We refer to Figure 7.27 for the precise locations of evaluation for the different quantities.

We employ deviation measures for magnetic quantities

$$r_{\boldsymbol{h}} = \frac{|h_1^s - h_1|}{|h_1|}, \qquad r_{\boldsymbol{b}} = \frac{|b_1^s - b_1|}{|b_1|}, \qquad r_{\boldsymbol{m}} = \frac{|m_1(b_1^s, h_1^s) - m_1(b_1, h_1)|}{|m_1(b_1, h_1)|}, \tag{7.65}$$

deformation measures based on displacements

$$r_{\boldsymbol{u},1} = \frac{|1 + u_1/a - F_{11}|}{|F_{11} - 1|}, \qquad r_{\boldsymbol{u},2} = \frac{|1/(1 + u_2/b) - F_{11}|}{|F_{11} - 1|}, \tag{7.66}$$

and deformation measures based on local strains

$$r_{\underline{\boldsymbol{F}},1} = \frac{|F_{11}^s - F_{11}|}{|F_{11} - 1|}, \qquad r_{\boldsymbol{u},1} = \frac{|1/F_{22}^s - F_{11}|}{|F_{11} - 1|}, \tag{7.67}$$

where in the last equation we have exploited incompressibility and plain strains giving $F_{11} = 1/F_{22}$.

Below we show plots of the maximum[17] r_i values obtained for various aspect ratios. In Figure 7.29 we depict the results for the deviations in the reconstruction of magnetic quantities $r_{\boldsymbol{h}}$, $r_{\boldsymbol{b}}$ and $r_{\boldsymbol{m}}$.

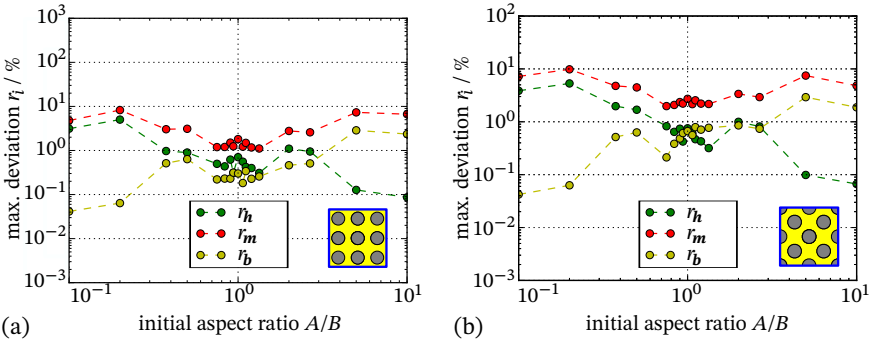

Figure 7.29: *Maximum* deviations (7.65) between magnetic quantities at the center of the specimen computed from measurable quantities and the corresponding true values. The results for microstructure orientation $\gamma = 0$ are shown in (a), those for $\gamma = pi/4$ in (b), respectively (Keip and Rambausek, 2017).

We observe quite similar results for microstructure orientations of $\gamma = 0$ and $\gamma = \pi/4$. Furthermore we see that the deviations are surprisingly large for aspect ratios far from 1. The explanation for this behavior are postprocessing errors in regions of high boundary curvature. As can be seen, there is always one graph of comparably good accuracy. This curve always corresponds to the quantity which is evaluated at the "flat" surface point,

[17] In the simulations we record all r_i at each load step. The maximum values are selected from that series for each r_i separately.

that is b_1^s for $A/B \to 1/10$ and h_1^s for $A/B \to 10/1$. The errors in turn are introduced by oscillations in the projection of $\underline{\boldsymbol{F}}$, $\boldsymbol{h}$ and $\boldsymbol{b}$ to a *continuous* space for postprocessing purposes. In Figure 7.30 we provide a detailed visualization of this phenomenon. From

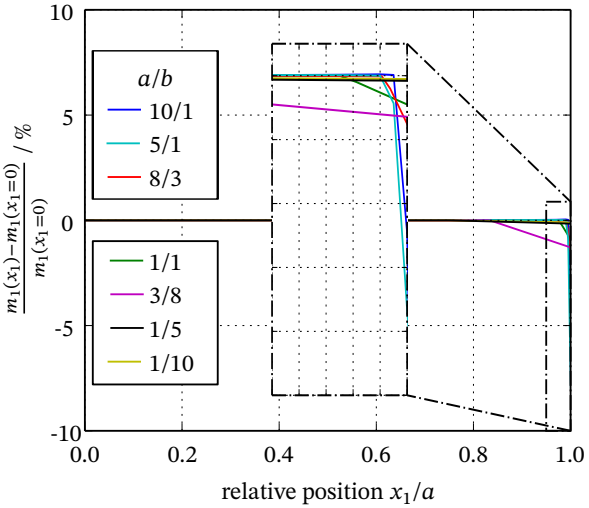

Figure 7.30: Relative deviation of the magnetization $m_1(x_1)$ along the x_1 axis from the magnetization $m_1(x_1 = 0)$ at the center. Significant deviations (inhomogeneities) can only be observed towards the boundary of the ellipse (near $(x_1/a = 1)$). These are postprocessing artifacts. In reality, the magnetization is almost perfectly uniform (Keip and Rambausek, 2017).

the latter figure we also see that the true deviations in the magnetic quantities are not the main concern for state reconstruction.

Figure 7.31 depicts plots of the deviations in deformation measures (7.66) to (7.67). Obviously, circular specimens lead to pronounced deviations in all four measures $r_{\boldsymbol{u},1}$, $r_{\boldsymbol{u},2}$, $r_{\underline{\boldsymbol{F}},1}$ and $r_{\underline{\boldsymbol{F}},2}$. The situation improves for $A/B \to 1/10$ as well as for $A/B \to 10/1$. However, the performance of the individual r_i depends on the aspect ratio such that no general recommendation can be given.

Next we turn to the determination of the stress state, which is the most delicate task in the reconstruction of internal state. There is no direct way to determine the stress exerted on the MRE specimen by the applied magnetic loads. It is, nevertheless, possible to approximately compute the stresses due to magnetic quantities, to which we have access via measurements. The key concept for what follows is the so-called Maxwell stress

$$\boldsymbol{\sigma}^{\mathrm{MW}} = \boldsymbol{h} \otimes \boldsymbol{b} - \frac{\mu_0}{2} (\boldsymbol{h} \cdot \boldsymbol{h}) \, \mathbf{1}. \tag{7.68}$$

Since this stress only relies only on the magnetic quantities $\boldsymbol{h}$ and $\boldsymbol{b}$ it is exists irrespec-

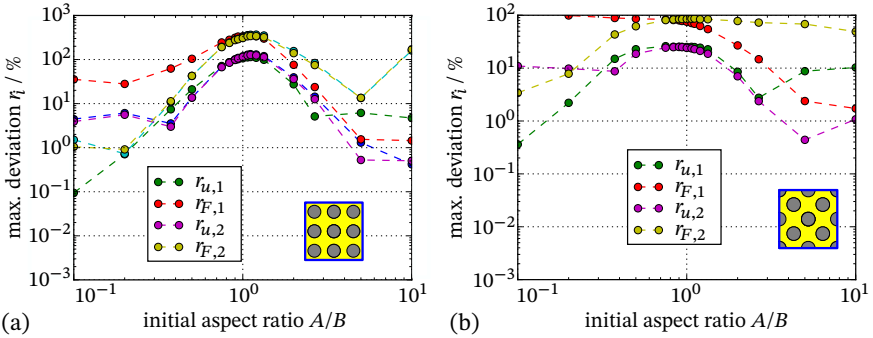

Figure 7.31: *Maximum* deviations between the deformation measures at the center of the specimen and estimates computed from corresponding measurable quantities (7.66) and (7.67). The results for microstructure orientation $\gamma = 0$ are shown in (a), those for $\gamma = pi/4$ in (b), respectively (Keip and Rambausek, 2017).

tive of matter and thus also in the surrounding of an MRE specimen. In vacuum the Maxwell stress is the only contribution to the total Cauchy-type stress $\boldsymbol{\sigma}$. Thus, (7.68) can be used to compute the resultant magneto-static force on a region in space via an integral over the boundary. Moreover, in vacuum we have $\boldsymbol{h} = \boldsymbol{b}/\mu_0$ and we may equivalently write $\boldsymbol{\sigma}^{\mathrm{MW}}$ only in terms of $\boldsymbol{h}$ or $\boldsymbol{b}$. The situation is different in (magnetizable) matter. Indeed, depending on the choice of primary variables, various expressions for the Maxwell stress *in matter* can be found in literature as summarized by Kankanala and Triantafyllidis (2004). While this is confusing in first place, one should keep in mind that the total stress is the central stress quantity (Kovetz, 2000; McMeeking and Landis, 2004) for modeling when matter is involved. Despite these complications we employ (7.68) which is the Maxwell stress consistent with our formulation of magneto-elasticity (Kankanala and Triantafyllidis, 2004). The traction that is exerted by the Maxwell stress on a body is

$$\boldsymbol{t}^{\mathrm{MW}} = \boldsymbol{\sigma}^{\mathrm{MW}} \cdot \boldsymbol{e}_{\mathrm{n}}, \tag{7.69}$$

which we will call Maxwell traction. Next, consider a point on an interface between a magnetized body and its empty surrounding. Assume that at this point we now $\boldsymbol{h}^{\mathrm{i}}$ and $\boldsymbol{b}^{\mathrm{i}}$ at the interior side and the outside pointing normal $\boldsymbol{e}_{\mathrm{n}}$. Then we employ the jump conditions (7.2) to compute $\boldsymbol{h}^{\mathrm{o}}$ and $\boldsymbol{b}^{\mathrm{o}}$ outside the specimen as

$$\boldsymbol{h}^{\mathrm{o}} = \left(\boldsymbol{h}^{\mathrm{i}} \cdot \boldsymbol{e}_{\mathrm{t}}\right) \boldsymbol{e}_{\mathrm{t}} + \frac{1}{\mu_0} \left(\boldsymbol{b}^{\mathrm{i}} \cdot \boldsymbol{e}_{\mathrm{n}}\right) \boldsymbol{e}_{\mathrm{n}} \quad \text{and} \quad \boldsymbol{b}^{\mathrm{o}} = \left(\boldsymbol{b}^{\mathrm{i}} \cdot \boldsymbol{e}_{\mathrm{n}}\right) \boldsymbol{e}_{\mathrm{n}} + \mu_0 \left(\boldsymbol{h}^{\mathrm{i}} \cdot \boldsymbol{e}_{\mathrm{t}}\right) \boldsymbol{e}_{\mathrm{t}} = \mu_0 \boldsymbol{h}^{\mathrm{o}}, \tag{7.70}$$

as visualized in Figure 7.32.

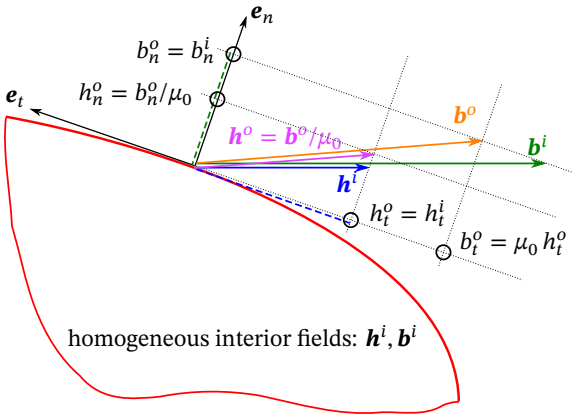

Figure 7.32: Magnetic jump conditions in absence of free currents and when only on side of the surface is magnetic.

Alternatively, we have $\boldsymbol{h}^{\mathrm{o}}$ in terms of $\boldsymbol{h}^{\mathrm{i}}$ and $\boldsymbol{m}^{\mathrm{i}}$

$$\boldsymbol{h}^{\mathrm{o}} = \boldsymbol{h}^{\mathrm{i}} + \left(\boldsymbol{m}^{\mathrm{i}} \cdot \boldsymbol{e}_{\mathrm{n}}\right) \boldsymbol{e}_{\mathrm{n}} \qquad \text{where} \qquad \boldsymbol{m}^{\mathrm{o}} = \boldsymbol{0}. \tag{7.71}$$

As a second ingredient, we decompose the total stress into a Maxwell-type term $\boldsymbol{\sigma}^{\mathrm{MW}}$ and a remaining[18] part $\widehat{\boldsymbol{\sigma}}$

$$\boldsymbol{\sigma} = \boldsymbol{\sigma}^{\mathrm{MW}} + \widehat{\boldsymbol{\sigma}}. \tag{7.72}$$

Since $\widehat{\boldsymbol{\sigma}} = 0$ in vacuum and $[\![\boldsymbol{\sigma}]\!] \cdot \boldsymbol{e}_{\mathrm{n}} = 0$ for vanishing *mechanical* tractions (see (7.8)) we obtain

$$\boldsymbol{\sigma}^{\mathrm{MW,i}} \cdot \boldsymbol{e}_{\mathrm{n}} + \widehat{\boldsymbol{\sigma}}^{\mathrm{i}} \cdot \boldsymbol{e}_{\mathrm{n}} = \boldsymbol{\sigma}^{\mathrm{MW,o}} \cdot \boldsymbol{e}_{\mathrm{n}} \tag{7.73}$$

and thus, with (7.71),

$$\hat{\boldsymbol{t}} = \widehat{\boldsymbol{\sigma}} \cdot \boldsymbol{e}_{\mathrm{n}} = [\![\boldsymbol{\sigma}^{\mathrm{MW}}]\!] \cdot \boldsymbol{e}_{\mathrm{n}} = [\![\boldsymbol{t}^{\mathrm{MW}}]\!] = \frac{\mu_0}{2} \left(\boldsymbol{m} \cdot \boldsymbol{e}_{\mathrm{n}}\right)^2 \cdot \boldsymbol{e}_{\mathrm{n}}, \tag{7.74}$$

where we dropped the superscript "i" for quantities $\widehat{\boldsymbol{\sigma}}$ and $\boldsymbol{m}$, which only exists in matter. The last result can be found, for example, in the works of Kankanala and Triantafyllidis (2004) and Bustamante et al. (2009b). The corresponding result for electro-elasticity was already known to Toupin (1956). The key point of (7.74) is that it does not directly depend on neither $\boldsymbol{h}^{\mathrm{i}}$ nor $\boldsymbol{b}^{\mathrm{i}}$. In general situations the derivation above is of limited sig-

[18] One might be tempted to call this part "mechanical". However, warned by the non-unique notion of Maxwell stress in magnetized matter we follow McMeeking and Landis (2004) and do not attribute any physical meaning to $\boldsymbol{\sigma}^{\mathrm{MW}}$ and $\widehat{\boldsymbol{\sigma}}$ as soon as both of them are non-zero simultaneously.

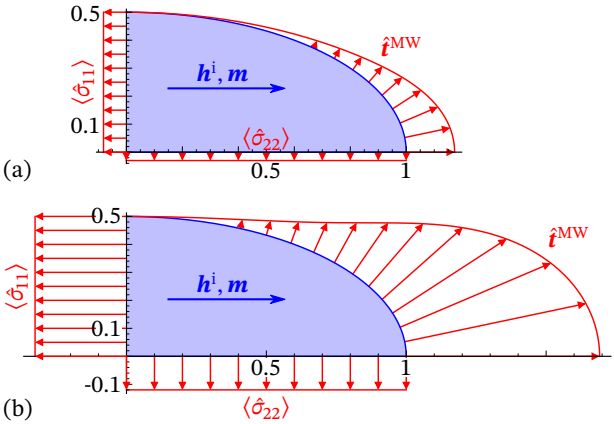

Figure 7.33: Free body diagrams for an elliptical, uniformly magnetized body with state $\{\boldsymbol{F} = \boldsymbol{1}, \boldsymbol{m}^{\mathrm{i}} = (0.5, 0)\}$ (a) and $\{\boldsymbol{F} = \boldsymbol{1}, \boldsymbol{m} = (1.0, 0)\}$ (b).

nificance. However, below we will investigate the case when the magnetic quantities are homogeneous inside a body, as is approximately the case for elliptical MRE specimens. For such a setting $\boldsymbol{\sigma}^{\mathrm{MW}}$ is also homogeneous inside the MRE $\mathcal{B}$ and hence can be removed from $(7.11a)_2$. We then arrive at reduced kinetic equations in the current configuration

$$\operatorname{div}\hat{\boldsymbol{\sigma}} = \boldsymbol{0} \quad \text{in } \mathcal{B}_{\mathrm{t}} \qquad \text{and} \qquad \hat{\boldsymbol{\sigma}} \cdot \boldsymbol{e}_{\mathrm{n}} = \hat{\boldsymbol{t}} \quad \text{on } \partial\mathcal{B}_t. \tag{7.75}$$

In the sequel we restrict ourselves to elliptical magnetic bodies with half-axes aligned with $\boldsymbol{e}_1$ and $\boldsymbol{e}_2$, respectively. Furthermore, we take $\boldsymbol{h} = h\boldsymbol{e}_1$ and $\boldsymbol{m} = m\boldsymbol{e}_1$. Then, consider a free body diagram of a quarter of such an ellipse as depicted in Figure 7.33.

The net force exerted by the traction $\hat{\boldsymbol{t}}$ is balanced by integrals of $\hat{\boldsymbol{\sigma}}$

$$\int_{x_2=0}^{b} \hat{\sigma}_{11}\,\mathrm{d}x_2 = \int_{s=0}^{s(\xi=\pi/2)} \hat{t}_1\,\mathrm{d}s(\xi) \quad \text{and} \quad \int_{x_1=0}^{a} \hat{\sigma}_{22}\,\mathrm{d}x_1 = \int_{s=0}^{s(\xi=\pi/2)} \hat{t}_2\,\mathrm{d}s(\xi), \tag{7.76}$$

where we made use of the fact that $\hat{\boldsymbol{\sigma}}$ has vanishing off-diagonal components in the basis $\{\boldsymbol{e}_1, \boldsymbol{e}_2\}$ along the cut due to symmetry. The left-hand-side integrals in (7.76) can be expressed in terms of average stress components $\langle\hat{\sigma}_{11}\rangle|_{\boldsymbol{e}_2}$ and $\langle\hat{\sigma}_{22}\rangle|_{\boldsymbol{e}_1}$ such that

$$\langle\hat{\sigma}_{11}\rangle|_{\boldsymbol{e}_2} = \frac{1}{b}\int_{s=0}^{s(\xi=\pi/2)} \hat{t}_1\,\mathrm{d}s(\xi) \qquad \text{and} \qquad \langle\hat{\sigma}_{22}\rangle|_{\boldsymbol{e}_1} = \frac{1}{a}\int_{s=0}^{s(\xi=\pi/2)} \hat{t}_2\,\mathrm{d}s(\xi). \tag{7.77}$$

In the course of state reconstruction we ask how well the stress state at the center of the ellipsoid can be approximated by the averages (7.77). In analogy to the deviation

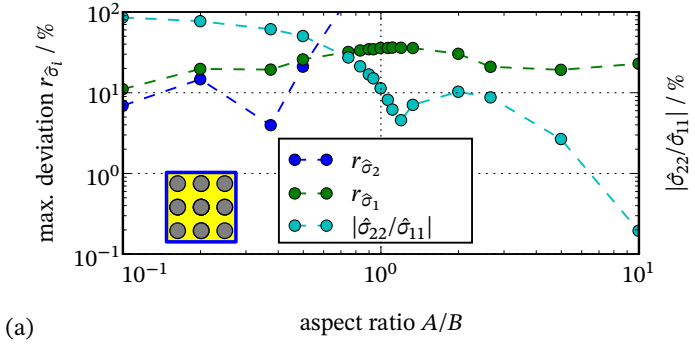

(a)

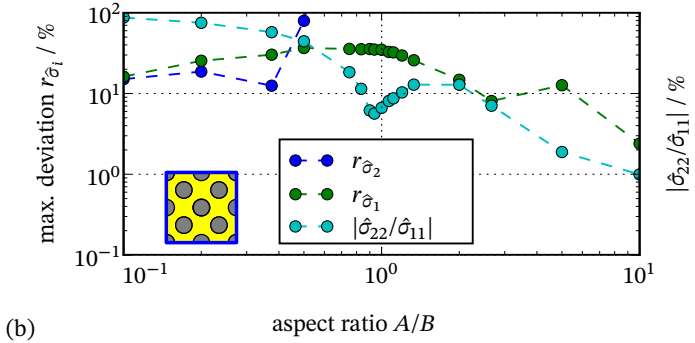

(b)

Figure 7.34: *Maximum* deviations (7.78) between stress components at the center of the specimen and their estimates. The results for microstructure orientation $\gamma = 0$ are shown in (a), those for $\gamma = pi/4$ in (b), respectively (Keip and Rambausek, 2017).

measures (7.65) to (7.67) we define

$$r_{\hat{\sigma}_1} = \frac{\left|\langle\hat{\sigma}_{11}\rangle|_{\boldsymbol{e}_2} - \hat{\sigma}_{11}\right|}{|\hat{\sigma}_{11}|} \qquad \text{and} \qquad r_{\hat{\sigma}_2} = \frac{\left|\langle\hat{\sigma}_{22}\rangle|_{\boldsymbol{e}_1} - \hat{\sigma}_{22}\right|}{|\hat{\sigma}_{22}|}, \tag{7.78}$$

where $\hat{\sigma}_{11}$ and $\hat{\sigma}_{22}$ are evaluated at the specimen center whereas the averages are computed by (7.77) based on "measured" magnetic and geometric quantities. Hence, $r_{\hat{\sigma}_1}$ and $r_{\hat{\sigma}_2}$ suffer from the overestimated errors in $\boldsymbol{r_m}$. Nevertheless, in Figure 7.34 we observe that it is possible to achieve deviations in the order of 10 %.

For small aspect ratios, the deviation $r_{\hat{\sigma}_2}$ is smaller whereas for high aspect ratio we observe small deviations $r_{\hat{\sigma}_1}$. Thus, there is at most one out of two averages that can be employed in the approximation of the stress state. The other component, however, can

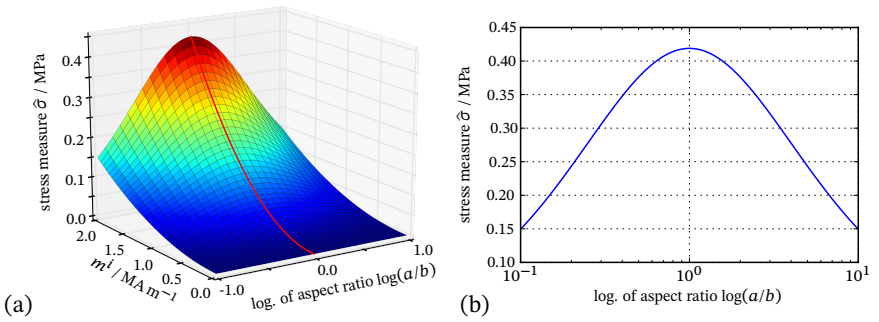

Figure 7.35: The deviatoric stress $\hat{\sigma}$ plotted over (a) the logarithmic current aspect ratio $\log(a/b)$ and magnetization m^{i} and (b) over the logarithmic current aspect ratio for fixed magnetization $m^i = 2.0\,\mathrm{MA\,m^{-1}}$. The solid red line in (a) corresponds to $a/b = 1$, the location of local extrema which is independent of the magnetization (Keip and Rambausek, 2017).

be directly estimated via the traction without the integral, that is

$$\hat{\sigma}_{11}(0,0) \approx \hat{t}_1(a,0) \qquad \text{and} \qquad \hat{\sigma}_{22}(0,0) \approx \hat{t}_2(0,b)\,, \tag{7.79}$$

where the former is appropriate for $A/B \to 1/10$ and the latter for $A/B \to 10/1$. For additional insight, Figure 7.34 also contains a graph representing the ratio $\hat{\sigma}_{22}/\hat{\sigma}_{11}$ which strongly varies over the aspect ratio.

To conclude this discussion we recall that the task of internal stress reconstruction is motivated by the shape-dependent magneto-mechanical response of MRE specimens. The results for the deviations r_i of approximations of the internal state based on experimentally accessible quantities suggest that this task is indeed possible, at least in the idealized setting under consideration. Thus we hope that the considerations above inspire experimentalists to craft new measurement setups that enable improved characterizations of real-world MREs.

We now revisit the physical interpretation of the stress $\widehat{\boldsymbol{\sigma}}$. For that purpose we investigate what we call "representative deviatoric stress state"

$$\hat{\sigma} = \frac{1}{2}\left(\langle \hat{\sigma}_{11} \rangle|_{\boldsymbol{e}_2} - \langle \hat{\sigma}_{22} \rangle|_{\boldsymbol{e}_1} \right), \tag{7.80}$$

in analogy to the deviatoric stress component characterizing the stress state of incompressible bodies in a plain-strain setting. We refer to the work of (Galipeau et al., 2014) where such a stress measure also plays a central role. By construction, $\hat{\sigma}$ carries information about the shape dependence of an elliptical MRE specimen's state. We hypothesize that $\widehat{\boldsymbol{\sigma}}$ has some *intrinsic* relevance for an MRE's deformation, which can not be said of $\boldsymbol{\sigma}^{\mathrm{MW}}$ when evaluated only inside the MRE. In Figure 7.35 we show plots of $\hat{\sigma}$ as a function of magnetization m_1 and *current* aspect ratio a/b.

There we see the pronounced maximum for an aspect ratio of 1 for any value of m_1. From this we expect that MRE specimens of approximately circular shape will exhibit a stronger tendency for elongation in field direction than specimens of "short" or lengthy shape. Indeed, this agrees with the graphs depicted in Figure 7.28. Moreover, since the plots of $\hat{\sigma}$ involve the *current* aspect ratio, the maximum for $a/b = 1$ explains the slight shifts of maximum deformation from *initial* aspect ratios $A/B = 1$ towards $A/B > 1$ for contracting and $A/B < 1$ for elongating specimens. Hence, we conclude that the averages $\langle \hat{\sigma}_{11} \rangle|_{\boldsymbol{e}_2}$ and $\langle \hat{\sigma}_{22} \rangle|_{\boldsymbol{e}_1}$ (or their "true" counterparts in the specimen center) are values that should be taken into account for the magneto-mechanical characterization of MREs.

7.4. An analytical model for the shape-dependent magneto-mechanical response of soft ellipsoidal magnetizable bodies

In the preceding subsection we highlighted the influence of the macroscopic shape of an MRE on its response to homogeneous external magnetic fields. As demonstrated, this effect is in the same order of magnitude the influence of an MRE's micro-morphology. This motivates the development of an analytical model that goes beyond the approach presented in Subsection 7.3.4. In what follows we consider magnetizable bodies in the shape of rotational ellipsoids. They shall consist of a material, which is mechanically soft as is the case for MREs. Regarding the magnetic properties, we deliberately opt for a simple saturation model that excludes intrinsic magneto-mechanical coupling. By that we ensure that the observed deformations in response to magnetic loads are driven by macroscopic effects only. The idea for the model presented below is based on the largely experimental work of Diguet et al. (2010), where the demagnetizing factor was employed to explain the shape-dependent response a cylindrical MRE specimens. As a second source of inspiration we mention the work of Liu (2014) containing an analytical model for the deformation of an ellipsoidal dielectric body. In fact, the approach presented below is equivalent to that discussed in Liu (2014). However, our derivation is different from Liu (2014) in that it relies on the demagnetizing factor as an accessible quantity governing the magneto-mechanical coupling similar to the macroscopic part of the model developed by Ivaneyko et al. (2014). As will be detailed below, by the removal of all local[19] coupling effects, we end up with a mechanism that solely relies on a quantity, which depends on the overall *shape* of a body. Hence, this mechanism has a non-local character and is even size-independent. What follows is a discussion of the magneto-mechanical part of our contribution (Rambausek and Keip, 2018a) concerned with the investigation of macroscopic magneto-electric coupling in soft bodies.

7.4.1. The total energy of a magnetized body

The starting point for the model is the energy of magnetized body expressed as (Brown, 1966)

$$\mathcal{J} = \int_{\mathcal{B}_t} \rho\psi\left(\underline{\boldsymbol{F}}, \boldsymbol{m}/\rho\right) - \frac{1}{2}\mu_0 \boldsymbol{m}\cdot\boldsymbol{h}_\mathrm{s}\left(\boldsymbol{m}, \mathcal{B}_t\right) - \mu_0 \boldsymbol{m}\cdot\boldsymbol{h}^\infty \, dV_t, \tag{7.81}$$

with ψ denoting the free-energy density per unit mass and ρ being the mass density. The magnetic field created by external devices is denoted as $\boldsymbol{h}^\infty$ and $\boldsymbol{h}_\mathrm{s}\left(\boldsymbol{m}, \mathcal{B}_t\right)$ is the body's self-current-potential. As indicated by its parametrization, $\boldsymbol{h}_\mathrm{s}\left(\boldsymbol{m}, \mathcal{B}_t\right)$ depends on the magnetization but also on the volume occupied by current configuration of the

[19] By "local" we mean that the value of some of quantity at a point x depends only on quantities evaluated within a bounded region of limited size containing x. Thus, we use "local" as in the sense of the principle of locality (Eringen, 1976; Truesdell and Noll, 2004; Tadmor et al., 2012).

body. In fact, the determination of the self-field for given $\boldsymbol{m}$ requires the solution of the corresponding magneto-static equations in whole $\mathbb{R}^3$, which naturally depend on the shape[20] of $\mathcal{B}_t$. Thus, the magnetic self-current-potential is of non-local nature in the sense outlined above.

Except for certain cases, we do not possess analytical solutions to the magneto-static problem of a magnetized body in free space. The determination of the quantities required for the evaluation of (7.81) is therefore not straight-forward in general. The nowadays standard procedure for this task is to bring (7.81) into an equivalent form like (7.15) via suitable (partial) Legendre transforms (Bustamante et al., 2008). From that, one obtains a variational formulation of the magneto-mechanical boundary value problem, which is then solved by means of numerical schemes, e.g. by the FEM as above. However, under certain assumptions to be discussed below, we may devise an analytical approach for the solution of a variational problem based on (7.81).

7.4.2. Specialization to ellipsoidal bodies undergoing homogeneous deformation

It is known that ellipsoidal magnetizable bodies exhibit uniform magnetization in response to homogeneous external magnetic fields. Moreover, in that case also all other magnetic quantities, i.e. $\boldsymbol{b}$ and $\boldsymbol{h}$, are uniform in the interior of such a body. Thus, there exist shape-dependent coefficients establishing relations between $\boldsymbol{m}$, $\boldsymbol{h}$ and $\boldsymbol{b}$ in $\mathcal{B}_t$. The classical equation connects $\boldsymbol{m}$ with $\boldsymbol{h}_\mathrm{s} = \boldsymbol{h} - \boldsymbol{h}^\infty$ (Osborn, 1945)

$$\boldsymbol{h}_\mathrm{s}(\boldsymbol{m}, \mathcal{B}_t) = -\boldsymbol{N}_d(\mathcal{B}_t) \cdot \boldsymbol{m}, \tag{7.82}$$

with the "demagnetizing factor" $\boldsymbol{N}_d(\mathcal{B}_t)$. With that, we rewrite (7.81) for a body with an ellipsoidal *current* configuration $\mathcal{B}_t$ and uniform $\underline{\boldsymbol{F}}$ exposed to homogeneous $\boldsymbol{h}^\infty$ as

$$\mathcal{J}/|\mathcal{B}_t| = \mathfrak{j} = \rho\psi\left(\underline{\boldsymbol{F}}, \boldsymbol{m}/\rho, \boldsymbol{p}/\rho\right) + \frac{1}{2}\mu_0 \boldsymbol{m} \cdot (\boldsymbol{N}_d \cdot \boldsymbol{m}) - \mu_0 \boldsymbol{m} \cdot \boldsymbol{h}^\infty. \tag{7.83}$$

Furthermore, for this case there exist analytical solutions for the magneto-static BVP. This allows to find closed-form expressions for $\boldsymbol{N}_d$ summarized by Osborn (1945). The assumption of uniform $\underline{\boldsymbol{F}}$ in $\mathcal{B}_t$ employed to arrive at (7.83) is an over-restriction of the body's kinematics. As a consequence, predictions made on a model based on this assumption suffer from an over-estimated stiffness. However, this does not have significant impact on what we want to show.

In order to further simplify (7.83) we restrict ourselves to the case of rotational ellipsoids with x_1 as rotation axis and $\boldsymbol{h}^\infty$ also aligned with x_1 (see Figure 7.36). In addition,

[20] The size of a (macroscopic) body is a mere scaling factor in this case.

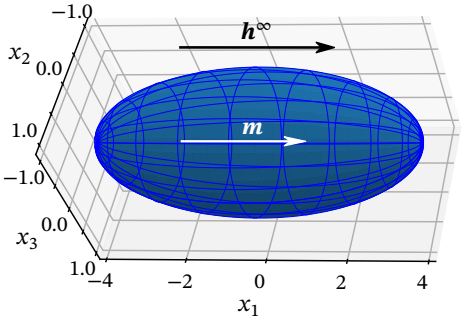

Figure 7.36: A rotational ellipsoid with rotation axis aligned with x_1 exposed to uniform external magnetic field h^∞.

we let the body consist of an isotropic and incompressible material. Then we may write

$$\underline{\boldsymbol{F}}(\lambda) = \begin{pmatrix} \lambda & 0 & 0 \\ 0 & \lambda^{-1/2} & 0 \\ 0 & 0 & \lambda^{-1/2} \end{pmatrix}, \qquad \boldsymbol{h}^\infty = \begin{pmatrix} h^\infty \\ 0 \\ 0 \end{pmatrix} \quad \text{and} \quad \boldsymbol{m} = \begin{pmatrix} m \\ 0 \\ 0 \end{pmatrix}. \tag{7.84}$$

Similarly, we write $\boldsymbol{N}_d$ as a function of the current aspect ratio $c = l/r$

$$\boldsymbol{N}_d(c) = \begin{pmatrix} N(c) & 0 & 0 \\ 0 & \frac{1-N(c)}{2} & 0 \\ 0 & 0 & \frac{1-N(c)}{2} \end{pmatrix}. \tag{7.85}$$

Since the current aspect ratio depends on the deformation we also introduce

$$\widehat{N}(\lambda; C) = N(c(\lambda; C)) \quad \text{with } c = \lambda^{\frac{3}{2}} C, \tag{7.86}$$

where $C = L/R$ denotes the initial aspect ratio. The actual expressions for $N(c)$ that will be employed in the examples are

$$N(c) = \frac{1}{k^2}\left[\frac{c}{2k}\ln\left(\frac{c+k}{c-k}\right) - 1\right] \qquad \text{with } k = \sqrt{c^2-1} \qquad \text{for } c \geq 1 \quad \text{and} \tag{7.87a}$$

$$N(c) = -\frac{1}{(ck)^2}\left[\frac{1}{k}\arcsin(ck) - 1\right] \quad \text{with } k = \sqrt{c^{-2}-1} \qquad \text{for } c < 1 \tag{7.87b}$$

as reported by Osborn (1945). The corresponding graphs are depicted in Figure 7.37.

Based on the above considerations we arrive at

$$\mathfrak{j}(\lambda, m; C, h^\infty) = \rho\widehat{\psi}(\lambda, m/\rho) + \frac{1}{2}\mu_0 m^2 \widehat{N}(\lambda; C) - \mu_0 m h^\infty. \tag{7.88}$$

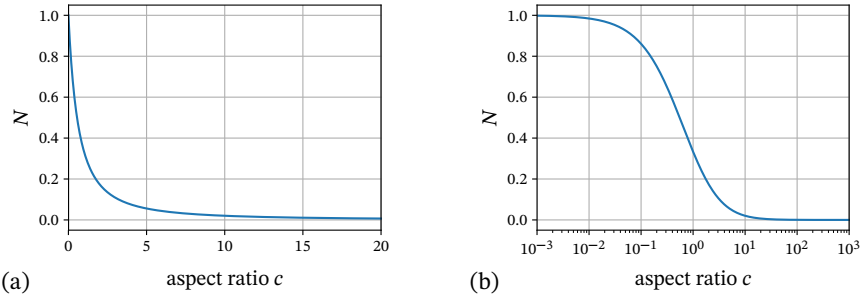

Figure 7.37: The demagnetizing-factor $N = (\boldsymbol{N}_d)_{11}$ for a rotational ellipsoid with rotation axis in x_1-direction as a function of the aspect ratio c. The function N is plotted over a linear c-axis in (a) and over a logarithmic c-axis in (b).

For the characterization of equilibrium states we recall that only isochoric and rotation-free deformations are considered. In these special circumstances, equilibrium can be expressed in terms of variations[21] with respect to λ and m

$$\delta \mathfrak{j} = \left[\rho \frac{\partial \widehat{\psi}}{\partial \lambda} + \frac{1}{2}\frac{\partial \widehat{N}}{\partial \lambda}\mu_0 m^2\right]\delta\lambda + \left[\rho \frac{\partial \widehat{\psi}}{\partial m} + \mu_0\left(\widehat{N}m - h^\infty\right)\right]\delta m = 0 \quad \forall\, \delta\lambda \text{ and } \delta m. \tag{7.89}$$

When we invoke (7.82) in the term going with δm, we obtain

$$\rho \frac{\partial \widehat{\psi}}{\partial m} = \mu_0 h, \tag{7.90}$$

which is the one-dimensional version of the classical magnetic constitutive relation.

For the results presented below we prescribed h^∞ and the initial aspect ratio C and solved the system of two nonlinear equations represented by (7.89) for λ and m.

7.4.3. Material models

Following (Liu and Sharma, 2013; Liu, 2014) we assume that the energy density per unit volume $\rho\widehat{\psi}$ can be decoupled in a mechanical and a magnetic contribution

$$\rho\widehat{\psi}(\lambda, m/\rho) = \widehat{\psi}^{\text{mech}}(\lambda) + \widehat{\psi}^{\text{magn}}(m). \tag{7.91}$$

This ensures that all magneto-mechanical coupling observed below is due to macroscopic structural effects, i.e. it depends on the distribution of material, and has nothing

[21] The interested reader is referred to Liu (2014) for a recent variational approach to magneto-electro-elasticity that partly inspired our analytical model.

to do with local coupling properties of the material itself. For the individual contributions to $\rho\widehat{\psi}$ we choose

$$\widehat{\psi}^{\text{mech}}(\lambda) = \frac{\mu}{2}\left(\lambda^2 + \frac{2}{\lambda} - 3\right) \quad \text{and} \tag{7.92a}$$

$$\widehat{\psi}^{\text{magn}}(m) = \mu_0 \frac{{m_\text{s}}^2}{2\chi_0^\text{m}}\left\{2\frac{m}{m_\text{s}}\,\text{artanh}\left[\frac{m}{m_\text{s}} + \ln\left(1 - \frac{m^2}{{m_\text{s}}^2}\right)\right]\right\}. \tag{7.92b}$$

For the shear modulus we take $\mu = 0.1\,\text{MPa}$ and for the saturation magnetization $m_\text{s} = 0.3\,\text{MA}\,\text{m}^{-1}$. These values are in accordance with literature on soft magnetic (composite) materials (Diguet et al., 2010; Spieler et al., 2013; Liu, 2014; Bodelot et al., 2018). Also note that the tensorial version of $\widehat{\psi}^{\text{magn}}$ given in (7.92b) represents the same material model as the magnetic contribution in (7.62). Indeed, it can be shown that that the energy density (7.92b) transforms into terms present in (7.62)[22] when (7.81) is transformed into (7.15).

7.4.4. Results

In Figure 7.38 we plot the deformation response in terms of λ versus the applied h^∞ for different initial susceptibilities χ_0^m and aspect ratios C.

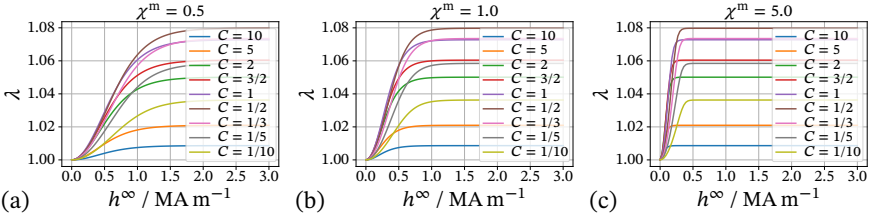

Figure 7.38: Deformation response of rotational ellipsoids with respect to external magnetic field. In the magnetic susceptibility for subplots (a), (b) and (c) are $\chi_m = 0.5$, $\chi_m = 1$ and $\chi_m = 5$, respectively (Rambausek and Keip, 2018a).

We observe that changes in χ_0^m lead to a horizontal scaling of the deformation response but do not have any effect on the deformation at saturation. As expected, C has pronounced influence on the magnitude of deformation. Moreover, in the non-saturated regime we see that prolate ellipsoids tend to show a greater magneto-mechanical sensitivity than oblate shapes. This leads to lines crossing each other at the onset of saturation.

Next we turn to the plots of $\lambda(C)$ for given χ_0^m and h^∞ shown in Figure 7.39. Subplot 7.39a shows the responses for rather low h^∞, from which we see that a higher χ_0^m

[22] The "energy density" (7.62) additionally contains terms which one could refer to as vacuum contributions present irrespective of the material to be modeled.

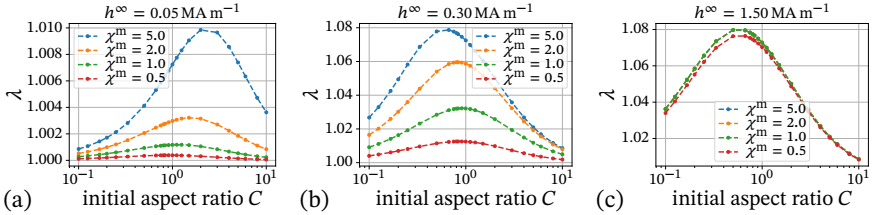

Figure 7.39: Deformation in response to external magnetic field over aspect ratio C for three different magnetic loads. For high magnetic loads (c) the influence of magnetic susceptibility vanishes due to magnetic saturation. However, the influence of shape remains (Rambausek and Keip, 2018a).

leads to a stronger response but also shifts the local maximum of a graph towards more prolate shapes. This effect comes from a greater sensitivity of magnetization with respect to h^∞ depicted in Figure 7.39. In Subplot 7.39b, where h^∞ takes on a moderate value, we still observe the deformation increasing with χ_0^m. However, here the local extrema already move towards oblate shapes. In Subplot 7.39c we are in the saturated state except for $\chi_0^\mathrm{m} = 0.5$. As expected from Figure 7.38, at saturation all curves coincide and the maximum deformation is obtained for ellipsoids with $C \approx 1/2$. This is in perfect agreement with the discussion in Section 7.3.3 and Figure 7.28 in particular.

We conclude that the analytical model based on the demagnetizing factor is capable of characterizing the shape effect also observed in the two-scale simulations in Subsection 7.3.3. Moreover, we highlight that our approach is equivalent to the analytical solution for a dielectric ellipsoid presented by Liu (2014) against which we validated our implementation. However, our derivation has the advantage that it factors out the source of macroscopic shape effects, setting it apart from the work of Liu (2014), where shape effects have not been discussed at all.

Chapter 8

Characterization of macrostructural magneto-electric coupling: an analytical study on ellipsoidal bodies

In Section 7.4 we discussed a model for a purely macroscopic magneto-mechanical coupling effect. The coupling was established via the demagnetizing factor, a concept also present in electrostatics. Hence, the derivation in Section 7.4 also applies to that discipline. But this means that we may combine both the magneto-mechanical and electro-mechanical coupling phenomena to achieve magneto-electric (ME) coupling. In that case the deformation, more precise the change of shape, acts as the mediator between the otherwise decoupled domains of magneto- and electro-statics. We term this ME coupling "non-local" which distinguishes it from "local" ME coupling intrinsic to the material occupying a certain point in space. Despite the latter is also often realized via the combination of magneto- and electro-mechanical effects (Spaldin and Fiebig, 2005), i.e. a product property (van Suchtelen, 1972), the underlying concepts are different.

To delve deeper into that topic, we remark that from an application perspective one is interested in the change of a magnetic (electric) quantity evaluated, e.g. averaged, over a specific region in space in response to the change in an electric (magnetic) quantity most often, but no necessarily, evaluated over the same region. Note that we say "evaluated over a region" because length scales play a crucial role. Local ME coupling is desirable when both regions are basically identical and the influence of the magnetic or, respectively, electric quantities outside that region should be excluded. However, the local ME coupling may still rely on non-local effects but on a smaller length scale. This is for example the case when we consider the macroscopic ME moduli obtained via homogenization of a micro-heterogeneous composite material: the macro-moduli are a local quantity from a macroscopic perspective, but in order to determine them, one solves a boundary value problem on a microscopic domain (Labusch et al., 2014; Schröder et al., 2016; Labusch et al., 2018).

By contrast, the non-local ME effect discussed below is largely independent of scale[1] since it does not require a true composite. The only ingredients are a (soft) elastic, magnetizable and polarizable body and the empty space surrounding the body. Despite that also this kind of non-local coupling depends on the presence of two regions with different properties, we do not regard it from the viewpoint of homogenization or composite materials. However, we believe that the term "product property" still applies.

[1] This at least applies to range of validity of standard continuum mechanics.

In what follows we extend the analytical model from Section 7.4 such that it also accounts for electrostatics. Accordingly, we will not reintroduce mechanical and magnetic quantities already present in that section. The model and results discussed below have already been published (Rambausek and Keip, 2018a). However, the derivation and presentation partly deviates from what can be found in that contribution.

8.1. The total energy of a magnetized and polarized elastic body

To begin with we combine the energetic contributions from elasticity, magneto- and electrostatics (Brown, 1966; Toupin, 1956; Bustamante et al., 2008, 2009b)

$$\mathcal{J} = \int_{\mathcal{B}_t} \rho\psi\left(\underline{\boldsymbol{F}}, \boldsymbol{m}/\rho, \boldsymbol{p}/\rho\right) - \frac{1}{2}\mu_0 \boldsymbol{m}\cdot\boldsymbol{h}_\mathrm{s}\left(\boldsymbol{m}, \mathcal{B}_t\right) - \mu_0 \boldsymbol{m}\cdot\boldsymbol{h}^\infty - \frac{1}{2}\boldsymbol{p}\cdot\boldsymbol{e}_\mathrm{s}\left(\boldsymbol{p}, \mathcal{B}_t\right) - \boldsymbol{p}\cdot\boldsymbol{e}^\infty \, dV_t, \tag{8.1}$$

where $\boldsymbol{p}$ is the polarization, $\boldsymbol{e}_\mathrm{s}$ the electric self-field and $\boldsymbol{e}^\infty$ the electric field due to external agencies.

Similar to its magnetic counterpart $\boldsymbol{h}_\mathrm{s}\left(\boldsymbol{m}, \mathcal{B}_t\right)$ the electric self-field $\boldsymbol{e}_\mathrm{s}\left(\boldsymbol{p}, \mathcal{B}_t\right)$ depends on the polarization and on the shape of the body. This is because the determination of $\boldsymbol{e}_\mathrm{s}$ also requires the solution of an electro-static BVP in whole $\mathbb{R}^3$. This is often ignored in the continuum mechanics community where typical examples consider a dielectric body between electrodes. The present setting, however, does not involve any attached electrodes and thus the interactions at the surface of the body cannot be ignored.

We assume that the current configuration of the body $\mathcal{B}_t$ is of ellipsoidal shape and that the material properties and deformation state are uniform. Then $\boldsymbol{p}$ and $\boldsymbol{m}$ and thus also $\boldsymbol{e}_\mathrm{s}$ and $\boldsymbol{h}_\mathrm{s}$ will be homogeneous in response to homogeneous $\boldsymbol{e}^\infty$ and $\boldsymbol{h}^\infty$. Thus we have the relations

$$\boldsymbol{e}_\mathrm{s}(\boldsymbol{p}, \mathcal{B}_t) = -\frac{1}{\epsilon_0}\boldsymbol{N}_d\left(\mathcal{B}_t\right)\cdot\boldsymbol{p} \qquad \text{and} \qquad \boldsymbol{h}_\mathrm{s}(\boldsymbol{m}, \mathcal{B}_t) = -\boldsymbol{N}_d\left(\mathcal{B}_t\right)\cdot\boldsymbol{m}, \tag{8.2}$$

respectively. We insert above expressions into (8.1) and obtain

$$\mathcal{J}/|\mathcal{B}_t| = \jmath = \rho\psi\left(\underline{\boldsymbol{F}}, \boldsymbol{m}/\rho, \boldsymbol{p}/\rho\right) + \frac{1}{2}\mu_0 \boldsymbol{m}\cdot(\boldsymbol{N}_d\cdot\boldsymbol{m}) - \mu_0\boldsymbol{m}\cdot\boldsymbol{h}^\infty + \frac{1}{2\epsilon_0}\boldsymbol{p}\cdot(\boldsymbol{N}_d\cdot\boldsymbol{p}) - \boldsymbol{p}\cdot\boldsymbol{e}^\infty. \tag{8.3}$$

Next we restrict ourselves further to the case of rotational ellipsoids consisting of incompressible isotropic material. Furthermore, we let the rotation axis of the ellipsoid, $\boldsymbol{h}^\infty$ and $\boldsymbol{e}^\infty$ be aligned with the x_1 direction. Accordingly we introduce the specializa-

tions

$$\boldsymbol{h}^{\infty} = \begin{pmatrix} h^{\infty} \\ 0 \\ 0 \end{pmatrix}, \qquad \boldsymbol{m} = \begin{pmatrix} m \\ 0 \\ 0 \end{pmatrix}, \qquad \boldsymbol{e}^{\infty} = \begin{pmatrix} e^{\infty} \\ 0 \\ 0 \end{pmatrix} \qquad \text{and} \qquad \boldsymbol{p} = \begin{pmatrix} p \\ 0 \\ 0 \end{pmatrix} \tag{8.4a}$$

as well as

$$\underline{\boldsymbol{F}}(\lambda) = \begin{pmatrix} \lambda & 0 & 0 \\ 0 & \lambda^{-1/2} & 0 \\ 0 & 0 & \lambda^{-1/2} \end{pmatrix} \qquad \text{and} \qquad \boldsymbol{N}_d(c) = \begin{pmatrix} N(c) & 0 & 0 \\ 0 & \frac{1-N(c)}{2} & 0 \\ 0 & 0 & \frac{1-N(c)}{2} \end{pmatrix} \tag{8.4b}$$

with current aspect ratio $c = l/r$. In order to relate N to the deformation we employ

$$\widehat{N}(\lambda; C) = N(\lambda^{3/2} C) \tag{8.5}$$

with initial aspect ratio $C = L/R$. For the closed form expressions for $N(c)$ we refer to (7.87) and Osborn (1945).

The above specializations inserted into (8.3) lead us to

$$\begin{aligned} &\mathcal{J}(\lambda, m, p; C, h^{\infty}, e^{\infty}) = \\ &\quad \rho\widehat{\psi}(\lambda, m/\rho) + \frac{1}{2}\mu_0 m^2 \widehat{N}(\lambda; C) - \mu_0 m h^{\infty} + \frac{1}{2\epsilon_0} p^2 \widehat{N}(\lambda; C) - p e^{\infty}, \end{aligned} \tag{8.6}$$

of which the first variation[2] with respect to $\{\lambda, p, m\}$ yields the equilibrium condition

$$\begin{aligned} \delta\mathcal{J} = &\left[\rho\frac{\partial\widehat{\psi}}{\partial\lambda} + \frac{\mu_0}{2}\frac{\partial\widehat{N}}{\partial\lambda}m^2 + \frac{1}{2\epsilon_0}\frac{\partial\widehat{N}}{\partial\lambda}p^2\right]\delta\lambda + \left[\rho\frac{\partial\widehat{\psi}}{\partial m} + \mu_0\left(\widehat{N}m - h^{\infty}\right)\right]\delta m \\ &+ \left[\rho\frac{\partial\widehat{\psi}}{\partial p} + \frac{\widehat{N}p}{\epsilon_0} - e^{\infty}\right]\delta p = 0 \qquad \forall\{\delta\lambda, \delta m, \delta p\}. \end{aligned} \tag{8.7}$$

[2]Note that the variation cannot be carried out this way in general. However, in the special setting under consideration the procedure is perfectly valid. We refer to Liu (2014) for more detailed derivations.

8.2. Material models

In order to exclude any material coupling we consider an energy density that can be additively decomposed as

$$\rho\widehat{\psi}(\lambda, m/\rho, p/\rho) = \widehat{\psi}^{\text{mech}}(\lambda) + \widehat{\psi}^{\text{magn}}(m) + \widehat{\psi}^{\text{elec}}(p), \tag{8.8}$$

where we chose for the individual energy contributions

$$\widehat{\psi}^{\text{mech}}(\lambda) = \frac{\mu}{2}\left(\lambda^2 + \frac{2}{\lambda} - 3\right), \tag{8.9a}$$

$$\widehat{\psi}^{\text{magn}}(m) = \mu_0 \frac{{m_\text{s}}^2}{2\chi_0^\text{m}} \left\{ 2\frac{m}{m_\text{s}} \operatorname{artanh}\left[\frac{m}{m_\text{s}} + \ln\left(1 - \frac{m^2}{{m_\text{s}}^2}\right)\right]\right\} \quad \text{and} \tag{8.9b}$$

$$\widehat{\psi}^{\text{elec}}(p) = \frac{p^2}{2\epsilon_0\chi^\text{e}} \tag{8.9c}$$

with the parameter χ^e denoting the electric susceptibility. The energy densities in the equation above correspond to an incompressible neo-Hookean elastic, saturation magnetic and linear dielectric material behavior, respectively. If not explicitly mentioned we employ the values $\mu = 0.1\,\text{MPa}$ and $m_\text{s} = 0.3\,\text{MA}\,\text{m}^{-1}$ in the examples below. Both values are within the range typical for soft magnetic composites such as MREs (Diguet et al., 2010; Spieler et al., 2013; Liu, 2014; Bodelot et al., 2018).

8.3. Shape-dependent electro-mechanical response

Before we eventually come the magneto-electric coupling we present results for electro-mechanical coupling similar to the results for magneto-mechanics in Section 7.4.4. We expect certain characteristics to be the same. However, the lack of saturation in the electric material model and the different range of values for the susceptibility will definitely lead to certain qualitatively different observations.

In Figure 8.1 we depict the deformation λ in response to applied electric field e^∞ for different values for the electric susceptibility χ^e and initial aspect ratio C. We observe

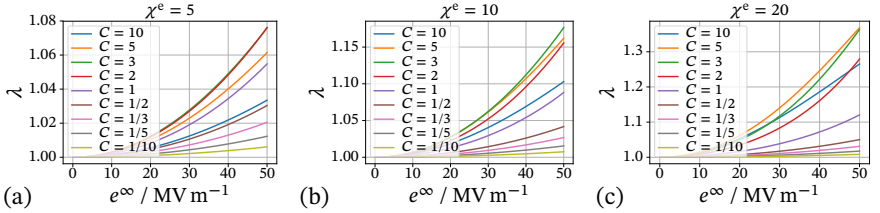

Figure 8.1: Deformation response of rotational ellipsoids with respect to external electric field. The electric susceptibilities are $\chi_e = 5$, $\chi_e = 10$ and $\chi_e = 20$ in (a), (b) and (c), respectively (Rambausek and Keip, 2018a).

that prolate ellipsoids tend to exhibit a stronger deformation than oblate ones and that the initial aspect ratio C for maximum deformation shifts to higher values with increasing χ^e. Moreover, in particular in Subplot 8.1c where $\chi^\mathrm{e} = 20$ but also in Subplot 8.1b we have intersecting graphs as a consequence of nonlinearities in the responses.

Figure 8.2 shows plots of the deformation versus the initial aspect ratio C. In all three

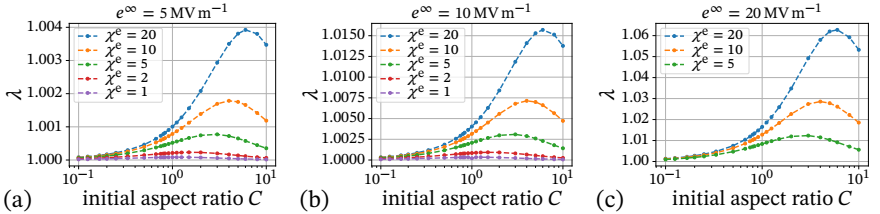

Figure 8.2: Deformation response of rotational ellipsoids with respect to external electric field plotted over aspect ratio C for different external electric fields. Keeping C fixed and change χ^e the location of maximum deformation moves to the right. In turn, changing see for fixed χ^e lets the maximum deformation move to the left (Rambausek and Keip, 2018a).

plots we again see that the aspect ratio for maximum deformation moves to higher values with increasing χ^e. However, when we compare the graphs for one χ^e from left to right (increasing electric load) we observe a slight shift of the extrema to smaller aspect ratios. The same tendency, but more pronounced, was also present in the magneto-

mechanical case (see Figure 7.39). We close the presentation of electro-mechanical results with Figure 8.3 where we show the polarization response plotted versus C.

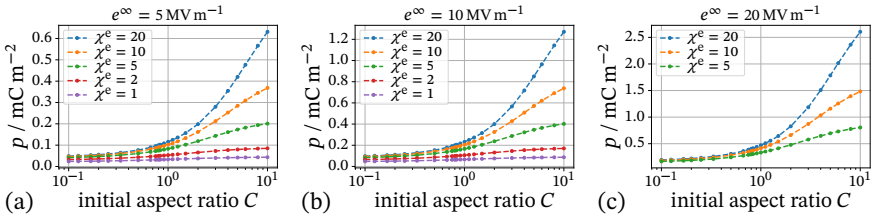

Figure 8.3: Electric polarization response of rotational ellipsoids with respect to external electric field over aspect ratio C for different external electric fields (Rambausek and Keip, 2018a).

8.4. Non-local deformation-mediated magneto-electric coupling

Recall that $\widehat{N}(\lambda; C)$ is the quantity responsible for magneto- and electro-mechanical coupling. From (8.7) and the energy densities (8.9) we also see that there is no direct magneto-electric coupling. It is however clear that the simultaneous action of magneto- and electro-mechanical coupling results in a magneto-electric effect. In the current section we characterize this effect in terms of changes in the electric field component $e = (\boldsymbol{e})_1$ inside the body in response to changes in the magnetic load $h^\infty = (\boldsymbol{h}^\infty)_1$ for prescribed $e^\infty = (\boldsymbol{e}^\infty)_1$. We start from

$$e = e^\infty + e_\mathrm{s} = e^\infty - \widehat{N}(\lambda; C)p \tag{8.10}$$

where we immediately see that e changes with λ through $\widehat{N}$ as schematically depicted in Figure 8.4. However, the situation is actually a bit more involved since, e.g., the po-

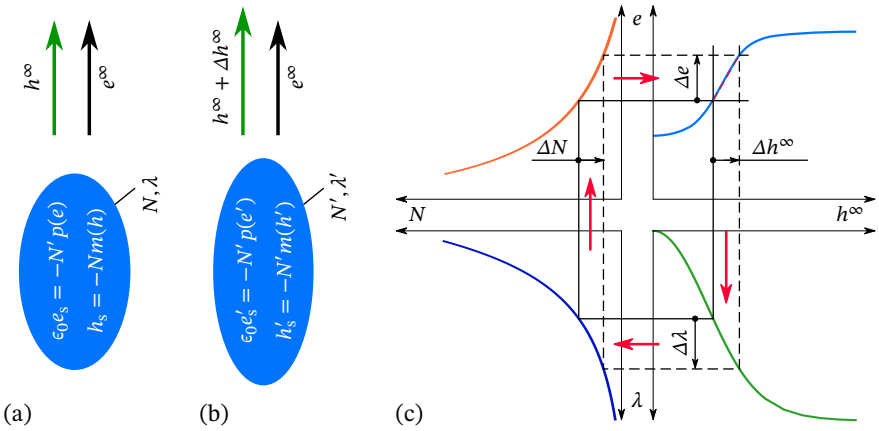

Figure 8.4: A sketch of non-local magneto-electric coupling through shape-effects. In (a) a deformed elliptical body exposed to external fields e^∞ and h^∞. For such a body a change in the external magnetic field Δh^∞ (b) leads to additional deformation $\lambda' = \lambda + \Delta\lambda$. As a consequence, the *shape property* N changes from N to N' which in turn yields a change Δe from e to e'. The diagram in (c) summarizes the deformation-mediated response of e with respect to a change in h^∞ for e^∞ being unchanged.

larization p will also change with $\widehat{N}$. Thus, we must consider systems at *equilibrium*. Therefore, we employ adjoint sensitivity analysis (see also Appendix C) to capture the sensitivity of e with respect to h^∞ while respecting this physical constraint. As a first step, we introduce a Lagrangian-type function

$$e^+(\lambda, m, p, \boldsymbol{\lambda}; h^\infty) = e(\widehat{N}(\lambda), p) - \delta\, \mathfrak{f}(\delta\{\lambda, m, p\} = \boldsymbol{\Lambda}; h^\infty) \tag{8.11}$$

with $\boldsymbol{\Lambda}$ being a Lagrange multiplier enforcing the equilibrium condition (8.7) and h^∞ explicitly mentioned as a parameter. The total differential of e^+ is obtained as

$$\begin{aligned}\mathrm{d}e^+ = &\left(\frac{\partial e}{\partial \widehat{N}}\frac{\partial \widehat{N}}{\partial \lambda} - \frac{\partial \delta \jmath(\delta\{\lambda, m, p\} = \boldsymbol{\Lambda}; h^\infty)}{\partial \lambda}\right)\mathrm{d}\lambda \\ &+ \left(\frac{\partial e}{\partial p} - \frac{\partial \delta \jmath(\delta\{\lambda, m, p\} = \boldsymbol{\Lambda}; h^\infty)}{\partial p}\right)\mathrm{d}p \\ &- \frac{\partial \delta \jmath(\delta\{\lambda, m, p\} = \boldsymbol{\Lambda}; h^\infty)}{\partial m}\,\mathrm{d}m - \frac{\partial \delta \jmath(\delta\{\lambda, m, p\} = \boldsymbol{\Lambda}; h^\infty)}{\partial \boldsymbol{\Lambda}}\,\mathrm{d}\boldsymbol{\Lambda} \\ &- \frac{\partial \delta \jmath(\delta\{\lambda, m, p\} = \boldsymbol{\Lambda}; h^\infty)}{\partial h^\infty}\,\mathrm{d}h^\infty, \end{aligned} \tag{8.12}$$

where we require the coefficients of $\{\mathrm{d}\lambda, \mathrm{d}m, \mathrm{d}p, \mathrm{d}\boldsymbol{\Lambda}\}$ to vanish. This gives us the equilibrium condition as equation for $\{\lambda, m, p\}$ as well as a system of three equations for the three components of $\boldsymbol{\Lambda}$. The corresponding solutions are denoted as $\hat{\boldsymbol{S}} = \{\hat{\lambda}, \hat{m}, \hat{p}, \hat{\boldsymbol{\Lambda}}\}$ and accordingly $\delta\hat{\jmath}(h^\infty) = \delta\jmath(\{\lambda, m, p, \delta\lambda, \delta m, \delta p\} = \hat{\boldsymbol{S}}; h^\infty)$. With $\hat{e} = e^+(\{\lambda, m, p, \boldsymbol{\Lambda}\} = \hat{\boldsymbol{S}})$ we arrive at

$$\mathrm{d}\hat{e} = -\frac{\partial \delta\hat{\jmath}(h^\infty)}{\partial h^\infty}\,\mathrm{d}h^\infty, \tag{8.13}$$

which represents the sensitivity of the electric field inside the body e with respect to h^∞ under the constraint (8.7). Of course, since e^∞ is regarded as a given constant parameter, $\mathrm{d}\hat{e} = \mathrm{d}\hat{e}_\mathrm{s}$. Note that we did not specify how to proceed from (8.12) to (8.13) in detail. In fact, when we first solve for $\{\lambda, m, p\}$ to fulfill the state constraint we may substitute $e = e^\infty - \widehat{N}p$ from (8.10) with

$$e = \rho\partial_p\widehat{\psi} \tag{8.14}$$

as can be seen from the last term in (8.7). The resulting system of equations for $\boldsymbol{\Lambda}$ then still hast the same coefficient matrix, but a different right-hand-side. Since we expect the coefficient matrix to be non-singular, if follows that the solutions for $\boldsymbol{\Lambda}$ cannot be identical in both cases. In fact, it turns out that the difference is in only $\hat{\Lambda}_3$, which does not affect the coefficient of $\mathrm{d}h^\infty$ in (8.13).

A rather direct approach to the ME sensitivity can be found in Rambausek and Keip (2018a). However, the adjoint approach, in particular the two-step version based on (8.14) can be directly generalized to more complicated BVPs and FE schemes.

For the results presented below we employed material parameters as mentioned in Section 8.2 and comparable to values reported in literature (Gallone et al., 2007; Vertechy et al., 2012).

Based on the above derivation, Figure 8.5a shows a *computed* version of the sketch Figure 8.4c. Figure 8.5b depicts the obtained ME sensitivity $\mathrm{d}\hat{e}/\,\mathrm{d}h^\infty$ and 8.5b the corresponding sensitivity of the polarization for which we exploited the relation $p = \epsilon_0\chi^\mathrm{e}e$ in accordance with (8.9c). In both of the sensitivity plots we observe that the sensitivities start with 0 for $h^\infty = 0$, which is expected because of the horizontal tangent in the

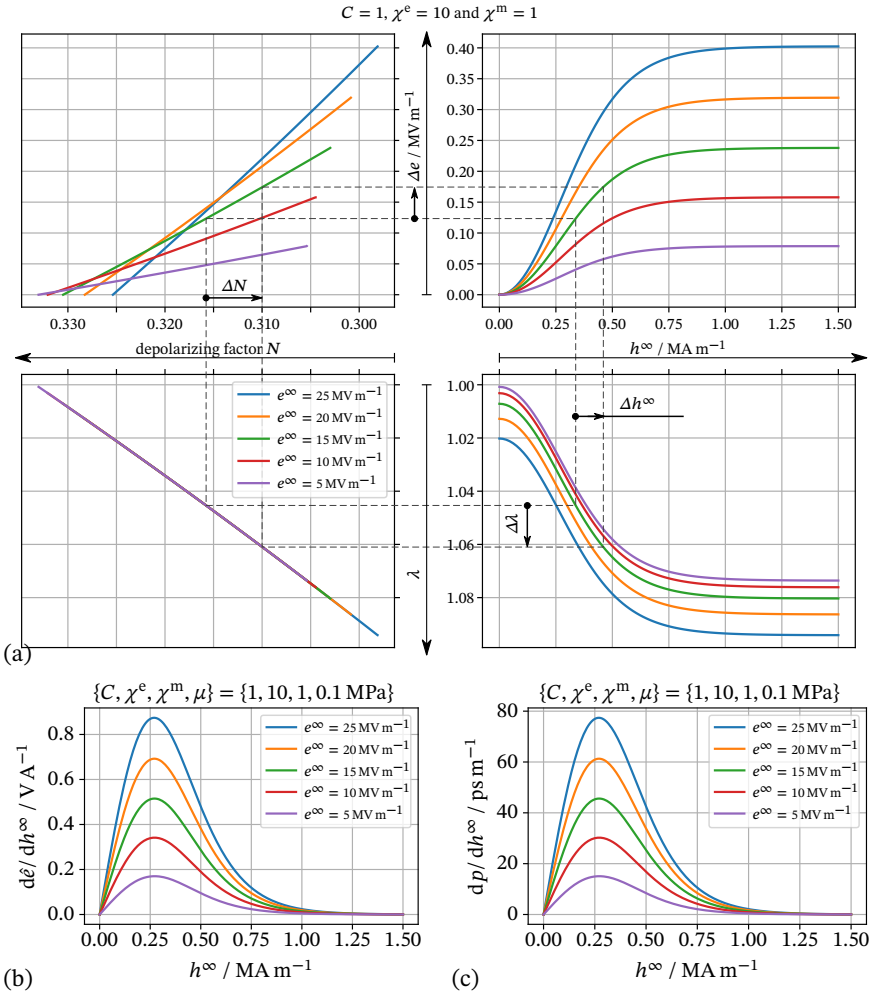

Figure 8.5: Non-local magneto-electric coupling: In (a) we depict a plot similar to the qualitative sketch in Figure 8.4c. Subplot (b) depicts the sensitivity of the electric field. In (c) we show the sensitivity of the polarization. The electric field e^∞ is given in $\mathrm{MV\,m^{-1}}$ (Rambausek and Keip, 2018a).

magneto-mechanical deformation response (see Figure 7.38). For moderate h^∞ the sensitivities then increase and attain their extrema close to $h^\infty = 0.25\,\mathrm{MA\,m^{-1}}$. For high applied magnetic loads the sensitivities eventually approach zero due to magnetic satu-

ration. We also see that the electric bias e^∞ increases the ME sensitivity. However, this behavior shall not be extrapolated since the whole BVP features nonlinearities which may change this tendency at some point.

In Figure 8.6 we show plots of the total magnetically induced change in the electric field (short induced electric field) defined as

$$\Delta\hat{e} = \hat{e}(h^\infty, e^\infty) - \hat{e}(h^\infty = 0, e^\infty) \tag{8.15}$$

for four different combinations of material parameters. By comparison of Subplots (a),

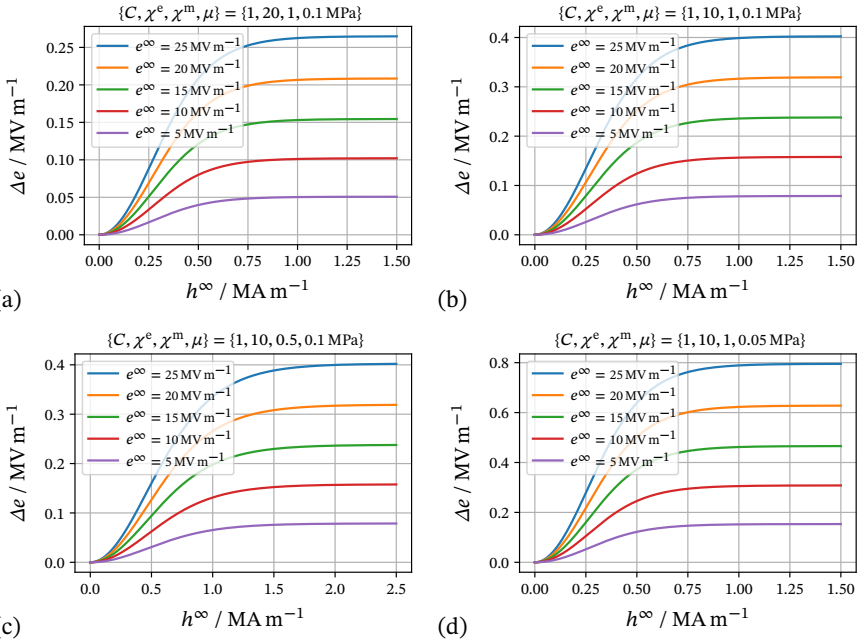

Figure 8.6: Electric field change $\Delta\hat{e} = \hat{e}(h^\infty) - \hat{e}(h^\infty = 0)$ induced by non-local magneto-electric coupling for four different sets of material parameters (Rambausek and Keip, 2018a).

(b) and (c) we see the interesting effect that a smaller χ^e leads to a higher induced field $\Delta\hat{e}$ whereas a change in χ^m leads to a horizontal scaling of the graphs. This is because we essentially evaluate the sensitivity of the electric field inside the ellipsoidal body. The picture is different for the sensitivities of the polarization $\boldsymbol{p}$ and the charge potential $\boldsymbol{d} = \epsilon_0\boldsymbol{e} + \boldsymbol{p}$. We also note that the sensitivity of $\boldsymbol{e}$ inside is identical to the sensitivity at a point at the surface where the external electric field is tangential to the surface. On the other hand, the sensitivity of $\boldsymbol{d}/\epsilon_0$ translates to the sensitivity of the electric field at the

surface where the external field is normal to the surface. A reduction of the mechanical parameter μ as expected leads to higher $\Delta\hat{e}$ (Figure 8.6d). The ME sensitivities, which are nothing else than the first derivative of $\Delta\hat{e}$ with respect to h^∞, are depicted in Figure 8.7.

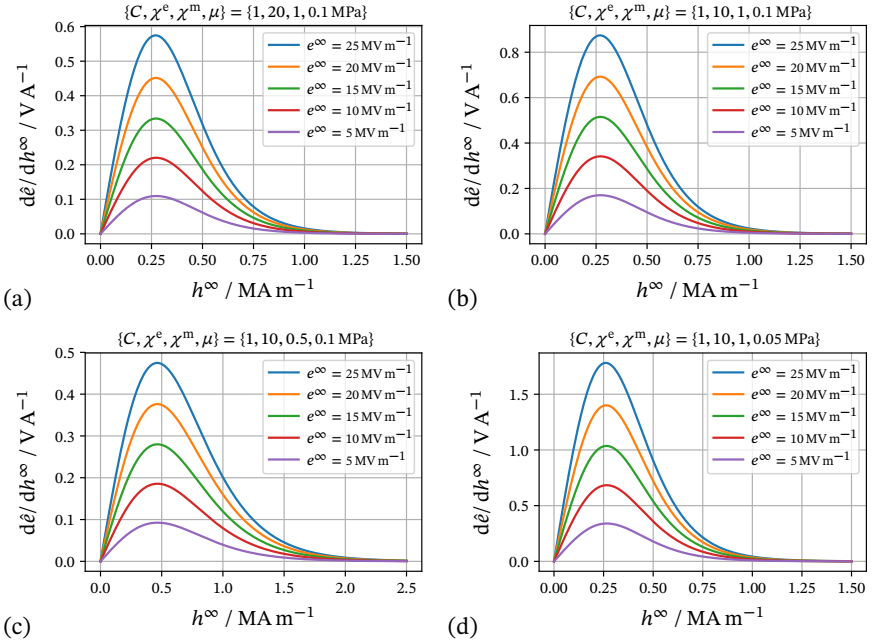

Figure 8.7: The non-local magneto-electric sensitivities corresponding to derivatives of the graphs in Figure 8.6 (Rambausek and Keip, 2018a).

Now we turn to the effect of the initial aspect ratio on the ME coupling performance. Figure 8.8 depicts the ME sensitivities for various aspect ratios $C \in [1/5, 5]$, where we find that ellipsoids with $C \in [3/2, 3]$ exhibit the highest sensitivities. Moreover, we observe that the value h^∞ for the extrema shows a certain dependence on C. Corresponding surface plots showing $\mathrm{d}\hat{e}/\,\mathrm{d}h^\infty$ over e^∞ and h^∞ for $C = 1$ and $C = 5$ are collected in Figure 8.9. In the case of $C = 1$ (Figure 8.9a) the ME sensitivity depends almost linearly on e^∞. In Subplot (b), by contrast, the relation is clearly nonlinear and suggests a local extremum occuring for some higher e^∞. To get a more complete impression of the shape influence, Figure 8.10 presents surface plots of $\mathrm{d}\hat{e}/\,\mathrm{d}h^\infty$ over C and h^∞. Obviously, slightly prolate shapes exhibit the highest ME sensitivities. Regarding the influence of the electric bias e^∞ on the C-location of the extremal sensitivity we only observe a slight shift towards $C = 1$ for higher e^∞. As with for the influence of χ^e different tendencies

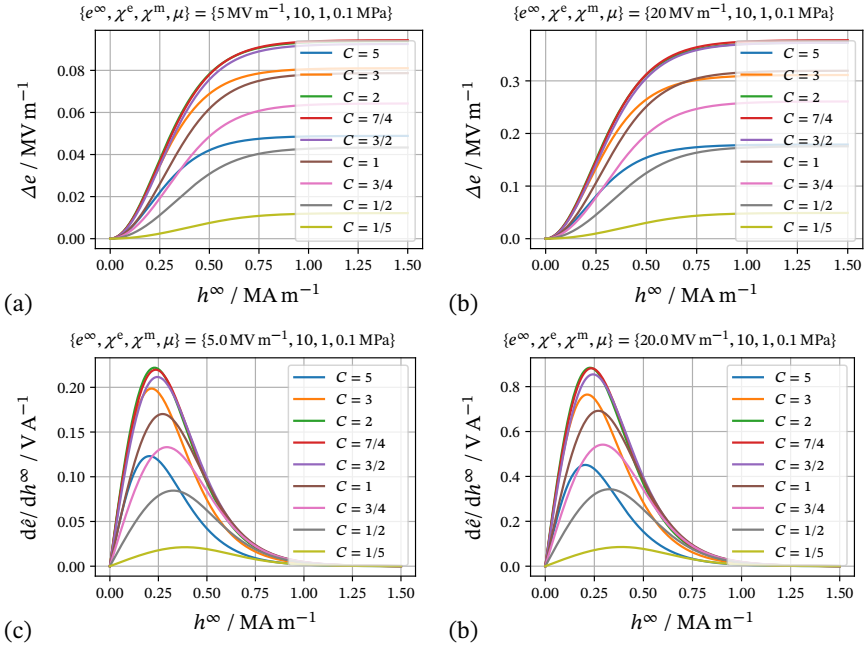

Figure 8.8: Induced electric field and magneto-electric sensitivities in dependence of the aspect ratio. Subplots (a) and (b) depict the induced electric field $\Delta\hat{e} = \hat{e}(h^\infty) - \hat{e}(h^\infty = 0)$. The corresponding sensitivities $\mathrm{d}\hat{e}/\,\mathrm{d}h^\infty$ can be found in (c) and (d) (Rambausek and Keip, 2018a).

may be observed for the sensitivities of $\boldsymbol{p}$ and $\boldsymbol{d}$.

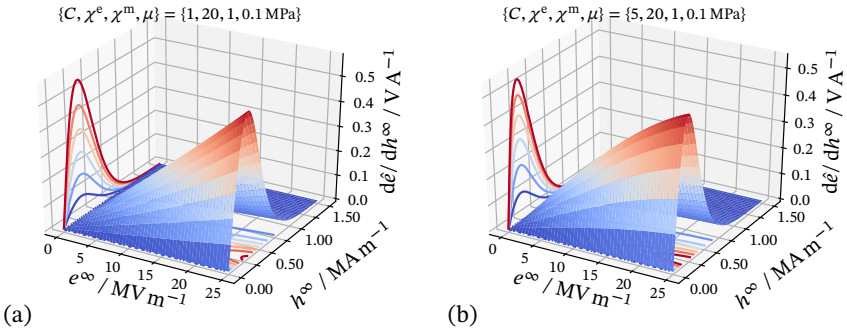

Figure 8.9: Surface plots of the magneto-electric sensitivity $\mathrm{d}\hat{e}/\mathrm{d}h^\infty$ as a function of the external fields e^∞ and h^∞ for initial aspect ratios $C = 1$ and $C = 5$ in (a) and (b), respectively (Rambausek and Keip, 2018a).

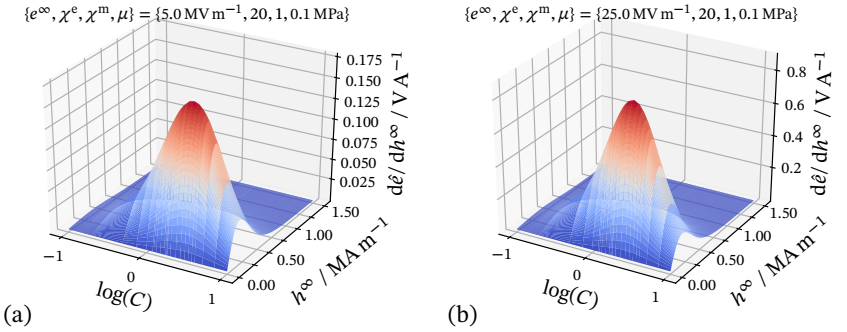

Figure 8.10: Surface plots of the magneto-electric sensitivity $\mathrm{d}\hat{e}/\mathrm{d}h^\infty$ as a function of the initial aspect ratio C and the external field h^∞. The external electric field was set to $e^\infty = 5\,\mathrm{MV\,m^{-1}}$ in (a) and to $e^\infty = 25\,\mathrm{MV\,m^{-1}}$ in (b) (Rambausek and Keip, 2018a).

8.5. Comparison with finite element simulations

The finite element implementation of magneto-electro-elasticity discussed below is a direct extension the magneto-mechanics framework presented in Section 7.1 and in Subsection 7.1.5 in particular. What we add is the electric potential ϕ^{e} as primary variable for the electric part of the coupled problem.

The referential (Lagrangian) electric field is obtained as

$$\boldsymbol{E} = -\operatorname{Grad}\phi^{\mathrm{e}}. \tag{8.16}$$

Dual to $\boldsymbol{E}$ we have the Lagrangian charge potential $\boldsymbol{D}$ better known as Lagrangian electric displacement. Their counterparts in the current configuration are related through

$$\boldsymbol{d} = \epsilon_0 \boldsymbol{e} + \boldsymbol{p} \qquad \text{with} \qquad \boldsymbol{e} = \underline{\boldsymbol{F}}^{-\mathrm{T}} \cdot \boldsymbol{E} \qquad \text{and} \qquad \boldsymbol{d} = \frac{1}{J}\underline{\boldsymbol{F}} \cdot \boldsymbol{D}. \tag{8.17}$$

The additional equations are the laws of Gauß and Faraday for electrostatics in their Lagrangian form together with the associated jump conditions

$$\operatorname{Curl}\boldsymbol{E} = \boldsymbol{0} \qquad \text{and} \qquad \operatorname{Div}\boldsymbol{D} = 0 \qquad \text{in } \Omega, \tag{8.18a}$$

$$[\![\boldsymbol{E}]\!] \times \boldsymbol{N} = \boldsymbol{0} \qquad \text{and} \qquad [\![\boldsymbol{D}]\!] \cdot \boldsymbol{N} = 0 \qquad \text{across } S. \tag{8.18b}$$

respectively. Furthermore, we explicitly account for incompressibility expressed as a kinematic constraint

$$J = \det\underline{\boldsymbol{F}} = 1 \quad \text{in } \mathcal{B}, \tag{8.19}$$

which will be enforced by means of a pressure-like Lagrange multiplier denoted as κ to avoid confusion with the scalar form of polarization p employed above.

8.5.1. Variational framework

With ϕ^{e} and κ as additional scalar-valued variables, we extend the variational formulation introduced in Subsection 7.1.2. The additions for the electric quantities are almost identical to the magnetic part. such that we proceed without much ado. For details on incompressibility we refer to Bonet and Wood (2008). The governing variational (saddle-point) principle reads as

$$\{\hat{\varphi}, \hat{\phi^{\mathrm{m}}}, \hat{\phi^{\mathrm{e}}}, \hat{\kappa}\} = \arg\left\{ \inf_{\substack{\varphi \\ \in \\ \mathscr{W}_{\varphi}}} \sup_{\substack{\phi^{\mathrm{m}} \\ \in \\ \mathscr{W}_{\phi^{\mathrm{m}}}}} \sup_{\substack{\phi^{\mathrm{e}} \\ \in \\ \mathscr{W}_{\phi^{\mathrm{e}}}}} \sup_{\substack{\kappa \\ \in \\ \mathscr{W}_{\kappa}}} \Pi(\varphi, \phi^{\mathrm{m}}, \phi^{\mathrm{e}}, \kappa) \right\}, \tag{8.20}$$

with Π in the absence of loading functionals given as

$$\Pi = \int_{\mathcal{B}} \Psi^{\mathrm{m}}\left(\underline{\boldsymbol{F}}, \boldsymbol{H}, \boldsymbol{E}\right) + \kappa(J-1)\, dV + \int_{\Omega\setminus\mathcal{B}} \Psi^{\mathrm{f}}\left(\underline{\boldsymbol{F}}, \boldsymbol{H}, \boldsymbol{E}\right)\, dV, \tag{8.21}$$

and spaces

$$\mathcal{W}_\varphi = \{\varphi \mid \varphi_\mathrm{i} \in \mathscr{H}(\mathrm{Grad}, \Omega),\ \pi_\varphi(\varphi) = \pi_\varphi(\varphi_\mathrm{D}) \text{ on } \partial\Omega_\varphi \cup \partial\mathcal{B}_\varphi\}, \tag{8.22a}$$

$$\mathcal{W}_{\phi^\mathrm{m}} = \{\phi^\mathrm{m} \mid \phi^\mathrm{m} \in \mathscr{H}(\mathrm{Grad}, \Omega),\ \phi^\mathrm{m} = \phi^\mathrm{m}_\mathrm{D} \text{ on } \partial\Omega_{\phi^\mathrm{m}}\}, \tag{8.22b}$$

$$\mathcal{W}_{\phi^\mathrm{e}} = \{\phi^\mathrm{e} \mid \phi^\mathrm{e} \in \mathscr{H}(\mathrm{Grad}, \Omega),\ \phi^\mathrm{e} = \phi^\mathrm{e}_\mathrm{D} \text{ on } \partial\Omega_{\phi^\mathrm{e}}\} \quad \text{and} \tag{8.22c}$$

$$\mathcal{W}_\kappa = L_2(\mathcal{B}). \tag{8.22d}$$

8.5.2. The discrete boundary value problem

In the FE simulations we consider a spherical free-space domain Ω_h in which we embed the ellipsoidal specimens $\mathcal{B}$ as depicted in Figure 8.11. To have a good approximation of

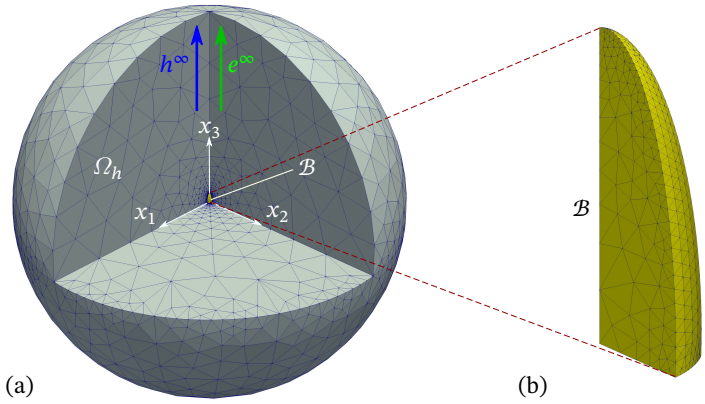

Figure 8.11: FE Boundary value problem for non-local magneto-electric coupling. An ellipsoidal body $\mathcal{B}$ is embedded into a spherical truncated free space Ω_h with $R^\mathcal{B}/R^{\Omega_h} = 1/20$. In (a) we depict the full discrete setting except for one octant to reveal the specimen. Since the problem has rotational symmetry around x_3 we only simulate the domain with $x_1 > 0$, $x_2 > 0 \wedge x_2 < x_1/2$ and $x_3 > 0$ with appropriate symmetry conditions. Subplot (b) shows the meshed specimen and indicates the exploitation of symmetry.

the BVP considered by the analytical model, the radius of Ω_h is twenty times the length of the major axis of the body $\mathcal{B}$.

The homogeneous external fields $\boldsymbol{e}^\infty$ and $\boldsymbol{h}^\infty$ enter the formulation via the decompositions

$$\phi^\mathrm{m} = -\boldsymbol{h}^\infty \cdot X + \phi^\mathrm{m}_\mathrm{p} \qquad \text{and} \qquad \phi^\mathrm{e} = -\boldsymbol{e}^\infty \cdot X + \phi^\mathrm{e}_\mathrm{p}, \tag{8.23}$$

as explained in Section 7.1.3 for the magnetic case. Accordingly the potentials $\phi^\mathrm{m}_\mathrm{p}$ and $\phi^\mathrm{e}_\mathrm{p}$ are the actual degrees of freedom in the FE implementation. Both of them are set to zero on the boundary of the truncated free space $\partial\Omega_h$ depicted in Figure 8.11.

For the discretization of the electric primary variable $\phi_{\mathrm{p}}^{\mathrm{e}}$ we employ exactly the same discretization as for $\phi_{\mathrm{p}}^{\mathrm{m}}$ (see Subsection 7.1.5). Throughout the current section we apply tetrahedral Lagrangian elements with shape functions of order 2 for all three fields φ, $\phi_{\mathrm{p}}^{\mathrm{m}}$ and $\phi_{\mathrm{p}}^{\mathrm{e}}$. The pressure κ is chosen element-wise constant, which in the present context turned out to yield a sufficiently stable numerical implementation.

For comparison with the analytical model we employ energy density functions consistent with (8.9). In the empty space $\Omega_h \setminus \mathcal{B}$ we use

$$\widehat{\Psi}^{\mathrm{f}}(\underline{\boldsymbol{F}}, \boldsymbol{H}, \boldsymbol{E}) = -\frac{J\epsilon_0}{2}\|\boldsymbol{e}\|^2 - \frac{J\mu_0}{2}\|\boldsymbol{h}\|^2 \tag{8.24}$$

whereas for the actual body $\mathcal{B}$ under consideration we employ

$$\widehat{\Psi}^{\mathrm{m}}(\underline{\boldsymbol{F}}, \boldsymbol{H}, \boldsymbol{E}) = \widehat{\Psi}^{\mathrm{f}} + \frac{\mu}{2}(\operatorname{tr}\boldsymbol{C} - \operatorname{tr}\mathbf{1}) - \epsilon_0\frac{\chi^{\mathrm{e}}}{2}\|\boldsymbol{e}\|^2 - \mu_0\frac{{m_{\mathrm{s}}}^2}{\chi_0^{\mathrm{m}}}\ln\left[\cosh\left(\frac{\chi_0^{\mathrm{m}}}{m_{\mathrm{s}}}\|\boldsymbol{h}\|\right)\right], \tag{8.25}$$

with material parameters given in Table 8.1. Note that $\widehat{\Psi}^{\mathrm{f}}$ as given in (8.24) does not include any elastic energy density. Hence, the resulting discrete system of equations will be singular. As a consequence, we apply a staggered solution scheme (Pelteret et al., 2016) where the electric and magnetic equations are solved throughout Ω_h but the fully coupled equations only in $\mathcal{B}$ plus a single layer of adjacent elements in free space. This is implemented by fixing the discrete mechanical degrees of freedom everywhere in $\Omega_h \setminus (\mathcal{B} \cup \partial\mathcal{B})$ during solution of (8.20). Then, in second step the mesh in the empty domain is updated using a pseudo-elastic energy.

Table 8.1: Material parameters employed in the comparison.

μ / MPa	χ^{e} / 1	χ_0^{m} / 1	m_{s} / MA m^{-1}
0.1	10.0	1.0	0.3

8.5.3. Results

For the determination of ME coupling in the FE simulations we consider the average 3-component of the electric field e_3 within the small domain $\mathcal{B}^{\mathrm{e}}$ indicated in Figure 8.12. The Lagrangian function analogous to (8.11)

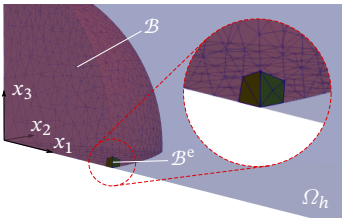

Figure 8.12: The domain $\mathcal{B}^{\mathrm{e}}$ within an magneto-electric ellipsoid (here: a sphere) for the evaluation of the electric field as quantity of interest.

$$e_h^+ = \frac{1}{\mathcal{B}^{\mathrm{e}}} \int_{\mathcal{B}^{\mathrm{e}}} \left(\underline{\boldsymbol{F}}^{-\mathrm{T}} \cdot \boldsymbol{E}\right)_3 \, dV - \delta\Pi\left(\delta\{\varphi_h, \phi^{\mathrm{m}}_{p,h}, \phi^{\mathrm{e}}_{p,h}, \varkappa\} = \boldsymbol{\Lambda}_h; h^\infty\right) \tag{8.26}$$

serves as the basis for adjoint sensitivity analysis as outlined in Subsection 8.4. We refer to Appendix C for a more general discussion of this technique.

In Figure 8.13 we compare analytical results to FE simulation for four different aspect ratios C. In subplots (c) and (d) the FE and the analytical model are in very good agreement, whereas for $C = 1$ (subplot (b)) the deviations are in the order of 20 %. However, for $C = 1/2$ the deviations decrease again to approximately 10 %. Despite that, the magnetic loads at which the maximum sensitivities are attained are practically the same for the analytical and the FE results.

Figure 8.14 show plots that directly compare the ME coupling for various aspect ratios C. We conclude that the analytical prediction of the aspect ratio that maximizes the ME coupling is quite accurate despite the deviations for aspect ratios close to $C = 1$. We also note that the FEM predicts optimal aspect ratios which are slightly smaller than the analytically predicted ones. This is a result of the over-constrained kinematics in the analytical model.

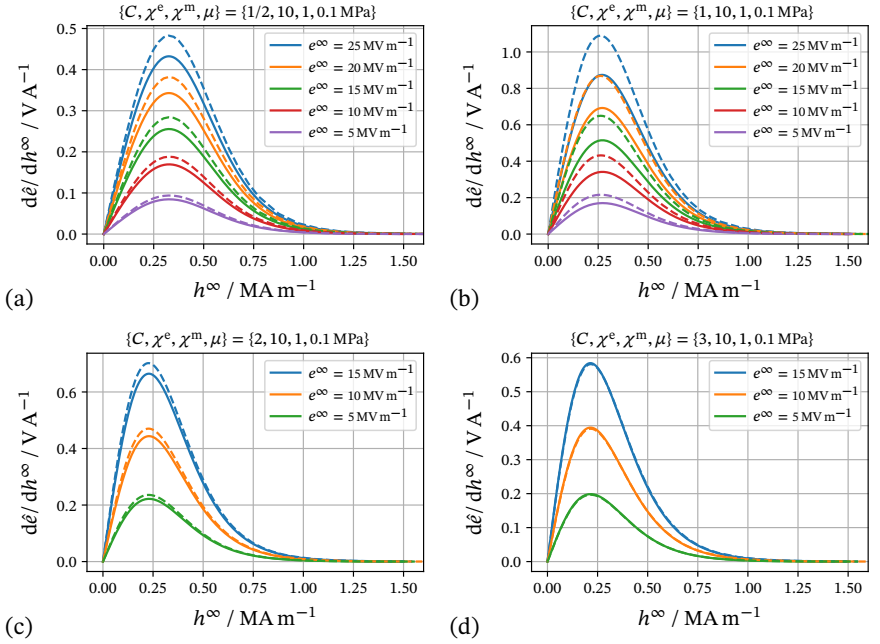

Figure 8.13: Comparison of magneto-electric sensitivities obtained with the proposed model and FE simulations. Note that for $C = 2$ and $C = 3$ the FE simulations suffered from stability issues. As a result we could not produce graphs for $e^\infty = \{20, 25\}\,\mathrm{MV\,m^{-1}}$ for the cases (c) and (d) (Rambausek and Keip, 2018a).

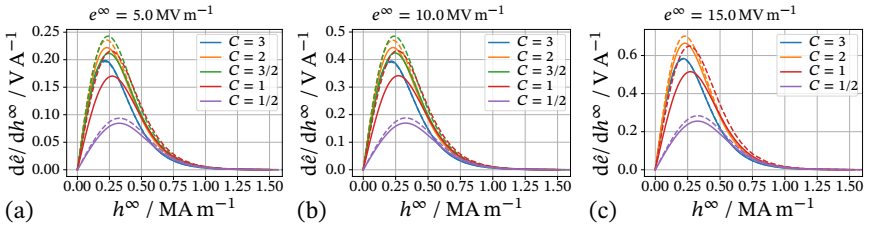

Figure 8.14: Comparison of the ME coupling for various aspect ratios C predicted by the analytical estimates and the FE simulations. In plot (c) the graph for $C = 3/2$ is omitted because of stability issues in the FE simulations for $h^\infty \approx 0.4\,\mathrm{MA\,m^{-1}}$ (Rambausek and Keip, 2018a).

Chapter 9

A constrained-minimization formulation for magneto-electro-elasticity at finite strains

In FE simulations in the field of finite-strain magneto-electro-elasticity we face the challenge of spurious magneto- and electro-mechanical interactions that occur most prominently in the convenient numerical implementations based on scalar potentials ϕ^{e} and ϕ^{m}. The effect of these spurious interactions are most severe in the vicinity of curved interfaces that separate regions or bodies with different electric or magnetic properties. Their effect is negligible in case of rather stiff material. It is, however, significant in very soft media irrespective[1] of their electric and magnetic properties. They even lead to artificial instabilities and crashes of numerical simulations in scenarios of practical interest.

The second important point is the field of stability analysis where one usually strives for minimizer-formulations that allow for the reliable detection of loss of stability indicated by negative eigenvalues. The convenient scalar-potential formulations, however, always have saddle-point structure and are thus not the first choice for that kind of problems. In turn, formulations based on vector potentials $\boldsymbol{A}^{\mathrm{e}}$ and $\boldsymbol{A}^{\mathrm{m}}$ for $\boldsymbol{D}$ and $\boldsymbol{B}$, respectively, fit the bill Psarra et al. (2017); Polukhov et al. (2018). Unfortunately, their implementation is more involved and the resulting systems of equations significantly increase and so does the computational effort (Bossavit, 1998a). Under certain conditions, mainly depending on the actual boundary conditions and material laws, it is possible to transform a vector-potential formulation of a BVP into a scalar-potential formulation. This was exploited in (Miehe et al., 2015, 2016) in the context of homogenization. In these works it was shown how one can still obtain positive definite matrices suitable for the stability analysis of the homogenized material, despite using scalar-potential formulations. Moreover, while in magnetostatics it is appropriate to identically fulfill $\mathrm{Div}\,\boldsymbol{B} = 0$, in electrostatics we have $\mathrm{Div}\,\boldsymbol{D} = q \neq 0$ in general. Thus, formulations employing $\boldsymbol{A}^{\mathrm{e}}$ cannot cover all scenarios of relevance.

The present chapter is dedicated to a variational framework for magneto-electro-elasticity that is motivated by the issue of spurious magneto- and electro-elastic interactions in scalar-potential formulations. Different from scalar-potential formulations the proposed "mixed" approach features a saddle-point structure coming from linearly constrained minimization. Hence, the resulting problems can be solved by powerful min-

[1] Because of that one can see that they are indeed spurious.

imization algorithms (Nocedal and Wright, 2006). This also renders our approach an attractive alternative to vector-potential formulations in terms of computational efficiency.

The remainder of the chapter is structured as follows: In Section 9.1 we provide a summary of the essential theory and then derive the constrained-minimization formulation. Section 9.3.1 contains numerical examples by which we compare the proposed mixed formulation with scalar-potential formulations. In Section 9.4 we compare the mixed formulation with various discretization schemes and formulations by means of a magneto-electro-mechanical BVP as considered in Section 8.5. Also note that the chapter is supposed to be largely self-contained and thus contains parts of the theory provided in greater detail in Chapter 4.

9.1. Theory

The theoretical basis for the content of present chapter is provided by the works (Brown, 1966; Dorfmann and Ogden, 2003; Dorfmann and Brigadnov, 2004; Kankanala and Triantafyllidis, 2004; Steigmann, 2004) on magneto-elasticity, the contributions (Toupin, 1956; Dorfmann and Ogden, 2005, 2006) on electro-elasticity and also by the publications (Pao and Hutter, 1975; Eringen and Maugin, 1990; Kovetz, 2000) on full magneto-electro-mechanics. Furthermore, we highlight the theoretical contributions of Ericksen (2006, 2007), Bustamante et al. (2008, 2009a) and Liu (2013, 2014) focusing on variational formulations relevant to the present scope.

After recalling the fundamental equations and constitutive relations, we introduce the constrained-minimization formulation and discuss the FE implementation thereof.

9.1.1. Fundamental equations of magneto-electro-elasticity

In the present context we consider the quasi-static Maxwell equations in presence of free-charge densities q and absence of free currents

$$\operatorname{div} \boldsymbol{d} = q, \qquad \operatorname{curl} \boldsymbol{h} = \boldsymbol{0} \tag{9.1a}$$

$$\operatorname{curl} \boldsymbol{e} = 0, \qquad \operatorname{div} \boldsymbol{b} = 0 \tag{9.1b}$$

valid in whole space $\mathbb{R}^3$. Across a quasi-statically moving surface $\mathcal{S}_t$ free of currents with unit normal $\boldsymbol{n}$ and surface charge q^{s} we have the jump conditions

$$[\![\boldsymbol{d}]\!] \cdot \boldsymbol{n} = q^{\mathrm{s}}, \qquad [\![\boldsymbol{h}]\!] \times \boldsymbol{n} = \boldsymbol{0} \tag{9.2a}$$

$$[\![\boldsymbol{e}]\!] \times \boldsymbol{n} = \boldsymbol{0}, \qquad [\![\boldsymbol{b}]\!] \cdot \boldsymbol{n} = 0. \tag{9.2b}$$

We point out that the grouping of equations in (9.1a) and (9.1b) is not by their electric or magnetic nature but rather along the more fundamental principle of charge conservation involving $\boldsymbol{d}$ and $\boldsymbol{h}$ as well as Faraday's law connecting $\boldsymbol{e}$ and $\boldsymbol{b}$ (Kovetz, 2000, Chapters 3 and 4). Accordingly, we refer to $\boldsymbol{d}$ as the charge potential, $\boldsymbol{h}$ as the current

potential, $\boldsymbol{e}$ as the electric field and $\boldsymbol{b}$ as the magnetic field. Additionally, we have the relations

$$\boldsymbol{d} = \epsilon_0 \boldsymbol{e} + \boldsymbol{p} \qquad \text{and} \qquad \boldsymbol{h} = \frac{\boldsymbol{b}}{\mu_0} - \boldsymbol{m} \tag{9.3}$$

with polarization $\boldsymbol{p}$ and magnetization $\boldsymbol{m}$ representing potentials for *bound* charges and currents, respectively. Naturally, $\boldsymbol{p} \equiv 0$ and $\boldsymbol{m} \equiv 0$ in vacuum.

Next, we introduce the electric potential ϕ^{e} and the magnetic vector potential $\boldsymbol{a}^{\mathrm{m}}$ which combine to the electro-magnetic 4-potential $\mathfrak{a} = (-\phi^{\mathrm{e}}, \boldsymbol{a}^{\mathrm{m}})$ (Kovetz, 2000, Chapter 4) and yield in the time-independent (quasi-static) case

$$\boldsymbol{e} = -\operatorname{grad} \phi^{\mathrm{e}} \qquad \text{and} \qquad \boldsymbol{b} = \operatorname{curl} \boldsymbol{a}^{\mathrm{m}}, \tag{9.4}$$

such that (9.1b) are fulfilled identically. In absence of free-charge and current densities we may, in analogy to ϕ^{e} and $\boldsymbol{a}^{\mathrm{m}}$, introduce the (auxiliary) electric vector potential $\boldsymbol{a}^{\mathrm{e}}$ and the scalar magnetic potential ϕ^{m}, respectively. Then,

$$\boldsymbol{d} = \operatorname{curl} \boldsymbol{a}^{\mathrm{e}} \iff \operatorname{div} \boldsymbol{d} = 0 \qquad \text{and} \qquad \boldsymbol{h} = -\operatorname{grad} \phi^{\mathrm{m}} \iff \operatorname{curl} \boldsymbol{h} = \boldsymbol{0}. \tag{9.5}$$

In addition to Maxwell's equations we consider the standard finite-strain framework for elasticity, which we already employed in magneto-mechanics in Chapter 7. The extension of magneto-mechanics to magneto-electro-mechanics does not add anything conceptually new in this regard. Thus, we below simply restate the most important mechanical equations in their form required below without much explanations. For further details and definitions we refer to Section 7.1.

We start with the deformation map $\varphi(X, t)$. At time t the deformation map assigns to a point $X \in \mathcal{B}$ the Eulerian coordinate $x = \varphi(X, t) \in \mathcal{B}_t$, where $\mathcal{B}_t$ denotes the current configuration of the body $\mathcal{B}$. From φ we obtain the deformation gradient $\underline{\boldsymbol{F}}$ as

$$\underline{\boldsymbol{F}} = \operatorname{Grad} \varphi(X), \tag{9.6}$$

which at the same time is the tangent map associated with φ. Note that we omitted the dependence of φ on t in the above equation. We will adhere to this notation for brevity as long as there is no chance of confusion. The differential operator Grad involves derivatives with respect to X and thus is the Lagrangian counterpart of grad $= \partial_x$. Similar considerations apply to the pairs {curl, Curl} and {div, Div}. Besides the kinematic quantities φ and $\underline{\boldsymbol{F}}$ we have the first Piola-Kirchhoff-type total stress $\underline{\boldsymbol{P}}$ accounting for magneto-electro-mechanical interactions. Along the lines of Section 7.1 we extend the Lagrangian coordinates X into the surrounding of $\mathcal{B}$, denoted as $\mathcal{B}'$ such that they cover the full "Lagrangian" space under consideration Ω. This in effect extends the domain of mechanical quantities to Ω. Then, the fields $\underline{\boldsymbol{F}}$ and $\underline{\boldsymbol{P}}$ fulfill the compatibility condition and balance of linear momentum

$$\operatorname{Curl} \underline{\boldsymbol{F}} = \boldsymbol{0} \qquad \text{and} \qquad \operatorname{Div} \underline{\boldsymbol{P}} = -\boldsymbol{f}_0 \qquad \text{in } \Omega, \tag{9.7}$$

Box 9.1: Transformation (pull-back) rules for various physical quantities

$$\phi^{\mathrm{e}}(X) = \phi^{\mathrm{e}}(x) \circ \varphi(X) \qquad \phi^{\mathrm{m}}(X) = \phi^{\mathrm{m}}(x) \circ \varphi(X) \tag{9.11a}$$

$$\boldsymbol{E}(X) = \underline{\boldsymbol{F}}^{\mathrm{T}} \cdot [\boldsymbol{e}(x) \circ \varphi(X)] \qquad \boldsymbol{H}(X) = \underline{\boldsymbol{F}}^{\mathrm{T}} \cdot [\boldsymbol{h}(x) \circ \varphi(X)] \tag{9.11b}$$

$$\boldsymbol{A}^{\mathrm{e}}(X) = \underline{\boldsymbol{F}}^{\mathrm{T}} \cdot [\boldsymbol{a}^{\mathrm{e}}(x) \circ \varphi(X)] \qquad \boldsymbol{A}^{\mathrm{m}}(X) = \underline{\boldsymbol{F}}^{\mathrm{T}} \cdot [\boldsymbol{a}^{\mathrm{m}}(x) \circ \varphi(X)] \tag{9.11c}$$

$$\boldsymbol{D}(X) = J\underline{\boldsymbol{F}}^{-1} \cdot [\boldsymbol{d}(x) \circ \varphi(X)] \qquad \boldsymbol{B}(X) = J\underline{\boldsymbol{F}}^{-1} \cdot [\boldsymbol{b}(x) \circ \varphi(X)] \tag{9.11d}$$

$$q_0^{\mathrm{s}}(X) = \|J\underline{\boldsymbol{F}}^{-\mathrm{T}} \cdot \boldsymbol{N}\| \, q^{\mathrm{s}}(x) \circ \varphi(X) \qquad \boldsymbol{t}_0(X) = \|J\underline{\boldsymbol{F}}^{-\mathrm{T}} \cdot \boldsymbol{N}\| \, \boldsymbol{t}(x) \circ \varphi(X) \tag{9.11e}$$

$$q_0(X) = Jq(x) \circ \varphi(X) \qquad \boldsymbol{f}_0(X) = J\boldsymbol{f}(x) \circ \varphi(X) \tag{9.11f}$$

respectively, where $\boldsymbol{f}_0$ denotes the mechanical body force density per unit volume in the initial (Lagrangian) configuration of the body $\mathcal{B}$. Clearly, $\boldsymbol{f}_0 = \boldsymbol{0}$ in $\Omega \setminus \mathcal{B}$. The corresponding jump conditions across a surface $\mathcal{S}$ with unit normal $\boldsymbol{N}$ read as

$$[\![\underline{\boldsymbol{F}}]\!] \times \boldsymbol{N} = \boldsymbol{0} \qquad \text{and} \qquad [\![\underline{\boldsymbol{P}}]\!] \cdot \boldsymbol{N} = -\boldsymbol{t}_0. \tag{9.8}$$

Note that we exclude phenomena like fracture, shear bands and contact as well as self-penetration ($J = \det \underline{\boldsymbol{F}} > 0$). Thus, we consider φ as continuous and $(9.8)_1$ is fulfilled identically.

Next we rewrite (9.1) and (9.2) in terms of Lagrangian quantities and operators. In the domain Ω we have

$$\operatorname{Div} \boldsymbol{D} = q_0, \qquad \operatorname{Curl} \boldsymbol{H} = \boldsymbol{0} \tag{9.9a}$$

$$\operatorname{Curl} \boldsymbol{E} = 0, \qquad \operatorname{Div} \boldsymbol{B} = 0 \tag{9.9b}$$

whereas the jump conditions across $\mathcal{S}$ take on the form

$$[\![\boldsymbol{D}]\!] \cdot \boldsymbol{N} = q_0^{\mathrm{s}}, \qquad [\![\boldsymbol{H}]\!] \times \boldsymbol{N} = \boldsymbol{0} \tag{9.10a}$$

$$[\![\boldsymbol{E}]\!] \times \boldsymbol{N} = \boldsymbol{0}, \qquad [\![\boldsymbol{B}]\!] \cdot \boldsymbol{N} = 0. \tag{9.10b}$$

The various transformations employed above are summarized in Box 9.1. We refer to Section 4.1 for more information on such transformations, i.e. pull-backs and push-forwards, respectively.

9.1.2. Constitutive relations

The structure of the field equations in Section 9.1.1 suggests the existence of constitutive relations for each of the pairs $\{\boldsymbol{E}, \boldsymbol{D}\}$, $\{\boldsymbol{B}, \boldsymbol{H}\}$ and $\{\underline{\boldsymbol{F}}, \underline{\boldsymbol{P}}\}$. We follow the works (Bustamante

et al., 2008, 2009a; Miehe et al., 2016) and employ an energy density

$$\Psi(\underline{\boldsymbol{F}}, \boldsymbol{D}, \boldsymbol{B}) = \psi(\underline{\boldsymbol{F}}, \boldsymbol{d} = \frac{1}{J}\underline{\boldsymbol{F}} \cdot \boldsymbol{D}, \boldsymbol{b} = \frac{1}{J}\underline{\boldsymbol{F}} \cdot \boldsymbol{B}) \tag{9.12}$$

from which we obtain the duals to $\{\underline{\boldsymbol{F}}, \boldsymbol{D}, \boldsymbol{B}\}$ as

$$\underline{\boldsymbol{P}} = \frac{\partial \Psi}{\partial \underline{\boldsymbol{F}}}, \qquad \boldsymbol{E} = \frac{\partial \Psi}{\partial \boldsymbol{D}} \qquad \text{and} \qquad \boldsymbol{H} = \frac{\partial \Psi}{\partial \boldsymbol{B}}. \tag{9.13}$$

For the modeling of truly incompressible material we either employ

$$\Psi^{\diamond}(\underline{\boldsymbol{F}}, \boldsymbol{D}, \boldsymbol{B}) = \Psi(\underline{\boldsymbol{F}}^{\diamond}, \boldsymbol{D}, \boldsymbol{B}) \quad \text{or} \quad \Psi^{\circ}(\underline{\boldsymbol{F}}, \boldsymbol{D}, \boldsymbol{B}) = \psi\left(\underline{\boldsymbol{F}}^{\diamond}, \frac{1}{J}\underline{\boldsymbol{F}} \cdot \boldsymbol{D}, \frac{1}{J}\underline{\boldsymbol{F}} \cdot \boldsymbol{B}\right), \tag{9.14}$$

where $\underline{\boldsymbol{F}}^{\diamond} = J^{-1/\dim}\underline{\boldsymbol{F}}$ denotes the distortional component of $\underline{\boldsymbol{F}}$, i.e. $\det \underline{\boldsymbol{F}}^{\diamond} \equiv 1$. Accordingly, the associated withtal stress components are

$$\underline{\boldsymbol{P}}^{\diamond} = \frac{\partial \Psi^{\diamond}}{\partial \underline{\boldsymbol{F}}} \qquad \text{and} \qquad \underline{\boldsymbol{P}}^{\circ} = \frac{\partial \Psi^{\circ}}{\partial \underline{\boldsymbol{F}}}. \tag{9.15}$$

They differ from the total stress $\underline{\boldsymbol{P}}$ by pressure terms (see also Section 9.1.3)

$$p^{\diamond} = (\underline{\boldsymbol{F}}^{\diamond})^{\mathrm{T}} \cdot (\underline{\boldsymbol{P}} - \underline{\boldsymbol{P}}^{\diamond}) \qquad \text{and} \qquad p^{\circ} = (\underline{\boldsymbol{F}}^{\diamond})^{\mathrm{T}} \cdot (\underline{\boldsymbol{P}} - \underline{\boldsymbol{P}}^{\circ}). \tag{9.16}$$

In our experience, the differences between results based on $\Psi^{\diamond}$ and Ψ° are negligible. However, in our tests, implementations based on Ψ° tended to be slightly more robust. Depending on whether Ψ° or $\Psi^{\diamond}$ is employed, we will denote a region of incompressible material as $\mathcal{B}^{\circ}$ or $\mathcal{B}^{\diamond}$, respectively. In derivations we will go with $\mathcal{B}^{\diamond}$ without loss of generality.

9.1.3. Variational principle

We consider a group of bodies $\mathcal{B} = \bigcup_i \mathcal{B}^i$ placed in an otherwise empty free-space domain Ω. The remaining empty domain is denoted as $\mathcal{B}' = \Omega \setminus \mathcal{B}$. Moreover, we exclude the possibility of frictional and non-permanent contact between the $\mathcal{B}^i$. Figure 9.1 essentially repeats Figure 4.5 to provide a sketch of the initial and current configurations. The variational principle to be constructed shall be energy-based such that it features a minimizer structure. Simultaneously, the formulation shall provide access to the scalar electric potential and allow for free charges. For this purpose we consider φ, $\boldsymbol{D}$ and $\boldsymbol{B}$ as primary variables

$$\varphi : \begin{cases} \Omega \times \mathcal{T} & \to \mathbb{R}^d \\ (X,t) & \mapsto \varphi(X,t) \end{cases} \quad \boldsymbol{D} : \begin{cases} \Omega \times \mathcal{T} & \to \mathbb{R}^d \\ (X,t) & \mapsto \boldsymbol{D}(X,t) \end{cases} \quad \boldsymbol{B} : \begin{cases} \Omega \times \mathcal{T} & \to \mathbb{R}^d \\ (X,t) & \mapsto \boldsymbol{B}(X,t). \end{cases} \tag{9.17}$$

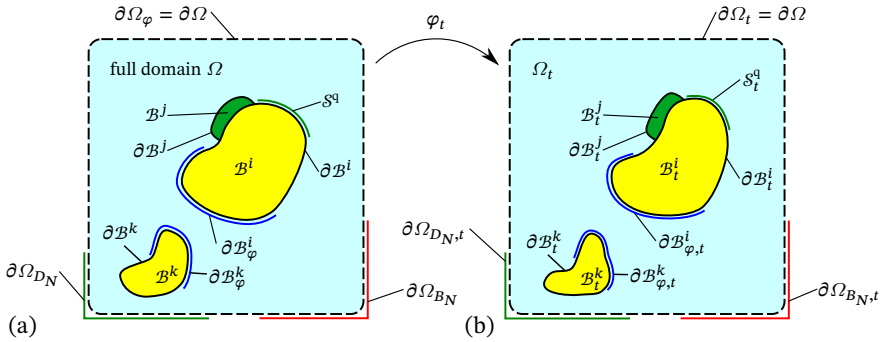

Figure 9.1: Bodies in free space: (a) initial and (b) current configuration. The bodies $\mathcal{B}^i$, $\mathcal{B}^j$ and $\mathcal{B}^k$ are embedded into Ω. On subsets of the boundaries denoted with subscripts, e.g. Ω_φ, Ω_{D_N} or Ω_{B_N}, we put constraints on the corresponding quantity in terms of essential (Dirichlet) boundary conditions. For simplicity we assume that $\partial\Omega_\varphi = \partial\Omega = \partial\Omega_t$ (Keip and Rambausek, 2016, 2017). The collection of all bodies is $\mathcal{B} = \bigcup_i \mathcal{B}^i \subset \Omega$. The "empty" part of Ω is denoted as $\mathcal{B}' = \Omega \setminus \mathcal{B}$.

Based on the considerations in Section 9.1.2 the total energy is then expressed as

$$\Pi(\varphi, \boldsymbol{D}, \boldsymbol{B}) = \Pi^{\text{int}} + \Pi^{\text{ext}} \tag{9.18}$$

where

$$\Pi^{\text{int}} = \int_{\mathcal{B}\setminus\mathcal{B}^\diamond} \Psi(\underline{\boldsymbol{F}}, \boldsymbol{D}, \boldsymbol{B})\, dV + \int_{\mathcal{B}^\diamond} \Psi^\diamond(\underline{\boldsymbol{F}}, \boldsymbol{D}, \boldsymbol{B})\, dV + \int_{\mathcal{B}'} \Psi^\infty(\underline{\boldsymbol{F}}, \boldsymbol{D}, \boldsymbol{B})\, dV \tag{9.19a}$$

and

$$\Pi^{\text{ext}} = -\int_{\mathcal{B}_t} \mathcal{P}^{\text{b}}\, dV - \int_{\partial\mathcal{B}_t\setminus\partial\mathcal{B}_{t;\varphi}} \mathcal{P}^{\text{t}}\, dV - \int_{\partial\Omega_t\setminus\partial\Omega_{t;D}} \mathcal{P}^{\text{e}}_\infty\, dV - \int_{\partial\Omega_t\setminus\partial\Omega_{t;B}} \mathcal{P}^{m}_\infty\, dV. \tag{9.19b}$$

The individual integrands in (9.19b) are defined such that

$$\boldsymbol{f} = \partial_\varphi \mathcal{P}^b, \qquad \boldsymbol{t} = \partial_\varphi \mathcal{P}^t, \qquad \phi^{\text{e}}_\infty \boldsymbol{n} = -\partial_{\boldsymbol{d}} \mathcal{P}^e_\infty \qquad \text{and} \qquad \phi^{\text{m}}_\infty \boldsymbol{n} = -\partial_{\boldsymbol{b}} \mathcal{P}^m_\infty. \tag{9.20}$$

When we characterize (meta-)stable equilibrium by a (local) infimum Π we must not forget to fulfill $(9.9a)_1$ and $(9.9b)_2$ as well as $(9.10a)_1$ and $(9.10b)_2$. As a next step, we introduce a Lagrangian functional $\mathcal{L}$ which includes all constraints under consideration

via Lagrange multipliers

$$\begin{aligned}\mathcal{L}(\varphi, \boldsymbol{D}, \boldsymbol{B}, p, \phi^e, \phi^m) = &\int_{\Omega\setminus\mathcal{B}^\circ} \Psi\left(\underline{\boldsymbol{F}}, \boldsymbol{D}, \boldsymbol{B}; X\right)\, dV + \int_{\mathcal{B}^\circ} \Psi^\circ\left(\underline{\boldsymbol{F}}, \boldsymbol{D}, \boldsymbol{B}; X\right) + p(J-1)\, dV \\ &+ \int_{\Omega\setminus\mathcal{S}^q} -\phi^e(\operatorname{Div}\boldsymbol{D} - q_0)\, dV + \int_{\mathcal{S}^q} -\phi^e\left(\llbracket\boldsymbol{D}\rrbracket\cdot\boldsymbol{N} - q_0^s\right)\, dA \\ &+ \int_{\Omega} -\phi^m(\operatorname{Div}\boldsymbol{B})\, dV + \Pi^{\text{ext}}. \end{aligned} \tag{9.21}$$

Any constraints not included in the above equation have to be built into the spaces for $\{\varphi, \boldsymbol{D}, \boldsymbol{B}\}$. In the case of $\boldsymbol{D}$ this practically means that the continuity of $\boldsymbol{D}\cdot\boldsymbol{N}$ is only relaxed on $\mathcal{S}^q$ but enforced by the space of $\boldsymbol{D}$ everywhere else. The variational principle corresponding to the Lagrangian (9.21) reads as

$$\left\{\hat{\varphi}, \hat{\boldsymbol{D}}, \hat{\boldsymbol{B}}, \hat{p}, \hat{\phi^e}, \hat{\phi^m}, \right\} = \arg\left\{ \inf_{\substack{\varphi \\ \in \\ \mathcal{W}_\varphi}} \inf_{\substack{\boldsymbol{D} \\ \in \\ \mathcal{W}_{\boldsymbol{D}}}} \inf_{\substack{\boldsymbol{B} \\ \in \\ \mathcal{W}_{\boldsymbol{B}}}} \inf_{\substack{p \\ \in \\ \mathcal{W}_p}} \sup_{\substack{\phi^e \\ \in \\ \mathcal{W}_\lambda}} \sup_{\substack{\phi^m \\ \in \\ \mathcal{W}_\lambda}} \mathcal{L}(\varphi, \boldsymbol{D}, \boldsymbol{B}, p, \phi^e, \phi^m) \right\}, \tag{9.22}$$

with the spaces $\mathcal{W}_i$ given as

$$\mathcal{W}_\varphi = \left\{ \varphi \mid \varphi_i \in \mathcal{H}(\text{Grad}, \Omega), \pi_\varphi(\varphi) = \pi_\varphi(\varphi_D) \text{ on } \partial\Omega \cup \left(\bigcup_i \partial\mathcal{B}^i_\varphi \right) \right\}, \tag{9.23a}$$

$$\mathcal{W}_{\boldsymbol{D}} = \{\boldsymbol{D} \mid \boldsymbol{D} \in \mathcal{H}(\text{Div}, \Omega\setminus\mathcal{S}^q), \boldsymbol{D}\cdot\boldsymbol{N} = D_N \text{ on } \partial\Omega_D,\ \llbracket\boldsymbol{D}\rrbracket\cdot\boldsymbol{N} \in L^2(\mathcal{S}^q)\}, \tag{9.23b}$$

$$\mathcal{W}_{\boldsymbol{B}} = \{\boldsymbol{B} \mid \boldsymbol{B} \in \mathcal{H}(\text{Div}, \Omega), \boldsymbol{B}\cdot\boldsymbol{N} = B_N \text{ on } \partial\Omega_B\}, \tag{9.23c}$$

$$\mathcal{W}_p = L^2(\mathcal{B}^\circ), \tag{9.23d}$$

$$\mathcal{W}_\lambda = L^2(\Omega). \tag{9.23e}$$

We remark here that the surface charges q_0^s are weakly imposed boundary conditions which could also be implemented within the FEM in a "strong" way by direct substitution. Moreover, the constraints on $\boldsymbol{D}\cdot\boldsymbol{N}$ and $\boldsymbol{B}\cdot\boldsymbol{N}$ could be weakly enforced.

It is noteworthy that the above variational principle is a constrained-minimization problem where all nonlinearities are contained in the potential Π and the incompressibility constraint (when present). The constraints on $\operatorname{Div}\boldsymbol{D}$, $\operatorname{Div}\boldsymbol{B}$ and $\llbracket\boldsymbol{D}\rrbracket\cdot\boldsymbol{N}$ are linear. In the discrete setting they attain particularly simple forms for a proper choice of finite elements such that they can be treated efficiently by appropriate optimization algorithms (Nocedal and Wright, 2006). The linear character of the constraints on $\boldsymbol{D}$ and $\boldsymbol{B}$ also sets the above formulation apart from saddle point problems resulting from formulations with scalar potentials ϕ^e and ϕ^m as primary variables (Pelteret et al., 2016). In such approaches the saddle-point structure is potentially far more complicated even without incompressibility since it is routed in partial Legendre-Fenchel transforms.

Stationary points and Euler-Lagrange equations
The first variation of the Lagrangian (9.21) yields

$$\begin{aligned}
\delta\mathcal{L} = &\int_{\Omega\setminus\mathcal{B}^\circ} \frac{\partial\Psi}{\partial\underline{\boldsymbol{F}}} : \frac{\partial\delta\boldsymbol{\varphi}}{\partial X} + \frac{\partial\Psi}{\partial\boldsymbol{D}}\cdot\delta\boldsymbol{D} + \frac{\partial\Psi}{\partial\boldsymbol{B}}\cdot\delta\boldsymbol{B}\,dV \\
&+ \int_{\mathcal{B}^\circ} \left(\frac{\partial\Psi^\circ}{\partial\underline{\boldsymbol{F}}} + pJ\underline{\boldsymbol{F}}^{-T}\right) : \frac{\partial\delta\boldsymbol{\varphi}}{\partial X} + \frac{\partial\Psi^\circ}{\partial\boldsymbol{D}}\cdot\delta\boldsymbol{D} + \frac{\partial\Psi^\circ}{\partial\boldsymbol{B}}\cdot\delta\boldsymbol{B} + \delta p(J-1)\,dV \\
&+ \int_{\Omega\setminus\mathcal{S}^\mathrm{q}} -\delta\phi^\mathrm{e}\,(\operatorname{Div}\boldsymbol{D} - q_0) - \phi^\mathrm{e}\operatorname{Div}\delta\boldsymbol{D}\,dV \\
&+ \int_{\mathcal{S}^\mathrm{q}} -\delta\phi^\mathrm{e}\,([\![\boldsymbol{D}]\!]\cdot\boldsymbol{N} - q_0^\mathrm{s}) - \phi^\mathrm{e}\,[\![\delta\boldsymbol{D}]\!]\cdot\boldsymbol{N}\,dA \\
&+ \int_{\Omega} -\delta\phi^\mathrm{m}\,(\operatorname{Div}\boldsymbol{B}) - \phi^\mathrm{m}\operatorname{Div}\delta\boldsymbol{B}\,dV \\
&+ \int_{\mathcal{B}_t} -\frac{\partial\mathcal{P}^\mathrm{b}}{\partial\boldsymbol{\varphi}}\cdot\delta\boldsymbol{\varphi}\,dV + \int_{\partial\mathcal{B}_t\setminus\partial\mathcal{B}_{t;\boldsymbol{\varphi}}} -\frac{\partial\mathcal{P}^\mathrm{t}}{\partial\boldsymbol{\varphi}}\cdot\delta\boldsymbol{\varphi}\,dV \\
&+ \int_{\partial\Omega_t\setminus\partial\Omega_{t;\boldsymbol{D}}} -\frac{\partial\mathcal{P}^\mathrm{e}_\infty}{\partial\boldsymbol{d}}\cdot\delta(J^{-1}\underline{\boldsymbol{F}}\cdot\boldsymbol{D})\,dV \\
&+ \int_{\partial\Omega_t\setminus\partial\Omega_{t;\boldsymbol{B}}} -\frac{\partial\mathcal{P}^\mathrm{m}_\infty}{\partial\boldsymbol{b}}\cdot\delta(J^{-1}\underline{\boldsymbol{F}}\cdot\boldsymbol{B})\,dV,
\end{aligned} \tag{9.24}$$

where we note that in case of a fixed free-space boundary $\partial\Omega = \partial\Omega_t$ we also have $\delta(J^{-1}\underline{\boldsymbol{F}}\cdot\boldsymbol{D}) = \delta\boldsymbol{D}$ and $\delta(J^{-1}\underline{\boldsymbol{F}}\cdot\boldsymbol{B}) = \delta\boldsymbol{B}$. This is assumed throughout the present

part of this thesis such that we may rearrange the above equation to obtain

$$\begin{aligned}
\delta\mathcal{L} = &\int_{\Omega\setminus\mathcal{B}^\circ} \frac{\partial\Psi}{\partial\underline{\boldsymbol{F}}} : \frac{\partial\delta\varphi}{\partial X}\,dV + \int_{\mathcal{B}^\circ}\left(\frac{\partial\Psi^\circ}{\partial\underline{\boldsymbol{F}}} + pJ\underline{\boldsymbol{F}}^{-T}\right) : \frac{\partial\delta\varphi}{\partial X}\,dV \\
&+ \int_{\mathcal{B}_t} -\frac{\partial\mathcal{P}^{\mathrm{b}}}{\partial\varphi}\cdot\delta\varphi\,dV + \int_{\partial\mathcal{B}_t\setminus\partial\mathcal{B}_{t;\varphi}} -\frac{\partial\mathcal{P}^{\mathrm{t}}}{\partial\varphi}\cdot\delta\varphi\,dV \\
&+ \int_{\Omega\setminus\mathcal{B}^\circ} \frac{\partial\Psi}{\partial\boldsymbol{D}}\cdot\delta\boldsymbol{D}\,dV + \int_{\mathcal{B}^\circ} \frac{\partial\Psi^\circ}{\partial\boldsymbol{D}}\cdot\delta\boldsymbol{D} + \,dV \\
&+ \int_{\Omega\setminus\mathcal{S}^{\mathrm{q}}} -\delta\phi^{\mathrm{e}}\,(\operatorname{Div}\boldsymbol{D} - q_0) - \phi^{\mathrm{e}}\operatorname{Div}\delta\boldsymbol{D}\,dV \\
&+ \int_{\mathcal{S}^{\mathrm{q}}} -\delta\phi^{\mathrm{e}}\,(\llbracket\boldsymbol{D}\rrbracket\cdot\boldsymbol{N} - q_0^{\mathrm{s}}) - \phi^{\mathrm{e}}\,\llbracket\delta\boldsymbol{D}\rrbracket\cdot\boldsymbol{N}\,dA + \int_{\partial\Omega\setminus\partial\Omega_D} -\frac{\partial\mathcal{P}_\infty^{\mathrm{e}}}{\partial\boldsymbol{D}}\cdot\delta\boldsymbol{D}\,dV \\
&+ \int_{\Omega\setminus\mathcal{B}^\circ} \frac{\partial\Psi}{\partial\boldsymbol{B}}\cdot\delta\boldsymbol{B}\,dV + \int_{\mathcal{B}^\circ} \frac{\partial\Psi^\circ}{\partial\boldsymbol{B}}\cdot\delta\boldsymbol{B} + \delta p(J-1)\,dV \\
&+ \int_{\Omega} -\delta\phi^{\mathrm{m}}\,(\operatorname{Div}\boldsymbol{B}) - \phi^{\mathrm{m}}\operatorname{Div}\delta\boldsymbol{B}\,dV + \int_{\partial\Omega\setminus\partial\Omega_B} -\frac{\partial\mathcal{P}_\infty^{\mathrm{m}}}{\partial\boldsymbol{B}}\cdot\delta\boldsymbol{B}\,dV. \qquad (9.25)
\end{aligned}$$

Via the usual procedure involving integration by parts and the application of the divergence theorem we arrive at the Euler-Lagrange equations summarized in Box 9.2.

9.1.4. Finite element discretization

The discretization of the function spaces given in (9.23) in terms of finite elements is more involved as for the magneto-elasticity formulation in Chapter 7. For $\mathscr{W}_\varphi$ we employ vector-valued continuous Lagrange elements, which are the natural choice for deformation or displacement degrees of freedom (DOFs). This reflects the interpretation of φ as vector-valued zero-form. The definition of $\mathscr{W}_{\boldsymbol{D}}$ has the complication of involving jump terms across geometrical features of co-dimension one, i.e. surfaces. While there are several possibilities to consider surface charges in finite element discretizations of the formulation above, in the scope of this thesis we opt for an approximation of such surfaces as volumes of small thickness. This makes $\mathscr{W}_{\boldsymbol{D}}$ and $\mathscr{W}_{\boldsymbol{B}}$ equivalent from an implementation perspective. The actual boundary conditions, however, will of course be different. We discretize $\mathscr{W}_{\boldsymbol{D}}$ and $\mathscr{W}_{\boldsymbol{B}}$ with $\mathscr{H}(\mathrm{Div})$-conforming elements such as Raviart-Thomas (RT), Brezzi-Douglas-Marini (BDM) and their generalizations to 3d: Nédélec face elements of first ($\mathrm{N1^f}$) and second kind ($\mathrm{N2^f}$), respectively. We refer to Raviart and Thomas (1977), Brezzi et al. (1985) and Nédélec (1980, 1986) for corresponding publications. The distinguishing feature of $\mathscr{H}(\mathrm{Div})$ elements is that their DoFs correspond to the values of a vector field (as the numerical *proxy* for a two-form, see Hiptmair (2002) and Arnold et al. (2006)) projected onto the element's boundary normal. In the case of two elements sharing a boundary and the associated degrees of freedom this practically

Box 9.2: Euler-Lagrange equations for the constrained-minimization principle for magneto-electro-mechanics.

balance-type equations

electric Gauß law	$\operatorname{Div} \boldsymbol{D} = q_0$	in $\Omega \setminus \mathcal{S}^{\mathrm{q}}$	(9.26a)
magnetic Gauß law	$\operatorname{Div} \boldsymbol{B} = 0$	in Ω	(9.26b)
balance of linear momentum	$\operatorname{Div} \underline{\boldsymbol{P}} = \boldsymbol{0}$	in $\Omega \setminus \mathcal{B}$	(9.26c)
	$\operatorname{Div} \underline{\boldsymbol{P}} = -\boldsymbol{f}_0^{\mathrm{b}}$	in $\mathcal{B}$	(9.26d)
incompressibility	$J = 1$	in $\mathcal{B}^\circ$	(9.26e)
auxiliary equation for the pressure	$p = 0$	in $\Omega \setminus \mathcal{B}^\circ$	(9.26f)

natural boundary conditions

prescribed tractions	$[\![\underline{\boldsymbol{P}}]\!] \cdot \boldsymbol{N} = \boldsymbol{t}^{\mathrm{mech}}$	on $\partial\mathcal{B} \setminus \partial\mathcal{B}_\varphi$	(9.27a)
prescribed surface charge	$[\![\boldsymbol{D}]\!] \cdot \boldsymbol{N} = q^{\mathrm{s}}$	on $\mathcal{S}^{\mathrm{q}}$	(9.27b)
prescribed electric potential	$\phi^e = \phi^e_\infty$	on $\partial\Omega \setminus \partial\Omega_D$	(9.27c)
prescribed scalar magnetic potential	$\phi^m = \phi^m_\infty$	on $\partial\Omega \setminus \partial\Omega_B$	(9.27d)

constitutive/kinematic relations

$\boldsymbol{H}$-field dual to $\boldsymbol{B}$	$\partial_{\boldsymbol{B}}\psi = -\operatorname{Grad}\phi^m = \boldsymbol{H}$	in $\Omega \setminus \mathcal{B}^\circ$	(9.28a)
	$\partial_{\boldsymbol{B}}\psi^\circ = -\operatorname{Grad}\phi^m = \boldsymbol{H}$	in $\mathcal{B}^\circ$	(9.28b)
electric field dual to $\boldsymbol{D}$	$\partial_{\boldsymbol{D}}\psi = -\operatorname{Grad}\phi^e = \boldsymbol{E}$	in $\Omega \setminus (\mathcal{B}^\circ \cup \mathcal{S}^{\mathrm{q}})$	(9.28c)
	$\partial_{\boldsymbol{D}}\psi^\circ = -\operatorname{Grad}\phi^e = \boldsymbol{E}$	in $\mathcal{B}^\circ \setminus \mathcal{S}^{\mathrm{q}}$	(9.28d)

results in discrete vector fields that conserve the flux across element boundaries. The difference between RT and BDM in two dimensions as well as between $\mathrm{N1^f}$ and $\mathrm{N2^f}$ in three dimensions is that BDM and $\mathrm{N2^f}$ of degree n contain all polynomials of degree $k \leq n$. By contrast, RT and $\mathrm{N1^f}$ only represent the polynomials of degree $k \leq n-1$ plus a special subset of the polynomials terms of degree $k = n$. Generic elements of the local spaces represented by the two dimensional triangular reference elements of order $n = 1$ are given below (Logg et al., 2012):

$$\boldsymbol{v}^{\mathrm{e}}_{\mathrm{RT},1}(\boldsymbol{\xi}, \underline{\mathrm{r}},) = \begin{pmatrix} \mathrm{r}_0 + \mathrm{r}_2\xi_1 \\ \mathrm{r}_1 + \mathrm{r}_2\xi_2 \end{pmatrix} \tag{9.29a}$$

and

$$\boldsymbol{v}^{\mathrm{e}}_{\mathrm{BDM},1}(\boldsymbol{\xi}, \underline{\mathrm{r}}, \underline{\mathrm{s}}) = \begin{pmatrix} \mathrm{r}_0 + \mathrm{r}_1\xi_1 + \mathrm{r}_2\xi_2 \\ \mathrm{s}_0 + \mathrm{s}_1\xi_1 + \mathrm{s}_2\xi_2 \end{pmatrix}. \tag{9.29b}$$

From this we see that the RT_1 element has three DOFs whereas the BDM_1 has six. Note that the parameter arrays $\underline{\mathrm{r}}$ and $\underline{\mathrm{s}}$ are neither the actual finite element DOFs nor do the given polynomials render finite element shape functions.

The crucial ingredient for $\mathscr{H}(\mathrm{Div})$-conforming elements is the flux across element boundaries. For a reference element as depicted in Figure 9.2 we have the fluxes

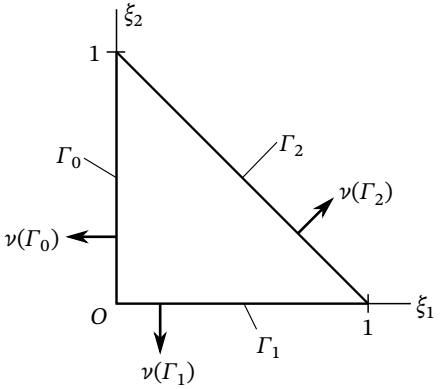

Figure 9.2: Triangular reference element with normal vectors.

$$\Phi_0 = \int_{\Gamma_0} \boldsymbol{v} \cdot \boldsymbol{\nu} \, \mathrm{d}\Gamma_0 = -\mathrm{r}_0, \; \Phi_1 = \int_{\Gamma_1} \boldsymbol{v} \cdot \boldsymbol{\nu} \, \mathrm{d}\Gamma_1 = -\mathrm{r}_1 \text{ and } \Phi_2 = \int_{\Gamma_2} \boldsymbol{v} \cdot \boldsymbol{\nu} \, \mathrm{d}\Gamma_2 = \sum_{i=1}^{3} \mathrm{r}_i, \tag{9.30}$$

where we substituted $\boldsymbol{v}$ by $\boldsymbol{v}_{\mathrm{RT},1}$ as given in (9.29a). From that we see that $\underline{\Phi} =$

(Φ_0, Φ_1, Φ_2) already fits our needs for the degrees of freedom for RT_1 elements. Next we obtain the basis functions by first expressing the r_i in terms of the fluxes Φ_i

$$\mathrm{r}_0 = -\Phi_0, \qquad \mathrm{r}_1 = -\Phi_1 \qquad \text{and} \qquad \mathrm{r}_2 = \Phi_0 + \Phi_1 + \Phi_2. \tag{9.31}$$

Inserting the above relations into (9.29a) we arrive at

$$\boldsymbol{v}^{\mathrm{e}}_{\mathrm{RT},1}(\boldsymbol{\xi}, \underline{\Phi}) = \begin{pmatrix} \xi_1 - 1 \\ \xi_2 \end{pmatrix} \Phi_0 + \begin{pmatrix} \xi_1 \\ \xi_2 - 1 \end{pmatrix} \Phi_1 + \begin{pmatrix} \xi_1 \\ \xi_2 \end{pmatrix} \Phi_2 = \underline{\mathbf{N}}_{\mathrm{RT},1} \cdot \underline{\Phi}. \tag{9.32}$$

The derivation of a FE basis for BDM, $\mathrm{N1}^{\mathrm{f}}$ and $\mathrm{N2}^{\mathrm{f}}$ elements of degree one can be carried out analogously. Note, however, that the fluxes Φ_i can only be directly used as DOFs for RT_1 and lowest order $\mathrm{N1}^{\mathrm{f}}$ elements. For BDM, $\mathrm{N2}^{\mathrm{f}}$ and higher order RT and $\mathrm{N1}^{\mathrm{f}}$ elements one has to choose appropriate momenta on $\partial\mathcal{T}$ and at a certain point also in $\mathcal{T}$ as further degrees of freedom (Boffi et al., 2013). For completeness we give the lowest order BDM basis functions based on (Boffi et al., 2013, Section 2.6.1) but reformulated for a reference triangle

$$\begin{aligned} \mathrm{N}_0 &= \begin{pmatrix} 0 \\ \xi_1 + \xi_2 - 1 \end{pmatrix} & \mathrm{N}_1 &= \begin{pmatrix} \xi_1 \\ -\xi_1 \end{pmatrix} & \mathrm{N}_2 &= \begin{pmatrix} \sqrt{2}\xi_1 \\ 0 \end{pmatrix} \\ \mathrm{N}_3 &= \begin{pmatrix} 0 \\ \sqrt{2}\xi_2 \end{pmatrix} & \mathrm{N}_4 &= \begin{pmatrix} -\xi_2 \\ \xi_2 \end{pmatrix} & \mathrm{N}_5 &= \begin{pmatrix} \xi_1 + \xi_2 - 1 \\ 0 \end{pmatrix}. \end{aligned} \tag{9.33}$$

For the multiplier fields ϕ^{e} and ϕ^{m} we employ discontinuous Lagrange elements of appropriate polynomial order. This means that if the $\mathscr{H}(\mathrm{Div})$-element for the corresponding field is of polynomial order n, the multiplier field is of order $n-1$ to ensure inf-sup stability.

For our numerical studies we rely on the implementation of the above finite elements provided by the FE toolbox `FEniCS` (Rognes et al., 2009; Logg and Wells, 2010; Logg et al., 2012; Alnæs et al., 2015) . Finally we would like to mention the website femtable.org which summarizes families of finite elements (Arnold and Logg, 2014) in the framework of the Finite Element Exterior Calculus (FEEC; see Arnold et al. (2006)).

Remark 9.1. From the boundary integrals involved in the construction of $\mathscr{H}(\mathrm{Div})$-elements outlined above it is clear that the orientation of the boundaries plays a role in assembly of global FE matrices. In fact, two adjacent elements somehow have to agree on the direction of the normal of their common boundary.

Remark 9.2. The combination of an $\mathscr{H}(\mathrm{Div})$ discretization for $\boldsymbol{D}$ with an L_2 field ϕ^{e} enforcing $\mathrm{Div}(\boldsymbol{D}) = q_0$ is, in case of a linear dielectric material, the electrostatic version of the classical mixed formulation of the Poisson equation.

9.1.5. Equivalence of vector-potential and mixed formulations

Below we briefly discuss the observation that the image of Curl A_3 is in certain cases identical to the space $\{\boldsymbol{B} \mid \boldsymbol{B} \in \mathscr{H}(\mathrm{Div}) \wedge \mathrm{Div}\,\boldsymbol{B} = 0\}$.

Equivalence of lowest order vector-potential and RT discretizations
The lowest order vector-potential discretization uses linear Lagrange elements for the out-of-plane component of the vector potential. Thus, computing the curl yields a divergence-free vector field $\boldsymbol{B}$ which is element-wise constant and fulfills $[\![\boldsymbol{B}]\!] \cdot \boldsymbol{N} = 0$ across inter-element boundaries. On the other hand, the divergence of (9.29a) vanishes if and only if $r_2 = 0$. What remains is again an element-wise constant vector field. The RT basis then ensures that the jumps normal to inter-element boundaries also vanish. Thus, both formulations yield identical representations of $\boldsymbol{B}$ under the constraint $\mathrm{Div}\,\boldsymbol{B} = 0$.

Equivalence of quadratic vector-potential and lowest order BDM discretizations
A similar statement can be made for BDM elements for $\boldsymbol{B}$ and quadratic Lagrange elements for A_3. The latter this time yields a space for $\boldsymbol{B}$ which is spanned by all divergence-free polynomials of degree less than or equal to one. Again we have $[\![\boldsymbol{B}]\!] \cdot \boldsymbol{N} = 0$. Lowest order BDM elements represent the full space of polynomials of degree less than or equal to one within one element. By construction they also fulfill $[\![\boldsymbol{B}]\!] \cdot \boldsymbol{N} = 0$. Constraining the divergence of $\boldsymbol{B}$ represented by linear BDM elements then naturally leads to the same space as Curl A_3.

Remark 9.3. The framework of FEEC (Arnold et al., 2006) suggests that such equivalence relations also exist in three dimensions. However, by contrast to the two-dimensional case, the "natural" (in FEEC) discretizations for vector-potentials are not Lagrange but Nédélec edge elements for first and second kind. We point out that we did not investigate this any further such that we prefer not to make a more rigorous statement in this regard. In particular, because we did not employ edge elements in any simulation we also did not yet feel the need to dig deeper.

9.1.6. Constitutive models

Throughout the remainder of the present chapter we employ prototypical magneto-electro-elastic energy densities. They will not only serve for the constrained-minimization formulation but also for classical scalar- and vector-potential based approaches.

The mechanical contribution (Holzapfel, 2000) is the same for all formulations

$$\Psi^{\mathrm{mech}}(\underline{\boldsymbol{F}}; \mu, \kappa) = \frac{\mu}{4}\left(\underline{\boldsymbol{F}}^{\diamond} : \underline{\boldsymbol{F}}^{\diamond} - \mathrm{Tr}\,\mathbf{1}\right) + \frac{\kappa}{4}\left(J^2 - 1 - 2\ln(J)\right), \tag{9.34}$$

with shear modulus μ and bulk modulus κ. In case of incompressibility, the purely volumetric term containing κ is omitted.

The additional magneto-electro-mechanical energy-density contribution

$$\Psi^{\mathrm{DB}}(\underline{\boldsymbol{F}}, \boldsymbol{D}, \boldsymbol{B}; \chi^{\mathrm{e}}, \chi^{\mathrm{m}}, m_{\mathrm{s}}) = \frac{J\|\boldsymbol{d}\|^2}{2\epsilon_0} - \frac{\chi^{\mathrm{e}}}{J+\chi^{\mathrm{e}}}\frac{J\|\boldsymbol{d}\|^2}{2\epsilon_0} + \frac{J\|\boldsymbol{b}\|^2}{2\mu_0} - \frac{m_{\mathrm{s}}}{\Xi}\ln\left[\cosh\left(\Xi\,\|\boldsymbol{b}\|\right)\right] \tag{9.35}$$

with

$$\Xi = \frac{J\chi^{\mathrm{m}}}{(J+\chi^{\mathrm{m}})\,m_{\mathrm{s}}\mu_0}$$

is employed for energy-based formulations, i.e. vector-potential or $\mathscr{H}(\mathrm{Div})$ constrained minimization schemes. In above equation χ^{e} denotes the electric susceptibility, χ^{m} the initial magnetic susceptibility and m_{s} denotes the saturation magnetization.

Conversely, the co-energy-density contribution

$$\begin{aligned}\Psi^{\mathrm{EH}}(\underline{\boldsymbol{F}}, \boldsymbol{E}, \boldsymbol{H}; \chi^{\mathrm{e}}, \chi^{\mathrm{m}}, m_{\mathrm{s}}) = &-\frac{\epsilon_0}{2}J\|\boldsymbol{e}\|^2 - \frac{\epsilon_0}{2}\chi^{\mathrm{e}}\|\boldsymbol{e}\|^2 - \frac{\mu_0}{2}J\|\boldsymbol{h}\|^2 \\ &- \frac{\mu_0 {m_{\mathrm{s}}}^2}{\chi^{\mathrm{m}}}\ln\left[\cosh\left(\frac{\chi^{\mathrm{m}}}{m_{\mathrm{s}}}\|\boldsymbol{h}\|\right)\right]\end{aligned} \tag{9.36}$$

is used in combination with scalar-potential formulations.

The (di)electric part of Ψ^{DB} corresponds to linear dielectric properties whereas the magnetic part feature saturation. The same holds for Ψ^{EH}. However, while the two dielectric contributions can be converted into each other through a partial Legendre transform, this is not possible for the magnetic saturation terms. The latter only show the same behavior for $\|\boldsymbol{H}\| \to 0$ and $\|\boldsymbol{H}\| \to \infty$, i.e. for lowest and highest field magnitudes.

The actual energy functions are composed of purely mechanical and magneto-electro-mechanical contributions

$$\Psi^{\mathrm{FDB}}(\underline{\boldsymbol{F}}, \boldsymbol{D}, \boldsymbol{B}; \mu, \kappa, \chi^{\mathrm{e}}, \chi^{\mathrm{m}}, m_{\mathrm{s}}) = \Psi^{\mathrm{mech}}(\underline{\boldsymbol{F}}; \mu, \kappa) + \Psi^{\mathrm{DB}}(\underline{\boldsymbol{F}}, \boldsymbol{D}, \boldsymbol{B}; \chi^{\mathrm{e}}, \chi^{\mathrm{m}}, m_{\mathrm{s}}) \tag{9.37a}$$

and

$$\Psi^{\mathrm{FEH}}(\underline{\boldsymbol{F}}, \boldsymbol{E}, \boldsymbol{H}; \mu, \kappa, \chi^{\mathrm{e}}, \chi^{\mathrm{m}}, m_{\mathrm{s}}) = \Psi^{\mathrm{mech}}(\underline{\boldsymbol{F}}; \mu, \kappa) + \Psi^{\mathrm{EH}}(\underline{\boldsymbol{F}}, \boldsymbol{E}, \boldsymbol{H}; \chi^{\mathrm{e}}, \chi^{\mathrm{m}}, m_{\mathrm{s}}). \tag{9.37b}$$

The actual values for the parameters $\{\mu, \kappa, \chi^{\mathrm{e}}, \chi^{\mathrm{m}}, m_{\mathrm{s}}\}$ are provided alongside the descriptions of the respective BVPs.

9.2. Representative magneto-electro-mechanical BVPs

Let us demonstrate some of the capabilities of the constrained-minimization scheme presented above. For this purpose we consider a capacitor-like setup in two and three dimensions. In both cases the “capacitors” consist of flat electrodes of finite thickness and extent and a magneto-electric-elastic medium in-between. Thus, the device will deform under applied electric loads, e.g. charged electrodes, but also in response to mag-

netic fields. The BVPs are solved by means of a monolithic scheme and the staggered scheme described in Appendix B. The material parameters employed for the free-space, the electrodes and the ME medium are listed in Table 9.1. The latter two are assumed to be incompressible, as indicated by $\varkappa = \infty$. Note that the elastic properties of the free space in case of the staggered scheme are only applied in the ALE update for $\mathcal{B}'$. Thus, the magnitude of the parameters μ and $\varkappa$ does not play a role for the coupled problem. By contrast, the monolithic scheme requires that the free space material is much softer than the other media.

Table 9.1: Material parameters for magneto-electric capacitor examples

Domain	μ / kPa	$\varkappa$ / kPa	χ^{e} / 1	χ^{m} / 1	m_{s} / MA m^{-1}
ME body	1×10^{2}	∞	1.0×10^{1}	1.0	0.3
Electrode	5×10^{1}	∞	1.0×10^{5}	0.0	0.0
Free (mono.)	3.846×10^{-1}	8.333×10^{-1}	0.0	0.0	0.0
Free (stag.)	3.846×10^{2}	8.333×10^{2}	0.0	0.0	0.0

9.2.1. A two-dimensional ME capacitor

The BVP under consideration is depicted in Figure 9.3.

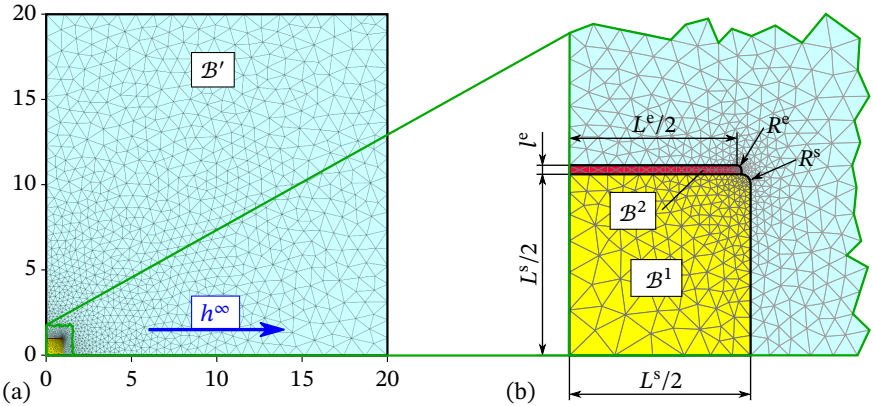

Figure 9.3: The square ME specimen ($\mathcal{B}^1$) with attached electrodes ($\mathcal{B}^2$) for electric loading surrounded by empty space $\mathcal{B}'$. Because of symmetry we depict only the first quadrant. The magnetic loading is performed via a homogeneous external magnetic field $\boldsymbol{h}^{\infty}$ in x_1-direction. The dimensions of the ME specimen and the electrode are given (in cm) as: $L^{\mathrm{s}} = 2$, $L^{\mathrm{e}} = 1.85$, $l^{\mathrm{e}} = 0.05$, $R^{\mathrm{s}} = 0.05$ and $R^{\mathrm{e}} = 0.025$. The out-of-plane dimension is 1 cm.

As usual $\varphi(X) = X$ on $\partial\Omega$. The magnetic field $\boldsymbol{h}^\infty$ in x_1-direction is applied via

$$\boldsymbol{B} \cdot \boldsymbol{N} = \boldsymbol{b} \cdot \boldsymbol{n} = \mu_0 \boldsymbol{h}^\infty \cdot \boldsymbol{n} \text{ on } \partial\Omega = \partial\Omega_t. \tag{9.38}$$

According to symmetry, $\phi^m(X_1 = 0) = 0$ and $\varphi_1(X_1 = 0) = X_1$. Moreover, we apply a volume charge density $q_0 = \bar{q}$ in the electrode $\mathcal{B}^2$. The symmetry condition $\phi^e(X_2 = 0) = 0$ corresponds to setting $q_0 = -\bar{q}$ in the opposite electrode. Furthermore, we have the electric boundary condition $\boldsymbol{D} \cdot \boldsymbol{N} = 0$ on $\partial\Omega$ and the symmetry condition $\boldsymbol{D} \cdot \boldsymbol{N} = 0$ where $X_1 = 0$.

In the simulations we first apply $\bar{q} \in \{0, 2, 4, 6\}\,\mathrm{C\,m^{-3}}$ and then, for each $\bar{q}$, ramp up the current potential $h^\infty = \|\boldsymbol{h}^\infty\|$ from $h^\infty = 0\,\mathrm{MA\,m^{-1}}$ to $h^\infty = 2.5\,\mathrm{MA\,m^{-1}}$.

Figure 9.4a depicts the deformation response in terms of the displacement component $u_1(X = (1,0)) = \varphi_1(X = (1,0)) - 1$ computed by the staggered scheme. We

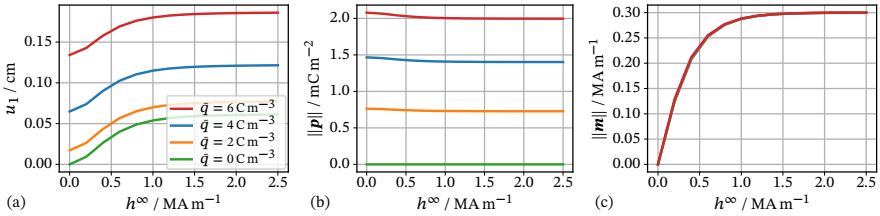

Figure 9.4: Line plots of (a) x_1-displacement at $X = (1,0)$, (b) polarisation $\|\boldsymbol{p}\|$ at $X = (0,0)$ and (c) magnetization $\|\boldsymbol{m}\|$ at $X = (0,0)$ for the two-dimensional ME capacitor example.

observe pronounced global deformations driven by electric and magnetic loads up to 20 %. The subplots (a) and (b) of Figure 9.4 show the magnitudes of polarization and magnetization near the origin. These graphs nicely reflect the electric and magnetic loading phases.

A comparison of the deformations obtained by the staggered scheme and the monolithic scheme, respectively, is shown in Figure 9.5. While both schemes are in good agreement from a global perspective, there are local differences in the vicinity of the electrode corners. Moreover, the staggered scheme is more robust than the monolithic scheme. The latter suffers from spurious magneto-electro-mechanical interactions in the free space $\mathcal{B}_t'$ (see also Section 9.3.1).

We close this first demonstrative example with plots of the electric field $\boldsymbol{e}$ and the magnetic $\boldsymbol{h}$-field in Figure 9.6.

9.2.2. A three-dimensional ME capacitor

Through rotation of the geometry in Figure 9.3 we obtain a three-dimensional ME capacitor shown in Figure 9.7. As depicted in Figure 9.7a the applied $\boldsymbol{h}^\infty$ is now aligned with the x_3 axis in order to not break rotational symmetry. Electric charge is applied in

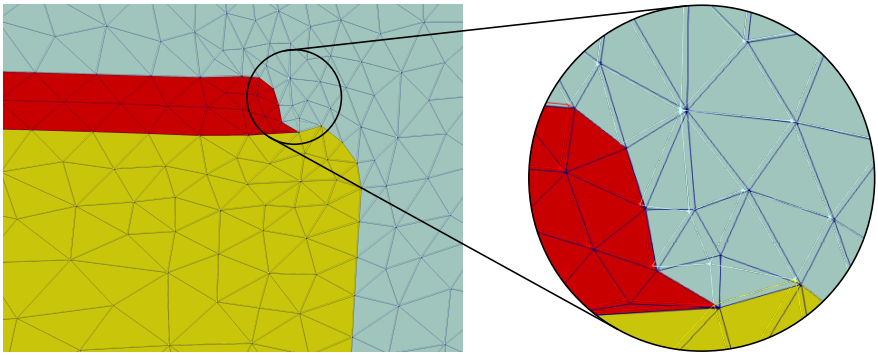

Figure 9.5: Comparison of the deformed configurations at $\bar{q} = 6\,\mathrm{C\,m^{-3}}$. The filled domains with dark mesh lines correspond to the staggered scheme whereas the light-colored mesh lines represent the result of the monolithic scheme. The differences are very small such that they become visible only in the detailed view on the right. They are most pronounced in the region of empty space near the "three-domain corner".

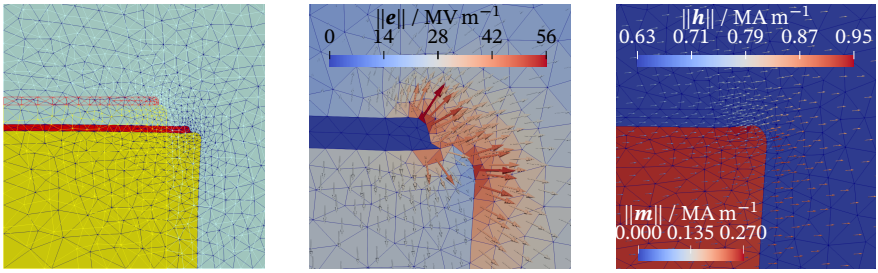

(a) deformed configuration (b) electric field $\boldsymbol{e}$ (c) magnetic field $\boldsymbol{h}$

Figure 9.6: Deformed (filled domains) and initial (wireframe) configuration for $\bar{q} = 6\,\mathrm{C\,m^{-3}}$ and $h^\infty = 2.5\,\mathrm{MA\,m^{-1}}$ (a), the electric field $\boldsymbol{e}$ near the corner for $\bar{q} = 6\,\mathrm{C\,m^{-3}}$ and $h^\infty = 2.5\,\mathrm{MA\,m^{-1}}$ (b) and the magnetic field $\boldsymbol{h}$ near the corner for $\bar{q} = 6\,\mathrm{C\,m^{-3}}$ and $h^\infty = 0.6\,\mathrm{MA\,m^{-1}}$ (c).

the same manner as in the previous subsection and will lead to a compression of the ME medium $\mathcal{B}^1$ in x_3 direction. The magnetic load, however, this time leads to extension in x_3 and thus works against the electrically driven deformation response.

Different from the two-dimensional example above we now prescribe $\boldsymbol{h}^\infty = (0, 0, h^\infty)$ via an external energy contribution

$$\Pi^{\mathrm{ext}} = \int_{\partial\Omega} (h^\infty X_3)(\boldsymbol{B} \cdot \boldsymbol{N})\, dA, \tag{9.39}$$

which is equivalent to the previous approach.

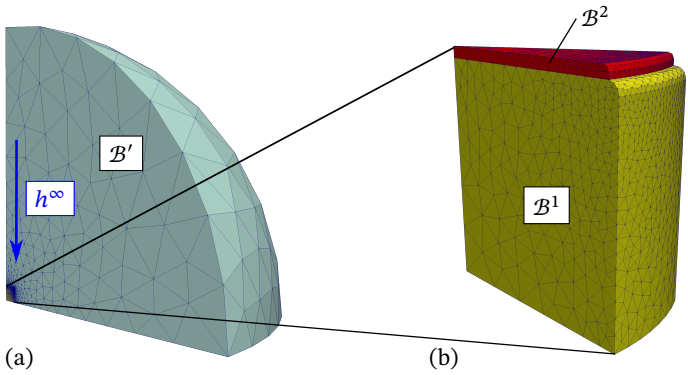

Figure 9.7: The cylindrical ME specimen ($\mathcal{B}^1$) with attached electrodes ($\mathcal{B}^2$) for electric loading surrounded by empty space $\mathcal{B}'$. We exploit symmetries with respect to the $x_3 = 0$-plane and the x_3-axis. We thus only consider the portion depicted. The magnetic loading is performed via a homogeneous external magnetic field $\boldsymbol{h}^\infty$ in negative x_3-direction. The ME body as well as the electrodes are simply constructed by rotation of the geometry depicted in Figure 9.3b. The surrounding empty space fills a sphere with radius 20 cm.

The remaining boundary and symmetry conditions can largely be applied in the usual manner. The major complication is the application of mechanical symmetry conditions. We implement them via Lagrange multipliers wherever the symmetry boundaries are not aligned with a coordinate plane.

For comparison with Figure 9.4 for the 2d case the corresponding plots of $u_1(1,0,0)$ as well as $\|\boldsymbol{p}(0,0,0)\|$ and $\|\boldsymbol{m}(0,0,0)\|$ are depicted in Figure 9.8. As expected, the

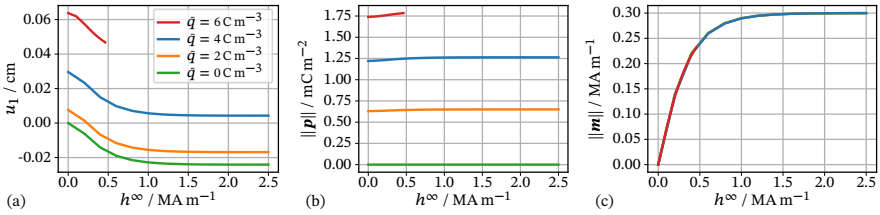

Figure 9.8: Line plots of (a) x_1-displacement at $\boldsymbol{X} = (1,0,0)$, (b) polarisation $\|\boldsymbol{p}\|$ at $\boldsymbol{X} = (0,0,0)$ and (c) magnetization $\|\boldsymbol{m}\|$ at $\boldsymbol{X} = (0,0,0)$ for the three-dimensional ME capacitor example. Despite adaptive load stepping we were not able to go beyond $h^\infty = 4.625 \times 10^{-1}\,\mathrm{MA\,m^{-1}}$ for $\bar{q} = 6\,\mathrm{C\,m^{-3}}$. This indicates an instability, the roots of which we, however, did not investigate further.

displacements are less pronounced than before. Note, however, that because of the 3d setting and rotational symmetry $u_1(1,0,0) = 6 \times 10^{-2}\,\mathrm{cm}$ roughly translates into

$u_3(0,0,1) = 12 \times 10^{-2}$ cm. In addition, we see from Figure 9.8 that the simulations fail somewhere near $\{\bar{q}, h^\infty\} = \{6\,\mathrm{C\,m^{-3}}, 0.4625\,\mathrm{MA\,m^{-1}}\}$. To see what is going on in this regime we show selected components of $\underline{\boldsymbol{F}}$ for both loadings

$$\{\bar{q}, h^\infty\} = \{6\,\mathrm{C\,m^{-3}}, 0\,\mathrm{MA\,m^{-1}}\} \tag{9.40a}$$

and

$$\{\bar{q}, h^\infty\} = \{6\,\mathrm{C\,m^{-3}}, 0.4625\,\mathrm{MA\,m^{-1}}\} \tag{9.40b}$$

in Figures 9.9 and 9.10. We observe oscillatory patterns in the vicinity of the line where

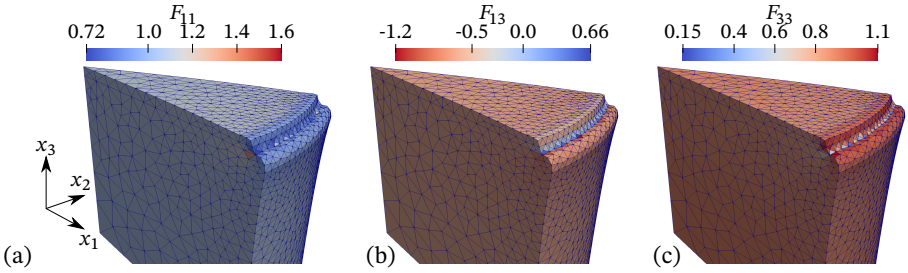

Figure 9.9: Selected components of the deformation gradient $\underline{\boldsymbol{F}}$ at load $\bar{q} = 6\,\mathrm{C\,m^{-3}}$ and $h^\infty = 0\,\mathrm{MA\,m^{-1}}$. At this stage we observe irregular patterns near the line where the body $\mathcal{B}^1$, the electrode $\mathcal{B}^2$ and the empty space domain $\mathcal{B}'$ meet. This reflects the fact that this state is close to a point of instability. We did not observe similar patterns for $\bar{q} \in \{0, 2, 4\}\,\mathrm{C\,m^{-3}}$ (not depicted).

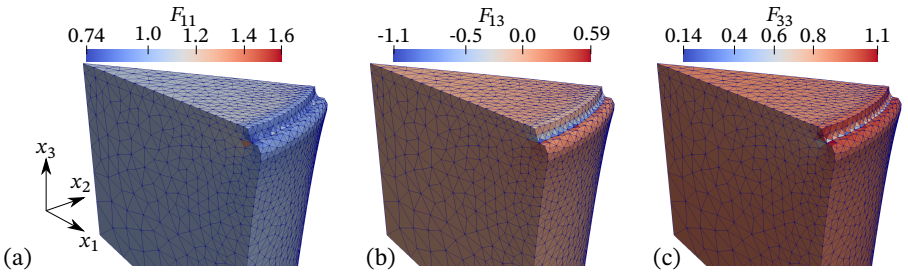

Figure 9.10: Selected components of the deformation gradient $\underline{\boldsymbol{F}}$ at load $\bar{q} = 6\,\mathrm{C\,m^{-3}}$ and $h^\infty = 0.4625\,\mathrm{MA\,m^{-1}}$. This was the last h^∞ loading stage that we could achieve for $\bar{q} = 6\,\mathrm{C\,m^{-3}}$. The plots are almost indistinguishable from those in Figure 9.9, which agrees with the corresponding line plot in Figure 9.8a.

the three domains $\mathcal{B}^1$, $\mathcal{B}^2$ and $\mathcal{B}'$ meet. We did not yet perform further investigations of this issue. Thus, we do not yet know whether this is a numerical artifact or a physical instability. Also note that we did not observe any issues of that kind for $\bar{q} \in \{0, 2, 4\}\,\mathrm{C\,m^{-3}}$.

Figure 9.11 presents the deformed configuration in the x_1-x_3-plane for loads $\bar{q} = 6\,\mathrm{C\,m^{-3}}$ and $h^\infty = 0.0\,\mathrm{MA\,m^{-1}}$. This state features to the largest displacement of the electrode throughout this example.

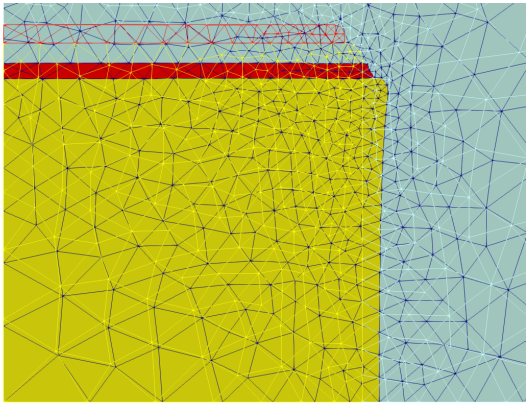

Figure 9.11: Deformed (filled domains) and initial (wireframe) configuration in the x_1-x_3 plane for $\bar{q} = 6\,\mathrm{C\,m^{-3}}$ and $h^\infty = 0.0\,\mathrm{MA\,m^{-1}}$.

The electric and magnetic fields at $\{\bar{q}, h^\infty\} = \{6\,\mathrm{C\,m^{-3}}, 0.4625\,\mathrm{MA\,m^{-1}}\}$ are visualized in Figure 9.12. One nicely observes the discontinuity $[\![\boldsymbol{h}]\!]\cdot\boldsymbol{N}$ across the interface between the ME medium $\mathcal{B}^1$ and the electrode $\mathcal{B}^2$ on the left-hand-side of the figure. On the right-hand-side we clearly see the electrodes acting as a source for the electric field $\boldsymbol{e}$.

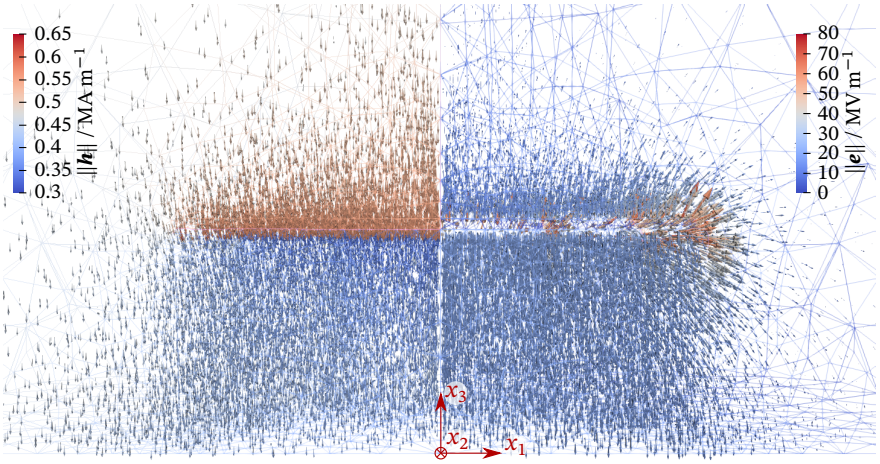

Figure 9.12: Magnetic field $\boldsymbol{h}$ (on the left) and electric field $\boldsymbol{e}$ (on the right) for $\bar{q} = 6\,\mathrm{C\,m^{-3}}$ and $h^{\infty} = 0.4625\,\mathrm{MA\,m^{-1}}$. The plots have been created by means of rotations and reflections of the actually simulated geometry.

9.3. Comparison with scalar- and vector-potential based formulations

In this section we compare the proposed constrained minimization formulation with established ones. The mathematical aspects of FE schemes for electro-statics and magneto-statics in terms of scalar- and vector-potentials are well-studied. We refer to Bossavit (1998a) and Hiptmair (2002) for some background on classical approaches. But also $\mathscr{H}(\mathrm{Div})$-conforming schemes are not new. Indeed, they have been studied for more than 40 years in different context. One of the prototypical problems is the mixed formulation of Poisson's equation. This can be used to describe Darcy's flow, but also linear electro-statics and linear magneto-statics in absence of free currents. Despite that, $\mathscr{H}(\mathrm{Div})$-conforming FE discretizations did not find their way into computational electro- and magneto-statics. Nevertheless, it is granted that all the formulations employed below work for electro- and magneto-statics, modulo certain restrictions such as absence of free currents (see Remark 9.4). Thus, we only investigate the behavior when coupled with mechanics.

The first peculiar effect is that FE simulations unexpectedly exhibit electro- and magneto-elastic interactions also in "passive", that is non-electric and non-magnetic (vacuum-like) media. This issue has not yet gained attention by the mathematics community and is also not documented in more engineering-oriented publications. One possible reason for this is that these interaction are only observable in very soft media, for example the free-space in a monolithic MEM solver or truly soft elastomers or biological tissue, both of which only recently entered the scene in the context of magneto-electro-elasticity. Therefore, we devote a couple of numerical examples to the demonstration of this issue.

The second aspect of interest is computational performance. Scalar-potential based schemes are superior to vector-potential schemes in this regard. However, they are not well-suited for stability analysis since scalar-potential formulations are not energy-based. Therefore, it is of interest to have a scheme that is better-suited for stability analysis but less expensive than vector-potential schemes.

Remark 9.4. A word on comparability. Scalar-potential based schemes as well as the constrained minimization formulation alone cannot account for free currents in magnetostatics in a natural way. On the other hand, vector-potentials fail to model volume charge distributions where one would have $\mathrm{Div}\,\boldsymbol{D} = q_0 \neq \mathrm{Div}\,\mathrm{Curl}\,\boldsymbol{A}^{\mathrm{e}}$. Consequently, comparisons of all three approaches are restricted to vanishing free charges and currents. Note that there is also the possibility of a scheme based on the $\boldsymbol{E}$ and $\boldsymbol{H}$ as primary fields. Such an approach is dual to the constrained minimization formulation in a restricted context. It is applicable in the same scenarios as vector potentials are.

9.3.1. Spurious magneto-elastic interactions

When we consider soft magneto-electro-elastic bodies the free space surrounding the body of interest often cannot be neglected. Thus, even in the case of a homogeneous body, the full BVP contains at least two different "materials", the body and the free space.

In our numerical studies based on a monolithic scalar-potential formulation of magneto-elasticity (see also Chapter 7), we observed spurious magneto-elastic interactions in the free space near to corners of magneto-elastic bodies. With spurious we mean that we see deformations in free-space that exceed the deformation of the body. This means that the free space does not only adapt itself to the deformation of the body but also "feels" magnetic forces on its own, which clearly should not be the case. Such effects can be reduced with rounding off corners, increasing the (artificial) stiffness of the free-space domain or resorting to a staggered solution scheme as described by Pelteret et al. (2016) or as in Appendix B. However, none of these measures is applicable in all cases of interest. This motivated our search for alternatives of which the constrained-minimization formulation is the result.

As a motivation for further research on this topic, the numerical examples below are designed to demonstrate the issue of spurious interactions. Nevertheless, they are not pathological corner cases.

9.3.1.1. A square dielectric elastomer in free space

We consider a square-shaped electro-elastic body $\mathcal{B}$ in a sufficiently large free-space environment Ω exposed to a homogeneous electric field e^∞ as depicted in Figure 9.13a. The mesh employed in the numerical simulation is shown in Figure 9.13b, which already indicates that we exploit the symmetry of the problem. Depending on the formulation, we model the materials by energy-density functions

$$\psi^{\mathrm{S}}(\underline{\boldsymbol{F}}, \boldsymbol{e}) = \frac{\mu}{2}\left(\operatorname{tr}\boldsymbol{C}^{\diamond} - 2\right) + \frac{\kappa}{4}\left(J^2 - 1 - 2\ln J\right) - \left(1 + \frac{\chi^{\mathrm{e}}}{J}\right)\frac{\epsilon_0 J\|\boldsymbol{e}\|^2}{2} \tag{9.41}$$

and

$$\psi^{\mathrm{M}}(\underline{\boldsymbol{F}}, \boldsymbol{d}) = \frac{\mu}{2}\left(\operatorname{tr}\boldsymbol{C}^{\diamond} - 2\right) + \frac{\kappa}{4}\left(J^2 - 1 - 2\ln J\right) + \left(1 - \frac{\chi^{\mathrm{e}}}{J + \chi^{\mathrm{e}}}\frac{J\|\boldsymbol{d}\|^2}{2\epsilon_0}\right), \tag{9.42}$$

where $\boldsymbol{C}^{\diamond} = (\underline{\boldsymbol{F}}^{\diamond})^{\mathrm{T}} \cdot \underline{\boldsymbol{F}}^{\diamond}$ denotes the right Cauchy-Green tensor computed with the distortional component of $\underline{\boldsymbol{F}}$. We refer to Holzapfel (2000) and McMeeking and Landis (2004) for the mechanical and dielectric terms, respectively. Both ψ^{S} and ψ^{M} are totally equivalent in the sense that they are connected through a (partial) Legendre transform of the dielectric energy contribution. To not make things overly complicated we do not consider strict incompressibility in this example. Table 9.2 summarizes the material parameters used for the body and the free space. We solve the BVP with a monolithic scheme. Hence, we require the free space to be mechanically much softer that the body.

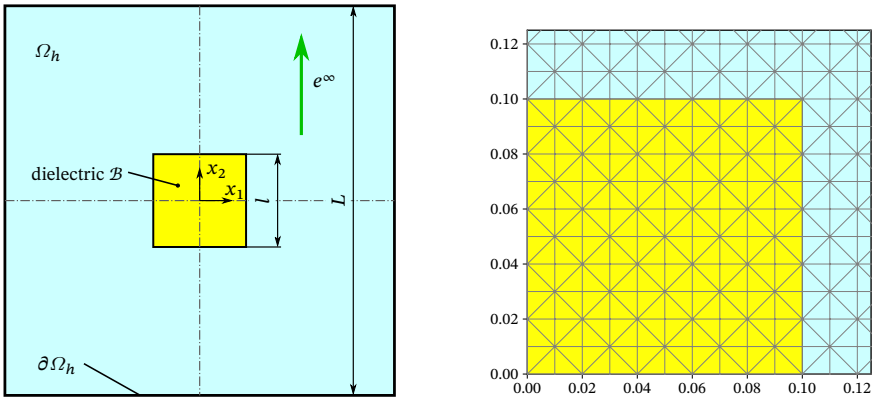

(a) (b)

Figure 9.13: Boundary value problem of a square EAP specimen exposed to a homogeneous external field $\boldsymbol{e}^\infty$ with surrounding space (a). The dimensions of the specimen $\mathcal{B}$ and the truncated free space Ω_h are given as $l = 0.1$ m and $L = 1$ m, respectively. The mesh for the first quadrant of the symmetric problem is shown in (b).

Table 9.2: Material parameters for ψ^{M} and ψ^{M} defined in (9.41)

Material	μ / MPa	κ / MPa	χ^{e} / 1
Body	76.923×10^{-3}	166.666×10^{-3}	10
Free space	1.000×10^{-4}	6.666×10^{-5}	0

Discretizations and loading

We discretize the deformation map φ with vector-valued quadratic Lagrange elements irrespective of the formulation of the electro-static part of the problem. As essential mechanical boundary conditions we have $x(1, X_2) = X$, $x(X_1, 1) = X$, $x_1(0, X_2) = 0$ and $x_2(X_1, 0) = 0$.

In case of the (scalar-)potential formulation we use scalar-valued quadratic Lagrange elements for ϕ^{e}. This corresponds to piecewise linear tangential-continuous $\boldsymbol{E}$-field and piecewise linear discontinuous $\boldsymbol{D}$. The loading is performed by prescribing $\phi^{\mathrm{e}}(x_1, L/2) = -\frac{L}{2}e^\infty$. Moreover, we also enforce $\phi^{\mathrm{e}}(X_1, 0) = 0$. Thus, at $X_1 = 0$ and $X_1 = 1$ the homogeneous natural boundary condition $\boldsymbol{D} \cdot \boldsymbol{N} = 0$ is in effect.

For the constrained-minimization formulations we use BDM and RT elements of degree one. In the case of BDM elements we have piecewise-linear normal-continuous $\boldsymbol{D}$ and piecewise-linear discontinuous $\boldsymbol{E}$. The same is true for RT elements. However, while for BDM elements $\boldsymbol{D} \cdot \boldsymbol{N}$ at element boundaries is a linear polynomial, the same expression is a constant for RT elements (see Section 9.1.4). As essential boundary con-

ditions we have $\boldsymbol{D} \cdot \boldsymbol{N} = \epsilon_0 e^\infty$ at $x_2 = L/2$ and $\boldsymbol{D} \cdot \boldsymbol{N} = 0$ at $x_1 \in \{0, 1\}$.

For completeness we also consider a vector potential formulation. We again employ *scalar*-valued quadratic Lagrange elements as we did for the electric (scalar) potential already before. This is due to the fact that in a two-dimensional setting only the out-of-plane component of the vector potential $\boldsymbol{A}^\mathrm{e}$, that is A_3^e, is non-zero. Hence, $\boldsymbol{B} = (\partial_{X_2} A_3^\mathrm{e}, -\partial_{X_1} A_3^\mathrm{e})^\mathrm{T}$. The electric loading is realized by setting $A_3^\mathrm{e}(x_1, L/2) = \epsilon_0 e^\infty (L/2 - x)$, $A_3^\mathrm{e}(0, x_2) = \epsilon_0 e^\infty L/2$ and $A_3^\mathrm{e}(1, x_2) = 0$. The vector potential leads to the same spaces for $\boldsymbol{D}$ and $\boldsymbol{E}$ as the BDM element for the constrained-minimization (mixed) approach. Thus, we expect identical results for these two discretizations.

Results

The results shown below serves as a motivation to further investigate phenomenon in the numerics of magneto-electro-elasticity that up to now has been neglected: errors in the numerical solution of electro-statics inject spurious source terms into the balance of linear momentum.

For the visualization of the issue at hand we plot the deformed configurations at $e^\infty = 27.5\,\mathrm{MV\,m^{-1}}$ for the ϕ^e and the $\boldsymbol{D}$-ϕ^e (BDM) formulations in Figure 9.14a and 9.14b, respectively. We clearly see the pronounced deformations in the free-space do-

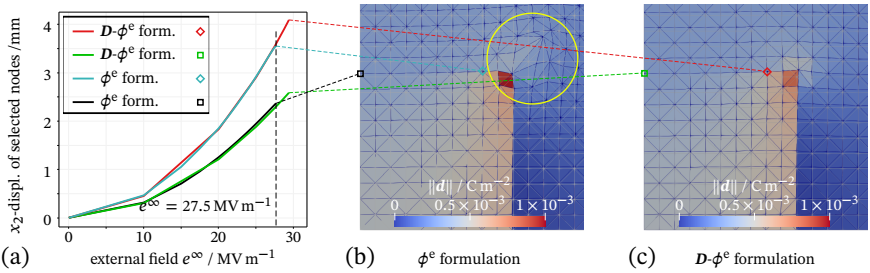

Figure 9.14: A square-shaped EAP exposed to homogeneous external field: In (a) we plot the absolute displacement of two points a the top boundary of the specimen. In (b) we show the deformed configuration obtained with the ϕ^e formulation at $t \approx 1$ corresponding to an electric field $e^\infty = 27.5\,\mathrm{MV\,m^{-1}}$. In (c) we show the state obtained with the $\boldsymbol{D}$-ϕ^e formulation.

main around the corner of the specimen in subplot (b). In (c), by contrast, no such dramatic effect is visible. Furthermore, we also see that the deformation of the specimen's corner in b) is not the same as in c).

Remark 9.5. In certain scenarios one can avoid such issues by means of a staggered scheme where all mechanical degrees of freedom in the free-space domain are fixed in during the solution of the coupled problem and adapted in a subsequent mesh update (Pelteret et al., 2016). However, this does not remove errors in the nodal forces at the boundary between body and free space. Moreover, when the environment of the body is not empty but a comparably soft medium, i.e. a carrier substance, a such a staggered

scheme does not seem appropriate.

9.3.1.2. A magnetic ellipse in a non-magnetic soft carrier box

Next we consider a rectangular box consisting of non-magnetic soft material that carries a rigid magnetic elliptical body in its interior. Let us for simplicity assume that the box has a rigid outer boundary and is itself embedded in free space. Due to symmetry we consider only a quarter of the problem as shown in Figure 9.15. Since the box has a

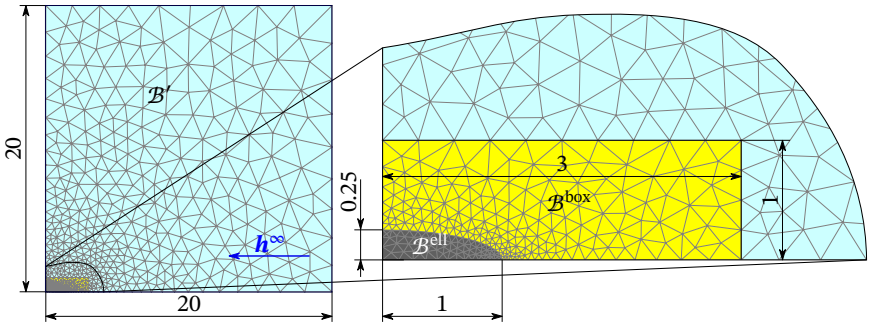

Figure 9.15: An elliptical body $\mathcal{B}^{\text{ell}}$ (rigid, magnetic) embedded in a carrier box $\mathcal{B}^{\text{box}}$ (soft, non-magnetic) exposed to an external h-field in x_1 direction. Dimensions in cm.

rigid outer boundary we simply block the mechanical degrees of freedom of the free space but also those of the rigid ellipse and of all the boundaries and interfaces. Hence, only the soft carrier medium may exhibit deformations. Because of that, the problem does not look particularly interesting at first sight. But recall the previous example. It differs from the present one mainly by the problem geometry. The two different meshes employed for this BVP are depicted in Figure 9.16

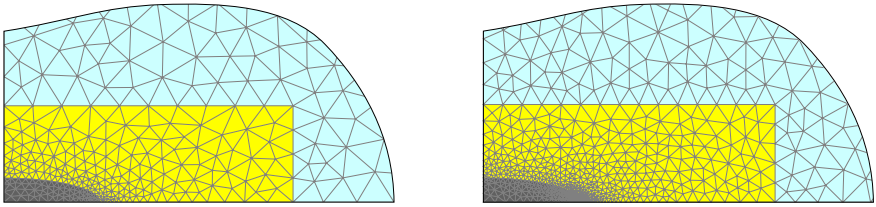

(a) mesh A (b) mesh B

Figure 9.16: Two basic meshes which mainly differ in the discretization of the curved boundary between ellipse and carrier box.

Table 9.3 list the material parameters. In the infinitesimal strain limit the mechanical

Table 9.3: Material parameters for the ellipse in the carrier box.

Domain	μ / kPa	κ / kPa	χ^{m} / 1	m_{s} / MA m^{-1}
Free space	—	—	0	0
Carrier	7.142 857	33.333 333	0	0
Ellipse	—	—	10	1

parameters for the carrier correspond to a Young's modulus of 20 kPa and a Poisson's ratio of 0.4.

Figure 9.17 decpits the mechanical response to the applied magnetic load for FE discretizations with scalar magnetic potential. As can be observed, mesh refinement re-

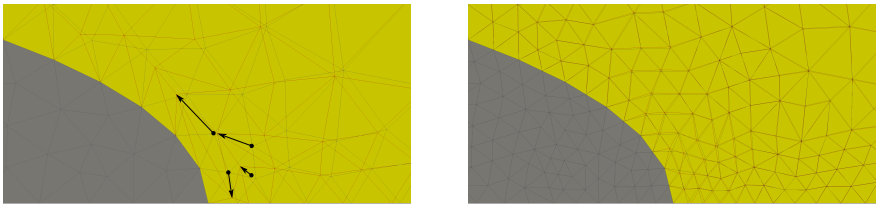

(a) (b)

Figure 9.17: Spurious deformations in the carrier medium obtained with scalar-potential based discretizations in terms of linear Lagrange elements. In (a) we observe pronounced deformations the original (unrefined) mesh. The refined mesh (b) is clearly better in this regard.

duces the excessive unphysical deformations. Interestingly, $\mathscr{H}(\mathrm{Div})$-based formulations as well as vector-potential formulations exhibit much less pronounced spurious deformations. We compare the different formulations in terms of the L_2 and the L_∞ norms of the displacement fields $\boldsymbol{u}$ in the carrier domain.

Figures 9.18 to 9.24 plot the results for various discretizations. In Figure 9.18 we see pronounced deformations in $\mathcal{B}^{\mathrm{box}}$ which are reduced for refined meshes. Moreover, in this context we observe that mesh B is much better in the L_∞ norm than in the L_2 norm. The former measures only the largest absolute displacement whether the latter corresponds to a weighted sum of all displacements. The L_∞ norm carries the more important information. Nevertheless, we believe that both norms together provide even more insight.

What we learn from Figures 9.19 and Figure 9.20 is that an the increase of the polynomial degree for ϕ^{m} reduces the spurious deformations whereas the increase of the degree for φ conversely increases them.

The displacement norms for the vector-potential based discretizations are depicted in Figures 9.21 and 9.22. In both cases, the displacements are discretized by quadratic La-

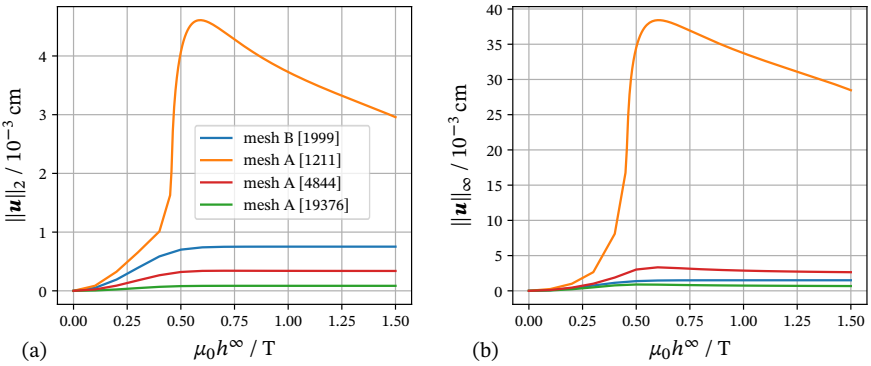

Figure 9.18: Norms of displacement fields in the non-magnetic carrier medium $\mathcal{B}^{\text{box}}$ for scalar-potential formulation with linear Lagrange elements for displacements and magnetic scalar potential. The numbers in braces within the legends are the overall number of elements in the mesh and as such indicate the level of (uniform) mesh refinement. Magnetic saturation limits the deformations. However, we observe a relaxation behavior which possibly reaches far into the magnetically saturated regime in certain cases.

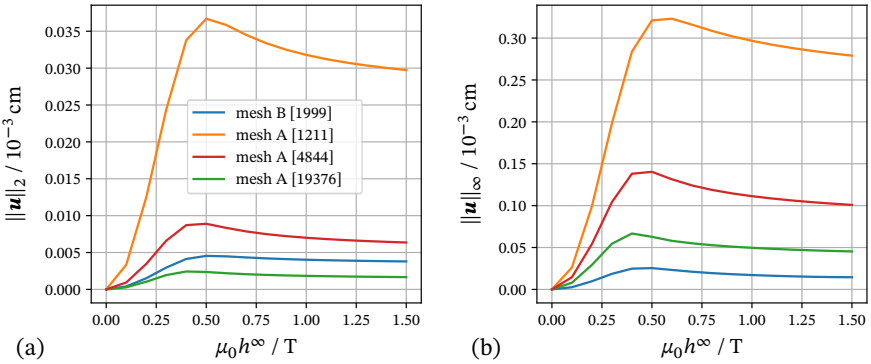

Figure 9.19: Norms of displacement fields in the non-magnetic carrier medium $\mathcal{B}^{\text{box}}$ for scalar-potential formulation with linear Lagrange elements for displacements and quadratic elements for the magnetic scalar potential. The numbers in braces within the legends are the overall number of elements in the mesh and as such indicate the level of (uniform) mesh refinement. Compared with Figure 9.18 we see a reduction in the displacement norms.

grange elements. When comparing Figure 9.21 with Figure 9.18 one despite the higher polynomial degree for displacements observes that both deformation measures for the

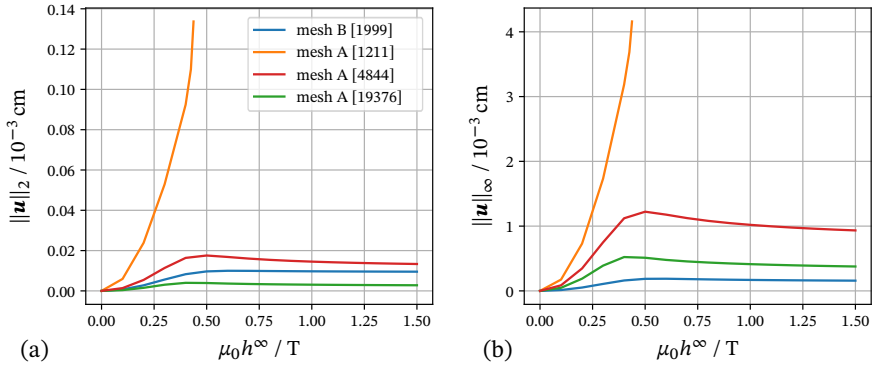

Figure 9.20: Norms of displacement fields in the non-magnetic carrier medium $\mathcal{B}^{\text{box}}$ for scalar-potential formulation with quadratic Lagrange elements for displacements and the magnetic scalar potential. The numbers in braces within the legends are the overall number of elements in the mesh and as such indicate the level of (uniform) mesh refinement. Compared with Figure 9.19 we somewhat unexpectedly see an increase in the displacement norms.

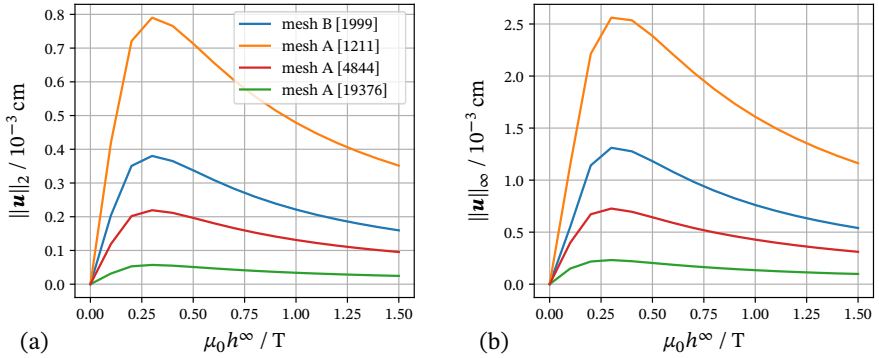

Figure 9.21: Norms of displacement fields in the non-magnetic carrier medium $\mathcal{B}^{\text{box}}$ for vector-potential formulation with quadratic Lagrange elements for displacements and linear magnetic vector potential. The numbers in braces within the legends are the overall number of elements in the mesh and as such indicate the level of (uniform) mesh refinement. Compared with Figure 9.20 for quadratic displacements and quadratic scalar potential we see a reduction of displacement norms despite the linear vector-potential.

vector potential are significantly smaller than those in for the scalar potential. Similar observations can be made from Figures 9.20 and 9.22. Another difference is the occurrence of local extrema in the graphs for the scalar potentials which are not present in

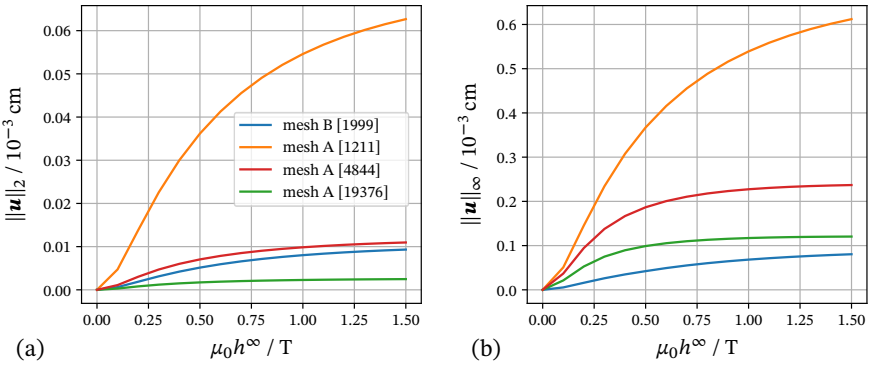

Figure 9.22: Norms of displacement fields in the non-magnetic carrier medium $\mathcal{B}^{\text{box}}$ for vector-potential formulation with quadratic Lagrange elements for displacements and magnetic vector potential. The numbers in braces within the legends are the overall number of elements in the mesh and as such indicate the level of (uniform) mesh refinement. As expected by the increase of polynomial degree for the vector potential the displacement norms are reduced further.

the vector potential cases. This might be due to the different material behaviour for intermediate magnetic loads.

The graphs for the $\mathscr{H}(\text{Div})$-conforming RT and BDM discretizations are shown in Figures 9.23 and 9.24, respectively. Obviously, the graphs in Figures 9.21 and 9.23 are identical. The same holds for Figures 9.22 and 9.24. This comes from the equivalence of the effective solution spaces as outlined in Section 9.1.5.

A common feature visible in all of the plots above is the effect of mesh refinement. However, we point out that not only the displacement become smaller, but also the FE cells. Thus, the distortion of the cells in the current configuration $\mathcal{B}_t^{\text{box}}$ may not be reduced. Figure 9.25 shows graphs of the ratios $\|u\|/\,\text{size}(cell)$ which apparently do not converge zero.

Our interpretation is that rather the spurious deformation *patterns* "converge" with the magnetic part of the problem. At the current state we have to admit that we do not possess a cure for this problem.

9.3.1.3. A nonmagnetic domain with a reentrant corner

Now we consider the synthesis of the examples from Sections 9.3.1 and 9.3.1.2. Let us, for the moment, set aside the question of the possibility of smooth(ened) boundaries to achieve improvements as observed in Section 9.3.1.2 and investigate the case of a single sharp reentrant corner.

Figure 9.26 shows the geometric setting. A soft nonmagnetic material wraps the reentrant corner. As before, we assume all boundaries and interfaces to be rigid and block

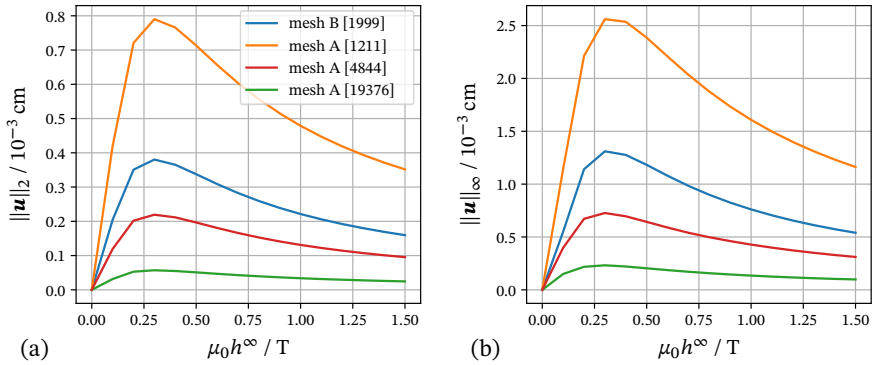

Figure 9.23: Norms of displacement fields in the non-magnetic carrier medium $\mathcal{B}^{\text{box}}$ for mixed formulation with quadratic Lagrange elements for displacements and RT elements for Lagrangian magnetic field $\boldsymbol{B}$. The numbers in braces within the legends are the overall number of elements in the mesh and as such indicate the level of (uniform) mesh refinement. The graphs are identical to those in Figure 9.21 which confirms the considerations from Section 9.1.5.

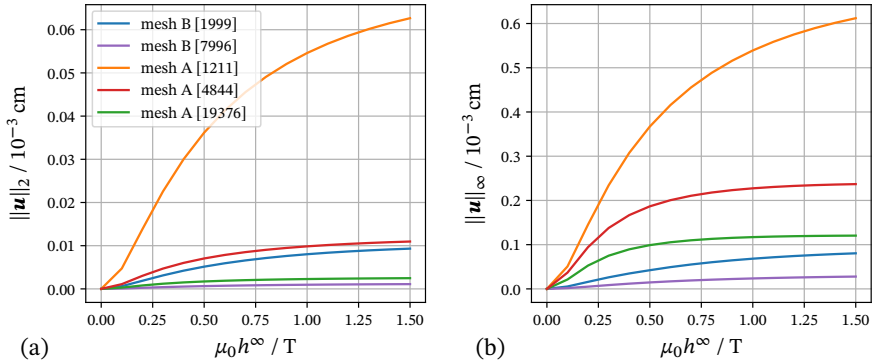

Figure 9.24: Norms of displacement fields in the non-magnetic carrier medium $\mathcal{B}^{\text{box}}$ for mixed formulation with quadratic Lagrange elements for displacements and BDM elements for Lagrangian magnetic field $\boldsymbol{B}$. The numbers in braces within the legends are the overall number of elements in the mesh and as such indicate the level of (uniform) mesh refinement. The graphs are identical to those in Figure 9.22 which confirms the considerations from Section 9.1.5.

the mechanical DOFs in $\mathcal{B}'$. In this case the solution of magnetostatic problem in the current configuration is decoupled from the mechanical problem. Thus, it reduces to Laplace's problem. Hence, we can employ the corresponding analytical solution for ϕ^{m}

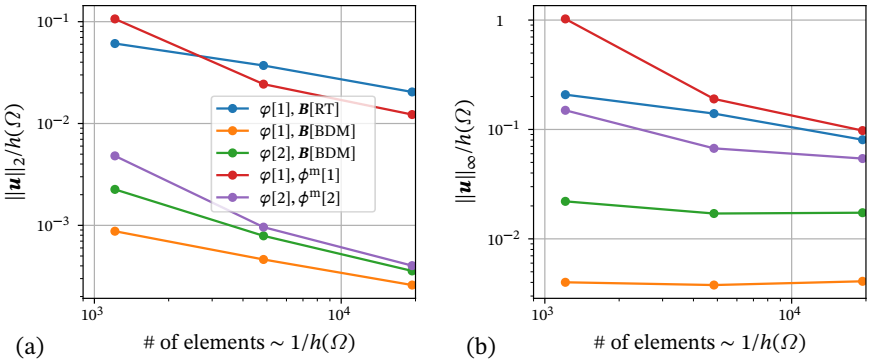

Figure 9.25: Norms of displacement fields in the non-magnetic carrier medium $\mathcal{B}^{\mathrm{box}}$ at saturated state weighted by minimal element size $h(\Omega)$. In (a) the norms seem to indicate a decrease of spurious deformations. However, we argue that this is rather to their localization, which also reduces the l_2 norm. In (b) we observe that the maximum deformations at some point reduce at the same pace as the element size. Our interpretation of this behavior is that the spurious deformation patterns converge with the magnetic part of the problem. Legend: The square braces indicate the polynomial degree and/or element type of a field's discretization.

(see, e.g. Babuška et al. (1995))

$$\phi_a^{\mathrm{m}}(X) = \overline{\phi^{\mathrm{m}}} r(X)^\alpha \sin(\alpha\Theta(X)) \tag{9.43}$$

with

$$\alpha = \frac{1}{3}, \quad r(X) = \sqrt{(X_1-5)^2 + (X_2-5)^2} \quad \text{and} \quad \Theta(X) = \arctan\left(\frac{X_1-5}{X_2-5}\right) + \frac{\pi}{2},$$

which is plotted in Figure 9.27. As boundary conditions we employ $\phi^{\mathrm{m}} = \phi_a^{\mathrm{m}} = 0$ where $X_1 \in [0,5] \wedge X_2 = 5$ and $\boldsymbol{B}\cdot\boldsymbol{N} = -\mu_0 \operatorname{Grad}\phi_a^{\mathrm{m}}$ elsewhere (Babuška et al., 1995).

The material laws and parameters are the same as before and can be found in Table 9.3. For the given boundary conditions the magnetic field features a singularity at the reentrant corner. It is well-known that this singularity deteriorates global convergence and has to be treated with care (Blum and Rannacher, 1987; Babuška et al., 1995; Oden and Feng, 1996). However, we are now not so much interested in convergence but in spurious deformations in the vicinity of a (sharp) corner.

We already know from the previous examples that there will be unphysical deformations in the non-magnetic domain. Therefore, we also expect unphysical forces in the same areas. Indeed, as shown in Figure 9.28, there are forces within $\mathcal{B}$. Please, note that there of course exist physical forces at the *boundaries* near the reentrant corner. However, we did not include them in the contour plots to not let them "shadow" the spurious forces in the interior.

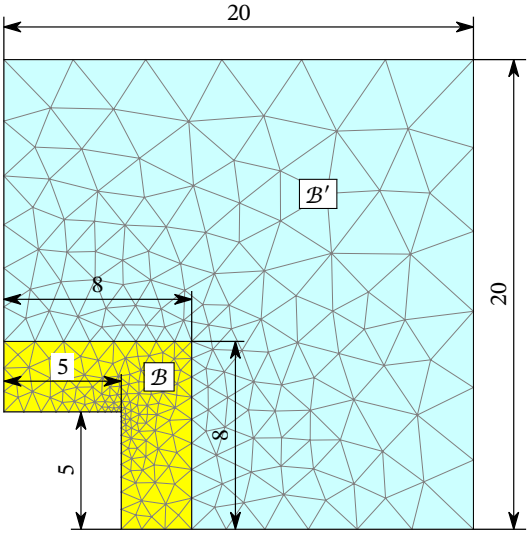

Figure 9.26: A reentrant corner embedded in a soft non-magnetic material $\mathcal{B}$ in free space $\mathcal{B}'$. The dimensions in the sketch re given in mm. The out-of-plane dimension is 1 mm.

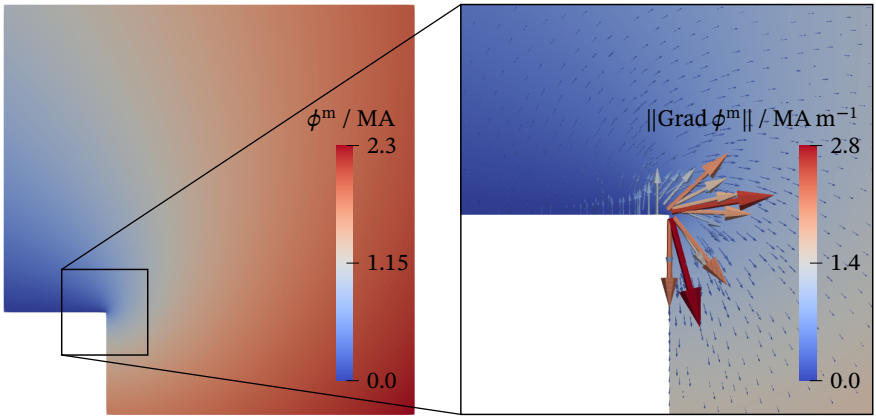

Figure 9.27: Analytical solutions for ϕ^{m} (a) and Grad ϕ^{m} (b). Note that Grad ϕ^{m} has a singularity at the reentrant corner. The colorbar for $\|\mathrm{Grad}\,\phi^{\mathrm{m}}\|$ is based on the numerical evaluation for which we omitted the corner point $X = (5, 5)$.

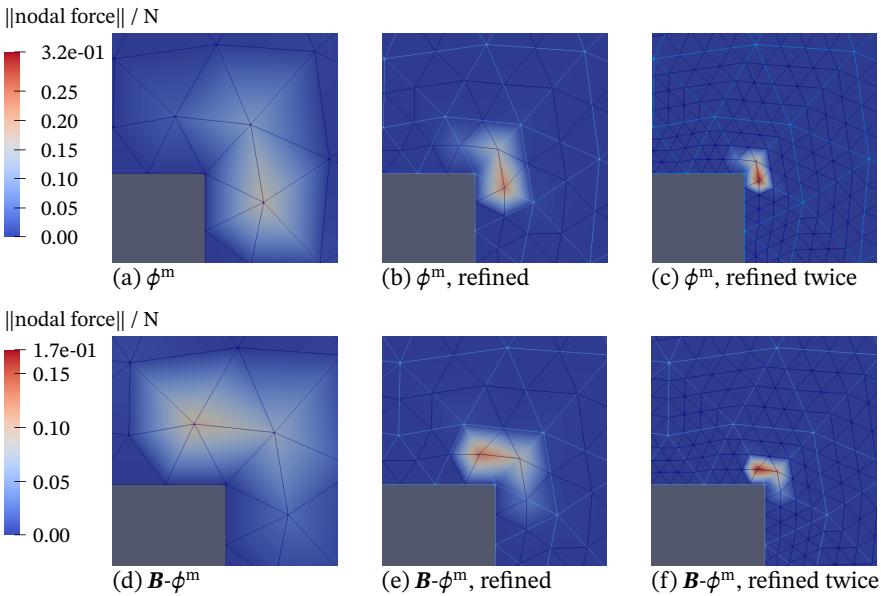

Figure 9.28: Contour plots of discrete nodal forces *within* $\mathcal{B}$ for the initially coarse mesh and refined meshes. The plots (a) to (c) are computed based on a linear scalar-potential discretization. Forces obtained with the mixed ($\mathscr{H}$(Div)-conforming) formulation discretized with RT elements are depicted in (d) to (f). Mesh refinement increases and localizes the discrete forces in the vicinity of the corner.

In the vicinity of the reentrant corner we observe pronounced nodal forces for both of the two formulations. However, the magnitudes differ and so does the "pattern" or distribution of forces. Moreover, in Figure 9.28 we see that mesh refinement not only localizes the discrete forces but also increases their extremal magnitude. At this point, one should have in mind that nodal forces are difficult to interpret, in particular in coupled problems. Therefore, we now turn to the actual (unphysical) deformations, which not only indicate a problem of accuracy but pose a threat to the robustness of numerical procedures. Figure 9.29 depicts the deformation responses for linear Lagrange elements for φ and BDM elements for $\boldsymbol{B}$ at "load" $\overline{\phi^{\mathrm{m}}} = 1\,\mathrm{MA}$.

The deformation localization is similar to the previously observed nodal force localization (see Figure 9.28). Also, while the magnitude of displacements is decreased by mesh refinement, the strains in the vicinity of the corner are increased at the same time. Obviously, mesh refinement is not the universal cure for the issue of spurious interactions in the present case. As a possible remedy we suggest to investigate the use of different levels of refinement for magnetic (or electric) and mechanical discretizations or similar ideas.

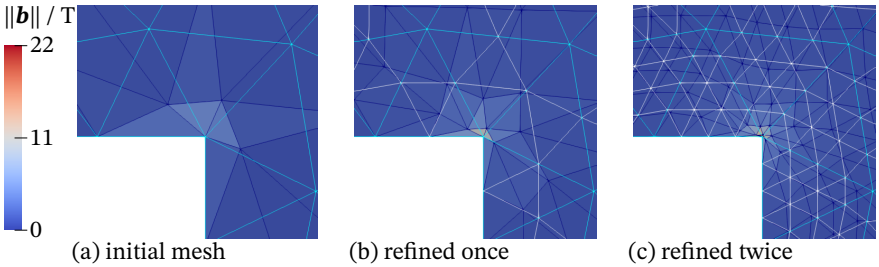

Figure 9.29: Spurious deformations in the vicinity of the reentrant corner for linear displacements and BDM elements. The colors indicate the magnitude of the magnetic field $\boldsymbol{b}$. Refinement clearly reduces the magnitude of displacements. However, the deformation is even increased in a small region close to the corner, whereas it is decreased elsewhere. At the same time, mesh refinement leads to a better resolution of $\boldsymbol{b}$.

All schemes discussed in the present thesis suffer from spurious interactions. However, their magnitude and also the deformation "patterns" or "modes" differ in general. Figure 9.30 compares the deformation responses at $\overline{\phi^{\mathrm{m}}} = 0.3\,\mathrm{MA}$ for linear Lagrange elements for φ combined with quadratic Lagrange elements for the scalar potential (Figure 9.30a) and BDM elements (Figure 9.30b), respectively. As depicted the

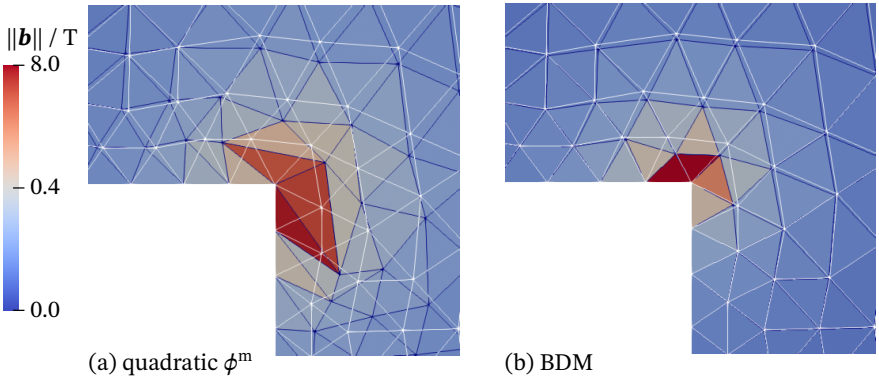

Figure 9.30: Spurious deformations in the vicinity of the reentrant corner for linear displacements combined with quadratic scalar potential (a) as well as BDM elements (b). The colors indicate the magnitude of the magnetic field $\boldsymbol{b}$. We show the deformed configurations for $\overline{\phi^{\mathrm{m}}} = 0.3\,\mathrm{MA}$ on the refined mesh with 1920 elements. Note the differences in deformation magnitude but also the deformation pattern. In (a) we observe that nodes try to move away from the corner parallel to the edges. By contrast, in (b) nodes seem to be attracted by the corner.

scalar-potential scheme features larger deformations than the BDM formulation. As

a consequence, the BDM discretization is applicable for higher loads than the scalar-potential scheme of comparable polynomial degree (linear $\boldsymbol{H}$).

9.3.1.4. Summary of observations on spurious interactions

Here we summarize our findings from Sections 9.3.1 to 9.3.1.3.

- Errors in the solution of the electro- and magnetostatic parts of the MEM problems are unavoidable. They cause more or less pronounced spurious deformations which cannot be removed by simple means, e.g. mesh refinement.
- The smoother a surface of discontuity in electric or magnetic properties is, the smaller are the spurious deformations.
- Different formulations and discretizations lead to different deformation patterns. It seems as if energy-based (vector-potential, contrained minimizaion) formulations perform better than scalar-potential based schemes in this regard.

9.3.2. Comparison of computational effort

In two dimensions scalar- and vector-potential formulations employ the same finite elements for discretization, i.e. scalar Lagrange elements. Thus, one cannot expect significant differences in computational performance, at least as long as direct linear solvers are used. The picture changes in three dimensions where the vector-potential is truly vector-valued. Moreover, in such a setting Nédélec edge elements provide the more natural discretization than vector-valued Lagrange elements (Bossavit, 1998a). Nevertheless, vector-valued Lagrange elements are the dominant discretization for vector-potentials in coupled magneto-electro-mechanics. We suspect that this is because edge element discretizations lose some of their advantages in coupled problems. For example, they are better suited for iterative solvers in magneto-statics (Bossavit, 1998a; Biro et al., 1996). In coupled magneto-elasticity, however, the construction of effective preconditioners is an open problem and iterative schemes, thus, are neither very efficient nor very common in the present context. Because of that, we will below only consider Lagrange elements for vector-potentials. Moreover, we restrict ourselves to Newton schemes with direct linear solvers for the solution of the discretized BVPs. Figure 9.31 depicts our magneto-electro-mechanical benchmark example. A soft dielectric box encloses an elastic magnetic sphere. Outside the box there is empty space. We apply electric and magnetic loads as fields $\boldsymbol{d}^{\infty} = (0, 0, 5 \times 10^{-5})\,\mathrm{C\,m^{-2}}$ and $\boldsymbol{b}^{\infty} = (0, 0, 2 \times 10^{-2})\,\mathrm{T}$, respectively.

The material parameters employed for the three domains are given in Table 9.4. The performance comparison is in terms of computational time required by the Newton solver to converge with a relative tolerance of $tol_{\mathrm{rel}} = 1 \times 10^{-12}$. The loads and tolerance are chosen such that 4 Newton iterations are required to converge, irrespective of the formulation and discretization. By that we ensure that the measured times listet

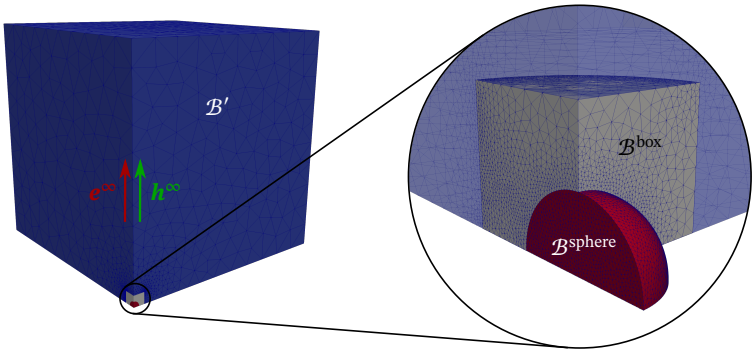

Figure 9.31: Boundary value problem for performance comparison. A magneto-electric sphere $\mathcal{B}^{\text{sphere}}$ of radius 1cm inside a dielectric cube $\mathcal{B}^{\text{box}}$ of side-length 4cm surrounded by cubical empty space $\mathcal{B}'$ of side-length 80cm. The magnetic and electric loads are applied in terms of homogeneous external fields $\boldsymbol{h}^\infty$ and $\boldsymbol{e}^\infty$, respectively. Because of symmetries we only consider one octant.

Table 9.4: Material parameters for performance comparison example

Domain	μ / kPa	κ / kPa	χ^{e} / 1	χ^{m} / 1	m_{s} / MA m^{-1}
Free space	—	—	0.0	0	0
Carrier	7.142 857	33.333 333	0.5	0	0
Sphere	337.837 838	5743.243 243	2.0	10	1

in Table 9.5 directly relate to the time required for the solution of the linear systems during the Newton steps. As linear solver we use the parallel direct solver `MUMPS` (Amestoy et al., 2001, 2006).

From Table 9.5 we see that scalar-potential formulations turn out to be most efficient, as expected. In second place we have the $\mathscr{H}(\text{Div})$-conforming schemes. Depending on the polynomial degrees of the sub-elements vector-potential scheme take up to five times longer until they converge. This is even the case despite that we implemented the Coulomb gauge via the penalty method. If we followed such an approach for the constraints $\text{Div}\,\boldsymbol{D} = 0$ and $\text{Div}\,\boldsymbol{B} = 0$, the mixed formulations would be even further ahead. Also note that the penalty method is not well suited for vector-potential discretizations with linear Lagrange elements. In that case, one cannot under-integrate the penalty term. Consequently, the solution severely lacks accuracy near surfaces of discontinuity in material parameters.

Improving performance

Despite their clear win over vector potentials, the $\mathscr{H}(\text{Div})$-conforming scheme are still considerably behind the scalar-potential approaches.

A possible route of improving the performance is to consider a weak enforcement of inter-element continuity of the $\mathscr{H}(\mathrm{Div})$ conforming element spaces as described in Brezzi and Fortin (1991, Chap. V) for the (mixed) Poisson problem and applied to fluid flow in porous media by Trykozko et al. (2001).

We also point out that the constraint term $\phi^{\mathrm{m}}(\mathrm{Div}\,\boldsymbol{B})$ leads to rather well-conditioned constraint-matrices such that null-space methods with nested iterative solvers for these constraints become an interesting option. As an example, the $\mathrm{N1}^f$-based discretization leads to discrete constraints

$$\delta\phi^{\mathrm{m}} \cdot \begin{bmatrix} \pm 1 & \pm 1 & \pm 1 & \pm 1 \end{bmatrix} \cdot \begin{bmatrix} \Phi_1 \\ \Phi_2 \\ \Phi_3 \\ \Phi_4 \end{bmatrix} \tag{9.44}$$

per element, where Φ_i are the DOFs associated with the fluxes of $\boldsymbol{B}$. We refer to Nocedal and Wright (2006) for further details on solvers for constrained optimization problems.

In three dimensions the storage requirements for the factorization of FE system matrices is prohibitive even for relatively small problems. Thus, one aims to apply iterative linear solvers like CG or GMRES and also multigrid methods. However, to estimate their computational effort for the solution of a linear system of equations one not only needs to know the effort for an vector-matrix multiplication but also the condition number of the matrix, which is decisive for convergence. For most problems discretized with finite elements it is required to use a preconditioner to achieve satisfactory convergence rates (Mardal and Winther, 2011). Unfortunately, there is no bullet-proof procedure for the construction of good preconditioners. This is particularly true for coupled problems. The interested reader is referred to Meister (2015) for a thorough introduction to linear systems of equations and to Hackbusch (1994) and Briggs et al. (2000) for multigrid methods. Concerning coupled problems we point out that preconditioners are often constructed only for a certain differential operator or PDE type, see e.g. Hiptmair (1998) and Hiptmair and Xu (2007) for multigrid preconditioners for Maxwell's equations and elliptical PDEs with $\mathscr{H}(\mathrm{Div})$- and $\mathscr{H}(\mathrm{Curl})$-conforming discretizations, respectively. However, the extension of such schemes to coupled PDEs and multiphysics is still an open problem. We refer to Shadid et al. (2016) as an example for recent progress in that direction.

Table 9.5: Performance of various discretizations in terms of computation time. The groups are selected based on the effective polynomial degrees of φ, $\boldsymbol{D}$ and $\boldsymbol{B}$.

Formulation	Discretization (*fields*: *FEEC elmt.*; ...)	# CPUs.	time / s
scalar pot.	$\varphi_i : \mathcal{P}_1\Lambda^0(\Delta_3);\ \phi^{\mathrm{e}}, \phi^{\mathrm{m}} : \mathcal{P}_1\Lambda^0(\Delta_3)$	1	36.77
vector pot.	$\varphi_i : \mathcal{P}_1\Lambda^0(\Delta_3);\ A_i^{\mathrm{e}}, A_i^{\mathrm{m}} : \mathcal{P}_1\Lambda^0(\Delta_3)$	1	129.61
$\mathscr{H}(\mathrm{Div})$	$\varphi_i : \mathcal{P}_1\Lambda^0(\Delta_3);\ \boldsymbol{D}, \boldsymbol{B} : \mathcal{P}_1^-\Lambda^2(\Delta_3);\ \phi^{\mathrm{e}}, \phi^{\mathrm{m}} : \mathcal{P}_0\Lambda^0(\Delta_3)$	1	89.40
scalar pot.	$\varphi_i : \mathcal{P}_2\Lambda^0(\Delta_3);\ \phi^{\mathrm{e}}, \phi^{\mathrm{m}} : \mathcal{P}_1\Lambda^0(\Delta_3)$	8	134.53
vector pot.	$\varphi_i : \mathcal{P}_2\Lambda^0(\Delta_3);\ A_i^{\mathrm{e}}, A_i^{\mathrm{m}} : \mathcal{P}_1\Lambda^0(\Delta_3)$	8	222.15
$\mathscr{H}(\mathrm{Div})$	$\varphi_i : \mathcal{P}_2\Lambda^0(\Delta_3);\ \boldsymbol{D}, \boldsymbol{B} : \mathcal{P}_1^-\Lambda^2(\Delta_3);\ \phi^{\mathrm{e}}, \phi^{\mathrm{m}} : \mathcal{P}_0\Lambda^0(\Delta_3)$	8	212.13
scalar pot.	$\varphi_i : \mathcal{P}_1\Lambda^0(\Delta_3);\ \phi^{\mathrm{e}}, \phi^{\mathrm{m}} : \mathcal{P}_2\Lambda^0(\Delta_3)$	8	61.48
vector pot.	$\varphi_i : \mathcal{P}_1\Lambda^0(\Delta_3);\ A_i^{\mathrm{e}}, A_i^{\mathrm{m}} : \mathcal{P}_2\Lambda^0(\Delta_3)$	8	721.21
$\mathscr{H}(\mathrm{Div})$	$\varphi_i : \mathcal{P}_1\Lambda^0(\Delta_3);\ \boldsymbol{D}, \boldsymbol{B} : \mathcal{P}_1\Lambda^2(\Delta_3);\ \phi^{\mathrm{e}}, \phi^{\mathrm{m}} : \mathcal{P}_0\Lambda^0(\Delta_3)$	8	155.70
scalar pot.	$\varphi_i : \mathcal{P}_2\Lambda^0(\Delta_3);\ \phi^{\mathrm{e}}, \phi^{\mathrm{m}} : \mathcal{P}_2\Lambda^0(\Delta_3)$	8	366.60
vector pot.	$\varphi_i : \mathcal{P}_2\Lambda^0(\Delta_3);\ A_i^{\mathrm{e}}, A_i^{\mathrm{m}} : \mathcal{P}_2\Lambda^0(\Delta_3)$	8	1560.31
$\mathscr{H}(\mathrm{Div})$	$\varphi_i : \mathcal{P}_2\Lambda^0(\Delta_3);\ \boldsymbol{D}, \boldsymbol{B} : \mathcal{P}_1\Lambda^2(\Delta_3);\ \phi^{\mathrm{e}}, \phi^{\mathrm{m}} : \mathcal{P}_0\Lambda^0(\Delta_3)$	8	631.65

9.4. Deformation-mediated magneto-electric coupling

In this section we return to the topic of Chapter 8, that is the transformation of a quasi-static change of the electric field into a change of the magnetic field and vice versa. One possibility to realize such a coupling is through mechanics, as we have seen in Chapter 8. As discussed therein, ME coupling can already be achieved with a simple spherical body. The only requirements are that the considered material is quite soft and that it can be magnetized and polarized.

Below we are interested in ME coupling in the spirit of Chapter 8. That is the change of the electric field in some region $\mathcal{B}^{\mathrm{e}}$ at the surface of $\mathcal{B}$ with respect to a change in the magnitude of the external magnetic field $\mu_0 h^\infty$. Accordingly, we again define the ME sensitivity via adjoint sensitivity analysis (see Section 8.4 and Appendix C) with quantity of interest α being

$$\alpha = e^{\mathrm{surf}} = \frac{1}{\mathcal{B}^{\mathrm{e}}} \int_{\mathcal{B}^{\mathrm{e}}} e_3 \, dV \tag{9.45}$$

and control variable $\beta = h^\infty$. The physical state and the equilibrium constraint are given by the magneto-electro-mechanical boundary value problem. The actual ME sensitivity will be denoted $\mathrm{d}\hat{e} \,/\, \mathrm{d}h^\infty$.

9.4.1. Macrostructural magneto-electric coupling of a spherical body in free space

We now consider the example of a spherical magneto-electro-elastic body exposed to homogeneous external magnetic and electric fields. Of particular interest are the non-local magneto-electric coupling properties of such a body. This setting resembles the setting investigated in Chapter 8 (see Section 8.5, in particular) but based on the new (mixed FE) formulation. For self-containedness of the present chapter, the BVP is shown in Figure 9.32.

The spherical body $\mathcal{B}$ is embedded in spherical truncated free space Ω_h. The ratio of radii is set to $R^{\mathcal{B}}/R^{\Omega} = 1/20$. We prescribe $\boldsymbol{h}^\infty = (0, 0, -h^\infty)$ and $\boldsymbol{e}^\infty = (0, 0, -e^\infty)$ through

$$\Pi^{\mathrm{ext}} = \int_{\partial\Omega} (h^\infty X_3)(\boldsymbol{B} \cdot \boldsymbol{N}) + (e^\infty X_3)(\boldsymbol{D} \cdot \boldsymbol{N}) \, dA. \tag{9.46}$$

As indicated in Figure 9.32b we exploit the symmetry of the problem. The domain employed in the simulations is given by a subset of the sphere such that $\Omega_h = \{X \mid (X_1 > 0) \wedge (X_2 < X_1/2) \wedge (X_3 > 0) \wedge (\|\boldsymbol{X}\| < R^{\Omega})\}$. At $X_1 = 0$ and $X_3 = 0$, we enforce the symmetry conditions on the deformation via trivial essential boundary conditions. We resort to weak enforcement with a Lagrange multiplier field ζ at $X_2 = X_1/2$. The symmetries of $\boldsymbol{d}$ and $\boldsymbol{b}$ are everywhere enforced as homogeneous essential and natural boundary conditions, respectively. The material for the body and the free space (treated in a monolithic way) is modeled by the energy-density function (9.37a) with parameters listed in Table 9.6. The domain $\mathcal{B}^{\mathrm{e}}$ where we evaluate (or "measure") $\boldsymbol{e}$ to obtain $\boldsymbol{e}^{\mathrm{surf}}$

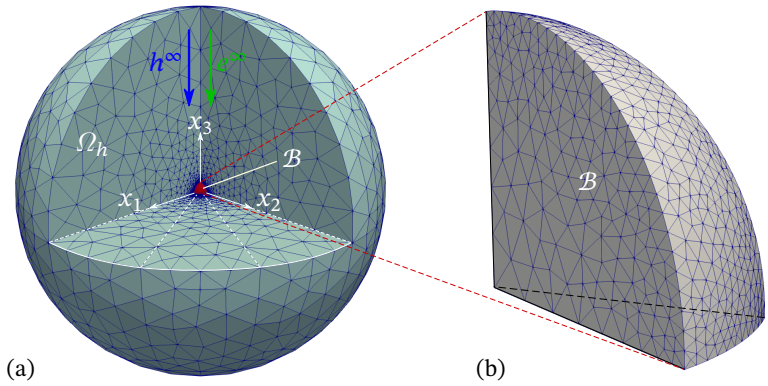

Figure 9.32: A spherical body $\mathcal{B}$ in a spherical truncated free space Ω_h with a ratio of radii $R^{\mathcal{B}}/R^{\Omega} = 1/20$. The body is exposed to homogeneous external magnetic and electric fields in negative x_3-direction, $\boldsymbol{h}^\infty$ and $\boldsymbol{e}^\infty$, respectively. In (a) we depict the full BVP with loading and free space. We only hide one octant in order to reveal the specimen. In (b) we picked out the specimen according to this reduced domain in order to visualize its (surface) mesh.

Table 9.6: Material parameters for magneto-electric capacitor examples

Domain	μ / kPa	κ / kPa	χ^{e} / 1	χ^{m} / 1	m_{s} / MA m^{-1}
ME sphere	1×10^2	∞	1.0×10^1	1.0	0.3
Free space	5×10^{-1}	3.333×10^{-1}	0.0	0.0	0.0

and its sensitivity with respect to h^∞ denoted as $\mathrm{d}\hat{e}/\,\mathrm{d}h^\infty$ is depicted in Figure 9.33.

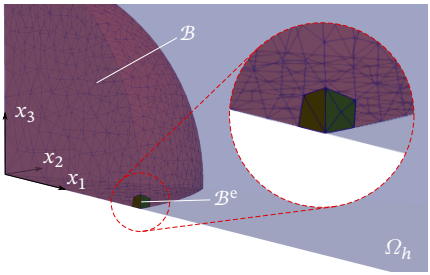

Figure 9.33: The domain $\mathcal{B}^{\mathrm{e}}$ for the evaluation of the electric field e^{surf} to determine the magneto-electric coupling properties of a spherical body.

We investigate the ME coupling for given external electric fields of magnitude $e^\infty \in$

$\{0, 5 \ldots 25\}\mathrm{MV\,m^{-1}}$. For each value of e^∞ we linearly increase the magnetic magnetic field from $\mu_0 h^\infty = 0$ to $\mu_0 h^\infty = \mu_0 1.5\,\mathrm{T}$. In Figure 9.34 we show line plots of e^{surf} and the corresponding ME sensitivity. Via cubic interpolation (Alfeld, 1984) we obtain the

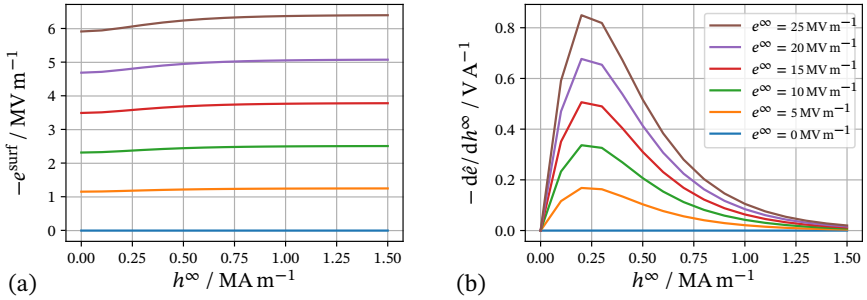

Figure 9.34: Magneto-electric coupling properties of a spherical body. The average electric field in $\mathcal{B}^{\mathrm{e}}$ at equilibrium denoted as e^{surf} is depicted in (a) for a range of external electric fields e^∞. Subplot (b) visualizes the (magneto-electric) sensitivity $\mathrm{d}\hat{e}/\mathrm{d}h^\infty$.

surface plot depicted in Figure 9.35. Both figures are in qualitative agreement with the

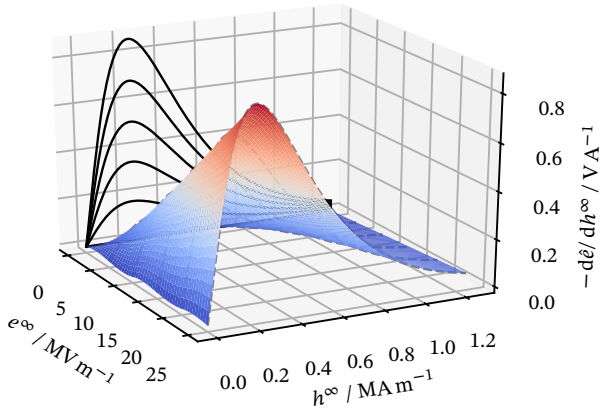

Figure 9.35: Surface plot of the magneto-electric sensitivity of a spherical body. The black lines correspond to smooth interpolations of the data points that lead to the line plots in Figure 9.34.

results presented in Section 8.4. Quantitative differences are not only due to the assumptions made in the derivation for the analytical model (see Section 8.5.3) but also come from the different material models employed. Indeed, the energy-density parametrized in $\underline{\boldsymbol{F}}$ and $\boldsymbol{h}$ that were employed in Chapter 8 cannot be Legendre-transformed into a

function in terms of $\underline{\boldsymbol{F}}$ and $\boldsymbol{b}$. While both material models account for magnetic saturation and also have the same asymptotic behavior at zero magnetic field, they in general differ in the non-saturated regime where the ME sensitivity is most pronounced.

9.4.2. A plate capacitor with a magneto-electro-elastic body as dielectric medium

The BVP for this example has already been described in Section 9.2.2. To recall the setup we repeat Figure 9.7 in Figure 9.36 below. To avoid unnecessary repetitions, we in the

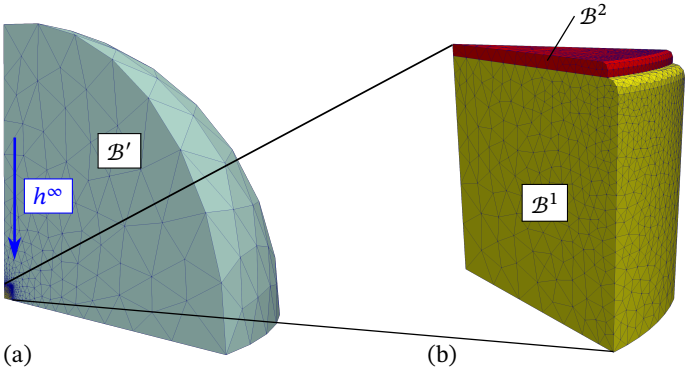

Figure 9.36: The cylindrical ME specimen ($\mathcal{B}^1$) with attached electrodes ($\mathcal{B}^2$) for electric loading surrounded by empty space $\mathcal{B}'$ (rep. of Figure 9.7). We exploit symmetries with respect to the $x_3 = 0$-plane and the x_3-axis. We thus only consider the portion depicted. The magnetic loading is performed via a homogeneous external magnetic field $\boldsymbol{h}^\infty$ in negative x_3-direction. The ME body as well as the electrodes are simply constructed by rotation of the geometry depicted in Figure 9.3b. The surrounding empty space fills a sphere with radius 20 cm.

present section simply show the results for the magneto-electric sensitivity, which is evaluated for a finite element inside the body adjacent to the surface and the symmetry plane $x_3 = 0$ as shown in Figure 8.12. Figure 9.37 depicts line plots of the QOI e^{surf} (a) and of the actual sensitivity $\mathrm{d}\hat{e}/\,\mathrm{d}h^\infty$ (b). The corresponding surface plot is shown in Figure 9.38. The results are quite similar to those for the sphere in Section 9.4.1 and in Section 8.4.

9.4.3. A spherical magneto-electro-elastic body partly covered with soft electrodes

This example is the synthesis of the two previous ones in Sections 9.4.1 and 9.4.2. The loading is performed the same way as in the the latter example, with the range for the

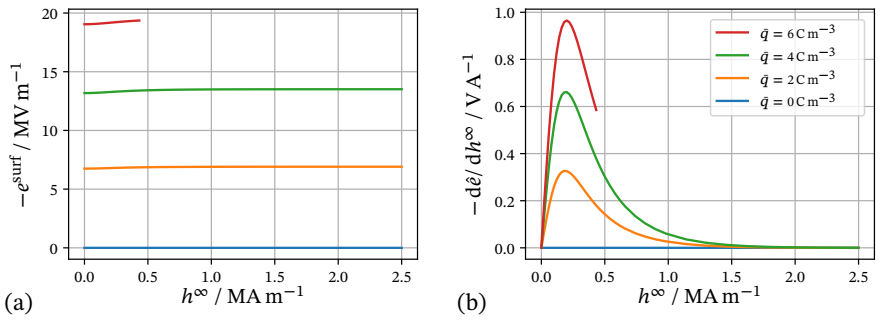

Figure 9.37: Magneto-electric coupling properties of a cylindrical capacitor. The average electric field in $\mathcal{B}^{\mathrm{e}}$ at equilibrium denoted as e^{surf} is depicted in (a) for a range of external electric fields e^∞. Subplot (b) visualizes the (magneto-electric) sensitivity $\mathrm{d}\hat{e}/\,\mathrm{d}h^\infty$.

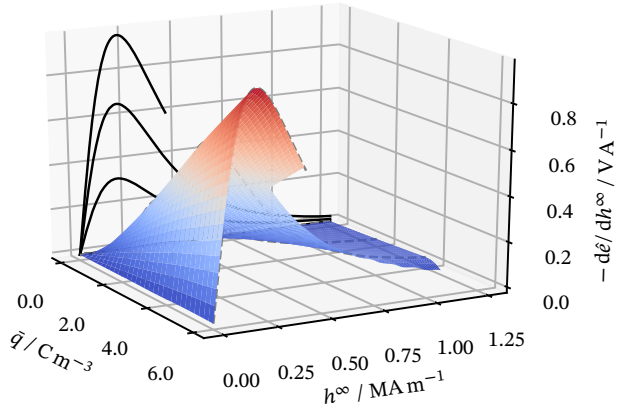

Figure 9.38: Magneto-electric sensitivity of a cylindrical capacitor. The black lines correspond to smooth interpolations of the data points that lead to the line plots in Figure 9.37.

prescribed charge density in the electrode $q_0 = \bar{q} \in \{0 \dots 3\}\,\mathrm{C\,m^{-3}}$ being the only difference. The overall setting is depicted in Figure 9.39. The domain of evaluation of the change in electric field is as in the previous example a FE cell inside the body adjacent to the surface and the symmetry plane $x_3 = 0$. For the present device we expect qualitatively similar results as before. As shown in Figure 9.40 this is indeed the case. However, the obtained sensitivities are of larger magnitude than for the cylindrical capacitor above (see Figure 9.37). We close the present section with the surface plot in Figure 9.41.

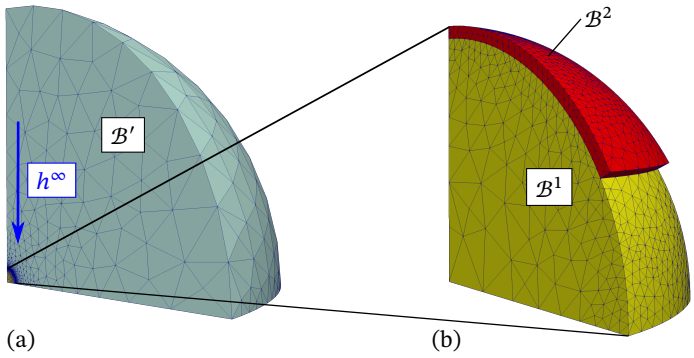

Figure 9.39: The spherical ME specimen ($\mathcal{B}^1$) with attached electrodes ($\mathcal{B}^2$) for electric loading surrounded by empty space $\mathcal{B}'$. The sphere has a radius of $r = 1$ cm. The thickness of the electrodes is $d = 0.05$ cm. They cover the sphere in the range $|x_3| \in [0.5, 1]$. The surrounding empty space fills a sphere with radius 20 cm. We exploit symmetries with respect to the $(x_3 = 0)$-plane and the x_3-axis such that only the portion depicted is actually considered in the simulations. The magnetic loading is performed via a homogeneous external magnetic field $\boldsymbol{h}^\infty$ in negative x_3-direction.

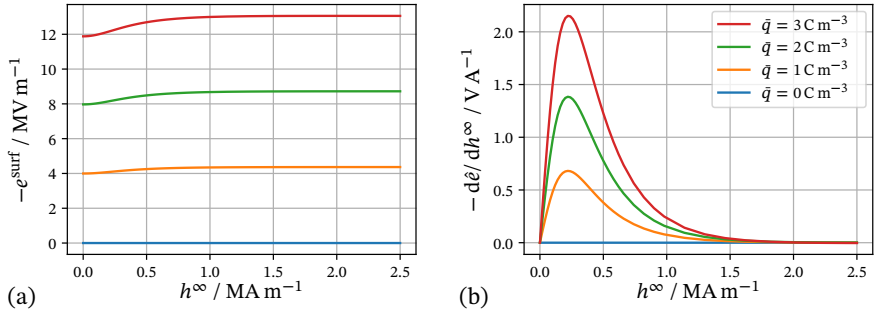

Figure 9.40: Magneto-electric coupling properties of a spherical body with electrodes. The average electric field in $\mathcal{B}^{\mathrm{e}}$ at equilibrium denoted as e^{surf} is depicted in (a) for a range of external electric fields e^∞. Subplot (b) visualizes the (magneto-electric) sensitivity $\mathrm{d}\hat{e}/\mathrm{d}h^\infty$.

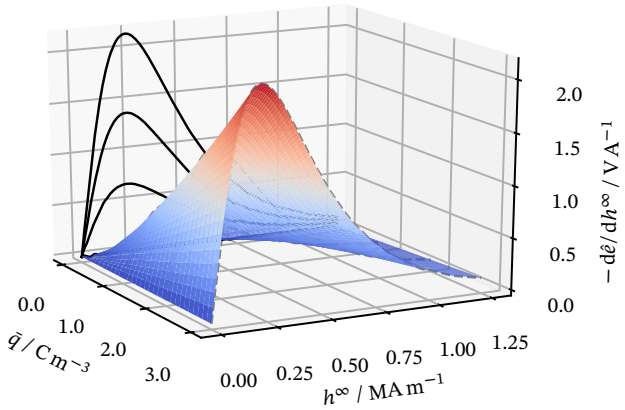

Figure 9.41: Magneto-electric sensitivity of a spherical body with electrodes. The black lines correspond to smooth interpolations of the data points that lead to the line plots in Figure 9.40.

Chapter 10

Two-scale studies on the magneto-electro-mechanical response of magnetorheological elastomers

In the present chapter we consider magnetorheological elastomers (MREs) as a prototypical soft magneto-electric composites. For studies focusing on their magneto-mechanical behavior only, we refer to Chapter 7 and references cited therein as well as to Section 11. In what follows we again account for the heterogeneous microstructure of MREs by computational homogenization along the lines of Miehe et al. (1999), Feyel and Chaboche (2000) and Terada and Kikuchi (2001). Early results of the research below have been published in Rambausek and Keip (2017, 2018b).

We consider a dielectric soft elastomer material for the matrix part of the representative volume element ($\mathcal{RVE}$). For the inclusions we assume quasi-rigid elastic and non-hysteretic but saturating magnetic behavior. Electrically, they are modeled as dielectrics with high electric susceptibility instead of as conductors. Such a choice is reasonable in the case of completely isolated particles in a quasi-static setting.

Below we first summarize a variational homogenization principle based on vector potential formulations in a two-dimensional setting following in Miehe et al. (2016).

We restrict ourselves to first-order homogenization schemes in the sense that we consider the macroscopic deformation gradient $\overline{\boldsymbol{F}}$, the Lagrangian free-charge potential $\overline{\boldsymbol{D}}$ and the Lagrangian magnetic field $\overline{\boldsymbol{B}}$ as inputs for the microscopic BVP. The corresponding purely microscopic fields vanish in an average sense. In turn we receive effective stresses $\overline{\boldsymbol{P}}$, the electric field $\overline{\boldsymbol{E}}$ and the free-current potential $\overline{\boldsymbol{H}}$ as constitutive response.

In what follows, we denote macroscopic quantities with an over-line and purely microscopic quantities with a tilde.

10.1. Variational homogenization BVP with magnetic and electric vector potentials

Since, as outlined above, no free charge densities are involved on the microscopic scale, we here may use a classical formulation based on vector potentials as already done by (Miehe et al., 2016) in the context of computational homogenization in finite-strain

magneto-electro-elasticity (see also Section 5.3.5 in Part I)

$$\overline{\Psi}^{\circ}\left(\overline{\underline{F}},\overline{\boldsymbol{D}},\overline{\boldsymbol{B}}\right) = \inf_{\substack{\varphi \\ \in \\ \mathscr{W}_{\varphi}(\overline{\underline{F}})}} \inf_{\substack{\boldsymbol{A}^{\mathrm{e}} \\ \in \\ \mathscr{W}_{\boldsymbol{A}}(\overline{\boldsymbol{D}})}} \inf_{\substack{\boldsymbol{A}^{\mathrm{m}} \\ \in \\ \mathscr{W}_{\boldsymbol{A}}(\overline{\boldsymbol{B}})}} \sup_{\substack{p \\ \in \\ \mathscr{W}_{p}}} \frac{1}{|\widetilde{\mathcal{B}}[\overline{X}]|} \int_{\widetilde{\mathcal{B}}[\overline{X}]} \Psi^{\circ}(\underline{\boldsymbol{F}}^{\diamond},\boldsymbol{D},\boldsymbol{B}) + p(J-1)\,dV \tag{10.1}$$

which we extended to incompressibility. The function spaces are given as

$$\mathscr{W}_{\varphi}(\overline{\underline{F}}) = \left\{\varphi \mid \varphi_i \in \mathscr{H}(\mathrm{Grad},\widetilde{\mathcal{B}}[\overline{X}]),\, \langle \mathrm{Grad}\,\varphi\rangle_{\widetilde{\mathcal{B}}} = \overline{\underline{F}},\; \widetilde{\varphi}|_{\partial\widetilde{\mathcal{B}}[\overline{X}]^{+}} = \widetilde{\varphi}|_{\partial\widetilde{\mathcal{B}}[\overline{X}]^{-}}\right\}, \tag{10.2a}$$

$$\mathscr{W}_{\boldsymbol{A}}(\overline{\boldsymbol{K}}) = \left\{\boldsymbol{A} \mid A_i \in \mathscr{H}(\mathrm{Grad},\widetilde{\mathcal{B}}[\overline{X}]),\, \langle \mathrm{Curl}\,\boldsymbol{A}\rangle_{\widetilde{\mathcal{B}}} = \overline{\boldsymbol{K}},\; \widetilde{\boldsymbol{A}}|_{\partial\widetilde{\mathcal{B}}[\overline{X}]^{+}} = \widetilde{\boldsymbol{A}}|_{\partial\widetilde{\mathcal{B}}[\overline{X}]^{-}}\right\}, \tag{10.2b}$$

$$\mathscr{W}_{p} = \left\{p \mid p \in \mathscr{L}^2(\widetilde{\mathcal{B}}[\overline{X}]),\, \langle p\rangle_{\widetilde{\mathcal{B}}} = 0\right\}, \tag{10.2c}$$

where $\overline{\boldsymbol{K}}$ stands for either $\overline{\boldsymbol{D}}$ or $\overline{\boldsymbol{B}}$, respectively. We note that in the case of strict incompressibility the pressure p is a Lagrange multiplier which is not exchanged with the macroscopic scale. The vector potential formulation automatically satisfies the homogeneous electric and magnetic Gauß laws $\mathrm{Div}\,\boldsymbol{D} = 0$ and $\mathrm{Div}\,\boldsymbol{B} = 0$, respectively.

The effective dual quantities are computed as

$$\overline{\underline{\boldsymbol{P}}'} = \frac{1}{|\widetilde{\mathcal{B}}[\overline{X}]|} \int_{\partial\widetilde{\mathcal{B}}[\overline{X}]} \left(\underline{\boldsymbol{P}}^{\circ}\cdot\boldsymbol{N}\right)\otimes X\,dA = \frac{1}{|\widetilde{\mathcal{B}}[\overline{X}]|} \int_{\widetilde{\mathcal{B}}[\overline{X}]} \underline{\boldsymbol{P}}^{\circ}\,dV, \tag{10.3a}$$

$$\overline{\boldsymbol{E}} = \frac{1}{|\widetilde{\mathcal{B}}[\overline{X}]|} \int_{\partial\widetilde{\mathcal{B}}[\overline{X}]} \widetilde{\boldsymbol{X}}\times(\boldsymbol{E}\times\boldsymbol{N})\,\mathrm{d}A = \frac{1}{|\widetilde{\mathcal{B}}[\overline{X}]|} \int_{\widetilde{\mathcal{B}}[\overline{X}]} \boldsymbol{E}\,dV \quad \text{and} \tag{10.3b}$$

$$\overline{\boldsymbol{H}} = \frac{1}{|\widetilde{\mathcal{B}}[\overline{X}]|} \int_{\partial\widetilde{\mathcal{B}}[\overline{X}]} \widetilde{\boldsymbol{X}}\times(\boldsymbol{H}\times\boldsymbol{N})\,\mathrm{d}A = \frac{1}{|\widetilde{\mathcal{B}}[\overline{X}]|} \int_{\widetilde{\mathcal{B}}[\overline{X}]} \boldsymbol{H}\,dV. \tag{10.3c}$$

The expression for $\underline{\boldsymbol{P}}^{\circ}$ is discussed in Section 9.1.2.

10.1.1. Vector-potential based homogenization principle in three dimensions

In three dimensions we have to take special care about the uniqueness of the vector potentials $\boldsymbol{A}^{\mathrm{e}}$ and $\boldsymbol{A}^{\mathrm{m}}$ (Semenov et al., 2006). Uniqueness is often established by *gauging*, with the Coulomb gauge $\mathrm{Div}\,\boldsymbol{A} = 0$ being the most popular choice for the present scope. In our implementation we augment (10.10) with penalty terms

$$\frac{1}{|\widetilde{\mathcal{B}}[\overline{X}]|} \int_{\widetilde{\mathcal{B}}[\overline{X}]} \Psi^{+}\,dV = \frac{1}{|\widetilde{\mathcal{B}}[\overline{X}]|} \int_{\widetilde{\mathcal{B}}[\overline{X}]} \frac{1}{\epsilon^{\mathrm{e}}}\left(\mathrm{Div}\,\boldsymbol{A}^{\mathrm{e}}\right)^2 + \frac{1}{\epsilon^{\mathrm{m}}}\left(\mathrm{Div}\,\boldsymbol{A}^{\mathrm{m}}\right)^2\,dV. \tag{10.4}$$

The polynomial degree of the finite elements for $\boldsymbol{A}^{\mathrm{e}}$ and $\boldsymbol{A}^{\mathrm{m}}$ has to be chosen such the respective penalty terms can be under-integrated (for numerical stability reasons). For simplicial meshes, second order polynomials for the vector potentials combined with a

first order quadrature rule for the penalties are a valid choice.

This formulation will only be employed in the scope of compressible magneto-elasticity in Section 11.3.

10.1.2. Vector-potential based homogenization principle in two dimensions

We start with the decomposition of the primary fields φ, $\boldsymbol{A}^{\mathrm{e}}$ and $\boldsymbol{A}^{\mathrm{m}}$ into macroscopic and microscopic contributions. For the present scope of first-order homogenization *in a two-dimensional setting* the vector potentials degenerate in the sense that only their out-of-plane component is non-zero. Hence, restricting to *two dimensions* where $\boldsymbol{a}\times\boldsymbol{b} = a_2b_1 - b_1a_2$ and the index 3 referring to the out-of-plane direction, we obtain

$$\varphi(X)|_{\widetilde{\mathcal{B}}[\overline{X}]} = \varphi(\overline{X};\widetilde{\boldsymbol{X}}) = \overline{\varphi}(\overline{X}) + \overline{\underline{\boldsymbol{F}}}(\overline{X})\cdot\widetilde{\boldsymbol{X}} + \widetilde{\varphi}(\widetilde{\boldsymbol{X}}), \tag{10.5}$$

$$A_3^{\mathrm{e}}(X)|_{\widetilde{\mathcal{B}}[\overline{X}]} = A_3^{\mathrm{e}}(\overline{X};\widetilde{\boldsymbol{X}}) = \overline{A}_3^{\mathrm{e}}(\overline{X}) + \overline{\boldsymbol{D}}(\overline{X})\times\widetilde{\boldsymbol{X}} + \widetilde{A}_3^{e}(\widetilde{\boldsymbol{X}}), \tag{10.6}$$

$$A_3^{\mathrm{m}}(X)|_{\widetilde{\mathcal{B}}[\overline{X}]} = A_3^{\mathrm{m}}(\overline{X};\widetilde{\boldsymbol{X}}) = \overline{A}_3^{\mathrm{m}}(\overline{X}) + \overline{\boldsymbol{B}}(\overline{X})\times\widetilde{\boldsymbol{X}} + \widetilde{A}_3^{\mathrm{m}}(\widetilde{\boldsymbol{X}}). \tag{10.7}$$

Accordingly, we have $\underline{\boldsymbol{F}}$, $\boldsymbol{D}$ and $\boldsymbol{B}$

$$\underline{\boldsymbol{F}}(\overline{X};\widetilde{\boldsymbol{X}}) := \operatorname{Grad}\varphi(X)|_{\widetilde{\mathcal{B}}[\overline{X}]} = \overline{\underline{\boldsymbol{F}}}(\overline{X}) + \widetilde{\operatorname{Grad}}\widetilde{\varphi}(\widetilde{\boldsymbol{X}}), \tag{10.8a}$$

$$\boldsymbol{D}(\overline{X};\widetilde{\boldsymbol{X}}) := \operatorname{Curl}A_3^{\mathrm{e}}(X)|_{\widetilde{\mathcal{B}}[\overline{X}]} = \overline{\boldsymbol{D}}(\overline{X}) + \widetilde{\operatorname{Curl}}\widetilde{A}_3^{\mathrm{e}}(\widetilde{\boldsymbol{X}}), \tag{10.8b}$$

$$\boldsymbol{B}(\overline{X};\widetilde{\boldsymbol{X}}) := \operatorname{Curl}A_3^{\mathrm{m}}(X)|_{\widetilde{\mathcal{B}}[\overline{X}]} = \overline{\boldsymbol{B}}(\overline{X}) + \widetilde{\operatorname{Curl}}\widetilde{A}_3^{\mathrm{m}}(\widetilde{\boldsymbol{X}}), \tag{10.8c}$$

with $\widetilde{\operatorname{Grad}}\{\bullet\}$ denoting the gradient with respect to $\widetilde{\boldsymbol{X}}$ and the two-dimensional Curl operators

$$\operatorname{Curl}\{\bullet\} = \begin{Bmatrix}\partial_{X_2}\{\bullet\}\\ -\partial_{X_1}\{\bullet\}\end{Bmatrix} \quad\text{and}\quad \widetilde{\operatorname{Curl}}\{\bullet\} = \begin{Bmatrix}\partial_{Y_2}\{\bullet\}\\ -\partial_{Y_1}\{\bullet\}\end{Bmatrix}. \tag{10.9}$$

Based on that the macroscopic energy density $\overline{\Psi}^{\circ}$ is given as

$$\overline{\Psi}^{\circ}\left(\overline{\underline{\boldsymbol{F}}},\overline{\boldsymbol{D}},\overline{\boldsymbol{B}}\right) = \inf_{\substack{\varphi\\ \in\\ \mathscr{W}_{\varphi}(\overline{\underline{\boldsymbol{F}}})}}\ \inf_{\substack{A_3^{\mathrm{e}}\\ \in\\ \mathscr{W}_A(\overline{\boldsymbol{D}})}}\ \inf_{\substack{A_3^{\mathrm{m}}\\ \in\\ \mathscr{W}_A(\overline{\boldsymbol{B}})}}\ \sup_{\substack{p\\ \in\\ \mathscr{W}_p}} \frac{1}{|\widetilde{\mathcal{B}}[\overline{X}]|}\int_{\widetilde{\mathcal{B}}[\overline{X}]} \Psi^{\circ}(\underline{\boldsymbol{F}}^{\circ},\boldsymbol{D},\boldsymbol{B}) + p(J-1)\,dV \tag{10.10}$$

with spaces

$$\mathscr{W}_{\varphi}(\overline{\underline{\boldsymbol{F}}}) = \left\{\varphi \mid \varphi_i \in \mathscr{H}(\operatorname{Grad},\widetilde{\mathcal{B}}[\overline{X}]),\ \langle\operatorname{Grad}\varphi\rangle_{\widetilde{\mathcal{B}}} = \overline{\underline{\boldsymbol{F}}},\ \widetilde{\varphi}|_{\partial\widetilde{\mathcal{B}}[\overline{X}]^+} = \widetilde{\varphi}|_{\partial\widetilde{\mathcal{B}}[\overline{X}]^-}\right\} \tag{10.11a}$$

$$\mathscr{W}_p = \left\{p \mid p \in \mathscr{L}^2(\widetilde{\mathcal{B}}[\overline{X}]),\ \langle p\rangle_{\widetilde{\mathcal{B}}} = 0\right\} \tag{10.11b}$$

$$\mathscr{W}_A(\overline{\boldsymbol{K}}) = \left\{A \mid A \in \mathscr{H}(\operatorname{Grad},\widetilde{\mathcal{B}}[\overline{X}]),\ \langle\operatorname{Curl}A\rangle_{\widetilde{\mathcal{B}}} = \overline{\boldsymbol{K}},\ \widetilde{A}\big|_{\partial\widetilde{\mathcal{B}}[\overline{X}]^+} = \widetilde{A}\big|_{\partial\widetilde{\mathcal{B}}[\overline{X}]^-}\right\}, \tag{10.11c}$$

where $\overline{\boldsymbol{K}}$ again stands for either $\overline{\boldsymbol{D}}$ or $\overline{\boldsymbol{B}}$, respectively. We refer to Danas (2017) for a detailed description of periodic boundary conditions suitable for the present scope.

10.2. A magneto-electric composite between two electrodes

The boundary value problem considered here is shown in Figure 10.1. Figure 10.2 de-

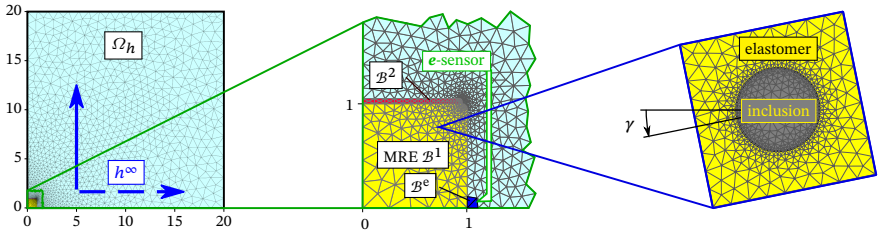

(a) MRE in free space (b) MRE body with electrode (c) $\mathcal{RVE}$ (micro)

Figure 10.1: The MRE capacitor: a square MRE specimen ($\mathcal{B}^1$) with attached electrodes ($\mathcal{B}^2$) for electric loading. Because of symmetry we depict and simulate only the first quadrant. The magnetic loading is performed via a homogeneous external field $\boldsymbol{h}^\infty$ either in x_1- or x_2-direction (indicated by the dashed and solid blue arrows). In the zoomed view of the specimen we indicate the location of a hypothetic electric-field sensor (in green) measuring the electric field somewhere in $\mathcal{B}^e$. The microscopic $\mathcal{RVE}$ is depicted at the very right.

picts the detailed dimensions of specimen and electrode.

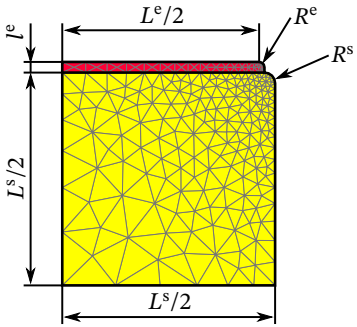

Figure 10.2: Detailed dimensions (in cm) of the MRE specimen and the electrode. The actual values are set to $L^s = 2$, $L^e = 1.85$, $l^e = 0.05$, $R^s = 0.05$ and $R^e = 0.025$ in cm. The out of plane dimension is 1cm.

We apply the magnetic field potential $\mu_0 \boldsymbol{h}^\infty$ in x_1 and x_2-direction by setting $\boldsymbol{B} \cdot \boldsymbol{N} = \boldsymbol{b} \cdot \boldsymbol{n} = \mu_0 \boldsymbol{h}^\infty \cdot \boldsymbol{n}$ at the free-space boundary (where $\boldsymbol{u} = \boldsymbol{0}$). The electric loading is applied

by prescribing the volume charge density $q_0 = \bar{q}$ in $\mathcal{B}^2$. This is naturally handled by the variational principle (9.22). The displacements vanish on the free-space boundary and fulfill symmetry conditions $u_1(x_1 = 0) = 0$ and $u_2(x_2 = 0) = 0$. We set $\boldsymbol{D} \cdot \boldsymbol{N} = 0$ at the free space boundary and at $x_1 = 0$. Furthermore, $\boldsymbol{B} \cdot \boldsymbol{N} = 0$ at boundaries with $\boldsymbol{N}$ normal to $\boldsymbol{h}^\infty$. For the electric potentials we have $\phi^e(x_2 = 0) = 0$ and the magnetic scalar potential ϕ^m vanishes at the symmetry boundary with $\boldsymbol{N}$ parallel to $\boldsymbol{h}^\infty$. As visualized, we also study the influence of the micro-structure orientation. In order to not break symmetry, we set the microstructure-angle to $\gamma = 0$ and $\gamma = \pi/4$ in our simulations.

The electrodes are modeled via a macroscopic energy density function also described by (9.37a) using (9.34) with parameters $\mu = 6.667 \times 10^{-1}$ MPa and (9.35) with $\chi^e = 1 \times 10^5$. All other parameters are set to zero. For the compressible free space we employ an energy function similar to (9.34) with $\mu = 1 \times 10^{-3}$ MPa and $\kappa = 6.667 \times 10^{-4}$ MPa as the only non-zero parameters.

For such a setting we expect that the body deforms under electric loading via the prescribed charge density $\bar{q}$ in the electrodes such that the distance between the electrodes is decreased when charge is increased[1]. Clearly, there will also be a response to applied magnetic fields because the magneto-electric body basically is an MRE. What we investigate below is the change of the electric state at the surface of the macroscopic body $\overline{\mathcal{B}}$ under prescribed but fixed electric load and changing magnetic load. Hence, we follow the same approach to magneto-electric *device* sensitivity as already done in Section 8.4 Section 9.4. However, different from the latter section, we now imagine the electric field to be measured by a sensor (see Figure 10.1) at or very close to the surface of the specimen near $x_2 = 0$. The corresponding sensitivity analysis is now based on the QOI given below which is again denoted as e^{surf}

$$e^{\text{surf}} = \frac{1}{|\mathcal{B}^{\text{e}}|} \int_{\mathcal{B}^{\text{e}}} (\boldsymbol{F}^{-\text{T}} \cdot \boldsymbol{E}) \cdot \boldsymbol{x}_2 \, dV, \tag{10.12}$$

where the domain $\mathcal{B}^{\text{e}}$ representing the location of field "measurement" is the small blue domain depicted in the center image of Figure 10.1.

We investigate four different setups in total: (i) $\boldsymbol{h}^\infty$ in x_1-direction and microstructure orientation $\gamma = 0$, (ii) $\boldsymbol{h}^\infty$ in x_2-direction and $\gamma = 0$, (iii) $\boldsymbol{h}^\infty$ in x_1-direction and $\gamma = \pi/4$ and (iv) $\boldsymbol{h}^\infty$ in x_2-direction and $\gamma = \pi/4$. For the magneto-electric sensor scenario that we have in mind, we first apply the electric load via the charge density $q_0 = \bar{q} \in \{0 \ldots 6\}\,\text{C m}^{-3}$ in the electrode[2] and then ramp $\boldsymbol{h}^\infty$ up $h^\infty = 1.5\,\text{MA m}^{-1}$ while holding q_0. The resulting values for the average electric field in $\mathcal{B}^{\text{e}}$ denoted as e^{surf} and

[1] The loading via prescribed charge as performed here corresponds to charging electrodes and then disconnecting them from the source before applying the magnetic loads. Then the charge contained in the electrodes is constant but the voltage is not fixed. Nevertheless, the results are expected to be comparable to a prescribed-voltage scenario for moderate deformations. We opted for such a model in order to demonstrate this possibility enabled by the proposed formulation. Such a way of prescribing loads could also be useful in the treatment of electrets (Harland et al., 2010; Alameh et al., 2015).

[2] For the employed thin electrode domains ($l^e = 0.05\,\text{cm}$) a volume charge density of $\hat{q} = 6\,\text{C m}^{-3}$ roughly corresponds to a surface charge density of $\bar{q}^s = 3\,\text{mC m}^{-2}$.

its sensitivities $\mathrm{d}\hat{e}/\,\mathrm{d}h^\infty$ for all of the four cases are shown in terms of line plots in Figures 10.3 and 10.4, respectively. Each plot contains an emblem indicating the direction

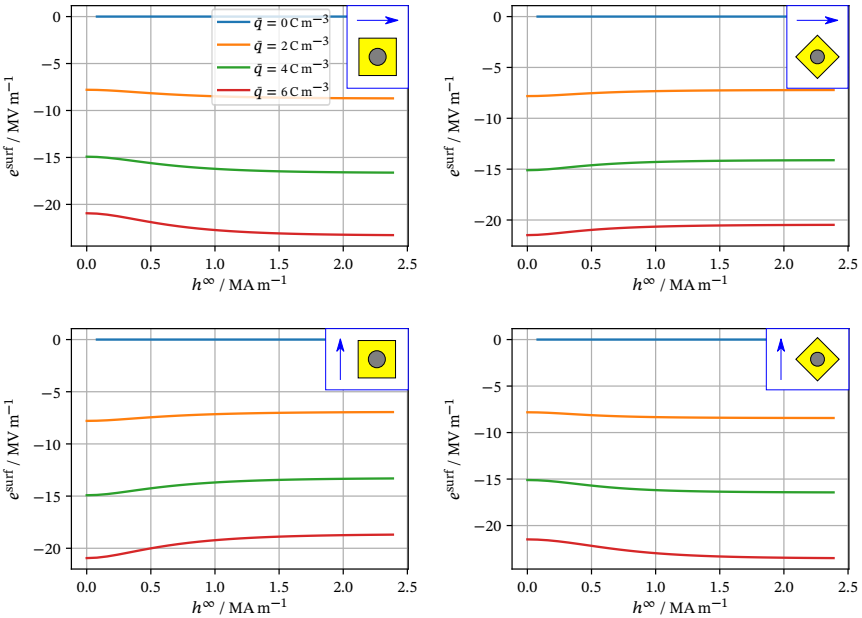

Figure 10.3: The electric field of interest e^{surf}, i.e. the average electric field in the region of detection $\mathcal{B}^{\mathrm{e}}$ for four different configurations. The emblems in each plot indicate the direction of $\boldsymbol{h}^\infty$ (blue arrow) and the orientation of the microstructure.

of applied $\boldsymbol{h}^\infty$ and microstructure orientation. All four plots share the same characteristics regarding the approximate location of the maximum and the decrease of the sensitivity for high magnetic field where saturation dominates. However, in contrast to Section 9.2.1 we now study a multiscale scenario and it is indeed observable that the microstructure orientation is capable of changing the sign of the magneto-electric device sensitivity. The same holds for the direction of the applied magnetic fields. Both effects come from the magneto-mechanical response of the MRE specimen (Keip and Rambausek, 2016). Moreover, depending on these two factors, the maximum sensitivity is not always obtained for the maximum electric load (Rambausek and Keip, 2018a). Indeed, in the top-right plot we observe almost coincident graphs for $\bar{q} = 4\,\mathrm{C\,m^{-3}}$ and $\bar{q} = 6\,\mathrm{C\,m^{-3}}$. The explanation of this behavior is not trivial. In fact, we observe the simultaneous action of different mechanisms: The first is the arrangement of the magnetic inclusions that is influenced by the applied electrical preloading. For a microstructure orientation of $\gamma = \pi/4$ the electrically induced deformation leads to a horizontal

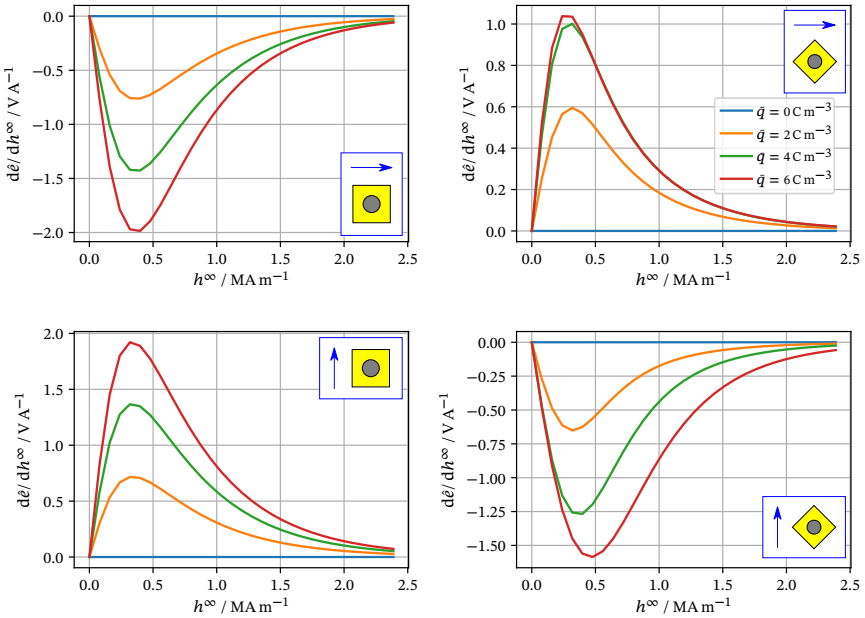

Figure 10.4: Magneto-electric device sensitivities $\mathrm{d}\hat{e}/\,\mathrm{d}h^\infty$ for four different configurations. The emblems in each plot indicate the direction of $\boldsymbol{h}^\infty$ (blue arrow) and the orientation of the microstructure. Each configuration yields the same qualitative figure (module sign). At a close look we however observe the almost coincident graphs for $\bar{q} = 4\,\mathrm{C\,m^{-3}}$ and $\bar{q} = 6\,\mathrm{C\,m^{-3}}$ in the top-right plot.

stretch of the pattern. For higher electric loads the initial $\pi/4$-line grid arrangement is deformed towards a pattern featuring horizontal and vertical lines. This in turn reduces the expected extension under horizontal magnetic field (Danas et al., 2012; Danas, 2017; Keip and Rambausek, 2017). Second, the evaluation of the magneto-electric device sensitivity is based on the electric field at the surface of the specimen. Under horizontal stretch of the specimen, the evaluation region moves away from the electrodes. Because of the comparably low effective electric susceptibility of the composite the electric field inside the MRE is inhomogeneous. Thus such a geometric effect also plays a role. Third, the mechanical properties change with deformation. These three effects together cause complex phenomena like the observed nonlinearity of the device sensitivity with respect to the electric (pre)loading.

Figure 10.5 depicts the corresponding surface plots again obtained via cubic interpolations. In Figure 10.6 we depict the magneto-electric material moduli at the center of the body plotted over the applied free-current potential $\boldsymbol{h}^\infty$. A strict comparison of device (non-local) and material (local) coupling is impossible because they describe two

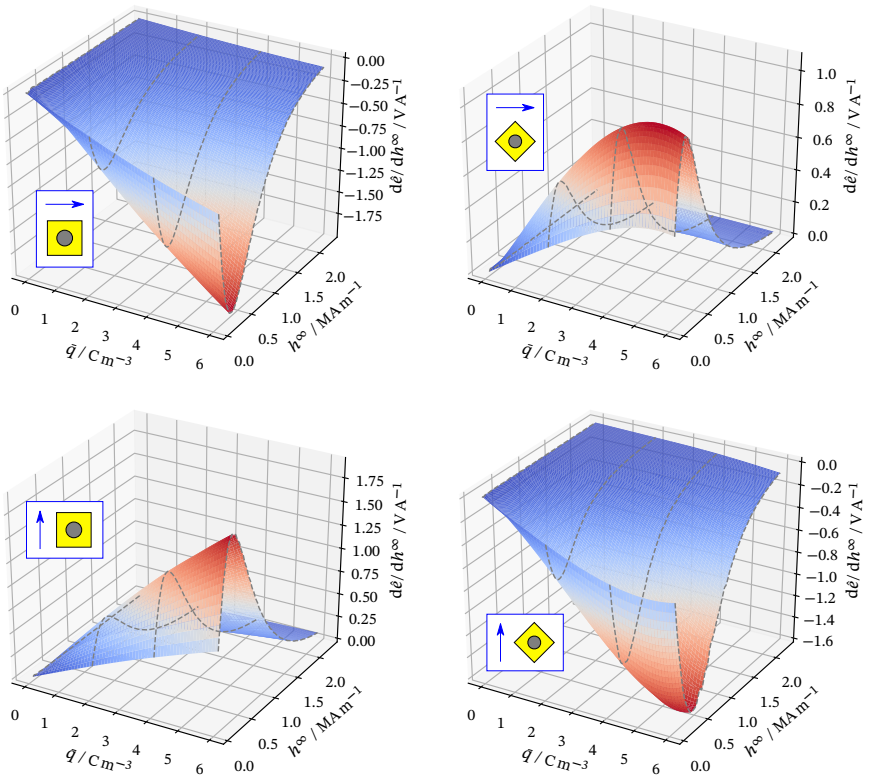

Figure 10.5: Surface plots of the magneto-electric device sensitivity $\mathrm{d}\hat{e}/\,\mathrm{d}h^\infty$. Again, the emblems in the subplots indicate the magnetic loading direction and the microstructure orientation. The dashed lines correspond to those shown in Figure 10.4.

different notions. Nevertheless, we observe that the magneto-electric material moduli and device sensitivities may even have different sign. We conclude that macroscopic effects which themselves are strongly influenced by the magneto- and electro-mechanical material properties govern the device sensitivity. The magneto-electric material properties, however, play a negligible role for the overall ME coupling in the present setting.

In order to give an idea of the electric field and the free current potential present in specimen and electrode we depict $\boldsymbol{e}$ and $\boldsymbol{h}$ in Figure 10.7a for $\bar{q} = 6\,\mathrm{C\,m^{-3}}$ and $h^\infty = 2.0\,\mathrm{MA\,m^{-1}}$ applied in horizontal direction. Figure 10.7b shows a detailed view of the electric field near the left end of electrode. There we observe pronounced field concentrations as expected for this scenario. For progress in the advanced numerical treatment of such field concentrations at sharp (re-entrant) corners we refer to the re-

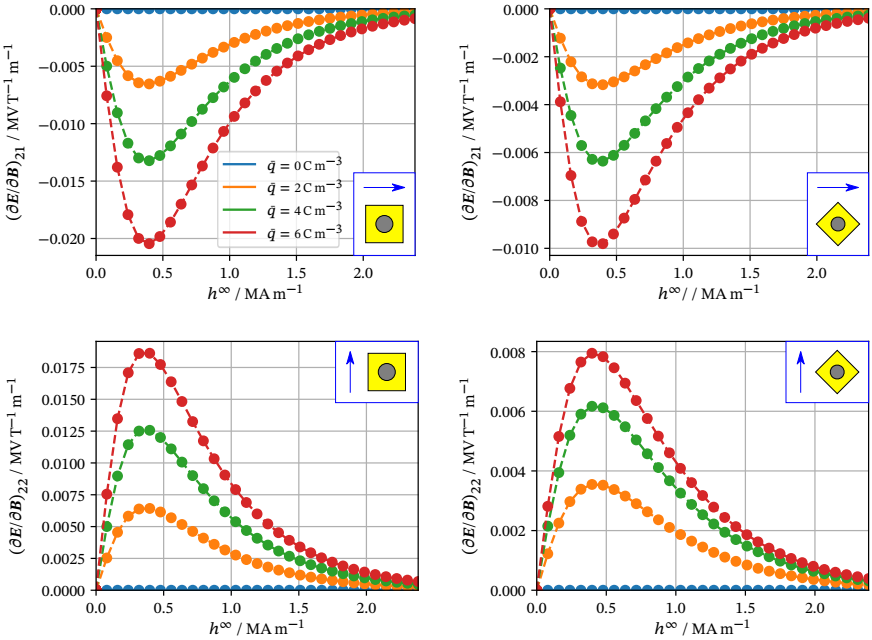

Figure 10.6: Line plots of the magneto-electric material moduli obtained via homogenization versus applied $\boldsymbol{h}$-field. Note that these moduli are macroscopically local quantities. They represent the change of referential electric field $\boldsymbol{E}$ with respect to the referential magnetic field $\boldsymbol{B}$ at a specific point on the macroscopic scale. The plots are obtained from $\mathcal{RVE}$s at the center of the MRE specimen. The emblems indicate the BVP configuration as in the two previous figures. The quantity plotted is in terms of referential quantities, whereas the magneto-electric device sensitivity is defined in terms of current quantities in a non-local manner.

cent works by Brandstetter (2015) and Brandstetter and Govindjee (2015). We close this example with showing the final deformed configurations in Figure 10.8 with the familiar emblems for the different BVP configurations.

10.3. A circular magneto-electric body under homogeneous external electric and magnetic fields

In this section the macroscopic MRE body of interest is of circular shape and no electrodes are attached to it this time. Instead, the electric loading is in terms of a homogeneous external electric field $\boldsymbol{e}^\infty$ similar to the magnetic loading as sketched in Figure 10.9. We prescribe $\boldsymbol{D} \cdot \boldsymbol{N} = \epsilon_0 \boldsymbol{e}^\infty \cdot \boldsymbol{n}$ at the top boundary where $x_2 = 20\,\text{cm}$ and

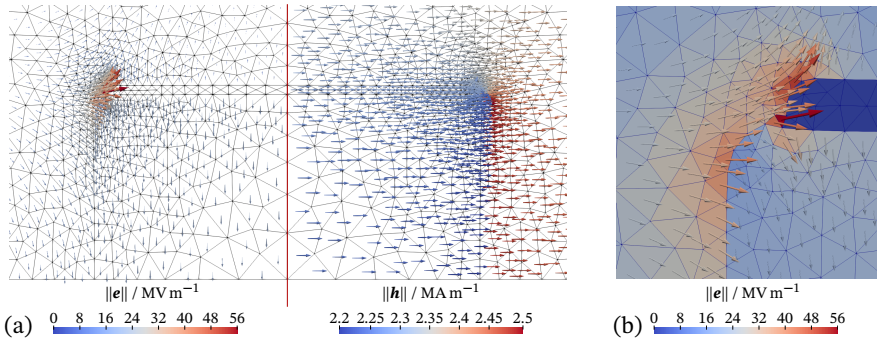

Figure 10.7: Free-current potential and electric field in specimen and electrode. In (a) we depict the electric field and the magnetic field on the left and right of the symmetry plane, respectively. As one can easily see, the electric field inside the electrode is practically zero as expected for a conductor-like material. In (b) we show a detailed view of electric field concentrations near the left boundary of the electrode. This is expected for the electrostatic part of the coupled problem. The discontinuities in the material properties have a similar effect on the solution in the free space as a re-entrant corner would have.

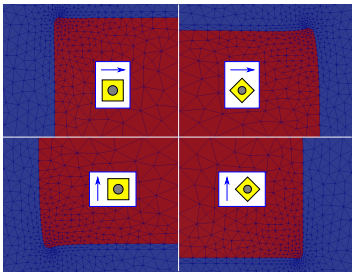

Figure 10.8: The deformed MRE specimens for $\bar{q} = 6\,\mathrm{C\,m^{-3}}$ and $h^\infty = 2.0\,\mathrm{MA\,m^{-1}}$ with emblems denoting the BVP configurations, i.e. the direction of $\boldsymbol{h}^\infty$ and microstructure orientation. Here we again observe differences in the responses coming from the symmetry of the microstructure.

$\boldsymbol{B} \cdot \boldsymbol{N} = \mu_0 \boldsymbol{h}^\infty \cdot \boldsymbol{n}$ at the free-space boundary with normal vector in direction of $\boldsymbol{h}^\infty$. The symmetry boundaries opposite to the respective Dirichlet boundaries have the corresponding scalar potential to vanish. The symmetry conditions for $\boldsymbol{D}$ and $\boldsymbol{B}$ on boundaries parallel to the corresponding applied field are expressed as $\boldsymbol{D} \cdot \boldsymbol{N} = 0$ and $\boldsymbol{B} \cdot \boldsymbol{N} = 0$, respectively. The displacement boundary conditions are as usual.

For the characterization of the magneto-electric device sensitivity we employ once more (10.12), whereby the evaluation domain $\mathcal{B}^\mathrm{e}$ is located right outside the MRE body near $x_2 = 0$ (see the central image in Figure 10.9). As we know from Rambausek and Keip (2018a) and Section 9.4.1 we observe magneto-electric device coupling also in such

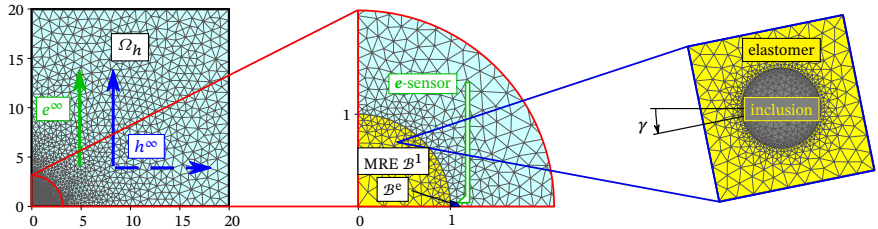

Figure 10.9: The circular MRE specimen ($\mathcal{B}^1$) exposed to homogeneous external fields $\boldsymbol{h}^\infty$ and $\boldsymbol{e}^\infty$, respectively. Because of symmetry we depict and simulate only the first quadrant. While $\boldsymbol{e}^\infty$ is always aligned with $\boldsymbol{x}_2$, $\boldsymbol{h}^\infty$ is either in x_1- or x_2-direction (indicated with dashed and solid blue arrows). The zoomed view of the specimen shows the location of a hypothetical electric-field sensor (in green) representing the evaluation of the electric field in the domain $\mathcal{B}^e$ as quantity of interest. The microscopic $\mathcal{RVE}$ is depicted at the very right. Lengths are given in cm.

an abstract setting. In contrast to Section 9.4.1 we now also account for the (idealized) microstructure of the MRE body. Along the lines of the previous multiscale example we here also consider microstructure orientations $\gamma = \{0, \pi/4\}$ and magnetic loading in directions x_1 and x_2. The external electric field is always in x_2 direction such that we end up with four different cases again. The results for the e^{surf} (the average of e_2 in $\mathcal{B}^e$) are depicted in Figure 10.10. The magneto-electric sensitivities $\mathrm{d}\hat{e}/\,\mathrm{d}h^\infty$ are summarized as line and surface plots in Figures 10.11 and 10.12, respectively.

The graphs in Figures 10.10, 10.11 and 10.12 are in line with the results from Sections 9.4 and 10.2. Compared with the setting with electrodes discussed in the previous example, we now obtain smaller sensitivities. However, the sign of the device sensitivity is still independent from the sign of the magneto-electric material moduli depicted in Figure 10.6. We conclude that also for the present example the effective magneto-electric material moduli do not significantly affect the ME device sensitivity.

The deformed configurations obtained at maximum electric and magnetic load are shown in Figure 10.13a. Figure 10.13b depicts the electric and magnetic quantities $\{\boldsymbol{e}, \boldsymbol{d}\}$ and $\{\boldsymbol{h}, \boldsymbol{b}\}$, respectively.

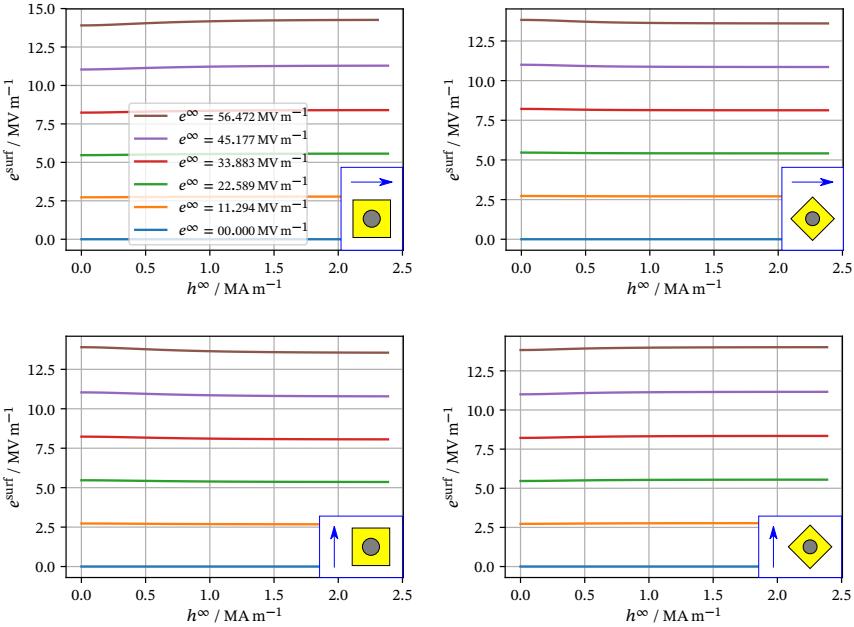

Figure 10.10: The quantity of interest e^{surf}, i.e. the average electric field in $\mathcal{B}^{\text{e}}$ for four different configurations. The emblems in each plot indicate the direction of applied $\boldsymbol{h}^{\infty}$ and the orientation of the microstructure. Compared with the graphs in Figure 10.3 in Section 10.2 the change over magnetic loading is less pronounced.

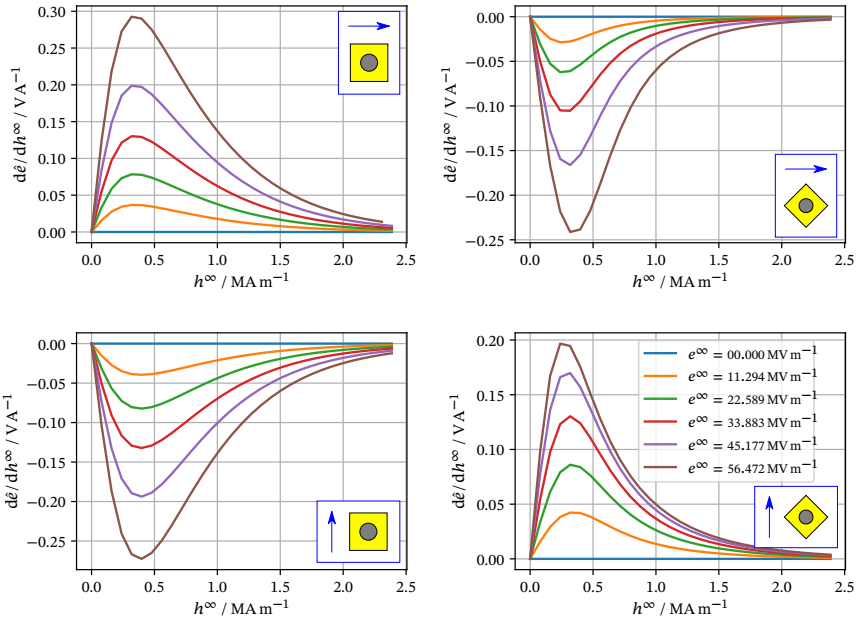

Figure 10.11: The magneto-electric device sensitivities $\mathrm{d}\hat{e}/\mathrm{d}h^\infty$ for four different BVP configurations. The emblems added to the plots indicate the direction of applied magnetic field and the orientation of the microstructure. The graphs are similar to those in Figure 10.4 in Section 10.2. The magnitude of the effect, however, is smaller than in the previous example. Nevertheless, also in the present case the sign of the magneto-electric sensitivity seems to be independent of the sign of the magneto-electric material moduli (see Figure 10.6).

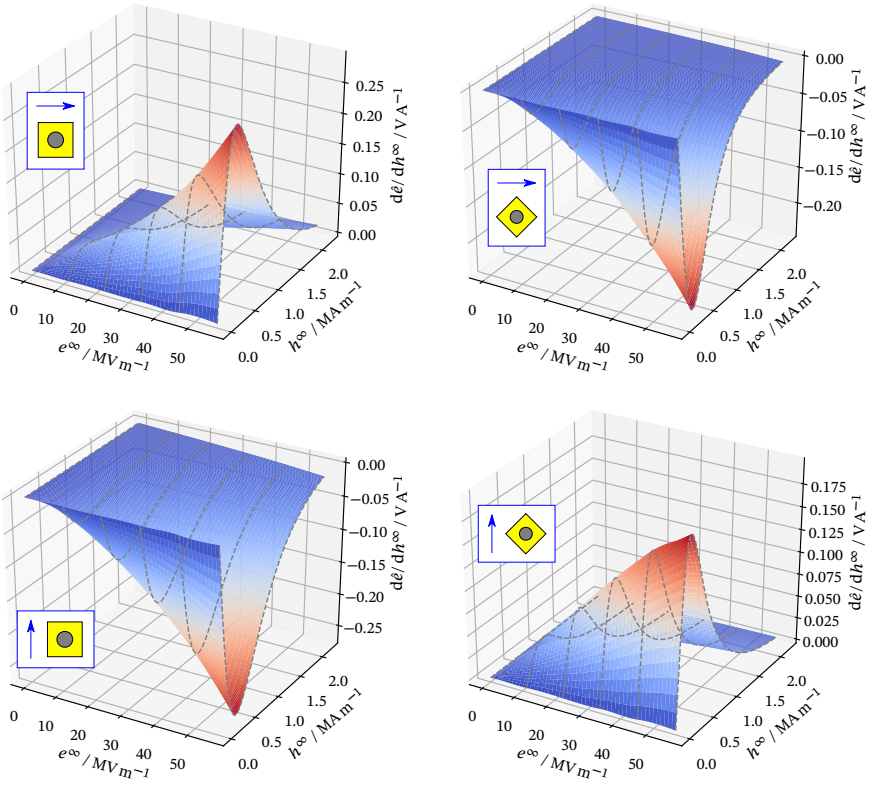

Figure 10.12: The magneto-electric device sensitivities $\mathrm{d}\hat{e}/\,\mathrm{d}h^\infty$ as surface plots corresponding to the line plots in Figure 10.11.

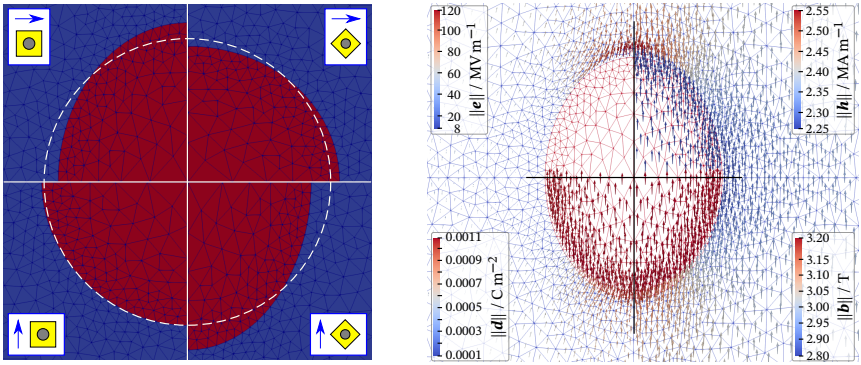

(a) (b)

Figure 10.13: The deformed configurations (a) and current electric as well as magnetic quantities in (b). In a) the dashed circle is the outline of the initial shape of the circular specimen. The emblems indicate the BVP configuration characterized by the direction of $\boldsymbol{h}^\infty$ and the microstructure orientation. In b) we plot $\boldsymbol{e}$, $\boldsymbol{h}$, $\boldsymbol{h}$ and $\boldsymbol{d}$ at the final state for microstructure orientation $\gamma = 0$ and $\boldsymbol{h}^\infty$ applied in vertical direction.

Chapter 11

Fourier-discretization of the constrained-minimization principle for computational homogenization

The fundamental idea for the numerical scheme presented below goes back to Vondřejc et al. (2014) and de Geus et al. (2017). In the latter publication the authors presented an implementation of a Fourier-based numerical homogenization scheme for finite elasticity. They departed from weak forms in a Galerkin fashion as customary rather for the FEM than for the Fourier community. The essential ingredient was the implementation of the compatibility constraint on the deformation gradient $\operatorname{Curl} \underline{\boldsymbol{F}} = \boldsymbol{0}$ via a projection in Fourier space. We recognized that this approach perfectly matches the magnetostatic part of constrained-minimization formulation of magneto-electro-elasticity as discussed in Chapter 9. Thus, we below provide a generalization of (de Geus et al., 2017) to fields with constraints on the divergence, e.g. $\operatorname{Div} \boldsymbol{B} = 0$, and an application to coupled magneto-elasticity. For a more general introduction to (computational) homogenization and a literature overview we refer to Chapter 5. The method and the results presented in this chapter can also be found in Rambausek et al. (2019).

11.1. The homogenization principle

The variational homogenization principle is the one described in Section 5.3.4. For convenience, we recall it in the current notation

$$\{\hat{\underline{\boldsymbol{F}}}, \hat{\boldsymbol{D}}, \hat{\boldsymbol{B}}\}\big|_{\widetilde{\mathcal{B}}} = \arg\left\{ \inf_{\underline{\boldsymbol{F}}, \boldsymbol{D}, \boldsymbol{B}} \int_{\widetilde{\mathcal{B}}} \Psi(\mathbf{C}, \boldsymbol{D}, \boldsymbol{B}) \, dV \right\} \tag{11.1}$$

or, equivalently,

$$\{\hat{\underline{\boldsymbol{F}}}, \hat{\boldsymbol{D}}, \hat{\boldsymbol{B}}\}\big|_{\widetilde{\mathcal{B}}} = \arg\left\{ \inf_{\underline{\boldsymbol{F}}, \boldsymbol{D}, \boldsymbol{B}} \langle \Psi(\mathbf{C}, \boldsymbol{D}, \boldsymbol{B}) \rangle_{\widetilde{\mathcal{B}}} \right\} \tag{11.2}$$

of which the specification is completed by the set of (periodic) function spaces

$$\mathscr{W}_{\underline{\boldsymbol{F}}}\left(\overline{\underline{\boldsymbol{F}}}; \widetilde{\mathcal{B}}\right) = \left\{ \underline{\boldsymbol{F}} \in \mathcal{H}\left(\operatorname{Curl}, \widetilde{\mathcal{B}}\right) \mid \operatorname{Curl} \underline{\boldsymbol{F}}_{i|} = 0, \langle \underline{\boldsymbol{F}} \rangle_{\widetilde{\mathcal{B}}} = \overline{\underline{\boldsymbol{F}}}, \underline{\boldsymbol{F}}\big|_{\widetilde{\boldsymbol{X}}^+} = \underline{\boldsymbol{F}}\big|_{\widetilde{\boldsymbol{X}}^-} \right\} \tag{11.3a}$$

$$\mathscr{W}_{\boldsymbol{D}}\left(\overline{\boldsymbol{D}}; \widetilde{\mathcal{B}}\right) = \left\{ \boldsymbol{D} \in \mathcal{H}\left(\operatorname{Div}, \widetilde{\mathcal{B}}\right) \mid \operatorname{Div} \boldsymbol{D} = 0, \langle \boldsymbol{D} \rangle_{\widetilde{\mathcal{B}}} = \overline{\boldsymbol{D}}, \boldsymbol{D}\big|_{\widetilde{\boldsymbol{X}}^+} = \boldsymbol{D}\big|_{\widetilde{\boldsymbol{X}}^-} \right\} \tag{11.3b}$$

$$\mathscr{W}_{\boldsymbol{B}}\left(\overline{\boldsymbol{B}}; \widetilde{\mathcal{B}}\right) = \left\{ \boldsymbol{B} \in \mathcal{H}\left(\operatorname{Div}, \widetilde{\mathcal{B}}\right) \mid \operatorname{Div} \boldsymbol{B} = 0, \langle \boldsymbol{B} \rangle_{\widetilde{\mathcal{B}}} = \overline{\boldsymbol{B}}, \boldsymbol{B}\big|_{\widetilde{\boldsymbol{X}}^+} = \boldsymbol{B}\big|_{\widetilde{\boldsymbol{X}}^-} \right\}. \tag{11.3c}$$

Therein, $\underline{\boldsymbol{F}}_{i|}$ refers to the ith row of $\underline{\boldsymbol{F}}$ to indicate that the Curl operates row-wise (on the second index) as also does the Div in, e.g., Div $\boldsymbol{P}$. Also note that we directly specified the periodicity of $\boldsymbol{B}$ and $\boldsymbol{D}$ instead of requiring periodicity of their normals (see Section 5.3.3).

In what follows, we will restrict ourselves to magneto-statics for brevity. Then, the Euler-Lagrange equations are

$$\left\langle \underline{\boldsymbol{P}} : \delta\widetilde{\underline{\boldsymbol{F}}} + \boldsymbol{H} \cdot \delta\widetilde{\boldsymbol{B}} \right\rangle_{\widetilde{\mathcal{B}}} = 0 \tag{11.4}$$

such that

$$\left\langle \underline{\boldsymbol{P}} : \delta\underline{\boldsymbol{F}} + \boldsymbol{H} \cdot \delta\boldsymbol{B} \right\rangle_{\widetilde{\mathcal{B}}} = \overline{\underline{\boldsymbol{P}}} : \delta\overline{\underline{\boldsymbol{F}}} + \overline{\boldsymbol{H}} \cdot \delta\overline{\boldsymbol{B}}. \tag{11.5}$$

11.2. Fourier discretization

Fourier discretizations are based on d-dimensional equidistant cartesian grids. Consider a hypercubic unit cell with dimensions $2L_1 \times \cdots \times 2L_d$ of which each dimension is divided into N_α intervals of equals length $h_\alpha = 2L_\alpha/N_\alpha$. The corresponding grid nodes are specified by location vectors

$$\boldsymbol{X}_{\underline{\mathbf{j}}} = \left(X^1_{j_1}, \ldots, X^d_{j_d}\right) \quad \text{with} \quad \underline{\mathbf{j}} = (j_1, \ldots, j_d) \quad \text{and} \quad X^\alpha_{j_\alpha} = -L_\alpha + h_\alpha(j_\alpha - \frac{1}{2}). \tag{11.6}$$

In the present thesis we will restrict ourselves to odd N_α. For even N_α the procedures are the same, only some formulae change. We refer to Trefethen (2000) for the case of even N_α and for a wide range of spectral methods and applications.

11.2.1. Fourier discretization in one dimension

In one dimension, a real-valued function $f(X)$ with periodicity $f(X + 2L) = f(X)$ of which we only know the values at N sampling points X_j can be represented as a finite Fourier series with $\xi(k) = k\pi/L$ for $k \in \mathbb{Z} \cap [-\lfloor N/2 \rfloor, \lfloor N/2 \rfloor]$

$$f_h(X) = \frac{1}{2}\check{f}^{\mathrm{c}}_0 + \sum_{k=1}^{\lfloor N/2 \rfloor} \left[\check{f}^{\mathrm{c}}_k \cos(\xi(k)X) + \check{f}^{\mathrm{s}}_k \sin(\xi(k)X)\right] = \sum_{k=-\lfloor N/2 \rfloor}^{\lfloor N/2 \rfloor} \check{f}_k e^{\imath\xi(k)X} \tag{11.7}$$

with

$$\check{f}_k = \frac{1}{2}\check{f}^{\mathrm{c}}_k - \frac{\imath}{2}\check{f}^{\mathrm{s}}_k, \quad \Re[\check{f}_k] = \Re[\check{f}_{-k}], \quad \text{and} \quad \Im[\check{f}_k] = -\Im[\check{f}_{-k}] \tag{11.8}$$

such that

$$f_h(X_j) = f(X_j) = f_j. \tag{11.9}$$

The Fourier coefficients $\check{f}_k$ are obtained as follows: First we exploit the fact that the integrals of both $\cos(\xi(k)X)$ and $\sin(\xi(k)X)$ over a domain of length $2L$ vanish by symmetry

for all $\xi(k) \neq 0$ and thus for $l \in \mathbb{Z} \cap [-\lfloor N/2 \rfloor, \lfloor N/2 \rfloor]$

$$\int_{-L}^{L} e^{\imath\xi(k)X} e^{-\imath\xi(l)X}\, dX = \int_{-L}^{L} e^{\imath\xi(k-l)X}\, dX = \begin{cases} 2L & \text{if } k = l \\ 0 & \text{otherwise.} \end{cases} \tag{11.10}$$

Interestingly, because of the symmetries of $\exp(\imath\xi(k)X)$, the integrals above can be evaluated *exactly* with the trapezoidal rule

$$\int_{-L}^{L} e^{\imath\xi(k-l)X}\, dX = \sum_{j=1}^{N} \frac{2L}{N} e^{\imath\xi(k-l)X_j} = \begin{cases} 2L & \text{if } k = l \\ 0 & \text{otherwise.} \end{cases} \tag{11.11}$$

Recall now that we only know $f(X)$ at sampling points X_j where we want $f(X_j) = f_j = f_h(X_j)$. By (11.7) we have

$$\int_{-L}^{L} f_h(X)\, e^{-\imath\xi(k)X}\, dX = \sum_{j=1}^{N} \frac{2L}{N} f_j\, e^{-\imath\xi(k)X_j} = \sum_{j=1}^{N} \frac{2L}{N} \check{f}_k \tag{11.12}$$

and thus

$$\check{f}_k = \frac{1}{N} \sum_{j=1}^{N} f_j\, e^{-\imath\xi(k)X_j}. \tag{11.13}$$

Next we consider a function $\delta^l(X)$ characterized by grid values

$$\delta^l(X_j) = \delta^l_j = \begin{cases} 1 & \text{if } l = j \\ 0 & \text{otherwise .} \end{cases} \tag{11.14}$$

This function is of particular interest because any function f given only by values f_j sampling points X_j can be written as a linear combination

$$f = \sum_{l=1}^{N} f_l \delta^l(X). \tag{11.15}$$

The discrete Fourier transform $\mathcal{F}$ of δ^l is simply

$$\mathcal{F}\left[\delta^l\right]_k = \frac{1}{N} \sum_{j=1}^{N} \delta^l_j e^{-\imath\xi(k)X_j} = \frac{1}{N} e^{-\imath\xi(k)X_l} \tag{11.16}$$

and thus

$$\delta^l_h(X) = \sum_{k=-\lfloor N/2 \rfloor}^{\lfloor N/2 \rfloor} \frac{1}{N} e^{\imath\xi(k)(X-X_l)} \quad \text{and} \quad \delta^l_h(X_j) = \delta^l_j = \sum_{k=-\lfloor N/2 \rfloor}^{\lfloor N/2 \rfloor} \frac{1}{N} e^{\imath\xi(k)(X_j-X_l)}. \tag{11.17}$$

Obviously, we may regard $\delta_h^l(X)$ as a trigonometric basis function for f_h such that

$$f_h(X) = \sum_{l=1}^{N} f_l \delta_h^l(X). \tag{11.18}$$

11.2.2. Multidimensional discrete Fourier transform

The generalizations of (11.8) and (11.13) from one-dimensional to n-dimensional equidistant grids are given as

$$f_h(\boldsymbol{X}) = \sum_{\underline{\mathbf{k}}=-\lfloor \underline{\mathbf{N}}/2 \rfloor}^{\lfloor \underline{\mathbf{N}}/2 \rfloor} \breve{f}_{\underline{\mathbf{k}}} e^{\imath \underline{\xi}(\underline{\mathbf{k}}) \cdot \boldsymbol{X}} \tag{11.19}$$

and

$$\breve{f}_{\underline{\mathbf{k}}} = \frac{1}{|N|} \sum_{\underline{\mathbf{j}}=\underline{1}}^{\underline{\mathbf{N}}} f_{\underline{\mathbf{j}}} e^{-\imath \underline{\xi}(\underline{\mathbf{k}}) \cdot \boldsymbol{X}_{\underline{\mathbf{j}}}} \tag{11.20}$$

where $\underline{\mathbf{N}} = \{N_1, \ldots, N_d\}$, $|\underline{\mathbf{N}}| = \prod_{\alpha=1}^{d} N_\alpha$ and the "wave-vector" $\underline{\xi}_\alpha(\underline{\mathbf{k}}) = \frac{k_\alpha \pi}{L_\alpha}$. For later use we introduce the conversions $f_h = \mathcal{F}^{-1}\left[\breve{f}\right]$, $\breve{f} = \mathcal{F}\left[f_h\right]$ such that $f_h = \mathcal{F}^{-1}\left[\mathcal{F}\left[f_h\right]\right]$.

11.2.3. Spatial derivatives in Fourier space

Consider first the partial derivatives of $f_h(\boldsymbol{X})$ which are obtained as

$$\frac{\partial f_h}{\partial X_\alpha} = \sum_{\underline{\mathbf{k}}=-\lfloor \underline{\mathbf{N}}/2 \rfloor}^{\lfloor \underline{\mathbf{N}}/2 \rfloor} \imath \underline{\xi}_\alpha \breve{f}_{\underline{\mathbf{k}}} e^{\imath \underline{\xi}(\underline{\mathbf{k}}) \cdot \boldsymbol{X}} \quad \Leftrightarrow \quad \mathcal{F}\left[\frac{\partial f_h}{\partial X_\alpha}\right]_{\underline{\mathbf{k}}} = \imath \underline{\xi}_\alpha(\underline{\mathbf{k}}) \mathcal{F}\left[f_h\right]_{\underline{\mathbf{k}}}. \tag{11.21}$$

Note that $k_\alpha = 0$ corresponds to a mode constant in direction α such the partial derivative in that direction vanishes as expected. Based on (11.21), we exploit the Cartesian setting to write

$$\mathcal{F}\left[\operatorname{Grad} f_h\right]_{\underline{\mathbf{k}}} = \imath \underline{\boldsymbol{\xi}}(\underline{\mathbf{k}}) \mathcal{F}\left[f_h\right]_{\underline{\mathbf{k}}}, \tag{11.22}$$

$$\mathcal{F}\left[\operatorname{Curl} \boldsymbol{f}_h\right]_{\underline{\mathbf{k}}} = \imath \underline{\boldsymbol{\xi}}(\underline{\mathbf{k}}) \times \mathcal{F}\left[\boldsymbol{f}_h\right]_{\underline{\mathbf{k}}} \quad \text{and} \tag{11.23}$$

$$\mathcal{F}\left[\operatorname{Div} \boldsymbol{f}_h\right]_{\underline{\mathbf{k}}} = \imath \underline{\boldsymbol{\xi}}(\underline{\mathbf{k}}) \cdot \mathcal{F}\left[\boldsymbol{f}_h\right]_{\underline{\mathbf{k}}}. \tag{11.24}$$

Obviously, (Cartesian) spatial derivatives become linear algebra operations in Fourier space. It is easy to see that the above operations fulfill the following identities for differential operators

$$\operatorname{Curl} \operatorname{Grad} f_h \equiv 0 \quad \Leftrightarrow \quad \imath^2 \underline{\boldsymbol{\xi}}(\underline{\mathbf{k}}) \times \underline{\boldsymbol{\xi}}(\underline{\mathbf{k}}) \breve{f}_{\underline{\mathbf{k}}} \equiv \mathbf{0} \tag{11.25}$$

and

$$\operatorname{Div}\operatorname{Curl}\boldsymbol{f}_h \equiv 0 \qquad \Leftrightarrow \qquad \imath^2\boldsymbol{\xi}(\underline{\mathbf{k}})\cdot\left(\boldsymbol{\xi}(\underline{\mathbf{k}})\times\check{\boldsymbol{f}}_{\underline{\mathbf{k}}}\right)\equiv 0. \tag{11.26}$$

11.2.4. The Helmholtz-Hodge decomposition in Fourier space

Recall the Helmholtz-Hodge decomposition of a vector field (4.85) from Section 4.1.7.11

$$\boldsymbol{v} = \boldsymbol{w} + \operatorname{grad} f + \operatorname{curl}\boldsymbol{u} \quad \text{with} \quad \operatorname{curl}\boldsymbol{w}=\boldsymbol{0}, \operatorname{div}\boldsymbol{w}=0 \tag{11.27}$$

such that

$$\operatorname{curl}\boldsymbol{v} = \operatorname{curl}\operatorname{curl}\boldsymbol{u} \quad \text{and} \quad \operatorname{div}\boldsymbol{v} = \operatorname{div}\operatorname{grad} f. \tag{11.28}$$

In Fourier space, this reads as

$$\check{\boldsymbol{v}}_{\underline{\mathbf{k}}} = \check{\boldsymbol{w}}_{\underline{\mathbf{k}}} + \boldsymbol{\xi}(\underline{\mathbf{k}})\check{f} + \boldsymbol{\xi}(\underline{\mathbf{k}})\times\check{\boldsymbol{u}}_{\underline{\mathbf{k}}} \tag{11.29}$$

such that

$$\mathcal{F}\left[\operatorname{Curl}\boldsymbol{v}\right]_{\underline{\mathbf{k}}} = \boldsymbol{\xi}(\underline{\mathbf{k}})\times\check{\boldsymbol{v}}_{\underline{\mathbf{k}}} = \boldsymbol{\xi}(\underline{\mathbf{k}})\times\left(\boldsymbol{\xi}(\underline{\mathbf{k}})\times\check{\boldsymbol{u}}_{\underline{\mathbf{k}}}\right) \tag{11.30}$$

and

$$\mathcal{F}\left[\operatorname{Div}\boldsymbol{v}\right]_{\underline{\mathbf{k}}} = \boldsymbol{\xi}(\underline{\mathbf{k}})\cdot\check{\boldsymbol{v}} = \boldsymbol{\xi}(\underline{\mathbf{k}})\cdot\boldsymbol{\xi}(\underline{\mathbf{k}})\check{f}_{\underline{\mathbf{k}}}. \tag{11.31}$$

From the requirement that $\boldsymbol{\xi}(\underline{\mathbf{k}})\cdot\check{\boldsymbol{w}}_{\underline{\mathbf{k}}}=0$ and $\boldsymbol{\xi}(\underline{\mathbf{k}})\times\check{\boldsymbol{w}}_{\underline{\mathbf{k}}}=\boldsymbol{0}$ we conclude that

$$\check{\boldsymbol{w}}_{\underline{\mathbf{k}}} = \begin{cases}\check{\boldsymbol{w}}_{\underline{\mathbf{0}}} & \text{if } \underline{\mathbf{k}}=\underline{\mathbf{0}}\\ \boldsymbol{0} & \text{otherwise.}\end{cases} \tag{11.32}$$

Since $\underline{\mathbf{k}}=\underline{\mathbf{0}}$ refers to the constant (average) mode we have $\check{\boldsymbol{w}}_{\underline{\mathbf{0}}} = \langle\boldsymbol{v}\rangle_{\widetilde{\mathcal{B}}}$ where $\widetilde{\mathcal{B}}[\overline{X}]$ is the periodic unit cell covered by the Cartesian grid. Hence, the non-constant Div-free part $\boldsymbol{\xi}(\underline{\mathbf{k}})\times\check{\boldsymbol{u}}_{\underline{\mathbf{k}}}$ of $\boldsymbol{v}$ in Fourier space is for $\underline{\mathbf{k}}\neq\underline{\mathbf{0}}$

$$\boldsymbol{\xi}(\underline{\mathbf{k}})\times\check{\boldsymbol{u}}_{\underline{\mathbf{k}}} = \check{\boldsymbol{v}}_{\underline{\mathbf{k}}} - \boldsymbol{\xi}(\underline{\mathbf{k}})\check{f}_{\underline{\mathbf{k}}} \tag{11.33}$$

whereas the Curl-free non-constant part is

$$\boldsymbol{\xi}(\underline{\mathbf{k}})\check{f}_{\underline{\mathbf{k}}} = \boldsymbol{\xi}(\underline{\mathbf{k}})\left(\frac{\boldsymbol{\xi}(\underline{\mathbf{k}})}{\|\boldsymbol{\xi}(\underline{\mathbf{k}})\|^2}\cdot\check{\boldsymbol{v}}_{\underline{\mathbf{k}}}\right) = \frac{\boldsymbol{\xi}(\underline{\mathbf{k}})\otimes\boldsymbol{\xi}(\underline{\mathbf{k}})}{\boldsymbol{\xi}(\underline{\mathbf{k}})\cdot\boldsymbol{\xi}(\underline{\mathbf{k}})}\cdot\check{\boldsymbol{v}}_{\underline{\mathbf{k}}} = \left(\boldsymbol{\eta}(\underline{\mathbf{k}})\otimes\boldsymbol{\eta}(\underline{\mathbf{k}})\right)\cdot\check{\boldsymbol{v}}_{\underline{\mathbf{k}}} \tag{11.34}$$

with

$$\boldsymbol{\eta}(\underline{\mathbf{k}}) := \begin{cases}\frac{\boldsymbol{\xi}(\underline{\mathbf{k}})}{\|\boldsymbol{\xi}(\underline{\mathbf{k}})\|} & \text{if } \underline{\mathbf{k}}\neq\underline{\mathbf{0}}\\ \boldsymbol{0} & \text{otherwise.}\end{cases} \tag{11.35}$$

From (11.34) we immediately see that

$$\boldsymbol{\xi}(\underline{\mathbf{k}})\times\check{\boldsymbol{u}}_{\underline{\mathbf{k}}} = \check{\boldsymbol{v}}_{\underline{\mathbf{k}}} - \left(\boldsymbol{\eta}(\underline{\mathbf{k}})\otimes\boldsymbol{\eta}(\underline{\mathbf{k}})\right)\cdot\check{\boldsymbol{v}}_{\underline{\mathbf{k}}} = \left(\boldsymbol{1}-\boldsymbol{\eta}(\underline{\mathbf{k}})\otimes\boldsymbol{\eta}(\underline{\mathbf{k}})\right)\cdot\check{\boldsymbol{v}}_{\underline{\mathbf{k}}}. \tag{11.36}$$

Thus, we have found two linear operators in Fourier space

$$\check{\underline{\boldsymbol{Y}}}_{\underline{\mathbf{k}}} := \boldsymbol{\eta}(\underline{\mathbf{k}}) \otimes \boldsymbol{\eta}(\underline{\mathbf{k}}) \qquad \text{and} \qquad \check{\underline{\boldsymbol{Z}}}_{\underline{\mathbf{k}}} := \mathbf{1} - \boldsymbol{\eta}(\underline{\mathbf{k}}) \otimes \boldsymbol{\eta}(\underline{\mathbf{k}}) = \mathbf{1} - \check{\underline{\boldsymbol{Y}}}_{\underline{\mathbf{k}}} \tag{11.37}$$

with the following properties:

$$\boldsymbol{\xi}(\underline{\mathbf{k}}) \times \left(\check{\underline{\boldsymbol{Y}}}_{\underline{\mathbf{k}}} \cdot \check{\boldsymbol{\upsilon}}_{\underline{\mathbf{k}}}\right) = \mathbf{0} \qquad \boldsymbol{\xi}(\underline{\mathbf{k}}) \cdot \left(\check{\underline{\boldsymbol{Z}}}_{\underline{\mathbf{k}}} \cdot \check{\boldsymbol{\upsilon}}_{\underline{\mathbf{k}}}\right) = 0 \tag{11.38a}$$

and

$$\check{\underline{\boldsymbol{Y}}}_{\underline{\mathbf{k}}} \cdot \check{\underline{\boldsymbol{Y}}}_{\underline{\mathbf{k}}} \cdot \check{\boldsymbol{\upsilon}}_{\underline{\mathbf{k}}} = \check{\underline{\boldsymbol{Y}}}_{\underline{\mathbf{k}}} \cdot \check{\boldsymbol{\upsilon}}_{\underline{\mathbf{k}}} \qquad \check{\underline{\boldsymbol{Z}}}_{\underline{\mathbf{k}}} \cdot \check{\underline{\boldsymbol{Z}}}_{\underline{\mathbf{k}}} \cdot \check{\boldsymbol{\upsilon}}_{\underline{\mathbf{k}}} = \check{\underline{\boldsymbol{Z}}}_{\underline{\mathbf{k}}} \cdot \check{\boldsymbol{\upsilon}}_{\underline{\mathbf{k}}}. \tag{11.38b}$$

The latter properties tell us that both $\underline{\boldsymbol{Z}}$ and $\underline{\boldsymbol{Y}}$ are projections, i.e. $\check{\underline{\boldsymbol{Y}}}_{\underline{\mathbf{k}}} \cdot \check{\underline{\boldsymbol{Y}}}_{\underline{\mathbf{k}}} = \check{\underline{\boldsymbol{Y}}}_{\underline{\mathbf{k}}}$ and $\check{\underline{\boldsymbol{Z}}}_{\underline{\mathbf{k}}} \cdot \check{\underline{\boldsymbol{Z}}}_{\underline{\mathbf{k}}} = \check{\underline{\boldsymbol{Z}}}_{\underline{\mathbf{k}}}$, respectively. The former, (11.38a), by the convolution relation for a linear operator $\mathbf{A}$ with discrete Fourier transform $\mathcal{F}[\mathbf{A}]$

$$\mathcal{F}[\mathbf{A} * \boldsymbol{\upsilon}]_{\underline{\mathbf{k}}} = \mathcal{F}[\mathbf{A}]_{\underline{\mathbf{k}}} \cdot \mathcal{F}[\boldsymbol{\upsilon}]_{\underline{\mathbf{k}}} \quad \text{with} \quad (\mathbf{A} * \boldsymbol{\upsilon})(\widetilde{\boldsymbol{X}}) = \int_{\widetilde{\mathcal{B}}} \mathbf{A}(\widetilde{\boldsymbol{X}} - \widetilde{\boldsymbol{Y}}) \cdot \boldsymbol{\upsilon}(\widetilde{\boldsymbol{Y}})\, dV(\widetilde{\boldsymbol{Y}}) \tag{11.39}$$

correspond to

$$\boldsymbol{\xi}(\underline{\mathbf{k}}) \times \left(\check{\underline{\boldsymbol{Y}}}_{\underline{\mathbf{k}}} \cdot \check{\boldsymbol{\upsilon}}_{\underline{\mathbf{k}}}\right) = \mathbf{0} \quad \Leftrightarrow \quad \mathrm{Curl}\left(\underline{\boldsymbol{Y}} * \boldsymbol{\upsilon}\right) = \mathbf{0} \tag{11.40}$$

and

$$\boldsymbol{\xi}(\underline{\mathbf{k}}) \cdot \left(\check{\underline{\boldsymbol{Z}}}_{\underline{\mathbf{k}}} \cdot \check{\boldsymbol{\upsilon}}_{\underline{\mathbf{k}}}\right) = 0 \quad \Leftrightarrow \quad \mathrm{Div}\left(\underline{\boldsymbol{Z}} * \boldsymbol{\upsilon}\right) = 0, \tag{11.41}$$

respectively.

11.2.5. Fourier discretization of the homogenization principle

The projections $\underline{\boldsymbol{Y}}$ and $\underline{\boldsymbol{Z}}$ will now be employed in Equations (11.4) and (11.5). The first essential step is to express $\underline{\boldsymbol{F}}$, of which the rows are Curl-free, and the Div-free $\boldsymbol{B}$ in terms of projections of the *unconstrained* fields $\widetilde{\underline{\boldsymbol{F}}}$ and $\widetilde{\boldsymbol{B}}$, i.e.

$$\underline{\boldsymbol{F}}_{i|} = \overline{\underline{\boldsymbol{F}}}_{i|} + \underline{\boldsymbol{Y}} * \widetilde{\underline{\boldsymbol{F}}}_{i|} \qquad \text{and} \qquad \boldsymbol{B} = \overline{\boldsymbol{B}} + \underline{\boldsymbol{Z}} * \widetilde{\boldsymbol{B}}. \tag{11.42}$$

With that we obtain

$$\left\langle \sum_i \underline{\boldsymbol{P}}_{i|} \cdot \left(\underline{\boldsymbol{Y}} * \delta\widetilde{\underline{\boldsymbol{F}}}_{i|}\right) + \boldsymbol{H} \cdot \left(\underline{\boldsymbol{Z}} * \delta\widetilde{\boldsymbol{B}}\right) \right\rangle_{\widetilde{\mathcal{B}}} = 0 \tag{11.43}$$

and

$$\left\langle \underline{\boldsymbol{P}} : \underline{\boldsymbol{F}} + \boldsymbol{H} \cdot \boldsymbol{B} \right\rangle_{\widetilde{\mathcal{B}}} = \overline{\underline{\boldsymbol{P}}} : \delta\overline{\underline{\boldsymbol{F}}} + \overline{\boldsymbol{H}} \cdot \delta\overline{\boldsymbol{B}}. \tag{11.44}$$

Expanding the volume averages and convolutions we have for (11.43)

$$\begin{aligned}
&\frac{1}{|\widetilde{\mathcal{B}}|}\int_{\widetilde{\mathcal{B}}}\int_{\widetilde{\mathcal{B}}}\sum_i \underline{\boldsymbol{P}}_{i|}(\widetilde{\boldsymbol{X}})\cdot\left(\underline{\boldsymbol{Y}}(\widetilde{\boldsymbol{X}}-\widetilde{\boldsymbol{Y}})\cdot\delta\underline{\widetilde{\boldsymbol{F}}}_{i|}(\widetilde{\boldsymbol{Y}})\right)dV(\widetilde{\boldsymbol{Y}})\,dV(\widetilde{\boldsymbol{X}})\\
&\quad+\frac{1}{|\widetilde{\mathcal{B}}|}\int_{\widetilde{\mathcal{B}}}\int_{\widetilde{\mathcal{B}}}\boldsymbol{H}(\widetilde{\boldsymbol{X}})\cdot\left(\underline{\boldsymbol{Z}}(\widetilde{\boldsymbol{X}}-\widetilde{\boldsymbol{Y}})\cdot\delta\widetilde{\boldsymbol{B}}(\widetilde{\boldsymbol{Y}})\right)dV(\widetilde{\boldsymbol{Y}})\,dV(\widetilde{\boldsymbol{X}})=\\
&\frac{1}{|\widetilde{\mathcal{B}}|}\int_{\widetilde{\mathcal{B}}}\sum_i\left(\underline{\boldsymbol{P}}_{i|}*\underline{\boldsymbol{Y}}\right)\cdot\delta\underline{\widetilde{\boldsymbol{F}}}_{i|}\,dV(\widetilde{\boldsymbol{Y}})+\frac{1}{|\widetilde{\mathcal{B}}|}\int_{\widetilde{\mathcal{B}}}\left(\boldsymbol{H}*\underline{\boldsymbol{Z}}\right)\cdot\delta\widetilde{\boldsymbol{B}}\,dV(\widetilde{\boldsymbol{Y}})=0
\end{aligned}\tag{11.45}$$

and hence

$$\sum_i \underline{\boldsymbol{P}}_{i|}*\underline{\boldsymbol{Y}}=\boldsymbol{0}\quad\text{and}\quad\boldsymbol{H}*\underline{\boldsymbol{Z}}=\boldsymbol{0}\quad\forall\widetilde{\boldsymbol{X}}\in\widetilde{\mathcal{B}}.\tag{11.46}$$

Next, we expand the unknowns $\underline{\boldsymbol{F}}$ and $\boldsymbol{B}$ similar to (11.18)

$$\underline{\boldsymbol{F}}(\widetilde{\boldsymbol{X}})=\sum_{\underline{\mathbf{j}}=\underline{\mathbf{1}}}^{\underline{\mathbf{N}}}\underline{\boldsymbol{F}}_{\underline{\mathbf{j}}}\delta_h^{\underline{\mathbf{j}}}(\widetilde{\boldsymbol{X}})\qquad\text{and}\qquad\boldsymbol{B}(\widetilde{\boldsymbol{X}})=\sum_{\underline{\mathbf{j}}=\underline{\mathbf{1}}}^{\underline{\mathbf{N}}}\boldsymbol{B}_{\underline{\mathbf{j}}}\delta_h^{\underline{\mathbf{j}}}(\widetilde{\boldsymbol{X}})\tag{11.47}$$

with

$$\delta_h^{\underline{\mathbf{j}}}(\widetilde{\boldsymbol{X}})=\frac{1}{|\underline{\mathbf{N}}|}\sum_{\underline{\mathbf{k}}=-\lfloor\underline{\mathbf{N}}/2\rfloor}^{\lfloor\underline{\mathbf{N}}/2\rfloor}e^{\imath\underline{\xi}(\underline{\mathbf{k}})\cdot(\widetilde{\boldsymbol{X}}-\widetilde{\boldsymbol{X}}_{\underline{\mathbf{j}}})}\tag{11.48}$$

and also do so for the unconstrained variations $\delta\underline{\widetilde{\boldsymbol{F}}}_{i|}$ and $\delta\widetilde{\boldsymbol{B}}$. Inserting these in (11.45) gives

$$\sum_{\underline{\mathbf{j}}=1}^{\underline{\mathbf{N}}}\sum_i\left\langle\delta_h^{\underline{\mathbf{j}}}\left(\underline{\boldsymbol{P}}_{i|}*\underline{\boldsymbol{Y}}\right)\right\rangle_{\widetilde{\mathcal{B}}}\cdot\left(\delta\underline{\widetilde{\boldsymbol{F}}}_{\underline{\mathbf{j}}}\right)_{i|}+\sum_{\underline{\mathbf{j}}=1}^{\underline{\mathbf{N}}}\left\langle\delta_h^{\underline{\mathbf{j}}}\left(\boldsymbol{H}*\underline{\boldsymbol{Z}}\right)\right\rangle_{\widetilde{\mathcal{B}}}\cdot\delta\widetilde{\boldsymbol{B}}_{\underline{\mathbf{j}}}=0.\tag{11.49}$$

We *approximate* the integral for the volume averages by the trapezoidal rule with evaluation points $\widetilde{\boldsymbol{X}}_{\underline{\mathbf{j}}}$ and exploit that $\delta_h^{\underline{\mathbf{j}}}(\widetilde{\boldsymbol{X}}_{\underline{\mathbf{l}}})=1$ for $\underline{\mathbf{l}}=\underline{\mathbf{j}}$ and 0 otherwise to arrive at

$$\sum_{\underline{\mathbf{j}}=\underline{\mathbf{1}}}^{\underline{\mathbf{N}}}\left[\sum_i\left(\underline{\boldsymbol{P}}_{i|}*\underline{\boldsymbol{Y}}\right)(\widetilde{\boldsymbol{X}}_{\underline{\mathbf{j}}})\cdot\left(\delta\underline{\widetilde{\boldsymbol{F}}}_{\underline{\mathbf{j}}}\right)_{i|}+\left(\boldsymbol{H}*\underline{\boldsymbol{Z}}\right)(\widetilde{\boldsymbol{X}}_{\underline{\mathbf{j}}})\cdot\delta\widetilde{\boldsymbol{B}}_{\underline{\mathbf{j}}}\right]=0.\tag{11.50}$$

Since $\delta\underline{\widetilde{\boldsymbol{F}}}(\widetilde{\boldsymbol{X}}_{\underline{\mathbf{j}}})$ and $\delta\widetilde{\boldsymbol{B}}(\widetilde{\boldsymbol{X}}_{\underline{\mathbf{j}}})$ are arbitrary we end up at the set of equations

$$(\underline{\boldsymbol{P}}_{i|}*\underline{\boldsymbol{Y}})(\widetilde{\boldsymbol{X}}_{\underline{\mathbf{j}}})=\boldsymbol{0}\qquad\text{and}\qquad(\boldsymbol{H}*\underline{\boldsymbol{Z}})(\widetilde{\boldsymbol{X}}_{\underline{\mathbf{j}}})=\boldsymbol{0}\qquad\forall\underline{\mathbf{j}}\in[\underline{\mathbf{1}},\underline{\mathbf{N}}].\tag{11.51}$$

The convolutions ask for a transform to Fourier space reading as

$$\mathcal{F}^{-1}\left[\mathcal{F}\left[\underline{\boldsymbol{P}}(\underline{\boldsymbol{F}},\boldsymbol{B})\right]:\underline{\mathbb{Y}}\right]_{\underline{\mathbf{j}}}=\underline{\boldsymbol{0}}\qquad\text{where}\qquad\left(\underline{\mathbb{Y}}_{\underline{\mathbf{k}}}\right)_{ijkl}=\left(\underline{\boldsymbol{Y}}_{\underline{\mathbf{k}}}\right)_{jl}\delta_{ik}\tag{11.52a}$$

and

$$\mathcal{F}^{-1}\left[\mathcal{F}\left[\boldsymbol{H}(\underline{\boldsymbol{F}},\boldsymbol{B})\right]\cdot\underline{\check{\boldsymbol{Z}}}\right]_{\underline{\mathbf{j}}}=\mathbf{0} \tag{11.52b}$$

$\forall\underline{\mathbf{j}}\in[\underline{\mathbf{1}},\underline{\mathbf{N}}]$ and with the "$\cdot$"- and ":"-products applied mode-wise. The equations above have been obtained along the lines of de Geus et al. (2017) and Rambausek et al. (2019). This approach is quite different form first versions of Fourier-based discretization schemes (Moulinec and Suquet, 1994, 1995).

Finally, we mention that at a solution $\{\underline{\boldsymbol{F}}^{[*]}(\overline{\boldsymbol{F}},\overline{\boldsymbol{B}}),\boldsymbol{B}^{[*]}(\overline{\boldsymbol{F}},\overline{\boldsymbol{B}})\}$ of the coupled equations (11.52) the effective dual quantities are obtained as the $\underline{\mathbf{0}}$-modes representing field averages, i.e.

$$\overline{\boldsymbol{P}}(\overline{\boldsymbol{F}},\overline{\boldsymbol{B}}):=\underline{\check{\boldsymbol{P}}}_{\underline{\mathbf{0}}}(\underline{\boldsymbol{F}}^{[*]},\boldsymbol{B}^{[*]})\qquad\text{and}\qquad\overline{\boldsymbol{H}}(\overline{\boldsymbol{F}},\overline{\boldsymbol{B}}):=\check{\boldsymbol{H}}_{\underline{\mathbf{0}}}(\underline{\boldsymbol{F}}^{[*]},\boldsymbol{B}^{[*]}). \tag{11.53}$$

11.2.6. Solution procedure

The discrete coupled magneto-mechanical system at the micro-scale (11.52) renders a set of nonlinear equations which can be solved by iterative schemes. Representative for a large class of such solvers we describe the Newton-scheme applied to (11.52) following Rambausek et al. (2019). The state at Newton iteration n is denoted as $\{\underline{\boldsymbol{F}}^{[n]},\boldsymbol{B}^{[n]}\}$. The corresponding increments are $\{\Delta\underline{\boldsymbol{F}}^{[n]},\Delta\boldsymbol{B}^{[n]}\}$ such that $\{\underline{\boldsymbol{F}}^{[n+1]},\boldsymbol{B}^{[n+1]}\}=\{\underline{\boldsymbol{F}}^{[n]}+\Delta\underline{\boldsymbol{F}}^{[n]},\boldsymbol{B}^{[n]}+\Delta\boldsymbol{B}^{[n]}\}$. Before entering the Newton loop we set the average of $\{\underline{\boldsymbol{F}}^{[0]},\boldsymbol{B}^{[0]}\}$ to the prescribed effective values. This is done in three steps:

1. $\underline{\check{\boldsymbol{F}}}^{[0]}=\mathcal{F}\left[\underline{\boldsymbol{F}}^{[0]}\right]$ and $\check{\boldsymbol{B}}^{[0]}=\mathcal{F}\left[\boldsymbol{B}^{[0]}\right]$ (11.54a)
2. $\underline{\check{\boldsymbol{F}}}^{[0]}_{\underline{\mathbf{0}}}=\overline{\boldsymbol{F}}$ and $\check{\boldsymbol{B}}^{[0]}_{\underline{\mathbf{0}}}=\overline{\boldsymbol{B}}$ (11.54b)
3. $\underline{\boldsymbol{F}}^{[0]}=\mathcal{F}^{-1}\left[\underline{\check{\boldsymbol{F}}}^{[0]}\right]$ and $\boldsymbol{B}^{[0]}=\mathcal{F}^{-1}\left[\check{\boldsymbol{B}}^{[0]}\right]$. (11.54c)

Next we need the linearization of (11.52). Linearity of the DFT allows us to simply write

$$\begin{pmatrix}\mathcal{F}^{-1}\left[\mathcal{F}\left[\Delta\underline{\boldsymbol{P}}(\underline{\boldsymbol{F}}^{[n]},\boldsymbol{B}^{[n]})\right]:\underline{\check{\mathbb{V}}}\right]\\ \mathcal{F}^{-1}\left[\mathcal{F}\left[\Delta\boldsymbol{H}(\underline{\boldsymbol{F}}^{[n]},\boldsymbol{B}^{[n]})\right]\cdot\underline{\check{\boldsymbol{Z}}}\right]\end{pmatrix}_{\underline{\mathbf{j}}}=-\begin{pmatrix}\mathcal{F}^{-1}\left[\mathcal{F}\left[\underline{\boldsymbol{P}}(\underline{\boldsymbol{F}}^{[n]},\boldsymbol{B}^{[n]})\right]:\underline{\check{\mathbb{V}}}\right]\\ \mathcal{F}^{-1}\left[\mathcal{F}\left[\boldsymbol{H}(\underline{\boldsymbol{F}}^{[n]},\boldsymbol{B}^{[n]})\right]\cdot\underline{\check{\boldsymbol{Z}}}\right]\end{pmatrix}_{\underline{\mathbf{j}}}\quad\forall\underline{\mathbf{j}}. \tag{11.55}$$

Expanding $\Delta\underline{\boldsymbol{P}}$ and $\Delta\boldsymbol{H}$ yields

$$\underbrace{\begin{pmatrix}\mathcal{F}^{-1}\left[\mathcal{F}\left[\partial_{\underline{\boldsymbol{F}}}\underline{\boldsymbol{P}}:\Delta\underline{\boldsymbol{F}}+\partial_{\boldsymbol{B}}\underline{\boldsymbol{P}}\cdot\Delta\boldsymbol{B}\right]^{[n]}:\underline{\check{\mathbb{V}}}\right]\\ \mathcal{F}^{-1}\left[\mathcal{F}\left[\partial_{\underline{\boldsymbol{F}}}\boldsymbol{H}:\Delta\underline{\boldsymbol{F}}+\partial_{\boldsymbol{B}}\boldsymbol{H}\cdot\Delta\boldsymbol{H}\right]^{[n]}\cdot\underline{\check{\boldsymbol{Z}}}\right]\end{pmatrix}_{\underline{\mathbf{j}}}}_{\underline{\mathbf{K}}_{\underline{\mathbf{j}}}(\Delta\underline{\boldsymbol{F}}^{[n]},\Delta\boldsymbol{B}^{[n]};\underline{\boldsymbol{F}}^{[n]},\boldsymbol{B}^{[n]})}=-\underbrace{\begin{pmatrix}\mathcal{F}^{-1}\left[\check{\underline{\boldsymbol{P}}}^{[n]}:\underline{\check{\mathbb{V}}}\right]\\ \mathcal{F}^{-1}\left[\check{\boldsymbol{H}}^{[n]}\cdot\underline{\check{\boldsymbol{Z}}}\right]\end{pmatrix}_{\underline{\mathbf{j}}}}_{\underline{\mathbf{R}}_{\underline{\mathbf{j}}}(\underline{\boldsymbol{F}}^{[n]},\boldsymbol{B}^{[n]})}\quad\forall\underline{\mathbf{j}}. \tag{11.56}$$

This is a system linear in $\Delta\underline{\boldsymbol{F}}^{[n]}$ and $\Delta\boldsymbol{B}^{[n]}$. Unfortunately, the corresponding matrix is dense because the trigonometric basis functions (11.48), by contrast to FE basis functions, do not have compact support. However, for iterative linear solvers such as the method of conjugate gradients (Hestenes and Stiefel, 1952) do not require an assembled matrix but only the action (the product) $\underline{\mathbf{K}}(\Delta\underline{\boldsymbol{F}}^{[n]}, \Delta\boldsymbol{B}^{[n]})$ of the underlying linear operator on $\Delta\underline{\boldsymbol{F}}^{[n]}$ and $\Delta\boldsymbol{B}^{[n]}$. In the context of Fourier based homogenization this was brought up by Brisard and Dormieux (2010) and Zeman et al. (2010). Moreover, due to the projection operators $\check{\mathbb{Y}}$ and $\check{\underline{\boldsymbol{Z}}}$ the volume average of $\underline{\mathbf{R}}$ and also of the action $\underline{\mathbf{K}}(\Delta\underline{\boldsymbol{F}}^{[n]}, \Delta\boldsymbol{B}^{[n]})$ vanish identically. Thus, $\Delta\overline{\boldsymbol{F}}^{[n]} = \boldsymbol{0}$ and $\Delta\overline{\boldsymbol{B}}^{[n]} = \boldsymbol{0}$.

In our implementation we employ the CG solver provided by `scipy`. As convergence criterion we employ $\|\underline{\mathbf{r}}\|/\|\underline{\mathbf{R}}\| \leq tol_{\mathrm{CG}}$, where $\underline{\mathbf{r}}$ is the linear solver residual and $tol_{\mathrm{CG}} = 5 \times 10^{-6}$ by default. If not explicitly mentioned we set the number of maximum CG iterations to size $\underline{\mathbf{R}}$ to bound the numerical effort for the solution of the linear system. The convergence criterion for the nonlinear (Newton) solver is $\|\underline{\mathbf{R}}\|/\sqrt{\operatorname{size}\underline{\mathbf{R}}} \leq tol_{\mathrm{NLS}}$, where tol_{NLS} defaults to 1×10^{-6}. The choice of tolerances tol_{CG} and tol_{NLS} has influence on the results shown below. In fact, we usually tried different values looking for a good compromise between robustness, accuracy and computational effort.

11.2.7. Computation of effective moduli

As in the case of twoscale FE schemes also for twoscale FE-Fourier schemes one key ingredient is the sensitivity of the micro-solutions with respect tochanges in the macroscopic inputs. We are already in possession of the operator $\underline{\mathbf{K}}$ allowing us to solve for $\{\Delta\underline{\boldsymbol{F}}, \Delta\boldsymbol{B}\}$. Analogous to the discussion in Sections 5.4.1 and 7.1.6 we only have to come up with appropriate right-hand-sides to obtain the desired sensitivities. For example, the sensitivities of a solution state $\{\Delta\underline{\boldsymbol{F}}^{[*]}, \Delta\boldsymbol{B}^{[*]}\}/\Delta\overline{\boldsymbol{F}}_{\alpha\beta}$ are obtained from the system

$$\begin{pmatrix} \mathcal{F}^{-1}\left[\mathcal{F}\left[\partial_{\underline{\boldsymbol{F}}}\underline{\boldsymbol{P}} : \Delta\underline{\boldsymbol{F}} + \partial_{\boldsymbol{B}}\underline{\boldsymbol{P}} \cdot \Delta\boldsymbol{B}\right]^{[*]} : \check{\mathbb{Y}}\right] \\ \mathcal{F}^{-1}\left[\mathcal{F}\left[\partial_{\underline{\boldsymbol{F}}}\boldsymbol{H} : \Delta\underline{\boldsymbol{F}} + \partial_{\boldsymbol{B}}\boldsymbol{H} \cdot \Delta\boldsymbol{H}\right]^{[*]} \cdot \check{\underline{\boldsymbol{Z}}}\right] \end{pmatrix}_{\underline{\mathbf{j}}} = -\begin{pmatrix} \mathcal{F}^{-1}\left[\mathcal{F}\left[\partial_{F_{\alpha\beta}}\underline{\boldsymbol{P}}^{[*]}\right] : \check{\mathbb{Y}}\right] \\ \mathcal{F}^{-1}\left[\mathcal{F}\left[\partial_{F_{\alpha\beta}}\boldsymbol{H}^{[*]}\right] \cdot \check{\underline{\boldsymbol{Z}}}\right] \end{pmatrix}_{\underline{\mathbf{j}}} \quad \forall \underline{\mathbf{j}}. \tag{11.57}$$

To indicate which sensitivity has been computed we write $\Delta\underline{\boldsymbol{F}}^{[*]}(\Delta\overline{\boldsymbol{F}}_{\alpha\beta})$ and $\Delta\boldsymbol{B}^{[*]}(\Delta\overline{\boldsymbol{F}}_{\alpha\beta})$. Similarly, for sensitivities with respect to $\overline{\boldsymbol{B}}$ we solve

$$\begin{pmatrix} \mathcal{F}^{-1}\left[\mathcal{F}\left[\partial_{\underline{\boldsymbol{F}}}\underline{\boldsymbol{P}} : \Delta\underline{\boldsymbol{F}} + \partial_{\boldsymbol{B}}\underline{\boldsymbol{P}} \cdot \Delta\boldsymbol{B}\right]^{[*]} : \check{\mathbb{Y}}\right] \\ \mathcal{F}^{-1}\left[\mathcal{F}\left[\partial_{\underline{\boldsymbol{F}}}\boldsymbol{H} : \Delta\underline{\boldsymbol{F}} + \partial_{\boldsymbol{B}}\boldsymbol{H} \cdot \Delta\boldsymbol{H}\right]^{[*]} \cdot \check{\underline{\boldsymbol{Z}}}\right] \end{pmatrix}_{\underline{\mathbf{j}}} = -\begin{pmatrix} \mathcal{F}^{-1}\left[\mathcal{F}\left[\partial_{B_\alpha}\underline{\boldsymbol{P}}^{[*]}\right] : \check{\mathbb{Y}}\right] \\ \mathcal{F}^{-1}\left[\mathcal{F}\left[\partial_{B_\alpha}\boldsymbol{H}^{[*]}\right] \cdot \check{\underline{\boldsymbol{Z}}}\right] \end{pmatrix}_{\underline{\mathbf{j}}} \quad \forall \underline{\mathbf{j}}. \tag{11.58}$$

Finally, the full expressions for the effective moduli are given as

$$\partial_{\overline{F}_{\alpha\beta}}\overline{\underline{P}} = \mathcal{F}\left[\partial_{F_{\alpha\beta}}\underline{P} + \partial_{\underline{F}}\underline{P} : \Delta\underline{F}^{[*]}(\Delta\underline{\overline{F}}_{\alpha\beta}) + \partial_{\boldsymbol{B}}\underline{P}\cdot\Delta\boldsymbol{B}^{[*]}(\Delta\underline{\overline{F}}_{\alpha\beta})\right]_{\underline{\mathbf{0}}} \tag{11.59a}$$

$$\partial_{\overline{F}_{\alpha\beta}}\overline{\boldsymbol{H}} = \mathcal{F}\left[\partial_{F_{\alpha\beta}}\boldsymbol{H} + \partial_{\underline{F}}\boldsymbol{H} : \Delta\underline{F}^{[*]}(\Delta\underline{\overline{F}}_{\alpha\beta}) + \partial_{\boldsymbol{B}}\boldsymbol{H}\cdot\Delta\boldsymbol{B}^{[*]}(\Delta\underline{\overline{F}}_{\alpha\beta})\right]_{\underline{\mathbf{0}}} \tag{11.59b}$$

$$\partial_{\overline{B}_{\alpha}}\overline{\underline{P}} = \mathcal{F}\left[\partial_{B_{\alpha}}\underline{P} + \partial_{\underline{F}}\underline{P} : \Delta\underline{F}^{[*]}(\Delta\overline{\boldsymbol{B}}_{\alpha}) + \partial_{\boldsymbol{B}}\underline{P}\cdot\Delta\boldsymbol{B}^{[*]}(\Delta\overline{\boldsymbol{B}}_{\alpha})\right]_{\underline{\mathbf{0}}} \tag{11.59c}$$

$$\partial_{\overline{B}_{\alpha}}\overline{\boldsymbol{H}} = \mathcal{F}\left[\partial_{B_{\alpha}}\boldsymbol{H} + \partial_{\underline{F}}\boldsymbol{H} : \Delta\underline{F}^{[*]}(\Delta\overline{\boldsymbol{B}}_{\alpha}) + \partial_{\boldsymbol{B}}\boldsymbol{H}\cdot\Delta\boldsymbol{B}^{[*]}(\Delta\overline{\boldsymbol{B}}_{\alpha})\right]_{\underline{\mathbf{0}}}. \tag{11.59d}$$

11.3. Numerical Examples

The results presented below are a subset of what can be found in the recent contribution Rambausek et al. (2019). Throughout this section we employ a generic magneto-mechanical energy-density function

$$\Psi(\underline{\boldsymbol{F}}, \boldsymbol{B}) = \frac{\mu}{2}\left(\operatorname{tr}\boldsymbol{C} - \operatorname{tr}\mathbf{1}\right) + \frac{\mu}{\beta}\left(J^{-\beta} - 1\right) + \frac{J\|\boldsymbol{b}\|^2}{2\mu_0} - \frac{m_{\mathrm{s}}}{\gamma}\ln\left[\cosh\left(\gamma\|\boldsymbol{b}\|\right)\right] \tag{11.60}$$

with

$$\boldsymbol{b} = \frac{1}{J}\underline{\boldsymbol{F}}\cdot\boldsymbol{B}, \quad \gamma = \frac{J\chi}{(J+\chi)m_{\mathrm{s}}\mu_0} \quad \text{and} \quad \mu_0 = 4\pi\times 10^{-1}\,\mu\mathrm{N/A}^2. \tag{11.61}$$

Furthermore we also consider a modified FFT scheme where the wave-vectors $\underline{\boldsymbol{\xi}}^{\mathrm{FD}}(\underline{\mathbf{k}})$ are defined through

$$\xi_{\alpha}^{\mathrm{FD}}(\underline{\mathbf{k}}) = \frac{\sin(\xi_{\alpha}(\underline{\mathbf{k}})h_{\alpha})}{h_{\alpha}}, \tag{11.62}$$

which corresponds to a finite difference (FD) approximation of derivatives. This approach is inspired by Berbenni et al. (2014) and has also been employed by Lebensohn and Needleman (2016) and Vidyasagar et al. (2017). Therein, this modification should reduce oscillations in the numerical solutions near material interfaces. However, because of different formulations, i.e. the present projection-based versus "classical" Green-operator-based approaches, observations regarding this FD modification are not directly transferable. In case of the current implementation, only the definitions of the projections operators $\underline{\boldsymbol{Y}}$ and $\underline{\boldsymbol{Z}}$ are affected by this change. In the examples below "FFT" we will refer to the "unmodified" scheme whereas FFT-FD denotes the modified one.

The finite element schemes which we for comparison employ on the microscale are described in Section 10.1. However, compared with the principles discussed in that section, we below drop the constraint of incompressibility. We choose second order basis functions for the deformation map and the magnetic vector potential. In three dimensions we set the weight of the penalty for the Coulomb gauge of the vector potential to

$\epsilon^{\mathrm{m}} = 1 \times 10^{-3}$.

11.3.1. Implementation of rotated microstructures

The unit cells under consideration in Section 11.3.3 are orthotropic. Hence, a rotation of the unit cells in the initial configuration with respect to the macroscopic body affects the overall response. The implementation of such rotations is easiest performed by considering a non-rotated unit cell and simply transform macroscopic inputs and effective responses. This is done as follows Rambausek et al. (2019): We start with the rotation of the co- and contravariant referential basis

$$\boldsymbol{E}'_I = \boldsymbol{Q} \cdot \boldsymbol{E}_I \qquad \text{and} \qquad \boldsymbol{E}'^I = \boldsymbol{Q}^{-1} \cdot \boldsymbol{E}^I, \tag{11.63}$$

respectively. Using the relation $\boldsymbol{Q}^{-1} = \boldsymbol{Q}^{\mathrm{T}}$ the macroscopic inputs $\{\overline{\underline{\boldsymbol{F}}}, \overline{\boldsymbol{B}}\}$ transform as

$$\overline{\underline{\boldsymbol{F}}}' = \overline{\underline{\boldsymbol{F}}} \cdot \boldsymbol{Q} \qquad \text{and} \qquad \overline{\boldsymbol{B}}' = \boldsymbol{Q}^{-1} \cdot \overline{\boldsymbol{B}}. \tag{11.64}$$

Correspondingly, the dual quantities of the rotated microstructure are obtained as

$$\boldsymbol{P} = \boldsymbol{P}' \cdot \boldsymbol{Q}^{-1} \qquad \text{and} \qquad \boldsymbol{H} = \boldsymbol{Q} \cdot \boldsymbol{H}'. \tag{11.65}$$

Finally, for the effective moduli we have the relations

$$\frac{\partial P_{iI}}{\partial F_{jJ}} = \frac{\partial P'_{iK}}{\partial F'_{jL}} Q^{-1}_{KI} Q^{-1}_{LJ}, \qquad \frac{\partial P_{iI}}{\partial B_J} = \frac{\partial P'_{iK}}{\partial B'_L} Q^{-1}_{KI} Q^{-1}_{LJ}, \tag{11.66a}$$

$$\frac{\partial H_I}{\partial F_{jJ}} = \frac{\partial H'_K}{\partial F'_{jL}} Q^{-1}_{KI} Q^{-1}_{LJ}, \qquad \frac{\partial H_I}{\partial B_J} = \frac{\partial H'_K}{\partial B'_L} Q^{-1}_{KI} Q^{-1}_{LJ}. \tag{11.66b}$$

11.3.2. A three-dimensional MRE unit cell

In the first example we consider a three-dimensional unit cell prototypical for an MRE. It consists of a soft non-magnetic matrix and a spherical magnetic inclusion occupying 20 % of the unit cell as depicted in Figure 11.1. The material parameters are summarized in Table 11.1, the load cases parameterized by a pseudo time t in Table 11.2.

Table 11.1: Material parameters for the 3d microstructure

domain	μ / MPa	β / 1	m_{s} / MA m^{-1}	χ / 1
inclusion	20	4.333	1	10
matrix	0.2	4.333	0	0

For a comparison of the pure FFT, the FFT-FD and the FE solver we show plots of the effective energies obtained in Figure 11.2.

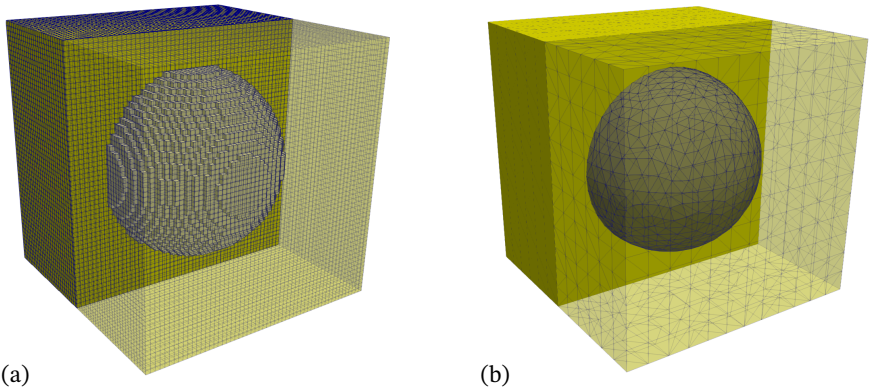

(a) (b)

Figure 11.1: Three-dimensional MRE microstructure discretized by a Cartesian grid (a) and a "body-fitted" tetrahedron mesh (b), respectively. The magnetic inclusion (gray) consumes 20 % of the unit cell's volume. The remaining 80 % are occupied by the elastomer matrix.

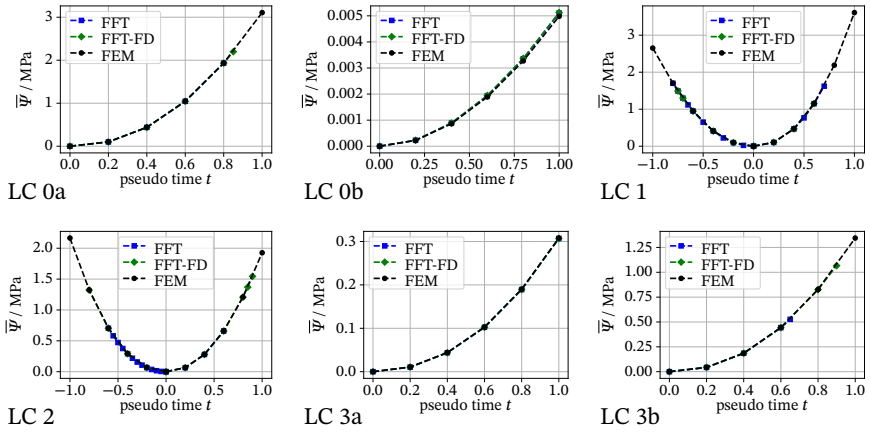

Figure 11.2: Effective energies of a 3d MRE unit cell under various load cases. We observe that the FFT schemes have problems in particular for coupled magneto-mechanical loads with high magnetic field. In most cases, the FFT-FD scheme is more robust than the unmodified FFT implementation. However, in LC 1, the FFT performs better that FFT-FD (Rambausek et al., 2019).

As depicted, both the FFT and FFT-FD schemes largely keep up with the FE solver. For magneto-mechanical loading with relatively high magnetic fields, however, they turn out to be not as robust. By that we mean that the CG solver failed to converge

Table 11.2: Load cases for the 3d microstructure

Label	$\overline{\underline{\boldsymbol{F}}} - \mathbf{1}$ / 1	$\overline{\boldsymbol{B}}$ / T
LC 0a	$\begin{bmatrix} 0 & 0 & 0 \\ 0 & 0 & 0 \\ 0 & 0 & 0 \end{bmatrix}$	$\begin{bmatrix} 0 \\ 0 \\ 3t \end{bmatrix}$
LC 0b	$\begin{bmatrix} -0.02t & 0 & 0 \\ 0 & -0.02t & 0 \\ 0 & 0 & 0.1t \end{bmatrix}$	$\begin{bmatrix} 0 \\ 0 \\ 0 \end{bmatrix}$
LC 1	$\begin{bmatrix} -0.02t & 0 & 0 \\ 0 & -0.02t & 0 \\ 0 & 0 & 0.1t \end{bmatrix}$	$\begin{bmatrix} 0 \\ 0 \\ 3t \end{bmatrix}$
LC 2	$\begin{bmatrix} -0.02t & 0 & 0 \\ 0 & -0.02t & 0 \\ 0 & 0 & 0.1t \end{bmatrix}$	$\begin{bmatrix} 2t \\ 1t \\ 1t \end{bmatrix}$
LC 3a	$\begin{bmatrix} 0 & 0.1t & 0.1t \\ 0 & 0 & 0.1t \\ 0 & 0 & 0 \end{bmatrix}$	$\begin{bmatrix} 0 \\ 0 \\ 1t \end{bmatrix}$
LC 3b	$\begin{bmatrix} 0 & 0.1t & 0.1t \\ 0 & 0 & 0.1t \\ 0 & 0 & 0 \end{bmatrix}$	$\begin{bmatrix} 0 \\ 0 \\ 2t \end{bmatrix}$

within a reasonable and practically feasible number of iterations. We did not observe such a degradation of performance for the mechanical loads. Moreover, in some cases FFT-FD can undergo higher loads than FFT. The differences are not dramatic and in some cases also FFT is more robust than FFT-FD.

To gain some insight we depict plots of section of deformed unit cells for LC 3a in Figures 11.3 and 11.4. We observe oscillations typical for FFT based schemes near the inclusion-matrix interface in deformation $\underline{\boldsymbol{F}}$ (Figure 11.3) and magnetization $\boldsymbol{m}$ (Figure 11.4). Nevertheless, the effective energy densities obtained by the FFT and FE solvers are in good agreement (see Figure 11.2).

11.3.3. Two-scale simulations in two dimensions

In the second example we consider the two-scale setting of which the macroscopic BVP is depicted in Figure 11.5. The underlying FFT and FE microstructure discretizations are depicted in Figure 11.6. The two sets of material parameters for the individual

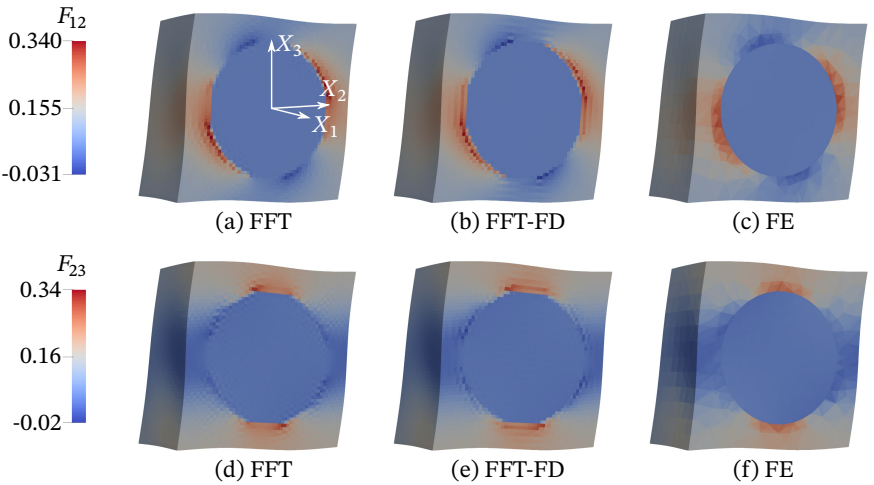

Figure 11.3: Deformed configurations of 3d MRE unit cells cut by the 2-3-plane for load case "3a" at $t = 1$. We see that the FFT-FD scheme does not remove the oscillations in $\underline{\boldsymbol{F}}$ as observable in the plot for FFT. However, the pattern is changed, which could be favorable for certain geometries (Rambausek et al., 2019).

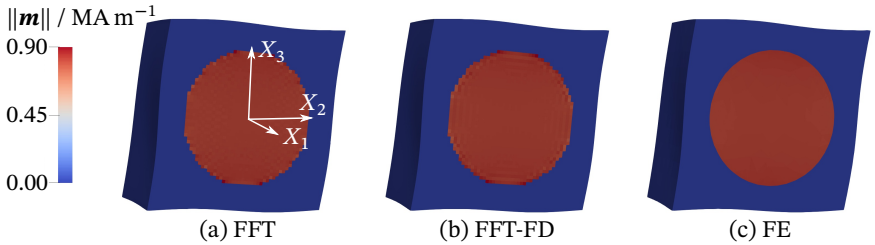

Figure 11.4: Magnetization in the deformed configuration of 3d MRE unit cells cut by the 2-3-plane for load case "3a" at $t = 1$. Also in the case of magnetization we observe oscillations near the inclusion-matrix interface for the FFT and FFT-FD scheme (Rambausek et al., 2019).

phases are given in Table 11.3

For the macroscopic BVP we employ the formulation described in Chapter 9 but without incompressibility. For the deformation map we choose second order Lagrange elements and the magnetic field $\overline{\boldsymbol{B}}$ is discretized by linear BDM elements. On the microscopic scale we employ the FFT, the FFT-FD and the vector-potential-based finite scheme with quadratic Lagrange elements applied to both the "pixel"-based (FE-V) and the "body-fitted" mesh (FE). We first show two-scale results obtained with the FFT-FD

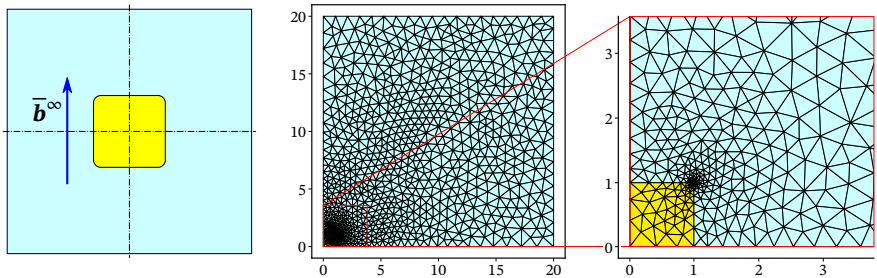

(a) overview (b) FE mesh (c) zoomed view

Figure 11.5: The macroscopic BVP for the two-scale simulation of an MRE in free space. The MRE body (yellow) is exposed to a uniform external magnetic field $\overline{\boldsymbol{b}}^{\infty}$ in vertical direction (a). Because of symmetry of the BVP we only discretize a quarter of the domain (b). A detailed view of the meshed MRE body is provided in (c). The body's corners are rounded ($r = 0.5$ mm) to avoid singularities in the magnetic response (Rambausek et al., 2019).

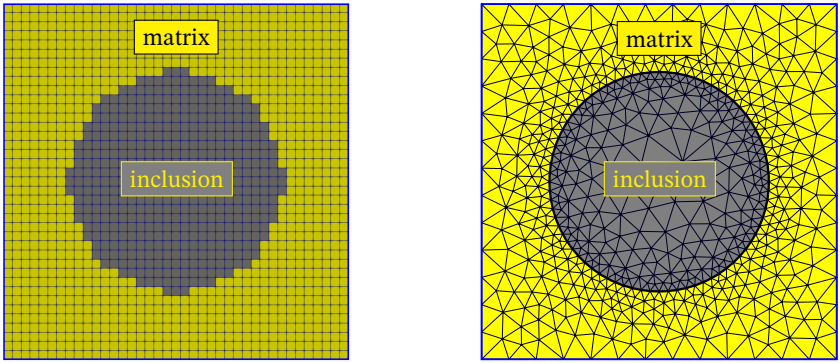

(a) grid ("pixels") (b) "body-fitted" mesh

Figure 11.6: Two discretizations of the two-dimensional MRE microstructure with a circular inclusion occupying 30 % of the unit cell's area. In (a) we show a 39×39 grid for FFT and voxel-FE (V-FE) schemes. Subplot (b) depicts a "body-fitted" FE mesh (Rambausek et al., 2019).

and the FE (body-fitted mesh) scheme. Figure 11.7 depicts plots of the macroscopic magnetization $\overline{\boldsymbol{m}}$ and displacements $\overline{u}_1 = \overline{\varphi}_1 - X_1$ and $\overline{u}_2 = \overline{\varphi}_2 - X_2$ at selected points for parameter set "a".

The corresponding results for the mechanically softer parameter set "b" are shown in Figure 11.8. In both Figures we observe almost identical effective magnetic responses but at the same time visibly deviating displacements. Despite these deviations, the point

Table 11.3: Material parameters for the two-scale FE-FFT example

set	domain	μ / N m^{-2}	β / 1	m_s / MA m^{-1}	χ / 1
a	inclusion	20	4.333	1	10
	matrix	0.2	4.333	0	0
b	inclusion	10	9.333	1.2	12
	matrix	0.1	9.333	0	0
a & b	free space	9.091×10^{-4}	0.250	0	0

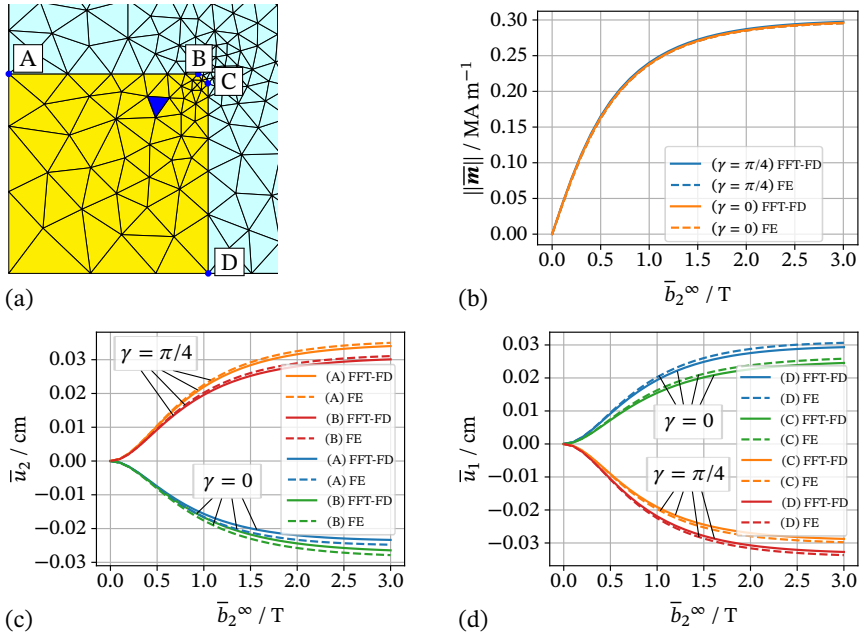

Figure 11.7: Macroscopic results for parameter set "a". The evaluation points are depicted in (a), actual results in (b) to (d). As depicted in (b) FE and FFT results for the magnetization are in excellent agreement. In the displacement responses shown in (c) and (d), however, we observe small deviations.

of instability[1] for parameters set "b" at $\overline{\boldsymbol{b}} \approx 1.3\,\mathrm{T}$ is the same for both FE and FFT em-

[1]We did not further investigate this point. The interested reader is referred to the contributions of, among others, Rudykh and Bertoldi (2013), Miehe et al. (2015), Miehe et al. (2016), Goshkoderia and Rudykh (2017) and

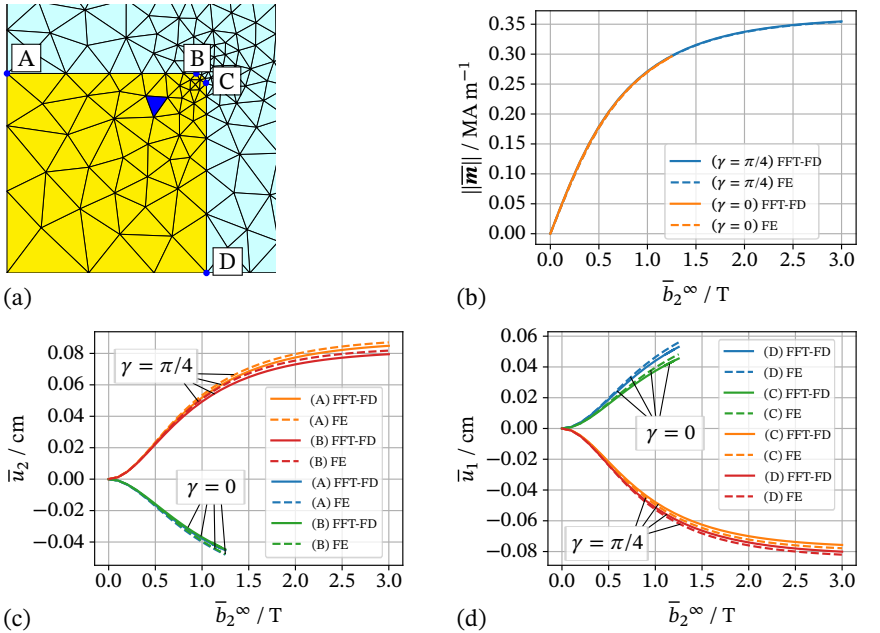

Figure 11.8: Macroscopic results for parameter set "b". The evaluation points are depicted in (a), actual results in (b) to (d). As for parameter set "a" in Figure 11.7 above, FE and FFT solvers yield practically identical results for the magnetization whereas we see small deviations in the mechanical responses. Moreover, the simulations crash for $\gamma = 0$ before the applied field $\overline{\boldsymbol{b}}^\infty$ reaches its maximum value. The point where this happens is the same for FE and FFT, which underlines their agreement (Rambausek et al., 2019).

ployed on the microscale.

The quantitative differences in the mechanical response ask for more detailed investigations of the effective responses. For this purpose we perform a comparison the FFT, FFT-FD, FE and V-FE schemes for different levels of grid/mesh refinements. The purely mechanical load applied is

$$\{\overline{\boldsymbol{F}}, \overline{\boldsymbol{B}}\} = \left\{\begin{bmatrix} 1.10 & 0.03 \\ 0.00 & -1.08 \end{bmatrix}, \begin{bmatrix} 0 \\ 0 \end{bmatrix}\right\}, \tag{11.67}$$

as material parameters we employ parameter set "b". The results for the effective energy density and two components of the effective first Piola-Kirchhoff stress are summarized in Table 11.4. Obviously, each scheme yields different results due to the rather coarse

Polukhov et al. (2018) on stability problems in the present scope.

Table 11.4: Comparison of FFT, FFT-FD, FE and V-FE for the mechanical load case (11.67)

quantity	FFT	FFT-FD	FE	V-FE
$\overline{\Psi}$ / MPa	3.772×10^{-3}	3.833×10^{-3}	3.678×10^{-3}	3.876×10^{-3}
$\overline{P}_{11}$ / MPa	49.012×10^{-3}	49.325×10^{-3}	48.371×10^{-3}	49.378×10^{-3}
$\overline{P}_{12}$ / MPa	4.198×10^{-3}	4.201×10^{-3}	4.131×10^{-3}	4.137×10^{-3}

discretization. We refer to Rambausek et al. (2019) for a corresponding convergence study.

Chapter 12

Conclusion and Outlook

The second part of this thesis presented research in magneto-electro-elasticity of soft composites. The prototypical material that motivated these investigations are magnetorheological elastomers (MREs) – composites of a soft elastomer matrix carrying magnetic inclusions. While mainly regarded as magneto-mechanical material as discussed in Chapter 7, this thesis also studied the magneto-*electro*-mechanical behavior (Chapters 8 and 9).

One of the key findings is the great importance of non-local macroscopic effects on the magneto-, the electro- and thus also on the magneto-electro-mechanical coupling properties of bodies. As shown by our two-scale studies this affects not only the design and optimization of structures and devices but also the design of experiments for the determination of material properties. Based on analytical considerations we were able to come up with recommendations for the latter task.

On the numerical side we characterize critical issues observed with existing finite element (FE) schemes in Section 9.3. In fact, the transfer of discretization errors between the magnetic (or the electric) and mechanical part of the coupled problem puts hard limits on the applicability of currently available FE schemes. We suspect that the problems observed are known to specialists in the field but may have not yet received enough attention because they only show up in certain applications involving soft media, not to say corner cases. In our test cases, finite element schemes based on face elements as well as vector-potential formulations performed better than scalar-potential-based discretizations. However, none of the implementations under investigation performed fully satisfactory. Increasing the understanding of this issue and eventually finding a cure is a formidable task for future work. As a side-result we in Section 9.3.2 report that in three-dimensional problems the proposed mixed formulations perform significantly better than vector-potential formulations when the arising linear systems are handled by direct solvers. A similar comparison for the case of iterative linear solvers would be of great interest. However, this requires the construction efficient and effective preconditioners for the coupled problem, which is still an open problem.

Also on the numerical side, we highlight the Fourier-based homogenization scheme for constrained-minimization formulations of magneto-elasticity presented in Chapter 11. Due to its mathematical structure the implementation is directly extensible to electro- and magneto-electro-elasticity.

Appendix A

Translations of objects and operations from modern differential geometry to classical vector and tensor calculus

For Euclidean space $\mathbb{R}^3$ and Cartesian coordinates we have the following relations between the exterior calculus of forms and classical vector/tensor calculus.

A.1. Objects

$$
\begin{aligned}
{}^0\mathfrak{a} = a \quad &\Leftrightarrow \quad a && && && \text{(A.1a)}\\
{}^1\mathfrak{a} \quad &\Leftrightarrow \quad \boldsymbol{a}\,(\cdot d\boldsymbol{l}) && ({}^1\mathfrak{a})_i \quad &\Leftrightarrow \quad a^i && \text{(A.1b)}\\
{}^2\mathfrak{a} \quad &\Leftrightarrow \quad \boldsymbol{a}\,(\cdot \boldsymbol{n}\, da) && ({}^2\mathfrak{a})_{\underline{jk}}\epsilon^{ijk} \quad &\Leftrightarrow \quad a^i && \text{(A.1c)}\\
{}^2\mathfrak{a} \quad &\Leftrightarrow \quad \mathbf{a}\,(:(\partial_{u^1} \otimes \partial_{u^2})) && ({}^2\mathfrak{a})_{ij} = -({}^2\mathfrak{a})_{ji} \quad &\Leftrightarrow \quad (\mathbf{a})_{ij} = -(\mathbf{a})_{ji} && \text{(A.1d)}\\
{}^2\underline{\mathfrak{s}} \quad &\Leftrightarrow \quad \underline{\boldsymbol{s}} && ({}^2\underline{\mathfrak{s}})_{\underline{ikl}} \quad &\Leftrightarrow \quad (\underline{\boldsymbol{s}})_i{}^j && \text{(A.1e)}\\
{}^3\mathfrak{a} \quad &\Leftrightarrow \quad a\,(\,dv) && && && \text{(A.1f)}
\end{aligned}
$$

A.2. Products

$$
\begin{aligned}
{}^1\mathfrak{a} \wedge {}^1\mathfrak{b} \quad &\Leftrightarrow \quad \boldsymbol{a} \times \boldsymbol{b}\,(\cdot \boldsymbol{n}\, da) && \text{(A.2a)}\\
{}^1\mathfrak{a} \wedge {}^2\mathfrak{b} \quad &\Leftrightarrow \quad \boldsymbol{a} \cdot \boldsymbol{b}\,(\,dv) && \text{(A.2b)}\\
\mathbb{i}_{\boldsymbol{v}}{}^1\mathfrak{a} \quad &\Leftrightarrow \quad \boldsymbol{a} \cdot \boldsymbol{v} && \text{(A.2c)}\\
\mathbb{i}_{\boldsymbol{v}}{}^2\mathfrak{a} \quad &\Leftrightarrow \quad \boldsymbol{a} \times \boldsymbol{v}\,(\cdot d\boldsymbol{l}) = -\boldsymbol{v} \times \boldsymbol{a}\,(\cdot d\boldsymbol{l}) && \text{(A.2d)}\\
\mathbb{i}_{\boldsymbol{v}}\, dv \quad &\Leftrightarrow \quad \boldsymbol{v}\,(\cdot \boldsymbol{n}\, da) && \text{(A.2e)}\\
{}^1\mathfrak{a}(\boldsymbol{v}) \quad &\Leftrightarrow \quad \boldsymbol{a} \cdot \boldsymbol{v} && \text{(A.2f)}\\
{}^2\mathfrak{a}(\boldsymbol{v}, \boldsymbol{w}) \quad &\Leftrightarrow \quad \mathbf{a} : (\boldsymbol{v} \otimes \boldsymbol{w}) = \boldsymbol{a} \cdot (\boldsymbol{v} \times \boldsymbol{w}) && \text{(A.2g)}\\
\mathbb{i}_{\boldsymbol{v}}{}^2\underline{\mathfrak{s}} \quad &\Leftrightarrow \quad \boldsymbol{v} \cdot \underline{\boldsymbol{s}}\,(\,dv) && \text{(A.2h)}\\
{}^2\underline{\mathfrak{s}}(\boldsymbol{\nabla}\boldsymbol{v}) \quad &\Leftrightarrow \quad \underline{\boldsymbol{s}} : \nabla \boldsymbol{v}\,(\,dv) && \text{(A.2i)}
\end{aligned}
$$

A.3. Derivatives

$$\mathbf{d}a \quad \Leftrightarrow \quad \nabla a = \operatorname{grad} a \,(\cdot d\boldsymbol{l}) \tag{A.3a}$$

$$\mathbf{d}^1\mathfrak{a} \quad \Leftrightarrow \quad \operatorname{curl} \boldsymbol{a} \,(\cdot \boldsymbol{n}\, da) \tag{A.3b}$$

$$\mathbf{d}^2\mathfrak{a} \quad \Leftrightarrow \quad \operatorname{div} \boldsymbol{a} \,(\, dv) \tag{A.3c}$$

$$\mathbb{d}(\mathbb{i}_{\boldsymbol{v}}{}^2\underline{\mathfrak{s}}) \quad \Leftrightarrow \quad \operatorname{div}(\boldsymbol{v} \cdot \underline{\boldsymbol{s}}) \tag{A.3d}$$

$$\mathbf{d}(\mathbb{i}_{\boldsymbol{v}}{}^2\underline{\mathfrak{s}}) \quad \Leftrightarrow \quad \operatorname{div}(\boldsymbol{v} \cdot \underline{\boldsymbol{s}}) \tag{A.3e}$$

A.4. Function spaces

$$\left\{{}^0\mathfrak{z} \mid {}^0\mathfrak{z} \in {}^0\Lambda, \{{}^0\mathfrak{z}, \mathbf{d}^0\mathfrak{z}\} \in \mathscr{L}^2\right\} =: \mathscr{H}({}^0\Lambda) \quad \Leftrightarrow \quad \mathscr{H}(\mathrm{Grad}) = \mathscr{H}^1 \tag{A.4a}$$

$$\left\{{}^1\mathfrak{z} \mid {}^1\mathfrak{z} \in {}^1\Lambda, \{{}^1\mathfrak{z}, \mathbf{d}^1\mathfrak{z}\} \in \mathscr{L}^2\right\} =: \mathscr{H}({}^1\Lambda) \quad \Leftrightarrow \quad \mathscr{H}(\mathrm{Curl}) \tag{A.4b}$$

$$\left\{{}^2\mathfrak{z} \mid {}^2\mathfrak{z} \in {}^2\Lambda, \{{}^2\mathfrak{z}, \mathbf{d}^2\mathfrak{z}\} \in \mathscr{L}^2\right\} =: \mathscr{H}({}^2\Lambda) \quad \Leftrightarrow \quad \mathscr{H}(\mathrm{Div}) \tag{A.4c}$$

Appendix B

A staggered solution scheme suitable for large deformation increments

The mechanical properties of the free-space ,e.g. air, $\mathcal{B}' = \Omega \setminus \mathcal{B}$ surrounding a (magneto-electric) deformable body $\mathcal{B}$ are usually negligible. However, if one treats body and surrounding in a monolithic way, one cannot simply assign zero mechanical energy to empty domain since the numerical BVP then would not be well-defined. If we do not want to set the mechanical parameters to small but non-zero values, we somehow have to fix or remove the discrete mechanical DOFs in this domain. In order to avoid self-penetration of the current configuration $\mathcal{B}'_t$ through the deformation or motion of the domain $\mathcal{B}$, $\mathcal{B}'_t$ has to be updated by an auxiliary mesh-motion or Arbitrary-Lagrangian-Eulerian(ALE)-type step. This is a well-known strategy (Bustamante et al., 2011; Pelteret et al., 2016) which we also employ in some examples in Part II. Our implementation of this approach largely follows Pelteret et al. (2016). However, we adapted their scheme such that it allows for updates of $\mathcal{B}'_t$ *within* Newton-Raphson-type schemes for the solution of the coupled nonlinear BVP. This has the advantage that load (and deformation) increments are not practically limited by the size of FE cells near the interface between $\mathcal{B}$ and $\mathcal{B}'$, i.e. $\partial\mathcal{B}$. This is important since otherwise mesh refinement would directly reduce possible load step sizes.

The proposed algorithm consists of three phases: First, the solution of the linearized discrete system of equations for the coupled MEM problem with deformation φ_h fixed in $\mathcal{B}'$. Then, if the deformation or motion of $\partial\mathcal{B}_t$ reaches a certain threshold, we solve an auxiliary problem in $\mathcal{B}'$ with boundary data from $\partial\mathcal{B}_t$ to obtain an updated $\mathcal{B}'_t$. As third step we recover magneto-electric equilibrium before turning to the next linearized magneto-electro-mechanical system. Before going into detail, we introduce the FE discretization operator $\mathcal{D}[\bullet]$ which establishes the abstract relation between a continuous object and its FE discretized counterpart, i.e. $\varphi_h = \mathcal{D}[\varphi]$. Furthermore, there is the projection $\mathcal{P}_\varphi[\bullet]$ which represent the extraction of φ or φ_h from its argument. Analogously, we have $\mathcal{P}_{\mathrm{ME}}[\bullet]$ for the magnetic and electric quantities. Such extractions can also be restricted to certain domains.

Example B.1. *Take the mixed formulation of electro-and magneto-statics combined with incompressible elasticity as an example. Let* $\underline{\mathrm{s}} = \mathcal{D}[\{\varphi, p, \boldsymbol{D}, \phi^e, \boldsymbol{B}, \phi^m\}]$ *denote the totality of discrete degrees of freedom of the MEM BVP in the full (truncated and discretized) domain* $\Omega_h = \mathcal{D}[\Omega]$*. Then,* $\varphi|_{\mathcal{B}} = \mathcal{P}_\varphi[\underline{\mathrm{s}}]\big|_{\mathcal{B}}$ *gives the deformation map restricted to* $\mathcal{B}$*.*

Furthermore, $\{\boldsymbol{D}, \phi^e, \boldsymbol{B}, \phi^m\}|_{\mathcal{B}'} = \mathcal{P}_{ME}[\underline{s}]\big|_{\mathcal{B}'}$ *selects the electric and magnetic variables restricted to the empty domain.*

Based on that we define the discrete residual vector $\underline{r}(\underline{s})$ and its linearization, the matrix $\underline{K}(\underline{s})$, through

$$\delta\underline{s} \cdot \underline{r}(\underline{s}) = -\mathcal{D}[\delta\mathcal{L}(\varphi, \boldsymbol{D}, \boldsymbol{B}, p, \phi^e, \phi^m)] \tag{B.1}$$

and

$$\delta\underline{s} \cdot \left(\underline{K}(\underline{s}) \cdot \Delta\underline{s}\right) = \mathcal{D}[\Delta\delta\mathcal{L}(\varphi, \boldsymbol{D}, \boldsymbol{B}, p, \phi^e, \phi^m)], \tag{B.2}$$

respectively.

B.1. The update of free space

When we do not assign any mechanical stiffness to $\mathcal{B}'$ the corresponding mechanical degrees of freedom have to be fixed during the solution of the coupled MEM problem. To adapt the current configuration of free space $\mathcal{B}'$ to the motion and deformation of $\mathcal{B}$ we formulate the "mesh-motion problem": For this purpose we employ the the deformation in $\mathcal{B}'$, denoted as $\xi = \varphi|_{\mathcal{B}'}$, and a hyperelastic energy density function $\Psi^{\text{mech}}(\underline{\boldsymbol{F}} = \text{Grad}\,\xi)$ to define an auxiliary mechanical BVP in $\mathcal{B}'$. Boundary conditions are given by the motion of $\partial\mathcal{B}_t$. DOFs at the outer free-space boundaries are fixed as usual. The actual variational problem is given as

$$\hat{\xi} = \arg\left\{ \inf_{\substack{\xi \\ \in \\ \mathcal{W}_\xi}} \int_{\mathcal{B}'} \Psi^{\text{mech}}\left(\text{Grad}\,\xi\right) dV \right\}, \tag{B.3}$$

with

$$\mathcal{W}_\xi = \{\xi \mid \xi_i \in \mathcal{H}\left(\text{Grad}, \mathcal{B}'\right), \xi = \varphi \text{ on } \partial\mathcal{B}, \xi = X \text{ on } \partial\Omega\}. \tag{B.4}$$

We solve this BVP every time when the accumulated maximum absolute deformation in $\mathcal{B}$ is greater than a certain fraction r_{mesh} of the smallest FE cell size. Because of the auxiliary mesh-motion nature of the above BVP its numerical solution does not need to be very accurate. Thus, an adaption of $\mathcal{B}'_t$ just to avoid self-penetration is sufficient. Hence, one or two Newton iterations already do the job in most cases.

B.2. The magneto-electric correction step

Since we may update φ_h in $\mathcal{B}'$ between Newton iterations for the MEM BVP, we need to account for the resulting perturbation of the magneto- and electrostatics states in $\mathcal{B}'_t$. We do so by solving the linearized MEM system only for $\Delta\underline{v} = \mathcal{P}_{\text{ME}}[\Delta\underline{s}]$ before returning to the full MEM problem. In our experience, this was sufficient for the Newton solver of the fully coupled problem to converge at an acceptable rate. This works exactly the

same for all formulations (and subsets) of magneto-electro-statics.

B.3. The complete algorithm

Algorithm 1 summarizes the procedure described above. The mesh motion criterion c_{mesh} (lines 5 and 6) can of course be replaced by some other appropriate indicator. Moreover, the mesh-motion and correction steps (lines 5 to 12) are "postprocessing" steps in the sense that they are independent of how the solution increments $\Delta\underline{s}$ are actually computed. Thus, the mesh update procedure is not restricted to Newton-Raphson schemes.

```
1  c_mesh ← 0 ;
2  while ||r(s)|| > tol do
3  |   solve K(s) · Δs = r(s) with P_φ[Δs]|_B' = 0 ;
4  |   s ← s + Δs ;
5  |   c_mesh ← c_mesh + ||Δs||_∞ ;
6  |   if c_mesh/r_mesh > min(size(FE cells)) then
7  |   |   c_mesh ← 0 ;
8  |   |   solve mesh-motion problem (B.3) for w = D[ξ̂];
9  |   |   P_φ[s]|_B' ← P_φ[w]|_B' ;
10 |   |   solve P_ME[K(s)] · Δv = P_ME[r(s)] for ME correction Δv;
11 |   |   P_ME[s] ← P_ME[s] + Δv ;
12 |   end
13 end
```

Algorithm 1: Newton-Raphson scheme with embedded algorithm for separate mesh motion step

Appendix C

Adjoint sensitivity analysis

In Chapters 8, 9 and 10 we employ adjoint sensitivity analysis to characterize magneto-electric sensitivities, i.e. the sensitivity of e with respect to h^∞ under equilibrium. Below we describe the general procedure. For this purpose we consider an abstract quantity of interest (QOI) α. The QOI α is function $\alpha(u, \beta)$ where u is some field like the deformation map φ or a collection of fields. We shall refer to it as "state". The variable "β" denotes either a single *control variable* or the set of control variables. An example for β would be the set of prescribed values φ_{D} for φ or an external field like $\boldsymbol{b}^\infty$. Then there also is some constraint $G(u; \beta) = 0$, usually governing physical equations, such that the *admissible* state $\hat{u} = u(\beta)$ where $\hat{u}$ is a solution of the constraint G for given β. Based on that we introduce a Lagrangian-type function

$$\alpha^+(u, \beta, \lambda) := \alpha(u, \beta) - \lambda G(u; \beta) \tag{C.1}$$

with λ being a Lagrange multiplier enforcing the equilibrium condition G. Alternatively, if G is a weak form $G(u, \delta u; \beta)$ of the (physical) constraints we write

$$\alpha^+(u, \beta, \lambda) := \alpha(u, \beta) - G(u, \delta u = \lambda; \beta). \tag{C.2}$$

In what follows we will work with version (C.2) since this is what directly maps to finite element solutions of the physical constraint (BVP). At a state $u = \hat{u}(\beta)$ we have $G(\hat{u}(\beta), \lambda, \beta) = 0$ and thus $\alpha^+(\hat{u}(\beta), \beta, \lambda) = \alpha(\hat{u}(\beta), \beta)$. Moreover, since $G(\hat{u}(\beta), \lambda, \beta) = 0$ it holds that $\partial\alpha^+(\hat{u}(\beta), \beta, \lambda)/\partial\lambda = 0$. Hence, we introduce $\hat{\alpha}^+(\beta) := \alpha^+(\hat{u}(\beta), \beta)$ which is independent of λ and evaluates to the same value as $\hat{\alpha}(\beta) := \alpha(\hat{u}(\beta), \beta)$.

The sensitivity we are looking for is the total derivative of α with respect to β under condition that the physical constraint is fulfilled. Let us compute the (total) differential of α^+

$$\mathrm{d}\alpha^+ = \frac{\partial\alpha}{\partial u}\,\mathrm{d}u + \frac{\partial\alpha}{\partial\beta}\,\mathrm{d}\beta - \frac{\partial G}{\partial u}\,\mathrm{d}u - \frac{\partial G}{\partial\beta}\,\mathrm{d}\beta - G(u, \delta u = \mathrm{d}\lambda; \beta) \tag{C.3}$$

with

$$G(u, \delta u = \mathrm{d}\lambda; \beta) = \frac{\partial G(u, \delta u = \lambda; \beta)}{\partial\lambda}\,\mathrm{d}\lambda. \tag{C.4}$$

If we in this linearized setting[1] manage to find a function $\hat{\alpha} = \hat{\alpha}(\beta)$ such that $\mathrm{d}\hat{\alpha} = \frac{\mathrm{d}\hat{\alpha}}{\mathrm{d}\beta}\,\mathrm{d}\beta$ or, equivalently, $\mathrm{d}\hat{\alpha}^+ = \frac{\mathrm{d}\hat{\alpha}^+}{\mathrm{d}\beta}\,\mathrm{d}\beta$ we actually find the desired sensitivity, i.e. $\frac{\mathrm{d}\hat{\alpha}(\beta)}{\mathrm{d}\beta}$. This is achieved by collecting the "components" of $\mathrm{d}u$ and $\mathrm{d}\lambda$ in (C.3) and finding u and λ such that all of these components vanish, i.e.

$$G(u, \delta u = \mathrm{d}\lambda; \beta) = 0 \qquad \Rightarrow \qquad \hat{u} \tag{C.5a}$$

and

$$\frac{\partial \alpha(u,\beta)}{\partial u}\,\mathrm{d}u - \frac{\partial G(u, \delta u = \lambda; \beta)}{\partial u}\,\mathrm{d}u = 0 \qquad \Rightarrow \qquad \hat{\lambda}. \tag{C.5b}$$

The first equation above is simply the requirement for a physically admissible state $\hat{u}(\beta)$. The second is an equation for λ with solution $\hat{\lambda}$ where we note that λ is in place of the test function δu and $\mathrm{d}u$, in place of the (incremental) solution Δu, has now the character of a test function. Thus, the linear operator (the matrix) in the system of equations for λ is the adjoint (Marsden and Hughes, 1994) of the operator encountered when solving for Δu, i.e.

$$\langle A\Delta u, \delta u\rangle_\delta = \langle \Delta u, A^\tau \delta u\rangle_\Delta \tag{C.6}$$

where A plays the role of $\partial G/\partial u$ and the subscripts δ and Δ indicate that δu and Δu do not need to have the same domain. Because of that we also write superscript τ instead of T for transpose, since we reserved the latter for the standard linear algebra notion (van der Giessen and Kollmann, 1996). The fact that λ replaces test functions also means that it has to respect the essential boundary conditions imposed on them, which are homogeneous in general.

To conclude this discussion we give the final expression for the sensitivity of the QOI α with respect tothe control variable β under consideration of physical constraints G

$$\mathrm{d}\hat{\alpha} = \frac{\mathrm{d}\hat{\alpha}}{\mathrm{d}\beta}\,\mathrm{d}\beta = \mathrm{d}\alpha^+(\hat{u}, \beta, \hat{\lambda}) = \left(\frac{\partial \alpha(\hat{u},\beta)}{\partial \beta} - \frac{\partial G(\hat{u}, \delta u = \hat{\lambda}; \beta)}{\partial \beta}\right)\mathrm{d}\beta. \tag{C.7}$$

[1] Recall the discussion of the differential of a function in Section 4.1.2.

Appendix D

Notes on software for scientific writing and computing

During the past couple of years I used a range software packages and libraries for numerical simulations, pre- and post-processing. The results presented in this Thesis have been obtained by `FEAP` (Taylor, 2014), `FEniCS` (Logg et al., 2012; Alnæs et al., 2015) and the python libraries `numpy` (Oliphant, 2006; van der Walt et al., 2011) and `scipy` (Virtanen et al., 2020). Mesh generation has been done with `Gmsh` (Geuzaine and Remacle, 2009) in combination with `meshio` (Schlömer, 2019a) and `pygmsh` (Schlömer, 2019b) Postprocessing has mainly been done with `Paraview`, `pandas` (McKinney, 2010) and `matplotlib` (Hunter, 2007).

The text production and typesetting was done with the `TeXLive` LaTeXdistribution, `Kile` and `TeXstudio`. Figures have been created and edited with inkscape.

Besides these powerful tools I used `IPython` (Perez and Granger, 2007) combined with `Jupyter` on an almost daily basis. All on top of several GNU/Linux-powered workstations.

List of Figures

List of Tables

List of Boxes

Bibliography

Abdulle, A., Weinan, E., Engquist, B., Vanden-Eijnden, E., 2012. The heterogeneous multiscale method. Acta Numerica 21, 1–87. doi:10.1017/S0962492912000025.

Aharonov, Y., Bohm, D., 1959. Significance of Electromagnetic Potentials in the Quantum Theory. Physical Review 115, 485–491. doi:10.1103/PhysRev.115.485.

Alameh, Z., Deng, Q., Liu, L., Sharma, P., 2015. Using electrets to design concurrent magnetoelectricity and piezoelectricity in soft materials. Journal of Materials Research 30, 93–100. doi:10.1557/jmr.2014.331.

Alfeld, P., 1984. A trivariate Clough-Tocher scheme for tetrahedral data. Computer Aided Geometric Design 1, 169–181. doi:10.1016/0167-8396(84)90029-3.

Alnæs, M.S., Blechta, J., Hake, J., Johansson, A., Kehlet, B., Logg, A., Richardson, C., Ring, J., Rognes, M.E., Wells, G.N., 2015. The FEniCS Project Version 1.5. Archive of Numerical Software 3, 9–23.

Alzetta, G., Arndt, D., Bangerth, W., Boddu, V., Brands, B., Davydov, D., Gassmoeller, R., Heister, T., Heltai, L., Kormann, K., Kronbichler, M., Maier, M., Pelteret, J.P., Turcksin, B., Wells, D., 2018. The `deal.II` library, version 9.0. Journal of Numerical Mathematics 26, 173–183. doi:10.1515/jnma-2018-0054.

Amestoy, P.R., Duff, I.S., Koster, J., L'Excellent, J.Y., 2001. A fully asynchronous multifrontal solver using distributed dynamic scheduling. SIAM Journal on Matrix Analysis and Applications 23, 15–41.

Amestoy, P.R., Guermouche, A., L'Excellent, J.Y., Pralet, S., 2006. Hybrid scheduling for the parallel solution of linear systems. Parallel Computing 32, 136–156.

Arnold, D.N., Falk, R.S., Winther, R., 2006. Finite element exterior calculus, homological techniques, and applications. Acta Numerica 15, 1–155. doi:10.1017/S0962492906210018.

Arnold, D.N., Logg, A., 2014. Periodic Table of the Finite Elements. SIAM News 47.

Babuška, I., Strouboulis, T., Upadhyay, C.S., Gangaraj, S.K., 1995. A posteriori estimation and adaptive control of the pollution error in theh-version of the finite element method. International Journal for Numerical Methods in Engineering 38, 4207–4235. doi:10.1002/nme.1620382408.

Bangerth, W., Hartmann, R., Kanschat, G., 2007. deal.II – a general purpose object oriented finite element library. ACM Trans. Math. Softw. 33, 24/1–24/27. doi:10.1145/1268776.1268779.

Bednarek, S., 1999. The giant magnetostriction in ferromagnetic composites within an elastomer matrix. Applied Physics A 68, 63–67. doi:10.1007/s003390050854.

Berbenni, S., Taupin, V., Djaka, K.S., Fressengeas, C., 2014. A numerical spectral approach for solving elasto-static field dislocation and g-disclination mechanics. International Journal of Solids and Structures 51, 4157–4175. doi:10.1016/j.ijsolstr.2014.08.009.

Bessa, M.A., Bostanabad, R., Liu, Z., Hu, A., Apley, D.W., Brinson, C., Chen, W., Liu, W.K., 2017. A framework for data-driven analysis of materials under uncertainty: Countering the curse of dimensionality. Computer Methods in Applied Mechanics and Engineering 320, 633–667. doi:10.1016/j.cma.2017.03.037.

Bhattacharjee, S., Matouš, K., 2016. A nonlinear manifold-based reduced order model for multiscale analysis of heterogeneous hyperelastic materials. Journal of Computational Physics 313, 635–653. doi:10.1016/j.jcp.2016.01.040.

Bibes, M., Barthélémy, A., 2008. Multiferroics: Towards a magnetoelectric memory. Nature Materials 7, 425–426. doi:10.1038/nmat2189.

Birkeland, K., 1894. Ueber die Strahlung electromagnetischer Energie im Raume. Annalen der Physik 288, 357–380. doi:10.1002/andp.18942880608.

Biro, O., Preis, K., Richter, K.R., 1996. On the use of the magnetic vector potential in the nodal and edge finite element analysis of 3d magnetostatic problems. IEEE Transactions on Magnetics 32, 651–654. doi:10.1109/20.497322.

Blatt, M., Burchardt, A., Dedner, A., Engwer, C., Fahlke, J., Flemisch, B., Gersbacher, C., Gräser, C., Gruber, F., Grüninger, C., Kempf, D., Klöfkorn, R., Malkmus, T., Müthing, S., Nolte, M., Piatkowski, M., Sander, O., 2016. The Distributed and Unified Numerics Environment, Version 2.4. Archive of Numerical Software Vol 4, Starting Point and Frequency: Year: 2013 . doi:10.11588/ans.2016.100.26526.

Blum, H., Rannacher, R., 1987. Extrapolation techniques for reducing the pollution effect or reentrant corners in the finite element method. Numerische Mathematik 52, 539–564. doi:10.1007/BF01400891.

Boczkowska, A., Awietjan, S., 2012. Microstructure and Properties of Magnetorheological Elastomers, in: Boczkowska, A. (Ed.), Advanced Elastomers - Technology, Properties and Applications. InTech. doi:10.5772/50430.

Bodelot, L., Voropaieff, J.P., Pössinger, T., 2018. Experimental investigation of the coupled magneto-mechanical response in magnetorheological elastomers. Experimental Mechanics 58, 207–221. doi:10.1007/s11340-017-0334-7.

de Boer, R., 1982. Vektor-und Tensorrechnung für Ingenieure. Springer.

Boffi, D., Brezzi, F., Fortin, M., 2013. Mixed Finite Element Methods and Applications. volume 44 of *Springer Series in Computational Mathematics*. Springer Berlin Heidelberg, Berlin, Heidelberg. doi:10.1007/978-3-642-36519-5.

Bonet, J., Gil, A.J., Ortigosa, R., 2015. A computational framework for polyconvex large strain elasticity. Computer Methods in Applied Mechanics and Engineering 283, 1061–1094. doi:10.1016/j.cma.2014.10.002.

Bonet, J., Wood, R.D., 2008. Nonlinear continuum mechanics for finite element analysis. 2nd ed., Cambridge University Press, Cambridge, UK; New York.

Böse, H., Rabindranath, R., Ehrlich, J., 2012. Soft magnetorheological elastomers as new actuators for valves , Soft magnetorheological elastomers as new actuators for valves. Journal of Intelligent Material Systems and Structures 23, 989–994. doi:10.1177/1045389X11433498.

Böse, H., Röder, R., 2009. Magnetorheological elastomers with high variability of their mechanical properties. Journal of Physics: Conference Series 149, 012090. doi:10.1088/1742-6596/149/1/012090.

Bossavit, A., 1998a. Computational Electromagnetism: Variational Formulations, Complementarity, Edge Elements. Academic Press.

Bossavit, A., 1998b. On the geometry of electromagnetism : (4): Maxwell's house. Journal of the Japan Society of Applied Electromagnetics 6, 318–326.

Bossavit, A., 2010. Discrete Magneto-Elasticity: A Geometrical Approach. IEEE Transactions on Magnetics 46, 3485–3491. doi:10.1109/TMAG.2010.2043346.

Bossavit, A., 2012. The premetric approach to electromagnetism in the 'waves are not vectors' debate. Advanced Electromagnetics 1, 97–102. doi:10.7716/aem.v1i1.66.

Bossavit, A., 2016. A note on the uniqueness of the Poynting vector and of the Maxwell tensor. International Journal of Numerical Modelling: Electronic Networks, Devices and Fields , n/a–n/adoi:10.1002/jnm.2214.

Brandstetter, G., 2015. A High-order Eulerian-Lagrangian Finite Element Method for Coupled Electro-mechanical Systems. Ph.D. thesis. UC Berkeley.

Brandstetter, G., Govindjee, S., 2015. A high-order immersed boundary discontinuous-Galerkin method for Poisson's equation with discontinuous coefficients and singular sources. International Journal for Numerical Methods in Engineering 101, 847–869. doi:10.1002/nme.4835.

Brenner, R., 2010. Computational approach for composite materials with coupled constitutive laws. Zeitschrift für angewandte Mathematik und Physik 61, 919–927. doi:10.1007/s00033-009-0045-8.

Brezzi, F., 1974. On the Existence, Uniqueness and Approximation of Saddle-Point Problems Arising from Lagrangian Multipliers. Publications mathématiques et informatique de Rennes S4, 1–26.

Brezzi, F., Douglas, J., Marini, L.D., 1985. Two families of mixed finite elements for second order elliptic problems. Numerische Mathematik 47, 217–235. doi:10.1007/BF01389710.

Brezzi, F., Fortin, M., 1991. Mixed and hybrid finite element methods. Number 15 in Springer series in computational mathematics, Springer-Verlag, New York.

Briggs, W.L., Henson, V.E., McCormick, S.F., 2000. A multigrid tutorial. 2. ed ed., SIAM, Philadelphia, Pa. OCLC: 247480475.

Brisard, S., Dormieux, L., 2010. FFT-based methods for the mechanics of composites: A general variational framework. Computational Materials Science 49, 663–671. doi:10.1016/j.commatsci.2010.06.009.

Brisard, S., Dormieux, L., 2012. Combining Galerkin approximation techniques with the principle of Hashin and Shtrikman to derive a new FFT-based numerical method for the homogenization of composites. Computer Methods in Applied Mechanics and Engineering 217-220, 197–212. doi:10.1016/j.cma.2012.01.003.

Brown, W.F.J., 1966. Magnetoelastic Interactions. Springer Tracts in Natural Philosophy, Springer-Verlag, Berlin Heidelberg.

Burke, W.L., 1996. Applied differential geometry. Reprinted ed., Cambridge: Cambridge Univ. Press. OCLC: 258055797.

Bustamante, R., 2009. Mathematical modelling of boundary conditions for magneto-sensitive elastomers: variational formulations. Journal of Engineering Mathematics 64, 285–301. doi:10.1007/s10665-008-9263-x.

Bustamante, R., Dorfmann, A., Ogden, R., 2008. On Variational Formulations in Nonlinear Magnetoelastostatics. Mathematics and Mechanics of Solids 13, 725–745. doi:10.1177/1081286507079832.

Bustamante, R., Dorfmann, A., Ogden, R.W., 2009a. Nonlinear electroelastostatics: a variational framework. Zeitschrift für angewandte Mathematik und Physik 60, 154–177. doi:10.1007/s00033-007-7145-0.

Bustamante, R., Dorfmann, A., Ogden, R.W., 2009b. On electric body forces and Maxwell stresses in nonlinearly electroelastic solids. International Journal of Engineering Science 47, 1131–1141. doi:10.1016/j.ijengsci.2008.10.010.

Bustamante, R., Dorfmann, A., Ogden, R.W., 2011. Numerical solution of finite geometry boundary-value problems in nonlinear magnetoelasticity. International Journal of Solids and Structures 48, 874–883. doi:10.1016/j.ijsolstr.2010.11.021.

Carrol, S., 2019. Lecture Notes on General Relativity. URL: https://ned.ipac.caltech.edu/level5/March01/Carroll3/Carroll5.html.

Chen, Q., Konrad, A., 1997. A review of finite element open boundary techniques for static and quasi-static electromagnetic field problems. IEEE Transactions on Magnetics 33, 663–676.

doi:10.1109/20.560095.

Crane, K., de Goes, F., Desbrun, M., Schröder, P., 2013. Digital Geometry Processing with Discrete Exterior Calculus, in: ACM SIGGRAPH 2013 Courses, ACM, New York, NY, USA. pp. 7:1–7:126. doi:10.1145/2504435.2504442. event-place: Anaheim, California.

Danas, K., 2017. Effective response of classical, auxetic and chiral magnetoelastic materials by use of a new variational principle. Journal of the Mechanics and Physics of Solids 105, 25–53. doi:10.1016/j.jmps.2017.04.016.

Danas, K., Kankanala, S.V., Triantafyllidis, N., 2012. Experiments and modeling of iron-particle-filled magnetorheological elastomers. Journal of the Mechanics and Physics of Solids 60, 120–138. doi:10.1016/j.jmps.2011.09.006.

Desbrun, M., Hirani, A.N., Marsden, J.E., 2003. Discrete exterior calculus for variational problems in computer vision and graphics, in: 42nd IEEE International Conference on Decision and Control (IEEE Cat. No.03CH37475), pp. 4902–4907 Vol.5. doi:10.1109/CDC.2003.1272393.

Diguet, G., Beaugnon, E., Cavaillé, J., 2010. Shape effect in the magnetostriction of ferromagnetic composite. Journal of Magnetism and Magnetic Materials 322, 3337–3341. doi:10.1016/j.jmmm.2010.06.020.

Dorfmann, A., Brigadnov, I.A., 2004. Constitutive modelling of magneto-sensitive Cauchy-elastic solids. Computational Materials Science 29, 270–282. doi:10.1016/j.commatsci.2003.10.004.

Dorfmann, A., Ogden, R.W., 2003. Magnetoelastic modelling of elastomers. European Journal of Mechanics-A/Solids 22, 497–507. doi:10.1007/s00707-003-0061-2.

Dorfmann, A., Ogden, R.W., 2005. Nonlinear electroelasticity. Acta Mechanica 174, 167–183. doi:10.1007/s00707-004-0202-2.

Dorfmann, A., Ogden, R.W., 2006. Nonlinear Electroelastic Deformations. Journal of Elasticity 82, 99–127. doi:10.1007/s10659-005-9028-y.

Doyle, T.C., Ericksen, J.L., 1956. Nonlinear Elasticity, in: Dryden, H.L., von Kármán, T. (Eds.), Advances in Applied Mechanics. Elsevier. volume 4, pp. 53–115. doi:10.1016/S0065-2156(08)70371-5.

Drugan, W.J., Willis, J.R., 1996. A micromechanics-based nonlocal constitutive equation and estimates of representative volume element size for elastic composites. Journal of the Mechanics and Physics of Solids 44, 497–524. doi:10.1016/0022-5096(96)00007-5.

Engquist, B., Souganidis, P.E., 2008. Asymptotic and numerical homogenization. Acta Numerica 17, 147–190. doi:10.1017/S0962492906360011.

Epstein, M., 2010. The Geometrical Language of Continuum Mechanics. Cambridge University Press.

Ericksen, J.L., 2006. A Modified Theory of Magnetic Effects in Elastic Materials. Mathematics and Mechanics of Solids 11, 23–47. doi:10.1177/1081286505055530.

Ericksen, J.L., 2007. Theory of Elastic Dielectrics Revisited. Archive for Rational Mechanics and Analysis 183, 299–313. doi:10.1007/s00205-006-0042-4.

Eringen, A.C., 1976. Polar and nonlocal field theories. volume 4 of *Continuum physics*. Academic Press, New York.

Eringen, A.C., Maugin, G.A., 1990. Electrodynamics of Continua I: Foundations and Solid Media. Springer-Verlag, New York.

Eshelby, J.D., Peierls, R.E., 1957. The determination of the elastic field of an ellipsoidal inclusion, and related problems. Proceedings of the Royal Society of London. Series A. Mathematical and Physical Sciences 241, 376–396. doi:10.1098/rspa.1957.0133.

Ethiraj, G., Sridhar, A., Miehe, C., 2015. Variational modeling and homogenization in dissipative

magneto-mechanics. GAMM-Mitteilungen 38, 75–101. doi:10.1002/gamm.201510004.

Eyre, D., Milton, G., 1999. A fast numerical scheme for computing the response of composites using grid refinement. The European Physical Journal 6, 41–47. doi:10.1051/epjap:1999150.

Fetisov, Y.K., Bush, A.A., Kamentsev, K.E., Ostashchenko, A.Y., Srinivasan, G., 2006. Ferrite-Piezoelectric Multilayers for Magnetic Field Sensors. IEEE Sensors Journal 6, 935–938. doi:10.1109/JSEN.2006.877989.

Feyel, F., Chaboche, J.L., 2000. FE^2 multiscale approach for modelling the elastoviscoplastic behaviour of long fibre SiC/Ti composite materials. Computer Methods in Applied Mechanics and Engineering 183, 309–330. doi:10.1016/S0045-7825(99)00224-8.

Feynman, R.P., Leighton, R.B., Sands, M., 2011. The Feynman Lectures on Physics, Vol. II: The New Millennium Edition: Mainly Electromagnetism and Matter. Basic Books.

Fiebig, M., 2005. Revival of the magnetoelectric effect. Journal of Physics D: Applied Physics 38, R123. doi:10.1088/0022-3727/38/8/R01.

Forest, S., 1998. Mechanics of generalized continua: construction by homogenizaton. Le Journal de Physique IV 08, Pr4–39–Pr4–48. doi:10.1051/jp4:1998405.

Forest, S., Trinh, D., 2011. Generalized continua and non-homogeneous boundary conditions in homogenisation methods. ZAMM - Journal of Applied Mathematics and Mechanics / Zeitschrift für Angewandte Mathematik und Mechanik 91, 90–109. doi:10.1002/zamm.201000109.

Frankel, T., 2011. The Geometry of Physics: An Introduction. Cambridge University Press.

Fritzen, F., Kunc, O., 2018. Two-stage data-driven homogenization for nonlinear solids using a reduced order model. European Journal of Mechanics - A/Solids 69, 201–220. doi:10.1016/j.euromechsol.2017.11.007.

Fritzen, F., Leuschner, M., 2013. Reduced basis hybrid computational homogenization based on a mixed incremental formulation. Computer Methods in Applied Mechanics and Engineering 260, 143–154. doi:10.1016/j.cma.2013.03.007.

Fritzen, F., Leuschner, M., 2015. Nonlinear reduced order homogenization of materials including cohesive interfaces. Computational Mechanics 56, 131–151. doi:10.1007/s00466-015-1163-0.

Galipeau, E., Ponte Castañeda, P., 2012. The effect of particle shape and distribution on the macroscopic behavior of magnetoelastic composites. International Journal of Solids and Structures 49, 1–17. doi:10.1016/j.ijsolstr.2011.08.014.

Galipeau, E., Ponte Castañeda, P., 2013a. A finite-strain constitutive model for magnetorheological elastomers: Magnetic torques and fiber rotations. Journal of the Mechanics and Physics of Solids 61, 1065–1090. doi:10.1016/j.jmps.2012.11.007.

Galipeau, E., Ponte Castañeda, P., 2013b. Giant field-induced strains in magnetoactive elastomer composites. Proceedings of the Royal Society A 469, 20130385. doi:10.1098/rspa.2013.0385.

Galipeau, E., Rudykh, S., deBotton, G., Ponte Castañeda, P., 2014. Magnetoactive elastomers with periodic and random microstructures. International Journal of Solids and Structures 51, 3012–3024. doi:10.1016/j.ijsolstr.2014.04.013.

Gallone, G., Carpi, F., De Rossi, D., Levita, G., Marchetti, A., 2007. Dielectric constant enhancement in a silicone elastomer filled with lead magnesium niobate–lead titanate. Materials Science and Engineering: C 27, 110–116. doi:10.1016/j.msec.2006.03.003.

Gambin, B., Kröner, E., 1989. Higher-Order Terms in the Homogenized Stress-Strain Relation of Periodic Elastic Media. physica status solidi (b) 151, 513–519. doi:10.1002/pssb.2221510211.

de Geus, T.W.J., Vondřejc, J., Zeman, J., Peerlings, R.H.J., Geers, M.G.D., 2017. Finite strain FFT-based non-linear solvers made simple. Computer Methods in Applied Mechanics and Engineering 318, 412–430. doi:10.1016/j.cma.2016.12.032.

Geuzaine, C., Remacle, J.F., 2009. Gmsh: A 3-D finite element mesh generator with built-in pre- and post-processing facilities. International Journal for Numerical Methods in Engineering 79, 1309–1331. doi:10.1002/nme.2579.

van der Giessen, E., Kollmann, F.G., 1996. On Mathematical Aspects of Dual Variables in Continuum Mechanics. Part 1: Mathematical Principles. ZAMM - Journal of Applied Mathematics and Mechanics / Zeitschrift für Angewandte Mathematik und Mechanik 76, 447–462. doi:10.1002/zamm.19960760807.

Gil, A.J., Ortigosa, R., 2016. A new framework for large strain electromechanics based on convex multi-variable strain energies: Variational formulation and material characterisation. Computer Methods in Applied Mechanics and Engineering 302, 293–328. doi:10.1016/j.cma.2015.11.036.

Göküzüm, F.S., Keip, M.A., 2018. An Algorithmically Consistent Macroscopic Tangent Operator for FFT-based Computational Homogenization. International Journal for Numerical Methods in Engineering 113, 581–600. doi:10.1002/nme.5627.

Goshkoderia, A., Rudykh, S., 2017. Stability of magnetoactive composites with periodic microstructures undergoing finite strains in the presence of a magnetic field. Composites Part B: Engineering 128, 19–29. doi:10.1016/j.compositesb.2017.06.014.

Green, A.E., Rivlin, R.S., 1964. On cauchy's equations of motion. Zeitschrift für angewandte Mathematik und Physik ZAMP 15, 290–292. doi:10.1007/BF01607019.

Gélébart, L., Mondon-Cancel, R., 2013. Non-linear extension of FFT-based methods accelerated by conjugate gradients to evaluate the mechanical behavior of composite materials. Computational Materials Science 77, 430–439. doi:10.1016/j.commatsci.2013.04.046.

Göküzüm, F.S., Nguyen, L.T.K., Keip, M.A., 2019. A multiscale FE-FFT framework for electroactive materials at finite strains. Computational Mechanics doi:10.1007/s00466-018-1657-7.

Hackbusch, W., 1994. Iterative Solution of Large Sparse Systems of Equations. volume 95 of *Applied Mathematical Sciences*. Springer New York, New York, NY. doi:10.1007/978-1-4612-4288-8.

Harland, B., Brownell, W.E., Spector, A.A., Sun, S.X., 2010. Voltage-induced bending and electromechanical coupling in lipid bilayers. Physical Review E 81, 031907. doi:10.1103/PhysRevE.81.031907.

Harsch, J., 2017a. A portable FE implementation of a ductile phase-field fracture model in crystal plasticity. Student project. University of Stuttgart, Institute of Applied Mechanics.

Harsch, J., 2017b. Programming Guidelines and Class Design for Material Model Subroutine. Student project. University of Stuttgart, Institute of Applied Mechanics.

Hashin, Z., Shtrikman, S., 1962a. On some variational principles in anisotropic and nonhomogeneous elasticity. Journal of the Mechanics and Physics of Solids 10, 335–342. doi:10.1016/0022-5096(62)90004-2.

Hashin, Z., Shtrikman, S., 1962b. A Variational Approach to the Theory of the Effective Magnetic Permeability of Multiphase Materials. Journal of Applied Physics 33, 3125–3131. doi:10.1063/1.1728579.

Hashin, Z., Shtrikman, S., 1962c. A variational approach to the theory of the elastic behaviour of polycrystals. Journal of the Mechanics and Physics of Solids 10, 343–352. doi:10.1016/0022-5096(62)90005-4.

Hashin, Z., Shtrikman, S., 1963. A variational approach to the theory of the elastic behaviour of multiphase materials. Journal of the Mechanics and Physics of Solids 11, 127–140. doi:10.1016/0022-5096(63)90060-7.

Hestenes, M., Stiefel, E., 1952. Methods of conjugate gradients for solving linear systems. Journal of Research of the National Bureau of Standards 49, 409. doi:10.6028/jres.049.044.

Hill, R., 1952. The Elastic Behaviour of a Crystalline Aggregate. Proceedings of the Physical Society. Section A 65, 349. doi:10.1088/0370-1298/65/5/307.

Hill, R., 1963. Elastic properties of reinforced solids: Some theoretical principles. Journal of the Mechanics and Physics of Solids 11, 357–372. doi:10.1016/0022-5096(63)90036-X.

Hill, R., 1964. Theory of mechanical properties of fibre-strengthened materials: I. Elastic behaviour. Journal of the Mechanics and Physics of Solids 12, 199–212. doi:10.1016/0022-5096(64)90019-5.

Hill, R., 1965a. Continuum micro-mechanics of elastoplastic polycrystals. Journal of the Mechanics and Physics of Solids 13, 89–101. doi:10.1016/0022-5096(65)90023-2.

Hill, R., 1965b. A self-consistent mechanics of composite materials. Journal of the Mechanics and Physics of Solids 13, 213–222. doi:10.1016/0022-5096(65)90010-4.

Hiptmair, R., 1998. Multigrid Method for Maxwell's Equations. SIAM Journal on Numerical Analysis 36, 204–225. doi:10.1137/S0036142997326203.

Hiptmair, R., 2002. Finite elements in computational electromagnetism. Acta Numerica 11, 237–339. doi:10.1017/S0962492902000041.

Hiptmair, R., Xu, J., 2007. Nodal Auxiliary Space Preconditioning in H(curl) and H(div) Spaces. SIAM Journal on Numerical Analysis 45, 2483–2509. doi:10.1137/060660588.

Hirani, A.N., 2003. Discrete exterior calculus. phd. California Institute of Technology.

Hirani, A.N., Nakshatrala, K.B., Chaudhry, J.H., 2015. Numerical Method for Darcy Flow Derived Using Discrete Exterior Calculus. International Journal for Computational Methods in Engineering Science and Mechanics 16, 151–169. doi:10.1080/15502287.2014.977500.

Holland, R.A., Thorup, K., Vonhof, M.J., Cochran, W.W., Wikelski, M., 2006. Navigation: Bat orientation using Earth's magnetic field. Nature 444, 702–702. doi:10.1038/444702a.

Holzapfel, G.A., 2000. Nonlinear solid mechanics: a continuum approach for engineering. Wiley, Chichester (New York).

Hou, T.Y., Wu, X.H., 1997. A Multiscale Finite Element Method for Elliptic Problems in Composite Materials and Porous Media. Journal of Computational Physics 134, 169–189. doi:10.1006/jcph.1997.5682.

Hughes, T.J.R., Feijóo, G.R., Mazzei, L., Quincy, J.B., 1998. The variational multiscale method—a paradigm for computational mechanics. Computer Methods in Applied Mechanics and Engineering 166, 3–24. doi:10.1016/S0045-7825(98)00079-6.

Hunter, J.D., 2007. Matplotlib: A 2D Graphics Environment. Computing in Science & Engineering 9, 90–95. doi:10.1109/MCSE.2007.55.

Hussein, M.I., Leamy, M.J., Ruzzene, M., 2014. Dynamics of Phononic Materials and Structures: Historical Origins, Recent Progress, and Future Outlook. Applied Mechanics Reviews 66, 040802–040802–38. doi:10.1115/1.4026911.

Ivaneyko, D., Toshchevikov, V., Saphiannikova, M., Heinrich, G., 2014. Mechanical properties of magneto-sensitive elastomers: unification of the continuum-mechanics and microscopic theoretical approaches. Soft Matter 10, 2213–2225. doi:10.1039/C3SM52440J.

James, R.D., Kinderlehrer, D., 1993. Theory of magnetostriction with applications to $Tb_xDy_{1-x}Fe_2$. Philosophical Magazine Part B 68, 237–274. doi:10.1080/01418639308226405.

Javili, A., Chatzigeorgiou, G., Steinmann, P., 2013. Computational homogenization in magneto-mechanics. International Journal of Solids and Structures 50, 4197–4216. doi:10.1016/j.ijsolstr.2013.08.024.

Jolly, M.R., Carlson, J.D., Muñoz, B.C., 1996. A model of the behaviour of magnetorheological materials. Smart Materials and Structures 5, 607–614. doi:10.1088/0964-1726/5/5/009.

Kabel, M., Böhlke, T., Schneider, M., 2014. Efficient fixed point and Newton-Krylov solvers for

FFT-based homogenization of elasticity at large deformations. Computational Mechanics 54, 1497–1514. doi:10.1007/s00466-014-1071-8.

Kalina, K.A., Brummund, J., Metsch, P., Kästner, M., Borin, D.Y., Linke, J.M., Odenbach, S., 2017. Modeling of magnetic hystereses in soft MREs filled with NdFeB particles. Smart Materials and Structures 26, 105019. doi:10.1088/1361-665X/aa7f81.

Kalina, K.A., Metsch, P., Kästner, M., 2016. Microscale modeling and simulation of magnetorheological elastomers at finite strains: A study on the influence of mechanical preloads. International Journal of Solids and Structures 102–103, 286–296. doi:10.1016/j.ijsolstr.2016.10.019.

Kallio, M., 2005. The elastic and damping properties of magnetorheological elastomers. Ph.D. thesis. Tampere University of Technology. VTT Technical Research Centre of Finland, Vuorimiehentie 5, P.O.Box 2000, FI–02044 VTT, Finland.

Kankanala, S.V., Triantafyllidis, N., 2004. On finitely strained magnetorheological elastomers. Journal of the Mechanics and Physics of Solids 52, 2869–2908. doi:10.1016/j.jmps.2004.04.007.

Kankanala, S.V., Triantafyllidis, N., 2008. Magnetoelastic buckling of a rectangular block in plane strain. Journal of the Mechanics and Physics of Solids 56, 1147–1169. doi:10.1016/j.jmps.2007.10.008.

Kanso, E., Arroyo, M., Tong, Y., Yavari, A., Marsden, J.G., Desbrun, M., 2007. On the geometric character of stress in continuum mechanics. Zeitschrift für angewandte Mathematik und Physik 58, 843–856. doi:10.1007/s00033-007-6141-8.

Keip, M.A., Rambausek, M., 2016. A multiscale approach to the computational characterization of magnetorheological elastomers. International Journal for Numerical Methods in Engineering 107, 338–360. doi:10.1002/nme.5178.

Keip, M.A., Rambausek, M., 2017. Computational and analytical investigations of shape effects in the experimental characterization of magnetorheological elastomers. International Journal of Solids and Structures 121, 1–20. doi:10.1016/j.ijsolstr.2017.04.012.

Keip, M.A., Schrade, D., Thai, H., Schröder, J., Svendsen, B., Müller, R., Gross, D., 2015. Coordinate-invariant phase field modeling of ferro-electrics, part II: Application to composites and polycrystals. GAMM-Mitteilungen 38, 115–131. doi:10.1002/gamm.201510006.

Keip, M.A., Steinmann, P., Schröder, J., 2014. Two-scale computational homogenization of electroelasticity at finite strains. Computer Methods in Applied Mechanics and Engineering 278, 62–79. doi:10.1016/j.cma.2014.04.020.

Klusemann, B., Ortiz, M., 2015. Acceleration of material-dominated calculations via phase-space simplicial subdivision and interpolation. International Journal for Numerical Methods in Engineering 103, 256–274. doi:10.1002/nme.4887.

Kochmann, J., Wulfinghoff, S., Reese, S., Mianroodi, J.R., Svendsen, B., 2016. Two-scale FE–FFT- and phase-field-based computational modeling of bulk microstructural evolution and macroscopic material behavior. Computer Methods in Applied Mechanics and Engineering 305, 89–110. doi:10.1016/j.cma.2016.03.001.

Kouznetsova, V., Brekelmans, W.a.M., Baaijens, F.P.T., 2001. An approach to micro-macro modeling of heterogeneous materials. Computational Mechanics 27, 37–48. doi:10.1007/s004660000212.

Kouznetsova, V., Geers, M.G.D., Brekelmans, W.a.M., 2002. Multi-scale constitutive modelling of heterogeneous materials with a gradient-enhanced computational homogenization scheme. International Journal for Numerical Methods in Engineering 54, 1235–1260. doi:10.1002/nme.541.

Kouznetsova, V.G., Geers, M.G.D., Brekelmans, W.A.M., 2004. Multi-scale second-order computa-

tional homogenization of multi-phase materials: a nested finite element solution strategy. Computer Methods in Applied Mechanics and Engineering 193, 5525–5550. doi:10.1016/j.cma.2003.12.073.

Kovetz, A., 2000. Electromagnetic Theory. Oxford University Press, Oxford.

Labusch, M., Etier, M., Lupascu, D.C., Schröder, J., Keip, M.A., 2014. Product properties of a two-phase magneto-electric composite: Synthesis and numerical modeling. Computational Mechanics 54, 71–83. doi:10.1007/s00466-014-1031-3.

Labusch, M., Schröder, J., Keip, M.A., 2018. An FE^2-Scheme for Magneto-Electro-Mechanically Coupled Boundary Value Problems, in: Ferroic Functional Materials. Springer, Cham. CISM International Centre for Mechanical Sciences, pp. 227–262. doi:10.1007/978-3-319-68883-1_5.

Larsson, F., Runesson, K., 2007. RVE computations with error control and adaptivity: the power of duality. Computational Mechanics 39, 647–661. doi:10.1007/s00466-006-0108-z.

Larsson, F., Runesson, K., Su, F., 2010. Variationally consistent computational homogenization of transient heat flow. International Journal for Numerical Methods in Engineering 81, 1659–1686. doi:10.1002/nme.2747.

Le, B.A., Yvonnet, J., He, Q.C., 2015. Computational homogenization of nonlinear elastic materials using neural networks. International Journal for Numerical Methods in Engineering 104, 1061–1084. doi:10.1002/nme.4953.

Le Bellac, M., Lévy-Leblond, J.M., 1973. Galilean electromagnetism. Il Nuovo Cimento B (1971-1996) 14, 217–234. doi:10.1007/BF02895715.

Lebensohn, R.A., 2001. N-site modeling of a 3D viscoplastic polycrystal using Fast Fourier Transform. Acta Materialia 49, 2723–2737. doi:10.1016/S1359-6454(01)00172-0.

Lebensohn, R.A., Needleman, A., 2016. Numerical implementation of non-local polycrystal plasticity using fast Fourier transforms. Journal of the Mechanics and Physics of Solids 97, 333–351. doi:10.1016/j.jmps.2016.03.023.

Lee, J., Boyd, J.G., Lagoudas, D.C., 2005. Effective properties of three-phase electro-magneto-elastic composites. International Journal of Engineering Science 43, 790–825. doi:10.1016/j.ijengsci.2005.01.004.

Lefèvre, V., Danas, K., Lopez-Pamies, O., 2017. A general result for the magnetoelastic response of isotropic suspensions of iron and ferrofluid particles in rubber, with applications to spherical and cylindrical specimens. Journal of the Mechanics and Physics of Solids 107, 343–364. doi:10.1016/j.jmps.2017.06.017.

Lefèvre, V., Lopez-Pamies, O., 2017a. Nonlinear electroelastic deformations of dielectric elastomer composites: II — Non-Gaussian elastic dielectrics. Journal of the Mechanics and Physics of Solids 99, 438–470. doi:10.1016/j.jmps.2016.07.005.

Lefèvre, V., Lopez-Pamies, O., 2017b. Nonlinear electroelastic deformations of dielectric elastomer composites: I—Ideal elastic dielectrics. Journal of the Mechanics and Physics of Solids 99, 409–437. doi:10.1016/j.jmps.2016.07.004.

Leok, M., 2004. Foundations of computational geometric mechanics. phd. California Institute of Technology. doi:https://thesis.library.caltech.edu/831/10/17_chapter_six_conclusions_mleok.pdf.

Leuschner, M., Fritzen, F., 2017. Fourier-Accelerated Nodal Solvers (FANS) for homogenization problems. Computational Mechanics , 1–34doi:10.1007/s00466-017-1501-5.

Lippmann, B.A., Schwinger, J., 1950. Variational Principles for Scattering Processes. I. Physical Review 79, 469–480. doi:10.1103/PhysRev.79.469.

Liu, L., 2013. On energy formulations of electrostatics for continuum media. Journal of the Me-

chanics and Physics of Solids 61, 968–990. doi:10.1016/j.jmps.2012.12.007.

Liu, L., 2014. An energy formulation of continuum magneto-electro-elasticity with applications. Journal of the Mechanics and Physics of Solids 63, 451–480. doi:10.1016/j.jmps.2013.08.001.

Liu, L., Sharma, P., 2013. Giant and universal magnetoelectric coupling in soft materials and concomitant ramifications for materials science and biology. Physical Review E 88, 040601. doi:10.1103/PhysRevE.88.040601.

Logg, A., Mardal, K.A., Wells, G.N., others, 2012. Automated Solution of Differential Equations by the Finite Element Method. Springer. doi:10.1007/978-3-642-23099-8.

Logg, A., Wells, G.N., 2010. DOLFIN: Automated finite element computing. ACM Transactions on Mathematical Software 37, 1–28. doi:10.1145/1731022.1731030.

Mardal, K.A., Winther, R., 2011. Preconditioning discretizations of systems of partial differential equations. Numerical Linear Algebra with Applications 18, 1–40. doi:10.1002/nla.716.

Marsden, J.E., Hughes, T.J.R., 1994. Mathematical foundations of elasticity. Dover, New York.

Martin, J.E., Anderson, R.A., Odinek, J., Adolf, D., Williamson, J., 2003. Controlling percolation in field-structured particle composites: Observations of giant thermoresistance, piezoresistance, and chemiresistance. Physical Review B 67, 094207. doi:10.1103/PhysRevB.67.094207.

Martin, J.E., Anderson, R.A., Read, D., Gulley, G., 2006. Magnetostriction of field-structured magnetoelastomers. Physical Review E 74, 051507. doi:10.1103/PhysRevE.74.051507.

McKinney, W., 2010. Data Structures for Statistical Computing in Python, in: van der Walt, S., Millman, J. (Eds.), Proceedings of the 9th Python in Science Conference, pp. 51–56.

McMeeking, R.M., Landis, C.M., 2004. Electrostatic Forces and Stored Energy for Deformable Dielectric Materials. Journal of Applied Mechanics 72, 581–590. doi:10.1115/1.1940661.

McMeeking, R.M., Landis, C.M., Jimenez, S.M.A., 2007. A principle of virtual work for combined electrostatic and mechanical loading of materials. International Journal of Non-Linear Mechanics 42, 831–838. doi:10.1016/j.ijnonlinmec.2007.03.008.

Meister, A., 2015. Numerik linearer Gleichungssysteme. Springer Fachmedien Wiesbaden, Wiesbaden. doi:10.1007/978-3-658-07200-1.

Michel, J.C., Moulinec, H., Suquet, P., 2001. A computational scheme for linear and non-linear composites with arbitrary phase contrast. International Journal for Numerical Methods in Engineering 52, 139–160. doi:10.1002/nme.275.

Miehe, C., Koch, A., 2002. Computational micro-to-macro transitions of discretized microstructures undergoing small strains. Archive of Applied Mechanics 72, 300–317. doi:10.1007/s00419-002-0212-2.

Miehe, C., Schotte, J., Schröder, J., 1999. Computational micro–macro transitions and overall moduli in the analysis of polycrystals at large strains. Computational Materials Science 16, 372–382. doi:10.1016/S0927-0256(99)00080-4.

Miehe, C., Schröder, J., Schotte, J., . Computational homogenization analysis in finite plasticity Simulation of texture development in polycrystalline materials. Computer Methods in Applied Mechanics and Engineering , 387–418doi:10.1016/S0045-7825(98)00218-7.

Miehe, C., Schröder, J., Becker, M., 2002. Computational homogenization analysis in finite elasticity: material and structural instabilities on the micro- and macro-scales of periodic composites and their interaction. Computer Methods in Applied Mechanics and Engineering 191, 4971–5005. doi:10.1016/S0045-7825(02)00391-2.

Miehe, C., Vallicotti, D., Teichtmeister, S., 2016. Homogenization and multiscale stability analysis in finite magneto-electro-elasticity. Application to soft matter EE, ME and MEE composites. Computer Methods in Applied Mechanics and Engineering 300, 294–346. doi:10.1016/j.cma.

2015.10.013.

Miehe, C., Vallicotti, D., Zäh, D., 2015. Computational structural and material stability analysis in finite electro-elasto-statics of electro-active materials. International Journal for Numerical Methods in Engineering 102, 1605–1637. doi:10.1002/nme.4855.

Milton, G.W., Kohn, R.V., 1988. Variational bounds on the effective moduli of anisotropic composites. Journal of the Mechanics and Physics of Solids 36, 597–629. doi:10.1016/0022-5096(88)90001-4.

Mohamed, M.S., Hirani, A.N., Samtaney, R., 2016. Discrete exterior calculus discretization of incompressible Navier–Stokes equations over surface simplicial meshes. Journal of Computational Physics 312, 175–191. doi:10.1016/j.jcp.2016.02.028.

Mora, C.V., Davison, M., Martin Wild, J., Walker, M.M., 2004. Magnetoreception and its trigeminal mediation in the homing pigeon. Nature 432, 508–511. doi:10.1038/nature03077.

Moulinec, H., Suquet, P., 1994. A fast numerical method for computing the linear and nonlinear mechanical properties of composites. Académie des Sciences 2, 1417–1423.

Moulinec, H., Suquet, P., 1995. A FFT-Based Numerical Method for Computing the Mechanical Properties of Composites from Images of their Microstructures, in: IUTAM Symposium on Microstructure-Property Interactions in Composite Materials. Springer, Dordrecht. Solid Mechanics and Its Applications, pp. 235–246. doi:10.1007/978-94-011-0059-5_20.

Moulinec, H., Suquet, P., Milton, G.W., 2018. Convergence of iterative methods based on Neumann series for composite materials: Theory and practice: Convergence of iterative methods. International Journal for Numerical Methods in Engineering 114, 1103–1130. doi:10.1002/nme.5777.

Nédélec, J.C., 1980. Mixed finite elements in $\mathbb{R}^3$. Numerische Mathematik 35, 315–341. doi:10.1007/BF01396415.

Nédélec, J.C., 1986. A new family of mixed finite elements in $\mathbb{R}3$. Numerische Mathematik 50, 57–81. doi:10.1007/BF01389668.

Nemat-Nasser, S., Hori, M., 2010. Micromechanics: overall properties of heterogeneous materials. 2. rev. ed., transferred to digital print. 2006 ed., Elsevier, Amsterdam. OCLC: 838314583.

Nocedal, J., Wright, S., 2006. Numerical Optimization. Springer Series in Operations Research and Financial Engineering, Springer New York.

Noll, W., 2006. A Frame-Free Formulation of Elasticity. Journal of Elasticity 83, 291–307. doi:10.1007/s10659-005-9046-9.

Oden, J., Feng, Y., 1996. Local and pollution error estimation for finite element approximations of elliptic boundary value problems. Journal of Computational and Applied Mathematics 74, 245–293. doi:10.1016/0377-0427(96)00027-1.

Oliphant, T.E., 2006. A guide to NumPy. volume 1. Trelgol Publishing USA.

Osborn, J.A., 1945. Demagnetizing Factors of the General Ellipsoid. Physical Review 67, 351–357. doi:10.1103/PhysRev.67.351.

Pao, Y.H., Hutter, K., 1975. Electrodynamics for moving elastic solids and viscous fluids. Proceedings of the IEEE 63, 1011–1021. doi:10.1109/PROC.1975.9878.

Pearle, P., Rizzi, A., 2017. Quantum-mechanical inclusion of the source in the Aharonov-Bohm effects. Physical Review A 95, 052123. doi:10.1103/PhysRevA.95.052123.

Pelteret, J.P., Davydov, D., McBride, A., Vu, D.K., Steinmann, P., 2016. Computational electro- and magneto-elasticity for quasi-incompressible media immersed in free space. International Journal for Numerical Methods in Engineering 108, 1307–1342. doi:10.1002/nme.5254.

Perez, F., Granger, B.E., 2007. IPython: A System for Interactive Scientific Computing. Computing in Science & Engineering 9, 21–29. doi:10.1109/MCSE.2007.53.

Polukhov, E., Vallicotti, D., Keip, M.A., 2018. Computational stability analysis of periodic elec-

troactive polymer composites across scales. Computer Methods in Applied Mechanics and Engineering 337, 165–197. doi:10.1016/j.cma.2018.01.020.

Ponte Castañeda, P., Galipeau, E., 2011. Homogenization-based constitutive models for magnetorheological elastomers at finite strain. Journal of the Mechanics and Physics of Solids 59, 194–215. doi:10.1016/j.jmps.2010.11.004.

Ponte-Castañeda, P., 1991. The effective mechanical properties of nonlinear isotropic composites. Journal of the Mechanics and Physics of Solids 39, 45–71. doi:10.1016/0022-5096(91)90030-R.

Pössinger, T., 2015. Experimental Characterization, Modeling and Simulation of Magneto-Rheological Elastomers. Ph.D. thesis. École Polytechnique.

Psarra, E., Bodelot, L., Danas, K., 2017. Two-field surface pattern control via marginally stable magnetorheological elastomers. Soft Matter 13, 6576–6584. doi:10.1039/C7SM00996H.

Psarra, E., Bodelot, L., Danas, K., 2019. Wrinkling to crinkling transitions and curvature localization in a magnetoelastic film bonded to a non-magnetic substrate. Journal of the Mechanics and Physics of Solids 133, 103734. doi:10.1016/j.jmps.2019.103734.

Rambausek, M., Göküzüm, F.S., Nguyen, L.T.K., Keip, M.A., 2019. A two-scale FE-FFT approach to nonlinear magneto-elasticity. International Journal for Numerical Methods in Engineering 117, 1117–1142. doi:10.1002/nme.5993.

Rambausek, M., Keip, M.A., 2017. Micro-and Macrostructural magneto-electric coupling in soft composites, in: 7th GACM Colloquium on Computational Mechanics for Young Scientists from Academia and Industry, pp. 600–605.

Rambausek, M., Keip, M.A., 2018a. Analytical estimation of non-local deformation-mediated magneto-electric coupling in soft composites. Proceedings of the Royal Society A 474, 20170803. doi:10.1098/rspa.2017.0803.

Rambausek, M., Keip, M.A., 2018b. Strain-mediated magneto-electric coupling in soft composites, in: Proceedings of the Third Seminar on the Mechanics of Multifunctional Materials, Prof. Dr.-Ing. habil. Jörg Schröder, Institute of Mechanics, Department of Civil Engineering, Faculty of Engineering, University of Duisburg-Essen, Bad Honnef, Germany. pp. 97–100.

Raviart, P.A., Thomas, J.M., 1977. A mixed finite element method for 2-nd order elliptic problems, in: Mathematical Aspects of Finite Element Methods. Springer, Berlin, Heidelberg. Lecture Notes in Mathematics, pp. 292–315. doi:10.1007/BFb0064470.

Reuss, A., 1929. Berechnung der Fließgrenze von Mischkristallen auf Grund der Plastizitätsbedingung für Einkristalle. ZAMM - Journal of Applied Mathematics and Mechanics / Zeitschrift für Angewandte Mathematik und Mechanik 9, 49–58. doi:10.1002/zamm.19290090104.

Rognes, M., Kirby, R., Logg, A., 2009. Efficient Assembly of $H(\mathrm{div})$ and $H(\mathrm{curl})$ Conforming Finite Elements. SIAM Journal on Scientific Computing 31, 4130–4151. doi:10.1137/08073901X.

Rudykh, S., Bertoldi, K., 2013. Stability of anisotropic magnetorheological elastomers in finite deformations: A micromechanical approach. Journal of the Mechanics and Physics of Solids 61, 949–967. doi:10.1016/j.jmps.2012.12.008.

Schlömer, N., 2019a. I/O for various mesh formats. URL: https://github.com/nschloe/meshio.

Schlömer, N., 2019b. Python interface for Gmsh. URL: https://github.com/nschloe/pygmsh.

Schlömerkemper, A., 2002. Magnetic forces in discrete and continuous systems. Ph.D. thesis. University of Leipzig. Leipzip, Germany.

Schlömerkemper, A., 2005. Mathematical Derivation of the Continuum Limit of the Magnetic Force between Two Parts of a Rigid Crystalline Material. Archive for Rational Mechanics and Analysis 176, 227–269. doi:10.1007/s00205-004-0354-1.

Schlömerkemper, A., Schmidt, B., 2009. Discrete-to-Continuum Limit of Magnetic Forces: Dependence on the Distance Between Bodies. Archive for Rational Mechanics and Analysis 192, 589–611. doi:10.1007/s00205-008-0134-4.

Schneider, M., Merkert, D., Kabel, M., 2017. FFT-based homogenization for microstructures discretized by linear hexahedral elements. International Journal for Numerical Methods in Engineering 109, 1461–1489. doi:10.1002/nme.5336.

Schröder, J., 2009. Derivation of the localization and homogenization conditions for electromechanically coupled problems. Computational Materials Science 46, 595–599. doi:10.1016/j.commatsci.2009.03.035.

Schröder, J., Keip, M.A., 2012. Two-scale homogenization of electromechanically coupled boundary value problems. Computational Mechanics 50, 229–244. doi:10.1007/s00466-012-0715-9.

Schröder, J., Labusch, M., Keip, M.A., 2016. Algorithmic two-scale transition for magneto-electro-mechanically coupled problems: FE^2-scheme: Localization and homogenization. Computer Methods in Applied Mechanics and Engineering 302, 253–280. doi:10.1016/j.cma.2015.10.005.

Schröder, J., Neff, P., 2003. Invariant formulation of hyperelastic transverse isotropy based on polyconvex free energy functions. International Journal of Solids and Structures 40, 401–445. doi:10.1016/S0020-7683(02)00458-4.

Schröder, J., Neff, P., Balzani, D., 2005. A variational approach for materially stable anisotropic hyperelasticity. International Journal of Solids and Structures 42, 4352–4371. doi:10.1016/j.ijsolstr.2004.11.021.

Scott, J.F., 2007. Applications of Modern Ferroelectrics. Science 315, 954–959. doi:10.1126/science.1129564.

Semenov, A.S., Kessler, H., Liskowsky, A., Balke, H., 2006. On a vector potential formulation for 3D electromechanical finite element analysis. Communications in Numerical Methods in Engineering 22, 357–375. doi:10.1002/cnm.818.

Shadid, J.N., Pawlowski, R.P., Cyr, E.C., Tuminaro, R.S., Chacón, L., Weber, P.D., 2016. Scalable implicit incompressible resistive MHD with stabilized FE and fully-coupled Newton-Krylov-AMG. Computer Methods in Applied Mechanics and Engineering 304, 1–25. doi:10.1016/j.cma.2016.01.019.

Smit, R.J.M., Brekelmans, W.A.M., Meijer, H.E.H., 1998. Prediction of the mechanical behavior of nonlinear heterogeneous systems by multi-level finite element modeling. Computer Methods in Applied Mechanics and Engineering 155, 181–192. doi:10.1016/S0045-7825(97)00139-4.

Spaldin, N.A., Fiebig, M., 2005. The Renaissance of Magnetoelectric Multiferroics. Science 309, 391–392. doi:10.1126/science.1113357.

Spencer, A.J.M., 1971. Part III. Theory of invariants, in: Eringen, A.C. (Ed.), Continuum Physics. Academic Press. volume 1, pp. 239–353.

Spieler, C., Kästner, M., Goldmann, J., Brummund, J., Ulbricht, V., 2013. XFEM modeling and homogenization of magnetoactive composites. Acta Mechanica 224, 2453–2469. doi:10.1007/s00707-013-0948-5.

Sridhar, A., Kouznetsova, V.G., Geers, M.G.D., 2016. Homogenization of locally resonant acoustic metamaterials towards an emergent enriched continuum. Computational Mechanics 57, 423–435. doi:10.1007/s00466-015-1254-y.

Steigmann, D.J., 2004. Equilibrium theory for magnetic elastomers and magnetoelastic membranes. International Journal of Non-Linear Mechanics 39, 1193–1216. doi:10.1016/j.ijnonlinmec.2003.08.002.

Steinmann, P., 2015. Geometrical Foundations of Continuum Mechanics. volume 2 of *Lecture*

Notes in Applied Mathematics and Mechanics. Springer Berlin Heidelberg, Berlin, Heidelberg. doi:10.1007/978-3-662-46460-1.

Stern, A., Tong, Y., Desbrun, M., Marsden, J.E., 2015. Geometric Computational Electrodynamics with Variational Integrators and Discrete Differential Forms, in: Chang, D.E., Holm, D.D., Patrick, G., Ratiu, T. (Eds.), Geometry, Mechanics, and Dynamics: The Legacy of Jerry Marsden. Springer New York, New York, NY. Fields Institute Communications, pp. 437–475. doi:10.1007/978-1-4939-2441-7_19.

van Suchtelen, J., 1972. Product properties: a new Application of composite materials. Philips Research Reports 27, 28–37.

Suo, Z., Zhao, X., Greene, W.H., 2008. A nonlinear field theory of deformable dielectrics. Journal of the Mechanics and Physics of Solids 56, 467–486. doi:10.1016/j.jmps.2007.05.021.

Svendsen, B., Chanda, T., 2005. Continuum thermodynamic formulation of models for electromagnetic thermoinelastic solids with application in electromagnetic metal forming. Continuum Mechanics and Thermodynamics 17, 1–16. doi:10.1007/s00161-004-0181-5.

Tadmor, E.B., Miller, R.E., Elliott, R.S., 2012. Continuum mechanics and thermodynamics: from fundamental concepts to governing equations. Cambridge University Press, Cambridge, UK ; New York.

Taylor, R.L., 2014. FEAP - finite element analysis program. URL: http://www.ce.berkeley/feap.

Temizer, İ., Wriggers, P., 2007. An adaptive method for homogenization in orthotropic nonlinear elasticity. Computer Methods in Applied Mechanics and Engineering 196, 3409–3423. doi:10.1016/j.cma.2007.03.017.

Terada, K., Kikuchi, N., 2001. A class of general algorithms for multi-scale analyses of heterogeneous media. Computer Methods in Applied Mechanics and Engineering 190, 5427–5464. doi:10.1016/S0045-7825(01)00179-7.

Terada, K., Saiki, I., Matsui, K., Yamakawa, Y., 2003. Two-scale kinematics and linearization for simultaneous two-scale analysis of periodic heterogeneous solids at finite strain. Computer Methods in Applied Mechanics and Engineering 192, 3531–3563. doi:10.1016/S0045-7825(03)00365-7.

Thomas, J.D., Triantafyllidis, N., 2009. On electromagnetic forming processes in finitely strained solids: Theory and examples. Journal of the Mechanics and Physics of Solids 57, 1391–1416. doi:10.1016/j.jmps.2009.04.004.

Tonti, E., 2013. The Mathematical Structure of Classical and Relativistic Physics. Modeling and Simulation in Science, Engineering and Technology, Springer New York, New York, NY. doi:10.1007/978-1-4614-7422-7.

Toupin, R.A., 1956. The Elastic Dielectric. Journal of Rational Mechanics and Analysis 5, 849–915.

Trefethen, L.N., 2000. Spectral Methods in MATLAB. Society for Industrial and Applied Mathematics. doi:10.1137/1.9780898719598.

Truesdell, C., Noll, W., 2004. The Non-Linear Field Theories of Mechanics. 3 ed., Springer-Verlag, Berlin Heidelberg. doi:10.1007/978-3-662-10388-3.

Trykozko, A., Zijl, W., Bossavit, A., 2001. Nodal and Mixed Finite Elements for the Numerical Homogenization of 3d Permeability. Computational Geosciences 5, 61–84. doi:10.1023/A:1011621529611.

Vertechy, R., Frisoli, A., Bergamasco, M., Carpi, F., Frediani, G., Rossi, D.D., 2012. Modeling and experimental validation of buckling dielectric elastomer actuators. Smart Materials and Structures 21, 094005. doi:10.1088/0964-1726/21/9/094005.

Vidyasagar, A., Tan, W.L., Kochmann, D.M., 2017. Predicting the effective response of bulk poly-

crystalline ferroelectric ceramics via improved spectral phase field methods. Journal of the Mechanics and Physics of Solids 106, 133–151. doi:10.1016/j.jmps.2017.05.017.

Virtanen, P., Gommers, R., Oliphant, T.E., Haberland, M., Reddy, T., Cournapeau, D., Burovski, E., Peterson, P., Weckesser, W., Bright, J., van der Walt, S.J., Brett, M., Wilson, J., Jarrod Millman, K., Mayorov, N., Nelson, A.R.J., Jones, E., Kern, R., Larson, E., Carey, C., Polat, İ., Feng, Y., Moore, E.W., Vand erPlas, J., Laxalde, D., Perktold, J., Cimrman, R., Henriksen, I., Quintero, E.A., Harris, C.R., Archibald, A.M., Ribeiro, A.H., Pedregosa, F., van Mulbregt, P., Contributors, S..., 2020. SciPy 1.0: Fundamental Algorithms for Scientific Computing in Python. Nature Methods 17, 261–272. doi:https://doi.org/10.1038/s41592-019-0686-2.

Voigt, W., 1887. Theoretische Studien über die Elasticitätsverhältnisse der Krystalle. I. Abhandlungen der Königlichen Gesellschaft der Wissenschaften in Göttingen 34, 3–52.

Vondřejc, J., Zeman, J., Marek, I., 2014. An FFT-based Galerkin method for homogenization of periodic media. Computers & Mathematics with Applications 68, 156–173. doi:10.1016/j.camwa.2014.05.014.

Vu, D.K., Steinmann, P., 2010. A 2-D coupled BEM–FEM simulation of electro-elastostatics at large strain. Computer Methods in Applied Mechanics and Engineering 199, 1124–1133. doi:10.1016/j.cma.2009.12.001.

Vu, D.K., Steinmann, P., 2012. On 3-D coupled BEM–FEM simulation of nonlinear electro-elastostatics. Computer Methods in Applied Mechanics and Engineering 201–204, 82–90. doi:10.1016/j.cma.2011.08.024.

van der Walt, S., Colbert, S.C., Varoquaux, G., 2011. The NumPy Array: A Structure for Efficient Numerical Computation. Computing in Science & Engineering 13, 22–30. doi:10.1109/MCSE.2011.37.

Willis, J., 1977. Bounds and self-consistent estimates for the overall properties of anisotropic composites. Journal of the Mechanics and Physics of Solids 25, 185–202. doi:10.1016/0022-5096(77)90022-9.

Willot, F., Abdallah, B., Pellegrini, Y.P., 2014. Fourier-based schemes with modified Green operator for computing the electrical response of heterogeneous media with accurate local fields. International Journal for Numerical Methods in Engineering 98, 518–533. doi:10.1002/nme.4641.

Wu, L.Q., Dickman, J.D., 2011. Magnetoreception in an Avian Brain in Part Mediated by Inner Ear Lagena. Current Biology 21, 418–423. doi:10.1016/j.cub.2011.01.058.

Yvonnet, J., Bonnet, G., 2014. A consistent nonlocal scheme based on filters for the homogenization of heterogeneous linear materials with non-separated scales. International Journal of Solids and Structures 51, 196–209. doi:10.1016/j.ijsolstr.2013.09.023.

Zabihyan, R., Mergheim, J., Javili, A., Steinmann, P., 2018. Aspects of computational homogenization in magneto-mechanics: Boundary conditions, RVE size and microstructure composition. International Journal of Solids and Structures 130-131, 105–121. doi:10.1016/j.ijsolstr.2017.10.009.

Zeman, J., de Geus, T.W.J., Vondřejc, J., Peerlings, R.H.J., Geers, M.G.D., 2017. A finite element perspective on nonlinear FFT-based micromechanical simulations. International Journal for Numerical Methods in Engineering 111, 903–926. doi:10.1002/nme.5481.

Zeman, J., Vondřejc, J., Novak, J., Marek, I., 2010. Accelerating a FFT-based solver for numerical homogenization of periodic media by conjugate gradients. Journal of Computational Physics 229, 8065–8071. doi:10.1016/j.jcp.2010.07.010.

Insitute of Applied Mechanics (IAM)
Chair of Materials Theory

Typical natural magnetic materials based on iron or other (mainly rare-earth) metals are rather hard and stiff. However, when particles of such magnetic materials are embedded in a soft elastomer matrix, a new composite material is created. It is deformable over a large elastic range and possesses magnetic properties at the same time. These so-called *magnetorheological elastomers* have been proposed for several innovative applications such as tunable shock absorbers, contactless controllable valves and haptic displays.

Beyond the coupled magneto-elastic properties, magnetorheological elastomers also exhibit magneto-electric coupling. Probably the most important industrial applications of this effect are novel types of sensors and detectors. Remarkably, the same coupling mechanism might be essential for *magneto-reception* – the ability of biological organisms to sense magnetic fields for orientation and navigation.

This thesis is concerned with theory and numerics of magneto-electro-elasticity. By that it contributes to a better understanding of fundamental mechanisms and phenomena that serve as the basis for the above-mentioned applications.

ISBN 978-3-937399-52-2